



# Semiconducting origamis : photonic resonators and topological applications

Rémi Briche

## ► To cite this version:

Rémi Briche. Semiconducting origamis : photonic resonators and topological applications. Other. Université de Lyon, 2021. English. NNT : 2021LYSEC032 . tel-03380651

**HAL Id: tel-03380651**

**<https://theses.hal.science/tel-03380651>**

Submitted on 15 Oct 2021

**HAL** is a multi-disciplinary open access archive for the deposit and dissemination of scientific research documents, whether they are published or not. The documents may come from teaching and research institutions in France or abroad, or from public or private research centers.

L'archive ouverte pluridisciplinaire **HAL**, est destinée au dépôt et à la diffusion de documents scientifiques de niveau recherche, publiés ou non, émanant des établissements d'enseignement et de recherche français ou étrangers, des laboratoires publics ou privés.

N° d'ordre NNT : 2021LYSEC32

# Thèse de doctorat de l'Université de Lyon opérée au sein de l'École Centrale de Lyon

École Doctorale N°34  
École Doctorale Matériaux de Lyon

Spécialité de doctorat : « Nanophotonique »

*Soutenue publiquement le 19/07/2021, par*

**Rémi BRICHE**

---

## Origamis semiconducteurs : résonateurs photoniques et applications à la topologie.

## Semiconducting Origamis: photonic resonators and topological applications.

---

Devant le jury composé de :

<b>Andreas RUEDIGER,</b>	Professeur, Centre Énergie Matériaux Télécommunications	Rapporteur
<b>Sophie BOUCHOULE,</b>	Directrice de recherche CNRS, C2N	Rapporteuse
<b>Yannick de WILDE,</b>	Directeur de recherche CNRS, Institut Langevin	Président du jury
<b>Pierre DELPLACE,</b>	Chercheur CNRS, École Normale Supérieure de Lyon	Examineur
<b>Jean-Louis LECLERCQ,</b>	Chercheur CNRS, Institut des Nanotechnologies de Lyon	Examineur
<b>Ségolène CALLARD,</b>	Professeur	Co-directrice de thèse
<b>Alexandre DANESCU,</b>	Maître de conférences	Co-directeur de thèse

École Centrale de Lyon  
Institut des Nanotechnologies de Lyon (INL)  
CNRS UMR 5270, 69134 Écully, France





---

## Remerciements

*Forsan et hæc olim meminisse juvabit.*

---

VIRGILE (ENÉIDE, I, 203)

J'adresse naturellement mes premiers remerciements à mes directeurs de thèse Ségolène CALLARD et Alexandre DANESCU sans qui cette aventure n'aurait tout simplement pas eu lieu. Je n'aurai sincèrement pas pu souhaiter meilleur encadrement que le vôtre tant vous avez fait preuve de disponibilité, d'attention et de bienveillance à l'égard de mon travail et de ma personne. J'ai beaucoup appris à vos côtés et vous avez toujours mis un point d'honneur à répondre patiemment à mes interrogations, mes doutes, à me débloquer et à parfaire mes productions écrites et orales, ce pour quoi je vous suis très reconnaissant.

Je remercie Sophie BOUCHOULE et Andreas RUEDIGER d'avoir accepté de rapporter ma thèse, pour leur lecture minutieuse du manuscrit, et de leur intérêt pour le sujet. Je remercie Pierre DELPLACE d'avoir assisté à ma soutenance en tant qu'examinateur et pour sa collaboration enrichissante dans le volet topologie. Merci d'avoir répondu à toutes mes questions de néophyte de la topologie. Je remercie aussi Jean-Louis LECLERCQ qui a aussi examiné cette thèse mais aussi et surtout qui a assuré la coordination du projet FOLDING dans laquelle cette dernière s'inscrit. Merci pour sa bienveillance, ses encouragements et son humanité, en autres. Je remercie enfin Yannick DE WILDE pour avoir accepté de présider le jury et pour les échanges constructifs sur les résultats obtenus.

Je tiens à remercier les directions successives du laboratoire INL au sein duquel j'ai réalisé ma thèse au cours de ces trois années et demi. Je remercie donc Catherine BRUCHEVALLIER et Christian SEASSAL pour leur aide dans l'organisation des Journées des Doctorants INL, ainsi que l'actuel directeur Bruno MASENELLI pour sa réactivité et sa bienveillance.

Je souhaite remercier chaleureusement Hai Son NGUYEN pour avoir été comme mon troisième directeur de thèse en m'accordant tant de précieuses minutes pour répondre à mes questions, m'aider à interpréter mes résultats, le tout en présentiel ou en visio, à toute heure et en tout lieu (même à vélo !). Son infatigable curiosité scientifique et son optimisme à toute épreuve ont été d'importants moteurs de ma thèse, la poussant notamment vers des ambitions topologiques, le tout avec beaucoup d'humour et de joie de vivre.

Je remercie aussi vivement Lydie FERRIER, fervente animatrice du GP Topologie, pour nos échanges enrichissants et constructifs sur les simulations et la fabrication, pour ta bienveillance, et pour nos discussions à bâtons rompus.

Je tiens à remercier tous les acteurs du projet ANR PHOLDING (ou « foldingue ») qui a financé ma thèse, incluant Jean-Louis LECLERCQ, Xavier LETARTRE, Pierre CREMILLIEU, Aziz BENAMROUCHE, et Philippe REGRENY. Un grand merci donc à Pierre CREMILLIEU d'avoir pris le temps de m'expliquer les différentes étapes de la fabrication des rouleaux photoniques au cours de nombreuses séances de salle blanche. Je ne cesse d'être impressionné par tous les merveilleux objets fabriqués. Merci à Philippe REGRENY pour ses dépôts épitaxiaux de qualité, indispensables briques de base aux futurs rouleaux, pour ses conseils et sa disponibilité. Merci à Xavier LETARTRE pour

---

son regard avisé et expérimenté sur le projet, son partage de ressources et de savoir-faire en simulation, et pour sa relecture attentive du manuscrit. Un grand merci à Aziz BENAMROUCHE de m'avoir formé au SNOM avec beaucoup de patience et de bienveillance. Je me souviendrai de ses images époustouflantes obtenues en quelques dizaines de minutes tandis que je captais leur pâle copie après quelques jours. Merci aussi d'avoir constamment amélioré le montage pour le rendre plus accessible et performant.

Je souhaite aussi remercier les membres du quatrième étage que j'ai côtoyé ces trois années toujours dans une bonne ambiance : Bertrand VILQUIN, Ingrid CAÑERO-INFANTE, José PENUELAS, Yves ROBACH, Christelle MONAT, Anne LAMIRAND, Sébastien CUEFF, Serge MAZAURIC, Christian GRILLET, Brice DEVIF. Je remercie en particulier Thérèse MARTIN et Yann DE ORDEÑANA pour m'avoir aidé dans toutes mes démarches administratives. Merci à Emmanuel DROUARD pour son aide sur les simulations et sur l'utilisation des clusters. Un grand merci à Sylvie GONCALVES pour avoir géré mes contrats doctoraux et pour m'avoir toujours accueilli dans la bonne humeur mêlée à beaucoup d'humour. Je remercie vivement Raphaël LOPEZ et Laurent CARREL pour leur aide dans mes tracasseries informatiques. Je remercie aussi tous les autres membres de l'équipe i-LUM qui ont partagé leurs compétences lors des réunions d'équipe.

Je remercie chaleureusement les doctorants et post-doctorants de la « bétailière » qui se renouvelle d'années en années et qui donnent vie à l'open-space du quatrième étage. Je remercie en particulier MachiaMalik de m'avoir formé aux simulations et au SNOM avec une grande patience, de nos enregistrements audio mémorables, Mister Demongodin (Jean la Neige) pour, entre autres, nos discussions philosophiques et nos fous rires dans la merveilleuse ville moutarde, Berry pour son talent indiscutable de conteur d'histoires, WikiRémi, inépuisable source de savoir et passionné d'abeilles (entre autres), Jérémy pour notre passion commune pour la musique, Jordan pour être tout simplement Jordan, mais aussi Tom WOOD, Florian DUBOIS, Thibaut LOUVET, et Thierry DESCHAMPS. Je remercie aussi les doctorants de la tribu ECLAUSion, Panthea, Greta, Kokou, Marina, Marko pour leur soutien et leur gentillesse.

Je remercie d'autre part tous les autres doctorants et post-doc des autres étages et équipes, Ha My DANG, Jimmy JOHN, Raphaël MERMET-LIAUDOZ, Milan SINOBAD, Alberto DELLA TORRE, avec qui j'ai pu discuter des vicissitudes de la thèse. En particulier, je tiens à remercier Eirini SARELLI avec qui j'ai été ravi d'être combiné et de former un duo choc au sein du Student Chapter. Je remercie aussi Paul BOUTEYRE pour son aide précieuse lors des sessions Fourier.

Je remercie aussi toute l'équipe organisatrice des JDD millésime 2018 avec à son bord Rachael TAITT, Xiao LI, Eirini SARELLI, Prabir MAHATO, Florian BERRY, et Nelly MOULIN qui a présidé cette édition d'une main de maître.

Je remercie vivement tous les membres de la chorale de Centrale Lyon avec qui j'ai pris un réel plaisir de chanter tous les lundis soir.

Je remercie chaleureusement tous mes amis Centraliens, Manon, Marie, Blandine E., Eliane, Benoît, Blandine P., Adrien, Camilo, Sécu, Florian, Elsa, Damien, Joris, Marc et Amélie pour chacune de nos retrouvailles toujours festives et joyeuses. Mention spéciale à Christophe avec qui j'ai partagé des sessions piscine, cinéma, ou encore

---

peinture !

Je n'oublie pas mes amis dijonnais, Coralie, Théo, Marie-Eve et Agnès pour tous les moments magiques passés à vos côtés et pour votre soutien tout au long de la thèse parfois éprouvante. C'est un grand honneur d'ouvrir le bal des soutenances de thèse !

Je remercie enfin ma famille, mon père, mes frères Nicolas, Olivier, Julien, leur conjointe respective, Clémence, Alexandra, Anne, mes merveilleux neveux, Jules, Gabin et Noé, pour leur soutien de tous les instants. A noter que je ne fabrique toujours pas de capes d'invisibilité !

Je tiens à remercier particulièrement ma mère pour m'avoir soutenu dans tous mes choix et pour avoir supporté et géré mes montagnes russes émotionnelles. Je ne serais sans doute pas arrivé jusque-là sans toi.

*A mes grands-parents, qui auraient été heureux de cet accomplissement.*

*A mon chat Cannabis, mon maître Yoda durant toutes ses années.*



---

## Abstract

Inspired from the Origami art of folding, the rolled-up nanotechnology has proved to be a competitive alternative toward the production of 3D microstructures through the self-rolling of pre-stressed membranes. This technique has enriched the palette of existing 3D microstructures, proposing unconventional geometries (tubes, coils, etc.) accessible with a large range of materials. Based on the stress-engineering method, a high degree of control over the size and geometry of the structures can be achieved, making them suitable in a wide range of applications. Among the variety of 3D architectures, rolled-up tubular microcavities have drawn great interest for optofluidic applications by combining their microchannel geometry and particular optical properties of the tube to produce highly sensitive fluid sensors.

Applying the stress-engineering method to fold more complex surfaces such as photonic nanostructured membranes generates a new class of 3D photonic micro-objects with original designs and tailored optical properties. Micrometer-sized patterning provides additional degrees of freedom with the modification of the dispersion of the planar membrane, leading to various optical functionalities including the guiding, the trapping, or the slowing of light. In particular, the combination between photonic crystal patterns and 3D rolled-up geometries offers new strategies for the management of light.

In this thesis, we propose the conception and characterization of “photon cages” based on the rolling of highly reflective 2D photonic crystal membranes. The reflecting walls allow to trap efficiently the light in the hollow low-index core, optimizing the overlap between the localized electromagnetic field and the surrounding medium, a keystone in sensing operations. Parameters of the photonic crystal membrane were adjusted to obtain an efficient reflector (reflectivity  $R > 95\%$ ) over a large spectral range ( $> 100$  nm) in near infrared domain. The cylindrical cavity resonator model and FDTD simulations were used to predict the optical response of the rolled-up membrane. Tubular cavities were then fabricated using stress engineering technique. Near-field optical measurements were carried out to investigate the modes in the hollow of the cavity, revealing the presence of cavity modes in compliance with theoretical computations, and bringing an experimental validation to the photon cage concept.

In this work, we also exploit the rolled-up nanotechnology to extend the analogy between solid-state and photonic structures toward the fabrication and characterization of photonic crystal analogues of carbon nanotubes. Numerical simulations were performed to design graphene-like photonic structures with a Dirac point centred at  $1.55\text{ }\mu\text{m}$ . Numerical calculations of the topological invariant and the band structure of graphene-like photonic ribbons with zig-zag edge shape demonstrated the existence of edge states. We calculated the optical dispersion of photonic microtubes in accordance with zone-folding predictions. We report highly reproducible fabrication of photonic nanotubes with honeycomb pattern. Preliminary angular-resolved spectral measurements of the structures have revealed dispersive features of the membrane wall but no signature of the microtube yet.

**Keywords:** rolled-up nanotechnology, photonic crystals, stress engineering, near-field optical microscopy, Fourier optics, topological edge states.



---

## Résumé

Inspirée de l'art du pliage papier Origami, la nanotechnologie par enroulement s'est avérée être une alternative compétitive à la production de microstructures 3D par auto-enroulement de nano-membranes précontraintes. Cette technique a élargi la palette de microstructures 3D en proposant des géométries originales (tubes, spires, etc.) associées à une large gamme de matériaux. Basée sur la méthode d'ingénierie des contraintes, elle permet aussi un contrôle très précis sur la taille et la géométrie des structures 3D obtenues, ainsi adaptées à un large éventail d'applications. Parmi les architectures 3D réalisables, les microcavités tubulaires ont suscité un grand intérêt pour les applications opto-fluidiques en combinant leur géométrie de microcanaux et les propriétés optiques particulières du tube pour produire des capteurs de fluide très sensibles.

L'ingénierie des contraintes appliquée au pliage de surfaces plus complexes, telles que des membranes photoniques microstructurées, aboutit à une nouvelle classe de micro-objets photoniques 3D aux formes et propriétés originales. La microstructuration offre des degrés de liberté supplémentaires en modifiant la dispersion de la membrane plane, permettant diverses fonctionnalités optiques tel que le guidage, le piégeage, ou le ralentissement de la lumière. En particulier, les combinaisons de réseaux cristallins avec des géométries 3D enroulées ouvrent de nouvelles stratégies de gestion de la lumière.

Dans cette thèse, nous proposons la conception et la caractérisation de « cages à photons » basées sur l'enroulement de membranes à cristaux photoniques 2D très réfléchissantes. Les parois réfléchissantes piègent alors efficacement la lumière dans le noyau creux à faible indice, optimisant l'interaction entre le champ électromagnétique localisé et le milieu environnant au fondement des applications de détection. Les paramètres de la membrane à cristal photonique ont été ajustés pour obtenir un réflecteur efficace (réflectivité  $R > 95\%$ ) sur une large gamme spectrale ( $> 100$  nm) dans le proche infrarouge. Le modèle de résonateur à cavité cylindrique et des simulations FDTD ont été utilisés pour prédire la réponse optique de la membrane enroulée. Les cavités tubulaires ont ensuite été fabriquées via la technique d'ingénierie des contraintes. Des mesures optiques en champ proche ont été réalisées pour étudier les modes à l'intérieur de la cavité, révélant la présence de modes de cavité prédite théoriquement, et apportant une validation expérimentale au concept de cage à photons.

Dans ce travail, nous exploitons également la nanotechnologie par enroulement afin d'étendre l'analogie entre les structures de la physique du solide et celles de la photonique à la conception d'analogues de nanotubes de carbone dans la classe des cristaux photoniques. Des simulations numériques ont été réalisées pour concevoir des structures photoniques de type graphène avec un point de Dirac centré à  $1,55\text{ }\mu\text{m}$ . Des calculs numériques d'invariant topologique et de structure de bandes de rubans photoniques, avec un réseau nid d'abeille et un bord en zigzag, ont démontré l'existence d'états de bord. Nous avons calculé la dispersion optique des microtubes photoniques qui concorde avec les prédictions de la méthode de repliement de zone. Nous rapportons la fabrication très reproductible de nanotubes photoniques avec motif en nid d'abeille. Des mesures spectrales et résolues en angle préliminaires des structures ont révélé des caractéristiques dispersives de la paroi de la membrane mais aucune signature du microtube pour le moment.

**Mots clés:** nanotechnologie par enroulement, cristaux photoniques, ingénierie de contraintes, champ proche optique, optique de Fourier, états de bords topologiques.





# Contents

<b>Contents</b>	<b>xi</b>
<b>List of figures</b>	<b>xiii</b>
<b>List of Tables</b>	<b>xix</b>
<b>Introduction</b>	<b>1</b>
<b>1 Origami-based photonic crystals</b>	<b>5</b>
1.1 Towards 3D rolled-up photonic structures . . . . .	6
1.2 Concept of tubular photon cages . . . . .	28
1.3 Photonic crystal analogues of solid-states structures . . . . .	43
1.4 Conclusion of the chapter . . . . .	60
1.5 References . . . . .	62
<b>2 Numerical, fabrication and optical characterization methods</b>	<b>75</b>
2.1 Simulations of optical properties . . . . .	76
2.2 Fabrication process . . . . .	85
2.3 Optical characterization . . . . .	97
2.4 Conclusion of the chapter . . . . .	105
2.5 References . . . . .	107
<b>3 Design and simulation of photon cages</b>	<b>109</b>
3.1 Introduction . . . . .	110
3.2 Design of the planar two-dimensional photonic crystal mirror . . . . .	111
3.3 Analytical model of the cylindrical cavity resonator . . . . .	120
3.4 Numerical study of tubular photon cages . . . . .	129
3.5 Conclusion of the chapter . . . . .	147
3.6 References . . . . .	148
<b>4 Fabrication and optical characterization of photon cages</b>	<b>149</b>
4.1 Fabrication of tubular photon cages . . . . .	150
4.2 Optical characterization of the photon cages . . . . .	155
4.3 Conclusion of the chapter . . . . .	171
<b>5 Photonic crystal analogues of carbon nanotubes</b>	<b>173</b>
5.1 Graphene VS honeycomb lattice photonic crystal . . . . .	174
5.2 Graphene ribbons and honeycomb lattice photonic crystal ribbons . . .	187
5.3 Carbon nanotubes and rolled-up honeycomb lattice photonic crystal . .	200
5.4 Conclusion of the chapter . . . . .	223
5.5 References . . . . .	224

<b>A</b>	<b>Mechanical model</b>	<b>I</b>
<b>B</b>	<b>1D SSH model</b>	<b>III</b>
<b>C</b>	<b>Fresnel coefficients</b>	<b>IV</b>
<b>D</b>	<b>Cylindrical cavity model</b>	<b>VI</b>
<b>E</b>	<b>Mode surface of FDTD modes</b>	<b>IX</b>
<b>F</b>	<b>Grazing reflection onto the PCM</b>	<b>X</b>
<b>G</b>	<b>Reflection of small radius photon cages</b>	<b>XI</b>
<b>H</b>	<b>Parameters of triangular-hole HC-PCM</b>	<b>XII</b>
<b>I</b>	<b>Résumé long en français</b>	<b>XIII</b>

# List of figures

1.1	Strategies for the bending of thin material sheets with non-uniform or uniform properties across the thickness. . . . .	7
1.2	Self-rolling of a prestrained InAs-GaAs membrane upon selective etching of underlying AlAs sacrificial layer. . . . .	9
1.3	Schematic introduction of pre-strains in a bilayer membrane. . . . .	10
1.4	Evolution of the curvature of a prestrained bilayer upon relaxation as a function of the thicknesses' ratio. . . . .	14
1.5	Results of scalability of rolled-up microtubes in literature. . . . .	15
1.6	Self-rolling of rectangular templates. . . . .	18
1.7	Planar templates for various rolled-up 3D microstructures. . . . .	19
1.8	Fabrication of micro-Origamis. . . . .	21
1.9	Examples of applications of rolled-up tubular microstructures in energy storage, optics and micromachines. . . . .	22
1.10	Whispering gallery modes (WGM) in tubular cavities. . . . .	24
1.11	Rolled-up tubular geometries for axial confinement of whispering gallery modes. . . . .	26
1.12	Rolled-up tubular microstructures for optofluidic applications. . . . .	27
1.13	Rolled-up tubular architectures for the detection of molecular mechanisms. . . . .	27
1.14	Hollow core microdevices for the confinement of light in air. . . . .	31
1.15	Concept of tubular photon cages based on 1D and 2D photonic crystal membranes. . . . .	33
1.16	Traditional designs of 1D, 2D and 3D photonic crystals. . . . .	34
1.17	Traditional designs of 1D and 2D photonic crystal membranes. . . . .	35
1.18	Guided and surface-addressable modes in photonic crystal membranes. . . . .	37
1.19	Ultra-compact vertical Fabry-Pérot cavities based on face-to-face 1D photonic crystal membrane mirrors. . . . .	40
1.20	Implementation of the photon cages concept with 1D PCM mirrors. . . . .	42
1.21	Structures and models for graphene, graphene ribbons, carbon nanotubes and their photonic crystal analogues. . . . .	44
1.22	Structure and dispersion of graphene. . . . .	45
1.23	Structure and dispersion of carbon nanotubes. . . . .	46
1.24	Classification of six objects with the genus number . . . . .	48
1.25	Evolution of the Hall resistance as a function of the magnetic field in the quantum Hall effect (QHE). . . . .	49
1.26	Edge states in the quantum Hall effect . . . . .	51
1.27	Su-Shrieffer-Heeger 1D model of the polyacetylene molecule . . . . .	53
1.28	Energy dispersion $E(k)$ of the two SSH model energy bands $E_+$ and $E_-$ along the 1D Brillouin zone when varying the hopping parameters $t$ and $t'$ . . . . .	54

1.29	Graphical determination of the winding number in the SSH model. . .	55
1.30	Photonic analogues of integer quantum Hall systems. . . . .	57
1.31	Photonic crystal analogue of quantum spin Hall systems. . . . .	58
1.32	Polaritonic SSH-like system. . . . .	59
2.1	Simulation of photonic crystal membranes' reflectivity spectra with the RCWA method. . . . .	77
2.2	Simulation of the optical spectral response of cylindrical cavities with the FDTD method. . . . .	79
2.3	Spectral response and cross-section map of the electric field intensity inside an InP-made tubular cavity. . . . .	81
2.4	FDTD model for the simulation of the band structure of an InP-based photonic crystal. . . . .	83
2.5	Geometrical properties of the honeycomb lattice in real and reciprocal spaces. . . . .	84
2.6	Typical band structure of a honeycomb lattice photonic crystal simulated with the FDTD method. . . . .	85
2.7	Schematized principle of the molecular beam epitaxy deposition and typical composition of a multi-layered precursor. . . . .	86
2.8	Principle of the reflection high energy electron diffraction for the control of the deposited material thicknesses. . . . .	89
2.9	Typical design of the planar mask for the realization of tubular rolled-up photonic crystal membrane. . . . .	90
2.10	Main steps of the electron-beam lithography for the production of the planar mask. . . . .	92
2.11	Main steps of the reactive ion etching for the transfer of the planar mask into the bilayer. . . . .	93
2.12	Main steps of the under-etching process. . . . .	95
2.13	Live frames of the under-etching process. . . . .	95
2.14	Geometry of the bowtie nanoaperture probe used for the near-field measurements. . . . .	99
2.15	Schematics of the customized scanning near-field optical microscopy. . .	100
2.16	Description of the approach and centering procedures of the near-field probe with respect to a tubular photon cage. . . . .	102
2.17	Fourier optics. . . . .	103
2.18	Setup for the realization of angle-resolved spectral measurements. . . .	105
3.1	Schematics of the planar photonic crystal membrane . . . . .	111
3.2	Evolution of the PCM's reflectivity for various thicknesses $h$ and air holes' radius $r$ . . . . .	112
3.3	Reflectivity spectra of the PCM for different holes' radius $r$ and period $a$	113
3.4	PCM's reflectivity spectra for various thicknesses $h$ . . . . .	114
3.5	Reflectivity spectra of the PCM and plain InP and gold membranes . .	115
3.6	Schematized orientations and polarizations of light at oblique incidence	116
3.7	PCM's reflectivity spectra at oblique incidence with orientation $\phi = 0^\circ$	117
3.8	PCM's reflectivity spectra at oblique incidence with orientation $\phi = 90^\circ$	118
3.9	Model of the cylindrical cavity resonator. . . . .	121
3.10	Dispersion diagrams of $TE_{m,n}$ modes for the first orders $(m, n)$ . . . .	123
3.11	Theoretical patterns of infinite cylindrical cavity modes. . . . .	124
3.12	Surface maps and profiles of $TE_{0,22}$ and $TE_{1,22}$ modes. . . . .	125

3.13	Spectral distribution and spacing of $p$ orders in a cavity of radius $\rho_c = 17.5 \mu m$ and varying length $L$ . . . . .	127
3.14	Maps of cavity modes in finite-length cylindrical cavities. . . . .	128
3.15	Numerical model of tubular rolled-up PCM. . . . .	131
3.16	FDTD model for the simulation of infinitely long tubular photon cages . . . . .	132
3.17	FDTD spectrum and maps of the modes in infinite tubular rolled-up PCM . . . . .	133
3.18	Spectral response of infinite tubular photon cages with electric and magnetic dipole excitation. . . . .	135
3.19	Maps and profiles of the modes in infinite tubular photon cages with electric and magnetic dipole excitation. . . . .	136
3.20	FDTD simulation model of a rolled-up PCM cavity of finite length $L$ and radius $\rho_{avg} \simeq 17.62 \mu m$ . . . . .	141
3.21	Spectrum of a tubular photon cage with length $L \sim 10 \mu m$ with an electric dipole excitation. . . . .	142
3.22	Maps and profiles of the modes simulated in finite-length tubular photon cages. . . . .	143
3.23	FDTD spectrum of a $50 \mu m$ -long tubular cavity of radius $\rho_c \simeq 17.62 \mu m$ simulated with an electric dipole excitation. . . . .	144
3.24	FDTD maps of the modes in a tubular cage with length $L = 50 \mu m$ and average radius $\rho_c \simeq 17.62 \mu m$ . . . . .	145
4.1	SEM picture of the planar design of a tubular photon cage. . . . .	152
4.2	SEM pictures of standing tubular photon cages. . . . .	153
4.3	FIB manipulation of a standing tubular photon cage. . . . .	155
4.4	SEM pictures of tubular photon cages on sample C2217. . . . .	156
4.5	SNOM maps inside a tubular photon cage specimen of sample C2217 for $\lambda = 1.450 \mu m$ to $1.580 \mu m$ at fixed insertion depth of the probe. . . . .	157
4.6	Analysis of a near-field map of a mode supported by a tubular photon cage. . . . .	158
4.7	Comparison of profiles . . . . .	160
4.8	SNOM scans in tubular photon cages of sample C2217 from $1530$ to $1532 nm$ with a $0.2 nm$ step. . . . .	161
4.9	Theoretical dispersion curves of $TE_{0,23,p}$ , $TE_{0,24,p}$ , $TE_{1,24,p}$ , and $TE_{1,23,p}$ modes. . . . .	162
4.10	SEM pictures of tubular photon cages on sample C2527. . . . .	164
4.11	SNOM maps for various wavelengths in tubular photon cages of sample C2527. . . . .	165
4.12	Analysis of the SNOM maps generated at $1.460 \mu m$ in a photon cage of sample C2527. . . . .	166
4.13	SNOM maps for various altitudes in tubular photon cages of sample C2527. . . . .	167
4.14	SEM pictures of tubular photon cages on sample C2579. . . . .	169
4.15	SNOM maps on top of tubular photon cages of sample C2579. . . . .	169
4.16	SNOM maps for various wavelengths in a tubular photon cage of sample C2579. . . . .	170
5.1	Energy diagrams and probability densities of the orbitals in a single carbon atom before and after $sp^2$ -type hybridization. . . . .	174
5.2	Schematized graphene honeycomb lattice structure in real and reciprocal space with the tight-binding parameters. . . . .	175

5.3	Surface plot and profile of the tight-binding graphene band structure. .	178
5.4	Maps of graphene tight-binding wavefunctions for various width of the Gaussian-like atomic orbital. . . . .	180
5.5	Band structure photonic graphene. . . . .	181
5.6	Numerical band structure of a circular-hole honeycomb lattice photonic crystal membrane. . . . .	183
5.7	Comparison between graphene tight-binding wavefunctions and maps of a circular-hole HC-PCM close to the Dirac point. . . . .	184
5.8	Structure and numerical band diagram of a triangular-hole HC-PCM. .	185
5.9	Comparison between graphene tight-binding wavefunctions and maps of a triangular-hole HC-PCM close to the Dirac point. . . . .	186
5.10	Illustration of different types of graphene ribbon edges . . . . .	189
5.11	Phase eigenvectors. . . . .	191
5.12	Evolution of the number of edge states for a graphene ribbon $\vec{T}(1,0)$ using discrete and integral formulation of the Zak phase. . . . .	192
5.13	Band structure of a circular air hole photonic crystal membrane along the Brillouin zone of a graphene ribbon of chirality $\vec{\Gamma}_{\perp}(1,0)$ . . . . .	194
5.14	Band structure of a triangular air hole photonic crystal membrane along the Brillouin zone of a graphene ribbon of chirality $\vec{\Gamma}_{\perp}(1,0)$ . . . . .	195
5.15	Schematics of the principle of a topological interface realized with a topologically non-trivial photonic crystal ribbon. . . . .	196
5.16	FDTD model and bandstructure of the honeycomb lattice photonic crystal ribbon of chirality $\vec{T}(1,0)$ . . . . .	197
5.17	Band structures of the topologically trivial triangular photonic crystal and the bulk ribbon defined with a supercell. . . . .	198
5.18	Band structure and map of the edge states in the topological interface between the ribbon $T(1,0)$ and trivial triangular lattice photonic crystals.	199
5.19	Planar unit cell of carbon nanotubes . . . . .	201
5.20	Illustration of the cutting lines method for the construction of the band diagram of a (6,6) armchair CNT. . . . .	204
5.21	Schematized cutting lines and zone-folding dispersion of carbon nanotubes with different chiralities. . . . .	205
5.22	One-dimensional topological model of carbon nanotubes. . . . .	207
5.23	Graphical determination of the winding number and topological classification of carbon nanotubes as a function of their chirality. . . . .	209
5.24	FDTD computation cell for the calculation of the band structure of unrolled CNT-like photonic microtube in the way of zone-folding. . . .	211
5.25	Simulated band structures of unrolled CNT-like photonic microtubes with circular air holes of different chiralities. . . . .	212
5.26	Computation unit cell and simulated band structures of unrolled CNT-like photonic microtubes with triangular air holes of different chiralities.	213
5.27	FDTD model of seamless rolled-up honeycomb lattice photonic crystal membrane microtubes with circular air holes. . . . .	214
5.28	FDTD band structures of CNT-like photonic microtubes compared to photonic zone-folding calculations with TE and TE-TM incident polarizations. . . . .	215
5.29	Scanning electron microscopy pictures of fabricated CNT-like photonic microtube with triangular air holes. . . . .	217
5.30	Geometry and zone-folding band structure of the zig-zag $\vec{C}_h(6,0)$ chirality.	218

5.31	Filtering of incident light components on microtube specimens for the measurement of dispersion of the tube along its axis. . . . .	219
5.32	Experimental band diagrams in reflectivity measured on zig-zag $\vec{C}_h(6, 0)$ zig-zag triangular air-hole honeycomb lattice photonic crystal microtube specimen. . . . .	219
5.33	Comparison of the experimental band diagrams in reflectivity of the real photonic microtubes with the band structure of a triangular-hole honeycomb lattice photonic crystal membrane. . . . .	221
5.34	Modelling of the microtube by an air-filled cavity and comparison of experimental and theoretical reflectivity spectra. . . . .	221
C.1	Schematized reflection and refraction of light at the interface between two dielectric media and onto a $d$ -thick dielectric slab. . . . .	IV
D.1	Plots of first kind Bessel functions $J_m(x)$ and their first derivative $J'_m(x)$ . VIII	
E.1	FDTD surface maps and profiles of cavity modes $TE_{0,22}$ and $TE_{1,23}$ in an infinite rolled-up PCM cavity of average radius $\rho_{\text{avg}} \simeq 1.62 \mu m$ . . . .	IX
F.1	Evolution of the angle of incidence $\theta$ in degrees as a function of the azimuthal order $m$ . Reflectivity of a $0.230 \mu m$ -thick photonic crystal membrane at oblique incidence. . . . .	X
G.1	Reflectivity of PCM structures fabricated on sample C2579. . . . .	XI
H.1	Triangle . . . . .	XII





# List of Tables

2.1	Harmonic inversion parameters of the resonances . . . . .	82
3.1	Spectral characteristics of the PCM's high reflectivity zone at oblique incidence. . . . .	119
3.2	Identification of cavity modes detected in FDTD spectrum of infinite tubular cavities. . . . .	138
3.3	Cutoff wavelengths $\lambda_{m,n,p}$ of finite cavity modes. . . . .	144
3.4	Cutoff wavelengths $\lambda_{\text{TE}_{1,22,p}}$ and $\lambda_{\text{TE}_{3,21,p}}$ in cylindrical cavity resonator of radius $\rho_c = 17.68 \mu m$ and length $L = 50 \mu m$ . . . . .	146
4.1	Composition of the C2217, C2527, and C2579 multi-layered stacks. . .	151
5.1	Evolution of the Zak phase and the number of edge states for photonic ribbons of chirality $\vec{T}(1, 0)$ as a function of $\alpha = k_{\parallel}/\Gamma_{\parallel}$ . . . . .	196
D.1	First five roots of the first derivative of first kind Bessel functions $J'_m$ with $m = 0, 1, 2, 3, 4$ . . . . .	VIII



# Introduction

History of nanophotonics has known a turning point with the development in the end of the 80s of photonic crystals as artificial photonic analogues of solid-state crystals. In particular, the analogy between the propagation of electrons in semi-conductors and the propagation of light in photonic crystals has opened new opportunities to achieve the spatial and temporal control of light, at the wavelength scale, in one, two or three directions. Moreover, the variety and tunability of the photonic crystal lattice patterns have offered a wide palette of optical functionalities such as the guiding, the trapping, or the slowing of light. For instance, 1D photonic crystals consisting of multi-layered dielectric stacks have served as reflective coating and high reflective mirrors in laser cavities. Similar effects have also been reported in 2D photonic crystals obtained by patterning dielectric substrate membranes. The realization of 3D photonic crystals exhibiting a complete photonic band gap has also aroused much interest toward the harnessing of light in all directions. However, the production of such 3D photonic crystal architectures generally involves complex fabrication technologies based for instance on the stacking of two-dimension layers, laser writing or drilling under different angles.

Toward the development of 3D photonic structures, the PHOLDING (for FoLDING PHOtonic Crystals: Semiconductors ORIGAMI) ANR project, in which this thesis is inscribed, has proposed to apply the technology of stress relaxation to photonic crystal membranes. Indeed, the mechanical elastic relaxation of pre-stressed patterned multilayers can give rise to 3D micro-object which final shapes are determined by the initial stress distribution. The fabricated structures are sometimes called "photonic origamis" as this fabrication process borrows the idea from the Japanese art of paper folding. The general purpose of this work is to explore the paths opened by this fabrication method to produce original photonic structures.

Among them, new families of 3D hollow optical micro-resonators with the peculiar properties of enabling a strong trapping and enhancement of light in a low index media, are especially targeted. In these microresonators, the confinement of light is based on the concept of "photon cages" which consists in enclosing a small region of space with a folded photonic crystal membrane designed to present a broad-band and high reflectivity in the wavelength range of interest. The idea is to achieve very open resonators where strong light-matter interaction can be exploited in optical devices comprising an active material embedded in a low index matrix like polymer, liquid or even gas. Indeed, hollow 3D resonators hold much interest for sensing operations as they not only maximize the 3D light confinement but also optimize the overlap between the electromagnetic field and potential sensing micro-sized targets. Using stress engineering technique, these 3D microresonators can be manufactured by rolling up 2D photonic crystal membranes to form tubular "photon cages". If the concept of photon cage has been studied theoretically at INL in the case of one-dimensional photonic crystal, no experimental validation has been brought yet. In this thesis, we first address the con-

ception and the optical characterization of tubular photon cages produced upon the rolling of 2D photonic crystal membranes mirrors. In particular, we aim at bringing an experimental proof of concept of the confinement of light inside the tubular photon cages.

Another application of photonic origamis deals with the common exploration of the correspondence between condensed matter and photonic systems. Indeed, the production of photonic crystal analogues of atomic crystals has paved the way to new perspectives in the light engineering. In particular, graphene-like photonic crystals have drawn interest as, like their electronic counterparts, they exhibit remarkable properties such as the presence of a Dirac point in their band diagram. By contrast with solid-state structures, photonic crystal equivalents present design flexibility through notably the change of their lattice parameters, allowing to explore new optical effects. In particular, beyond the linear dispersion around the Dirac point, it has been proved that by opening a gap around this peculiar point, topological edges states could be observed.

Stress-engineering based fabrication also allows us to pursue the analogy and explore the properties of carbon nanotubes photonic crystal analogues, namely rolled-up honeycomb lattice photonic crystal membrane microtube. Indeed, depending on the direction of rolling of the graphene sheet, also known as the chirality, the carbon nanotubes may (or not) present a band-gap. Therefore, a natural question we address in this work concerns the existence of a rolling-induced band gap in the case of the photonic micro-tubes. If so, another legitimate question that we raise deals with the topological nature of this gap.

In Chapter 1, we first introduce the rolled-up nanotechnology based on the self-rolling of stress-engineered nanomembranes, as a competitive micro-fabrication method to the challenging production of 3D micro-objects. On the basis of the multiple reviews recently published, we present a update state of the art of the technique, giving an overview of the range of materials, the variety of the 3D architectures accessible with the technique, and the scope of applications. We focus notably on the utilization of tubular microstructures as photonic microcavities with tunable optical properties. In the second section, we present the concept of photon cages based on the deformation of highly reflective photonic crystal membranes as a alternative solution to the confinement of light in air. We explain the mechanisms behind the reflective properties of photonic crystal. We then formulate the first objective of this thesis dealing with the conception of tubular photon cages based on the rolling of highly reflective 2D photonic crystal membranes. In the third section, after reviewing the properties of graphene and carbon nanotubes, we introduce the second objective of the thesis which concerns the production and optical characterization of photonic crystal analogues of carbon nanotubes.

In Chapter, 2, we present the numerical, fabrication, and optical characterization methods used in this thesis to achieve the conception and characterization of the rolled-up photonic crystal microtubes. The first section focuses on two numerical tools, the rigorous coupled-wave analysis and the finite-difference time-domain method, employed to simulate the optical response of planar and rolled-up photonic crystals. The second section details the fabrication processes of the rolled-up microstructures, involving the production of the multi-layered precursors by epitaxial deposition, the design and fabrication of the planar mask by e-beam lithography and reactive ion etching process, and the rolling of the photonic crystal membrane by underetching. In the last section,

we describe the two main techniques used in this thesis to perform the optical characterization of the fabricated rolled-up photonic structures, namely scanning near-field optical measurements and angular-resolved spectral measurements.

In Chapter 3, we address the design and the simulation of the tubular photon cages. The first section deals with the conception of a broadband and high performance 2D photonic crystal membrane mirror constituting the membrane wall of photon cages. The second section concentrates on the simulation of optical response of the photonic cages with infinite and finite size, using the analytical model of the cylindrical cavity resonator and more realist modelling of the rolled-up structures.

In Chapter 4, we complete the study of the tubular photon cages with the fabrication and optical characterization steps. In the first section, we present the main results of the fabrication of the rolled-up photonic crystal membranes, precisising the composition of the multi-layered stack, the conception of the planar mask and describing one typical sample. In the second section, we present and analyze the near-field optical measurements carried out inside different specimens of tubular cages and bring the experimental proof of the the confinement of light in the air-filled hollow part of the tubular photon cages.

In Chapter 5, we tackle the conception and explore the optical properties of photonic crystal analogues of carbon nanotubes. In the first section, after reviewing the structural and electronic dispersion of graphene approached with the tight-binding model, we present the simulated photonic dispersion of a honeycomb lattice photonic crystal membrane constituting the building block of the carbon nanotube-like photonic microtube. In the second section, we first describe the topological properties of graphene ribbons following the literature. We then assess numerically the topological behaviour of their photonic crystal equivalents, ribbons of honeycomb lattice photonic crystal membranes, by estimating the topological invariants and simulating the photonic band diagram at the edge of the ribbon. In the third section, we review the structural properties, the electronic dispersion using the zone-folding method and the topological classification of carbon nanotubes with respect to their chirality. We then investigate the optical properties of their photonic crystal analogues by simulating numerically the photonic band structure on planar and rolled-up structures. We present afterward main fabrication results of the photonic microtubes, precisising their composition and evaluating the quality of the rolled-up microstructures as well as the reproducibility of the method. We finally present preliminary results on the optical characterization of the fabricated honeycomb lattice photonic crystal microtubes through angular-resolved spectral measurements allowing to extract experimental photonic band diagrams.



# Chapter 1

## Origami-based photonic crystals

*Light thinks it travels faster than anything but it is wrong.  
No matter how fast light travels, it finds the darkness has always got  
there first, and is waiting for it.*

---

TERRY PRATCHETT (REAPER MAN)

### Contents

---

<b>1.1</b>	<b>Towards 3D rolled-up photonic structures . . . . .</b>	<b>6</b>
1.1.1	Introduction to the rolled-up nanotechnology . . . . .	6
1.1.2	Optical microcavities with tunable properties . . . . .	24
<b>1.2</b>	<b>Concept of tubular photon cages . . . . .</b>	<b>28</b>
1.2.1	Confining light in low-index media . . . . .	28
1.2.2	Tubular photon cages . . . . .	32
1.2.3	Photonic crystal membrane mirrors . . . . .	34
1.2.4	Tubular photon cages based on 1D photonic crystal membranes	41
1.2.5	Tubular photon cages based on 2D photonic crystal membranes	43
<b>1.3</b>	<b>Photonic crystal analogues of solid-states structures . . . . .</b>	<b>43</b>
1.3.1	Electronic dispersions of graphene and carbon nanotubes . .	44
1.3.2	Topology in physics: introduction to concepts and models . .	48
1.3.3	Photonic crystal analogues of carbon nanotubes . . . . .	59
<b>1.4</b>	<b>Conclusion of the chapter . . . . .</b>	<b>60</b>
<b>1.5</b>	<b>References . . . . .</b>	<b>62</b>

---



In this chapter, we introduce the rolled-up fabrication technique with a focus on its application to the fabrication of photonic structures. We will then see how the use of this manufacturing method, with the use of photonic crystal membranes, is relevant for making hollow photonic resonators, which allow light to be strongly confined in a low index medium. A part from this application, we will show that the rolled-up of a photonic crystal membrane also makes it possible to explore the field of correspondences between electronic systems of condensed matter and photonic systems. In this work, we are interested in the link between carbon nanotubes and their photonic analogues obtained by the rolled-up technique. More precisely, we will study the relationships that can be established between these systems at the level of their dispersion band diagrams and their topological properties. These aspects, including elements of topology useful to understand our study, will be presented in the last part of this chapter.

## 1.1 Towards 3D rolled-up photonic structures

This section introduces the rolled-up nanotechnology based on the self-rolling of pre-stressed planar nano-membranes, and developed in the last two decades to address the challenging fabrication of 3D micro-structures. It will explain at first the main mechanisms at stake: the introduction of an inhomogeneous strain in the membrane and the bending predicted by the classical plate theory when releasing the stress. It will then give an insight into the large variety of 3D micro-objects achievable with this technique, considering the multiple combinations of 3D geometries and materials. It will finally focus on the use of tubular rolled-up microstructures in photonic applications such as lasing and optofluidic sensing.

### 1.1.1 Introduction to the rolled-up nanotechnology

#### In the scope of 3D fabrication techniques

The production of 3D micro-structures has raised scientific enthusiasm in the last decades owing, among other motivations, to the growing demand for the miniaturisation of devices and the reduction of energy consumption. The development of microstructures with complex 3D architectures has also opened new horizons for the production of 3D micro-objects exhibiting novel functionalities [1] which find applications in a wide variety of fields such as biology [2], electronics [3–5], photonics [6], to name but a few. However, the production of such 3D microstructures remains challenging as existing fabrication techniques strive to interweave all at once high pattern resolution, materials flexibility, variety of 3D shapes and scaling properties.

The case of 3D optical metamaterials epitomizes the delicate transition between theoretical predictions and their practical realization at the micro- and nanometer scales. Indeed, metamaterials as 3D assembly of artificial optical elements have drawn a peculiar attention on account of their outstanding range of optical functionalities such as negative refraction, perfect lensing effect or invisibility cloaking [7]. Despite achievements in the microwave regime, the transposition to optical frequencies, hence with micro- and nanometer resolution, encounters challenging fabrication requirements owing partly to the multi-scale nature of the structures. Indeed, conventional planar technologies, including UV or electron-beam lithography for instance, enable the planar patterning of material layers with a resolution up to few nanometers but limit to simple 3D stacking layout [8]. In parallel, other 3D fabrication methods have recently been

developed to push the limits of 2D planar fabrication. In particular, 3D printing [9–11] or laser direct writing (LDW) [12–17] methods have proved their efficiency to create a large range of complex 3D forms from various materials and with competitive resolution. Nevertheless, their sequential nature implies significant fabrication duration and thus impedes the scaling-up or the production of high-aspect ratio microstructures.

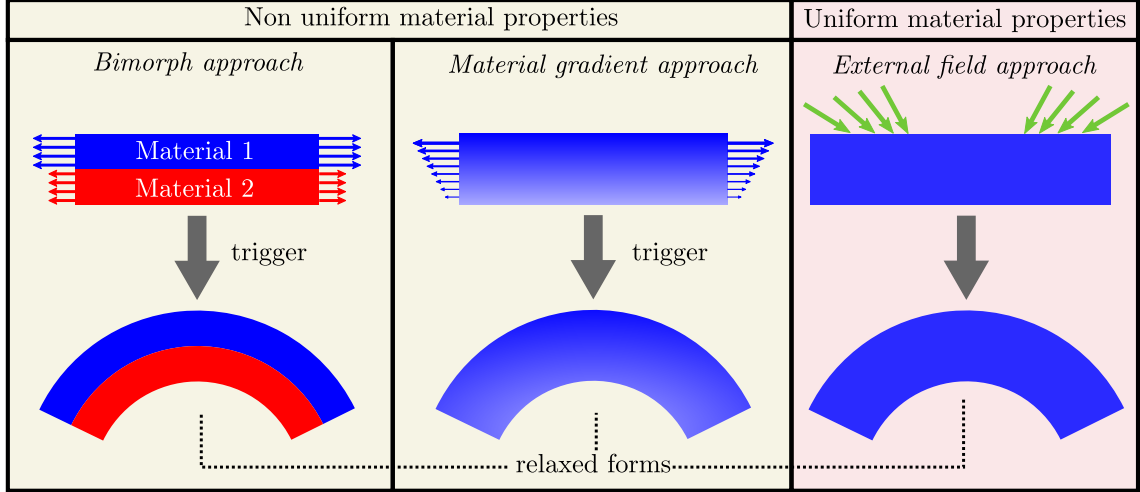


FIGURE 1.1: Strategies for the bending of thin material sheets with non-uniform or uniform properties across the thickness. In the bimorph and material gradient approaches, the coloured arrows represent the vertical distribution of the internal forces in the membranes. In the external field approach, external forces symbolized by green oblique arrows are applied on the membrane. In the three configurations, opposite forces (not depicted on the drawings) are needed to maintain the static equilibrium of the membranes which relax into a downwards curved form upon a proper trigger mechanism. Drawings inspired from [18].

### Rolling at the micro- and nano-scale: the Origami technique

Another strategy toward the fabrication of 3D microstructures has emerged drawing inspiration from the Origami art of folding which turns planar templates, originally planar paper-based templates, into 3D architectures. Transposing the concept at micro- and nanometric scales, the key point in the production of Origami-based 3D micro-objects rests upon the folding of thin material films. The folding of thin material layers can be achieved according to two mechanisms: the bending by generating an in-plane moment or the buckling by applying compressive forces on the layer. Two generic methods described below and schematized on the two colour-shaded panels on Figure 1.1 allow to bend or buckle thin material layer systems. The ensemble of methods fall into the generic framework of the so-called *rolled-up nanotechnology* [19].

On the right panel, the material properties of the layer represented by a blue patch are distributed uniformly along the thickness of the layer. The bending of the layer is then carried out by the application of an external force depicted as incident green arrows, it is so-called the *external field approach*. This method involves driving forces of various natures such as capillary [20] or magnetic [21] effects. Moreover, a buckling phenomenon may occur when the entire film thickness experiences compressive forces [22].

On the two left panels, the system corresponds either to a bilayer system (*bimorph approach*) or to a single material layer (*material gradient approach*), both defined by a non-uniform distribution of material properties (elastic modulus, lattice parameters) across the total thickness. In general, we introduce a differential strain in the material

layers which causes the bending of system. In particular, in the *bimorph approach*, two material layers with mismatch strains are adjoined together whereas in the *material gradient approach*, the strain changes gradually along the thickness of the single material layer. Among the driving mechanisms employed to induce strain in material membranes, we can cite *residual stress*, *swelling*, *liquid crystal alignment* and *shape-memory effect*, described in [18].

### Stress-engineering

In particular, the *residual stress*, obtained through *compressive* or *tensile* strain, is typically introduced in crystalline material layer during epitaxial growth. It is generally considered as an undesirable effect of the film growth as it may generate crystal defects such as dislocations or roughening on the deposited film in case of large amount of pre-stress. However, it can also be advantageously exploited toward the bending of a bilayer system composed of two prestrained material layers. For instance, the thermal growth of a metallic film on top of a  $\text{SiO}_2$  layer induces *compressive* and *tensile* prestrains, respectively, owing to the different thermal expansion coefficients of the materials [23]. Opposing forces in the two layers generate a nonzero bending moment which result in the bending of the bilayer upon release from its substrate.

In a similar way, Prinz *et al.* have exploited in a series of seminal works [24–26], the prestrains induced in semi-conducting material films inherently to epitaxial deposition techniques, to roll material bilayers up. We schematize in Figure 1.2.a) the process originally proposed to produce free-standing rolled-up InAs/GaAs membranes. The fabrication scheme begins with the epitaxial growth of successive AlAs, InAs and GaAs material layers on top of an InP substrate, with thicknesses controlled down to the atomic monolayer (ML). In Figure 1.2, each layers are depicted as periodic assemblies of rectangular shapes in order to emphasize their crystallographic nature. The length of each rectangles indicates the lattice parameter of the material composing the layer in both horizontal and vertical directions. We remark that the epitaxial growth supposes the adjustment of the in-plane lattice parameters of deposited layers to that of the substrate.

This adjustment is inherent to the lattice mismatch between the materials of the deposited and substrate layers. In particular, the different lattice parameters of InAs ( $a_{\text{InAs}} \simeq 6.06 \text{ \AA}$ ) and GaAs ( $a_{\text{GaAs}} \simeq 5.65 \text{ \AA}$ ) materials induces respective *compressive* and *tensile* forces in the layers, symbolized by thick black arrows of opposite directions. The selective etching of the underlying sacrificial AlAs layer releases the pre-strains in the InAs/GaAs bilayer. Opposite forces in the bilayer generates a nonzero moment noted  $M$  which induces a natural curvature of the bilayer membrane. We demonstrate in later developments that, in the framework of a linear elastic mechanical model, the induced curvature, defined by the curvature radius  $\rho$ , depends mainly on the thicknesses and the composition of the layers. Moreover, for rectangular shapes, the dimensions and the orientation of the planar precursor determines the number of rolling and the 3D shape of the final structures. Therefore, the SEM picture of Figure 1.2.b) shows a typical array of high aspect ratio microtubes obtained in [27] at the end of one fabrication cycle. The diameter of the so-formed cylindrical microstructures reaches about  $2 \mu\text{m}$  for wall thickness estimated to about  $10 \text{ nm}$  and lengths reckoned to few centimetres. Additional realizations were carried out in [27] while varying the thickness of InGaAs and GaAs layers of a InGaAs-GaAs bilayer, down to few ML, and the Indium (In) proportion  $x$  of the  $\text{In}_x\text{Ga}_{1-x}\text{As}$  layer to achieve diameters within  $[2 \text{ nm} - 2 \mu\text{m}]$ . The cross-sectional high resolution transmission electronic microscopy (HRTEM) view

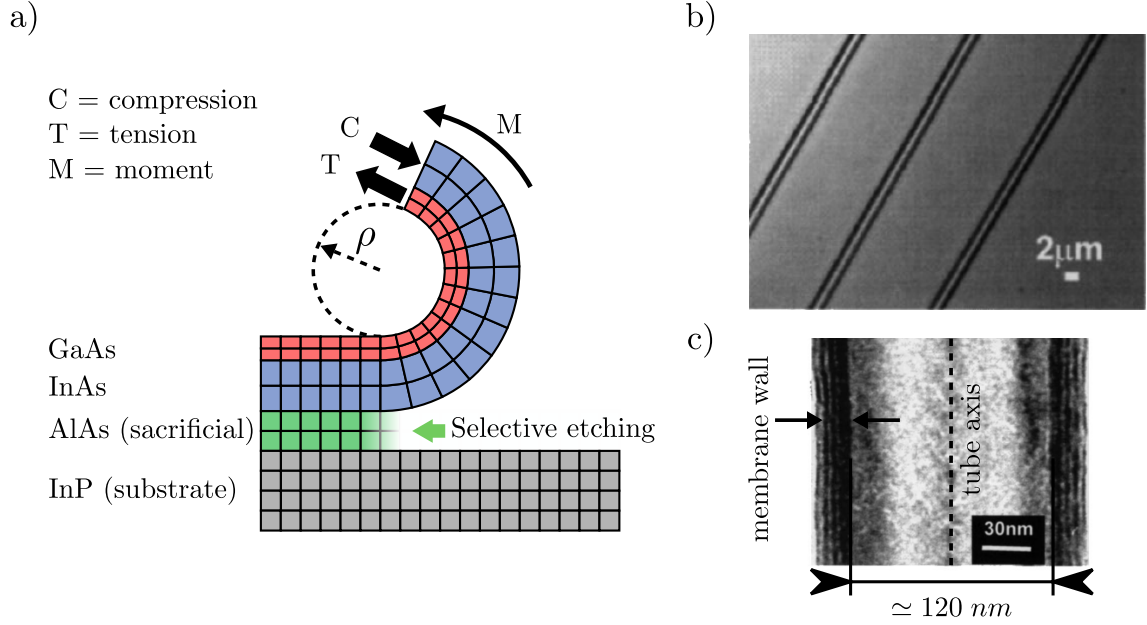


FIGURE 1.2: a) Schematized self-rolling of a prestrained InAs-GaAs membrane upon selective etching of underlying AlAs sacrificial layer. The periodic assemblies of rectangular shapes reproduces the crystalline nature of the material layers grown epitaxially. Tension and compression in InAs and GaAs layers generate a non-zero moment for the bilayer which starts to curve with a radius  $\rho$ . b) SEM picture of an array of rolled-up InAs-GaAs microtubes obtained in [27]. c) Cross-sectional SEM picture, also extracted from [27], of a multilayered InAs-GaAs microtube.

in Figure 1.2.c) of a microtube based on InGaAs-GaAs bilayer reveals the multi-layered nature of the membrane wall composed of a 4 ML-thick InGaAs layer adjoined to a 4 ML-thick GaAs layer. This example also demonstrates the successful implementation of the rolled-up nanotechnology for the rolling of extremely thin layers of only few microlayers thickness.

### Theoretical expression of the induced curvature

The systematic production of rolled-up micromembranes upon relaxation of induced *residual strain* necessitates to find the relation between the structural parameters of the bilayer membrane (composition and thickness) and the curvature radius  $\rho$  of the final multilayered microstructure. To this end, we use a mechanical model derived from the thin plates theory, also known as the Love-Kirchhoff theory, which applies especially to the study of bending of single and multi-layer structures. In this model, we consider the simplest system composed of two crystalline material layers  $A_1$  and  $A_2$  defined by their respective lattice parameters  $a_1$  and  $a_2$  verifying, for instance,  $a_2 < a_1$ . The two separated layers are depicted on Figure 1.3.a) using the same schematic representation of crystalline layers in Figure 1.2.a).

We seek to describe the mechanical behaviour of the bilayer  $A_1$ - $A_2$  formed after the epitaxial deposition of layer  $A_2$  onto layer  $A_1$ . We define a *reference configuration* for which layer  $A_1$  is naturally relaxed while layer  $A_2$  fits its crystallographic parameters to that of  $A_1$  substrate layer. The study of the mechanical behaviour of the bilayer decomposes into two steps. We first establish the constitutive relations of the two layers with respect to the reference configuration. We determine then the behaviour in the *free bilayer* when subjected to null forces and moments since, in practice, the prestrained bilayer is free when it detaches from the substrate during the etching of

the sacrificial layer. We emphasize the independence of the final result with respect to the choice of the reference configuration.

Assuming a *linear elastic* behaviour and *plane stresses* for each layer, we can write the constitutive relation for each material layer  $i$  ( $i = \{1, 2\}$ ) in the following form:

$$\boldsymbol{\sigma} = \mathbb{C}^{(i)} [\boldsymbol{\varepsilon} + \mathbf{m}^{(i)}], \quad (1.1)$$

where  $\boldsymbol{\sigma}$ ,  $\boldsymbol{\varepsilon}$  designate respectively the stress and strain symmetric second-order (6 independent components) tensors. The elements  $\mathbb{C}^{(i)}$  and  $\mathbf{m}^{(i)}$  stand respectively for the fourth-order (21 independent terms) *Hooke* tensor and the pre-strain of the  $i$ -th layer, i.e. the strain with respect to the fixed reference configuration, of thermal and/or microscopic origin. In the case of materials defined by a cubic crystal system, which includes Indium Phosphide (InP) and Gallium Phosphide (GaP) semiconductors, and using the Voigt notation, the Equation (1.1) reduces to:

$$\begin{pmatrix} \sigma_{11} \\ \sigma_{22} \\ \sigma_{33} \\ \sigma_{23} \\ \sigma_{13} \\ \sigma_{12} \end{pmatrix} = \begin{pmatrix} C_{11} & C_{12} & C_{12} & 0 & 0 & 0 \\ & C_{11} & C_{12} & 0 & 0 & 0 \\ & & C_{11} & 0 & 0 & 0 \\ & & & C_{44} & 0 & 0 \\ & \text{sym} & & & C_{44} & 0 \\ & & & & & C_{44} \end{pmatrix} \begin{pmatrix} \varepsilon_{11} + m_{11} \\ \varepsilon_{22} + m_{22} \\ \varepsilon_{33} + m_{33} \\ 2\varepsilon_{23} \\ 2\varepsilon_{13} \\ 2\varepsilon_{12} \end{pmatrix}. \quad (1.2)$$

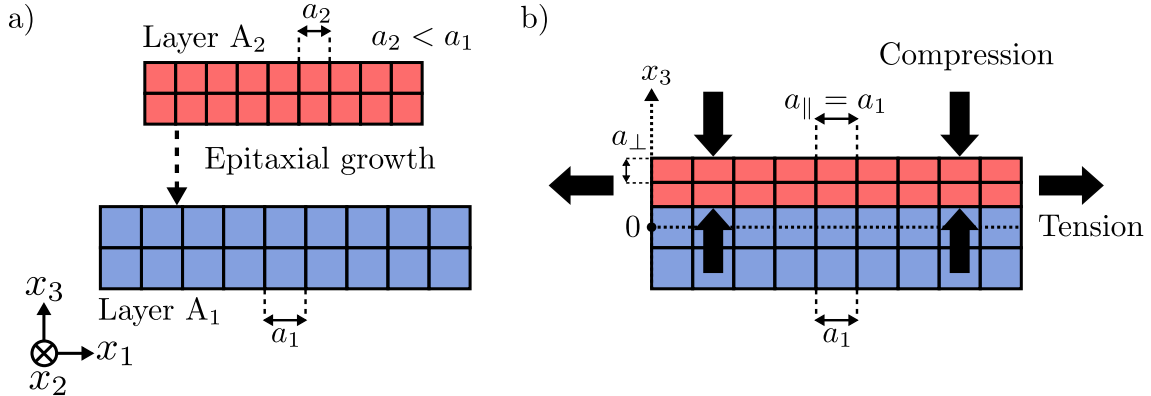


FIGURE 1.3: Schematic introduction of pre-strains in a bilayer membrane. a) Layer A<sub>2</sub> with lattice parameter  $a_2$  is grown epitaxially on substrate layer A<sub>1</sub> with lattice parameter  $a_1 > a_2$ . The periodic assemblies of square forms symbolizes the cubic crystallographic nature of the layers in the  $(x_1, x_3)$  plane. b) After deposition and due to the lattice mismatch, layer A<sub>2</sub> undergoes bi-axial tensile strains and compression in the  $x_3$  vertical direction.

We form the material bilayer A<sub>1</sub>-A<sub>2</sub> by depositing epitaxially layer A<sub>2</sub> on layer A<sub>1</sub> as sketched on Figure 1.3.b). The epitaxial growth imposes that the material layer A<sub>2</sub> adopts the cristallographic structure and orientation of the supporting layer A<sub>1</sub>. Therefore, in the plane of the membrane, namely along both directions  $x_1$  and  $x_2$ , the lattice parameter of layer A<sub>2</sub> fits with that of A<sub>1</sub>:  $a_{\parallel} = a_1$ . For simplicity, we represent the lattice matching exclusively along the  $x_1$  direction but identical mechanism occurs along the  $x_2$  axis due to the cubic symmetry. Moreover, inherently to the deposition method, the structural parameters of layer A<sub>2</sub>, at a given deposited thickness, evolve freely along the  $x_3$  axis normal to the membrane plane. The situation then changes in the course of the growth due to the increase in the thickness of the deposited layer, such that the amount of stress in the membrane changes too. However, in our model, we

only consider plane stresses in the membrane to calculate the final induced curvature of the bilayer.

In the reference configuration, the layer  $A_1$  is characterized by  $\mathbf{m}^{(1)} = \mathbf{0}$ , such that the constitutive law merely reads:

$$\boldsymbol{\sigma} = \mathbb{C}^{(1)} \boldsymbol{\varepsilon}. \quad (1.3)$$

Conversely, on account of the lattice mismatch, the constitutive law of layer  $A_2$  with respect to relaxed layer  $A_1$  expresses as:

$$\begin{pmatrix} \sigma_{11} \\ \sigma_{22} \\ \sigma_{33} \\ \sigma_{23} \\ \sigma_{13} \\ \sigma_{12} \end{pmatrix} = \mathbb{C}^{(2)} \begin{pmatrix} \varepsilon_{11} + m \\ \varepsilon_{22} + m \\ \varepsilon_{33} + \varepsilon_{33}^0 \\ 2\varepsilon_{23} \\ 2\varepsilon_{13} \\ 2\varepsilon_{12} \end{pmatrix}, \quad (1.4)$$

where the misfit parameter  $m$  defines as:

$$m = \frac{a_1 - a_2}{a_2}. \quad (1.5)$$

In other words, layer  $A_2$  undergoes a biaxial strain  $m$  in the membrane plane while  $\varepsilon_{33}^0$  indicates the strain in the out-of-plane direction, in the reference configuration. Moreover, the growth process supposes that the material layers form freely in the vertical direction which allows to consider plane stresses, namely  $\sigma_{23} = \sigma_{13} = \sigma_{33} = 0$ , in the bilayer system. In particular, the application of plane-stress assumptions in the reference configuration gives the following expression of the out-of-plane strain:

$$\varepsilon_{33}^0 = -2m \frac{C_{12}^{(2)}}{C_{11}^{(2)}}, \quad (1.6)$$

while the remaining relations  $\sigma_{23} = \sigma_{13} = 0$  always hold true.

In particular, if  $a_2 < a_1$ , hence  $m > 0$ , we infer that, with respect to its natural relaxed configuration, the layer  $A_2$  undergoes:

- a *tensile* strain; as a consequence, in-plane compressive strains  $\varepsilon_{11}, \varepsilon_{22} < 0$  are needed to satisfy  $\sigma_{11} = \sigma_{22} = 0$ ;
- a *compressive* strain  $\varepsilon_{33}^0 < 0$  in the out-of-plane direction, as a tensile strain  $\varepsilon_{33} > 0$  cancels out the stress component  $\sigma_{33}$ ,

as schematized with thick black arrows on Figure 1.3.b). Furthermore, for both materials, the application of the plane-stress assumption  $\sigma_{33} = 0$  using Equations 1.4 and 1.6 leads to an expression of  $\varepsilon_{33}$  depending exclusively on  $\varepsilon_{11}$  and  $\varepsilon_{22}$ :

$$\varepsilon_{33} = -\frac{C_{12}^{(i)}}{C_{11}^{(i)}} (\varepsilon_{11} + \varepsilon_{22}). \quad (1.7)$$

Combining Equations 1.4 and 1.7, the constitutive relation for layer  $A_2$  rewrites in a more compact way as:

$$\begin{pmatrix} \sigma_{11} \\ \sigma_{22} \\ \sigma_{12} \end{pmatrix} = \begin{pmatrix} \hat{C}_{11} & \hat{C}_{12} & 0 \\ & \hat{C}_{11} & 0 \\ \text{sym} & & C_{44} \end{pmatrix} \begin{pmatrix} \varepsilon_{11} + m \\ \varepsilon_{22} + m \\ 2\varepsilon_{12} \end{pmatrix} \quad (1.8)$$

where the coefficients  $\hat{C}_{11}$  and  $\hat{C}_{12}$  defined by:

$$\hat{C}_{11} = C_{11} - \frac{C_{12}^2}{C_{11}}, \quad (1.9)$$

$$\hat{C}_{12} = C_{12} - \frac{C_{12}^2}{C_{11}}, \quad (1.10)$$

refer to the *reduced elastic constants* in the formalism of the classical plate theory of Love-Kirchhoff. The reduced form of the constitutive law of layer  $A_i$  writes then:

$$\boldsymbol{\sigma} = \hat{\mathbb{C}}^{(i)} [\boldsymbol{\varepsilon} + \mathbf{m}^{(i)}], \quad (1.11)$$

where  $\mathbf{m}^{(1)} = [0 \ 0 \ 0]^t$  and  $\mathbf{m}^{(2)} = [m \ m \ 0]^t$ .

We have demonstrated so far the introduction of biaxial pre-strains in the mismatched layer  $A_2$  inherent to its epitaxial growth on relaxed layer  $A_1$ , and directly related to the lattice mismatch  $m$ . We have also established a compact expression of the constitutive law for both material layers  $A_1$  and  $A_2$  with the assumption of plane stresses. The second step consists then in determining the behaviour of the bilayer in response to the internal strain in layer  $A_2$ .

We consider the bifilm  $A_1$ - $A_2$  as a thin plate due to its small thickness as compared to lateral dimensions. The study of the motion of the bilayer reduces then to the study of the motion of its mid-surface. The mid-surface refers to the plane located at the middle of the bilayer thickness, taken as the origin of the  $x_3$  coordinate. In the Kirchhoff-Love theory for thin plates, the kinematic assumptions formulate as:

$$\begin{aligned} u_1(x_1, x_2, x_3) &= u_1^0(x_1, x_2) - x_3 \frac{\partial u_3}{\partial x_1}, \\ u_2(x_1, x_2, x_3) &= u_2^0(x_1, x_2) - x_3 \frac{\partial u_3}{\partial x_2}, \\ u_3(x_1, x_2) &= u_3^0(x_1, x_2), \end{aligned} \quad (1.12)$$

where  $\mathbf{u} = (u_1, u_2, u_3)$  designates the displacement field in the mid-surface along the directions  $x_1$ ,  $x_2$  and  $x_3$ , respectively. The motion of the mid-surface described in Equation (1.12) combines therefore in-plane ( $u_1^0$ ,  $u_2^0$ ) and out-of-plane ( $u_3^0$ ) displacements completed by the conservation of the angles between the normal to the mid-plane and the in-plane directions.

Supposing small deformations, the strain components  $\varepsilon_{ij}$  with  $(i, j) = \{1, 2, 3\}$  relates to the displacement field  $\mathbf{u} = (u_1, u_2, u_3)$  with the Green-Lagrange operator as:

$$\varepsilon_{i,j} = \frac{1}{2} \left( \frac{\partial u_i}{\partial x_j} + \frac{\partial u_j}{\partial x_i} \right). \quad (1.13)$$

From Equation (1.13), we verify that  $\varepsilon_{23} = \varepsilon_{13} = 0$  which validates the plane stresses assumptions  $\sigma_{23} = \sigma_{13} = 0$ , so that we can rewrite the in-plane strain in the following form:

$$\boldsymbol{\varepsilon} = \begin{pmatrix} \varepsilon_{11} \\ \varepsilon_{22} \\ 2\varepsilon_{12} \end{pmatrix} = \begin{pmatrix} \varepsilon_{11}^0 \\ \varepsilon_{22}^0 \\ 2\varepsilon_{12}^0 \end{pmatrix} + x_3 \begin{pmatrix} \kappa_{11} \\ \kappa_{22} \\ 2\kappa_{12} \end{pmatrix} \equiv \boldsymbol{\varepsilon}^0 + x_3 \boldsymbol{\kappa}, \quad (1.14)$$

where  $\boldsymbol{\varepsilon}^0 = (\varepsilon_{11}^0, \varepsilon_{22}^0, \varepsilon_{12}^0)$  refer to the *bilayer membrane strains* and express according to Equation (1.13) as:

$$\varepsilon_{11}^0 = \frac{\partial u_1^0}{\partial x_1}, \quad \varepsilon_{22}^0 = \frac{\partial u_2^0}{\partial x_2}, \quad \varepsilon_{12}^0 = \frac{1}{2} \left( \frac{\partial u_1^0}{\partial x_2} + \frac{\partial u_2^0}{\partial x_1} \right), \quad (1.15)$$

whereas  $\boldsymbol{\kappa} = (\kappa_{11}, \kappa_{22}, \kappa_{12})$  corresponds to the *bilayer membrane* (linearized) *curvatures*, expressed in  $m^{-1}$ , given also according to Equation (1.13) by:

$$\kappa_{11} = -\frac{\partial^2 u_3}{\partial x^2}, \quad \kappa_{22} = -\frac{\partial^2 u_3}{\partial x_2^2}, \quad \kappa_{12} = -\frac{\partial^2 u_3}{\partial x_1 \partial x_2}. \quad (1.16)$$

We notice for instance that for  $\kappa_{11} > 0$ , the bilayer membrane acquires along the  $x_1$  direction a natural *convex* shape.

In the framework of the plate theory, efforts and moments are defined as average quantities over the thickness of the plate, and calculated from the displacement fields known on the mid-surface. Therefore, we evaluate the efforts  $\mathbf{F}$  in the bilayer membrane by integrating, over the membrane thickness  $h = h_1 + h_2$ , the reduced constitutive laws established in Equation (1.11) for each layer:

$$\mathbf{F} = \int_{-h/2}^{h/2} \boldsymbol{\sigma} dx_3 = \int_{-h/2}^{h/2} \hat{\mathbb{C}} [\boldsymbol{\varepsilon} + \mathbf{m}]. \quad (1.17)$$

Similarly, we obtain the expression of the moments  $\mathbf{M}$  in the bilayer membrane by integrating, over the total thickness  $h$ , the reduced constitutive laws multiplied by  $x_3$ :

$$\mathbf{M} = \int_{-h/2}^{h/2} x_3 \boldsymbol{\sigma} dx_3 = \int_{-h/2}^{h/2} x_3 \hat{\mathbb{C}} [\boldsymbol{\varepsilon} + \mathbf{m}]. \quad (1.18)$$

Neglecting boundary effects, in the case of a *free* bilayer membrane, the strains  $\boldsymbol{\varepsilon}^0$  and curvatures  $\boldsymbol{\kappa}$  adjust to realize zero efforts and moments in the membrane, noted  $\mathbf{F}$  and  $\mathbf{M}$  respectively. Null efforts and moments in the membrane traduces by the two systems  $\mathbf{F} = \mathbf{0}$  and  $\mathbf{M} = \mathbf{0}$  each composed of three equations. The third equations of both systems leads to  $\varepsilon_{12}^0 = \kappa_{12} = 0$  while the four remaining equations admit a solution for  $\varepsilon_{11}^0 = \varepsilon_{22}^0 \equiv \varepsilon$  and  $\kappa_{11}^0 = \kappa_{22}^0 \equiv \kappa$ . The resolution of the previous systems, detailed in Appendix A, gives then the following general solution:

$$\varepsilon = \frac{-m\xi(\xi^3 + 3C\xi^2 + 3C\xi + C)}{C^2 + 2C\xi(2\xi^2 + 3\xi + 2) + \xi^4}, \quad \hat{\kappa} = \frac{-6mC\xi^2(1 + \xi)}{C^2 + 2C\xi(2\xi^2 + 3\xi + 2) + \xi^4}, \quad (1.19)$$

where  $C = E_1(1 - \nu_2)/E_2(1 - \nu_1)$  designates the *elastic contrast* defined with  $E_i$  and  $\nu_i$  ( $i = \{1, 2\}$ ) the Young modulus and Poisson coefficients of the  $i$ -th material layer, and  $\xi = h_2/h_1$ . We retrieve the historical results obtained in Timoshenko's theoretical macroscopic study on the bending of bi-metal structures [28].

In particular, for  $C = 1$ , the solutions reduce simply to:

$$\varepsilon = \frac{-m\xi}{1 + \xi}, \quad \hat{\kappa} = \frac{-6m\xi^2}{(1 + \xi)^3}, \quad (1.20)$$

with  $\hat{\kappa} = h_2\kappa$ .

In conclusion, the linear elastic model applied to the prestrained bilayer  $A_1$ - $A_2$  brings out the following remarks, on the basis of the key expressions obtained in Equation (1.20):

- The *free bilayer* undergoes an in-plane deformation  $\varepsilon$  and spontaneously rolls up with a normalized curvature  $\hat{\kappa}$ , both of which depending proportionally to the lattice mismatch  $m \neq 0$ ;



- In particular, we examine the two possible configurations according to the sign of  $m$ 
  - $m > 0$  (layer  $A_2$  under *tension*): the free bilayer relaxes in *compression* since  $\epsilon < 0$  and forms a *convex* shape as  $\hat{\kappa} < 0$ ;
  - $m < 0$  (layer  $A_2$  under *compression*): the free bilayer relaxes in *extension* since  $\epsilon > 0$  and forms a *concave* shape as  $\hat{\kappa} > 0$ ;
- We also point out the extreme evolutions of bilayer strains and curvatures for a given  $m$ :
  - $h_1 \gg h_2$ :  $\xi \rightarrow 0$  and the bilayer remains in planar configuration as strain  $\epsilon$  and curvature both tend to zero;
  - $h_2 \gg h_1$ :  $\xi \rightarrow \infty$  and the bilayer should stay in planar form as  $\hat{\kappa} \rightarrow 0$  but  $\epsilon \rightarrow -m$ . In practice, the uniform deposition of layer  $A_2$  is compromised above a critical thickness depending on the lattice mismatch and experimental conditions;
  - $h_2 = h_1 = h/2$ :  $\xi = 1$ , the curvature  $\kappa$  reaches its maximum value for a fixed  $h$  as plotted on Figure 1.4 for different misfit  $m$ ;

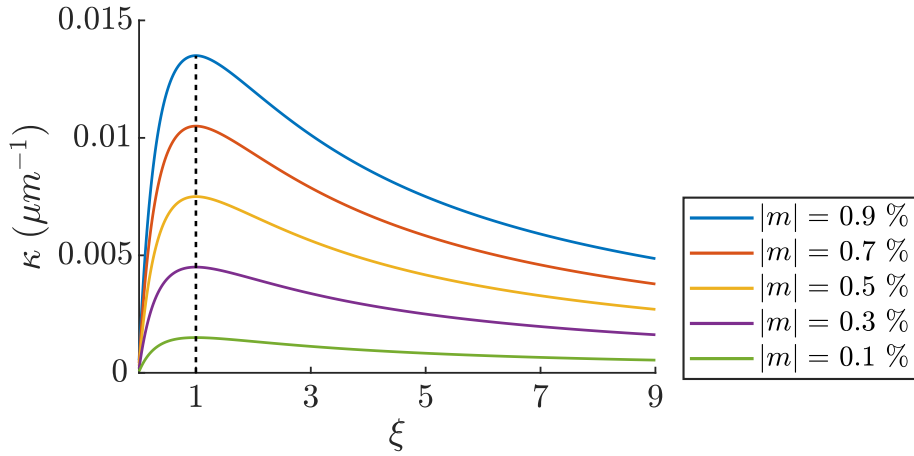


FIGURE 1.4: Evolution of the curvature  $\kappa$  (in  $\mu m^{-1}$ ) of a prestrained bilayer upon relaxation, for different prestrain  $m$  (in %), as a function of the ratio  $\xi = h_2/h_1$  with  $h_1$  and  $h_2$  the thicknesses of the two layers. The total thickness of the bilayer  $h = h_1 + h_2$  is fixed to one micron.

Above all and most interestingly, we deduce the expression of the curvature radius  $\rho$  of the rolled-up membrane directly from Equation (1.20) as:

$$\rho = \frac{1}{\kappa} = \frac{h_2}{\hat{\kappa}} = \frac{h_2(1 + \xi)^3}{-6m\xi^2}, \quad \text{if } C = 1. \quad (1.21)$$

We note that the previous expression holds true for materials with similar mechanical behaviour, namely  $C = 1$ . In particular, we report small deviations (inferior to few %) of the real radius  $\rho$  as compared to the exact expression in Equation (1.21) owing to the very close values of our materials' elastic constants.

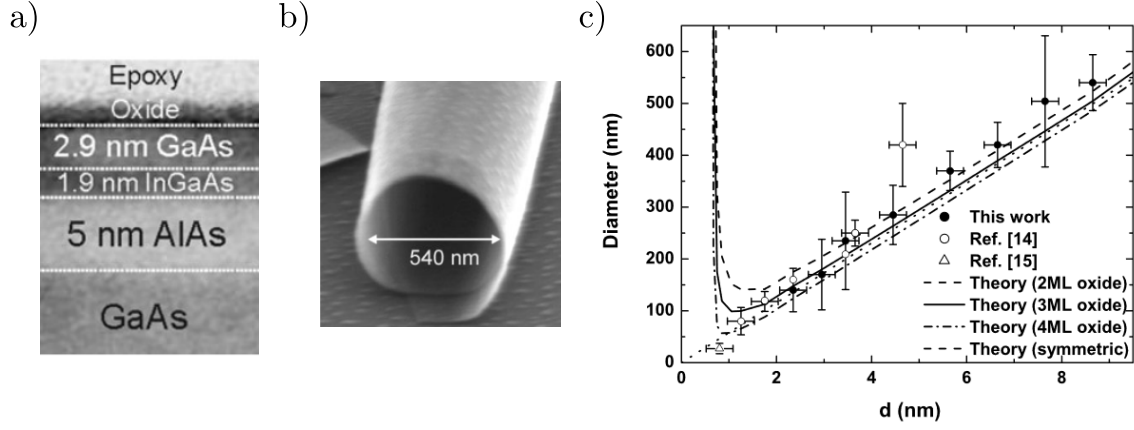


FIGURE 1.5: Study of the scalability of rolled-up microtubes from [29]. a) Cross-sectional transmission electronic microscopy (TEM) picture of a multi-layered semiconductor stack grown by molecular beam epitaxy (MBE). The oxide layer forms after exposition of the sample to ambient conditions. b) TEM picture of a specimen of rolled-up InGaAs-GaAs microtubes formed after selective etching of the AlAs layer. c) Evolution of the diameter of the microtubes calculated theoretically and experimentally as a function of the thickness  $d$  of the InGaAs-GaAs bilayer. Different theoretical curves are proposed according to the oxide monolayers (ML) subtracted to the estimation of the bilayer thickness. In the symmetric case, InGaAs and GaAs material have identical thicknesses.

### Validity of the model for microscopic rolls

Deneke and al. have then confronted in [29] theoretical and experimental estimations of the curvature radius of rolled-up InGaAs-GaAs bilayers to assess the accuracy of the mechanical model established hereinabove. Successive layers of AlAs, InGaAs, GaAs materials are first deposited through MBE process on top of a GaAs substrate as illustrated on the cross-sectional transmission electronic microscopy (TEM) image in Figure 1.5.a. The GaAs is grown intentionally thicker to compensate the formation of a thin layer of oxide (few ML-thick) on top of the multi-layered stack after exposition of the sample to ambient conditions, and to obtain a symmetric bilayer. Moreover, the total thickness of the bilayer  $d$  ranges from 7.4 ML to 33.6 ML. After the selective removal of the AlAs sacrificial layer, the InGaAs-GaAs prestrained bilayers relax by rolling into tubular shapes as showed on the TEM picture of Figure 1.5.b). The diameters of the microtubes measured experimentally for increasing thickness  $d$  are reported on the graph of Figure 1.5.c) and confronted to dashed line plots representing theoretical predictions taking or not into account the oxide layer. The results of previous works from same authors have also been added.

The evolution of experimental data points and theoretical curves shows a rather close fit over the entire range of thicknesses. This agreement is explained by the fact that the misfit  $m$  represents the only source of energy in the bilayer system. Consequently, at the equilibrium, the non-homogeneity which stems from the spatial distribution of the initial misfit is such that in each point the strain is lower than that imposed by the lattice mismatch. The slight experimental deviations observed at large diameters can be attributed to the imprecision in the determination of the concentration of Indium element. These results finally demonstrate the relevance of the mechanical model to predict precisely the relaxation of pre-strained bilayers and the induced curvature of the free bilayer membrane. The agreement between the small-strains theory and the experimental data explains by the unique contribution of small strains but large displacements/rotations in the roll-up process.

### Material compatibility

The material flexibility in 3D micro-fabrication techniques plays a crucial role as it determines not only their field of applications but also the potential integration of the 3D micro-objects in more complex devices or platforms. Concerning the generic rolled-up nanotechnology, the range of accessible materials has evolved jointly with the advances and technical improvements to offer thus far a wide variety of materials to be scrolled up. To investigate this range, we need to consider the anatomy of the multi-layered precursor produced beforehand and composed traditionally of functional layers including the pre-strained layers and a sacrificial layer deposited on top a substrate layer. The key process of the rolling of the functional layers relies on the relaxation of the pre-strained layers by the removal of the sacrificial layer. This removal is performed generally by a wet etching of the layer. It implies therefore an appropriate choice of the etching solution to eliminate selectively the sacrificial layer while preserving the upper functional material layers, which limits *de facto* the range of possible materials. We summarize hereinafter the main strategies adopted to extend the material choice towards the fabrication of rolled-up microstructures compatible with various applications, as described in details in [30].

Originally, sacrificial layers employed to realize rolled-up membranes were grown out of inorganic materials, using epitaxial deposition methods. Therefore, pioneer works of Prinz *et al.* [27] report the deposition of a AlAs layer as sacrificial layer on top of InP substrate and supporting InGaAs-GaAs pre-strained bilayer. Benefiting, among other assets, from the high-quality fabrication and the precise control of induced prestrain in material layers grown epitaxially, semiconducting crystalline III-V compounds, including AlGaAs, AlSb, AsSb or CdTe, have also extended the list of potential sacrificial layers. The removal of such layers is commonly and efficiently carried out in hydrofluoric (HF)-based etchant. Prinz and its team also managed later to roll membranes based on Silicon (Si) materials as in [26] for which the pre-strained bifilm composed of two layers of doped Si and GeSi lie on top an undoped Si sacrificial layer. The *under-etching*, namely the removal of the sacrificial layer, occurs by immersing the sample in a  $\text{NH}_4\text{OH}$  etching solution. We can mention multiple advantages in using Si-based material structures. First, the deposition technique is no more restrained to sophisticated and costly MBE method which consequently widens the choice of deposited materials. Second, the fabrication technique based on mature semiconductor industry ensures compatibility with planar technology and potential on-chip integration of the 3D microstructures. However, it is noteworthy that some of the etching solutions remain highly toxic, such as HF solutions, making the fabrication process incompatible with bioapplications. Research works have then focused on finding more bio- and eco-friendly etchant. For instance, etching solutions based on water [31] and  $\text{H}_2\text{O}_2$  [32] have proved to remove efficiently and selectively Ge and  $\text{GeO}_2$  sacrificial layers, respectively.

As an alternative to inorganic compounds which imply complex and multi-steps fabrication process, the utilisation of organic sacrificial layers offers multiple assets. For instance, the deposition of a photoresist sacrificial layer enables the deposition of various materials including platinum (Pt) and aluminium oxyde ( $\text{Al}_2\text{O}_3$ ) as demonstrated in [33]. Moreover, the photoresist layer often associates with traditional lithographic processes to realize a planar mask for the patterning of the upper functional layers. Finally, dry-etching of polymethyl methacrylate (PMMA) sacrificial layers by a heating procedure [34] have been proposed to circumvent surface tension issues encountered when drying wet-etched-based rolled-up microstructures.

In conclusion, the material range accessible with the rolled-up nanotechnology in-

timately relates to the choice of the sacrificial layer and its corresponding etchant. Indeed, the deposition of the sacrificial layer supposes a compatibility with the growth of upper functional layers which include the pre-strained films. Moreover, as a key process of the rolling of the membrane, the etching of the sacrificial layer shall exhibit high selectivity properties in order to limit at best deterioration of the upper layers. Current solutions entail the use of inorganic and organic sacrificial layers with corresponding etching solutions exhibiting competitive etching efficiency and selectivity. The decision will depend mostly on the type of targeted applications, favouring III-V and Si-based material for integration in semiconductor technology, while an organic sacrificial layer appears suitable for bio-related perspectives.

### **Accessible 3D shapes: rolling direction and planar design**

We have introduced the principle of the rolled-up nanotechnology applicable to a wide range of materials to achieve the rolling of pre-strained bilayer membranes. We have illustrated the method with typical achievements of epitaxially-grown membranes rolled up into elementary tubular shapes. Although extensively used and praised for its simplicity and geometrical functionalities [35, 36], the tubular shape constitutes a tiny part of the large variety of 3D architectures accessible with the rolled-up microfabrication method. It is noteworthy that the final 3D shape of the microstructure results from an appropriate and predetermined design of the precursor planar template. We denote therefore three major leverages of action on the 2D design which allow to develop *a priori* any targeted 3D architecture: the orientation, the dimensions and finally the overall shape of the planar design.

We first examine the impact of the orientation of a simple planar design, a rectangular strip, on the 3D shape of a self-rolling pre-strained bilayer membrane, following the work in [37]. The pre-strained bifilm consists of two crystalline layers of SiGe and Si materials epitaxially grown successively on top of a SiGe sacrificial layer. As mentioned previously, the key step toward the rolling of a pre-strained bilayer membrane entails the removal of the sacrificial layer which relaxes strains in the membrane and triggers its spontaneous rolling. In crystalline sacrificial layers, the etching of the material exhibits anisotropic behaviour. In other words, the etching rate varies according to the direction of crystalline planes. In particular, for Si and Ge materials, the etching occurs more compliantly, namely requiring minimal energy, in the crystallographic direction  $\langle 100 \rangle$  defined according to Miller indices. Therefore, the planar design organizes in two sets of multiple rectangular strips with prescribed orientation as depicted on Figure 1.6.a). On the left panel, the strips orient both along and perpendicularly to the crystallographic direction  $\langle 100 \rangle$  whereas the strips of the right panel point in the  $\langle 110 \rangle$  direction and perpendicularly. The SEM pictures presented below the planar designs show the resulting rolled-up microstructures obtained after the *under-etching* process. It comes out that the strips along the most compliant direction  $\langle 100 \rangle$  roll naturally into nanorings while the strips along  $\langle 110 \rangle$  form nanocoils. This simple experiment demonstrates the importance of the orientation of the planar design with respect to preferential etching directions defined in the crystal lattice of the sacrificial layer. The orientation of the planar template introduces therefore another degree of freedom for the fabrication of complex 3D forms.

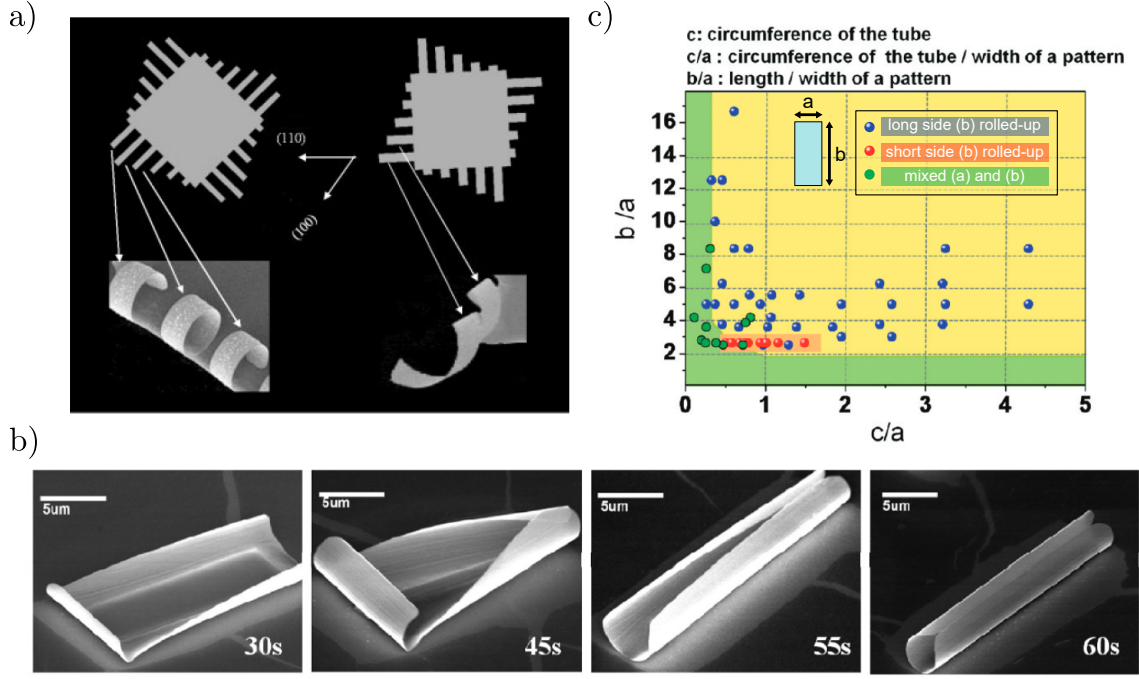


FIGURE 1.6: a) Upper SEM pictures: planar strips of prestrained SiGe-Si membrane oriented along (110) or (100) crystallographic directions. Lower SEM pictures: the strips oriented along (100) (or (110)) direction roll into nanotubes (or nanocoils) upon strain relaxation [37]. b) SEM snapshots showing the self-rolling of a  $10 \times 25 \mu\text{m}^2$  rectangular InGaAs/GaAs membrane after 30, 45, 55 and 60 seconds from the beginning of the isotropic under-etching process. c) Distribution of the rolling direction for rectangular-shaped membrane with dimensions  $b$  and  $a$  (inset drawing) as a function of the ratios  $b/a$  and  $c/a$  where  $c$  designates the circumference of the fabricated microtube. The complete rolling can occur along the short side  $a$  (blue dots), along the long side  $b$  (red dots), or along both sides (green dots). Adapted from [38].

In the same way, Chun *et al.* have investigated [38] the effect of a change in the dimensions of a rectangular planar pattern on the shape of the final rolled-up microstructure. In particular, they analysed the self-rolling of a  $10 \times 25 \mu\text{m}^2$  rectangle of InGaAs/GaAs pre-strained bilayer triggered by the isotropic etching of the underlying AlGaAs sacrificial layer. To this end, they monitored the evolution of the under-etching by generating SEM snapshots of the microstructure, represented on Figure 1.6.b), after 30, 45, 55 and 60 seconds from the beginning of the process. After 30 seconds, the bending of the bilayer initiates on each sides of the rectangle characterized by identical etching rates. However, at 45 seconds, the situation seems to reach a deadlock owing to opposing bending effects perpendicularly to the length and width of the rectangular pattern. The bending perpendicularly to the width finally concedes to enable a complete rolling of the membrane perpendicularly to the length into a  $3 \mu\text{m}$  diameter microtube. We also notice the elastic behaviour of the membrane which returns back to its initial configuration along the width while maintaining the integrity of the final structure. Varying the width  $a$  and the length  $b$  of the rectangular pattern, Chun and its team has also conducted a systematic study on the rolling behaviour of the membrane. The graph of Figure 1.6.c) present the main results of this study as a function of the ratio  $c/a$  and  $b/a$ , where  $c$  denotes the circumference of the final microtube. Blue and red dots indicate that the complete rolling of the membrane occurs perpendicularly to the length and the width (red dots), respectively, of the rectangular pattern. The green dots represent a mixed state for which rolling of the membrane in both directions are observed. The study reveals a predominant rolling of the bilayer membrane along the width. Numerical finite element calculations corroborate the observed trend

which explains by the relaxation of the membrane internal strains over a larger area when the etching occurs along the width. Nevertheless, the few cases of rolling along the length highlights in practice a more complex interplay between energetic considerations, etching kinetics and deformation history of the membrane, at the origin of the rolling direction. Moreover, several strategies have proved their efficiency to ensure the rolling of a pre-strained membrane along a prescribed direction from a rectangular template. Among them, we can mention the shallow etching [39], which involves a preliminary mesa-structuration of the bilayer, the glancing angle deposition (GLAD) [33] which exploits the shadowed material deposition on a tilted substrate and finally the utilization of wrinkled pre-strained membranes [40].

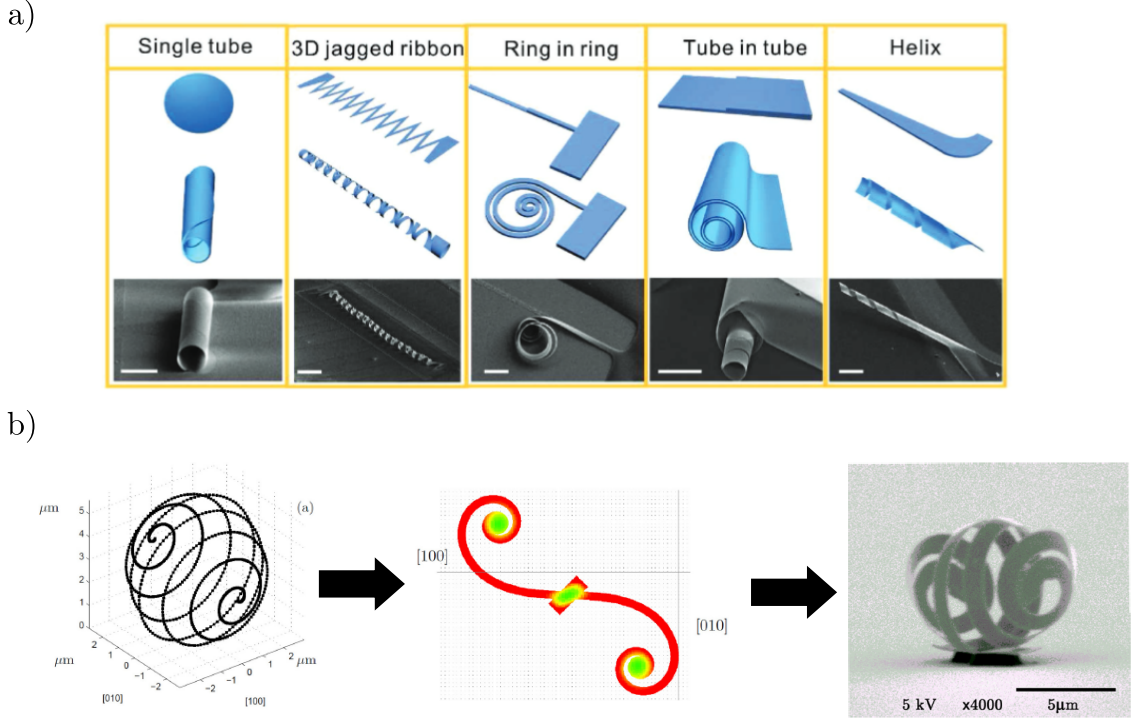


FIGURE 1.7: a) Table of five distinct targeted 3D geometries with the rolled-up nanotechnology. First row: planar templates. Second row: predicted 3D shapes from the previous planar designs. Third row: SEM pictures of 3D-shaped nanocrystalline (NC) diamond membranes after self-rolling according to the planar designs [41]. b) *Inverse etching process* for the production of 3D spiral curved geometry. First plot: discretized 3D spiral curve. Second plot: planar template of the 3D spiral curve calculated with a projection algorithm and oriented with respect to the crystallographic directions  $[100]$  and  $[010]$ . The colour gradient indicates the exposure dose for the lithography process optimized with Monte-Carlo method. SEM picture: 3D spiral microstructure obtained by self-rolling of a prestrained InP-InGaP membrane according to the predicted planar template [42].

The realization of microstructures rolling up into more complex 3D shapes relies therefore essentially on a proper adjustment of the orientation, with respect to potential preferential etching direction, the dimensions and the overall shape of the initial planar membranes. In this way, Tian and al. have managed in [41] the production of microstructures with various 3D shapes by the rolling of pre-strained membranes patterned beforehand according to prescribed planar templates depicted on Figure 1.7.a). The patterning of the nanocrystalline (NC) diamond membranes, exhibiting isotropic material properties, was achieved by lithography and reactive ion etching (RIE) processes. Figure 1.7.a) divides into four columns with illustrations of the predefined 2D pattern on the first row, of the predicted 3D shape on the second row, and the SEM picture of the fabricated microstructure on the third row. In particular, the under-

etching of a circular pattern (first column) results in a traditional tubular form with varying wall thickness along the length of the tube. In the same way, a jagged ribbon (second column) rolls into a spring-like microstructure. An additional patterning of the membrane with RIE process allows for the realization of ribbons with modulated thickness. The relaxation of the membrane leads then to the creation of nested rings or tubes as shown in the third and fourth columns, respectively. Finally, the release of a membrane patterned into an asymmetric ribbon reminding of hockey sticks produces an helical geometry in accordance with numerical predictions. For the latter pattern, the minimisation of the total energy of the structure accounts for the rolling into a helical geometry instead of a tubular shape.

It is worth noticing that the previous results rely on the prediction of the 3D shape of a prescribed planar template of the membrane after stress relaxation. However, it is most likely to reason in the reverse way for the conception of a 3D microdevice. Therefore, the issue could be formulated as: what is the corresponding planar geometry which leads to the construction of a predefined 3D shape after relaxation of the membrane? At INL, in the heteroepitaxy team, we have addressed in [42] the so-called *reverse etching process* for high aspect ratio structures such as ribbons, toward the fabrication of face-to-face chiral spherical mirrors represented by the left 3D curve in Figure 1.7.b). Precisely, we have proposed an algorithm to flatten a discretized polygonal version of the 3D curve onto the design plane. The resulting planar design is depicted on the central plot of Figure 1.7.b). The color gradient indicates the variation of the exposure dose parameter optimized numerically so as to prevent proximity effects during the electron beam lithography. Finally, the fabricated structure, represented on the right SEM picture of Figure 1.7.b), and obtained after the relaxation of a prestrained InAsP/InGaP bilayer according to the simulated planar design, reproduces well the targeted 3D geometry. Alexandre Danescu *et al.* have also introduced in a recent paper [43] a stress-engineering method to fabricate geodesic objects such as the spherical version of the *truncated icosahedron* associated to the  $C_{60}$  fullerene molecule. For the latter structure, geodesic of the sphere replace the straight segments of the original polyhedron. The projection of the parabolic arcs onto tangent planes of the sphere form therefore the precursor planar template. We finally mention that the realization of peculiar 3D architectures, such as conical shapes, requires a non-uniform distribution of the strain in the bilayer membrane according to theoretical and numerical simulations reported in [44].

Lastly, we report another stress-relaxation method developed by other groups to fabricate 3D micro-structures based on the realization of folds connecting the planar design, in the way of Origami planar templates. This technique applies in [45] to the self-assembly of cubic hollow micro-containers. The planar pattern of the targeted cubic form, as schematized in Figure 1.8.a), consists of an cruciform-like assembly of square faces, each of them connected with black-shaded hinges. The self-assembly of the faces relies on the bending of the hinges, namely trilayers of photoresist polymer, Chromium (Cr) and Copper (Cu) materials, which play the role of real folds. The thermal evaporation of successive layers of Cr and Cu material layers forms a prestrained metallic bilayer owing to thermal expansion mismatch and to tensile strains accumulated in the Cr layer during the growth. A photoresist polymer layer grown on top of the metallic bilayer and covering part of the Ni layer acts as motion trigger. Indeed, the heating of the sample softens the photoresist and allows for the relaxation of strains into the metallic bilayer which causes its bending. The thickness of the Cr layer is adjusted to achieve a  $90^\circ$  angle between each faces of the cube. The metallic



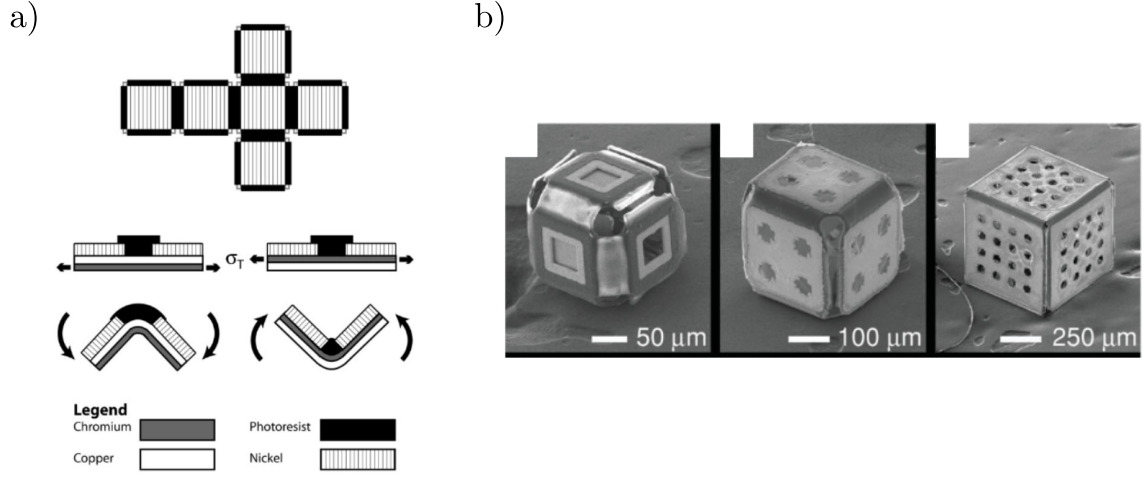


FIGURE 1.8: Fabrication of micro-Origamis. a) Upper drawing: planar template for the production of a 3D cubic microstructure with the rolled-up nanotechnology. Middle drawing: the faces of the cube consists of a Nickel material layer on top of a prestrained Copper/Chromium (Cu/Cr) or Chromium/Copper (Cr/Cu) bilayer. They are connected with photoresist polymer hinges which also maintains their planeness. Lower drawing: the heating of the sample softens the photoresist which triggers downwards or upwards bending of the Cr/Cu bilayer. A proper adjustment of the thickness of the Cr layer enables a  $90^\circ$  angle between faces upon bending. b) SEM pictures of cubic microstructures after bending of the previous planar pattern with three distinct patterns on the faces.

bilayer bends either downwards or upwards depending on the deposition order of Cr and Cu layers as depicted on the last sketch of Figure 1.8.a). The three SEM pictures on Figure 1.8.b) illustrates fabricated hollow cubic microstructures upon relaxation of the previous planar template with  $50 \mu m$ -sized faces. The faces of the cube are lithographically patterned beforehand to functionalize the surface of the 3D micro-objects.

### Multi-function 3D microstructures

Several reviews [19, 30, 46, 47] published in the last decade attest to the material flexibility and the variety of 3D shapes henceforth accessible with the rolled-up nanotechnology. They also measure the full scope of these versatile 3D rolled-up micro-objects through their utilization as multi-functional devices spanning a wide range of domains: microelectronics, biology, energy storage, photonics, among others. To give an insight on the field of applications, we present three different rolled-up systems dedicated to the enhancement of energy storage, the realization of original optical materials and the development of micro-/nano-motors as illustrated on the tree panels of Figure 1.9.



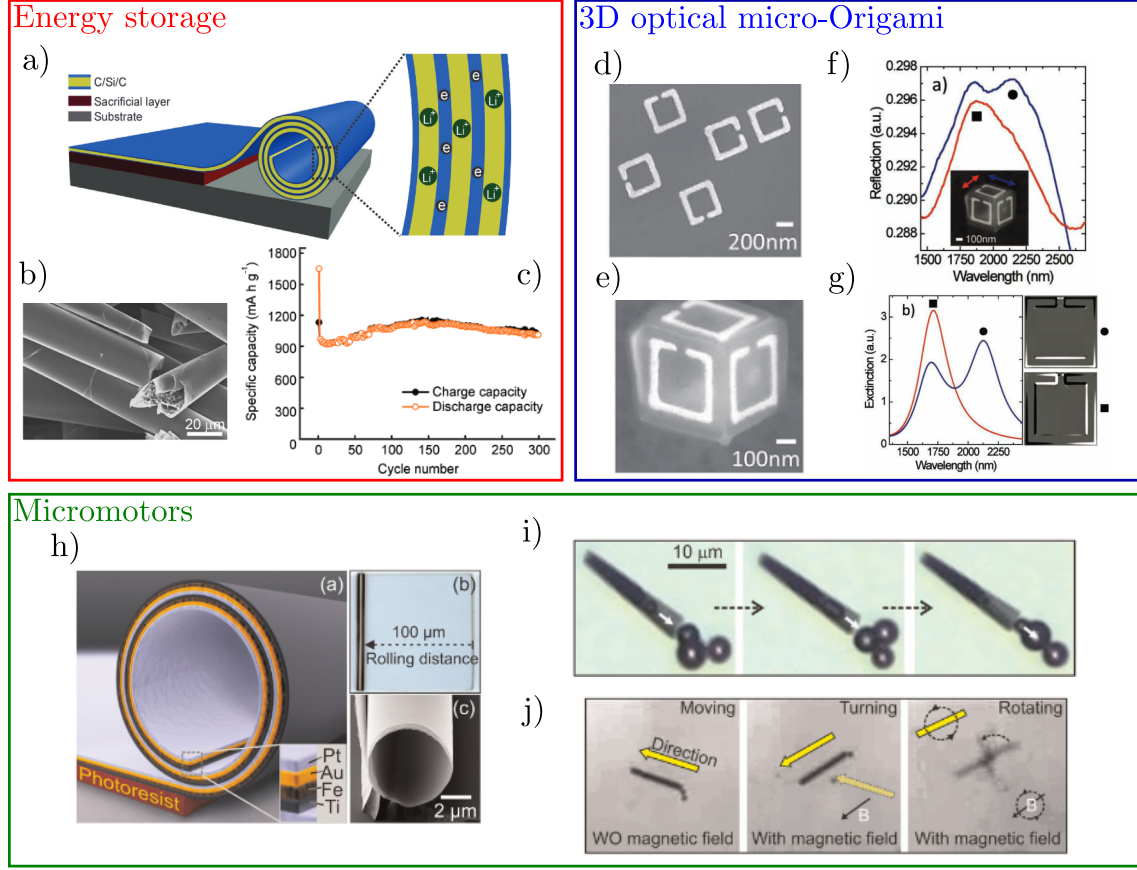


FIGURE 1.9: a) Schematized rolled-up Carbon (C)/Silicon (Si)/Carbon (C) membrane, upon etching of the burried-in sacrificial layer, which serves as the anode of a Lithium-ion battery. b) SEM picture of multiple overlapping rolled-up anodes obtained after one fabrication cycle. c) Evolution of the charge and discharge capacity of the battery as a function of the number of charge/discharge cycles [48]. SEM pictures of d) the planar template of a cubic Origami with Au split-ring resonators (SRR) patterned on  $\text{Al}_2\text{O}_3$  faces; e) a typical cubic microstructure obtained after under-etching process. f) Experimental reflection spectrum of the cubic photonic Origami for incident field polarized along (red curve) or perpendicularly (blue curve) to the gap of the SRR as indicated on the inset SEM picture. g) Simulated extinction spectrum of the cubic photonic Origami for the two polarizations previously mentioned. The lateral maps represent the charge distribution simulated in the SRR at the wavelengths identified by square and disk markers [49]. h) Left sketch: membrane composed of Titanium (Ti), Iron (Fe), Gold (Au) and Platinum (Pt) material layers rolling up after removal of photoresist sacrificial layer. Upper right SEM picture: fabricated microtube after the rolling of the membrane over  $100\ \mu\text{m}$  distance. Lower right SEM picture: SEM perspective view of the microtube. i) Live frames of the motion of the microtube due to thrust force created by catalytic reaction of surrounding  $\text{H}_2\text{O}_2$  solution with the Pt membrane surface and ejected out of the tube. j) Modification of the motion direction of the microtube by the application of a magnetic field to achieve turn and rotations.

The first application deals with the improvement of the performances of Lithium-ion accumulators based on Silicon (Si) anode [48]. Though Si material provides high theoretical performances (estimated to  $4200\ \text{mA.h.g}^{-1}$ ), the battery suffers in reality from capacity retention due to large volume deformation of the Si electrode during charge/discharge cycles. An alternative architecture of the anode electrode was then proposed to circumvent the actual bottleneck. It consists of a trilayer composed of successive Carbon (C), Si and another C layers, rolled up after stress-relaxation through under-etching process into a multi-wall microtube as schematized on Figure 1.9.a). The SEM picture of Figure 1.9.b) shows fabricated electrodes with diameters in the range of  $20\ \mu\text{m}$ . The specific capacity during charge and discharge of the so-formed

Li-ion batterie was then measured for 300 cycles which results in the plot of Figure 1.9.c). We observe that both charge and discharge capacities maintain at a high level until 150 cycles from which they start to reduce very slowly. In particular, we notice that after 300 cycles, the capacity reaches its value obtained after the second cycle. These promising results explain partly by the role of carbon layers which ensure good electronic transport properties while preserving the mechanical integrity of Si layers severely tested during the cycling. The rolled-up shape confers therefore a better stability to the Li-ion battery, hence enhanced performances.

The fabrication of 3D microstructures finds also interest in the realization of 3D micro-objects with tunable optical response. We present thus the creation of 3D optical micro-Origamis based on the self-folding of the planar template illustrated on the SEM picture of Figure 1.9.d) into a cubic form. Each of the four faces in  $\text{Al}_2\text{O}_3$  material of the final cube represented on SEM picture of Figure 1.9.e) are patterned lithographically with gold split-ring resonator (SRR) structures. The simulation and experimental measurement of the optical response of the so-formed optical cubic object gives respectively the two plots depicted on Figure 1.9.f) and g). The red and blue curve indicate the optical response for two polarizations of the field, along and orthogonal to the gap of the SRR, respectively, as represented on the inset image of Figure 1.9.f). We notice that the polarization dependence of the optical spectra predicted in the simulation is retrieved in the experiment. The differences observed in the experimental spectrum stem from the presence of metallic hinges at the edges of each faces of the cube which broaden and shifts the peaks. The two inset pictures in Figure 1.9.g) show the charge distribution of the modes indicated by square and circle black dots which correspond to the first and second order dipole modes, respectively. We finally remark that the SRR constitutes the traditional building block of metamaterials as they exhibit a strong magnetic response. The periodic repetition along the three directions of SRR elements, namely arrays of the previous cubic microstructures, forms a metamaterial which should generate a negative refraction effect. Therefore, we can envision to create such structure to achieve negative refraction at optical frequencies.

The third application relies on the fabrication of micro-/nano-motors, namely micro-/nano-machines capable of moving into complex, generally liquid, media. In particular, micro-/nano-motors with a tubular geometry are referred to as micro-/nano-jets or rockets as they draw inspiration, in terms of shape and propulsion mechanism, from macroscale prototypes. Solovev *et al.* have thus achieved the creation of micro-jets [50] based on the self-rolling of a pre-strained Ti/Fe/Au/Pt multi-layered stack as depicted in Figure 1.9.h). In practice, the multi-layered membrane rolls up over a distance of about  $100\ \mu\text{m}$  into a  $2\ \mu\text{m}$  radius microtube as represented on the SEM pictures of Figure 1.9.h). The catalytic decomposition of the Pt layer into a surrounding hydrogen peroxide ( $\text{H}_2\text{O}_2$ ) solution drives the motion of the microtube. Indeed, the chemical reaction generates bubbles which are ejected at one end of the microtube. The ejection generates a thrust force which propels the microtube in the opposite direction as showed on the time-lapse pictures in Figure 1.9.i). The Fe layer also enables to control the direction of the motion by applying a magnetic field. The pictures of Figure 1.9.j) demonstrate that the direction of the motion follows the orientation of the magnetic field so that turning and rotating movements of the microtube can be achieved. Consequently, such tubular micro-objects can cumulate various functionalities such as cargo collection, transport and delivery, which hold much promise for biomedical drug delivery applications. Finally, the functionalization of the outer layer can also serve to capture and isolate targeted molecules.

### 1.1.2 Optical microcavities with tunable properties

Among the variety of 3D rolled-up architectures, tubular microstructures have drawn a particular interest over the last decades for the realization of low-threshold microlasers and opto-fluidic detection devices.

Indeed, the tubular shape, owing to inherent openness and geometry, acts as a microfluidic channel as it can both host fluidic substances in the hollow part, potentially carrying micro- or nano-sized sensing targets, and transport them towards other devices. Cylindrical geometries with high surface-to-volume ratio also maximizes the area of interaction between the analytes and the sensor surface, so as to achieve high sensitivity and reduce the amount of fluid to inject.

Moreover, the rolled-up nanotechnology enables the simultaneous fabrication of multiple tubular microstructures with controlled geometry (orientation, dimensions, shape) resulting in high-yield and low cost fabrication process compatible with mass production. The tunability of the geometric parameters (diameter, wall thickness) for the realization of micro- and nano-sized tubes allows to miniaturize the sensors and hence to increase their density in devices. Finally, the material flexibility of the rolled-up microfabrication enables the fonctionnalization of the microtube surfaces for label-free detection and its integration on lab-on-chip devices.

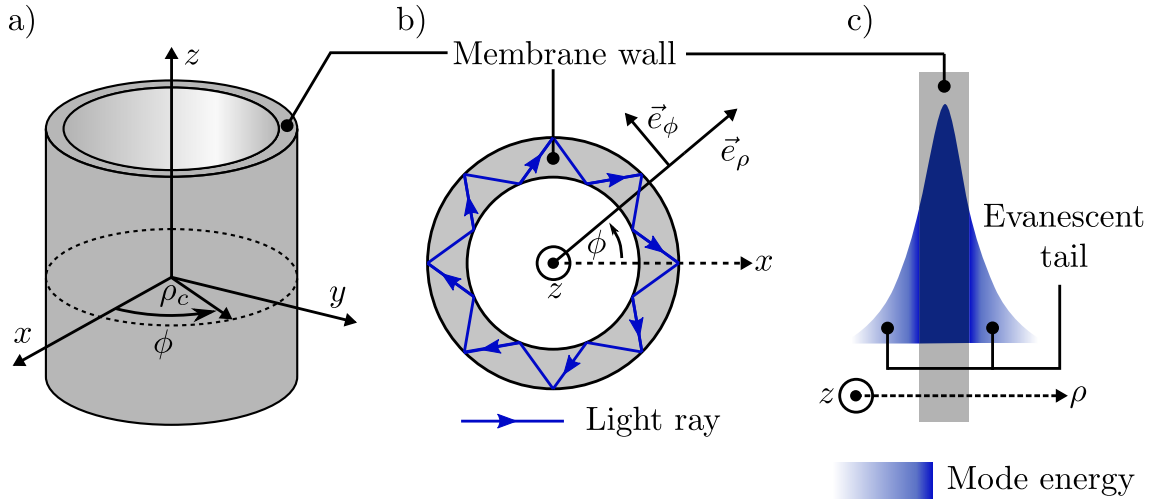


FIGURE 1.10: Schematics of whispering gallery modes (WGM) in tubular cavity. a) A tubular cavity with a radius  $\rho_c$  in the cylindrical coordinate system; b) Cross-section view of the cavity: WGM forms by *total internal reflection* of light rays (blue arrows) at the interface between the membrane wall and the outside of the cavity. c) Spatial distribution of the WGM electromagnetic energy.

From the optical point of view, tubular microstructures have turned to be high-performance cylindrical optical microcavities with tunable properties [51]. As in planar optical ring resonators, the light can be confined in the membrane wall of a microtube of radius  $\rho_c$  as schematized on Figure 1.10.a) by *total internal reflection* occurring at the interface between high and low refractive index media. It forms whispering gallery modes (WGMs) circulating around the microtubes as illustrated on Figure 1.10.b) which satisfy the following condition for constructive interference after round trip:

$$n_{\text{eff}}L = \lambda_m m, \quad (1.22)$$

where  $n_{\text{eff}}$  stands for the effective refractive index of the mode,  $L = 2\pi\rho$  corresponds to the perimeter of the microtube of radius  $\rho$ ,  $\lambda_m$  refers to the vacuum wavelength of the  $m$ -th mode and  $m$  denotes the azimuthal order. The azimuthal order  $m$  indicate the

number of spatial variations of the electromagnetic fields of the mode in the azimuthal direction with respect to the cylindrical coordinate reference. Moreover, though most of the energy of WGM is confined in the membrane wall, the remaining part, also called the *evanescent tail*, leaks out on both sides of the membrane as sketched on Figure 1.10.c). Therefore, the effective index  $n_{\text{eff}}$  takes into account the optical refractive indices of both the cavity membrane wall and the surrounding medium. According to Equation (1.22), we understand that a change in either  $n_{\text{eff}}$  or  $\rho$  ( $L = 2\pi\rho$ ) implies a spectral shift of the modes, which constitutes the detection principle of optical microtubular sensors.

In practice, Kipp *et al.* have first demonstrated [52], at cryogenic temperatures and at near-infrared wavelengths, the presence of WGM in photoluminescence spectra of self-standing rolled-up InGaAs/GaAs microtubes embedded with active InAs quantum dots (QDs). The WGM appear as sharp peaks standing out of the broad QDs luminescence background and strictly polarized along the axis of the microtubes. Furthermore, the spectral positions and spacing of the modes concur with theoretical predictions expressed in Equation (1.22). They also reported an energy shift within 15-19 meV of the modes for a change of 50 nm of the microtube radius (about 4%), which bodes well for high sensitivity detection purposes. However, estimations of the quality factors  $Q$  of the modes ( $Q \simeq 3000$ ) stay well below theoretical computations owing to optical losses at the discontinuities of radii of the spiral-like microtubes. Finally, it is noteworthy that the proper detection of the WGM requires the suspension of the microtubes achieved for instance by a U-shaped planar design of the membrane. Indeed, this operation prevents from optical leakage into the substrate which reduces the lifetime of photons in the cavity and leads to weak and broad peaks hardly detectable. Moreover, the breaking of the rotational symmetry due to the spiral shape of rolled-up microtubes lifts the degeneracy of the two modes travelling around the microtubes in *clockwise* and *counterclockwise* directions [53].

Songmuang *et al.* have also detected WGM in rolled-up  $\text{SiO}_x/\text{Si}$  microtubes at room temperature and in the visible range [54]. They observed inversely proportional dependence between the spectral spacing of WGM and the diameter of microtubes consistently with Equation (1.22) and finite difference simulations. For smaller diameters, hence thinner membrane wall, the evanescent part of WGM widens and the quality factor  $Q$  of the mode diminishes leading to a broad bandwidth of the mode. Bolaños Quiñones *et al.* have reproduced in [55] a similar study with different diameters of microtubes based on rolled-up  $\text{SiO}_2$ - $\text{SiO}$  bilayer membrane resulting from various thickness of the bilayer as plotted in Figure 1.11.a). The photoluminescence spectra of the microtubes labelled (I) to (IV) presented in Figure 1.11.b) confirm that the spacing and the bandwidth of the WGMs increase for smaller diameter of the microtube. We also notice that below a critical diameter located between (I) and (II) specimens, the WGMs peaks exhibit very weak intensities and very large bandwidths so that they become indistinguishable. The same paper demonstrates that the shifting of the WGMs energy can also be achieved by post-fabrication deposition of  $\text{Al}_2\text{O}_3$  material layer which modifies the outer radius of the microtubes.

In addition to azimuthal confinement of light, the specific design of one rolling edge allows to achieve confinement along the axis of rolled-up microtubes. Therefore, Strelow and al. have proved in [56] and [57] the axial confinement of WGMs in semiconducting rolled-up microtubes owing to the parabolic-shaped lobe designed at one rolling edge as sketched on Figure 1.11.c). At fixed azimuthal order  $m$ , the WGMs decomposes in harmonics with increasing energies and localized in the lobe. The evolution of the

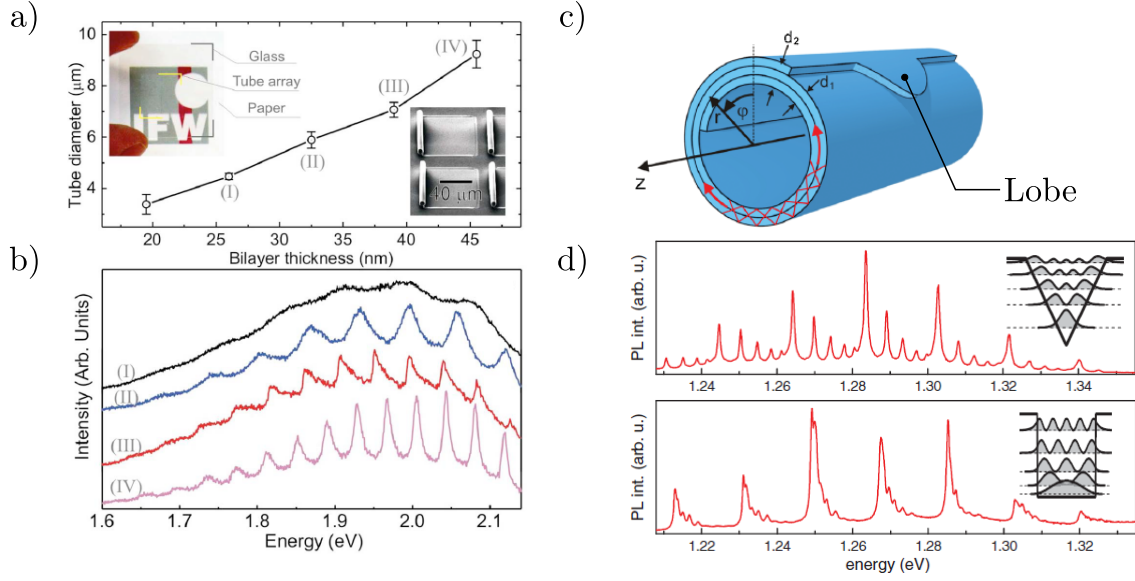


FIGURE 1.11: From [55]: a) Evolution of the diameter of microtubes based on rolled-up SiO<sub>2</sub>-SiO bilayer membrane as a function of the bilayer thickness. Inset picture in upper left corner: macroscopic view of the sample containing arrays of tubes deposited on glass substrate. Inset picture in lower right corner: SEM picture of the fabricated microtubes. b) Micro-photoluminescence spectra of microtubes with diameters labelled (I) to (IV) in the previous plot. c) Schematized rolled-up microtube with a parabolic lobe at one rolling edge. d) PL spectra of rolled-up multi-layered InAlGaAs-InGaAs-AlGaAs-GaAs microtube with triangular (upper plot) and rectangular (lower plot) shape of the lobe. Adapted from [56].

energies and the spatial distribution of the axial modes agree very well with theoretical predictions based on adiabatic approximation and numerical computations. Finally, it is shown the distribution in energies of the axial modes can be tuned by the shape of the lobe as represented on PL spectra of triangular and rectangular lobe in Figure 1.11.d).

A fine tuning of the structural parameters of microtubes allows then to achieve efficient azimuthal and axial confinement of WGMs by minimizing potential sources of optical losses. This enables the generation of high quality factor WGMs, estimated to 5000 in rolled-up microstructures made of low-loss SiO<sub>2</sub> material layer [58]. It has also concretized with the realization of coherent emission in semiconducting microtubes composed of QDs [59] or quantum wells (QWs) [60] layers as the gain medium optically or electrically [61] pumped. Most interestingly, these so-formed microlasers exhibit very low thresholds evaluated to few μW in [62] and [63].

Optical tubular microcavities as microfluidic channels endowed with resonant optical properties described previously have turned out to be ideal candidates for the production of opto-fluidic detection devices. Bernardi and al. have first developed an on-chip refractometer based on a rolled-up Si-SiO<sub>x</sub> microtube as sketched on Figure 1.12.a). An analyte solution is introduced at one end of the microtube and the optical response of the microtube is collected via PL measurements with a laser excitation source. The optical sensing mechanism relies on the variation of the effective refractive index  $n_{\text{eff}}$  of WGM due to the introduction of an analyte solution in the hollow part of the tube. This index variation explains by the interaction between the WGM and the surrounding solution in the evanescent tail which triggers a shift of the energy of the mode according to Equation (1.22). The graph in Figure 1.12.b) presents three different PL spectra recorded at different positions on the microtube where the hollow core is filled with air (blue curve), air and solution (dark curve), and solution (red curve).

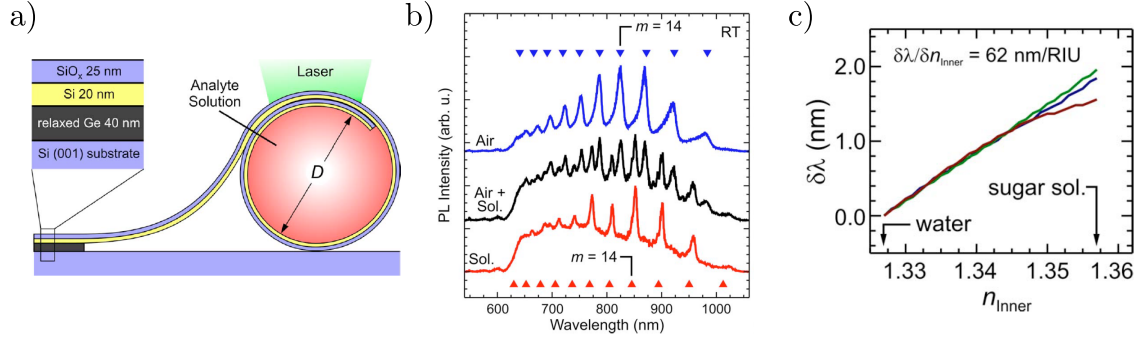


FIGURE 1.12: a) Schematized principle of an optofluidic refractometer based on Si-SiO<sub>x</sub> bilayer rolled up into microtubular shape after etching of underlying Ge layer. The optical response of the microtube is collected via photoluminescence (PL) measurements by laser excitation on the top of the microtube. The analyte solution is introduced at one end of the microtube. b) PL spectra of the microtube filled respectively with air (upper blue curve), with air and the analyte solution (middle dark curve) and with the solution (lower red curve). c) Spectral shifts of the WGM with order  $m = 14$  (blue curve), 15 (green curve) and 16 (red curve) as a function of the refractive index  $n_{\text{Inner}}$  of the hollow core of the tube. Extracted from [64].

We observe a redshift of the WGM peaks when the analyte solution replaces the air as surrounding medium of the tubular microcavity. In the intermediate situation where the tube is filled with air and the solution, we retrieve peaks of both air and solution spectra. The evolution of the spectral shift  $\delta\lambda$  (nm) of three WGMs with  $m = 14, 15$  and 16 as a function of the inner index  $n_{\text{Inner}}$  are plotted as green, red and blue curves, respectively, on Figure 1.12.c). The sensitivity of the device,  $\delta\lambda/\delta n_{\text{Inner}}$ , estimates then to about 62 nm/RIU, where  $n_{\text{Inner}}$  expresses in refractive index units (RIU).

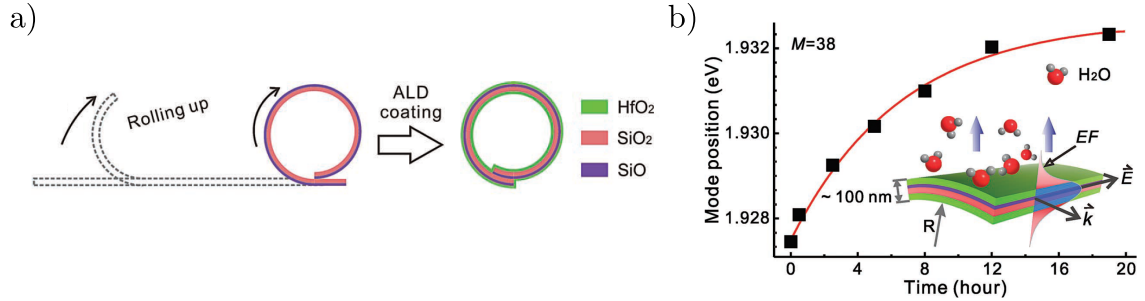


FIGURE 1.13: a) Schematized rolling of SiO-SiO<sub>2</sub> bilayer into a microtube and post-fabrication deposition of HfO<sub>2</sub> layer by atomic layer deposition (ALD). b) Temporal evolution of the energy position of one WGM generated in the previous microtube during the desorption of water molecules on the surface. Extracted from [65].

The axial confinement of the light and the enlargement of the evanescent zone, achieved by a proper shape of the microtube rolling edge and thinner membrane wall, increases the sensitivity up to 80 nm/RIU [66]. Furthermore, the fabrication of size-tunable rolled-up microtubes sensors compatible with Si-based technology enables on-chip integration along with the specific capture and detection of micro- or nano-sized targets carried in biological medium [67]. The reduction of the microchannel cross-section also limits advantageously the required volume of analyte solution down to picoliters. Finally, the functionalization of rolled-up microtubes surfaces leads to specific and label-free detection. In particular, Ma and al. have accomplished in [65] the coating of rolled-up SiO-SiO<sub>2</sub> microtubes with HfO<sub>2</sub> material grown by atomic layer deposition (ALD) as schematized in Figure 1.13.a). This operation increases both the effective refractive index which enhances light confinement in the membrane wall, and



favours adsorption of water molecules owing to higher polarity of  $\text{HfO}_2$  material. They have then performed real-time monitoring of water molecules desorption on the micro-tube surface with photoluminescence measurements of one WGM energy as plotted in Figure 1.13.b). This study provides quantitative information on the dynamic molecular process such as the thickness of the water layer adsorbed onto the microtube surface.

## 1.2 Concept of tubular photon cages

In the previous section, we have introduced the rolled-up nanotechnology as a promising route to produce versatile 3D micro-objects from the self-rolling of planar nanomembranes. In particular, the production of a targeted 3D geometry entails two essential steps preceding the rolling: a specific engineering of the strain in the membrane and the design of the planar template. Following the fabrication scheme inherited from Prinz pioneer works, these two stages are carried out respectively via traditional bottom-up (epitaxial growth) and top-down (lithography and etching) approaches. This leads generally to the production of 3D rolled-up non-structured membranes with controlled dimensions and 3D shapes. The same top-down processes can also be employed to imprint patterns on the initial planar membrane so as to provide the final rolled-up 3D micro-object with additional (new) functionalities. In particular, photonic crystal membranes (PCM), formed by 1D or 2D periodic repetition of subwavelength patterns, accomplish various optical behaviours such as the guiding, the confinement or the routing of light, suitable for a wide range of applications, including waveguides, lasers, or even mirrors. The rolled-up nanotechnology applied to the rolling of PCM provides therefore a new strategy for the creation of 3D photonic micro-objects with original 3D architectures and customized optical functions. This strategy was already approached theoretically in [68] for the production of tubular rolled-up PCM exhibiting a complete photonic bandgap, yet without experimental validation.

In this section, we introduce the concept of photon cages based on the deformation of highly reflective 1D or 2D PCM so as to form 3D photonic micro-resonators capable of confining the light in air and along multiple directions. In particular, we propose the practical realization of tubular-shaped photon cages resulting from the rolling of 2D PCM mirrors.

### 1.2.1 Confining light in low-index media

Traditional routes to manipulate light often occur in high refractive index media. Indeed, in optical fibres, total internal reflection (TIR) ensures the guiding of light exclusively in high index cores encircled by a lower-index cladding. As another example, photonic crystal slabs as 1D or 2D periodic corrugations in a high index material layer, have turned to be choice components for the realization of various optical functionalities such as the trapping [69, 70] or the guiding of light in the membrane. However, in several applications, there has been a high demand to realize the confinement of light in low-index media so as to enhance the light-matter interactions. In particular, a keystone of sensing applications consists in optimizing the overlap between the mode field and the sensing targets. The latter correspond to either micro- or nano-sized targets often carried in low refractive index fluid or to the fluid itself. This optimized interaction serves for instance to the achievement of highest possible sensitivities with minimum required volume of analyte solution.

In particular, for opto-fluidic sensors based on rolled-up tubular optical microcavities described in Section 1.1.2, the sensing mechanism relies on the interaction between WGMs formed inside the membrane wall and the sensing targets hosted in the hollow core of the microtube. Precisely, the overlap between the electromagnetic energy and the analyte solution restricts to the evanescent tail of the WGMs generated at the surface of the microtubes. The optimization of the light-matter interactions supposes therefore the production of high aspect ratio microtubes to compensate the narrow penetration of the mode energy in the air-filled core.

Among existing strategies to tackle the confinement of light in air, two specific guidance schemes have drawn much attention since the end of the 20th century involving the *photonic band gap effect* and the *anti-resonant effect*.

The development of hollow core waveguides based on the *photonic band gap effect* (PBG) originates in the combination of optical fibres and photonic crystal designs. The traditional optical fibre, guiding light within doped silica ( $\text{SiO}_2$ ) core surrounded by a  $\text{SiO}_2$  cladding, has for long time maintained its reputation as unrivalled candidate for low-loss optical transmission, especially at telecom wavelengths. Since its first implementation, improvements in the fabrication technique have increased significantly the purity of silica material, bringing down the attenuation to its current lowest limit. However, remaining optical losses stem from the Rayleigh scattering which occurs inevitably owing to thermal fluctuations in the course of the fabrication process. It is also noteworthy that Rayleigh scattering scales in  $1/\lambda^4$  which impedes the use of conventional optical fibres at lower wavelengths, knowing that losses due to molecules vibrations predominate at higher wavelengths. To cope with this deadlock, researchers have approached the question differently, by proposing to rejuvenate the design of the optical fibre rather than delving into incremental improvements of the traditional architecture. Reversing the original trend, the confinement of light in low-index medium, in air particularly, has thus become a tantalizing method to circumvent optical losses inherent to material properties.

The first practical implementation of the guidance of light in air based on the PBG effect came along with the advent of photonic crystals popularized by the seminal paper of Yablonovitch [71], a milestone in photonics. Indeed, Yeh and Yariv have first laid down theoretical foundations in [72] for the realization of a 1D photonic crystal reflector, or Bragg reflector. Precisely, they showed that a multi-layered stack composed of alternating layers of high and low index material with prescribed thicknesses can constitute an efficient mirror along the direction normal to the stack. The explanation of such optical behaviour relates to the existence of a photonic band gap which prohibits the propagation of light along the stack. Consequently, incident light in air, with frequencies within the gap, gets reflected after striking on the Bragg stack. Facing two Bragg mirrors, we obtain a hollow-core waveguide as proposed and demonstrated experimentally in [73]. Most interestingly, rolling the Bragg mirror stack leads to the creation of a hollow-core fibre as suggested in [74] where light propagates in the air-filled core unlike conventional fibres. Fink *et al.* have thus reported in [75] the first realization of a Bragg fibre obtained by rolling a Bragg mirror composed of 9 alternations of polystyrene ( $n \simeq 1.6$ ) and tellurium ( $n \simeq 4.8$ ) micrometre-thick layers and operating in the infrared regime, near  $10 \mu\text{m}$ . Unfortunately close in appellations, the Bragg fiber should not to be confused with Bragg fiber gratings which incorporate the Bragg mirror in the core of the fiber. Fink's team also demonstrated omnidirectionality of the Bragg mirror wall owing to the extension of the photonic band gap in the reciprocal space of conserved wavevectors. The performances of Bragg fibers as omnidirectional



dielectric reflector were then confirmed in [76] with a stratified structure of alternating polyethylene sulfide (PES) and chalcogenide  $\text{As}_2\text{Se}_3$  glass layers as depicted on the SEM picture of Figure 1.14.a). The close-up SEM view zooms on the multi-layered stack encircled by the PES cladding layer. The high optical index contrast obtained with the two materials,  $\Delta n \simeq 1.25$ , results in a large photonic bandgap centered at around  $3 \mu\text{m}$ . The article also proves the tunability of the position of the bandgap by the control of the thicknesses of the material layers, achieving a shift of the high reflection properties up to  $10 \mu\text{m}$ .

The guidance of light in air via *the photonic band gap effect* was then extended to the fabrication of hollow-core fibres with transverse micro-structures defined according to a prescribed 2D lattice pattern. Cregan *et al.* have thus produced in [77] first specimens of so-called *photonic crystal fibers* (PCFs), also referred as *holey fibres*, based on a triangular lattice of air holes. In practice, the fibre was created by jointing long silica rods together following the triangular lattice pattern as shown on the SEM picture of Figure 1.14.b). The 2D photonic crystal presents a full broad photonic band gap in the dispersion diagram, hence enables omni-directional reflection on the crystal, provided a high air-filling factor of the lattice. Therefore, by omitting seven rods in the centre of the fibre, a defect mode is created which frequency lies within the band gap so that the light can propagate in the air-filled core.

Bragg fibers and PCF represent therefore promising members of the next generation of fibers. Indeed, their ability to guide light in air and their design flexibility make them suitable for a wide variety of applications entailing strong light-matter interactions. However, there is still room for improvement to reach low levels of optical losses recorded with conventional optical fibres, and determined mostly by the quality of the photonic mirror. For both Bragg fibers and PCF, the performances of the mirror enhance with increasing size of the 2D lattice, namely the number of layers and silica rods, at the expense of the final device compactness. Moreover, the fabrication of high-performance PCF remains quite challenging as broad photonic band gap requires high air-filling factor lattice, hence ultra-thin silica rods. Finally, the surface roughness of the silica rods contributes to a significant leakage of the air-core mode due to light scattering phenomenon.

Concurrently, hollow core waveguides based on *anti-resonance effects* have also drawn much attention for their ability to guide light in air-filled cores. We note that the generic term of anti-resonant microstructures actually encompasses multiple hollow-core micro-sized designs. Such structures usually exploit a combination of anti-resonances and inhibited coupling between the hollow core and the cladding modes to realize the propagation of light in air.

A first class of anti-resonant waveguides, anti-resonant reflecting optical waveguides (ARROWs), has been developed in the early works of Duguay and his team [78]. The article explains the strategy to confine light in a  $\text{SiO}_2$  core surrounded by air on one side and layers of Si and  $\text{SiO}_2$  on the other side. At the air- $\text{SiO}_2$  interface, light stays confined in the core through traditional TIR phenomenon. However, at the  $\text{SiO}_2$ -Si- $\text{SiO}_2$  interfaces, the guidance mechanism in the core relies on anti-resonances of the cladding Si and  $\text{SiO}_2$  thin films which both act as Fabry-Pérot etalons in series. More precisely, in between two transmission resonances of one etalon, reflected light waves from the upper and lower boundary interfere constructively. It results in a high reflection signal, namely a low-loss propagation of light in the silica core. Unlike PCF, the high reflection zones span large spectral windows which makes ARROWs suitable for a large range of applications. The same approach was then applied to

the creation of hollow-core ARROWs with the aim of propagating light in air. The SEM picture of Figure 1.14.c) presents a typical architecture of a hollow-core ARROW fabricated and characterized in [79]. Thin layers of  $\text{SiO}_2$  and silicon nitride ( $\text{SiN}$ ) deposited on a Si substrate with predefined thicknesses serve as Fabry-Pérot resonators and encircle a  $12 \times 3.5 \mu\text{m}^2$  rectangular air-filled cross-section to achieve transverse and lateral confinement. We note that the thick cap layer of silica material maintains the mechanical stability of the final waveguide. When coupled with  $785 \text{ nm}$  laser excitation, the hollow-core waveguide exhibits a single mode propagation with optical losses estimated to  $6.5 \text{ dB/cm}$ . The optimization of the design and fabrication processes of ARROWs have been investigated during the last decades [80, 81] in order to lower down the level of losses.

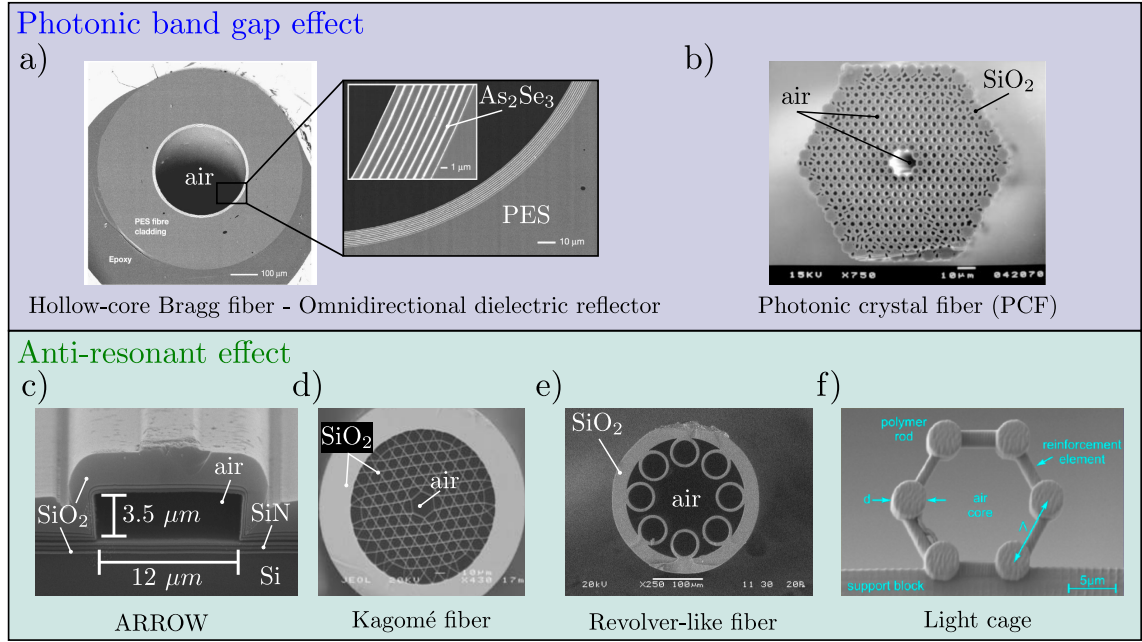


FIGURE 1.14: Hollow-core microdevices exploiting photonic band gap (upper blue-shaded panel) or anti-resonant (lower green-shaded panel) effects for the confinement of light in air. SEM pictures of a) a hollow-core Bragg fiber [76]. Close-up view on the alternating layers of chalcogenide  $\text{As}_2\text{Se}_3$  glass ( $n \simeq 2.8$ ), in bright white, and polyether sulphone (PES) polymer ( $n \simeq 1.55$ ), in light gray, forming the Bragg mirror and surrounding the air core. The cladding is also made of PES material. b) a hollow-core photonic crystal fiber (HC-PCF) [77]: triangular lattice of silica ( $\text{SiO}_2$ ) rods where the air core is formed by omitting seven rods. c) an anti-resonant reflecting optical waveguide (ARROW) [79]: alternating  $\text{SiO}_2$  and silicon nitride ( $\text{SiN}$ ) deposited on Si substrate and surrounding a rectangular air core. A silica cap lies over the multi-layered structure to ensure mechanical stability. d) a silica fiber with kagomé lattice cladding [82]. e) a revolver-like fibre: eight inner non-touching silica capillaries attached to a silica jacket. f) light cage formed by six polymer strands arranged around an hexagonal air core [83];

Anti-resonant hollow-core waveguides with cylindrical geometries and microstructured cladding were also explored as an alternative to PCF to achieve low-loss transmission of light in air. In particular, Kagomé fibers consist of Kagomé lattice silica cladding attached to a thick silica tubular jacket with an air core left in the centre as shown on the SEM image of Figure 1.14.d) extracted from [82]. They exhibit high transmission bands where the light strongly localizes in the hollow core but little in the cladding elements. Wrongly attributed to photonic band gap effects, the guidance mechanism of light in the hollow core actually results from weak interaction between core and cladding modes, in the way of bound states in the continuum (BICs). This

is attested by the low, but nonzero, density of optical states (DOS) simulated numerically for the Kagomé fiber. We note that a reduction of the cladding element thickness blueshifts the operational domain of the fiber. The performances of Kagomé fibers were then further improved by removing competitive resonances emerging in the cladding struts by the design of hypocycloid-shaped hollow cores [84].

Exploiting similar guidance mechanisms, hollow-core revolver-like fibers [85] have also become serious contenders to efficient confinement of light in air. The SEM picture in Figure 1.14.e) depicts a hollow-core revolver-like fiber produced in [86] and composed of eight silica glass capillaries arranged circularly on a silica tubular shelf. The overlap between the core and cladding modes is strongly reduced by avoiding contact between capillaries and by the negative curvature of the hollow core. Advanced versions of hollow-core revolver-like fibers, also known as nested anti-resonant nodeless fibres (NANFs) [87], include a second series of nested capillaries with smaller diameters. The additional air-glass interfaces reinforce the reflection phenomenon and allow then to minimize leakage of the core modes. Such hollow-core have proved to outperform traditional optical fibres by achieving low losses between 600 and 1100 nm [88] in which Rayleigh scattering normally predominates.

We finally mention the very recent development of *light cages* in [83] as assembly of high aspect-ratio polymer strands around an hexagonal shaped hollow core as illustrated on the SEM picture of Figure 1.14.f). Guidance of light in the core again involves anti-resonant effect between core modes and cladding super-modes generated by the coupling between each single strand modes. As compared to previous hollow-core waveguide designs, light cages presents at least three distinctive assets. First, they show diffractionless propagation in the core which covers large and tunable [89] spectral window from the UV to the near-infrared. Second, the openness of the microstructures allow any fluids for direct access to the core, hence to the modal fields. Third, a very high fraction of the core mode energy (above 99.9 %) is contained in the hollow section. For the three reasons above, light cages provide a very attractive platform for the realization of diverse applications such as ultrafast spectroscopy [90], opto-fluidic sensing, non-linear optics, directly integrated onto on-chip devices.

### 1.2.2 Tubular photon cages

At INL, another approach for the confinement of light in air has been developed via the realization of *photon cages*. Photon cages designate 3D photonic micro-resonators resulting from the bending of 1D or 2D planar photonic crystal membrane (PCM) mirrors which aim to confine light in air or low-index media. Among conceivable 3D architectures, we have focused our attention on tubular photon cages obtained consequently by the rolling of PCM mirrors into a cylindrical shape. We have indeed stressed in Section 1.1.2 the advantages of using a tubular geometry which can both act as a micro-channel and optical sensor, highly desirable features for opto-fluidic detection purposes.

We present schematically in Figure 1.15 the production scheme of tubular photon cages which divides into two key steps. In the first stage represented in the left blue panel, 1D (upper drawing) or 2D (lower drawing) planar PCM are properly designed to exhibit high reflective properties symbolized by the yellow-shaded light beam bouncing on the mirror-like microstructures. The second step described in the right red panel involves the folding of the 1D (upper drawing) or 2D (lower drawing) PCM mirror into a cylindrical geometry so as to form 3D hollow photonic microresonators. Indeed, the

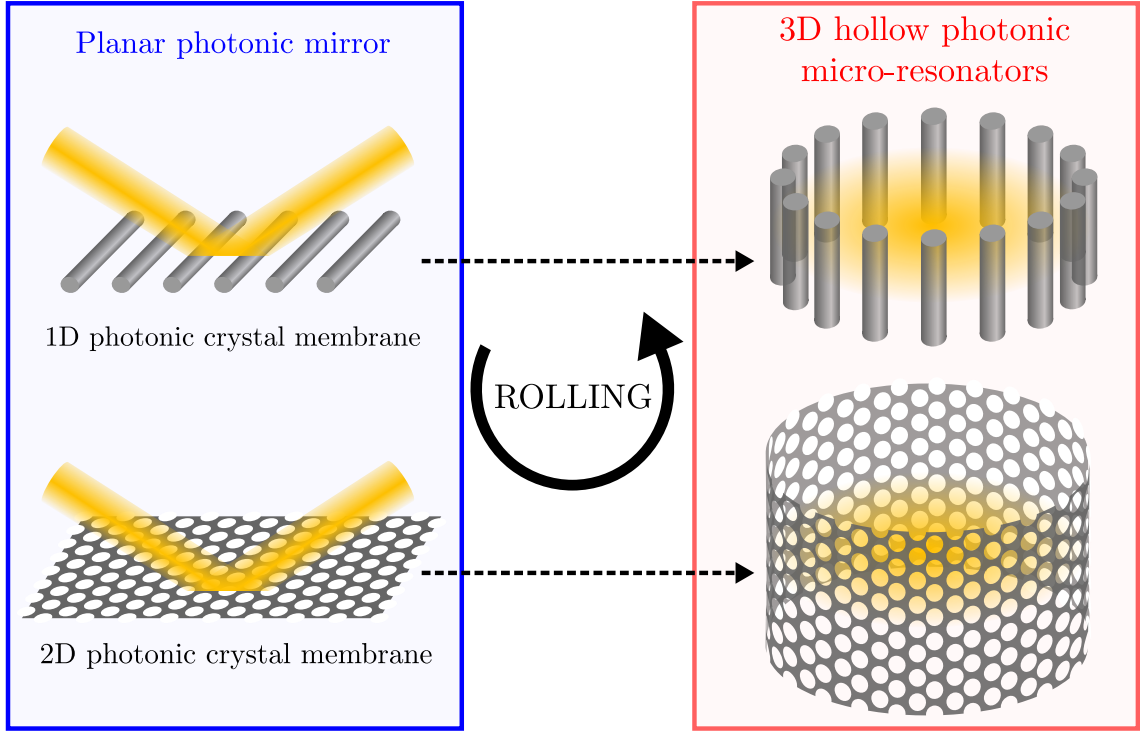


FIGURE 1.15: Schematized production of hollow tubular photon cages. Left panel: planar photonic mirrors consisting of photonic crystal membranes (PCM) with 1D (upper drawing) or 2D (lower drawing) periodicity. Right panel: hollow cylindrical photonic micro-resonators, also called tubular *photon cages*, obtained after rolling the planar 1D (upper drawing) or 2D (lower drawing) PCM mirrors up.

reflecting PCM wall allows to trap the light in the hollow core of the tubular cavity as depicted by the yellow-shaded light halo emerging in the cross-section of the so-formed cylinders.

We highlight the originality of the concept of tubular-shaped photon cages which differ from hollow cylindrical waveguides (PCF and anti-resonant structures) introduced earlier according to the following points:

- Unlike photonic crystal fibers (PCF), the optical response of photon cages results from the optical features of 1D or 2D photonic crystal membranes (PCMs) as monolayer diffracting microstructures. This improves *de facto* the compactness of the final micro-objects.
- Unlike PCF, reflecting properties of the PCM do not rely on the existence of photonic band gaps but rather on the coupling between photonic crystal modes and radiative modes as it will be explained later.
- Contrary to PCF and anti-resonant waveguides, photon cages take advantage of strongly resonant modes in air able to sustain temporally and spatially in long micro-structures. High concentration of light in air is highly desirable for optimized overlap between mode fields and surrounding medium, a keystone in sensing applications.

In the following parts, we delve into the practical conception of tubular photon cages which entails two main steps already mentioned: the production of 1D or 2D PCM mirrors and the rolling of the photonic mirrors into a cylindrical shape. We start by explaining the physical principles at the basis of the high reflection behaviour

observed in 1D or 2D PCM which find various applications in the creation of compact photonic micro-devices. We also provide main guidelines for the design of PCMs with the aim of producing high-performance and broadband photonic mirrors operating at optical frequencies.

### 1.2.3 Photonic crystal membrane mirrors

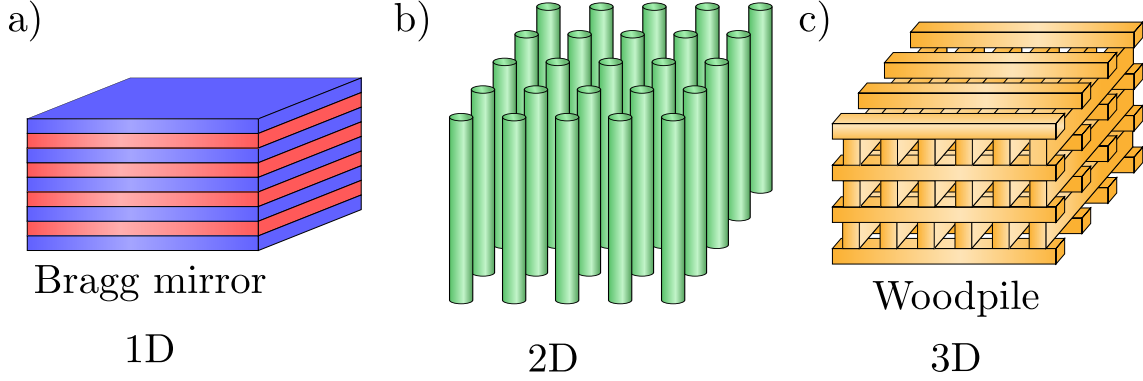


FIGURE 1.16: Typical designs of photonic crystals periodic in one (a), two (b) and three (c) directions. The colours indicate the different dielectric constants of the constitutive materials. The 1D and 3D photonic crystals correspond to a Bragg mirror and a woodpile design, respectively.

Before apprehending the case of photonic crystal membranes (PCM) and in anticipation to further developments of the thesis, we find appropriate to recall some general methodological points in the study of photonic crystals. First of all, we call photonic crystals (PCs) the analogues of solid-state crystals where 1D, 2D or 3D periodic modulations at the wavelength scale of the dielectric constant of a medium replace original atoms and molecules arranged in a lattice system. Concretely, the three drawings of Figure 1.16 illustrate three generic PC designs where the periodicity is achieved in one, two and three directions. The different colours indicate the different dielectric constants of the constitutive materials. We define therefore a PC by specifying its periodicity, its lattice type whenever applicable, and the optical properties of the dielectric medium.

We use Maxwell's equations to describe the propagation of light in any medium. These equations relate temporal and spatial evolutions of electric  $\vec{E}(\vec{r}, t)$  and magnetic  $\vec{H}(\vec{r}, t)$  fields in the medium. In particular, in the absence of free charges and currents, and assuming a linear, homogeneous, transparent and isotropic behaviour for all the constitutive materials of the medium defined by the dielectric constant  $\varepsilon(\vec{r})$  with  $\vec{r}$  the spatial position, Maxwell's equations formulate as:

$$\begin{aligned} \vec{\nabla} \cdot \vec{H}(\vec{r}, t) &= 0, & \vec{\nabla} \times \vec{H}(\vec{r}, t) &= \varepsilon_0 \varepsilon(\vec{r}) \frac{\partial \vec{E}(\vec{r}, t)}{\partial t}, \\ \vec{\nabla} \cdot [\varepsilon(\vec{r}) \vec{E}(\vec{r}, t)] &= 0, & \vec{\nabla} \times \vec{E}(\vec{r}, t) &= -\mu_0 \frac{\partial \vec{H}(\vec{r}, t)}{\partial t}, \end{aligned} \quad (1.23)$$

where  $\varepsilon_0$  and  $\mu_0$  designate the vacuum permittivity and permeability, respectively. Assuming time harmonic fields, namely  $\vec{H}(\vec{r}, t) = \vec{H}(\vec{r}) e^{j\omega t}$  with  $\omega$  the angular frequency, we can decouple the curl equations in the system 1.23 to obtain the following *master equation* for  $\vec{H}(\vec{r})$ :

$$\vec{\nabla} \times \left( \frac{1}{\varepsilon(\vec{r})} \vec{\nabla} \times \vec{H}(\vec{r}) \right) = \left( \frac{\omega}{c} \right)^2 \vec{H}(\vec{r}), \quad (1.24)$$

with  $c = 1/\sqrt{\varepsilon_0\mu_0}$ , the speed of light. We note that we can establish a similar equation for the electric field. Identifying the left term to an operator  $\hat{\Theta}$  acting on  $\vec{H}(\vec{r})$ , the previous equation assimilates to an eigenvalue problem. The resolution of Equation (1.24) consists then in finding all the eigenvalues  $(\omega/c)^2 \geq 0$  and associate eigenvectors  $\vec{H}(\vec{r})$ , also called *modes* of the system. Moreover, we notice that the Hermitian nature of the  $\Theta$  operator ensures the positivity of the eigenvalues.

In the specific case of periodic structures such as PCs, we search for modes in the form of *Bloch waves* defined as:

$$\vec{H}_{\vec{k}}(\vec{r}) = \vec{h}_{\vec{k}}(\vec{r})e^{j\vec{k}\cdot\vec{r}}, \quad (1.25)$$

where the function  $h_{\vec{k}}(\vec{r})$  shares the same periodicity as the PC lattice. In other words the function  $h_{\vec{k}}$  verifies  $h_{\vec{k}}(\vec{r} + \vec{R}) = h_{\vec{k}}(\vec{r})$  for any lattice vector  $\vec{R}$ . The term  $\vec{k}$  with  $\|\vec{k}\| = 2\pi/\lambda$  stands for the wave vector defined in the reciprocal lattice and  $\lambda$ , the wavelength. The resolution of Equation (1.24) in a periodic system finally yields a set of  $n$  eigenvalues  $\omega_n(\vec{k})$ , called photonic *bands* of the system, which dependence in  $\vec{k}$  is referred to as the *dispersion relation*, the *dispersion diagram* or even the *band structure*. We also remark that  $\vec{H}_{\vec{k}}(\vec{r} + \vec{R}) = \vec{H}_{\vec{k}}(\vec{r})$  implies the relation  $\vec{k} \cdot \vec{R} = 2n\pi$  ( $n \in \mathbb{Z}$ ) which defines the lattice vectors in the reciprocal space also called  $\vec{k}$ -space. Most importantly, the modes of the system  $\vec{H}_{\vec{k}}(\vec{r})$  can be completely characterized by their behaviour in the primitive cell of the reciprocal lattice, also known as the *Brillouin zone*.

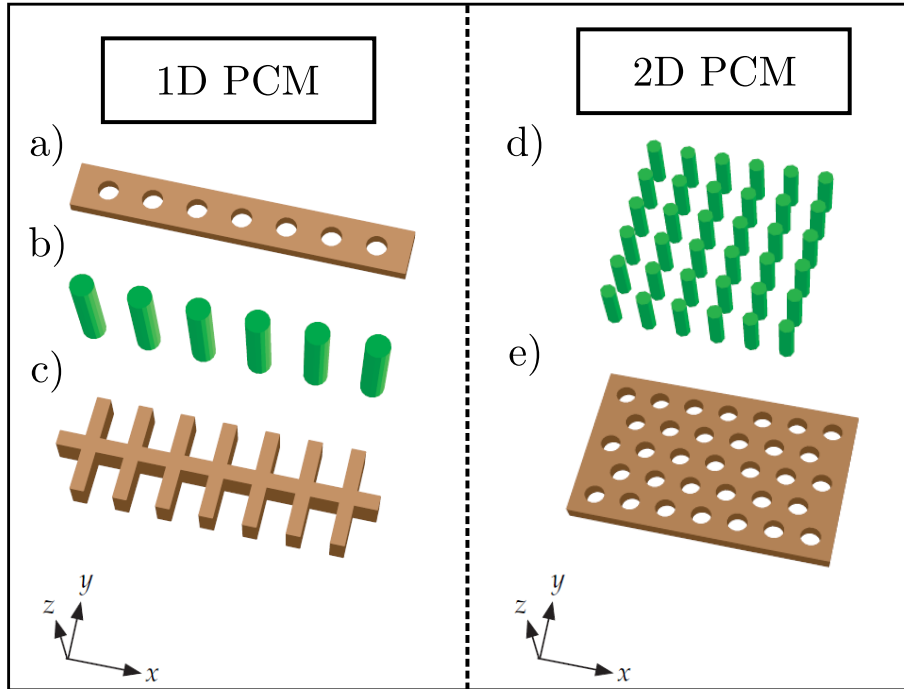


FIGURE 1.17: Photonic crystal membrane (PCM) designs. 1D periodicity: a) air holes in dielectric membrane, b) dielectric pillars, c) fishbone-like grating; 2D periodicity: d) square lattice of dielectric pillars, e) triangular lattice of air holes in a dielectric membrane. Adapted from [91].

For sufficiently high optical index contrast in PC, strong coupling between modes occur and leads to the formation of photonic band gaps (PBGs) visible in the dispersion diagram. Similarly to their electronic counterparts, a PBG delimits a range of frequencies and directions ( $\vec{k}$ ) for which the propagation of light inside the PC is forbidden. In other words, the existence of a PBG traduces into a null density of optical

states (DOS). A complete PBG refers to the extreme case for which the propagation of light is forbidden along all possible directions. The utilization of PBGs of PC microstructures have thus raised much interest toward the harnessing of photons along unique or multiple directions of space. However, though the quest for 3D confinement of light reveals great potential, its implementation with 3D PC showing complete PBG still faces fabrication challenges.

Alternatively, lots of efforts were gathered on the more convenient production of 1D or 2D PC with a finite thickness, also known as photonic crystal membranes (PCM). Possible designs of 1D PCM are presented in Figure 1.17 and consist of a unidimensional periodic assembly of air holes in a dielectric membrane (a), of dielectric rods (b), or of dielectric slits embedded in a fishbone-like architecture (c). Similarly, we construct a 2D PCM by either arranging dielectric pillars (d) or drilling air holes in a dielectric membrane (e) according to a predefined 2D lattice system. The accessibility of PCM designs as compared to 3D PC is explained by the compatibility of their fabrication with standard planar technologies extensively used in the semiconductor industry. Consequently, single-layer PCMs represent ideal building blocks for the creation of versatile integrated photonic devices with a high degree of compactness.

In the field of integrated optics, planar photonic devices usually operate in the waveguide regime which forbids any interaction between guided modes and radiated or free-space modes. In a waveguiding slab, the in-plane confinement of light is achieved via the *index-guiding* effect. In other words, the guidance of the modes results from the vertical optical index distribution in the slab in the way of total internal reflection (TIR) phenomenon. However, this vertical confinement is perfect (partial) for the modes which lie under (above) the light line in the dispersion diagram of the photonic membrane. We illustrate these notions in the case of a PCM as depicted on Figure 1.18 consisting of a 1D periodic assembly, of period  $a$ , of blue-shaded high-optical-index rectangular rods embedded in air. For simplicity, we drew a cross-section view of the PCM supposing that the rods extend infinitely in the remaining in-plane direction. The central plot schematizes the dispersion diagram of the PCM for the first two bands as a function of the in-plane component  $k_{\parallel} = |\vec{k}_{\parallel}|$  of the wavevector along the periodicity. Owing to the optical index contrast, a photonic band gap appears at the edge of the Brillouin zone for  $k_{\parallel} = \pi/a$ . The black dashed line corresponds to the *light line* defined by the equation  $\omega = ck_{\parallel}$  which delimits two principal optical regimes of the photonic membrane:

- the *waveguide* regime (white-shaded zone) for the modes located below the light line also called *guided* modes as they travel in the PCM without interacting with radiated modes. Consequently, the mode identified by a red dot and labelled as number (2) in the diagram pertains to the class of guided modes which only propagate laterally in the PCM as sketched with red arrows on the right panel.
- the *free-space* regime (gray-shaded zone) for the modes lying above the light line also referred to as *surface-addressable* modes or *leaky* modes. In this case, PCM modes can couple resonantly with radiated modes provided that they share identical in-plane components  $k_{\parallel}$  and wavelengths. The resulting modes, such as the green dot mode labelled (2), exhibit a hybrid nature as one part propagates in the PCM (red arrows) while the other radiates in the out-of-plane direction (green arrows) as represented on the left panel.

Toward the realization of integrated photonic circuits, one generally seeks to design photonic building blocks, such as PCMs, which operate in the waveguide regime. In-



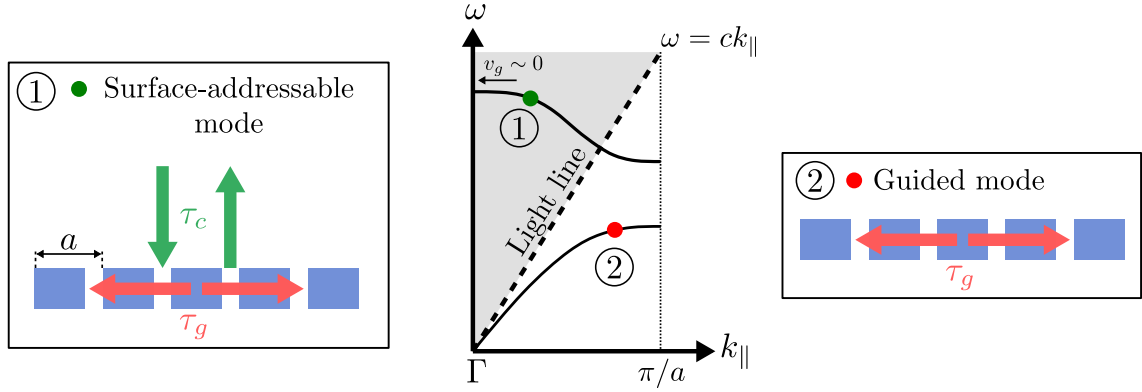


FIGURE 1.18: Schematized dispersion diagram of a 1D photonic crystal membrane (PCM) consisting of an  $a$ -periodic assembly of high-index infinitely long rectangular rods. Two kinds of modes exist according to their position with respect to the light line (black dashed line) of equation  $\omega = ck_{\parallel}$ . The term  $k_{\parallel}$  designates the in-plane component of the wavevector, evolving along the  $\pi/a$ -long part of the 1D Brillouin zone. Surface-addressable modes located above the light line, like mode 1 (green dot), propagate in the PCM with the time constant  $\tau_g$  but they can also couple with radiated modes with the time constant  $\tau_c$ . Conversely, the modes below the light line, like mode 2 (red dot), are guided in the photonic slab as represented on the right panel.

deed, the coupling between guided modes and the radiation continuum hinders proper in-plane guidance as it generates substantial out-of-plane optical losses. However, approaching the issue from a different perspective, we can take advantage of this resonant out-coupling to achieve the control of light in the third (vertical) dimension of planar photonic devices. Moreover, the optimization of the interplay between guided and radiated modes enables tailored optical responses in transmission and reflection of the planar devices. It leads then to the realization of a new class of planar photonic objects addressable in the vertical direction, so-called 2.5D photonic microstructures.

In practice, guided-mode resonances in patterned photonic slab manifest themselves by sharp resonant features in the reflection and transmission spectra. Wang *et al.* have thus proposed a theoretical model [92] to predict the optical properties of 1D PCM with infinite lateral size illuminated at normal and oblique incidence. The model highlights abrupt transitions in the reflection and transmission responses attributed to the diffractive coupling of the PCM guided modes. The article also provides design rules for the production of optical devices with various optical functionalities including optical filters, polarized lasers or even optical switches. In the same way, Astratov *et al.* have investigated in [93] the reflection behaviour of 2D PCM consisting of waveguides patterned with deep air holes. They also reported sharp features in the reflectivity spectrum measured for different guided modes lying above the light line, hence able to couple with free-space modes. Moreover, they showed a great consistency between the positions of the leaky modes in the experimental and numerical band diagrams. It is noteworthy that the strength of the resonance increases as the position of the mode in the band structure gets closer to the high symmetry point  $\Gamma$  where the PCM is shined at normal incidence. We finally mention the works of Pottage *et al.* who approached theoretically in [94] the vertical-cavity surface-emitting resonances produced in AlGaAs-made 2D PCM. The resonances are characterized by high quality factors and thus suitable for the realization of compact vertical emission lasers.

The previous studies have managed to predict the optical properties of PCMs with infinite lateral size. In reality, we need to take into account the finite section of laser beam sources which illuminate the real PCM structures. Using a phenomenological



model, Letartre *et al.* have therefore examined in [95] the impact of the finite lateral size of a 1D PCM on the quality of the surface-addressable modes, also called guided-mode resonances. In the next developments, we consider a 1D PCM illuminated by a laser beam with a finite section  $S$ . Following the above-mentioned model, the bandwidth  $\delta\omega$  of the resonant features expresses, in first approximation, as:

$$\delta\omega \simeq \frac{1}{\tau_c} + \frac{1}{\tau_g}, \quad (1.26)$$

where  $\tau_c$  evaluates the average lifetime of the photons within the illuminated area before reemission into free-space while  $\tau_g$  measures the temporal stay of photons in the illuminated area before escaping laterally across the PCM. The left panel of Figure 1.18 schematizes the hybrid nature of the guided mode with associate coupling rates. Introducing the average group velocity  $V_g$  of the resonant guided mode, the escape lateral time approximates to:

$$\tau_g \simeq \frac{\sqrt{S}}{V_g}. \quad (1.27)$$

Contrary to waveguide applications, we emphasize that lateral optical losses hamper efficient out-of-plane coupling. Indeed, they impede guided modes from interacting with free-space modes and degrade the resonance consequently. We understand then that the optimization of resonant out-coupling requires the longest stay of the guided modes within the illuminated area before escaping laterally, namely  $\tau_g \gg \tau_c$ . Using Equation (1.27), we obtain that the previous condition rewrites as  $V_g \ll \sqrt{S}/\tau_c$  which implies a strong slowdown of guided photons in the PCM. Such situation typically occurs around extrema of dispersion diagrams, such as in  $\Gamma$  where the incident radiation impinges on the PCM at normal incidence. Indeed, around  $\Gamma$ , the dispersion flattens so that the group velocity of guided modes  $V_g = d\omega/dk$  tends to zero. Consequently, the guided modes in question, also called *slow Bloch modes*, become stationnary.

The flattening of the dispersion band near a zero group-velocity point  $P(k_p, \omega_p)$  is characterized by the parabolic approximation:

$$\omega \simeq \omega_p + \frac{1}{2}\alpha\delta k^2, \quad (1.28)$$

where  $\delta k$  evaluates the distance in the  $k$ -space to the extremum and  $\alpha = d^2\omega/dk^2$  corresponds to the second derivative, namely the curvature, of one dispersion band. The expression of the group velocity changes to  $V_g \simeq \alpha\delta k$ . We deduce that the reduction of lateral losses reduces to the minimization of the curvature  $\alpha$  around the extremum of the PCM dispersion. In particular, 1D or 2D PCM characterized by high refractive index contrast exhibit very low curvatures around extrema of their dispersion diagrams, hence achieve efficient lateral confinement of light. We note that these extrema correspond generally to high symmetry points of the PC reciprocal lattice. As mentioned above, the coupling between guided and radiated modes in  $\Gamma$  results in a resonant emission in the out-of-plane (vertical) direction of the PCM. Equivalently, any external radiation hitting the PCM at normal incidence ( $\Gamma$ ) and matching with a guided mode wavelength gets reflected efficiently back into free space<sup>1</sup>. Provided low lateral losses, the spectral characteristics of the resonance, namely its bandwidth  $\delta\omega \sim 1/\tau_c$  and position, are

<sup>1</sup>Bound states in the continuum (BICs) constitute notable exceptions: though lying above the light line, the symmetry properties of those guided modes impede them from coupling to free-space modes. The reflectivity spectrum of the PCM helps to clarify the nature of guided modes above the light line showing either peaks for guided-mode resonance or dips for BICs.

mainly determined by the structural parameters of the PCM: the lattice period, the filling factor and the thickness of the membrane. The possibility to tailor the emission of photons in the third dimension of planar PCM has thus spurred the realization of multiple, versatile and tunable photonic devices.

Guided-mode resonances in PCM have for instance been employed to produce surface-addressable photonic devices. Mouette *et al.* have thus reported in [96] the fabrication of a high quality factor  $Q$  vertical-emission micro-laser based on graphene lattice InP-based PCM embedded with active quantum well layers. The structural parameters of the PCM are first adjusted to achieve the flattest bands possible around  $\Gamma$  at about  $1.5\ \mu\text{m}$ , the central emission wavelength of the active layers. This operation reduces lateral losses in the PCM as explained beforehand and enhances spontaneous emission of the optically pumped active medium in the vertical direction of the PCM. The so-formed micro-laser operates near  $1.5\ \mu\text{m}$  at room temperature and exhibits very low power thresholds, down to  $40\ \mu\text{W}$ , for a given design of the photonic crystal.

The tunability of the properties of PCM guided resonances also shows high interest for the realization of diverse optical functionalities. The works of Ding *et al.* have thus revealed in [97] the high potential of 1D dielectric gratings in the conception of a wide collection of passive optical devices including narrow linewidth bandpass filters, wide-band reflectors, or even polarizers. Most interestingly, the authors have conducted a systematic study to elucidate the influence of the grating profile (symmetries, geometric parameters, index modulations) on the spectral features of the guided-mode resonances (density, linewidth, spectral locations and polarization dependence). Letartre *et al.* have also proposed in [95] design schemes of a new class of switching devices based on the combination of PCM and micro-opto-electro-mechanical systems (MOEMS), so called PC-MOEMS. The PC-MOEMS structures comprise suspended high-index membranes assembled vertically, some of which are laterally patterned to form 1D or 2D PCM. The PCM layers act as highly-efficient reflectors with predetermined spectral characteristics. Switching optical response of the overall device is therefore carried out by the vertical displacement of some of the constitutive layers via electric actuation.

Finally, PCMs have also proved to be ideal candidates for the conception of compact, broadband, non-absorbing and highly-efficient micro-sized mirrors. Mateus *et al.* have thus reported the development of ultra-broadband mirrors [98] based on single-layer 1D high-index gratings. In particular, they have adjusted in [99] the grating structural parameters to achieve a very high reflectivity ( $R > 98.5\%$ ) spanning a  $500\ \text{nm}$ -wide infrared range from  $1.12\ \mu\text{m}$  to  $1.62\ \mu\text{m}$ . It is noteworthy that the high and broadband reflective behaviour was obtained with incident light polarized exclusively along the dielectric slits of the grating. In a similar way, Lousse *et al.* have demonstrated in [100] high-reflective response of 2D PCM based on a square lattice of air holes etched in a high-index dielectric membrane. They have also showed that the mirror-like behaviour was maintained for a wide range of angles of incidence and for both TE (electric field along the membrane plane) and TM (out-of-plane electric field) polarizations unlike polarization-selective 1D PCM mirror. In addition, polarization sensitivity of 2D PCM reflectors can be achieved by breaking the  $90^\circ$ -rotational symmetry of the lattice, namely by modifying the air holes' shape. The works of Boutami *et al.* in [101] also reported a high and broadband reflective response with a controllable polarization dependence of a 2D square lattice of air holes in an InP membrane illuminated at normal incidence. Moreover, they proved that the large bandwidth of the high-reflectivity zone actually originates from the merging of two slow Bloch modes

distinguishable when slightly detuning the PCM geometrical parameters.

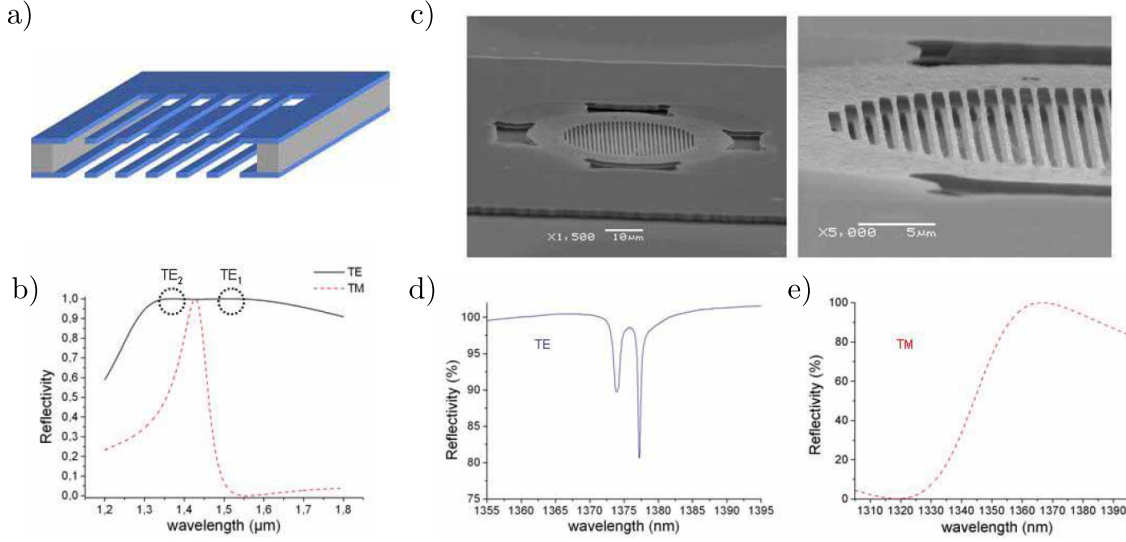


FIGURE 1.19: a) Schematics of an ultra-compact vertical Fabry-Pérot cavity composed of two suspended PCM made of 1D periodic repetition of high-index slits. b) Reflectivity spectra of the cavity for TE and TM polarized light simulated for the cavity design. c) Overall (left picture) and close-up (right picture) SEM views of a vertical cavity obtained after one fabrication cycle. Reflectivity spectra of the fabricated cavity for TE (d) and TM (e) polarized incident light.

High-performance mirrors are needed for instance to produce high-quality factor resonant microcavities. Such cavities serve as building blocks of microlasers characterized by low power thresholds and low linewidths. In the class of vertical cavity surface emitting lasers (VCSELs), two distributed Bragg reflectors (DBRs) are traditionally used to form a Fabry-Pérot resonant cavity which encloses the gain medium. DBRs are multilayers stacks composed of pairs of high and low refractive index material layers. For a fixed number of pairs, the index contrast dictates the DBR reflection performances. Indeed, a high (low) contrast results in a high (low) and broadband (narrow) reflectivity. However, the epitaxial growth of the layers limits the choice of materials and imposes low index modulations. Consequently, an important number of pairs of layers and high fabrication tolerances are required to attain sufficiently high reflectivity of the DBRs, yet at the cost of the size of the overall device [102]. By contrast, exceptional reflective properties of PCM arise in the out-of-plane direction of single-layer dielectric membranes laterally patterned providing more design flexibility and high compactness above all.

PCM mirrors have thus naturally and progressively succeeded conventional bulky DBRs for the fabrication of ultra-compact and low-consumption VCSELs. At INL, Boutami *et al.* have first brought theoretical and experimental proof in [103] of the potential of a tunable hybrid Fabry-Pérot filter combining a top 1D PCM mirror with a bottom 3 layer-thick Bragg reflector. The size of the cavity, adjustable via electrical actuation of some layers, fixes the spectral range of the filter. The device belongs therefore to the generic family of PC-MOEMS introduced previously. Most importantly, it was shown that the single-layer PCM mirror exhibits competitive high reflective behaviour in comparison to the Bragg stack. Furthermore, estimations of the quality factor of the filter were in the same order of magnitude than those assessed with traditional two Bragg reflectors. Nevertheless, the authors stress that the performances of the hybrid filter remains largely underestimated due to structural technical deficiencies of the device including the bending of the PCM layer. The same team has then extended the use

of the hybrid cavity in [104] to create a compact, directive and polarization-selective VCSEL operating at around  $1.5 \mu\text{m}$  at room temperature.

A ultimate version of PCM-based vertical Fabry-Pérot cavity was also implemented by our team in [105] where two 1D PCM mirrors replace the two traditional Bragg reflectors as sketched on Figure 1.19.a). This structure typically belongs to the historical expertise of the nanophotonic team at INL. Its design achieves the highest degree of compactness as compared to conventional DBRs-based vertical cavity and hybrid cavity. A proper adjustment of the PCM geometrical parameters leads to the reflection spectra showed in Figure 1.19.b) for both TE (straight black line) and TM (dashed red line) polarized light at normal incidence. A high and broadband reflectivity zone is observed exclusively for TE polarization. It covers a large spectral range around  $1.5 \mu\text{m}$  which stems from the merging of two slow Bloch modes  $\text{TE}_1$  and  $\text{TE}_2$  identified on the plot. On the contrary, the reflectivity for TM polarization reaches high levels on a narrow spectral interval. The two SEM pictures in Figure 1.19.c) present two perspective views of a cavity sample characterized by the two suspended 1D PCM mirrors. The optical response of the cavity is then measured for TE and TM polarized light at normal incidence which results in the two spectra represented in Figure 1.19.d) and e), respectively. We distinguish two resonant modes for TE polarization which correspond to the first two modes of the Fabry-Pérot cavity formed due to the finite lateral size of the PCM. The fundamental mode detected at the largest wavelength ( $\sim 1.377 \mu\text{m}$ ) gives the narrowest peak and quality factor  $Q$  estimated to 3,000 for a simulated value of 30,000. The difference between numerical and experimental estimations of  $Q$  is attributed to different filling factors of the top and bottom PCM mirrors which also account for the slight spectral shift of the resonant peaks. Conversely, the reflectivity spectrum for TM polarized light displays a very broad resonance shifted toward  $1.32 \mu\text{m}$  for a high reflectivity peak of the PCM mirrors recorded at around  $1.4 \mu\text{m}$ .

#### 1.2.4 Tubular photon cages based on 1D photonic crystal membranes

The first implementation of the concept of tubular photon cages was proposed by our team in [106] via the deformation of a 1D PCM mirror. We recap hereinafter the main results of the study which considers a 1D PCM consisting of a  $\Lambda$ -periodic assembly of silicon (Si) pillars of diameter  $d$  as depicted on the left drawing of Figure 1.20.a). The tubular photon cage is obtained by virtually rolling the 1D PCM reflector. In practice, the pillars are arranged circularly to form a cylindrical cavity with a radius  $\rho_c$  as schematized on the right drawing of 1.20.a). We note that the perimeter of the cylindrical cage corresponds exactly to an integer number of the lattice period  $\Lambda$  so as to produce a seamless hollow tube. In principle, assuming the robustness of the reflection properties of the PCM against bending, the light gets confined in the hollow part of the tubular cavity by reflection onto the PCM mirror wall. The conception of the 1D PCM-based tubular cages divides then into two steps: the design of the planar PCM mirror followed by the simulation of the optical resonant properties of the final cylindrical cavity.

First of all, the structural parameters of the 1D PCM were adjusted to achieve a broadband high reflective behaviour around the operational wavelength of  $1.5 \mu\text{m}$  at normal incidence. Therefore, with the following setting  $\Lambda = 1 \mu\text{m}$  and  $d = 270 \text{ nm}$ , the PCM reflectivity, noted  $R$  and plotted as a blue curve on Figure 1.20.b), maintains above a 99.8 % limit over the spectral interval  $[1.35 - 1.55] \mu\text{m}$ . The high reflective properties are observed only for TE polarization, for which the electric field orients

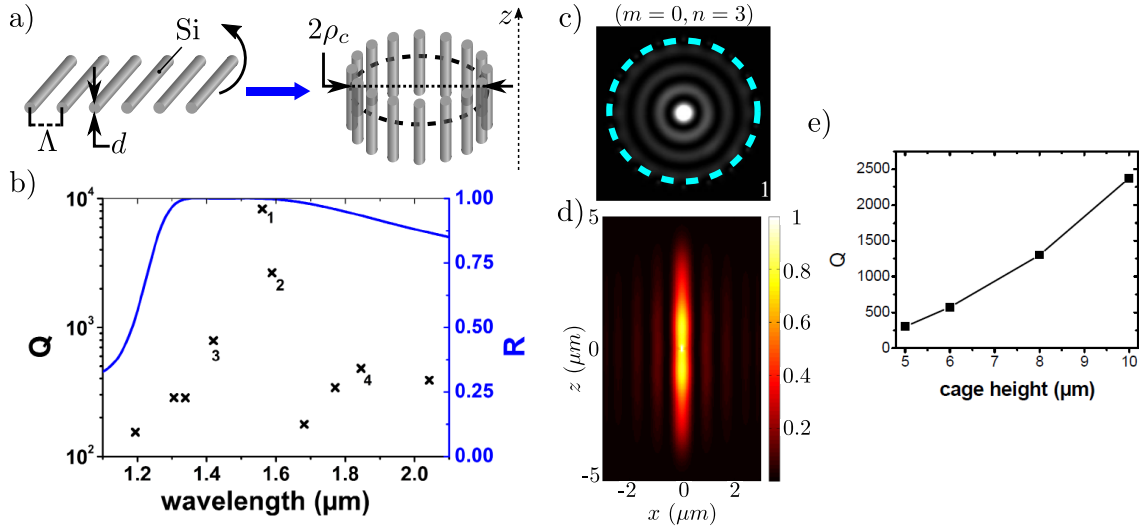


FIGURE 1.20: Implementation of the photon cages concept with 1D PCM mirrors. a)  $\Lambda$ -periodic assembly of silicon (Si) rods with a diameter  $d$  arranged circularly to form a tubular cavity with  $\rho_c$  radius. b) Spectral evolution of the 1D PCM reflectivity for TE polarized light and of the quality factor  $Q$  of some of the resonant modes supported by the final cylindrical cavity. c) Map of the electric field intensity in the cross-section of a 18 pillars cavity (dashed blue contour) at the resonant mode labelled 1 in the previous spectrum and identified as the cylindrical cavity mode  $TE(m=0, n=3)$ . d) Map of the electric field intensity along the axis of a  $10\ \mu\text{m}$ -long cavity of mode  $TE(0,3)$  with null axial order. e) Evolution of the  $Q$  factors of the mode  $TE(0,3)$  as a function of the height of the cavity. Plots b) to e) extracted from [106].

along the bars<sup>2</sup>. Simulations of the optical properties of a cylindrical cavity with 18 infinitely long pillars have then demonstrated the existence of resonant modes in the hollow core. The quality factors  $Q$  of some of those modes are reported in the graph of Figure 1.20.b) with black crosses. The recorded high  $Q$  values not only attest of the strong confinement of light inside the tubular cage but also confirm the robustness of the 1D PCM mirror against bending. Moreover, the spectral evolution of the  $Q$  factors globally follows the reflectivity curve of the planar PCM mirror at normal incidence. The analysis of the modes profiles shows that the resonant modes correspond to cylindrical cavity modes, noted  $TE(m, n)$ , described by two integers  $m$  and  $n$  which define respectively the number of azimuthal and radial antinodes of the fields. The mode labelled "1" in graph b) thus identifies to mode  $TE(0, 3)$  as the map of the electric field intensity over the cavity cross-section in Figure 1.20.c) presents three radial antinodes but no azimuthal antinode. More generally, the family of modes  $TE(0, n)$  shows a high concentration of the electromagnetic energy in the centre of the cavity desirable in sensing, non-linear, or optical trapping applications.

Finally, a strong confinement of the light is also observed along the axis of cylindrical cavities with finite heights as attested in Figure 1.20.d) by the electric intensity map of the mode  $TE(0, 3)$  along a  $10\ \mu\text{m}$ -long cavity. Indeed, the tubular photonic cavity acts in the vertical direction as a Fabry-Pérot resonator due to the impedance mismatch between the inside and the outside regions. However, optical losses in the vertical direction remain predominant and only long cavities, namely long pillars, can afford to preserve the high  $Q$  factors of the modes as indicated on the graph of Figure 1.20.e).

Although theoretically promising, the practical realization of 1D PCM-based photon cages able to confine light in air and along the three directions faces significant tech-

<sup>2</sup>We note that the TE polarization ( $\vec{E} = E_z \vec{e}_z$ ) in the present study corresponds to the TM polarization in the cylindrical cavity model introduced in Chapter 2

nological challenges. Indeed, the fabrication technique based on top-down approaches imposes a limit length of the pillars ( $\sim 10 \mu m$ ) and generates strong sidewall roughness which deteriorates significantly the optical mode properties. As a consequence, the concept of tubular photon cages based on deformed 1D PCM mirrors has not yet found an experimental validation.

### 1.2.5 Tubular photon cages based on 2D photonic crystal membranes

In this work, we propose to realize photon cages based on 2D PCM to overcome most of the trickiest technical and theoretical bottlenecks encountered in the 1D PCM version. First, unlike 1D PCM reflectors, high reflective properties of 2D PCM can be maintained for both TE and TM polarizations which preserves the confinement ability of the final 3D microstructures. Second, the rolled-up nanotechnology offers an ideal platform for the production of rolled-up 2D PCM. Indeed, the technical process integrates the patterning of the membrane into a 2D PCM and the rolling of the membrane with high control and precision on the structural parameters and on the final 3D shape.

Hence, in the first part of this thesis work, we propose to bring the proof of concept of tubular photon cages based on rolled-up 2D PCM mirrors. To address this issue, the following steps has been performed and will be presented in the next chapters:

- the design and optical simulation of the 2D PCM mirror;
- the design and optical simulation of the rolled-up PCM cavity;
- the fabrication of the rolled-up PCM cavity following the rolled-up nanotechnology processes;
- the optical characterization and the demonstration of the 3D confinement of light inside the tubular cavity;

## 1.3 Photonic crystal analogues of solid-states structures

In the previous section, we have shown a typical combination of a photonic crystal design showing high reflection properties with a rolled-up tubular geometry for the production of 3D hollow optical micro-resonators. However, other photonic crystal designs can be chosen to endow the final 3D photonic micro-objects with customized optical functionalities. In particular, the honeycomb pattern has a special status as it is the only lattice to be encountered in natural structures such as graphene. Graphene has drawn attention due its outstanding properties in terms of electronic transport and mechanical flexibility, among others. In a similar way, derivative of graphene, such as graphene ribbons and carbon nanotubes (rolled-up graphene) have also showed much interest due to their peculiar electronic and topological properties. In this thesis, we intend to explore the analogies between the electronic and topological properties of graphene and its derivates, and the optical and topological properties of their photonic crystal analogues as summarized in In Figure 1.21.

In this section, we will first briefly review the interesting properties of the electronic dispersion relations of graphene and carbon nanotubes. To apprehend the topological properties of these structures, we will then introduce some notions of topology including the definitions of important quantities such as the Berry phase and the Chern number in the case of the quantum Hall effect in a 2D gas of electrons. This will allow us then

to specify the concepts of edge states and bulk-edge correspondence. We will finally show how we can take advantage of these effects in photonics and more specifically in the framework of this thesis.

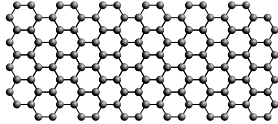
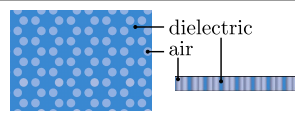
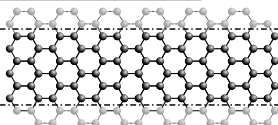
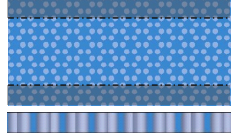
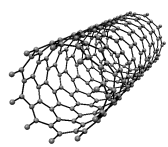
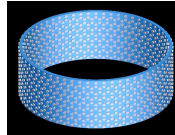
Solid-state		Photonic crystal domain	
Structure	Model/properties	Model/properties	Structure
<b>Graphene</b> 	<i>Tight-binding model</i> ▶ Energy bands ▶ Wavefunctions	<i>Numeric simulations</i> ▶ Energy bands ▶ Modes' distributions	<b>Honeycomb lattice (HC-PCM) photonic crystal membrane</b> 
<b>Graphene ribbons</b> 	<i>Tight-binding model</i> ▶ Energy bands <i>1D topological system</i> ▶ Topology	<i>Numeric simulations</i> ▶ Energy bands ▶ Topology	<b>Ribbons of HC-PCM</b> 
<b>Carbon nanotubes (CNTs)</b> 	<i>Zone-folding method</i> ▶ Energy bands <i>1D topological system</i> ▶ Topology	<i>Numeric simulations</i> ▶ Energy bands ▶ Topology	<b>Rolled-up HC-PCM</b> 

FIGURE 1.21: Summary of the structures and models used to describe the properties of solid-state graphene, graphene ribbons and carbon nanotubes on the left panel and the their analogues in the class of photonic crystals, honeycomb lattice photonic crystal membrane (HC-PCM), ribbons of HC-PCM and rolled-up HC-PCM on the right panel.

### 1.3.1 Electronic dispersions of graphene and carbon nanotubes

#### Graphene

Graphene is the name given for a single planar layer of carbon atoms arranged according to a honeycomb lattice as depicted in Figure 1.22.a). It constitutes the building material of other allotropes of carbon, including fullerenes, carbon nanotubes and graphite evolving along 0, 1 and 3 dimensions of space represented in 1.22.a). Long considered a pure theoretical material, graphene has come into the spotlight of condensed matter physics when first produced and characterized in 2004 by Geim and Novoselov [107]. The latter seminal works, awarded by the 2010 Nobel Prize, have notably reported the exceptional mobility (up to  $10^5 \text{ cm}^2 \cdot (\text{V} \cdot \text{s})^{-1}$ ) of charge carriers at room temperature, revealing the potential of graphene in micro-electronics.

By contrast to its rather recent experimental evidence, the description of graphene electronic structure dates back to 1947 by Wallace [108] as intermediary result to approach graphite band structure. Indeed, at that time, graphene only served as academic material as it was not presumed to exist owing to thermodynamical unstability predicted for 2D materials [109]. Graphene peculiar electronic properties originate from the interaction between electrons moving around carbon atoms and the periodic potential created across the honeycomb crystallographic system. We summarize below the main features of graphene electronic band structure obtained through the tight-binding approach. A detailed description of the tight-binding model and its application to derive graphene electronic structure will be the subject of the first developpements of Chapter 5. The honeycomb lattice schematized in 1.22.b) consists of two sublattices A



and B translated by linear combination of lattice vectors ( $\vec{a}_1, \vec{a}_2$ ). From another point of view, the honeycomb system corresponds to a triangular lattices of lattice vectors ( $\vec{a}_1, \vec{a}_2$ ) applied to the basis of sublattices A and B. The associate reciprocal lattice forms a triangular lattice of lattice basis ( $\vec{b}_1, \vec{b}_2$ ) with a primitive unit cell (green-shaded zone) referred to as the First Brillouin zone (FBZ) delimited by high-symmetry vertices  $\Gamma, K, K'$  and M.

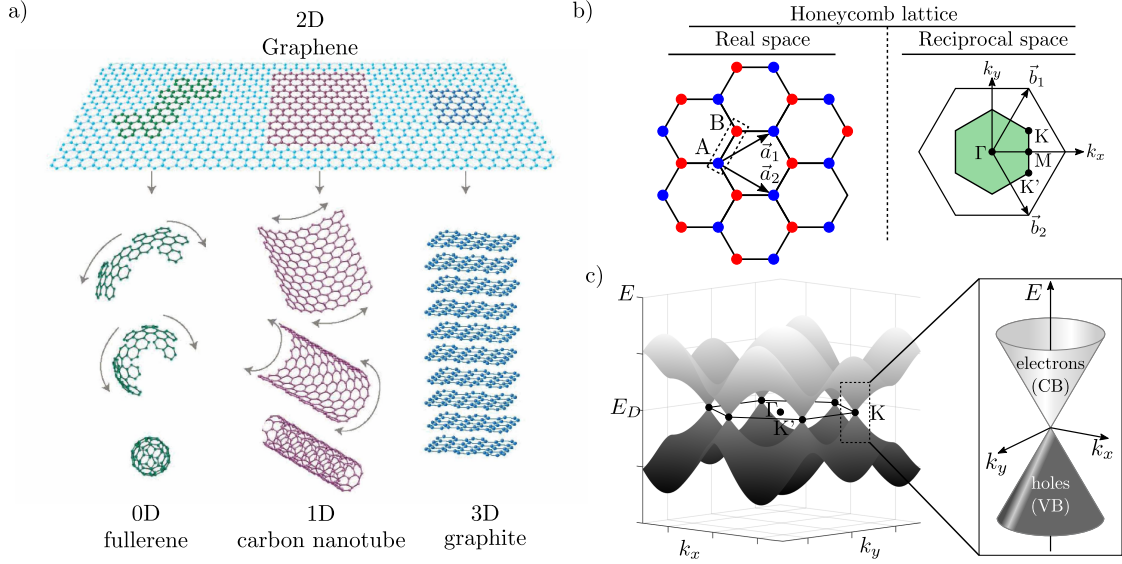


FIGURE 1.22: a) Allotropes of carbons with zero (fullerene), one (carbon nanotubes), two (graphene) and three (graphite) dimensions. Annotated version of [107] b) Honeycomb lattice crystallographic system in real and reciprocal space. c) Graphene energy band structure plotted in the first Brillouin zone delimited by high-symmetry points K and K'. Close-up view: conical dispersion around the K point.

The tight-binding approach applied to electrons hopping to nearest neighbours leads to the low energy band dispersion plotted in Figure 1.22.c) in the FBZ. We note that this model provides an correct reproduction of graphene band structure only over a restricted range of momentum  $\vec{k}$  close to the Dirac points introduced below [110]. A more accurate description would include hopping of electrons to second and third nearest neighbours. The originality of graphene electronic structure relies on two features revealed by the modelled bands. First, conduction and valence bands, noted CB and VB, touch at the Fermi level at high-symmetry points K and K' of the FBZ. Therefore, graphene can be considered both as a zero-overlap semi-metal (zero density of states in K and K') and a zero-gap semiconductor (band crossing). Second, the energy dispersion evolves linearly around K and K' as depicted on the close-up conical section around K point in Figure 1.22.c). Indeed, a first order development of the dispersion relation around K (equivalently K') at  $\vec{k} = \vec{\Gamma K} + \delta\vec{k}$ ,  $|\delta\vec{k}| \ll |\vec{\Gamma K}|$ , expresses as:

$$E_{\pm}(\delta\vec{k}) = \pm \hbar v_F |\delta\vec{k}|, \quad (1.29)$$

where  $E_{\pm}$  designates upper and lower energy bands and  $v_F$  refers to the Fermi velocity evaluating to about  $10^6 \text{ m.s}^{-1}$  for graphene. We recognize a typical form of Dirac's equation describing massless relativist particles. Electrons in the honeycomb lattice mimic relativist particles with zero-rest mass and an effective speed of light  $v_F \sim c/300$  and  $c$  the speed of light in vacuum. The so-formed quasiparticles are then called massless Dirac fermions while K, K' points and the conical dispersion are referred



to as the Dirac points and Dirac cone, respectively. The original dispersion relation reported confers therefore graphene with exceptional electronic transport properties, holding much interest for the production of high performance microelectronic devices. We also mention that graphene provides a choice material platform to investigate quantum electrodynamics (QED) phenomena driven by the Dirac's relativist behaviour of the charge carriers, including fractional quantum Hall effect (QHE) [111] and Klein tunneling effect [112, 113].

### Carbon nanotubes

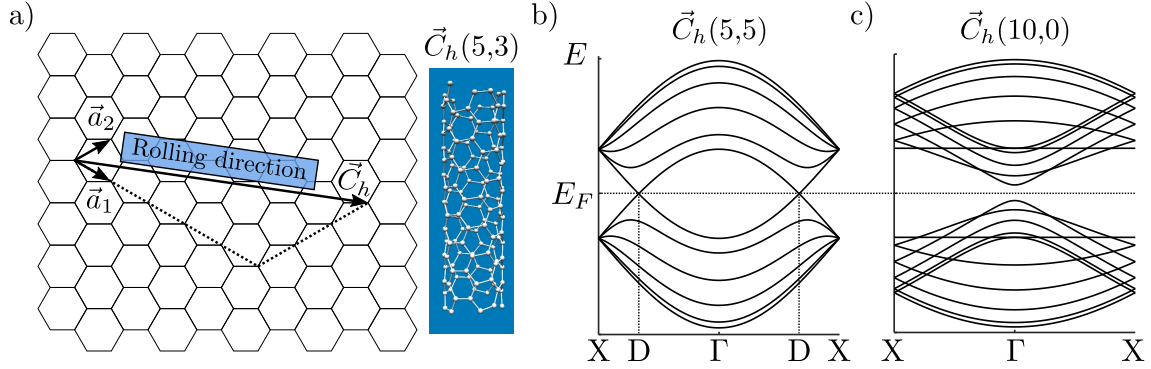


FIGURE 1.23: a) Schematics: representation of the chiral vector  $\vec{C}_h = 5\vec{a}_1 + 3\vec{a}_2$  in the graphene honeycomb lattice. Picture: illustration of the carbon nanotube (CNT) obtained after rolling a graphene sheet along  $\vec{C}_h$ . b) Energy dispersion diagrams of CNTs with chiralities (5,5) and (10,0) calculated along the 1D Brillouin zones X- $\Gamma$ -X with the zone-folding approach.

Carbon nanotubes (CNTs) consist of graphene sheets rolled up into hollow cylinders with nanometric diameter and micrometric length. The first realization of CNTs was reported by Iijima in 1991 [114] using arc-discharge evaporation method. The grown CNTs comprised coaxial rolled-up graphene tubes in number from 2 to 50, so called multi-walled carbon nanotubes (MWCNTs) by contrast with single-walled carbon nanotubes (SWCNTs). The direction of rolling of the graphene sheet, known as the *chirality*, is determined by the *chiral vector*  $\vec{C}_h = m\vec{a}_1 + n\vec{a}_2$  defined by its coordinates  $(m, n)$ , called the *chiral indices*, in graphene sheet basis  $(\vec{a}_1, \vec{a}_2)$ . In the following, we adopt the notation  $\vec{C}_h(m, n)$  for the chiral vector or the chirality of the CNTs equivalently. We illustrate in Figure 1.23.a) the rolling of a graphene sheet along  $\vec{C}_h(5, 3)$  drawn on the honeycomb lattice, into the tube depicted on the right picture. Specific configurations  $(m, m)$  and  $(m, 0)$  correspond to armchair and zig-zag nanotubes, respectively, exhibiting mirror symmetry with respect to any plane containing the tube's axis. The chirality is an essential parameter in the description of CNTs as it not only fixes the tubes' geometry, including their diameter  $d_t = |\vec{C}_h|/\pi$ , but also dictates most of their physical properties, including their electronic and topological nature.

Electronic properties of CNTs can be derived, in first approximation, from graphene electronic structure using the zone-folding approach detailed in Chapter 5 following the classical development in [115]. We highlight below the main steps and features of the model, considering tubes with infinite length and large curvature. Supposing the rolling of a graphene sheet into a seamless tube, periodic boundary conditions apply along the circumferential direction. It implies the quantization of the orthoradial component of the momentum, noted  $k_\perp$ , to verify the phase matching condition after one circulation of the electronic waves around the tube. Conversely, due to the translation symmetry

along the tubes' axis, the axial component of the momentum, noted  $k_{\parallel}$ , takes continuous values. In the  $\vec{k}$ -space, the periodic boundary conditions manifest by  $k_{\perp}$ -lines located at the quantized values of  $k_{\perp}$  oriented along  $k_{\parallel}$  directions, coinciding with the tube axis. Moreover, the number of lines and their spacing depend on the tube chirality.

In the zone-folding approach, we construct a CNT's band structure by superimposing sections of graphene band structure along the  $k_{\perp}$ -lines, so called *cutting lines*, over graphene Brillouin zone. In particular, for a given chirality, the CNT will behave as a metal if one of the sections contains a Dirac point. Therefore, the tube's band structure will present a band crossing at the Fermi level ( $E = E_F$ ). Indeed, we observe such a crossing on armchair  $\vec{C}_h(5, 5)$  tubes' energy dispersion plotted in Figure 1.23.b) along the  $\Gamma$ -X Brillouin zone parallel to the tube's axis. We also draw the attention on the tunability of the band crossing position along the  $\vec{k}$ -path depending on the tube's chirality. Therefore, we find a band intersection for armchair  $\vec{C}_h(5, 5)$  tubes in between  $\Gamma$  and X symmetry points as inferred from the reading of Figure 1.23.b), whereas the crossing lies in  $\Gamma$  for metallic zig-zag  $\vec{C}_h(3, 0)$  tubes, for instance. On the contrary, a band gap opens at the Fermi level when no cutting lines intersect with any Dirac point, conferring semi-conducting properties to the CNT as revealed, for instance, on the band structure of zig-zag tubes  $\vec{C}_h(10, 0)$  in Figure 1.23.c). Another important result concerning semi-conducting CNTs demonstrates the dependence of the band gap width upon the inverse of their diameter  $d_t$ .

In comparison to *ab initio* calculations, zone folding provides reliable estimations of energy dispersion of CNTs with large diameters, typically above 1.5 nm [116]. For diameters between 0.5 and 1 nm, the method still manages to predict correctly the electronic behaviour (metallic or semi-conducting) of the tubes though it overestimates energy levels. However, below 1 nm-diameter, the zone-folding model fails completely to reproduce CNTs' energy diagrams, handing over to *ab initio* results. Indeed, for these diameters, curvature effects can be no more neglected as they affect the lattice structural properties in modifying angles and distances between atoms and allowing hybridization between in-plane ( $\sigma$ ) and out-of-plane ( $\pi$ ) electronic orbitals. Nevertheless, the zone-folding remains a powerful tool showing tremendous efficiency by giving quick calculations of band structures of large nanotubes, irrespective to the number of carbon atoms.

Apart from the interesting dispersion properties, graphene [117], graphene ribbons and carbon nanotubes have also raised a significant interest owing to their topological potential. In particular, considering SWNTs as 1D topological systems, Okuyama *et al.* have established in [118] a topological classification of the tubes as a function of their chirality. It comes out from this study that almost every SWNTs exhibit topological properties characterized by the emergence of edge states at the two ends of the tubes, except for armchair specimens and the chirality  $\vec{C}_h(n, m)$  verifying  $n = m + 1$ .

To get a better insight on the potential of these topological properties, we will introduce in the following part some of the general notions, quantities, and models involved when dealing with topology in physics. In particular, these concepts will be useful to apprehend the topological properties of graphene ribbons and carbon nanotubes developed in **Chapter V**.

### 1.3.2 Topology in physics: introduction to concepts and models

#### Topology formalism

Originally, topology is a branch of mathematics which studies the invariance of objects' geometrical properties under continuous deformation. A classical example illustrated in Figure 1.24 shows that a sphere and a spoon, though characterized by distinct geometries, belong to the same topological class. Indeed, there exists a continuous deformation implying bending, stretching or compression, for instance, which allows transforming one structure into the other. Similarly, a torus and coffee cup, or a double torus and tea pot share identical topologies. On the contrary, turning a sphere into a torus requires discontinuous deformation including cutting, tearing or attachment so that the two objects present distinct topologies.

Mathematically, we characterize different topologies with integers called *topological invariants* which are preserved under arbitrary continuous deformations of the systems. In the previous example, the topological invariant is the genus number  $g$  which defines the number of holes within closed surfaces. Objects sharing the same topological invariant are said *topologically equivalent*. Moreover, we call *topological transition*, the transition between objects of distinct topological invariants. We emphasize that topological invariants, including the genus number, define global and not local properties (local curvature) of the systems though both are connected via the Gauss-Bonnet theorem:

$$\frac{1}{2\pi} \int_S \mathcal{K} dS = 2(1 - g), \quad (1.30)$$

where the genus number  $g$  directly relates to integral of the Gauss curvature  $\mathcal{K}$  (local property) of closed surfaces  $S$ .

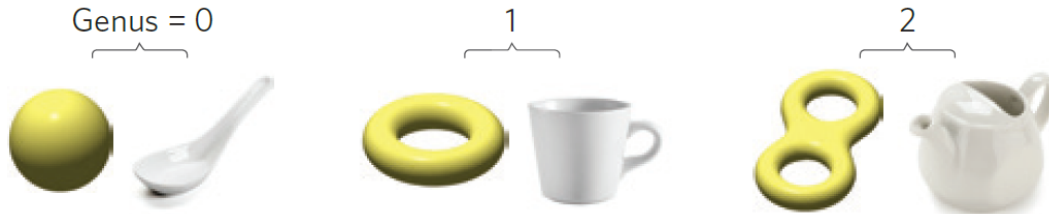


FIGURE 1.24: Six objects classified in three pairs of topologies characterized by distinct genus numbers corresponding to the number of holes of the objects. Adapted from [119].

#### Quantum Hall effect: introduction to the Berry phase and Chern number

In solid-state physics, we traditionally determine the electronic behaviour of a solid material, being either metallic, insulating or semiconducting, by the reading of its energy band structure. However, beyond the energy dispersion, the *geometrical* properties of the electronic states on the bands along the momentum space can also influence the electronic properties of the material. More precisely, these geometrical properties, encoded in the *Berry phase* [120], are associated to a topological invariant characterizing each of the band. We illustrate this concept below, in the framework of the quantum Hall effect, and define the topological quantities that are the Berry phase and the Chern number. We may consult, for instance, Dalibard's lecture notes available in [121], for a detailed development on the Berry phase expression.

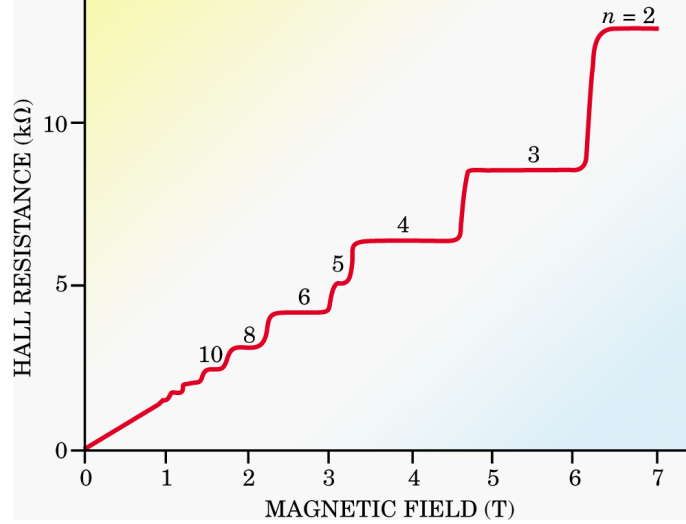


FIGURE 1.25: Quantum Hall effect (QHE). Evolution of the Hall resistance in a 2D gas of electrons at very low temperature as a function of the norm of the out-of-plane magnetic field. For high values of the magnetic field, the Hall resistance increases in a steplike way with plateaus at integral values of the fine-structure constant  $e^2/h$ . Adapted from [122].

The first historical connection between topology and physical phenomena dates back to the discovery of the quantum Hall effect (QHE), in 1981. Studying the evolution of the Hall conductance in a two-dimensional electron gas at very low temperatures subject to intense out-of-plane magnetic field, von Klitzing reported [123, 124] a staircase of plateaus schematized in Figure 1.25 for the Hall resistance (inverse of Hall conductance). Moreover, he was able to measure, with unanticipated precision ( $\sim 10^{-10}$ ), the successive values of the Hall conductance as integer multiples of the fine-structure constant  $e^2/h$ :

$$\sigma_{xy} = n \frac{e^2}{h}, \quad n \in \mathbb{N}^*, \quad (1.31)$$

irrespective to the defects of the samples. Apart from the tremendous consequences in metrology, the highly robust integral quantization of the conductance hinted at a topological origin of the phenomenon first intuited by Laughlin [125] and confirmed by Thouless *et al.* in [126]. Precisely, they established the connection between the integral values of the Hall conductance and a topological invariant called the *Chern* number.

We review below some of the critical steps leading to the landmark result which are detailed, for instance, in the following review [127]. We introduce notably the concepts of Berry connection, Berry curvature and Berry phase that will be useful in further developments.

The concept of Berry phase deals with the adiabatic [128] evolution of a quantum system described by a Hamiltonian  $\hat{H}_{\boldsymbol{\lambda}}$  depending on the the time-varying parameter  $\boldsymbol{\lambda} = (\lambda_1, \lambda_2, \dots, \lambda_d)$  of dimension  $d$  in the general case. The adiabatic condition refers to the slow variation of  $\boldsymbol{\lambda}(t)$  in time. Such a condition will be quantified later. We consider that  $\boldsymbol{\lambda}(t)$  describes a closed path  $C$  in parameter space from initial time  $t = t_i$  to final time  $t = t_f$ , which traduces by  $\boldsymbol{\lambda}(t_f) = \boldsymbol{\lambda}(t_i)$ . Assuming non-degenerate quantum states at any time  $t$ , the adiabatic theorem stipulates that the final and initial states of the system noted  $|\psi(t_f)\rangle$  and  $|\psi(t_i)\rangle$ , respectively, differ by a phase factor  $\Phi$ :

$$|\psi(t_f)\rangle = e^{i\Phi} |\psi(t_i)\rangle. \quad (1.32)$$

In particular, this phase factor  $\Phi$  contains two contributions:

- a *dynamic* phase related to the time integral of the energy  $E(t)$  by  $1/\hbar$  factor;
- a *geometrical* phase or *Berry phase* noted  $\gamma$  depending on the closed path  $C$ .

In particular, we note  $\{|\psi_{\lambda}^{(n)}\rangle\}$  a basis of eigenstates associate to the eigenvalues  $E_{\lambda}^{(n)}$  of the Hamiltonian  $\hat{H}_{\lambda}$  for the  $n$ -th band and verifying:

$$\hat{H}_{\lambda}|\psi_{\lambda}^{(n)}\rangle = E_{\lambda}^{(n)}|\psi_{\lambda}^{(n)}\rangle. \quad (1.33)$$

We suppose the system prepared in a given eigenstate of the  $n$ -th band at  $t = t_i$ , namely  $|\psi(t_i)\rangle = |\psi_{\lambda(t_i)}^{(n)}\rangle$ . In the adiabatic approximation, condition expressed by  $\epsilon \ll 1$  with

$$\epsilon = \frac{|\langle \psi_{\lambda}^{(n)} | \left( \frac{d}{dt} \psi_{\lambda}^{(m)} \right) \rangle|}{|E_{\lambda}^{(n)} - E_{\lambda}^{(m)}|} \Big|_{\min}^{\max}, \quad (1.34)$$

the state of the system at  $t$  stays in the  $n$ -th band to become:

$$|\psi(t)\rangle \simeq e^{i\Phi(t)}|\psi_{\lambda(t_i)}^{(n)}\rangle. \quad (1.35)$$

In particular, the Berry phase acquired upon the variation of  $\lambda$  from  $t_i$  to  $t_f$  over the closed path  $C$  on the  $n$ -th band is defined by<sup>3</sup>:

$$\gamma^{(n)} = \oint_C i \langle \psi_{\lambda}^{(n)} | \nabla_{\lambda} \psi_{\lambda}^{(n)} \rangle d\lambda. \quad (1.36)$$

For the sake of compactness, we introduce the *Berry connection*  $\mathcal{A}_{\lambda}^{(n)}$  defined for each eigenstate of the Hamiltonian  $\hat{H}_{\lambda}$  as:

$$\mathcal{A}_{\lambda}^{(n)} = i \langle \psi_{\lambda}^{(n)} | \nabla_{\lambda} \psi_{\lambda}^{(n)} \rangle, \quad (1.37)$$

so that the Berry phase rewrites then in the following form:

$$\gamma^{(n)} = \oint_C \mathcal{A}_{\lambda}^{(n)} d\lambda. \quad (1.38)$$

To circumvent the difficult direct evaluation of  $|\nabla_{\lambda} \psi_{\lambda}^{(n)}\rangle$  in Equation (1.37), we transform Equation (1.38) into a surface integral via Stokes' theorem:

$$\gamma^{(n)} = \iint_S \mathbf{n} \cdot \Omega_{\lambda}^{(n)} dS. \quad (1.39)$$

with  $dS$  a small surface element in the parameter space,  $S$  a surface over the enclosing contour  $C$ ,  $\mathbf{n}$  the normal to the surface  $S$  and  $\Omega_{\lambda}^{(n)}$  the *Berry curvature* defined according to:

$$\Omega_{\lambda}^{(n)} = \nabla_{\lambda} \times \mathcal{A}_{\lambda}^{(n)}. \quad (1.40)$$

Back to our description of the QHE, we assimilate the Bloch Hamiltonian  $\hat{H}_{\mathbf{k}}$  describing the system with the eigenstates  $u_{n,\mathbf{k}}$  to the generic form  $\hat{H}_{\lambda}$  where the control

<sup>3</sup>Note that the dynamical part of the phase factor expresses as  $\Phi_{\text{dyn}} = -\frac{1}{\hbar} \int_0^{t_f} E_{\lambda(t_f)}^{(n)} dt$

parameter  $\lambda$  identifies with the momentum  $\mathbf{k}$  varying over the first Brillouin zone. Considering the first Brillouin zone (FBZ) as a closed path, the geometrical phase acquired by the system prepared initially in state  $u_{n,\mathbf{k}}$  when  $\mathbf{k}$  varies across the FBZ expresses as:

$$\gamma^{(n)} = \iint_{S_{\text{FBZ}}} \mathbf{n} \cdot \boldsymbol{\Omega}_{\mathbf{k}}^{(n)} d\mathbf{k}, \quad (1.41)$$

where  $\boldsymbol{\Omega}_{\mathbf{k}}^{(n)}$  encodes the geometrical properties of the  $n$ -th band. We finally notice that Equation (1.41) bears strong analogies with the Gauss-Bonnet theorem formulated in Equation (1.30). Indeed, we can relate the surface integral of the Berry curvature of the  $n$ -th band over the Brillouin zone to a topological invariant, the Chern number  $C_n$  defined by:

$$C_n = \frac{1}{2\pi} \iint_{S_{\text{FBZ}}} \mathbf{n} \cdot \boldsymbol{\Omega}_{\mathbf{k}}^{(n)} d\mathbf{k}. \quad (1.42)$$

In particular, we identify the Chern number with the integer number of the fine-structure constant  $e^2/h$  found in the Hall conductance in Equation (1.31).

The characterization of the system energy bands with an integer reveals therefore the profound topological origin of the Hall conductance quantization. More generally, we call *Chern insulators* 2D insulating systems which topological properties are defined by a nonzero Chern number.

### Edge states

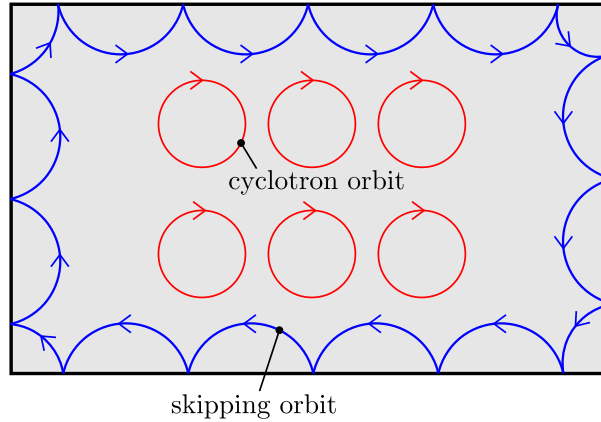


FIGURE 1.26: Electrons trajectories in the bulk (red) and at the edges (blue) in the quantum Hall effect.

Another topological manifestation of the QHE deals with the emergence of electronic states which propagate at the boundary of the systems and that we call *edge states*. In particular, in the QHE, the edge states have a *chiral* nature signifying that they propagate in a one-way direction along the boundary of the sample while being immune to backscattering effect when encountering any defects in the sample. This phenomenon leads to the precise and robust quantization of the Hall conductance. More generally, we note that the existence of chiral edge states in systems show great interest as they allow for dissipationless electronic transport in theory.

We can picture the emergence of edge states in the QHE by using a semi-classical approach in which the electrons in a 2D semiconducting system subjected to a large magnetic field follow circular cyclotron orbits as schematized in Figure 1.26, characterized by quantized energy levels (Landau levels). These electrons can not participate to

the electronic conduction in the sample, forming an insulating bulk. However, close to the sample edges, the electrons only complete one half of the orbital trajectory before reaching a boundary of the system. These electrons are not constrained and travel along the sample boundaries to form conducting channels called edge states. Therefore, the system consists therefore in an insulating bulk characterized by a *non-trivial* (non-zero) topological invariant and conducting edges, which defines a *topological insulator*.

### Bulk-edge correspondence

The relation between the number of edge states and the topological invariant which describes the geometry of the system energy bands constitutes the *bulk-edge correspondence* [129]. In the QHE, it traduces by the coincidence between the number of edge states contributing to the edge current and the sum of Chern numbers of each bulk energy bands filled with electronic states.

More generally, the notion of bulk-edge correspondence encompasses the idea that edge states always appear at the interface between two insulators of different topologies. In other words, it tells that if two gapped systems which gap are characterized by distinct topological invariants are put in contact, the gap must close to pass from one system to the other. This transition is called *topological phase transition* and leads to the emergence of states which energy lies within the gaps of the two systems and which is localized spatially in the interface region. In the quantum Hall system, the 2D insulator defined by a non-zero topological invariant interfaces the vacuum of trivial topology (zero topological invariant), guaranteeing the existence of edge states at the boundary of the insulator.

### Topology and symmetries of the system

The following part presents briefly the intimate relation between the topological properties of the system and its symmetries for the realization of topological phases of matter.

The essential ingredient behind the non-trivial topology of the quantum Hall system lies in the **breaking of the time-reversal (TR) symmetry** realized by the application of a magnetic field. The TR symmetry breaking accounts notably for the chiral nature of the edge states propagating in either clockwise or counterclockwise.

However, we note that strong magnetic fields are generally required to break the TR symmetry in the systems. Alternatively, Haldane has showed in [130] that graphene tight-binding model considering complex next-nearest-neighbour hopping also breaks the TR symmetry and results in a gap-opening at the Dirac points characterized by non-trivial topology. Moreover, the generalization of the Haldane model, also known as the quantum anomalous Hall effect, has lead to the realization of topological insulators (TI) characterized by a non-zero Chern number without any applied magnetic fields [131].

For systems preserving the TR symmetry, we can show that Chern number cancels out. However, a novel 2D topological state of matter involving systems which preserve TR symmetry, known as quantum spin Hall systems, has then been proposed successively by Kane and Mele in [132] and Bernevig *et al.* in [133]. In particular, Kane and Mele have investigated the effect of spin-orbit coupling in the Haldane model on graphene while Bernevig *et al.* have studied the spin-orbit coupling generated in strained semiconductor. Both models have reported a new state of matter consisting of two copies of a Chern insulator for the spin up and the spin down characterized by

opposite Chern numbers  $C_{\text{up}}$  and  $C_{\text{down}} = -C_{\text{up}}$ , respectively. We obtain a zero total Chern number and the TR symmetry is preserved due to the opposite magnetic fields of the two spins. Provided that no spin-flip processes occur, the two spin components behave as two independent Chern insulators sharing the same number of edge states but with opposite direction, so called *helical edge states*. Such topological insulators are better known as the quantum spin-Hall insulators and characterized by a  $\mathbb{Z}_2$  topological invariant taking either 0 (trivial) or 1 (non-trivial) values exclusively, first realized experimentally in HgTe/(Hg,Cd)Te quantum wells [134].

More generally, in the case of non-interacting fermionic systems, we can deduce from the knowledge of the preserved symmetries and the dimension, the associated topological phase and the type of topological invariant (0,  $\mathbb{Z}$  or Chern number,  $\mathbb{Z}_2$ ), following the classification established in the literature [135].

We have introduced so far the topological properties of 2D insulating systems. However, topological phases of matter have also been reported in 1D systems. We outline in the following the main results of a classical 1D topological model known as the SSH model. Most interestingly, we will show in **Chapter V** that the SSH model can also be employed to predict the topology of carbon nanotubes and graphene ribbon.

### Topology of 1D systems: SSH model

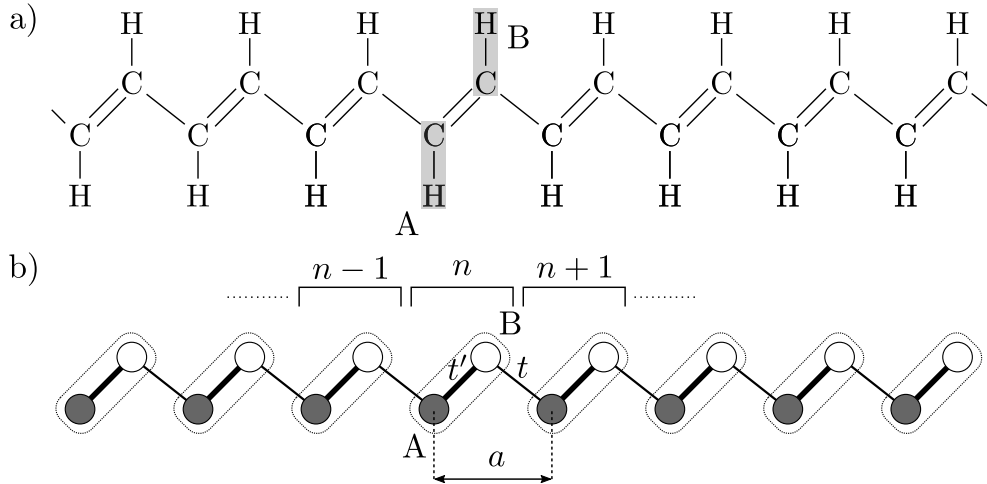


FIGURE 1.27: a) Polyacetylene polymer consisting of carbon atoms linked each other with simple and double bounds. b) Su-Schrieffer-Heeger 1D model of the polyacetylene molecule: chain of dimers A-B repeated with a period  $a$ . The parameters  $t$  and  $t'$  stands for the energy scale of the hopping of electrons from one site to the adjacent one to reproduce the single and double bounds of the molecule.

The Su-Schrieffer-Heeger model originates from the seminal theoretical study conducted by Su, Schrieffer and Heeger in 1979 of electronic conduction in long polymer chains such as the polyactelene ( $\text{CH}_x$ ) schematized in Figure 1.27.a. This conjugated polymer present alternating simple and double bounds which links the carbon atoms to each other.

In the SSH model, the molecule is modelled by a simple chain of dimers A-B. Similarly to the tight-binding approach, electrons on sublattice A or B can hop toward the neareast neighbour sublattice with the tunneling amplitudes  $t$  or  $t'$  replacing the double and simple bounds, respectively, as sketched in Figure 1.27.b.

We first summarize the topological properties of an infinite chain of dimers A-B with a period  $a$  where  $n$  indexes the position of each dimer along the chain. Considering



nearest-neighbour hopping, we can show that (see Appendix B) the Bloch Hamiltonian of the system expresses as:

$$H_k = \begin{pmatrix} 0 & t' + te^{-ika} \\ t' + te^{ika} & 0 \end{pmatrix} \quad (1.43)$$

, where  $k$  designates the momentum. Introducing the set of Pauli matrices  $\vec{\sigma} = (\sigma_x, \sigma_y, \sigma_z)$ , the Bloch Hamiltonian adopts the compact and more generic form:

$$H_k = \vec{g}(k) \cdot \vec{\sigma} \quad (1.44)$$

where  $\vec{g}(k) = (g_x(k), g_y(k), g_z(k)) = (t' + t \cos(ka), t \sin(ka), 0)$  from which we deduce directly the two SSH energy bands corresponding to the eigenvalues of  $H_k$ :

$$E_{\pm}(k) = \pm |\vec{g}(k)| = \pm |t' + te^{ika}|. \quad (1.45)$$

We present in Figure 1.28.a, b, c, d and e, the energy dispersion of the two SSH bands along the 1D Brillouin zone of size  $2\pi/a$  for different ratio of the hopping parameters  $t = 0$ ,  $t < t'$ ,  $t = t'$ ,  $t > t'$  and  $t' = 0$ . We observe that the two bands remain disjointed for almost every case expect for  $t = t'$  for which they intersect.

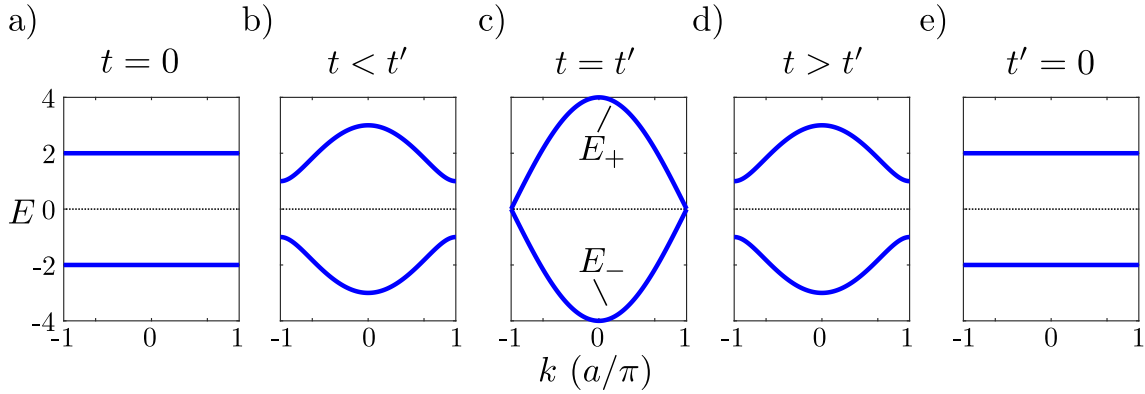


FIGURE 1.28: Energy dispersion  $E(k)$  of the two SSH model energy bands  $E_+$  and  $E_-$  along the 1D Brillouin zone when varying the hopping parameters  $t$  and  $t'$ .

However, the energy diagrams do not provide any information concerning the topology of the bands which is encoded in the evolution of the eigenvectors over the Brillouin zone. A possible choice for normalized eigenvectors of the Bloch Hamiltonian  $H_k$  associated to the eigenvalues  $E_{\pm}$  writes as:

$$|u_k^{(\pm)}\rangle = \frac{1}{\sqrt{2}} \begin{pmatrix} \pm e^{i\theta(k)} \\ 1 \end{pmatrix}, \quad (1.46)$$

where we have introduced the complex argument  $\theta(k) = \arctan(g_y(k)/g_x(k))$  which is well defined over the Brillouin zone expect for  $t = t'$  (band crossing). We can calculate, therefore, the Berry connection defined in Equation (1.37), for the SSH system:

$$\mathcal{A}_k^{(\pm)} = i \langle u_k^{(\pm)} | \nabla_k u_k^{(\pm)} \rangle = -\frac{1}{2} \frac{d\theta(k)}{dk}, \quad (1.47)$$

and the Berry phase corresponding to the integral of the Berry connection over the Brillouin zone according to Equation (1.40):

$$\gamma = \int_{-\pi/a}^{\pi/a} \mathcal{A}_k^{(\pm)} dk = -\frac{1}{2} \int_{-\pi/a}^{\pi/a} \frac{d\theta(k)}{dk} dk, \quad (1.48)$$

also known as the Zak phase that we note  $\mathcal{Z}$  [136] which interprets geometrically as the winding number  $w$  of  $\vec{g}(k)$  in the complex plane around the origin when  $k$  runs through the Brillouin zone:

$$w = -\frac{1}{\pi}\mathcal{Z} = \frac{1}{2\pi} \int_{-\pi/a}^{\pi/a} \frac{d\theta(k)}{dk} dk = \frac{1}{2\pi} [\theta_{-\pi/a} - \theta_{\pi/a}]. \quad (1.49)$$

We present in Figure 1.29.a and b the trajectories of  $\vec{g}(k)$  in the complex plane when the momentum  $k$  varies from  $-\pi/a$  to  $\pi/a$  for the two configurations  $t < t'$  and  $t > t'$  leading to two gapped bands. In both configuration, the vector  $\vec{g}(k)$  describes a circle of radius  $t$  and centred on  $(t', 0)$ . However, we distinguish two positions of the circle with respect to the origin, leading to two distinct topologies of the bands:

- For  $t < t'$ : the circle locates in the half plane where  $g_x > 0$  and for  $g_y > 0$  but it does not enclose the origin. We obtain therefore a zero Zak phase and by definition  $w = 0$ : the energy bands are topologically **trivial**.
- For  $t > t'$ : the circle encloses one time the origin. We obtain a Zak phase  $\mathcal{Z} = -\pi$ , hence a winding number  $w = 1$ : the energy bands are topologically **non-trivial**.

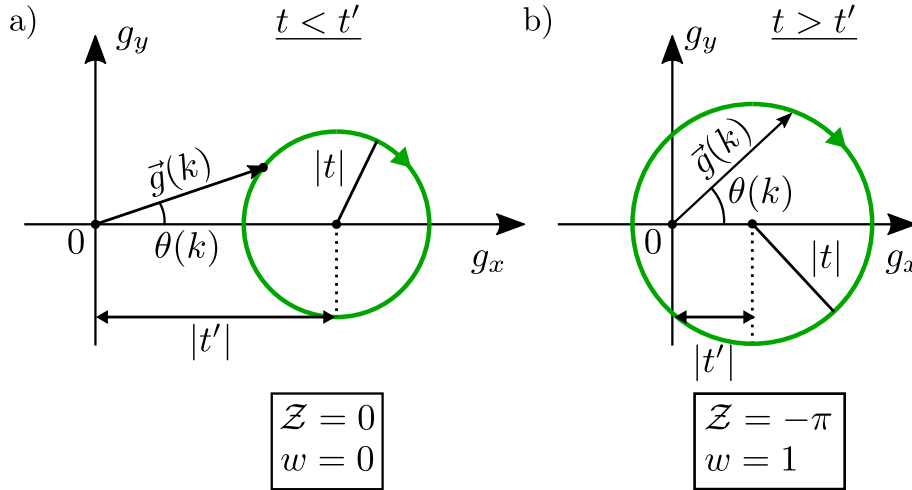


FIGURE 1.29: Graphical determination of the winding number in the SSH model. Trajectories of  $\vec{g}(k)$  in the complex plane when  $k$  varies along the Brillouin zone for a)  $t < t'$  and b)  $t > t'$ .

We emphasize that the transition from one insulating phase to the other implies the closing of the gap which constitutes the hallmark of a topological phase transition.

To reveal the non-trivial topology of the SSH insulators, we need to create an interface between the SSH chain and topologically trivial systems. A straightforward way consists in considering a finite chain with open boundary conditions constituted of  $N$  dimers enclosed by topologically trivial vacuum.

In [137], Delplace *et al.* have constructed the eigenstates of the finite chain as linear combination of bulk eigenvectors  $|u_k^{(\pm)}\rangle$  and  $|u_{-k}^{(\pm)}\rangle$  with opposite momentum, imposing the cancelling of the total wavefunction at the A or B site near 0-th and  $N$ -th dimer, similarly to standing waves. Through a graphical resolution method, they found  $2N$  and  $2(N-1)$  bulk states for  $t' > t$  and  $t' < t$  (depending on the ratio  $t'/t$ ), respectively. As demonstrated above, the value of the Zak phase controls the topological properties of the bands depending on the ratio  $t'/t$ , and consequently, the number of solutions in the finite chain. In particular, the two missing states in the case of  $t' < t$  corresponds

to a zero-energy edge states localized at the end of the chain. They also emphasize that these results stay valid in the limit of large  $N$  number of dimers.

We stress that the zero energy of the edge states is ensured by the chiral symmetry of the SSH 1D chain composed of two sublattices. The breaking of this symmetry by, for instance, the addition of a staggered potential on one sublattice, does not guarantee edge states with zero energy level and Zak phase taking multiple of  $\pi$  values.

As mentioned previously, the SSH model can be used to assess the topological properties of graphene ribbons and carbon nanotubes which can be both be considered as 1D version of graphene. In particular, Delplace *et al.* have established a method derived from the SSH model to predict the existence of edge states in graphene ribbons for large range of ribbons' edges [137] and formulate the bulk-edge correspondence. Similarly, Okuyama *et al.* [118] have established an analytical formulation of the Zak phase of the carbon nanotubes which depends on their chirality, leading to a topological classification of the nanotubes. We note that the results of both studies will be reviewed in details in Chapter 5.

### Topological photonics

The concepts of robust topological phases of matter highlight historically in solid-state structures have raised a huge scientific interest and permeated into multiple domains toward the conception of mechanical, acoustic or photonic topological insulators. We present below some of the strategies and achievements developed in the photonic field to emulate the physics of solid-state topological insulators. In particular, topologically-protected photonic edge states show much potential for the realization of dissipationless optical devices.

We start by presenting photonic analogues of integer quantum Hall systems which breaks the time-reversal symmetry and which topology can be characterized by an integer-valued Chern number. Such systems give rise to topologically-protected chiral edge states propagating in one exclusive direction. The first example developed by Wang *et al.* in [138] consists of a magneto-optical photonic crystal operating in the microwave regime. Precisely, the photonic crystal structure depicted in Figure 1.30.a is composed of a period array of ferrite rods of vanadium-doped calciumiron-garnet (VCIG) (blue rods) interfacing a metal wall (yellow material). In particular, when subjected to a high static magnetic field, the photonic crystal exhibits a strong gyro-magnetic response which results in a gap opening in the energy band diagram characterized by a non-trivial topology. Since the metal wall reflecting gap shows trivial topology, a topologically-protected edge states emerges at the frontiers between the metal wall and the photonic crystal, accordingly to the bulk-edge correspondence. The energy of this edge state lies within the gap of the photonic crystal. The breaking of the time-reversal symmetry by the application of a magnetic field implies that the edge state is related to a Chern topological invariant. The topological robustness of the edge state against backscattering is highlighted in the numerical simulation presented in Figure 1.30.b where the edge state circumvent a large obstacle. Such striking effect present multiple advantages in contrast with traditional optical waveguides which backscattering on defects causes significant transmission losses.

However, the transposition of such systems in the optical regime appears challenging as photonic crystal structures ordinary exhibits weak magneto-optical response in that spectral range. Alternative methods were then developed to circumvent this bottleneck and achieve the breaking of time-reversal symmetry. In particular, the approach used by Rechtsman *et al.* in [139] consists in using one dimension which plays the role

temporal coordinate in the paraxial equation for the diffraction of light. Therefore, breaking the reversal symmetry along this dimension generates topologically protected chiral edge states in the transverse plane. In practice, the authors have proposed an array of evanescently coupled helical waveguides oriented along the  $z$  axis and arranged according to a honeycomb lattice as schematized in Figure 1.30.c. The helical shape of the waveguides ensures to break the  $z$ -reversal symmetry and results in the emergence of chiral edge states at the boundary of the waveguide. We show, for instance, in Figure 1.30.d the experimental observation of a chiral edge state propagating in one-way direction along the waveguide boundary in the transverse plane.

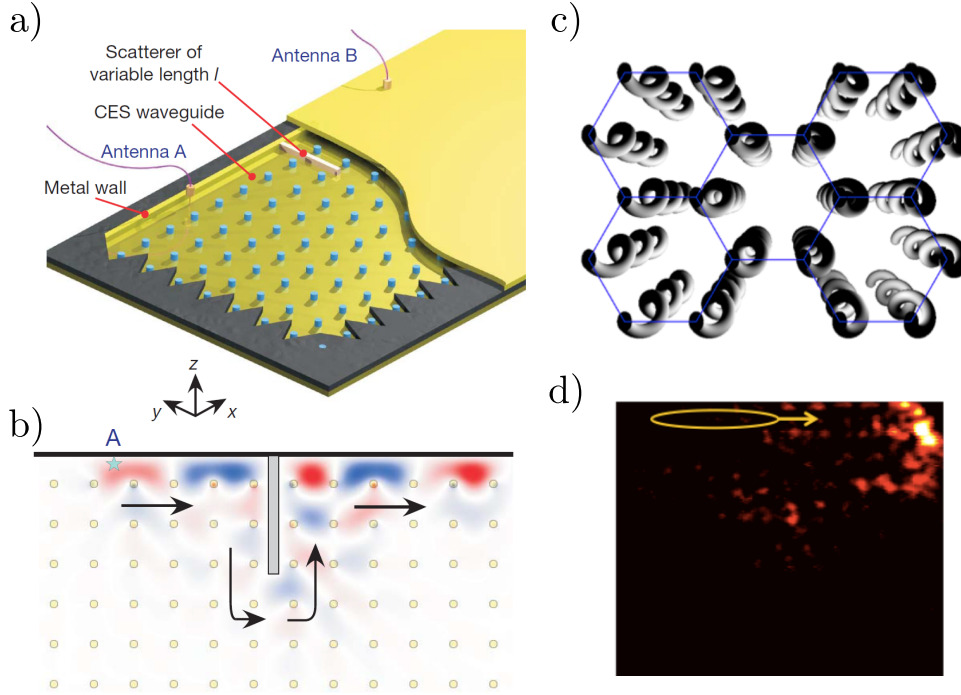


FIGURE 1.30: Photonic analogues of integer quantum Hall systems. a) Schematics of a magneto-optical photonic crystal composed of ferrite rods of vanadium-doped calciumiron-garnet (VCIG) (blue rods) interfacing a metal wall (yellow material). b) Simulation of the propagation of the chiral edge states along the interface between the metal and the photonic crystal with a large obstacle inserted along the path. Adapted from [138]. c) Schematics of a honeycomb lattice of helical-shape waveguide. d) Experimental observation of the chiral edge state propagating along the boundary of the waveguide array. Adapted from [139].

Another class of photonic topological insulators correspond to the implementation of quantum spin Hall effect for photons using photonic crystals as proposed originally by Wu *et al.* in [140]. In the approach of Wu, the structure is composed of dielectric rods arranged in air according to a honeycomb lattice. Such geometry results in a photonic Dirac dispersion at high-symmetry points K and K' of the honeycomb Brillouin zone. In particular, the authors have shown that, for transverse magnetic polarization, the magnetic field distribution calculated on the lower and upper band of the Dirac dispersion present  $(p_x, p_y)$  and  $(d_{xy}, d_{x^2-y^2})$  orbital like symmetry acting then as a pseudospin basis. Consequently, the bands are characterized by nonzero pseudospin Chern numbers analogue to  $\mathbb{Z}_2$  topological insulator and finite-sized crystals with non-trivial topology exhibit two helical edge states within their gap with opposite velocities. Such a concept has also been developed and demonstrated experimentally by Barik *et al.* in the infrared domain with photonic crystal slabs illustrated in Figure 1.31.a and b. Precisely, the structure consists of two interfacing photonic crystal membranes consisting

of triangular air holes etched in a GaAs material and arranged according to a stretched or shrunk honeycomb lattice. The deformation of the honeycomb lattice, while preserving the  $C_3$  rotational symmetry, results in a gap opening for the two regions as represented in Figure 1.31.c characterized by distinct topologies. Consequently, helical edge states with opposite circular polarization  $\sigma^+$  and  $\sigma^-$  emerge at the interface between the two photonic crystal patterns.

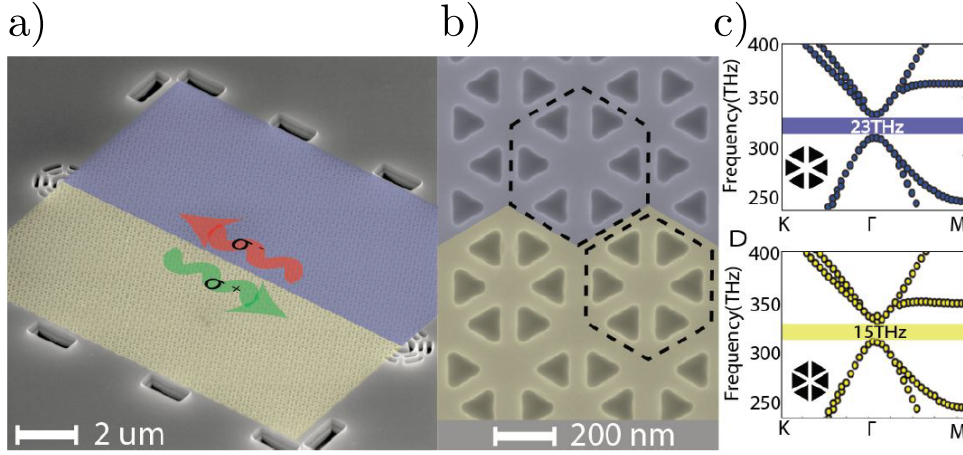


FIGURE 1.31: a) Scanning electron microscopy (SEM) picture of a quantum spin Hall photonic system. Helical edge states of circular polarization  $\sigma^+$  and  $\sigma^-$  with opposite directions emerging at the interface between photonic crystal membranes with trivial and non-trivial spin Hall topologies. b) SEM picture of the interface between a shrunk and expanded honeycomb lattice photonic crystal pattern composed of triangular air holes etched in GaAs material. c) Simulated band diagrams of the shrunk and expanded photonic crystals. Adapted from [141].

Our last example deals with the realization of a photonic equivalent of the 1D photonic SSH system using a polaritonic platform. The 1D polaritonic system consists of a zig-zag assembly of semiconducting micropillars made of two vertically facing distributed Bragg mirrors (DBRs) enclosing quantum wells (QWs), as represented in Figure 1.32.a. Each single micropillar support two kinds of photonic modes:  $s$  modes with a cylindrical symmetry and two degenerate  $p$  modes with anti-symmetric orbital orthogonal to each other as sketched in Figure 1.32.b. The diagram represents a spectrally-resolved real-space emission of a single micropillar revealing the two types of orbitals at different energy levels. The reproduction of the SSH model relies on the coupling between the  $p$  orbitals of adjacent micropillars. The strength of the coupling between two consecutive pillars depends on to the orientation the axis linking them, being one order of magnitude higher for facing orbitals lobes, and mimicking the SSH hopping energies  $t$  and  $t'$ . In particular, the  $p_y$  subspace which starts (ends) with a weak coupling between the first (last) two pillars gives rise to an edge state appearing as a flat band within the energy band gap of the  $p$  bands as showed on the energy-momentum photoluminescence diagram in Figure 1.32.c. The real-space photoluminescence image in Figure 1.32.d also reveals the localization of the edge state in the first pillar exclusively.

We have showed in this part that the topological concepts originally developed for solid-states structures have been transposed successfully to the photonic domain with the creation of topological insulators showing chiral or helical edge states. The existence of such unidirectional edge states holds much interest toward the realization of dissipationless waveguides or topologically protected laser. We have also reported the potential of the photonic crystal platform with the creation of photonic topological

insulators from honeycomb lattice photonic crystals. Similarly, we can wonder whether we can retrieve the topological properties predicted for carbon nanotubes but with rolled-up version of graphene-like photonic crystal. We will show in the following that the rolled-up nanotechnology represents an ideal platform to address the previous question.

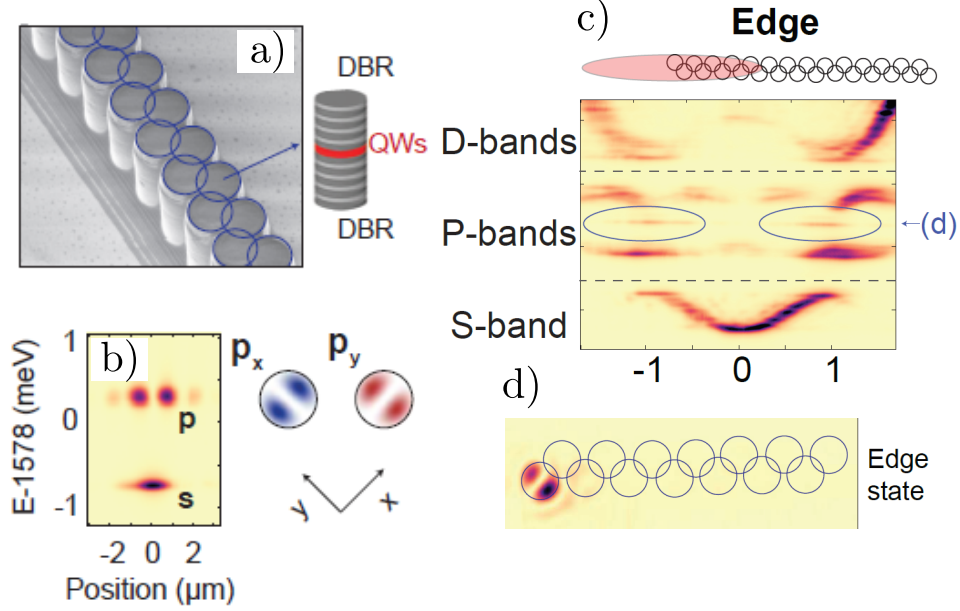


FIGURE 1.32: a) Scanning electron microscopy (SEM) picture of the 1D zig-zag array of semiconducting micropillars mimicking the 1D SSH chain. The drawing on the left represents a single micropillar formed by quantum wells embedded between two distributed Bragg mirrors. b) Spectrally-resolved real-space emission diagram of a single micropillar supporting one  $s$  and two degenerate  $p$  orbitals. Drawing: schematized distribution of the two anti-symmetric degenerate orbitals  $p_x$  and  $p_y$ . c) Energy-momentum photoluminescence emission diagram of a finite-size polaritonic chain exploiting  $p_y$ -like orbitals and collected at the edge. d) Real-space photoluminescence image of the edge state forming on the boundary of the photonic chain. Adapted from [142].

### 1.3.3 Photonic crystal analogues of carbon nanotubes

The exceptional properties of graphene have sparked a considerable interest in the scientific community to emulate Dirac physics in other material platforms. Indeed, the emergence of Dirac cones intimately relates to the honeycomb lattice arrangement. Therefore, artificial structures reproducing the honeycomb lattice system, dubbed artificial graphenes [143], should present similar dispersive features as revealed for graphene.

For instance, centimeter-size dielectric cylindrical rods arranged in 2D honeycomb lattice simulating graphene in the microwave domain, exhibit typical Dirac dispersion [144]. Another example of artificial graphene consists of a honeycomb lattice of silicon pillars hosting polaritons [145] which interaction mimics the behaviour of Dirac relativist fermions. Beyond the mere analogy, the tunability of artificial graphene systems offers a suitable testing ground to get a new insight on graphene physics and measure physical phenomena hardly appreciable or technically demanding in graphene specimen. For instance, appropriate modifications of artificial graphene structural parameters allows the manipulation, the creation or even the removal of Dirac points, and the emergence of topological effects [146, 147].



The photonic crystal platform represents an alternative way of producing graphene photonic analogues. Inspired from solid-states crystal, photonic crystals bear *de facto* complementary physics proper to crystallographic systems. Indeed, in solid (photonic) crystals, electronic (photonic) states express in the form of Bloch functions (waves). The energy electronic (photonic) dispersion manifests itself through successive bands separated by electronic (photonic) band gaps prohibiting the propagation of electrons (photons) for a certain range of energies and directions.

However, unlike solid crystal, photonic counterparts offer design flexibility through changes of lattice parameters, suitable for dispersion engineering, for instance. Moreover, the scalability of Maxwell's equations allows transposing designs and associate physical effects within any targeted spectral range. Finally, the dispersion characteristics of photonic structures are more easily accessible through common far-field optical measurements. In particular, the production of honeycomb lattice photonic crystal membranes (HC-PCM), exhibiting Dirac dispersion, has raised a significant interest in the last decades for the realization of topological effects [140, 148] as reported earlier.

In the present thesis, **we propose to extend the analogy toward the production and the optical characterization of carbon nanotubes (CNTs) equivalents in the class of photonic crystals**, so far unexplored. Indeed, the rolled-up nanotechnology represents a suitable technological platform to design HC-PCM and roll them up into hollow cylindrical forms. Moreover, the rolled-up technology allows a precise control on the structural parameters of the planar template, hence on the chirality and the diameter of the final tubular photonic structure. We intend notably, in this work, to answer the following questions:

- Does the photonic dispersion of the CNT photonic crystal analogues varies as a function of the tube's chirality, resulting in band gaps or Dirac points with tunable positions ?
- Does the band gap of the photonic microtubes exhibit topological properties?

Before tackling these issues, we will investigate the optical and topological properties of intermediary structures that are the photonic crystal equivalents of graphene and graphene ribbons.

## 1.4 Conclusion of the chapter

We have showed in this chapter that the rolled-up nanotechnology represents a competitive alternative to the fabrication of 3D versatile micro-objects. The principle of this technique relies on the self-rolling of pre-strained membranes characterized by micron-sized thickness. The production of a 3D prescribed geometry involves two essential steps: the strain engineering and the design of the 2D template of the membranes. Popular 3D architectures produced with the rolled-up nanotechnology include microtubes, microcoils, or helices. Furthermore, the large range of materials covered by the micro-fabrication, comprising metals, semiconductors, or polymers, enables the utilisation of the so-formed 3D micro-objects for various applications. In particular, tubular-shaped microstructures, acting both as microchannels and optical microresonators, have held much promises in the realization of compact and efficient opto-fluidic sensing devices.

In this thesis, our approach consists in using the rolled-up nanotechnology to roll photonic crystal membranes to form two kinds of structures: photon cages and photonic crystal analogues of carbon nanotubes.

In the first place, we address the conception of tubular photon cages based on the rolling of 2D photonic crystal membrane mirror using the rolled-up nanotechnology and capable of confining light in air. Our objective consists in bringing a experimental proof of concept of photon cages.

In the second place, we intend to explore theoretically and experimentally the optical and topological properties of photonic crystal analogues of carbon nanotubes consisting of rolled-up honeycomb lattice photonic crystal membranes. In the light of the electronic and topological properties of carbon nanotubes, we aim at answering the two following questions. How does the photonic dispersion of the CNT-like photonic microtube evolve as a function of the microtube's chirality ? Does the photonic microtubes exhibit non-trivial topological properties ?

In the following chapter, we introduce the numerical and fabrication methods to realize the different steps of the conception of the previous structures: the design, the simulation of the optical properties, the fabrication and the optical characterization of the structures.



## 1.5 References

- [1] Z. Ren and P.-X. Gao, “A review of helical nanostructures: growth theories, synthesis strategies and properties,” *Nanoscale*, vol. 6, pp. 9366–9400, July 2014. Publisher: The Royal Society of Chemistry. 6
- [2] S. M. Douglas, H. Dietz, T. Liedl, B. Högberg, F. Graf, and W. M. Shih, “Self-assembly of DNA into nanoscale three-dimensional shapes,” *Nature*, vol. 459, pp. 414–418, May 2009. Number: 7245 Publisher: Nature Publishing Group. 6
- [3] Y. L. Kong, I. A. Tamargo, H. Kim, B. N. Johnson, M. K. Gupta, T.-W. Koh, H.-A. Chin, D. A. Steingart, B. P. Rand, and M. C. McAlpine, “3D Printed Quantum Dot Light-Emitting Diodes,” *Nano Lett.*, vol. 14, pp. 7017–7023, Dec. 2014. Publisher: American Chemical Society. 6
- [4] A. Javey, Nam, R. S. Friedman, H. Yan, and C. M. Lieber, “Layer-by-Layer Assembly of Nanowires for Three-Dimensional, Multifunctional Electronics,” *Nano Lett.*, vol. 7, pp. 773–777, Mar. 2007. Publisher: American Chemical Society.
- [5] M. S. Mannoor, Z. Jiang, T. James, Y. L. Kong, K. A. Malatesta, W. O. Soboyejo, N. Verma, D. H. Gracias, and M. C. McAlpine, “3D Printed Bionic Ears,” *Nano Lett.*, vol. 13, pp. 2634–2639, June 2013. Publisher: American Chemical Society. 6
- [6] D. B. Burckel, J. R. Wendt, G. A. T. Eyck, A. R. Ellis, I. Brener, and M. B. Sinclair, “Fabrication of 3D Metamaterial Resonators Using Self-Aligned Membrane Projection Lithography,” *Advanced Materials*, vol. 22, no. 29, pp. 3171–3175, 2010. \_eprint: <https://onlinelibrary.wiley.com/doi/pdf/10.1002/adma.200904153>. 6
- [7] K. Sakoda, ed., *Electromagnetic Metamaterials: Modern Insights into Macroscopic Electromagnetic Fields*. Springer Series in Materials Science, Springer Singapore, 2019. 6
- [8] N. Liu, H. Guo, L. Fu, S. Kaiser, H. Schweizer, and H. Giessen, “Three-dimensional photonic metamaterials at optical frequencies,” *Nature Materials*, vol. 7, pp. 31–37, Jan. 2008. Number: 1 Publisher: Nature Publishing Group. 6
- [9] T. D. Ngo, A. Kashani, G. Imbalzano, K. T. Q. Nguyen, and D. Hui, “Additive manufacturing (3D printing): A review of materials, methods, applications and challenges,” *Composites Part B: Engineering*, vol. 143, pp. 172–196, June 2018. 7
- [10] K. B. Fritzler and V. Y. Prinz, “3D printing methods for micro- and nanostructures,” *Phys.-Usp.*, vol. 62, p. 54, Jan. 2019. Publisher: IOP Publishing.
- [11] J. Li and M. Pumera, “3D printing of functional microrobots,” *Chem. Soc. Rev.*, Jan. 2021. Publisher: The Royal Society of Chemistry. 7
- [12] A. Selimis, V. Mironov, and M. Farsari, “Direct laser writing: Principles and materials for scaffold 3D printing,” *Microelectronic Engineering*, vol. 132, pp. 83–89, Jan. 2015. 7

- [13] T. Gissibl, S. Thiele, A. Herkommer, and H. Giessen, “Two-photon direct laser writing of ultracompact multi-lens objectives,” *Nature Photonics*, vol. 10, pp. 554–560, Aug. 2016.
- [14] M. P. Lim, X. Guo, E. L. Grunblatt, G. M. Clifton, A. N. Gonzalez, and C. N. LaFratta, “Augmenting mask-based lithography with direct laser writing to increase resolution and speed,” *Opt. Express, OE*, vol. 26, pp. 7085–7090, Mar. 2018. Publisher: Optical Society of America.
- [15] J. Lölsberg, A. Cinar, D. Felder, G. Linz, S. Djeljadini, and M. Wessling, “Two-Photon Vertical-Flow Lithography for Microtube Synthesis,” *Small*, vol. 15, no. 33, p. 1901356, 2019. \_eprint: <https://onlinelibrary.wiley.com/doi/pdf/10.1002/sml.201901356>.
- [16] D. Li, C. Liu, Y. Yang, L. Wang, and Y. Shen, “Micro-rocket robot with all-optic actuating and tracking in blood,” *Light: Science & Applications*, vol. 9, p. 84, May 2020. Number: 1 Publisher: Nature Publishing Group.
- [17] C. Maibohm, O. F. Silvestre, J. Borme, M. Sinou, K. Heggarty, and J. B. Nieder, “Multi-beam two-photon polymerization for fast large area 3D periodic structure fabrication for bioapplications,” *Scientific Reports*, vol. 10, p. 8740, May 2020. Number: 1 Publisher: Nature Publishing Group. 7
- [18] U. S. Dixit and S. K. Dwivedy, eds., *Mechanical Sciences: The Way Forward*. Springer Singapore, 2021. 7, 8
- [19] C. Xu, X. Wu, G. Huang, and Y. Mei, “Rolled-up Nanotechnology: Materials Issue and Geometry Capability,” *Advanced Materials Technologies*, vol. 4, no. 1, p. 1800486, 2019. 7, 21
- [20] C. Py, P. Reverdy, L. Doppler, J. Bico, B. Roman, and C. N. Baroud, “Capillary Origami: Spontaneous Wrapping of a Droplet with an Elastic Sheet,” *Phys. Rev. Lett.*, vol. 98, p. 156103, Apr. 2007. Publisher: American Physical Society. 7
- [21] W. Hu, G. Z. Lum, M. Mastrangeli, and M. Sitti, “Small-scale soft-bodied robot with multimodal locomotion,” *Nature*, vol. 554, pp. 81–85, Feb. 2018. Number: 7690 Publisher: Nature Publishing Group. 7
- [22] Z. Yan, F. Zhang, J. Wang, F. Liu, X. Guo, K. Nan, Q. Lin, M. Gao, D. Xiao, Y. Shi, Y. Qiu, H. Luan, J. H. Kim, Y. Wang, H. Luo, M. Han, Y. Huang, Y. Zhang, and J. A. Rogers, “Controlled Mechanical Buckling for Origami-Inspired Construction of 3D Microstructures in Advanced Materials,” *Advanced Functional Materials*, vol. 26, no. 16, pp. 2629–2639, 2016. \_eprint: <https://onlinelibrary.wiley.com/doi/pdf/10.1002/adfm.201504901>. 7
- [23] E. Moiseeva, Y. M. Senousy, S. McNamara, and C. K. Harnett, “Single-mask microfabrication of three-dimensional objects from strained bimorphs,” *J. Microelect. Microeng.*, vol. 17, pp. N63–N68, Aug. 2007. Publisher: IOP Publishing. 8
- [24] V. Y. Prinz, V. A. Seleznev, A. K. Gutakovskiy, A. V. Chehovskiy, V. V. Preobrazhenskii, M. A. Putyato, and T. A. Gavrilova, “Free-standing and overgrown InGaAs/GaAs nanotubes, nanohelices and their arrays,” *Physica E: Low-dimensional Systems and Nanostructures*, vol. 6, pp. 828–831, Feb. 2000. 8

- [25] S. V. Golod, V. Y. Prinz, V. I. Mashanov, and A. K. Gutakovsky, “Fabrication of conducting GeSi/Si micro- and nanotubes and helical microcoils,” *Semicond. Sci. Technol.*, vol. 16, pp. 181–185, Feb. 2001. Publisher: IOP Publishing.
- [26] V. Y. Prinz, D. Grützmacher, A. Beyer, C. David, B. Ketterer, and E. Deckardt, “A new technique for fabricating three-dimensional micro- and nanostructures of various shapes,” *Nanotechnology*, vol. 12, no. 4, p. 399, 2001. 8, 16
- [27] V. Y. Prinz, V. A. Seleznev, A. K. Gutakovsky, A. V. Chehovskiy, V. V. Preobrazhenskii, M. A. Putyato, and T. A. Gavrilova, “Free-standing and overgrown InGaAs/GaAs nanotubes, nanohelices and their arrays,” *Physica E: Low-dimensional Systems and Nanostructures*, vol. 6, pp. 828–831, Feb. 2000. 8, 9, 16
- [28] S. Timoshenko, “Analysis of Bi-Metal Thermostats,” *J. Opt. Soc. Am., JOSA*, vol. 11, pp. 233–255, Sept. 1925. Publisher: Optical Society of America. 13
- [29] C. Deneke, C. M. Iler, N. Y. Jin-Phillipp, and O. G. Schmidt, “Diameter scalability of rolled-up In(Ga)As/GaAs nanotubes,” *Semicond. Sci. Technol.*, vol. 17, pp. 1278–1281, Nov. 2002. 15
- [30] B. Xu, X. Lin, and Y. Mei, “Versatile Rolling Origami to Fabricate Functional and Smart Materials,” *Cell Reports Physical Science*, vol. 1, p. 100244, Nov. 2020. 16, 21
- [31] C. S. Martinez-Cisneros, S. Sanchez, W. Xi, and O. G. Schmidt, “Ultracompact Three-Dimensional Tubular Conductivity Microsensors for Ionic and Biosensing Applications,” *Nano Lett.*, vol. 14, pp. 2219–2224, Apr. 2014. Publisher: American Chemical Society. 16
- [32] S. Miao, S. He, M. Liang, G. Lin, B. Cai, and O. G. Schmidt, “Microtubular Fuel Cell with Ultrahigh Power Output per Footprint,” *Advanced Materials*, vol. 29, no. 34, p. 1607046, 2017. \_eprint: <https://onlinelibrary.wiley.com/doi/pdf/10.1002/adma.201607046>. 16
- [33] Y. Mei, G. Huang, A. A. Solovev, E. B. Ureña, I. Mönch, F. Ding, T. Reindl, R. K. Y. Fu, P. K. Chu, and O. G. Schmidt, “Versatile Approach for Integrative and Functionalized Tubes by Strain Engineering of Nanomembranes on Polymers,” *Advanced Materials*, vol. 20, no. 21, pp. 4085–4090, 2008. 16, 19
- [34] J. Li, J. Zhang, W. Gao, G. Huang, Z. Di, R. Liu, J. Wang, and Y. Mei, “Dry-Released Nanotubes and Nanoengines by Particle-Assisted Rolling,” *Advanced Materials*, vol. 25, no. 27, pp. 3715–3721, 2013. \_eprint: <https://onlinelibrary.wiley.com/doi/pdf/10.1002/adma.201301208>. 16
- [35] O. G. Schmidt and K. Eberl, “Nanotechnology: Thin solid films roll up into nanotubes,” *Nature*, vol. 410, p. 168, Mar. 2001. 17
- [36] O. G. Schmidt and N. Y. Jin-Phillipp, “Free-standing SiGe-based nanopipelines on Si (001) substrates,” *Appl. Phys. Lett.*, vol. 78, pp. 3310–3312, May 2001. Publisher: American Institute of Physics. 17

- [37] M. Huang, C. Boone, M. Roberts, D. E. Savage, M. G. Lagally, N. Shaji, H. Qin, R. Blick, J. A. Nairn, and F. Liu, “Nanomechanical Architecture of Strained Bilayer Thin Films: From Design Principles to Experimental Fabrication,” *Advanced Materials*, vol. 17, no. 23, pp. 2860–2864, 2005. 17, 18
- [38] I. S. Chun, A. Challa, B. Derickson, K. J. Hsia, and X. Li, “Geometry Effect on the Strain-Induced Self-Rolling of Semiconductor Membranes,” *Nano Lett.*, vol. 10, pp. 3927–3932, Oct. 2010. 18
- [39] A. B. V. ev and V. Y. Prinz, “Directional rolling of strained heterofilms,” *Semicond. Sci. Technol.*, vol. 17, pp. 614–616, May 2002. Publisher: IOP Publishing. 19
- [40] P. Cendula, S. Kiravittaya, I. Mönch, J. Schumann, and O. G. Schmidt, “Directional Roll-up of Nanomembranes Mediated by Wrinkling,” *Nano Lett.*, vol. 11, pp. 236–240, Jan. 2011. Publisher: American Chemical Society. 19
- [41] Z. Tian, L. Zhang, Y. Fang, B. Xu, S. Tang, N. Hu, Z. An, Z. Chen, and Y. Mei, “Deterministic Self-Rolling of Ultrathin Nanocrystalline Diamond Nanomembranes for 3D Tubular/Helical Architecture,” *Advanced Materials*, vol. 29, no. 13, p. 1604572, 2017. \_eprint: <https://onlinelibrary.wiley.com/doi/pdf/10.1002/adma.201604572>. 19
- [42] A. Danescu, C. Chevalier, G. Grenet, P. Regreny, X. Letartre, and J. L. Leclercq, “Spherical curves design for micro-origami using intrinsic stress relaxation,” *Appl. Phys. Lett.*, vol. 102, p. 123111, Mar. 2013. 19, 20
- [43] A. Danescu, P. Regreny, P. Cremillieu, and J.-L. Leclercq, “Fabrication of self-rolling geodesic objects and photonic crystal tubes,” *Nanotechnology*, vol. 29, p. 285301, July 2018. 20
- [44] A. Danescu and I. R. Ionescu, “Shell design from planar pre-stressed structures,” *Mathematics and Mechanics of Solids*, vol. 25, pp. 1247–1266, June 2020. Publisher: SAGE Publications Ltd STM. 20
- [45] T. G. Leong, B. R. Benson, E. K. Call, and D. H. Gracias, “Thin Film Stress Driven Self-Folding of Microstructured Containers,” *Small*, vol. 4, no. 10, pp. 1605–1609, 2008. \_eprint: <https://onlinelibrary.wiley.com/doi/pdf/10.1002/smll.200800280>. 20
- [46] B. Xu, B. Zhang, L. Wang, G. Huang, and Y. Mei, “Tubular Micro/Nanomachines: From the Basics to Recent Advances,” *Advanced Functional Materials*, vol. 28, no. 25, p. 1705872, 2018. 21
- [47] D. Karnaushenko, T. Kang, V. K. Bandari, F. Zhu, and O. G. Schmidt, “3D Self-Assembled Microelectronic Devices: Concepts, Materials, Applications,” *Advanced Materials*, vol. 32, no. 15, p. 1902994, 2020. \_eprint: <https://onlinelibrary.wiley.com/doi/pdf/10.1002/adma.201902994>. 21
- [48] J. Deng, H. Ji, C. Yan, J. Zhang, W. Si, S. Baunack, S. Oswald, Y. Mei, and O. G. Schmidt, “Naturally Rolled-Up C/Si/C Trilayer Nanomembranes as Stable Anodes for Lithium-Ion Batteries with Remarkable Cycling Performance,” *Angewandte Chemie International Edition*, vol. 52, no. 8, pp. 2326–2330, 2013. 22

- [49] J.-H. Cho, M. D. Keung, N. Verellen, L. Lagae, V. V. Moshchalkov, P. V. Dorpe, and D. H. Gracias, “Nanoscale Origami for 3D Optics,” *Small*, vol. 7, no. 14, pp. 1943–1948, 2011. 22
- [50] A. A. Solovev, Y. Mei, E. B. Ureña, G. Huang, and O. G. Schmidt, “Catalytic Microtubular Jet Engines Self-Propelled by Accumulated Gas Bubbles,” *Small*, vol. 5, no. 14, pp. 1688–1692, 2009. \_eprint: <https://onlinelibrary.wiley.com/doi/pdf/10.1002/sml.200900021>. 23
- [51] X. Li, “Self-rolled-up microtube ring resonators: a review of geometrical and resonant properties,” *Adv. Opt. Photon., AOP*, vol. 3, pp. 366–387, Dec. 2011. 24
- [52] T. Kipp, H. Welsch, C. Strelow, C. Heyn, and D. Heitmann, “Optical Modes in Semiconductor Microtube Ring Resonators,” *Phys. Rev. Lett.*, vol. 96, p. 077403, Feb. 2006. 25
- [53] M. Hosoda and T. Shigaki, “Degeneracy breaking of optical resonance modes in rolled-up spiral microtubes,” *Appl. Phys. Lett.*, vol. 90, p. 181107, Apr. 2007. Publisher: American Institute of Physics. 25
- [54] R. Songmuang, A. Rastelli, S. Mendach, and O. G. Schmidt, “SiO<sub>x</sub>-Si radial superlattices and microtube optical ring resonators,” *Appl. Phys. Lett.*, vol. 90, p. 091905, Feb. 2007. 25
- [55] V. A. B. Quiñones, G. Huang, J. D. Plumhof, S. Kiravittaya, A. Rastelli, Y. Mei, and O. G. Schmidt, “Optical resonance tuning and polarization of thin-walled tubular microcavities,” *Opt. Lett., OL*, vol. 34, pp. 2345–2347, Aug. 2009. Publisher: Optical Society of America. 25, 26
- [56] C. Strelow, H. Rehberg, C. M. Schultz, H. Welsch, C. Heyn, D. Heitmann, and T. Kipp, “Optical Microcavities Formed by Semiconductor Microtubes Using a Bottlelike Geometry,” *Phys. Rev. Lett.*, vol. 101, p. 127403, Sept. 2008. 25, 26
- [57] C. Strelow, C. M. Schultz, H. Rehberg, M. Sauer, H. Welsch, A. Stemmann, C. Heyn, D. Heitmann, and T. Kipp, “Light confinement and mode splitting in rolled-up semiconductor microtube bottle resonators,” *Phys. Rev. B*, vol. 85, p. 155329, Apr. 2012. 25
- [58] S. Böttner, S. Li, J. Trommer, S. Kiravittaya, and O. G. Schmidt, “Sharp whispering-gallery modes in rolled-up vertical SiO<sub>2</sub> microcavities with quality factors exceeding 5000,” *Opt. Lett., OL*, vol. 37, pp. 5136–5138, Dec. 2012. 26
- [59] F. Li, Z. Mi, and S. Vicknesh, “Coherent emission from ultrathin-walled spiral InGaAs/GaAs quantum dot microtubes,” *Opt. Lett., OL*, vol. 34, pp. 2915–2917, Oct. 2009. Publisher: Optical Society of America. 26
- [60] Y. Li, L. Feng, X. Su, Q. Li, F. Yun, G. Yuan, and J. Han, “Whispering gallery mode lasing from InGaN/GaN quantum well microtube,” *Opt. Express, OE*, vol. 25, pp. 18072–18080, July 2017. Publisher: Optical Society of America. 26
- [61] M. H. T. Dastjerdi, M. Djavid, and Z. Mi, “An electrically injected rolled-up semiconductor tube laser,” *Appl. Phys. Lett.*, vol. 106, p. 021114, Jan. 2015. 26

- [62] F. Li and Z. Mi, “Optically pumped rolled-up InGaAs/GaAs quantum dot microtube lasers,” *Opt. Express*, vol. 17, p. 19933, Oct. 2009. 26
- [63] P. Bianucci, S. Mukherjee, M. H. T. Dastjerdi, P. J. Poole, and Z. Mi, “Self-organized InAs/InGaAsP quantum dot tube lasers,” *Appl. Phys. Lett.*, vol. 101, p. 031104, July 2012. 26
- [64] A. Bernardi, S. Kiravittaya, A. Rastelli, R. Songmuang, D. J. Thurmer, M. Benyoucef, and O. G. Schmidt, “On-chip Si/SiO<sub>x</sub> microtube refractometer,” *Appl. Phys. Lett.*, vol. 93, p. 094106, Sept. 2008. 27
- [65] L. Ma, S. Li, V. A. B. Quiñones, L. Yang, W. Xi, M. Jorgensen, S. Baunack, Y. Mei, S. Kiravittaya, and O. G. Schmidt, “Dynamic Molecular Processes Detected by Microtubular Opto-chemical Sensors Self-Assembled from Prestrained Nanomembranes,” *Advanced Materials*, vol. 25, pp. 2357–2361, Apr. 2013. 27
- [66] V. A. Bolaños Quiñones, L. Ma, S. Li, M. Jorgensen, S. Kiravittaya, and O. G. Schmidt, “Localized optical resonances in low refractive index rolled-up microtube cavity for liquid-core optofluidic detection,” *Appl. Phys. Lett.*, vol. 101, p. 151107, Oct. 2012. 27
- [67] E. J. Smith, S. Schulze, S. Kiravittaya, Y. Mei, S. Sanchez, and O. G. Schmidt, “Lab-in-a-Tube: Detection of Individual Mouse Cells for Analysis in Flexible Split-Wall Microtube Resonator Sensors,” *Nano Lett.*, vol. 11, pp. 4037–4042, Oct. 2011. 27
- [68] M. R. Jorgensen, S. Giudicatti, and O. G. Schmidt, “Diamond lattice photonic crystals from rolled-up membranes,” *Phys. Rev. A*, vol. 87, p. 041803, Apr. 2013. Publisher: American Physical Society. 28
- [69] K. J. Vahala, “Optical microcavities,” *Nature*, vol. 424, pp. 839–846, Aug. 2003. 28
- [70] M. Notomi, “Strong Light Confinement With Periodicity,” *Proceedings of the IEEE*, vol. 99, pp. 1768–1779, Oct. 2011. Conference Name: Proceedings of the IEEE. 28
- [71] E. Yablonovitch, “Inhibited Spontaneous Emission in Solid-State Physics and Electronics,” *Phys. Rev. Lett.*, vol. 58, pp. 2059–2062, May 1987. 29
- [72] P. Yeh and A. Yariv, “Bragg reflection waveguides,” *Optics Communications*, vol. 19, pp. 427–430, Dec. 1976. 29
- [73] A. Y. Cho, A. Yariv, and P. Yeh, “Observation of confined propagation in Bragg waveguides,” *Appl. Phys. Lett.*, vol. 30, pp. 471–472, May 1977. Publisher: American Institute of Physics. 29
- [74] P. Yeh, A. Yariv, and E. Marom, “Theory of Bragg fiber\*,” *J. Opt. Soc. Am., JOS A*, vol. 68, pp. 1196–1201, Sept. 1978. Publisher: Optical Society of America. 29
- [75] Y. Fink, J. N. Winn, S. Fan, C. Chen, J. Michel, J. D. Joannopoulos, and E. L. Thomas, “A Dielectric Omnidirectional Reflector,” *Science*, vol. 282, pp. 1679–1682, Nov. 1998. Publisher: American Association for the Advancement of Science Section: Report. 29

- [76] B. Temelkuran, S. D. Hart, G. Benoit, J. D. Joannopoulos, and Y. Fink, “Wavelength-scalable hollow optical fibres with large photonic bandgaps for CO<sub>2</sub> laser transmission,” *Nature*, vol. 420, pp. 650–653, Dec. 2002. Number: 6916 Publisher: Nature Publishing Group. 30, 31
- [77] R. F. Cregan, B. J. Mangan, J. C. Knight, T. A. Birks, P. S. J. Russell, P. J. Roberts, and D. C. Allan, “Single-Mode Photonic Band Gap Guidance of Light in Air,” *Science*, vol. 285, pp. 1537–1539, Sept. 1999. Publisher: American Association for the Advancement of Science Section: Report. 30, 31
- [78] M. A. Duguay, Y. Kokubun, T. L. Koch, and L. Pfeiffer, “Antiresonant reflecting optical waveguides in SiO<sub>2</sub>-Si multilayer structures,” *Appl. Phys. Lett.*, vol. 49, pp. 13–15, July 1986. Publisher: American Institute of Physics. 30
- [79] D. Yin, H. Schmidt, J. P. Barber, and A. R. Hawkins, “Integrated ARROW waveguides with hollow cores,” *Opt. Express, OE*, vol. 12, pp. 2710–2715, June 2004. Publisher: Optical Society of America. 31
- [80] D. Yin, J. P. Barber, A. R. Hawkins, and H. Schmidt, “Waveguide loss optimization in hollow-core ARROW waveguides,” *Opt. Express*, vol. 13, no. 23, p. 9331, 2005. 31
- [81] E. J. Lunt, B. Wu, J. M. Keeley, P. Measor, H. Schmidt, and A. R. Hawkins, “Hollow ARROW Waveguides on Self-Aligned Pedestals for Improved Geometry and Transmission,” *IEEE Photonics Technology Letters*, vol. 22, pp. 1147–1149, Aug. 2010. Conference Name: IEEE Photonics Technology Letters. 31
- [82] F. Couny, F. Benabid, P. J. Roberts, P. S. Light, and M. G. Raymer, “Generation and Photonic Guidance of Multi-Octave Optical-Frequency Combs,” *Science*, vol. 318, pp. 1118–1121, Nov. 2007. Publisher: American Association for the Advancement of Science Section: Report. 31
- [83] C. Jain, A. Braun, J. Gargiulo, B. Jang, G. Li, H. Lehmann, S. A. Maier, and M. A. Schmidt, “Hollow Core Light Cage: Trapping Light Behind Bars,” *ACS Photonics*, vol. 6, pp. 649–658, Mar. 2019. 31, 32
- [84] Y. Y. Wang, N. V. Wheeler, F. Couny, P. J. Roberts, and F. Benabid, “Low loss broadband transmission in hypocycloid-core Kagome hollow-core photonic crystal fiber,” *Opt. Lett., OL*, vol. 36, pp. 669–671, Mar. 2011. Publisher: Optical Society of America. 32
- [85] I. A. Bufetov, A. F. Kosolapov, A. D. Pryamikov, A. V. Gladyshev, A. N. Kolyadin, A. A. Krylov, Y. P. Yatsenko, and A. S. Biriukov, “Revolver Hollow Core Optical Fibers,” *Fibers*, vol. 6, p. 39, June 2018. Number: 2 Publisher: Multidisciplinary Digital Publishing Institute. 32
- [86] A. N. Kolyadin, A. F. Kosolapov, A. D. Pryamikov, A. S. Biriukov, V. G. Plotnichenko, and E. M. Dianov, “Light transmission in negative curvature hollow core fiber in extremely high material loss region,” *Opt. Express, OE*, vol. 21, pp. 9514–9519, Apr. 2013. Publisher: Optical Society of America. 32
- [87] F. Poletti, “Nested antiresonant nodeless hollow core fiber,” *Opt. Express, OE*, vol. 22, pp. 23807–23828, Oct. 2014. Publisher: Optical Society of America. 32

- [88] H. Sakr, Y. Chen, G. T. Jasion, T. D. Bradley, J. R. Hayes, H. C. H. Mulvad, I. A. Davidson, E. Numkam Fokoua, and F. Poletti, “Hollow core optical fibres with comparable attenuation to silica fibres between 600 and 1100 nm,” *Nature Communications*, vol. 11, p. 6030, Nov. 2020. Number: 1 Publisher: Nature Publishing Group. 32
- [89] B. Jang, J. Gargiulo, M. Ziegler, R. F. Ando, U. Hübner, S. A. Maier, and M. A. Schmidt, “Fine-tuning of the optical properties of hollow-core light cages using dielectric nanofilms,” *Opt. Lett., OL*, vol. 45, pp. 196–199, Jan. 2020. 32
- [90] J. Kim, B. Jang, J. Gargiulo, J. Bürger, J. Zhao, S. Upendar, T. Weiss, S. A. Maier, and M. A. Schmidt, “The Optofluidic Light Cage – On-Chip Integrated Spectroscopy Using an Antiresonance Hollow Core Waveguide,” *Anal. Chem.*, vol. 93, pp. 752–760, Jan. 2021. Publisher: American Chemical Society. 32
- [91] S. G. Johnson, A. Mekis, S. Fan, and J. D. Joannopoulos, “Molding the flow of light,” *Computing in Science Engineering*, vol. 3, pp. 38–47, Nov. 2001. Conference Name: Computing in Science Engineering. 35
- [92] S. S. Wang and R. Magnusson, “Theory and applications of guided-mode resonance filters,” *Appl. Opt., AO*, vol. 32, pp. 2606–2613, May 1993. Publisher: Optical Society of America. 37
- [93] V. N. Astratov, I. S. Culshaw, R. M. Stevenson, D. M. Whittaker, M. S. Skolnick, T. F. Krauss, and R. M. D. L. Rue, “Resonant Coupling of Near-Infrared Radiation to Photonic Band Structure Waveguides,” *J. Lightwave Technol., JLT*, vol. 17, p. 2050, Nov. 1999. Publisher: IEEE. 37
- [94] J. M. Pottage, E. Silvestre, and P. S. J. Russell, “Vertical-cavity surface-emitting resonances in photonic crystal films,” *J. Opt. Soc. Am. A, JOSAA*, vol. 18, pp. 442–447, Feb. 2001. Publisher: Optical Society of America. 37
- [95] X. Letartre, J. Mouette, J. L. Leclercq, P. R. Romeo, C. Seassal, and P. Viktorovitch, “Switching Devices With Spatial and Spectral Resolution Combining Photonic Crystal and MOEMS Structures,” *J. Lightwave Technol., JLT*, vol. 21, p. 1691, July 2003. 38, 39
- [96] J. Mouette, C. Seassal, X. Letartre, P. Rojo-Romeo, J. Leclercq, P. Regreny, P. Viktorovitch, E. Jalaguier, R. Perreau, and H. Moriceau, “Very low threshold vertical emitting laser operation in InP graphite photonic crystal slab on silicon,” *Electronics Letters*, vol. 39, pp. 526–528, Mar. 2003. 39
- [97] Y. Ding and R. Magnusson, “Resonant leaky-mode spectral-band engineering and device applications,” *Opt. Express, OE*, vol. 12, pp. 5661–5674, Nov. 2004. 39
- [98] C. Mateus, M. Huang, Y. Deng, A. Neureuther, and C. Chang-Hasnain, “Ultra-broadband mirror using low-index cladded subwavelength grating,” *IEEE Photonics Technology Letters*, vol. 16, pp. 518–520, Feb. 2004. 39
- [99] C. Mateus, M. Huang, L. Chen, C. Chang-Hasnain, and Y. Suzuki, “Broadband mirror (1.12-1.62  $\mu\text{m}$ ) using a subwavelength grating,” *IEEE Photonics Technology Letters*, vol. 16, pp. 1676–1678, July 2004. 39



- [100] V. Lousse, W. Suh, O. Kilic, S. Kim, O. Solgaard, and S. Fan, “Angular and polarization properties of a photonic crystal slab mirror,” *Opt. Express, OE*, vol. 12, pp. 1575–1582, Apr. 2004. Publisher: Optical Society of America. 39
- [101] S. Boutami, B. B. Bakir, H. Hattori, X. Letartre, J. Leclercq, P. Rojo-Romeo, M. Garrigues, C. Seassal, and P. Viktorovitch, “Broadband and compact 2-D photonic crystal reflectors with controllable polarization dependence,” *IEEE Photonics Technology Letters*, vol. 18, pp. 835–837, Apr. 2006. Conference Name: IEEE Photonics Technology Letters. 39
- [102] A. E. Willner, “Lasers: All mirrors are not created equal,” *Nature Photonics*, vol. 1, pp. 87–88, Feb. 2007. 40
- [103] S. Boutami, B. Ben Bakir, J.-L. Leclercq, X. Letartre, P. Rojo-Romeo, M. Garrigues, P. Viktorovitch, I. Sagnes, L. Legratiet, and M. Strassner, “Highly selective and compact tunable MOEMS photonic crystal Fabry-Perot filter,” *Opt. Express*, vol. 14, no. 8, p. 3129, 2006. 40
- [104] S. Boutami, B. Benbakir, J.-L. Leclercq, and P. Viktorovitch, “Compact and polarization controlled  $1.55\mu\text{m}$  vertical-cavity surface-emitting laser using single-layer photonic crystal mirror,” *Applied Physics Letters*, vol. 91, p. 071105, Aug. 2007. 41
- [105] S. Boutami, B. Benbakir, X. Letartre, J. L. Leclercq, P. Regreny, and P. Viktorovitch, “Ultimate vertical Fabry-Perot cavity based on single-layer photonic crystal mirrors,” *Optics Express*, vol. 15, no. 19, p. 12443, 2007. 41
- [106] C. Sieutat, R. Peretti, J.-L. Leclercq, P. Viktorovitch, and X. Letartre, “Strong confinement of light in low index materials: the Photon Cage,” *Opt. Express, OE*, vol. 21, pp. 20015–20022, Aug. 2013. 41, 42
- [107] K. S. Novoselov, A. K. Geim, S. V. Morozov, D. Jiang, Y. Zhang, S. V. Dubonos, I. V. Grigorieva, and A. A. Firsov, “Electric Field Effect in Atomically Thin Carbon Films,” *Science*, vol. 306, pp. 666–669, Oct. 2004. Publisher: American Association for the Advancement of Science Section: Report. 44, 45
- [108] P. R. Wallace, “The Band Theory of Graphite,” *Phys. Rev.*, vol. 71, pp. 622–634, May 1947. Publisher: American Physical Society. 44
- [109] R. Peierls, “Quelques propriétés typiques des corps solides,” *Annales de l’institut Henri Poincaré*, vol. 5, no. 3, pp. 177–222, 1935. 44
- [110] S. Reich, J. Maultzsch, C. Thomsen, and P. Ordejón, “Tight-binding description of graphene,” *Phys. Rev. B*, vol. 66, p. 035412, July 2002. Publisher: American Physical Society. 45
- [111] K. I. Bolotin, F. Ghahari, M. D. Shulman, H. L. Stormer, and P. Kim, “Observation of the fractional quantum Hall effect in graphene,” *Nature*, vol. 462, pp. 196–199, Nov. 2009. Number: 7270 Publisher: Nature Publishing Group. 46
- [112] T. Ozawa, A. Amo, J. Bloch, and I. Carusotto, “Klein tunneling in driven-dissipative photonic graphene,” *Phys. Rev. A*, vol. 96, p. 013813, July 2017. Publisher: American Physical Society. 46

- [113] P. E. Allain and J. N. Fuchs, “Klein tunneling in graphene: optics with massless electrons,” *Eur. Phys. J. B*, vol. 83, pp. 301–317, Oct. 2011. arXiv: 1104.5632. 46
- [114] S. Iijima, “Helical microtubules of graphitic carbon,” *Nature*, vol. 354, pp. 56–58, Nov. 1991. Number: 6348 Publisher: Nature Publishing Group. 46
- [115] G. G. Samsonidze, A. R. Saito, D. A. Jorio, E. M. A. Pimenta, E. A. G. Souza Filho, F. A. Grüneis, D. G. Dresselhaus, and M. S. Dresselhaus, “The Concept of Cutting Lines in Carbon Nanotube Science,” *Journal of Nanoscience and Nanotechnology*, vol. 3, pp. 431–458, Dec. 2003. 46
- [116] S. Reich, C. T. physicien, C. Thomsen, and J. Maultzsch, *Carbon Nanotubes: Basic Concepts and Physical Properties*. John Wiley & Sons, Mar. 2004. Google-Books-ID: w\_xpdFx0C4MC. 47
- [117] T. Ando and Y. Zheng, “Hall conductivity of a two-dimensional graphite system,” *Phys. Rev. B*, vol. 65, p. 245420, June 2002. Publisher: American Physical Society. 47
- [118] R. Okuyama, W. Izumida, and M. Eto, “Topological classification of the single-wall carbon nanotube,” *Phys. Rev. B*, vol. 99, p. 115409, Mar. 2019. 47, 56
- [119] L. Lu, J. D. Joannopoulos, and M. Soljačić, “Topological Photonics,” *Nature Photonics*, vol. 8, pp. 821–829, Nov. 2014. arXiv: 1408.6730. 48
- [120] M. V. Berry, “Quantal phase factors accompanying adiabatic changes,” *Proceedings of the Royal Society of London. A. Mathematical and Physical Sciences*, vol. 392, pp. 45–57, Mar. 1984. Publisher: Royal Society. 48
- [121] J. Dalibard, “La matière topologique et son exploration avec les gaz quantiques,” p. 155. 48
- [122] J. E. Avron, D. Osadchy, and R. Seiler, “A Topological Look at the Quantum Hall Effect,” *Physics Today*, vol. 56, pp. 38–42, Aug. 2003. Publisher: American Institute of Physics. 49
- [123] K. v. Klitzing, G. Dorda, and M. Pepper, “New Method for High-Accuracy Determination of the Fine-Structure Constant Based on Quantized Hall Resistance,” *Phys. Rev. Lett.*, vol. 45, pp. 494–497, Aug. 1980. Publisher: American Physical Society. 49
- [124] K. von Klitzing, “The quantized Hall effect,” *Rev. Mod. Phys.*, vol. 58, pp. 519–531, July 1986. Publisher: American Physical Society. 49
- [125] R. B. Laughlin, “Quantized Hall conductivity in two dimensions,” *Phys. Rev. B*, vol. 23, pp. 5632–5633, May 1981. Publisher: American Physical Society. 49
- [126] D. J. Thouless, M. Kohmoto, M. P. Nightingale, and M. den Nijs, “Quantized Hall Conductance in a Two-Dimensional Periodic Potential,” *Phys. Rev. Lett.*, vol. 49, pp. 405–408, Aug. 1982. Publisher: American Physical Society. 49

- [127] T. Ozawa, H. M. Price, A. Amo, N. Goldman, M. Hafezi, L. Lu, M. Rechtsman, D. Schuster, J. Simon, O. Zilberberg, and I. Carusotto, “Topological Photonics,” *arXiv:1802.04173 [cond-mat, physics:physics, physics:quant-ph]*, Feb. 2018. arXiv: 1802.04173. 49
- [128] A. Messiah, *Quantum Mechanics, Chapter XVII, § 13, t. II*. Amsterdam: North-Holland Publishing Company, 1961. 49
- [129] Y. Hatsugai, “Chern number and edge states in the integer quantum Hall effect,” *Phys. Rev. Lett.*, vol. 71, pp. 3697–3700, Nov. 1993. Publisher: American Physical Society. 52
- [130] F. D. M. Haldane, “Model for a Quantum Hall Effect without Landau Levels: Condensed-Matter Realization of the ”Parity Anomaly”,” *Phys. Rev. Lett.*, vol. 61, pp. 2015–2018, Oct. 1988. Publisher: American Physical Society. 52
- [131] C.-Z. Chang, J. Zhang, X. Feng, J. Shen, Z. Zhang, M. Guo, K. Li, Y. Ou, P. Wei, L.-L. Wang, Z.-Q. Ji, Y. Feng, S. Ji, X. Chen, J. Jia, X. Dai, Z. Fang, S.-C. Zhang, K. He, Y. Wang, L. Lu, X.-C. Ma, and Q.-K. Xue, “Experimental Observation of the Quantum Anomalous Hall Effect in a Magnetic Topological Insulator,” *Science*, vol. 340, pp. 167–170, Apr. 2013. Publisher: American Association for the Advancement of Science Section: Report. 52
- [132] C. L. Kane and E. J. Mele, “Quantum Spin Hall Effect in Graphene,” *Phys. Rev. Lett.*, vol. 95, p. 226801, Nov. 2005. Publisher: American Physical Society. 52
- [133] B. A. Bernevig and S.-C. Zhang, “Quantum Spin Hall Effect,” *Phys. Rev. Lett.*, vol. 96, p. 106802, Mar. 2006. Publisher: American Physical Society. 52
- [134] M. König, S. Wiedmann, C. Brüne, A. Roth, H. Buhmann, L. W. Molenkamp, X.-L. Qi, and S.-C. Zhang, “Quantum Spin Hall Insulator State in HgTe Quantum Wells,” *Science*, vol. 318, pp. 766–770, Nov. 2007. Publisher: American Association for the Advancement of Science Section: Research Article. 53
- [135] A. Kitaev, “Periodic table for topological insulators and superconductors,” *AIP Conference Proceedings*, vol. 1134, pp. 22–30, May 2009. Publisher: American Institute of Physics. 53
- [136] J. Zak, “Berry’s phase for energy bands in solids,” *Phys. Rev. Lett.*, vol. 62, pp. 2747–2750, June 1989. Publisher: American Physical Society. 55
- [137] P. Delplace, D. Ullmo, and G. Montambaux, “Zak phase and the existence of edge states in graphene,” *Phys. Rev. B*, vol. 84, p. 195452, Nov. 2011. Publisher: American Physical Society. 55, 56
- [138] Z. Wang, Y. Chong, J. D. Joannopoulos, and M. Soljačić, “Observation of unidirectional backscattering-immune topological electromagnetic states,” *Nature*, vol. 461, pp. 772–775, Oct. 2009. Number: 7265 Publisher: Nature Publishing Group. 56, 57
- [139] M. C. Rechtsman, J. M. Zeuner, Y. Plotnik, Y. Lumer, D. Podolsky, F. Dreisow, S. Nolte, M. Segev, and A. Szameit, “Photonic Floquet topological insulators,” *Nature*, vol. 496, pp. 196–200, Apr. 2013. Number: 7444 Publisher: Nature Publishing Group. 56, 57

- [140] L.-H. Wu and X. Hu, “Scheme for Achieving a Topological Photonic Crystal by Using Dielectric Material,” *Phys. Rev. Lett.*, vol. 114, p. 223901, June 2015. 57, 60
- [141] S. Barik, A. Karasahin, C. Flower, T. Cai, H. Miyake, W. DeGottardi, M. Hafezi, and E. Waks, “A topological quantum optics interface,” *Science*, vol. 359, pp. 666–668, Feb. 2018. 58
- [142] P. St-Jean, V. Goblot, E. Galopin, A. Lemaître, T. Ozawa, L. Le Gratiet, I. Sagnes, J. Bloch, and A. Amo, “Lasing in topological edge states of a one-dimensional lattice,” *Nature Photon*, vol. 11, pp. 651–656, Oct. 2017. Number: 10 Publisher: Nature Publishing Group. 59
- [143] M. Polini, F. Guinea, M. Lewenstein, H. C. Manoharan, and V. Pellegrini, “Artificial graphene as a tunable Dirac material,” *Nature Nanotech*, vol. 8, pp. 625–633, Sept. 2013. arXiv: 1304.0750. 59
- [144] M. Bellec, U. Kuhl, G. Montambaux, and F. Mortessagne, “Topological Transition of Dirac Points in a Microwave Experiment,” *Phys. Rev. Lett.*, vol. 110, p. 033902, Jan. 2013. Publisher: American Physical Society. 59
- [145] T. Jacqmin, I. Carusotto, I. Sagnes, M. Abbarchi, D. Solnyshkov, G. Malpuech, E. Galopin, A. Lemaître, J. Bloch, and A. Amo, “Direct Observation of Dirac Cones and a Flatband in a Honeycomb Lattice for Polaritons,” *Phys. Rev. Lett.*, vol. 112, p. 116402, Mar. 2014. Publisher: American Physical Society. 59
- [146] G. Montambaux, “Artificial graphenes: Dirac matter beyond condensed matter,” *Comptes Rendus Physique*, vol. 19, pp. 285–305, July 2018. 59
- [147] L. Tarruell, D. Greif, T. Uehlinger, G. Jotzu, and T. Esslinger, “Creating, moving and merging Dirac points with a Fermi gas in a tunable honeycomb lattice,” *Nature*, vol. 483, pp. 302–305, Mar. 2012. Number: 7389 Publisher: Nature Publishing Group. 59
- [148] S. Barik, H. Miyake, W. DeGottardi, E. Waks, and M. Hafezi, “Two-dimensionally confined topological edge states in photonic crystals,” *New J. Phys.*, vol. 18, no. 11, p. 113013, 2016. 60



# Chapter 2

## Numerical, fabrication and optical characterization methods

*La vie est brève :  
un peu d'espoir,  
un peu de rêve ...  
et puis-bonsoir !*

---

ANONYME

### Contents

---

<b>2.1</b>	<b>Simulations of optical properties . . . . .</b>	<b>76</b>
2.1.1	Rigorous coupled-wave analysis . . . . .	76
2.1.2	Finite difference time domain simulations . . . . .	78
<b>2.2</b>	<b>Fabrication process . . . . .</b>	<b>85</b>
2.2.1	Production of the precursor multi-layered stacks . . . . .	86
2.2.2	Design, fabrication and transfer of the planar mask . . . . .	90
2.2.3	Rolling the photonic crystal membrane . . . . .	95
2.2.4	Conclusion . . . . .	96
<b>2.3</b>	<b>Optical characterization . . . . .</b>	<b>97</b>
2.3.1	Scanning near-field optical microscopy (SNOM) . . . . .	97
2.3.2	Angle-resolved spectral measurements . . . . .	102
<b>2.4</b>	<b>Conclusion of the chapter . . . . .</b>	<b>105</b>
<b>2.5</b>	<b>References . . . . .</b>	<b>107</b>

---

In this chapter, we present the ensemble of methods which allow the conception and the characterization from the the planar photonic crystal membranes (PCM) building blocks to the final rolled-up microstructures. The first section focuses on the numerical methods employed to simulate the optical responses of the planar photonic membranes and the cylindrical cavities.

## 2.1 Simulations of optical properties

The description of the propagation of light in any structure entails the resolution of Maxwell's equations. However, for lack of simple analytical solutions in the general case, this resolution implies the use of numerical methods. The most appealing numerical methods provide a wide choice of tunable parameters, optical outputs and apply to almost any complex architectures, but often at the cost of high memory resources and simulation time. Alternatively, some methods have restrained their field of action to calculate optical properties of specific geometries such as periodic structures at minor computing cost and with great precision.

This section introduces the two main numerical methods used in this thesis to apprehend optical properties of planar and rolled-up photonic structures: the rigorous coupled-wave analysis (RCWA) and the finite-difference time-domain (FDTD) method. For both method, we first explain the principle of resolution and the domain of applicability. We specify then the different outputs or the accessible optical properties. We finally illustrate the application of the methods on typical structures in anticipation to the results of later chapters.

### 2.1.1 Rigorous coupled-wave analysis

The rigorous coupled-wave analysis (RCWA), also known as the Fourier modal method (FMM), is a rigorous and semi-analytical method of computing electromagnetics popularized by Moharam and Gaylord in 1980s [1, 2]. It relies on the numerical resolution of Maxwell's equations in the spatial frequency domain for the particular subset of structures with in-plane periodicity but out-of-plane uniformity such as 2D photonic crystal membranes (PCM). The method is said rigorous as the solution tends toward the exact solution for an infinite number of spatial harmonics, and semi-analytical as we search for analytical solutions in the out-of-plane direction but in-plane numeric solutions. The accuracy of the solutions depends essentially on the number of harmonics denoted  $N$ , and convergence testing is therefore needed to attest the validity of the results.

The RCWA simulates the response of photonic structures to incident plane wave excitation. It provides optical properties such as reflection, transmission, and absorption efficiencies. In particular, we exploit the method to extract the reflectivity spectra of 2D PCM at normal and oblique incidences related to the dispersion of guided resonances. Guided-mode resonances located above the light line are also accessible through angle-resolved far-field optical measurements described in later Section 2.3. We can therefore compare both diagrams afterward. In this thesis, we use the free-access  $S^4$  solver developed by Fan group [3] in the Stanford Electrical Engineering Department to conduct the RCWA calculations.

In addressing the conception of the 2D PCM wall of future tubular photonic cages, our strategy aims at adjusting the lattice parameters and the membrane thickness to achieve a high reflective behavior on a broad spectral range at normal incidence.

We note that the RCWA method is efficient to estimate rapidly the reflectivity while sweeping the value of the lattice parameters. Typically, in our case, we calculate the reflectivity spectrum at normal incidence of a 2D PCM consisting of a triangular lattice with a period  $a$  of air holes of radius  $r$  etched in an  $h$ -thick InP-based, as sketched on the top and section views of Figure 2.1.a). We indicate the lattice vectors  $\vec{a}_1$  and  $\vec{a}_2$  of the lattice system. The calculations zone reduces to the green-shaded primitive cell assuming infinite lateral size of the PCM. We chose a linear polarization of the incident plane wave with the electric field pointing to the  $x$ -axis direction. We fix the value of  $a$  and  $r$  to 1 and  $0.4 \mu\text{m}$ , respectively, while performing a sweep of  $h$  from  $0.21$  to  $0.23 \mu\text{m}$ . We set the number of spatial harmonics  $N$  to 20 as for the demonstration. We propose two representations of the simulated PCM reflectivity spectrum to properly visualize the intensity of the reflection on the curves of Figure b) along with the spectral dynamics of the guided resonances (GR) on the maps of Figure c). In particular, owing to the emergence and redshift of  $\text{GR}_3$ , we observe that  $\text{GR}_1$  redshifts and combines with  $\text{GR}_2$  to form a large band of high reflectivity.

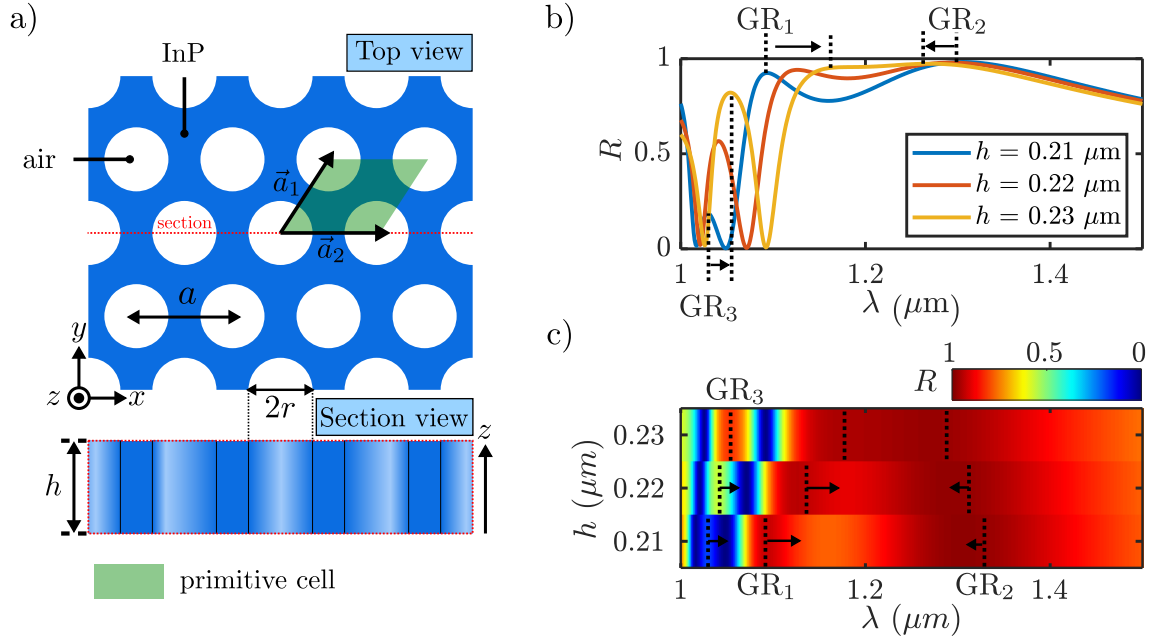


FIGURE 2.1: a) Top view of the PCM: schematized triangular lattice, with a period  $a$ , of air holes of radius  $r$  etched in an InP-based dielectric membrane. The lattice basis  $(\vec{a}_1, \vec{a}_2)$  covers the green-shaded primitive cell. Section view of the PCM: section of the  $h$ -thick membrane along the red dashed line in the top view. b) Reflectivity spectra  $R(\lambda)$  of the PCM for different thicknesses  $h = 0.21, 0.22, 0.23 \mu\text{m}$  calculated with the RCWA method. c) Map version of b).

In principle, the RCWA only gives access to the dispersion of the PCM guided resonances which couples with the incident plane wave, but not to that of remaining PCM guided modes unless introducing an artificial double period or material absorption. It also shows less efficiency in calculating the dispersion of high-index-contrast structures as the finite truncation of Fourier harmonics leads to Gibbs phenomenon. Finally, the RCWA algorithm essentially applies to multi-layered structures with in-plane patterning for some layers. Instead, to tackle the simulation of the optical response of more complex 3D structures such as rolled-up PCM, we use the finite difference time domain method (FDTD) described below.



## 2.1.2 Finite difference time domain simulations

### Introduction

The finite-difference time-domain (FDTD) method has proved to be one of the most popular and powerful numerical tools of computational electromagnetics. The FDTD algorithm, first implemented by Yee in 1966, directly resolves Maxwell's equation in time and spatial domains replacing partial derivatives with finite differences. The popularity of the FDTD method relies on several reasons. First, it represents a robust and accurate resolution method. Indeed, sources of numerical errors are known and easily corrigible. Moreover, the reduction of spatial and time discretization allows achieving the closest prediction to reality. Second, it is suitable to test the impulse response of structures over a wide spectral range. Third, it provides a systematic approach that applies to any structures regardless of geometries and dispersion properties. In other terms, the problem needs no reformulation when varying the system but adaptation of the spatial mesh. Finally, we can extract various optical properties from time-varying outputs, including spectra and band structures. We conduct the following FDTD simulations with the LUMERICAL FDTD solver.

We will use the FDTD method in this thesis to calculate spectrale responses, maps of the electromagnetic fields and band structures. First, we illustrate the calculation of the spectral response, maps of the electromagnetic fields and the quality factors of the modes supported by a plain InP-made hollow cylindrical cavity. We extend the simulation scheme in Chapter 3 to predict tubular photon cages' spectral responses. Second, we describe the simulation setting to calculate the dispersion diagrams of a honeycomb lattice photonic crystal (PC) in anticipation of Chapter 5 developments.

### Illustration of the spectral properties of plain InP-based microtubes

We first draw a seamless tube made of InP material modelled as a pink-shaded microtube on the LUMERICAL 3D CAD views presented in Figures 2.2.a), b), and c). We load the InP material's optical dispersion properties from the *InP-Palik* reference experimental data available in the LUMERICAL bank of materials. The reference dispersion is fitted within the spectral range  $[1.275-1.875] \mu m$  with a polynomial function of order and a fit tolerance set to 6 and 0.1 by default. Note that the previous parameters stay valid for future simulations involving InP-based structures within the same spectral window unless otherwise stated. We fix the inner radius  $\rho_{in}$  of the tube to  $17.5 \mu m$  and the membrane wall thickness  $h$  to  $0.228 \mu m$  for comparison with real structures. We simulate for the demonstration an infinitely long microtube so that the calculation zone only extends in the cross-section of the cavity.

We define then the main parameters of the FDTD computation zone delimited by an orange contour in Figure 2.2.a) and covering the cavity cross-section.

- The simulation time  $t_s$  set to 10 ps. An appropriate value of  $t_s$  supposes a complete decay of the electromagnetic energy inside of the computation zone at the end of the simulation. The FDTD solver proposes an auto-shutoff level that estimates the remaining energy in the simulation region. Proper termination of the simulation at  $t_s$  sees the level reaching a threshold value set by default to  $1.10^{-5}$  of the initial energy. In high-quality factor cavities, the electromagnetic energy decreases very slowly so that a proper decay occurs for high  $t_s$ . Such a situation requires a specific methodology explained below.

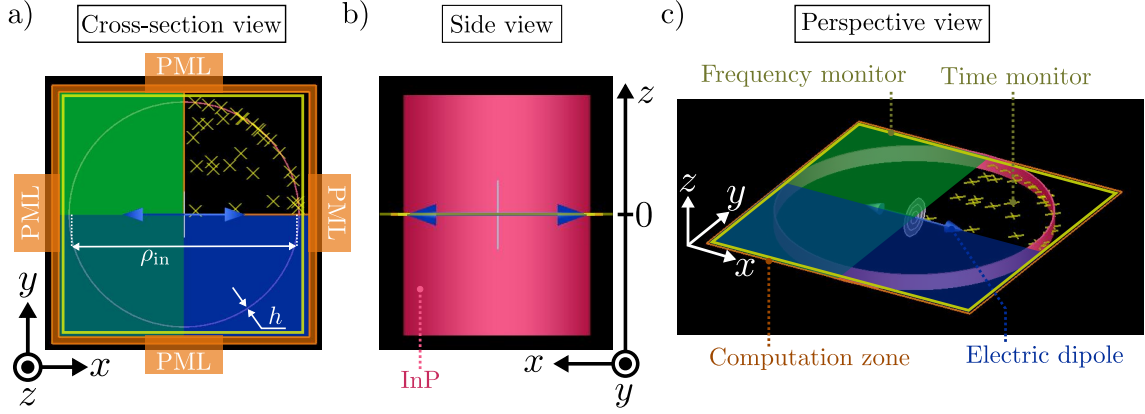


FIGURE 2.2: Cross-section (a), side (b) and perspective (c) views: FDTD model in LUMERICAL CAD environment for the calculation of the spectral response of a plain cylindrical InP-based cavity of inner radius  $\rho_{in}$  and membrane thickness  $h$ . The blue arrow and the yellow crosses schematize the dipole source excitation and the time point monitors. We apply perfect matched layers (PML), symmetric (blue zone), and anti-symmetric (green zone) boundary conditions on the borders of the simulation region outlined in orange.

- The spatial and temporal sampling. The implementation of the FDTD algorithm implies a Cartesian mesh with rectangular mesh cells. Inherently to the FDTD method, the spatial mesh of the computation zone constitutes one of the main sources of numerical errors. To minimize the errors, the LUMERICAL solver proposes an adaptive mesh which automatically adjusts the mesh size to the material's optical properties. Concretely, the mesh size becomes smaller in higher optical index and highly absorbent materials. Different levels of mesh accuracy, from 1 to 6, are available and reduces the mesh size to achieve better precision, however, at the cost of higher computation time. We chose a mesh accuracy of 2 which enables rapid calculations with a minimum mesh size  $\Delta$  in the order of  $0.04 \mu m$ . We also use the conformal technology to refine the mesh at interfaces between different materials. Finally, the time step  $dt$  is automatically adjusted to the value of  $\Delta$  to ensure numerical stability of the simulation<sup>1</sup>.
- The boundary conditions. We apply perfect matched layers (PML) boundary conditions (BC) to the four borders of the simulation region as indicated in Figure 2.2.a). The PML boundaries absorb incident light when eventually escaping out of finite-size structures. They contain layers of absorbing material impedance matched with the surrounding medium to achieve a minimal reflection. The LUMERICAL FDTD solver proposes various PML profiles characterized by different absorption efficiencies. Here, we use the lowest demanding setting of PML referred to as *normal* profile. The distance of the PML boundaries to the structure also influences the absorption efficiency. For high PML-structure proximity, the PML may interact with the evanescent tail of modes and generate spurious reflections. We position the PML frontiers at about  $2.3 \mu m$  to the microtube outer radius in both x and y directions<sup>2</sup>.

Following the definition of the computation zone, we introduce the two main ingre-

<sup>1</sup>The numerical stability is guaranteed when  $dt$  fulfils the Courant-Friedrichs-Lewy (CFL) stability criterion:  $dt \leq \Delta/(\sqrt{d}c_0)$  where  $d$  and  $c_0$  designate the structure dimensionality and the speed of light, respectively

<sup>2</sup>We satisfy the solver's recommendation of placing the PML at least half of a maximum excitation wavelength (here,  $1.875 \mu m$ ) to the structure's boundaries.

dients for the simulation of the cavity spectral response: the excitation source and the monitors. We describe below the tunable parameters for both objects.

- The excitation source. Oscillating electric or magnetic dipole are suitable sources for investigating the cavity modes as they radiate in almost every direction. We use a single oscillating electric dipole centred in the cavity cross-section and oriented along the  $x$ -axis direction as illustrated in Figure 2.2. It allows preferential excitation of modes with pure axial magnetic components: ( $H_x = H_y = 0, H_z \neq 0$ ) referred to as TE modes in Chapter 3. Moreover, we exploit symmetries shared by the dipole and the cavity to reduce the computation time. In particular, we apply symmetric (anti-symmetric) boundary conditions over the blue-shaded (green-shaded) half-plane  $y \leq 0$  ( $x \leq 0$ ). It restricts the computation zone to the quadrant with positive coordinates  $x, y \geq 0$  and decreases the computation time by a factor of 4. Finally, we set the emission Gaussian-shaped bandwidth of the dipole from 1.275 to 1.875  $\mu m$ .
- The monitors. We use time point monitors, symbolized by yellow crosses in Figure 2.2.a), to collect the temporal evolution of the electric  $E_{x,y,z}(t)$  and magnetic  $H_{x,y,z}(t)$  field components at a given position  $(x, y, z)$ . We disperse two groups of 15 time monitors, in the hollow core and the cavity membrane wall, at random positions over the computation zone, as depicted in Figure 2.2.a). The monitors' arbitrary positions ensure to maximize the spatial overlap with the cavity modes' fields.

Once the simulation terminated, we collect the time data and perform two operations to recover the cavity spectral response:

- The apodization of the time signals. When dealing with high-quality factor ( $Q$ ) modes, a complete decay of the field may be impossible or require substantial  $t_s$ . Consequently, the cavity spectrum results from the Fourier transform of time signals truncated with a rectangular window, hence convolved to a sinc function in the frequency domain. To avoid such phenomenon, we apodize the time signals before the Fourier transform with a Gaussian window of bandwidth  $\Delta t$  and centred on  $t_c$ . In the frequency domain, the spectral features convolve to a Gaussian envelope with a bandwidth inversely proportional to  $\Delta t$ . We adjust the apodization parameters to remove the source pulse's contribution and the signal ending and finally collect the cavity modes' signatures exclusively. Due to apodization, straightforward estimations of the modes'  $Q$  factors from the spectral peaks' bandwidths are not reliable as overestimated. We extract thus  $Q$  values with a post-treatment of time signals based on harmonic inversion as explained later. We apodize the time signals of every electric fields' components with the following parameters:  $t_c = 0.5t_s$  and  $\Delta t = 0.15t_s$ .
- The Fourier transform of the time signals. We construct the cavity spectrum  $I(\lambda)$  by adding square Fourier transforms of each electric field components' pre-apodized times signals;

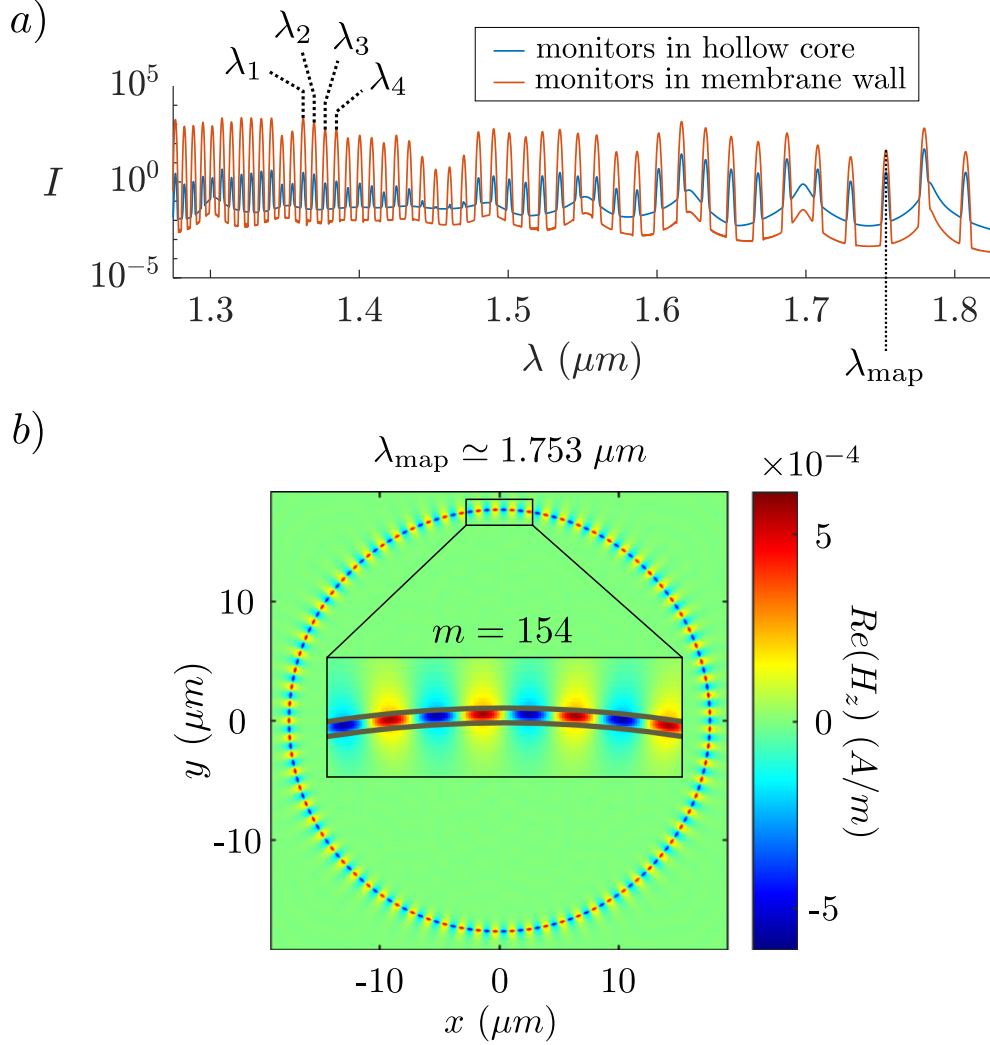


FIGURE 2.3: a) Electric field intensity spectra  $I(\lambda)$  of the InP-made microtube extracted from time monitors data in the hollow core (blue curve) and the membrane wall of the cavity. b) Map of the real axial magnetic component  $H_z$  at the excitation wavelength  $\lambda_{\text{map}} \simeq 1.753 \mu\text{m}$ .

We present in Figure 2.3.a) the spectral responses  $I(\lambda)$  calculated in the hollow core (blue curve) and the membrane wall (orange curve) of the InP-made cylindrical cavity, in logarithmic scale and within the spectral range  $[1.275\text{-}1.875] \mu\text{m}$ . Both spectra coincide exactly and contain successive peaks with a spectral spacing increasing with the wavelength.

We investigate the nature of the modes detected in the spectra of Figure 2.3.a) by calculating maps of the fields in the cavity cross-section. To this end, we place a frequency monitor (yellow outline) covering the computation zone area as represented in Figures 2.2.a) and c). The frequency monitor records the fields' time signals at each point of the computation zone mesh and performs a Fourier transformation of the time signals at a given frequency. We have simulated, for instance, the spatial distribution of the real magnetic field component  $H_z$  at the resonance frequency  $f_{\text{map}} = 171 \text{ THz}$  (i.e. at  $\lambda_{\text{map}} = 1.753 \mu\text{m}$ ) represented in Figure 2.3.b). We notice azimuthal oscillations of the field in the way of whispering gallery modes with an azimuthal order  $m = 154$ . The mode evolves exclusively in the membrane wall outlined in dashed grey line, around the tube circumference. We find similar mode patterns at the wavelengths of the other peaks with  $m$  decreasing for higher wavelengths.

We finally estimate the quality factors  $Q$  of the detected modes. We mentioned

earlier the difficulty to extract reliable  $Q$  values directly from the spectrum of a cavity supporting slowly decaying modes. Instead, we perform *harmonic inversion* assuming a specific form  $s(t)$  of the truncated time signals:

$$s(t) = \sum_r A_r \sin(\omega_r t + \phi_r) e^{-\alpha_r t}, \quad (2.1)$$

as a combination of sine functions of amplitude  $A_r$ , phase  $\phi_r$ , and pulsation  $\omega_r$  multiplied to an exponentially decaying envelope of decay rate  $\alpha_r$ . Therefore, the quality factor of the mode at  $\omega_r$  simply relates to the decay rate according to  $Q = \omega_r/2\alpha_r$ . We use the free-access solver *Harminv* based on filter diagonalization method (FDM) to find the parameters of the sine and exponential functions. In particular, we applied the method to estimate the  $Q$  factors of the four modes detected at  $\lambda_1$ ,  $\lambda_2$ ,  $\lambda_3$  and  $\lambda_4$  in Figure 2.3.a). We gather the results in Table 2.1 where we give the sine parameters for each resonance and a coarse estimation of the relative error  $e_r$  on the resonance pulsation. We confirm the high  $Q$  values of the modes which justifies the apodization procedure.

$r$	$f_r$ (THz)	$\lambda_r$ ( $\mu m$ )	$\alpha_r$ ( $10^{10}.s^{-1}$ )	$Q_r$ ( $10^4$ )	$A_r$ ( $10^{-5}.V/m$ )	$\varphi_r$ (rad)	$e_r$
1	220.03	1.3625	4.82	1.44	5.06	-1.46	$2.27 \times 10^{-8}$
2	218.86	1.3698	4.68	1.47	8.68	-1.33	$5.68 \times 10^{-9}$
3	217.67	1.3773	4.43	1.54	4.87	-2.96	$8.42 \times 10^{-9}$
4	216.49	1.3848	4.13	1.65	6.71	-3.08	$5.21 \times 10^{-9}$

TABLE 2.1: Parameters of the resonances detected between 1.36 and 1.39  $\mu m$  in the spectrum in Figure 2.3.a) following the *harmonic inversion* decomposition of Equation (2.1). We specify for each resonance  $r$  ( $r = 1, 2, 3, 4$ ): the frequency  $f_r$ , the wavelength  $\lambda_r$ , the decay rate  $\alpha_r$ , the sine amplitude  $A_r$ , the phase  $\varphi_r$  and the relative error  $e_r$  on the frequency.

### Band structure of a honeycomb lattice photonic crystal

In the present section, we expound on the generic methodology to simulate band diagrams of photonic structures. In particular, we apply the method for the computation of the band structure of a honeycomb lattice photonic crystal (PC). Similarly to the simulation of tubular cavities' spectral response, we detail successively the modelled structure, the FDTD parameters and the exploitation of the simulation results to construct the final diagrams.

We present in Figure 2.4 PC structure modelled with LUMERICAL CAD environment. It consists of a honeycomb lattice with a period  $a_h = 0.232 \mu m$  of air holes (grey circles) with a radius  $r = 0.067 \mu m$  etched in InP material (blue background). We define a non-dispersive medium with refractive index 3.16, playing the role of the InP material at around 1.55  $\mu m$ .

The following steps delimit and set the solver region's parameters. Considering the periodicity of the crystal, the calculation of the dispersive properties reduces to the study of a single unit cell. The smallest unit cell of the honeycomb crystallographic system forms a rhombus shape and encompasses two sites (black dots), as sketched in Figure 2.5.a). Indeed, the repetition of the unit cell according to all linear combinations in the vector basis  $(\vec{a}_1, \vec{a}_2)$  spans the entire lattice. However, the solver implements the FDTD algorithm with a Cartesian mesh, imposing a rectangular computation zone.

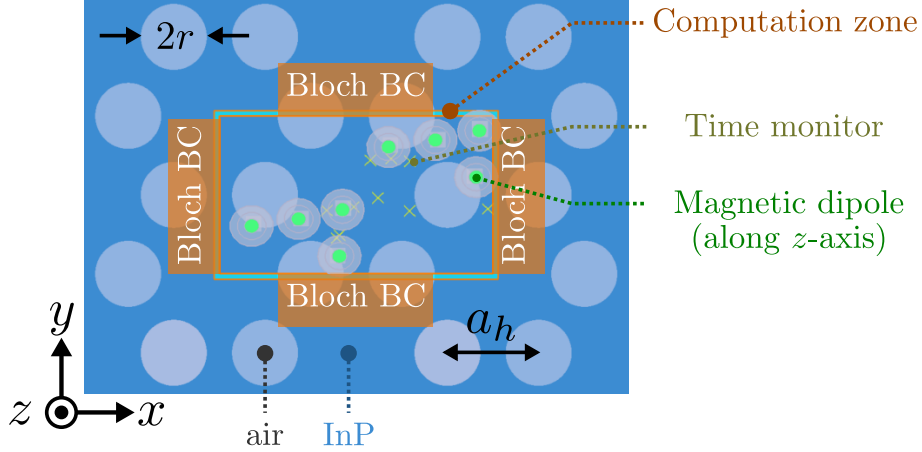


FIGURE 2.4: CAD view of the FDTD model for 2D simulation of the band structure of a honeycomb lattice (period  $a_h$ ) of air holes of radius  $r$  etched in InP material (optical refractive index  $n_{\text{InP}} \sim 3.16$  at  $1.5 \mu\text{m}$ ). Bloch boundary conditions (BC) allows the periodic repetition of the FDTD computation zone (orange outline) to form the photonic crystal pattern. Out-of-plane magnetic dipoles (green arrows) excite the modes with transverse electric (TE) polarization for which the electric field orients in the PC plane. Time monitors (yellow crosses) record the time evolution of the electromagnetic fields.

Therefore, we define a rectangular computation cell outlined in orange in Figure 2.4, ensuring the reproduction of the honeycomb crystal pattern when replicated laterally. We note that the solver region encompasses two honeycomb lattice unit cells. We explain later necessary adjustments to retrieve the original PC's periodicity and avoid artificial band folding in the final dispersion diagram. We use the conformal technology to mesh the computation cell with the solver mesh accuracy set to 3.

We apply Bloch boundary conditions (BCs) to emulate the crystal's periodicity. By contrast with pure periodic BCs, which strictly copies the electromagnetic fields from one unit cell to another, the Bloch BCs also applies a phase correction. Indeed, in periodic media, we search for propagating solutions in the form of Bloch waves:

$$\vec{E}(\vec{r}) = \vec{u}(\vec{r})e^{j\vec{k}\cdot\vec{r}}, \quad (2.2)$$

with  $\vec{u}(\vec{r})$  an envelope term sharing the same periodicity as the PC and  $e^{j\vec{k}\cdot\vec{r}}$  a plane wave propagating in the direction of the wavevector  $\vec{k} = k_x\vec{e}_x + k_y\vec{e}_y$ . The periodicity condition expresses then as:

$$\vec{E}(\vec{r} + \vec{R}) = \vec{u}(\vec{r} + \vec{R})e^{j\vec{k}\cdot(\vec{r} + \vec{R})} = \vec{E}(\vec{r})e^{j\vec{k}\cdot\vec{R}}, \quad (2.3)$$

where  $\vec{R}$  designates any combination of the lattice vectors  $\vec{R} = \alpha\vec{a}_1 + \beta\vec{a}_2$ ,  $(\alpha, \beta) \in \mathbb{Z}^2$  such that  $\vec{u}$  verifies  $\vec{u}(\vec{r} + \vec{R}) = \vec{u}(\vec{r})$ . Therefore, we identify the term  $\vec{k}\cdot\vec{R}$  in Equation (2.3) as the Bloch phase correction evoked earlier. We will show that the setting of  $\vec{k}$  is the heart of the band structure calculation. We also remark that the phase shifts  $\vec{k}\cdot\vec{R}$  and  $(\vec{k} + \vec{G})\cdot\vec{R}$  results in the same Bloch solution  $\vec{E}(\vec{r})$  on condition that  $\vec{G}$  verifies  $\vec{G}\cdot\vec{R} = 2\pi$ . The latter relation defines the reciprocal lattice, also called  $\vec{k}$ -space, where the lattice vector  $\vec{G}$  decomposes in a predefined reciprocal vector basis  $(\vec{a}_1^*, \vec{a}_2^*)$ . In particular, the reciprocal lattice of the honeycomb pattern corresponds to a triangular lattice as depicted on Figure 2.5.b) with a green-shaded primitive cell referred to as the first Brillouin zone (FBZ). Due to the  $C_6$  (or  $2\pi/3$ ) rotational symmetry, the study of the dispersion properties in the  $\vec{k}$ -space ultimately reduces to the blue-shaded area, also known as the irreducible FBZ.

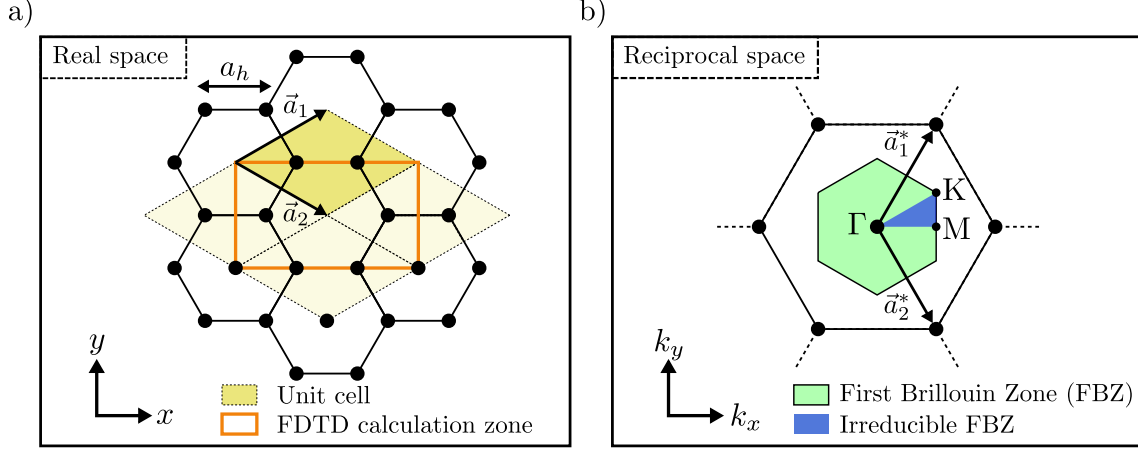


FIGURE 2.5: a) Schematics of the honeycomb crystallographic system. The lattice basis  $(\vec{a}_1, \vec{a}_2)$  covers the unit cell shaded in yellow containing two atomic sites (black dots). We superimpose the FDTD computation zone (orange outline) used for the simulation of the band structure of a honeycomb lattice PCM. The calculation zone encompasses two unit cells. b) Schematics of the reciprocal lattice associated to the honeycomb crystal, corresponding to a triangular lattice constructed from the basis  $(\vec{a}_1^*, \vec{a}_2^*)$ . The green-shaded area delimits the primitive cell or Wigner-Seitz cell, referred to as the first Brillouin zone (FBZ). Due to  $C_6$  (or  $2\pi/3$ ) rotational symmetry, the study of the FBZ reduces to the blue-shaded irreducible zone enclosed by the high-symmetry points  $\Gamma$ ,  $K$  and  $M$ .

We add then sources and time monitors within the computation cell to inject the excitation signal and collect the temporal evolutions of the fields. We dispose multiple magnetic dipole sources oriented in the out-of-plane direction as represented in Figure 2.4 to excite exclusively transverse electric (TE) modes defined by  $E_z = 0$ . We adjust their spectral bandwidth to span the interval [10-300] THz, or equivalently [1-23]  $\mu\text{m}$ . We have noticed earlier that the solver region actually contains two honeycomb lattice unit cells as depicted in Figure 2.5.a). Without a proper setting of the dipoles' locations and phase shifts, we simulate the band structure of the superlattice and generate spurious modes by artificial band folding. To constrain the study to one honeycomb unit cell, we create a first set of dipoles with arbitrary positions contained in the bottom corner of dimensions  $3a_h/2 \times \sqrt{3}a_h/2$ . We then copy the set of dipoles and place it at identical positions in the second unit cell located in the upper right corner of the solver cell. We finally phase match the second series of dipoles by adding a phase offset  $\Delta\theta = -180\vec{k} \cdot \Delta\vec{r}/\pi$  with  $\Delta\vec{r}$  the position offset to the first reference set of dipoles.

The simulation of the PC band structure consists in calculating the spectral response for each wavevectors  $\vec{k}$  along the irreducible FBZ passing by the high-symmetry points  $\Gamma$ ,  $K$  and  $M$ . In practice, we obtain the spectrum for each  $\vec{k}$  by Fourier transform of the time data collected by the time monitors and apodized beforehand with  $t_c = 0.5t_s$  and  $\Delta t = 0.125t_s$ ,  $t_s = 1000 \text{ fs}$ . We then assemble all the spectra to construct a raster version of the dispersion diagram as plotted in Figure 2.6.a) in normalized frequencies units  $a_h/\lambda$ . We deduce the band structure as represented in 2.6.b) by extracting the modes of higher intensity exclusively.

### Conclusion on the FDTD method

In conclusion, we have showed in this section the relevance of the FDTD method to complete the RCWA predictions and simulate:

- the spectral response, the modes' profiles and quality factors  $Q$  supported by



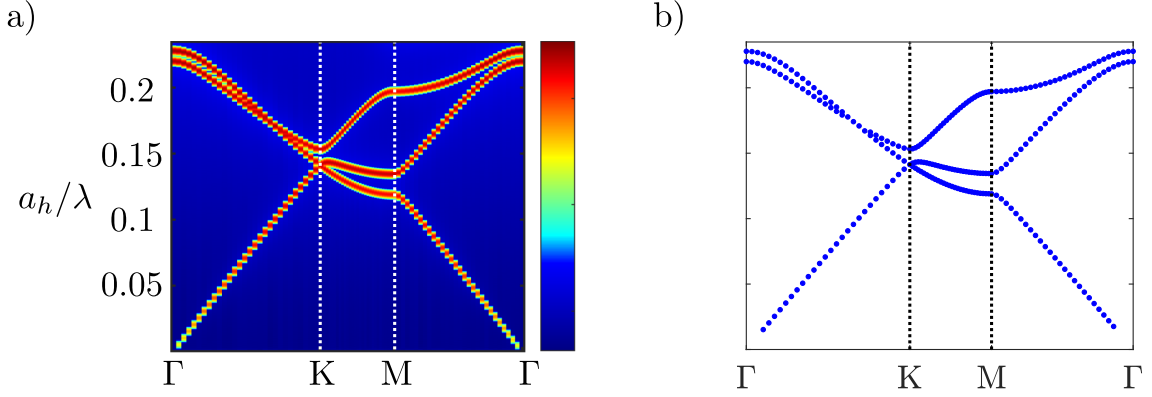


FIGURE 2.6: a) Dispersion diagram of a honeycomb lattice photonic crystal (PC) with a period  $a = 0.232 \mu\text{m}$  and air holes of radius  $r = 0.067 \mu\text{m}$  in InP material simulated with the FDTD method (Lumerical solver) for incident TE polarization (electric field contained in the PC). The diagram represents the dispersion expressed in normalized frequencies  $a_h/\lambda$  along the irreducible FBZ with high-symmetry vertices  $\Gamma$ , K and M. b) Extracted bands of the previous diagram.

tubular micro-structures as illustrated with a non-structured InP-made micro-tube,

- the band structure of periodic photonic structures applied on a honeycomb lattice InP-based photonic crystal.

In both configurations, a refinement of the settings leads to more accurate results but often at the expense of higher computation time and memory requirements. As a guide, for the simulation of 3D structures, the computation time (memory requirements) evolves in proportion to  $1/\Delta^4$  ( $1/\Delta^3$ ) where  $\Delta$  designates the smaller mesh size. In particular, the simulation of tubular photon cages implies substantial computing resources due to the multi-scale nature of the structures. We use in this case the Newton computer cluster facilities available at the École Centrale de Lyon to perform parallel calculations and achieve reasonable simulation time.

## 2.2 Fabrication process

In this section, we introduce the fabrication scheme of 2D photonic crystal membranes (PCM) rolled-up into tubular shapes which structural parameters have been adjusted via numerical simulations presented earlier. We employ the method in the present thesis for the production of both tubular photon cages and rolled-up honeycomb lattice PCM as analogues of carbon nanotubes in the class of photonic crystals. The overall process relies on the rolled-up nanotechnology which enables the rolling of pre-strained nano-membranes into prescribed 3D geometries upon relaxation. In particular, the production of the tubular patterned rolled-up membranes divides into three main successive stages:

- the production of precursor stress-engineered multi-layered stacks;
- the design, fabrication and transfer of the planar mask;
- the self-rolling of the photonic membrane into a cylindrical shape.

We describe hereinafter the technical processes involved at each of the previous steps and we elucidate the critical parameters that influence the structural parameters of the final rolled-up structures.



### 2.2.1 Production of the precursor multi-layered stacks

The first step in the fabrication of rolled-up nanomembranes is dedicated to the production of a precursor multi-layered stack composed of a sacrificial layer and a pre-strained bilayer deposited successively on top of a substrate layer. We have demonstrated in Chapter 1 that the amount of strain introduced in the bilayer and the thicknesses of the layers determine the induced curvature of the final rolled-up microstructures according to Equation (1.21) in Chapter 1. In particular, we will show that the epitaxial growth is a suitable technique to achieve the deposition of material layers with a high degree of control on the thicknesses and the composition directly related to the amount of stress. In the later developments, the constitutive material layers are essentially made out of III-V alloys such as Indium Phosphide (InP). This choice is motivated by the wide use of InP-based devices in photonic integrated circuits (PIC) to realize active as well as passive optical on-chip functionalities.

#### Epitaxial growth of material layers

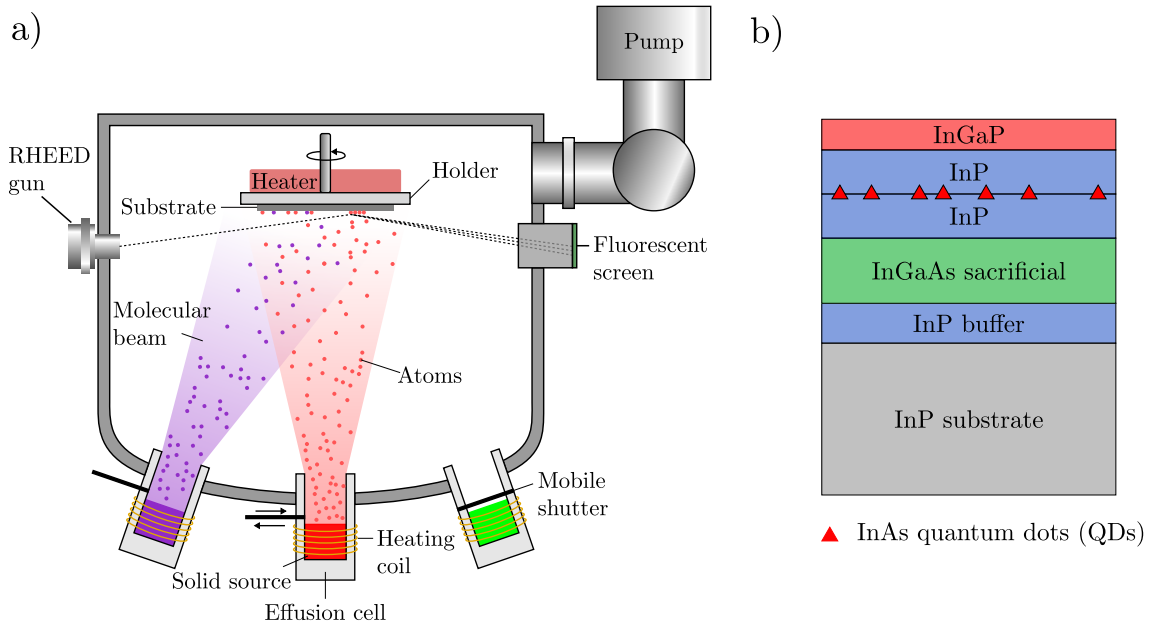


FIGURE 2.7: a) Illustration of the molecular beam epitaxy (MBE) deposition technique. Solid material sources are heated in effusion cells until evaporation. Due to the high vacuum environment performed by set of pumps, the so-formed gases of atoms moves towards the substrate in the form of molecular beams. The molecules condensates on the heated substrate and arrange to form material layers with atomic precision. Mechanical shutters allow to vary the composition of the layers by closing effusion cells. The deposition of the material layers are monitored via reflection high energy electron diffraction (RHEED) method for which an electron beam hits the sample surface at grazing incidence and reflects on a fluorescent screen. b) Typical precursor multi-layered stack obtained after the MBE process and used for the rolling of pre-strained InP-InGaP bilayer.

The deposition of material layers was performed via the molecular beam epitaxy (MBE) deposition technique by Philippe Regreny at INL within the NanoLyon platform. In a ultra-high vacuum (UHV) environment (down to  $10^{-10}$  Torr), the MBE growth allows for the preparation of very thin crystalline material films with atomic precision and a high control on the composition and the surface quality of the layers. This technique is used to deposit successive layers of InP, Indium Gallium Arsenide (InGaAs), InP and Indium Gallium Phosphide (InGaP) material on top of a nominal

(100)-oriented InP substrate to form the multi-layered stack depicted on Figure 2.7.b). In particular, the InGaAs film corresponds to the sacrificial layer and the InP-InGaP bifilm to the pre-strained bilayer. Moreover, the InP layer deposited right after the InP substrate acts as a buffer layer which smooths the substrate surface by covering roughness irregularities. The MBE deposition method also allows to insert planes of active nanostructures, such as InAs quantum dots (QDs) represented on the drawing as red triangles, in between InP-based layers. This operation endows the final structure with active optical properties accessible through photo-luminescence characterization.

Technically, material solid sources with III-V elements, namely Indium (In), Gallium (Ga), and Arsenide (As), are placed and heated in Knudsen-type effusion cells embedded in a chamber as illustrated in Figure 2.7.a), until sublimation to form gases of particles (colored dots). Due to its pyrophoric behaviour, Phosphorus (P) is treated separately in specific valved cracker cells to obtain beams of  $P_2$  dimers. The high vacuum conditions achieved in the chamber reduce drastically the collisions between the particles and increase significantly their mean free path. Therefore, the gases of atoms migrate almost in a straight line, as *molecular beams* (purple and red envelopes), towards the substrate. The substrate is also heated but at a lower temperature than settled for effusion cells, to prompt the condensation of the atomic vapours and maintain molecular dynamics at the surface. Several mechanisms contribute then to the growth of the layer. The impinging atoms are first retained at the surface of the substrate through physical adsorption and become so-called *adatoms*, but diffuse efficiently via the thermal agitation. They come to stabilize either by binding with other atoms and forming nucleation sites or by incorporating to existing material steps. These processes also compete with the re-evaporation by thermal desorption or the inter-diffusion of adatoms, according to the temperature of the substrate.

### Control of composition and thicknesses of the layers

Using the mechanical model introduced in Chapter 1, we can precisely predict the curvature  $\kappa$  adopted by a free pre-strained bilayer composed of a mismatched layer  $A_2$  deposited on a substrate layer  $A_1$ . The pre-strain introduced in the bifilm originates from the epitaxial pseudomorphic growth of  $A_2$  onto  $A_1$  which imposes layer  $A_2$  to adopt the same in-plane lattice parameters as the substrate layer  $A_1$ . The layer  $A_2$  undergoes therefore a pre-strain directly related to the mismatch of lattice parameters expressed as  $m = (a_1 - a_2)/a_1$ , also called misfit parameter, with  $a_1$  and  $a_2$  the lattice parameters of  $A_1$  and  $A_2$ , respectively. According to the model, for an elastic contrast close to one (which is the case here), the curvature solely depends on the thicknesses  $h_1$  and  $h_2$  and on the misfit parameter  $m$ . In our configuration, we identify layers  $A_1$  and  $A_2$  of the model with the top InP and InGaP layers of the multi-layered stack. Using Vegard's law, the lattice constant of the layer InGaP approximates as  $a_2 = a_{\text{In}_{1-x}\text{Ga}_x\text{P}} = xa_{\text{GaP}} + (1-x)a_{\text{InP}}$  where  $x$  denotes the composition in Gallium element of the InGaP layer. The proportion  $x$  therefore dictates the mismatch  $m$  and hence the amount of pre-strain in the InP-InGaP bilayer. Eventually, the induced curvature of the final rolled-up microstructure is determined by the thicknesses of InP and InGaP films and the composition  $x$  in the InGaP material layer. It is noteworthy that the mechanical model gives accurate predictions provided that the bilayer undergoes small strains which implies low  $x$  values. The fabrication of a rolled-up InP-InGaP membrane with prescribed structural parameters (membrane wall thickness, curvature radius) demands a tight control on the thicknesses and Gallium composition of the InP and InGaP layers.

Thermal and pressure conditions are therefore key parameters of the overall process

as they influence the composition and the thickness the deposited layers. They also determine the surface quality of as well as the speed of growth. Indeed, the high vacuum conditions in the chamber, obtained by a complex set of turbo-molecular and ionic pumps, ensure a very low level of contamination of the sample and a layer-by-layer deposition rate. The thickness of the layer and the speed of growth depend on the material flows controlled by the temperature of the effusion cells. Moreover, mechanical shutters in front of each effusion cells, as depicted on Figure 2.7, enable a quasi-instantaneous interruption of the atomic flows which results in abrupt material heterostructures and a precise control of the alloys' composition. Finally, the substrate is placed on a rotating platform, at the convergence of the atomic flows, to obtain the most homogeneous deposition possible.

### Growth modes and critical thickness

In the course of the epitaxial growth, the deposited InGaP material layer accumulates elastic energy per unit area  $E_{\text{elas}}$  which expresses as [4]:

$$E_{\text{elas}} = \frac{E}{1 - \nu} m^2 h_2, \quad (2.4)$$

where  $E$  and  $\nu$  refer to the elastic modulus and Poisson's ratio of InGaP material. According to Equation (2.4), for a given misfit  $m$ ,  $E_{\text{elas}}$  increases linearly with the thickness  $h_2$ . However, the layer-by-layer deposition is guaranteed below a critical thickness  $h_c$ : this regime is also called *Frank-van der Merwe* growth. Above  $h_c$ , the deposited layer acquires sufficient energy to create dislocations and relax strains into the formation of islands, a regime referred to as the 3D *Volmer-Weber* growth mode. An intermediate regime or *Stranski-Krastanov* growth mode combines both a layer-by-layer deposition and the formation of islands above the critical thickness. The value of the limit thickness  $h_c$  depends on the misfit  $m$  and on the growth parameters such as the temperature or the growth speed. In particular, for typical Gallium proportions  $x$  in the InGaP layer in the order of 0.1, we have estimated the critical thickness to  $h_c \simeq 70 \text{ nm}$ .

### Growth of optically active quantum dashes (QDas)

Generally an undesired effect for the uniform deposition of thin material films, the growth of islands can be exploited to create quasi zero-dimensional nanostructures of semiconducting material: quantum dots (QDs). On account of quantum confinement effects, QDs exhibit photoluminescent properties which emission wavelengths vary according to their size and material composition. These tunable optical properties together with low threshold current density have for instance made QDs-based materials ideal candidates in the production of low-threshold lasers [5, 6]. Originally implemented on GaAs substrates, the method was extended to InP substrates and enabled the formation of InAs quantum dashes (QDas) with an emission wavelength close to the  $1.5 \mu\text{m}$  standard telecommunication wavelength [7–9]. In particular, we used this method to grow in some of the samples a plane of self-organized InAs-QDas in between two InP layers [8] as represented by red triangles on Figure 2.7. This operation was performed with the aim of characterizing the optical response of the final rolled-up structure through photoluminescent measurements.

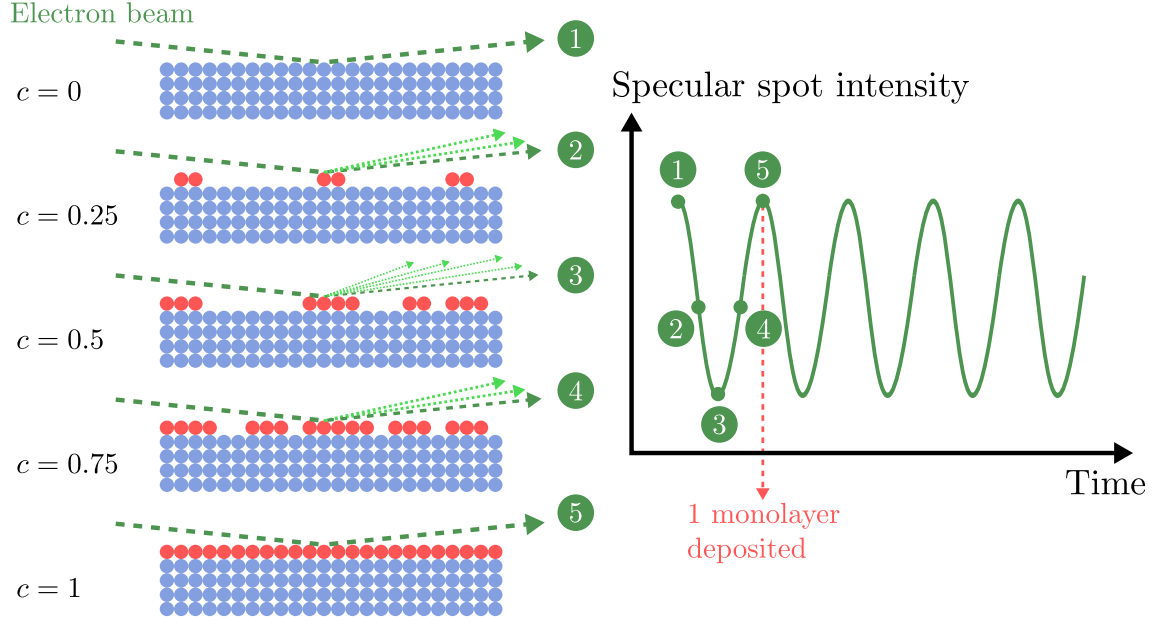


FIGURE 2.8: Schematic view of the monitoring of the epitaxial growth via reflection high energy electron diffraction (RHEED). The drawings on the left represent different stages of the deposition of red material on a substrate crystalline blue material quantified by the covering rate  $0 \leq c \leq 1$ . An electron beam (dark green dashed line) is sent onto the surface of the sample at grazing incidence and only the specular reflection (dark green dashed reflected line) is detected. On the right, we plot the evolution of the specular spot intensity as a function of the time of the deposition. We indicate the position of the five stages of the left drawings.

### Real-time and *in-situ* control of thickness via RHEED measurements

Previous remarks have stressed the crucial role of thicknesses  $h_1$  and  $h_2$  not only on the value of the curvature of the final rolled-up microstructure but also on the evolution of the growth mode. It is hence of paramount importance to control precisely their values to meet the targeted dimensions of the final microtubes and ensure the desired type of deposition. Toward this goal, real-time and *in-situ* reflection high energy electron diffraction (RHEED) measurements are performed to monitor the growth of material films. An electron beam generated by an electron gun is sent onto the multi-layered structure at grazing incidence, as depicted on Figure 2.7.a). When the beam hits the sample, it deflects by reflection and diffraction phenomena. Small incidence angles, typically 1 or 2 degrees, allow the analysis of surface layers exclusively. The deviated beams are then collected onto a fluorescent screen. In particular, the intensity of the reflected (specular) spot is measured and its cyclic evolution can be directly related to the surface roughness, namely the filling of the surface by the atoms, as represented on Figure 2.8. The parameter  $c$  designates the coverage rate of the sample surface. In the first place, few incoming atoms arrange on the surface of the multi-layered structure and hardly perturb the reflected beam. As more atoms impinge on the surface and cluster to form the layer, they also diffract the beam leading to a decrease of the reflected intensity ( $c = 0.25$ ). When the surface is half filled ( $c = 0.5$ ), diffraction phenomena predominate and the reflected signal reaches a minimum. Then, the deposition follows on until the total reconstruction of the surface while the intensity rises gradually until its initial and maximum value ( $c = 1$ ). The deposition of the material is monitored down to the atomic monolayer. Indeed, the thickness of the deposited layer can be estimated by counting the oscillations of the intensity during the growth which corresponds to the number of material mono-layers directly deposited onto the sample surface. Finally,

RHEED measurements are also exploited to detect the transition between two growth modes. In particular, the transition from a layer-by-layer deposition to the formation of islands makes the oscillations in the reflection intensity vanish.

### 2.2.2 Design, fabrication and transfer of the planar mask

The next step of the fabrication of tubular rolled-up PCM involves the design, the fabrication and the transfer of the planar mask into the InGaP-InP bilayer. In particular, the design of the planar mask plays a crucial role in the overall process as it determines the structural and optical properties of the final 3D rolled-up micro-object as we explained it in Chapter 1. We detail hereinafter the technical processes employed in the conception of the mask along with the key parameters which influence the geometrical and physical properties of the final 3D rolled-up microstructures.

#### Design of the planar mask

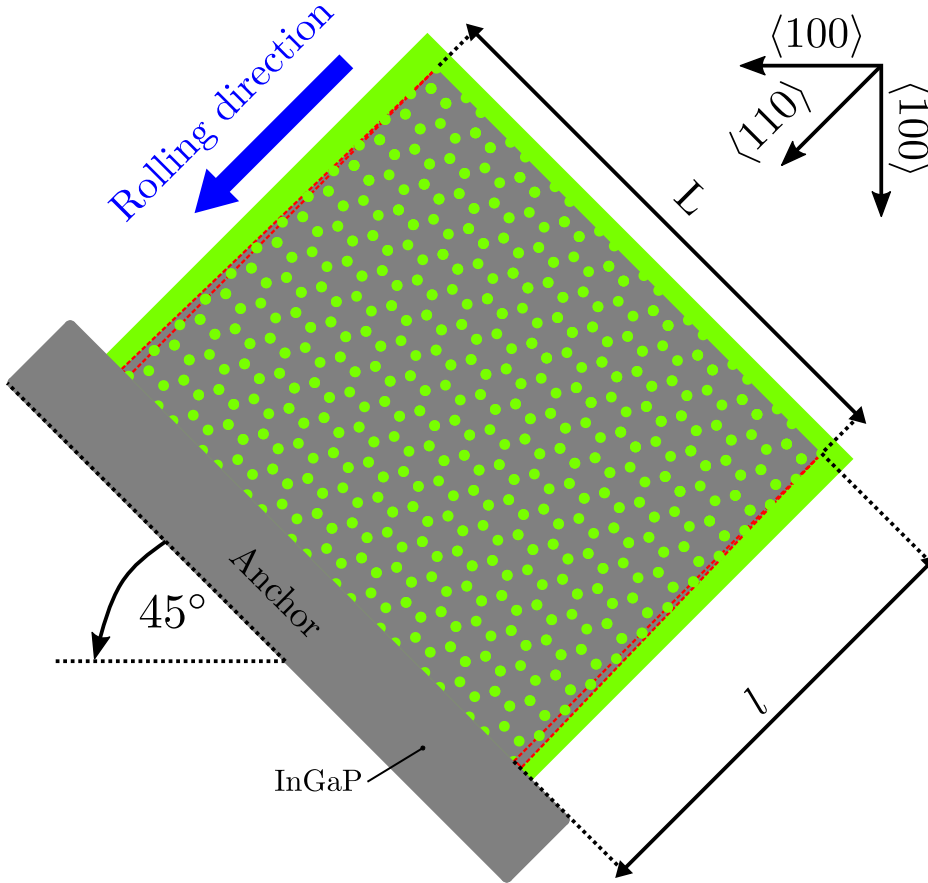


FIGURE 2.9: Design of the planar mask for the production of a rolled-up honeycomb lattice PCM attached to the substrate. Colour coding is borrowed from ELPHY pattern generator hardware used for the electron beam lithography. Green colour indicates the region exposed to the electron beam. The whole design is tilted with an angle  $\theta$  along the fastest direction of under-etching, supposed here to be (110) crystallographic direction.

The planar template fulfil three distinct functionalities. It first contains the photonic crystal pattern which will endow the InP-InGaP bilayer membrane with appropriate optical properties. The orientation, dimensions and overall shape of the mask

control the shape and dimensions of the final 3D rolled-up micro-object. Finally, the template comprises specific design features which realize the attachment of the future 3D microstructure to the substrate. We illustrate the three previous points with the planar mask represented on Figure 2.9 used for the production of tubular rolled-up honeycomb lattice PCM. The design is drawn and converted into a GDSII file in the ELPHY pattern generator hardware which is then readable by the electron beam lithography device. Light green coloured regions indicate the areas that will be exposed later to the electron beam for the fabrication of the mask.

The central part of the planar template concerns the photonic crystal pattern which consists of green-shaded air holes arranged according to a honeycomb lattice. The lattice parameters, namely the dimensions of the holes and the lattice period, result from the numerical simulations performed to achieve predefined optical properties of the PCM. Moreover, the orientation of the lattice can be adjusted to realize the rolling of the PCM according to a given chirality.

The overall shape, the dimensions and the orientation of the photonic crystal pattern are then adjusted to obtain the rolling of the PCM into a tubular shape with prescribed radius  $\rho_c$  and length  $L$ . We have shown in Chapter 1 that the rolling of a rectangular membrane leads to the production of a hollow cylindrical shape. Assuming the rolling direction along the blue arrow, the dimension  $l$  fixes the number of winding as it corresponds to  $n$  times the perimeter  $2\pi\rho_c$  of the final tube. In particular, for integer values of  $n$ , the PCM achieves  $n$  complete rolling. Furthermore, the other dimension  $L$  matches with the length of the cylinder. Green-shaded strips surrounds the rectangular pattern to initiate the later under-etching process by facilitating the penetration of the etching solution toward the buried-in sacrificial layer. Considering the anisotropic etching of the crystalline InGaAs sacrificial layer, the PCM will roll along the dimension  $l$  if the fastest etching direction coincide with the direction of  $l$ . Due to the pseudomorphic epitaxial growth, the InGaAs layer shares the same crystallographic structure as the nominal  $\langle 100 \rangle$ -InP substrate. Moreover, the lateral faces of the sample correspond to the cleavage  $\langle 100 \rangle$  planes of InP cubic crystalline material from which we identify at  $45^\circ$  the direction  $\langle 110 \rangle$  of fastest etching rate. Therefore, we orient the planar template at  $45^\circ$  with respect to the cleavage planes of the sample as depicted on Figure 2.9 to ensure the rolling of the PCM along the dimension  $l$ . However, the under-etching equivalently occurs along the dimension  $L$  owing to the rotational symmetries of the cubic crystallographic system. To favour the rolling along  $l$ , we add a extra band of InP material with gradually increasing thickness outlined with a red dashed line which slows down the etching along  $L$ .

The rolling of the PCM stops at the level of the anchor schematized on Figure 2.9. This specific design feature also allows to hold the rolled-up structures to the substrate. Complex anchor can be conceived to realize additional functionalities. In particular, in later **Chapter III**, we design a special anchor to perform the vertical lifting of the rolled-up microtubes which facilitates the optical characterization of the microtubes in the hollow part.

### **Fabrication of the planar mask: electron-beam lithography**

The fabrication of the planar mask via electron-beam (e-beam) lithography process and the following etching process have been performed in NanoLyon by Pierre Cremillieu whom I accompany during the fabrication sessions. The e-beam lithography consists in patterning an electron-sensitive resist deposited on top of the sample by scanning its surface with an electron beam. Unlike diffraction-limited optical methods, the use

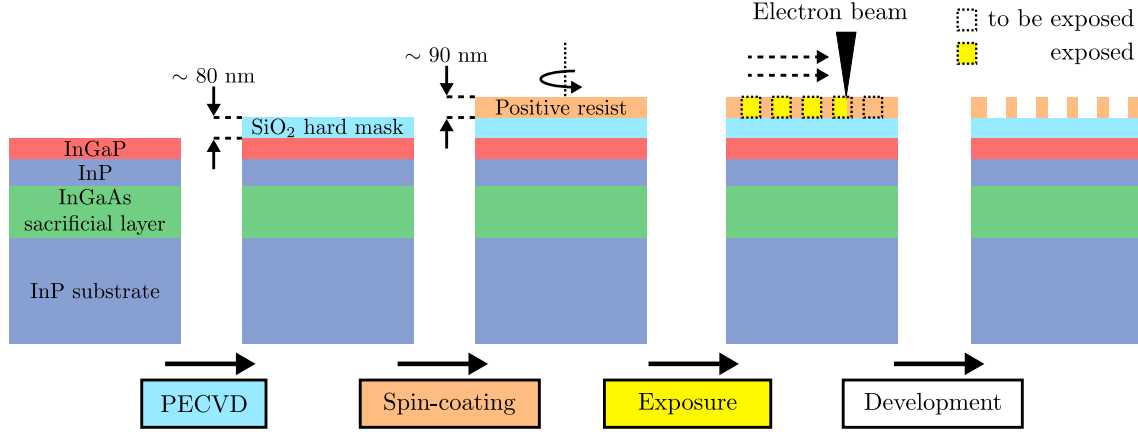


FIGURE 2.10: Sketches of the electron-beam (e-beam) lithography steps: deposition of the  $\text{SiO}_2$  hard mask by plasma-enhanced chemical vapor deposition (PECVD) on top of InGaP/InP/InGaAs/InP(substrate) stack; spin-coating of the resist; the resist is exposed to the electron beam according to the targeted design; development of the resist to obtain the planar mask.

of electronic matter waves allows to achieve very high resolution, down to few tens of nanometers. The path followed by the electron beam corresponds to the planar design produced in the earlier step. In practice, a 80 nm-thick  $\text{SiO}_2$  layer is deposited by plasma-enhanced chemical vapor deposition (PECVD), on top of the multi-layered stack. This intermediate layer will serve as a hard mask and will guide the etching of the lower layers as the resist tends to degrade more easily in contact with the etching plasma. A resist with reference AR-P 6200.04 is spin-coated on top of the hard mask during 60 seconds with a rotation speed and an acceleration of 4000 and 3000 rpm, respectively. Under these conditions, the resist deposits uniformly onto the hard mask until a thickness of about 90 nm which optimizes the resolution and the contrast of the lithography. A soft-bake of the sample is performed afterwards at  $150^\circ\text{C}$ , also during 60 seconds, to improve the adherence of the resist to the substrate.

The writing of the patterns is realized by the deflection of the electron beam across the surface of the resist with electrostatic lenses, according to the targeted design. A blanking system allows to turn the beam off and leave unexposed parts of the resist. Following the writing procedure, the sample is immersed into a developing solution with reference AR 600-546, during 45 seconds. A positive resist is used for which the exposure to the e-beam improves its solubility in the developing solution: the exposed parts are removed by dissolution to form the patterns. The development is stopped by plunging the sample into an isopropanol solution and the patterned resist is cleansed in deionized water to remove residual solvent, each operations lasting 30 seconds. The sketches in Figure 2.10 summarize the primary steps of the e-beam lithography process.

The exposure and the development of the resist are two determinant processes for the quality of the lithography evaluated by the concordance between the targeted planar design and the resulting patterned resist. Unlike UV lithography, the e-beam lithography is a serial process: the electron beam irradiates successively elementary areas separated by a distance  $s$  or *step size* and during a time  $t_d$  or *dwell time*. The step size is fixed with respect to the size of the smallest pattern to be produced. Knowing the beam current  $I$  and the area dose  $D$  which measures the charge per units of area required to fully develop the resist, the dwell time is deduced with the relation:

$$D = \frac{I \times t_d}{s^2}. \quad (2.5)$$

Typical values of the area dose reach hundreds of  $\mu\text{C}/\text{cm}^2$ . The exposure dose plays a key role in the final resolution of the patterns. During the exposure, the electrons interact with the resist to break chemical bonds and make it more soluble in the developer. However, they can also undergo scattering events which contribute to a broadening of the exposed area by the increase of the original electron beam diameter. This leads to a degradation of the resolution of the patterns. Indeed, the electrons can collide elastically with the atoms of the resist or back-scatter in the substrate and diffuse out of the exposed area. Inelastic electrons-matter interactions are observed for which the electrons transfer part of their kinetic energy to the atoms which ionize and expel electrons, called secondary electrons. Those electrons can migrate towards the resist and generate other electrons by the same processes. Scattering phenomena result therefore in the widening of the exposed area, also called *proximity effect*. The importance of proximity effects depends on multiple factors as the nature of the substrate, the electron beam current or the thickness of the resist. Therefore, for each patterns of each sample, we generally vary the dose factor, the fraction of the area dose set to  $100 \mu\text{C}/\text{cm}^2$ , to find the best compromise between high resolution of the patterns and sufficient exposure of the resist. For each value of the dose, the appropriate dwell time is calculated using Equation (2.5).

#### Transfer of the planar mask: reactive ion etching (RIE)

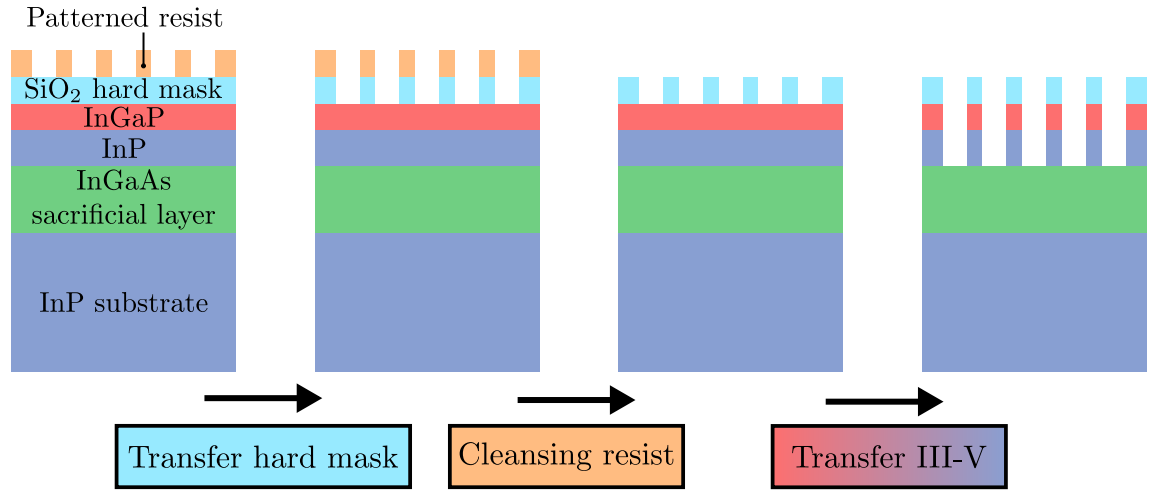


FIGURE 2.11: Schematized steps of the transfer of the planar mask into the InP-InGaP bilayer. The photonic crystal pattern imprinted on the resist is first transferred into the hard mask through reactive ion etching (RIE). The resist is then removed and the planar mask is also transferred via RIE successively across InGaP and InP layers until the top of the InGaAs sacrificial layer to form the photonic crystal membrane (PCM).

The electron-beam lithography process leads to the formation of a planar mask out of the resist layer which reproduces the photonic crystal pattern. The next step towards the formation of the photonic crystal membrane consists in using the mask as a stencil to transfer its pattern into the successive lower layers of the sample until the bottom of the InGaP/InP bilayer, by reactive ion etching (RIE). This etching technique relies on the bombardment of the sample by a plasma of reactive particles. The plasma, a gas of charged particles, generates by the application of a powerful radio frequency (RF) oscillating signal which triggers the ionization of gases of molecules surrounding the sample. The ejected electrons tend to accumulate on the wafer which supports the sample by the action of the RF signal whereas the much more massive



ions exhibit weak response. This leads to the formation of a strong polarization tension which makes the newly created ions accelerate towards the sample. The etching occurs when the ions access the lower layers through the patterned resist and sputter the molecules of the layer surface by transferring part of their kinetic energy, also called *physical* (or dry) etching. However, the ions can also be adsorbed on the layer surface and react chemically with the molecules, corresponding to the so-called *chemical* (or wet) etching. Therefore, the RIE technique combines advantages of both physical and chemical etching mechanisms, to achieve high anisotropic etching profile together with high etching rate.

In practice, the RIE process follows several steps of a recipe for which the nature of the gases in the plasma are adapted for each layer to be etched. Furthermore, the following parameters, the gases flow rates expressed in standard cubic centimetres per minute (sccm) units, the temperature of the substrate  $T_s$ , the pressure in the chamber  $P_c$ , the RF power  $P_{RF}$  and the etching time, have been adjusted to carry out a directional, selective and complete etching of the different layers. Starting from the multi-layered stack represented on the first left drawing of Figure 2.11, the pattern of the resist is first transferred into the SiO<sub>2</sub> hard mask layer by introducing a gas mixture composed of CHF<sub>3</sub> at 100 sccm and O<sub>2</sub> at 3 sccm,  $T_s = 20^\circ\text{C}$ ,  $P_c = 10\text{ mTorr}$  and  $P_{RF} = 140\text{ W}$ . The small fraction of O<sub>2</sub> is used here to impede the competitive formation of CHF<sub>3</sub> polymers without degrading the O<sub>2</sub>-sensitive resist. The resist is then entirely removed with a plasma composed exclusively of O<sub>2</sub> gas at 100 sccm,  $P_c = 100\text{ mTorr}$  and  $P_{RF} = 100\text{ W}$ . The high pressure tends here to favour the chemical attack of the resist compared to the physical bombardment by plasma ions. The pattern of the hard mask is next transferred down into the InGaP/InP bilayer by introducing a combination of H<sub>2</sub> and CH<sub>4</sub> gases at 60 sccm and 20 sccm, respectively, with  $P_c = 30\text{ mTorr}$  and  $P_{RF} = 120\text{ W}$ . The temperature of the sample is brought to  $T_s = 90^\circ\text{C}$  to make the etch polymer by-products more volatile, hence easier to eliminate by pumping. Otherwise, the hybrid compounds can stick to the etching sidewalls or redeposit on the surface of the layer, which obstructs the etching process. A cleaning step is also performed, with the same conditions as for the cleansing of the resist, to remove all the residual carbon composites formed with CH<sub>4</sub> derivatives to protect the etching sidewalls. Finally, a purge of the chamber is realized to dispose of any residuals of reactive gases. The main steps of the RIE process are pictured on Figure 2.11.

The key point of the RIE processes is to find the correct etching time to ensure the complete etching of the layers, that is commonly called end point detection (EPD). To this end, *in-situ* and real-time laser reflectometry are performed which enables to monitor precisely and non-destructively the etching of the different layers. Technically, a laser beam ( $\lambda = 672.2\text{ nm}$ ) is focused at normal incidence onto a reference rectangular zone which undergoes the etching process, and the reflected intensity is recorded on a CCD camera. The shape of the laser beam spot is also checked on the camera and it should be the most circular, otherwise it means that the sample is tilted which can distort the reflectivity measurements and affect the directionality of the etching. In the course of the etching, the thickness of the layer  $d$  reduces and it satisfies, for quantized values, the Bragg condition for constructive interferences between reflected light rays:  $2n_{\text{med}}d = p\lambda$ , with  $n_{\text{med}}$  the refractive index of the layer and  $p \in \mathbb{Z}$ . Therefore, we can follow the advance of the etching of the layer through the oscillations of the reflected intensity. The etching end point is detected when the oscillations of the intensity vanish, meaning that the layer is completely etched.

### 2.2.3 Rolling the photonic crystal membrane

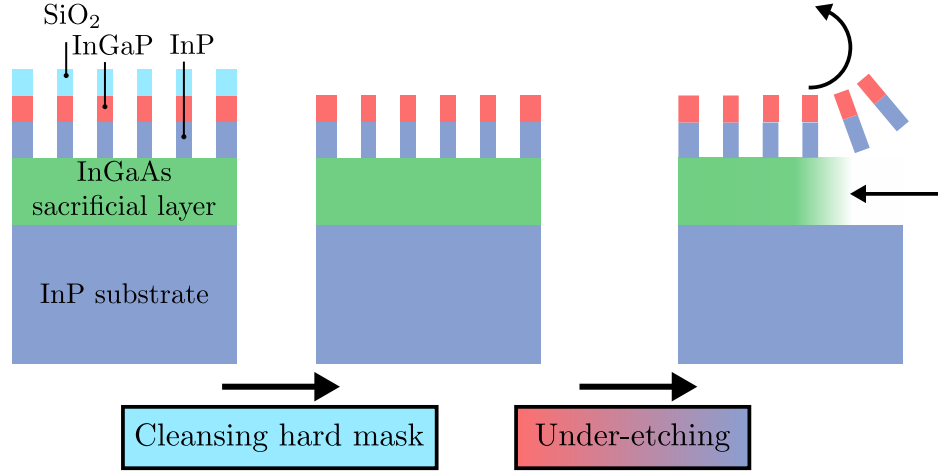


FIGURE 2.12: Sketched steps of the under-etching process. The  $\text{SiO}_2$  hard mask is first removed via a cleansing operation. The self-rolling of the InP-InGaP bilayer is then triggered by the removal of the sacrificial InGaAs layer by under-etching process in solution.

#### Under-etching

During the precedent steps, the transfer of the photonic crystal pattern into the InGaP/InP bilayer was performed by reactive ion etching (RIE) process. The next stage consists in triggering the self-rolling of the bilayer by releasing the accumulated strains via the etching of the burried-in InGaAs sacrificial layer, so called *under-etching*. The  $\text{SiO}_2$  hard mask is removed beforehand by immersing the sample into a buffer oxyde etch (BOE), a mixture of a fluoride ammonium solution and fluorhydric (HF) acid during 2 minutes. The under-etching of the InGaAs layer is then carried out by wet etching of the sample into a  $\text{FeCl}_3$  solution diluted in electrodeionized (EDI) water. Both steps are sketched on Figure 2.12. We note the selectivity of this solution with respect to the lower InP layer. The volume ratio of the mixture  $\text{FeCl}_3$ /EDI determines the kinetics of the reaction: a slow evolution of the etching is obtained with a highly diluted  $\text{FeCl}_3$  solution. The ratio can thus be adapted to control the speed of the reaction and to avoid damaging the sample by over-etching undesired parts of the original design.

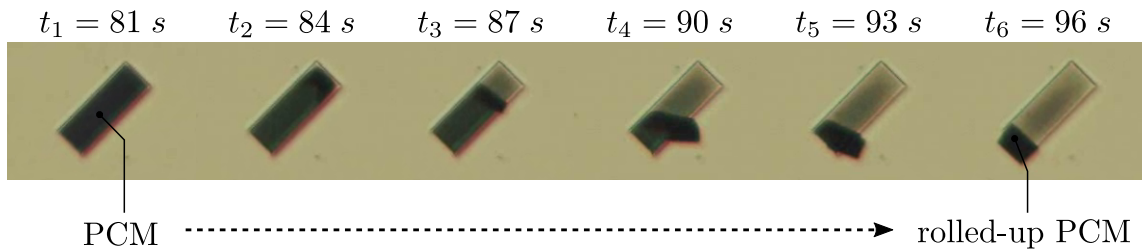


FIGURE 2.13: Live frames extracted from HIROX microscope recorded video of the under-etching process in  $\text{FeCl}_3$ /EDI solution of volumic ratio 3/80.

The advance of the etching and the self-rolling of the membranes are tracked by observing the immersed structures under a 3D numerical Hirox optical microscope. Figure 2.13 shows six snapshots of the under-etching of one PCM specimen in a 3/80

volumic ration  $\text{FeCl}_3/\text{EDI}$  solution taken at  $t_1 = 81$  s from the beginning of the process with a spacing of 3 seconds. We note that the self-rolling of the photonic membrane evolves rapidly as only 15 seconds are needed to terminate the process and obtain an horizontal rolled-up microtubes at  $t_6 = 96$  s. In the meantime, the membrane starts detaching from the substrate competitively along both edges of the rectangular planar template as represented on the frame at  $t_2 = 84$  s. At  $t_3 = 87$  s, the rolling along the longest edge of the rectangle prevails on the shorter edge. The rolling trajectory slightly deviates on the right on pictures recorded at  $t_4 = 90$  s and  $t_5 = 93$  s and rectifies at  $t_6 = 96$  s to give a rolled-up PCM microtube which axis is aligned with the shortest edge of the rectangular design. Once almost every membranes have rolled up into a tubular shape after about 2 minutes and 20 seconds, the reaction is stopped by pouring water on the sample and removing progressively any residuals of  $\text{FeCl}_3$  compound. A special care is applied to always maintain a liquid meniscus on top of the structures, while transferring the sample from one liquid to another, as capillarity forces tend to deform them or drag them off the substrate.

### Drying

The final step of the fabrication process entails the drying of the sample by the removal of the liquid through evaporation. The critical point of this process is to manage to extract the liquid without degrading the rolled-up structures. To this end, a supercritical drying is performed, a standard method employed for the drying of food or the preparation of biological samples, to achieve the liquid evaporation while maintaining the structural integrity of the rolled-up structures. Indeed, during the liquid-gas phase transition, surface tension and capillary forces exert on surrounding solid elements as the liquid rises towards the surface to turn into gas. As a consequence, such phenomenon may damage the rolled-up microstructures being dragged off or pressed against the substrate in the course of the liquid ascent. On the contrary, supercritical drying avoids crossing the liquid-gas boundary in the temperature-pressure phase diagram by going around the critical point. Beyond that point, liquid and gas phases become indistinguishable and form a superfluidic phase. As the solvent reaches the supercritical region, temperature and pressure conditions are then adjusted to pass through the gas region and achieve a complete extraction of the solvent by evaporation. In practice, liquid carbon dioxide ( $\text{CO}_2$ ) at approximately 70 bar is used to attain a critical point located at a relatively low temperature of about  $31^\circ\text{C}$  which hence limits thermal degradation of the solid structures. Initially immersed in water, the sample is first transferred into acetone solvent which shows almost complete miscibility with liquid  $\text{CO}_2$ , and position it into a chamber at ambient conditions. Adjusting the chamber temperature to few Celsius degrees to maintain a liquid phase, liquid  $\text{CO}_2$  is poured on the sample to replace progressively the acetone. The temperature is increased up to  $37^\circ\text{C}$  to pass  $\text{CO}_2$  critical point and obtain a superfluidic phase. The pressure is finally diminished to enter the gas region and to evaporate completely  $\text{CO}_2$  solvent.

### 2.2.4 Conclusion

In conclusion, we have described in this section the fabrication cycle of photonic crystal membranes (PCM) rolled up into tubular shapes on the basis of the rolled-up nanotechnology. The whole process divides into three main steps, namely the production of a multi-layered InP-based stack, the conception of the PCM planar mask and the rolling

of the PCM up into a horizontal cylinder. We summarize below the critical parameters of the technical processes involved at each stages which allow the realization of high-quality photonic microtubes with a high degree of control on structural properties defined beforehand by numerical simulations.

- The production of the multi-layered InP(substrate)-InGaAs(sacrificial)-InP-InGaP precursor is performed by molecular beam epitaxy (MBE) deposition technique. This method enables the growth of crystalline material layers with atomic precision and precise composition controlled respectively by real-time *in-situ* RHEED and *ex-situ* X-ray diffraction measurements. Consequently, we can achieve a high control on the curvature radius and membrane wall thickness of the final tubular geometry directly related to thicknesses and composition of InP-InGaP bilayer. However, we have stressed that the uniform deposition of layers is guaranteed up to a critical thickness depending on material composition and growth parameters.
- The planar mask plays a crucial role as it defines the photonic crystal pattern and the template to achieve the rolling of the PCM into a cylindrical geometry. Its production is carried out through electron-beam lithography on a resist characterized by nanometric resolution controlled by the exposure dose. It is then transferred across the InP-InGaP bilayer via reactive ion etching (RIE) process as a combination of physical and chemical mechanisms which leads to vertical etching slope.
- Chemical etching of the buried-in InGaAs sacrificial layer, or *under-etching*, triggers the self-rolling of the PCM into an horizontal tube. The kinetics of the reaction is controlled by the dilution rate of the etching solution and monitored by *in-situ* real time microscopy observation. The fabrication cycle ends up with the supercritical drying of the sample which preserves the structural integrity of the rolled-up microstructures.

## 2.3 Optical characterization

The present section introduces the two principal methods used in the thesis to perform the optical characterization of rolled-up photonic structures. We present in the first place a customized near-field optical microscope (SNOM) setup providing maps of the modes confined inside tubular photon cages via raster scan of the electric field intensity. We explain in the second place the principles of angular-resolved reflectivity and photoluminescence measurements conducted on rolled-up photonic structures to extract experimental dispersion diagrams. Both experimental techniques results are thus available for comparison with simulation results.

### 2.3.1 Scanning near-field optical microscopy (SNOM)

#### Principles of near-field optical measurements

Incident light diffracted on any object generates two types of electromagnetic fields. The first type corresponds to *propagating* waves carrying low spatial frequency information, namely large details of the object compared to the excitation wavelength  $\lambda$ . The propagating field evolves far distances to the sample, so-called the *far-field*. Conversely, the second type, labelled as the *evanescent* field, forms non-propagating waves located

within few nanometers from the sample surface, so-called the *near-field*. It encodes high spatial frequencies, namely the subwavelength-sized details of the sample.

Traditional optical devices collect the propagating part in the far-field and filter out high spatial frequencies contained in the evanescent waves. The filter's cutoff frequency determines the resolving power achievable in classical optics. For instance, Abbe's criterion evaluates the maximum resolution  $\Delta x$  attainable with optical microscopes to  $\Delta x = 0.6\lambda/\text{NA}$ , with  $\lambda$  the wavelength of the incoming light and NA the numerical aperture of the optical elements.

The detection of the evanescent waves containing high spectral information is at the heart of the near-field optics microscopy, referred to as the scanning near-field optical microscopy (SNOM), allowing higher lateral resolution than diffraction-limited optics. In a series of seminal works in early 1928, Synge has laid the theoretical foundations of the SNOM. The idea consisted in localized illumination through a subwavelength aperture realized in a metallic film placed at a subwavelength distance of the sample surface. The lateral displacement of the aperture across the sample surface would image subwavelength details. Most importantly, Synge had identified the two main critical parameters determining the final lateral resolution: the size of the aperture and the aperture-sample distance.

It was not until the 70s that practical realizations of SNOM confirmed the potential of near-field optics to obtain subwavelength-resolved images. First, in the microwave domain with Ash and Nichols, then at optical frequencies with Pohl's works, for instance, the lateral resolution attained  $1/60$  and  $1/20$  of the excitation wavelength, respectively. The modern versions of SNOM result from technological advances and specifically the development of scanning probe microscopy (SPM), including scanning tunnelling microscopy (STM) and atomic force microscopy (AFM). In particular, SNOM probes have evolved toward tapered fibres with a sharp nanometer-sized tip to collect samples' near-field [10]. Moreover, scanning stages borrowed from AFM setups allows precise control of the vertical and lateral position of the probe based on tubular piezoelectric actuators. In general, the probe mounted on a tuning fork vibrates parallel to the sample surface. Close to the sample, shear forces damp the oscillations of the probe owing to attractive interaction. Maintaining a constant oscillations' amplitude by a feedback system on the extension of the piezoelectric tubes leads to a constant probe-sample distance while scanning the sample's surface. In addition to the optical signal collected by the probe, outputs of the feedback loop provide topographic information on the sample's surface. Finally, current SNOM setups show versatility differing in probes' nature and the operational mode, working in illumination, collection or illumination-collection modes. In the next part, we highlight particularly the relevance of the SNOM technique to perform the optical characterization of fabricated tubular photon cages and extract the modal response.

### Optical characterization of tubular cavities

In principle, owing to the high reflective properties of the membrane wall, tubular photon cages achieve efficient confinement of light in the hollow air-filled core, both in the transverse and axial directions. Consequently, the modes emerging in the cavities exhibit low leakage in free space, rendering conventional far-field detection methods inaccessible. A possible strategy to extract the modal response consists of inserting an emitter or a dipole to probe the modes directly inside the cavity.

Toward this goal, the SNOM method represents a suitable platform for multiple reasons. First, the SNOM scanner stage enables a precise centring and controlled insertion

of the probe in the hollow part of the tubular cavities. Second, the SNOM illumination-collection operation mode allows simultaneous optical excitation and collection of the cavity modal response. Indeed, nano-aperture probes act both as nano-antennas and nano-detectors.

In particular, we use in the thesis a specific type of nano-aperture probe, the bowtie nano-aperture (BNA) probe, which fabrication divides into three steps. The first step involves forming the probe tip by the polymerization of a photosensitive polymer on top of a monomode SMF-28 fibre. The operation produces a tapered tip jointed and aligned to the fibre's core as schematized in Figure 2.14 to ensure optimum coupling conditions. The next step consists in covering the tip with a 0.1  $\mu\text{m}$ -thick Aluminum (Al) coating prior to the nano-aperture creation. The apex of the tip is finally patterned into a bowtie shape via focused ion beam (FIB) milling as schematized in Figure 2.14, allowing a high resolution of the final form.

The so-formed BNA holds much interest as it acts as a nano-antenna with a resonant behaviour at 1.55  $\mu\text{m}$  for incident light polarized exclusively along the gap symbolized by an orange arrow in Figure 2.14. Moreover, Mivelle *et al.* have reported in [11] an intense concentration of light, at the resonance, along the gap with an enhancement factor estimated to 120, increasing the probe collection efficiency dramatically. The BNA probe fulfils therefore the requirements of illumination-collection mode, acting as an integrated nano-source and a highly efficient nanocollector. The BNA polarization sensitivity also allows to filter the modes for which the electric field orients perpendicularly to the cavity axis exclusively, called transverse electric (TE) modes in later chapters. The polarization selectivity is all the more valuable as it facilitates the detection and discrimination of a certain kind of modes in case of high modal density of tubular cavities. The probes used in this thesis were fabricated by Dusan Nedeljkovic in Novalite company and Thierry Grosjean in the FEMTO-ST laboratory in the framework of the ANR NANOEC project involving the INL. We may refer to Thanh-Phong Vo's thesis [12] for a detailed fabrication process and analysis of BNA probes' properties.

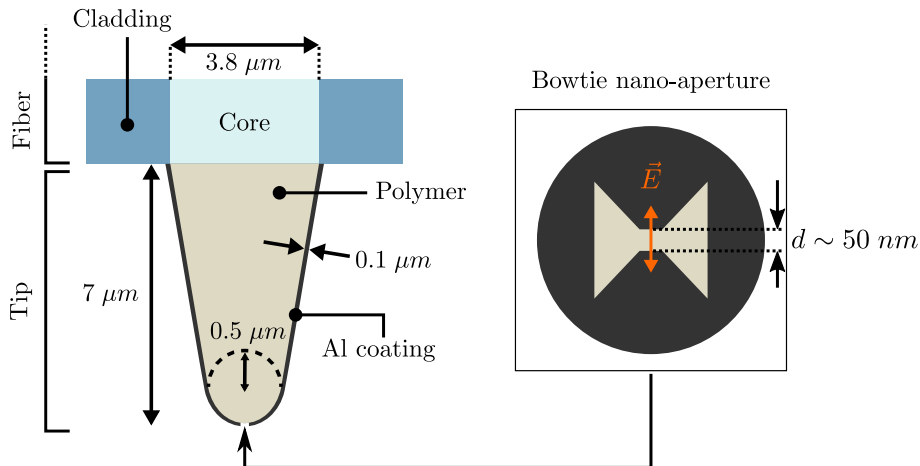


FIGURE 2.14: Bowtie-nanoaperture (BNA) probe. Left schematics: polymer tip grown on top of a monomode fiber and covered with an Aluminum (Al) coating. Right schematics: bowtie nano-aperture at the apex of the tip. The BNA behaves as a nanoantenna with resonant behaviour at about 1.55  $\mu\text{m}$  for incident light polarized along the bowtie gap (orange arrow).

In summary, we have pointed out the advantages of using a BNA probe to assess the modal response of tubular photon cages. Indeed, the BNA tip shows versatility combining the ability to inject and collect the optical signal (illumination-collection

mode), polarization sensitivity, and high resolution imaging. In contrast, other metal-coated aperture probes exhibit lower signal throughput and polarization independence while apertureless dielectric probes generate scan pictures with lower spatial resolution. However, the optical characterization of the tubular microstructures necessitates the insertion of the probe inside the cavities. It implies customizing the conventional SNOM set-up to drive the probe's tip carefully down into the photonic tubular cavities. We present in the following part the tailored SNOM set-up assembled at INL by Aziz Benamrouche to tackle the probe's insertion and measure photon cages' optical response.

### Customized SNOM setup

In addition to functionalities proper to the illumination-collection mode, the customized SNOM setup includes a specific positioning stage combined with a visualization system to achieve a controlled approach of the probe into the cavities.

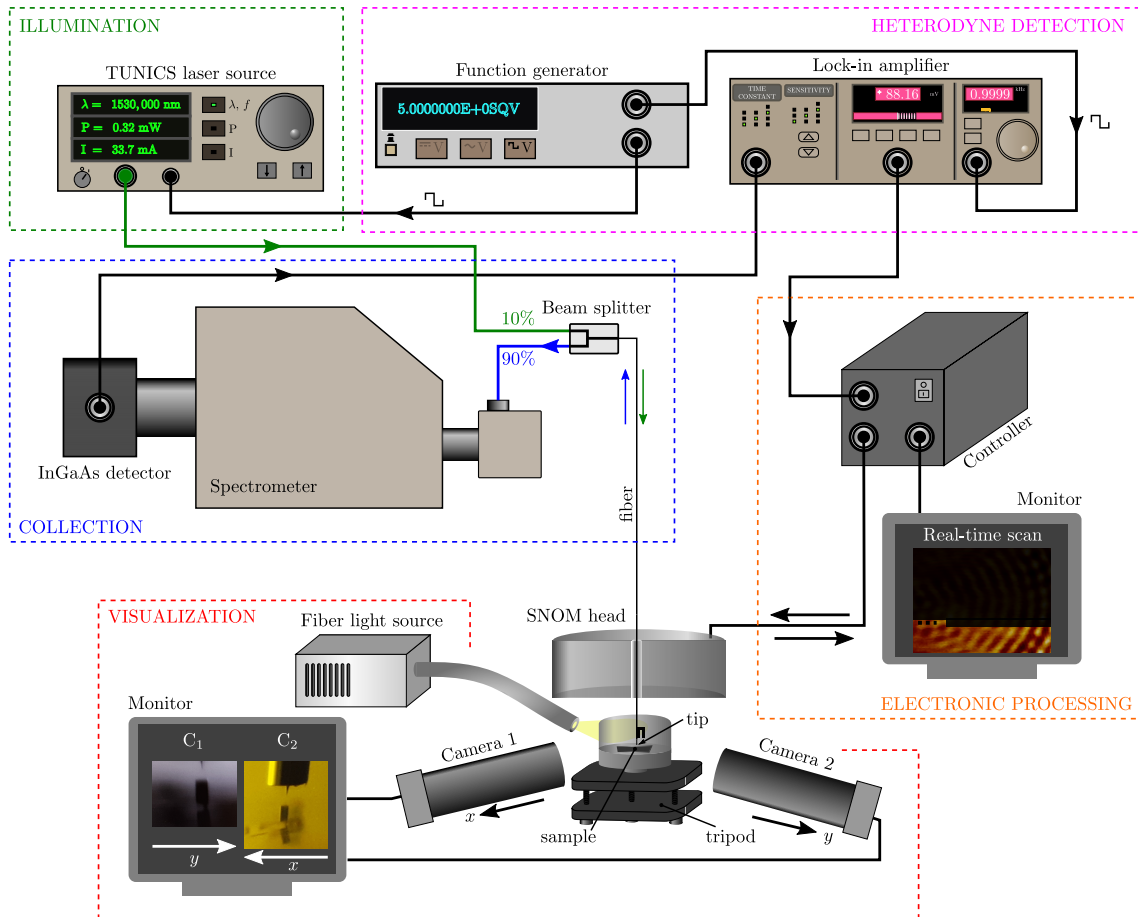


FIGURE 2.15: Schematics of the customized scanning near-field optical microscopy (SNOM) setup operating in illumination-collection mode to extract maps of the modes inside tubular photon cages.

The visualization panel in the bottom right corner of Figure 2.15 encompasses both the scanning and monitoring systems. The probe mounted on a SNOM head (NT-MDT product) translates parallel to the sample via the action of piezoelectric tubes. A tuning fork glued to the probe ensures the sole vertical stability of the fibre-probe ensemble. A screw on the top of the SNOM head allows a coarse vertical approach of the probe toward the sample, refined then by a step-by-step motor. We place the sample on a Teflon pedestal positioned on a tripod stage. The driving-in of each tripod's

constitutive screws determines the orientation of the sample. It aims to align the axis of the tubular cavities with the probe's axis. We illuminate the sample-probe system with a fibre light source diffused by the Teflon wall for visualization purposes. Two visible-range cameras (0.58-7X, 0.004-0.550 N.A., Navitar products), labelled  $C_1$  and  $C_2$  in Figure 2.15 and oriented perpendicularly, capture the probe-sample ensemble to guide the probe alignment procedure and avoid any contact between the tip and the microstructures.

The illumination section shows the TUNICS laser source, which provides the excitation signal in the probe with a tunable wavelength ranging from 1.450 to 1.580  $\mu m$  down to 0.1  $nm$  precision. We maintain the source power below 0.5  $mW$  to avoid thermal degradation of the BNA probe. At the tip level, the BNA radiates the excitation signal and collect the electric field that travels back into the fibre towards a beam splitter.

In the collection panel, the beam splitter divides excitation and collected signals with a ratio of 10/90. We record the entire spectral range of the collected signal in the spectrometer. The InGaAs detector, cooled down by a Peltier system, converts the optical signal into electronic data.

We install a heterodyne detection system to improve the signal-to-noise ratio. In principle, a function generator modulates the source excitation with a 1  $kHz$  rectangular carrier signal. Based on the modulation signal, the lock-in amplifier filters the optical signal at the output of the InGaAs detector and discards the remaining noise. The controller unit finally processes the filtered optical signal to make it readable by a computer and generate maps of the electric field intensity.

To sum up, we have described the main components of the customized SNOM setup used in the present thesis to assess the optical response of tubular photon cages. By contrast with traditional SNOM setups, ours incorporates specific monitoring and positioning systems to achieve the insertion of the probe inside the cavities. Precisely, it enables the careful approach, the alignment and the centring of the probe according to a targeted tubular cavity's surface, a condition to realize reliable measurements. We detail in the next part the three procedures abovementioned, hence requiring special care.

### Preparation of SNOM measurements

The extraction of modes' profiles in the hollow core of tubular photonic cavities requires approach, alignment and centring procedures of the probe to the microstructures' surfaces.

The first step consists of a coarse approach of the probe's tip toward the sample's surface by manipulating the SNOM head's screw. We monitor the operation via the two orthogonal cameras to evaluate the distance to the sample and avoid damaging the tip. Once both the tip and sample become visible, we move the sample and modify the cameras' focus to observe both the probe and a targeted cavity distinctly. We adjust the orientation of the sample via the tripod's screws to align vertically the tip and the cavity. We perform preliminary scans to attest the quality of the alignment over the cavity's cross-section.

The second step entails a refined approach of the probe's tip using the step-by-step motor while proceeding to the final settings of the camera's focus. The snapshot represented in Figure 2.16 shows a general view of the probe and the tilted sample. The inset close-up view from the numerical zoom attests to the high-quality vertical alignment between the tip and the standing cage.



In the third step, we drive the tip in the close vicinity to the cavity's bottom face as schematized in Figure 2.16.b), and we launch a scan spanning a large area. We present in Figure 2.16.c) the resulting  $40 \times 40 \mu m^2$  map of the electric field intensity recorded at an excitation wavelength  $\lambda = 1.530 \mu m$  over a  $30 \mu m$ -diameter cavity. We estimate the lateral resolution of the scan to  $80 nm$ , allowing the observation of modes with fine details. The scan reveals concentric azimuthal patterns, suggesting the probe's sensitivity to cavity's modes. It also indicates approximately the cavity's position. As a guide, we have outlined in black dashed line the membrane wall of the  $30 \mu m$ -diameter cavity based on the central azimuthal ring. We refine the centring of the probe to the cavity's axis with similar scans.

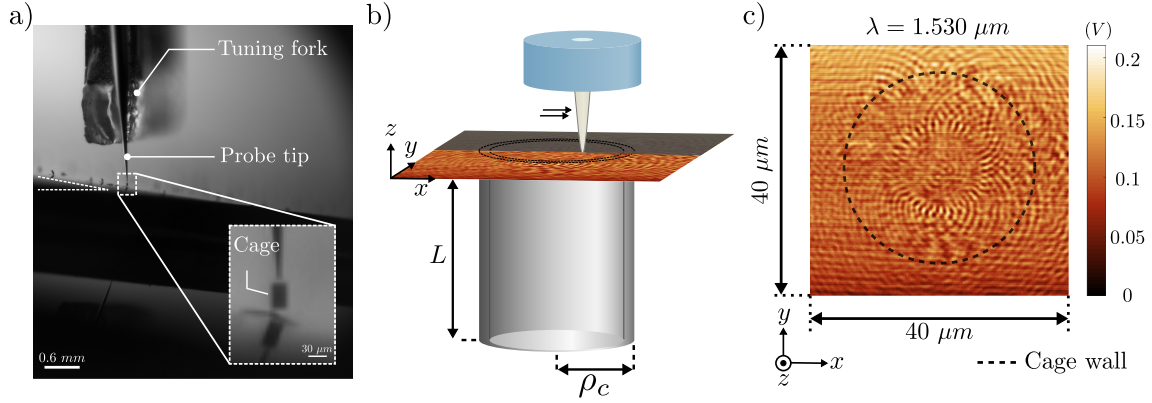


FIGURE 2.16: a) Snapshot of the SNOM probe with the tip approaching the surface of a photon cage specimen. Inset picture: numerical zoom to show the vertical alignment of the probe and the tubular photonic structure. b) Schematics of the probe scanning the very top of the photon cage of radius  $\rho_c$  and length  $L$ . c) Map of the electric field intensity recorded at the excitation wavelength  $\lambda = 1.530 \mu m$  on the top of the cage, spanning a  $40 \times 40 \mu m^2$  zone. The black dashed line delimits the cage membrane wall.

### Conclusion of SNOM optical characterization method

In this section, we have presented the scanning near-field optical microscopy (SNOM) as a suitable technique for probing the modes confined inside tubular photon cages, according to the following key points:

- In the illumination-collection mode, the SNOM aperture probe inserted inside the cavity simultaneously injects the excitation signal and collects the optical response, overcoming far-field detection bottlenecks.
- We use a bowtie nano-aperture (BNA) probe, which acts as an integrated nano-source, a highly efficient nano-collector and exhibits polarization selectivity.
- A customized SNOM setup allows us to achieve a careful approach, a very satisfying vertical alignment, and the centring of the probe to the cavities' axis.
- After insertion inside the cavities, we generate maps of the modes by a raster scan of the electric field in the cross-section.

### 2.3.2 Angle-resolved spectral measurements

Angle-resolved spectroscopy consists in the measurement of both spectral and angular dispersion information of structures' modes. Combining both information, we recon-

struct experimentally the band diagrams of fabricated structures and confront them to theoretical predictions.

### Principle of angle-resolved measurements

By definition, the construction of a band diagram requires the acquisition of the modes' wavelengths and wave vectors. On the one hand, spectroscopic measurements allow collecting spectral information of the modes. Fourier optics, on the other hand, provides information related to the modes' wave vector. In particular, Fourier optics relies on Fraunhofer diffraction, which establishes a proportional relation between the far-field distribution and the spatial Fourier transform of the field amplitude. In practice, we observe the spatial frequencies distribution by projecting the far-field amplitude in the focal plane of a converging lens, also called the Fourier plane. The lens acts, therefore, as a Fourier transforming system.

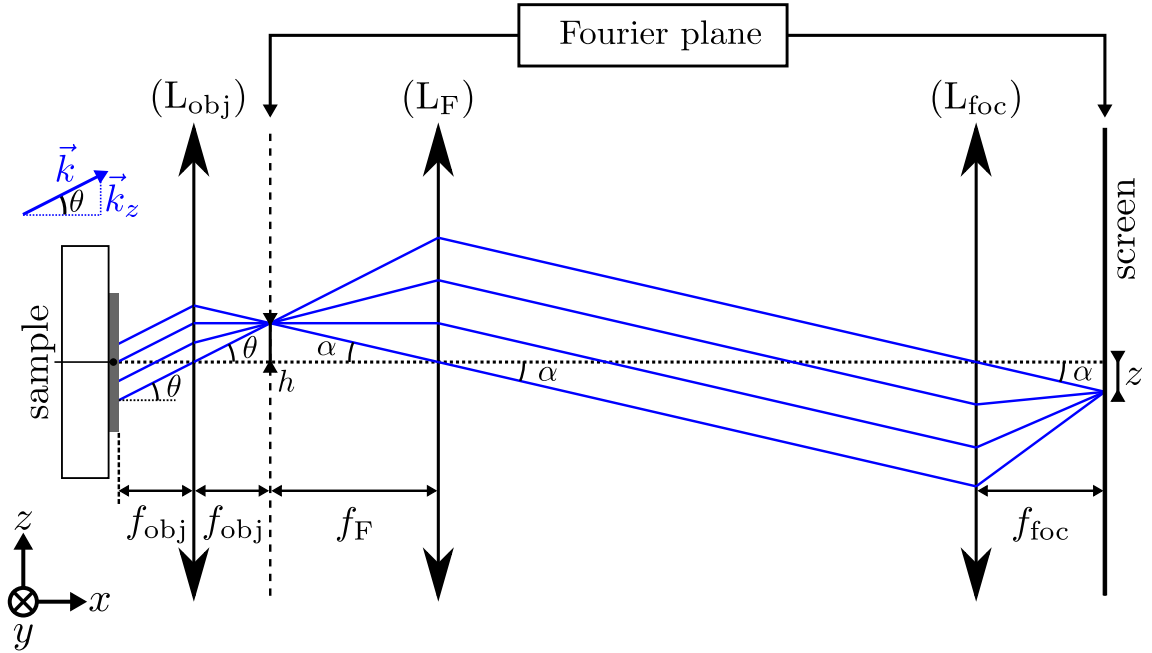


FIGURE 2.17: Simplified schematics of the Fourier optics setup allowing the imaging of the Fourier components of the sample's emission.

We present in Figure 2.17 a simplified schematics of the Fourier optics setup used to extract wave vector components of the structures' modes. It comprises three converging lenses noted ( $L_{obj}$ ), ( $L_F$ ), and ( $L_{foc}$ ) standing for the objective, Fourier and focalization lenses, respectively, placed in between the sample and a projection system (screen or CCD sensor). We explain, in first approximation, the propagation of light emitted from the sample toward the screen using geometrical optics considerations. Therefore, in the general case, a plane wave at incidence  $\theta$  to the normal of the sample surface (here coinciding with the  $x$  axis) focuses in the focal plane of  $L_{obj}$  at a distance  $h$  to the optical axis (horizontal dashed line). Noting  $f_{obj}$  the objective focal distance, basic trigonometry implies the following relation between  $\theta$  and  $h$ :

$$\tan \theta = \frac{h}{f_{obj}}. \quad (2.6)$$

Placing the Fourier lens ( $L_F$ ) at its focal distance  $f_F$  to the objective focal plane, the plane wave Fourier components project on the screen, at the focal distance  $f_{foc}$ .

Similarly to Equation (2.6), we relate the angle  $\alpha$  with the spatial coordinates  $h$  and  $z$ :

$$\tan \alpha = \frac{h}{f_F} = \frac{z}{f_{\text{foc}}}. \quad (2.7)$$

Finally, identifying  $h$  in Equations 2.6 and 2.8, we deduce the relation between the angular dispersion  $\theta$  and the  $z$  coordinate:

$$\tan \theta = \frac{f_F}{f_{\text{foc}} f_{\text{obj}}} z = Cz, \quad (2.8)$$

with the ratio  $C$  of the lenses' focal distances. In practice, the objective numerical aperture, noted NA, limits the angle of incidence  $\theta$  to a maximum value  $\theta_{\text{max}} = \arcsin(\text{NA})$ , corresponding to a maximum coordinate  $z_{\text{max}}$ . We determine, therefore, the ratio  $C$  according to:

$$C = \frac{\tan(\theta_{\text{max}})}{z_{\text{max}}}. \quad (2.9)$$

Moreover, the projection of the wave vector onto the  $z$  axis writes as:

$$k_z = \vec{k} \cdot \vec{e}_z = |\vec{k}| \sin \theta = \frac{2\pi}{\lambda} \sin \theta, \quad (2.10)$$

where  $\lambda$  designates the wavelength of the plane wave. Finally, combining Equations 2.8 and 2.10, we obtain the following relation:

$$\boxed{k_z = \frac{2\pi}{\lambda} \sin(\arctan(Cz))}, \quad (2.11)$$

which associates the image formed at  $z$  with a unique wave vector component  $k_z$ .

Therefore, the measurement of the angular dispersion on the screen gives access to the Fourier transform components of the plane wave. Combined with the spectral information dispersed along the other direction of the screen (here the  $y$  axis), we build the dispersion diagram  $\lambda = f(\vec{k})$  of the sample. However, we only extract the dispersion of the structures' modes located above the light line, hence able to couple to the radiation continuum, but not pure guided modes. Moreover, owing to the two-dimensional screen, we record in our example the dispersion along the  $z$  axis direction related to the wave vector component  $k_z$  exclusively. In practice, we fix the  $k$ -direction of the dispersion diagram by performing a spatial filtering of the image collected on the screen with a slit aligned with the targeted direction. Finally, we note the possible visualization of the sample in real space by removing the Fourier lens.

### Presentation of the setup

We show in Figure 2.18 a schematics of the setup dedicated to angle-resolved spectral measurements. It comprises notably the successive converging lenses (objective, Fourier and focalization), the slit, and the spectrometer mentioned earlier.

The setup offers two operation modes collecting either the photoluminescence response of samples embedded with quantum dashes (QDas) or the reflection signal. In the photoluminescence mode, we pump the structures with a laser diode (PDL 800-D, PicoQuant) emitting picosecond impulsions at 968 nm. In the reflectivity mode, we illuminate the sample when with an halogen lamp (SLS-301, Thorlabs). We change the from reflectivity to photoluminescence configuration by rotating a mirror to guide the laser beam toward the sample.

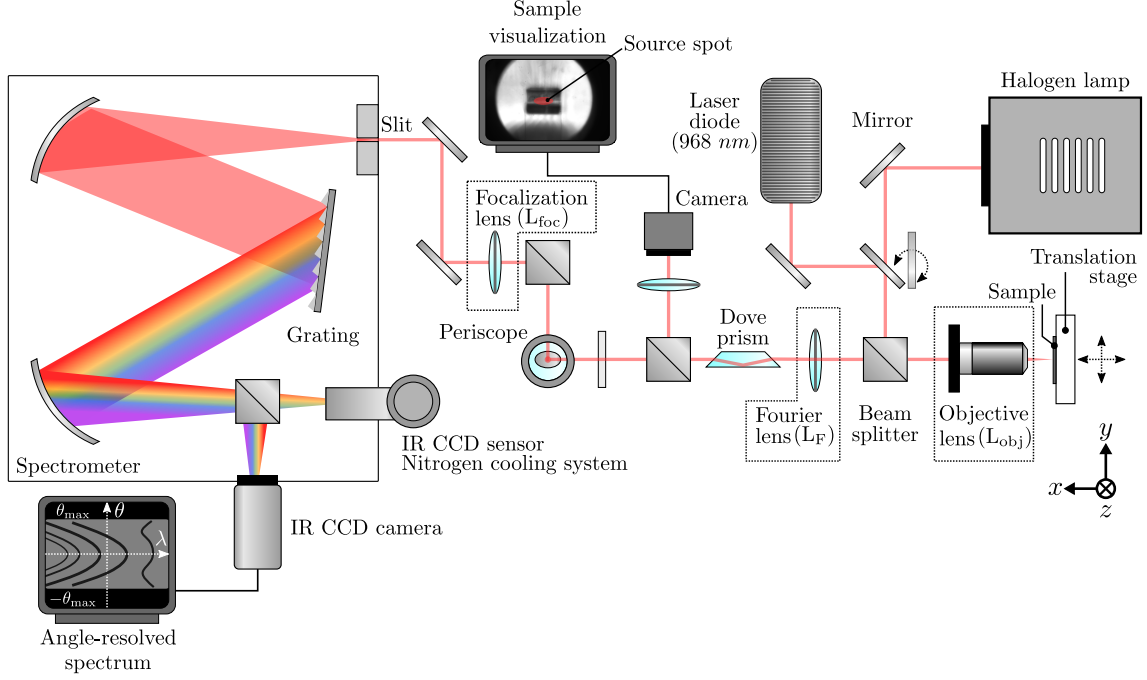


FIGURE 2.18: Setup for the realization of angle-resolved spectral measurements on photonic microstructures to retrieve their band diagrams experimentally.

The sample is mounted on a translation stage to adjust its position to the objective focal distance and align the structures with respect to the optical axis, hence the excitation spot. The objective both focuses the excitation signal onto the structures and collect the photoluminescence or reflection response. We use an objective lens of numerical aperture (NA) of 0.42 or 0.8 to observe angles of  $\pm 25^\circ$  or  $\pm 53^\circ$  corresponding to maximum wave vector norms of  $1.7$  or  $3.2 \mu\text{m}^{-1}$ . Large (small) values of NA enlarges (reduces) the angular limit of the dispersion while focusing the excitation spot on a smaller (larger) zone of the sample. The measurement of the modes' dispersion along the axis of photonic tubular cavities necessitates to align the tubes' axis along the slit orientation. To this end, the Dove prism allows to rotate the direction of the light beam collected by the objective with respect to the sample surface normal.

The spectrometer contains a grating monochromator which disperses spectrally the collected signal. Three gratings noted A, B and C with periods of 150, 600 and 900 lines/mm provide a spectral resolution of 120, 20 and 10 nm, respectively. However, a smaller resolution requires several measurements to cover a large spectral range.

An infrared camera finally collects the dispersed optical signal on a matrix of  $620 \times 512$  pixels consisting of InGaAs sensors with a detection range from 0.9 to  $1.7 \mu\text{m}$ . Thermoelectric cooling system and circulating water allows the reduction of the electronic noise.

## 2.4 Conclusion of the chapter

In this chapter, we have introduced the different methods of simulation, fabrication and optical characterization for the conception and study of rolled-up PCM microstructures.

In the first section, we have presented the rigorous coupled-wave analysis (RCWA) and the finite-difference time-domain (FDTD) methods employed to the simulation of:

- the PCM reflectivity spectrum at normal and oblique incidence (RCWA);

- the spectral response of tubular cavities (FDTD method)
- the band structure of periodic photonic structures, regardless of the geometry (FDTD method).

In the second section, we have detailed the fabrication process of rolled-up PCM microtubes composed of the following main steps:

- the production of the multi-layered precursors by molecular beam epitaxy (MBE);
- the design, fabrication and transfer of the planar PCM mask by successive e-beam lithography and reactive ion etching procedures;
- the rolling of the PCM into a tubular shape by under-etching process and the drying of the sample;

In the third section, we have described the two main setups dedicated to the optical characterization of the fabricated tubular micro-objects:

- a customized scanning near-field optical microscopy (SNOM) setup to map the modes confined into tubular photon cages;
- an angle-resolved spectroscopy setup to construct the band diagram of fabricated structures by collecting the photoluminescence or reflection signal.

In particular, we apply the previous methods in the following chapter for the conception and characterization of tubular photon cages.

## 2.5 References

- [1] M. G. Moharam and T. K. Gaylord, “Rigorous coupled-wave analysis of planar-grating diffraction,” *J. Opt. Soc. Am., JOSAA*, vol. 71, pp. 811–818, July 1981. Publisher: Optical Society of America. 76
- [2] M. G. Moharam and T. K. Gaylord, “Rigorous coupled-wave analysis of metallic surface-relief gratings,” *J. Opt. Soc. Am. A, JOSAA*, vol. 3, pp. 1780–1787, Nov. 1986. Publisher: Optical Society of America. 76
- [3] V. Liu and S. Fan, “S4 : A free electromagnetic solver for layered periodic structures,” *Computer Physics Communications*, vol. 183, pp. 2233–2244, Oct. 2012. 76
- [4] E. P. O’Reilly, “Valence band engineering in strained-layer structures,” *Semicond. Sci. Technol.*, vol. 4, pp. 121–137, Mar. 1989. Publisher: IOP Publishing. 88
- [5] G. Liu, A. Stintz, H. Li, K. Malloy, and L. Lester, “Extremely low room-temperature threshold current density diode lasers using InAs dots in In<sub>0.15</sub>Ga<sub>0.85</sub>As quantum well,” *Electronics Letters*, vol. 35, pp. 1163–1165, July 1999. Conference Name: Electronics Letters. 88
- [6] O. Shchekin, G. Park, D. Huffaker, Q. Mo, and D. Deppe, “Low-threshold continuous-wave two-stack quantum-dot laser with reduced temperature sensitivity,” *IEEE Photonics Technology Letters*, vol. 12, pp. 1120–1122, Sept. 2000. Conference Name: IEEE Photonics Technology Letters. 88
- [7] R. Schwertberger, D. Gold, J. Reithmaier, and A. Forchel, “Long-wavelength InP-based quantum-dash lasers,” *IEEE Photonics Technology Letters*, vol. 14, pp. 735–737, June 2002. Conference Name: IEEE Photonics Technology Letters. 88
- [8] B. Salem, N. Chauvin, T. Benyattou, G. Guillot, C. Bru-Chevallier, G. Bremond, C. Monat, P. Rojo-Romeo, and M. Gendry, “Optical investigation of single self-organized InAs/InP quantum dashes emitting in the 1.3–1.5  $\mu\text{m}$  range,” *Nanotechnology*, vol. 16, pp. 444–447, Feb. 2005. Publisher: IOP Publishing. 88
- [9] J. P. Reithmaier, G. Eisenstein, and A. Forchel, “InAs/InP Quantum-Dash Lasers and Amplifiers,” *Proceedings of the IEEE*, vol. 95, pp. 1779–1790, Sept. 2007. Conference Name: Proceedings of the IEEE. 88
- [10] D. Courjon and C. Bainier, *Le champ proche optique: théorie et applications*. Collection technique et scientifique des télécommunications, Paris: Springer, 2001. OCLC: 248507312. 98
- [11] M. Mivelle, I. A. Ibrahim, F. Baida, G. W. Burr, D. Nedeljkovic, D. Charraut, J.-Y. Rauch, R. Salut, and T. Grosjean, “Bowtie nano-aperture as interface between near-fields and a single-mode fiber,” *Opt. Express, OE*, vol. 18, pp. 15964–15974, July 2010. 99
- [12] T. P. Vo, *Optical near-field characterization of Slow-Bloch Mode based photonic crystal devices*. Theses, Ecole Centrale de Lyon, Sept. 2011. 99



# Chapter 3

## Design and simulation of photon cages

*Qui craint de souffrir, il souffre déjà de ce qu'il craint.*

---

MICHEL DE MONTAIGNE (ESSAIS, III, 13)

### Contents

---

<b>3.1</b>	<b>Introduction</b>	<b>110</b>
<b>3.2</b>	<b>Design of the planar two-dimensional photonic crystal mirror</b>	<b>111</b>
3.2.1	Reflection properties at normal incidence	111
3.2.2	Comparison with non-structured membranes	114
3.2.3	Reflection properties at oblique incidence	116
<b>3.3</b>	<b>Analytical model of the cylindrical cavity resonator</b>	<b>120</b>
3.3.1	Introduction to the model	120
3.3.2	Infinite cylindrical cavities	121
3.3.3	Finite length cylindrical cavities	126
<b>3.4</b>	<b>Numerical study of tubular photon cages</b>	<b>129</b>
3.4.1	Numerical model of tubular photon cages	130
3.4.2	Simulations of infinite cavities	130
3.4.3	Simulations of finite cavities	139
<b>3.5</b>	<b>Conclusion of the chapter</b>	<b>147</b>
<b>3.6</b>	<b>References</b>	<b>148</b>

---



### 3.1 Introduction

In the previous chapter, we have introduced the main tools to achieve the conception of rolled-up PCM microstructures, including the design, simulation, fabrication, and optical characterization steps. In the following two chapters, we focus on realizing tubular photon cages consisting of rolled-up 2D PCM mirrors and capable of 3D confinement of light in air. In particular, the present chapter deals with the design and the optical simulation of the cages. The first section presents the conception of a broadband and highly efficient 2D PCM mirror acting as the cages' membrane wall. Moreover, we compare the reflection performances of the PCM mirror with a standard gold mirror and an equivalent non-structured InP-made membrane. We finally assess the robustness of the PCM mirror at oblique incidences. The second section concentrates on the theoretical estimations of the tubular photon cages' optical properties. We use in first approximation the analytical model of the cylindrical cavity resonator to apprehend the modal response of the 3D hollow microresonators. We perform then finite-difference time-domain (FDTD) simulations to approach the optical response of the photon cages more realistically. We finally evaluate the consistency of both models.

## 3.2 Design of the planar two-dimensional photonic crystal mirror

Photon cages are 3D tubular photonic micro-resonators based on the bending of 1D or 2D photonic crystal membranes (PCM). The reflection properties of the PCM enables the trapping of light in the hollow part of the micro-cavities. The efficiency of this confinement depends on the performances of the PCM mirror. We explained in 1.2 that proper engineering of the dispersion of the modes supported by the PCM, by adjusting the photonic crystal lattice parameters, can enhance and extend the spectral range of the PCM reflection properties. On the model of 1D PCM photon cages previously introduced, we realize photon cages based on 2D PCM. Therefore, this section aims to produce the building block of those photon cages: the 2D PCM mirror. In the first part, we present the PCM structure and adjust the lattice parameters to achieve broadband and efficient reflective behaviour in the near-infrared domain around  $1.55 \mu\text{m}$ , the telecommunication wavelength. We assess the reflectivity of the PCM numerically, at normal incidence, using the RCWA method. In the second part, we compare the PCM's reflectivity to an equivalent gold mirror and plain InP membrane to assess the advantages of microstructure on the PCM mirror's performances. We finally evaluate the robustness of the PCM high reflectivity at oblique incidence through RCWA simulations.

### 3.2.1 Reflection properties at normal incidence

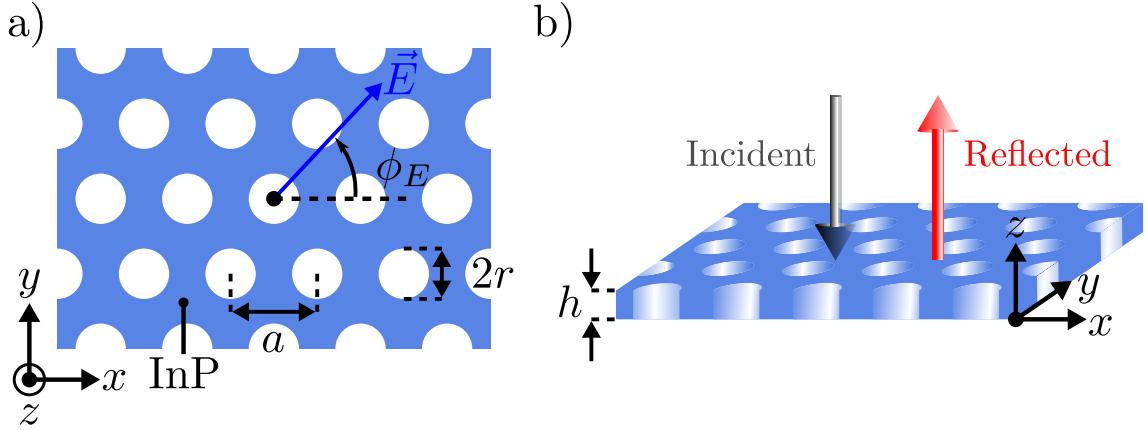


FIGURE 3.1: a) Schematics of the photonic crystal membrane (PCM): a triangular lattice, with a period  $a$ , of air holes (white circles) of radius  $r$ , etched in an Indium Phosphide (InP) membrane (blue background). The electric field  $\vec{E}$  orients in the plane of the PCM with the angle  $\phi_E$  taken from the  $x$  axis. b) Schematic perspective view of the reflection of incident light onto the PCM of thickness  $h$ .

We chose a 2D photonic crystal pattern as depicted in Figure 3.1.a), consisting of a triangular lattice, with a period  $a$ , of circular air holes (white holes) with a radius  $r$  etched in a dielectric membrane made of Indium Phosphide (InP) material (pale blue). The optical dispersion of the InP material comes from the model established in [1]. We simulate the optical response of the suspended PCM with thickness  $h$  and infinite lateral extension to a plane wave excitation, using the RCWA method through the  $S^4$  software. We extract the spectral evolution of the reflectivity  $R(\lambda)$  (red arrow) of the PCM at normal incidence as schematized on the perspective view of the PCM in Figure 3.1.b). It is noteworthy that transverse electric (TE) and transverse magnetic (TM)

polarizations coincide at normal incidence. However, we identify the orientation of the electric field  $\vec{E}$  in the PCM plane ( $xy$  plane) with the angle  $\phi_E$  formed with the  $x$  axis as shown in Figure 3.1.a). The thickness  $h$  refers to the thickness of a homogeneous layer of InP.<sup>1</sup> We also notice that any polarization decomposes linearly for instance in the basis of the directions  $\phi_E = 0^\circ$  and  $\phi_E = 60^\circ$ . Since both directions are equivalent due to the  $C_6$  lattice symmetry, the optical response of the PCM at normal incidence is therefore isotropic. Consequently, we restrain the computation of the PCM reflectivity to the orientation  $\phi_E = 0^\circ$  ( $\vec{E}$  along the  $x$  axis). The purpose of the calculations is to find a set of parameters ( $a, r, h$ ) to achieve high reflection behaviour ( $R(\lambda) > 95\%$ ) of the PCM on a broad ( $> 100 \text{ nm}$ ) spectral interval.

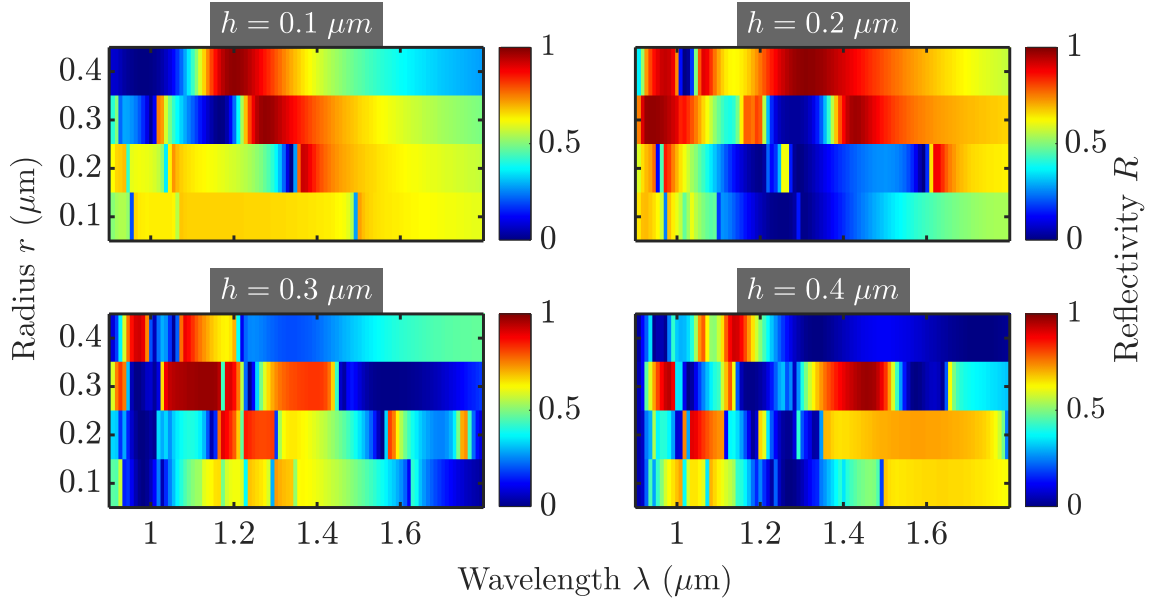


FIGURE 3.2: Maps of the PCM reflectivity  $R$  within the spectral window  $[0.9 - 1.8] \mu\text{m}$  for different PCM thickness  $h = 0.1, 0.2, 0.3, 0.4 \mu\text{m}$  and varying radius of the holes  $r = 0.1, 0.2, 0.3, 0.4 \mu\text{m}$ . The lattice period is fixed at  $a = 1 \mu\text{m}$ .

We carry out a first series of computations of the PCM reflectivity  $R(\lambda)$  at normal incidence in the interval  $[0.9 - 1.8] \mu\text{m}$ . We explore a large spectral window deliberately to observe the dynamics of the PCM modes while varying the structural parameters. Starting with a period  $a = 1 \mu\text{m}$ , a sweep of the radius  $r$  and the thickness  $h$  allows to select a first set of parameter  $(r, h)$  for which we observe a large spectral band of high reflectivity. The four plot areas in Figure 3.2 report the simulation results for four values of the thickness  $h = 0.1, 0.2, 0.3$  and  $0.4 \mu\text{m}$ . For each value of  $h$ , the plot area divides into four reflectivity spectra corresponding to a radius  $r$  ranging from  $0.1$  to  $0.4 \mu\text{m}$ . We ensure that  $r < a/2$  to avoid the overlapping between two adjacent holes. We conducted the simulations with a low number of diffraction orders ( $N = 20$ ) to obtain a rapid and qualitative trend of the reflectivity for each setting. At first glance, several combinations  $(r, h)$  are acceptable as the corresponding spectra present broad ( $> 100 \text{ nm}$ ) (reddish) intervals of high reflectivity ( $R > 0.9$ ), called HR zones thereafter for high-reflectivity zones. The HR zones correspond to PCM guided resonances characterized by large bandwidths. We focus afterwards on the combination  $(r = 0.4, h = 0.2) \mu\text{m}$  which exhibits a HR zone spanning from  $1.24$  to  $1.4 \mu\text{m}$ .

<sup>1</sup>In reality, the fabricated membrane consists of an InGaP/InP bilayer. However, supposing small proportions of Gallium (Ga) element in the InGaP layer, we expect similar optical behaviour of InGaP and InP layers.

The second step for the adjustment of the PCM parameters aims to shift and centre the HR zone around the wavelength of interest  $1.55 \mu\text{m}$ . Toward this goal, we fix the membrane thickness  $h = 0.2 \mu\text{m}$  and we increase the radius  $r$  and the period  $a$  simultaneously, maintaining a constant ratio  $r/a = 0.4$ . The reflectivity spectra of the PCM for  $r$  ranging from  $0.45 \mu\text{m}$  to  $0.5 \mu\text{m}$  are displayed in Figure 3.3. We observe that the HR zone undergoes a redshift as  $r$  and  $a$  increase. In particular, for  $r = 0.480 \mu\text{m}$  and  $a = r/0.4 = 1.2 \mu\text{m}$ , the HR zone is approximately centred on the targeted wavelength of  $1.55 \mu\text{m}$  and the reflectivity reaches a maximum value of nearly 99 %.

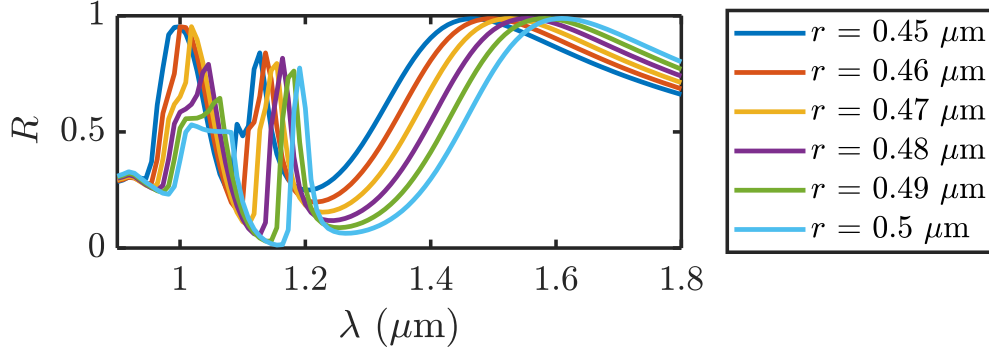


FIGURE 3.3: Spectra of the PCM reflectivity  $R(\lambda)$  within the spectral window  $[0.9 - 1.8] \mu\text{m}$  for increasing value of the air holes' radius  $r$  between  $0.45$  and  $0.5 \mu\text{m}$  and the lattice period  $a$  but constant ratio  $r/a$  fixed at  $0.4$ . The PCM thickness  $h$  is set to  $0.2 \mu\text{m}$ .

We finally perform a finer tuning of the thickness  $h$  to improve the PCM reflective behaviour at normal incidence. Indeed, higher-order membrane modes add to the dispersion diagram of thicker PCM, increasing the probability of two leaky modes (or guided resonances) to overlap and form a wider HR zone. The reflectivity  $R(\lambda)$  spectra are shown in Figure 3.4.a) for thicknesses  $h$  varying gradually from  $0.2$  to  $0.25 \mu\text{m}$  with a  $10 \text{ nm}$  step. We also present a mapped version of the previous plot Figure 3.4.b) to visualize the dynamics of the modes properly. At  $h = 0.2 \mu\text{m}$ , we distinguish three distinct spectral features: the HR zone at around  $1.6 \mu\text{m}$  and two additional leaky modes that we note  $\text{LM}_1$  and  $\text{LM}_2$  which maximum of reflectivity locates at about  $1.3$  and  $1.8 \mu\text{m}$ , respectively. The two modes  $\text{LM}_1$  and  $\text{LM}_2$  undergo a strong redshift and a spectral broadening as the thickness  $h$  increases. By contrast, the HR zone hardly evolves for higher  $h$  and the wavelength of the reflectivity maximum only redshifts by  $0.6 \%$  of its initial value of  $1.55 \mu\text{m}$  for  $h = 0.2 \mu\text{m}$ . At  $h = 0.25 \mu\text{m}$ , the situation favourably evolves towards the merging between  $\text{LM}_2$  and the HR zone, forming a broader and highly efficient HR zone. However, the modification of the thickness  $h$  is not inconsequential at the level of:

- the optical properties of the PCM mirror: the thickness  $h$  influences both the value and the bandwidth of the planar PCM reflectivity  $R(\lambda)$ . In particular, we have shown earlier that an increase of  $h$  leads to a more efficient and broadband PCM mirror.
- the optical properties of the tubular cavity knowing that the curvature radius  $\rho_c$  of the final tubular cage increases with  $h$  according to Equation (1.21) in Chapter 1. On the one hand, large values of the radius  $\rho_c$  with respect to the PCM geometrical parameters  $(a, r)$  preserves the reflection properties of the planar PCM mirror. On the other hand, rolled-up PCM with a large curvature radius

form highly multi-modal tubular microcavities with degraded performances, as shown in later sections.

- the structural properties of the tubular cavity produced by the self-rolling of an epitaxially grown InP/InGaP bilayer of total thickness  $h = h_1 + h_2$  with  $h_1, h_2$  the thicknesses of InP and InGaP individual layers. The epitaxial growth imposes a critical value of  $h_2$ , noted  $h_c$ , above which relaxation phenomenon can occur within the deposited InGaP layer. In particular, for Gallium (Ga) compositions  $x$  in the order of 0.1, we report a critical thickness  $h_c \simeq 80 \text{ nm}$  consistently with the  $70 \text{ nm}$  limit found in other works [3] for  $x = 0.2 - 0.25$ .

According to Equation (1.21) in Chapter 1, given  $h_2 = 80 \text{ nm}$  and  $x = 0.1$ , the radius of the final cylindrical cavity  $\rho_c$  varies from about  $17.36 \mu\text{m}$  to  $23.94 \mu\text{m}$  ( $\sim 38 \%$  raise) as  $h$  ranges from  $0.2$  to  $0.25 \mu\text{m}$ . We finally find a good compromise between a broad reflecting behaviour of the PCM and a relatively low value of  $\rho_c$  by fixing the PCM thickness to  $h = 0.23 \mu\text{m}$ .

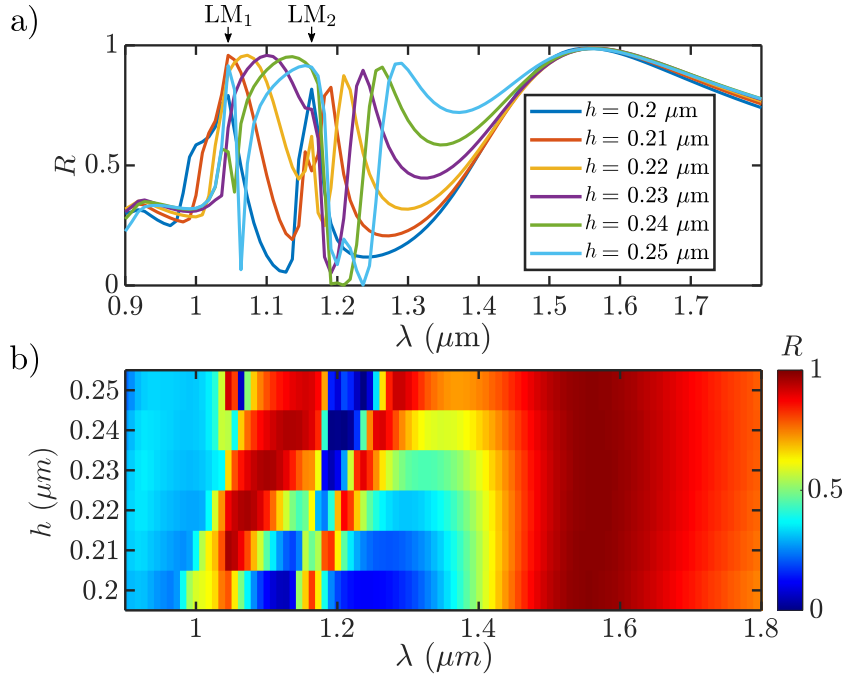


FIGURE 3.4: a) Spectrum of the PCM reflectivity  $R$  within the spectral window  $[0.9-1.8] \mu\text{m}$  for given  $r = 0.4a$ ,  $a = 1.2 \mu\text{m}$  and varying thickness  $h$  from  $0.2$  to  $0.25 \mu\text{m}$ . b) Mapped version of the previous graph.

We have designed a broadband and efficient PCM mirror with lattice parameters ( $a = 1.2, r = 0.48$ )  $\mu\text{m}$  and thickness  $h = 0.230 \mu\text{m}$ . It exhibits a high reflecting behaviour, namely  $R > 0.95$ , at normal incidence within a  $130 \text{ nm}$ -large near-infrared interval ( $[1.53 - 1.66] \mu\text{m}$ ). The PCM reflectivity  $R$  reaches a maximum value of about  $0.99$  near  $1.56 \mu\text{m}$ , close to the standard telecommunication wavelength. Most interestingly and unlike 1D PCM mirrors, the reflection properties of the 2D PCM do not depend on the electric field's orientation at normal incidence.

### 3.2.2 Comparison with non-structured membranes

We have also compared the reflection performances of the PCM at normal incidence to that of a non-structured gold mirror and InP membrane within the spectral window  $[1.4 - 1.8] \mu\text{m}$ .

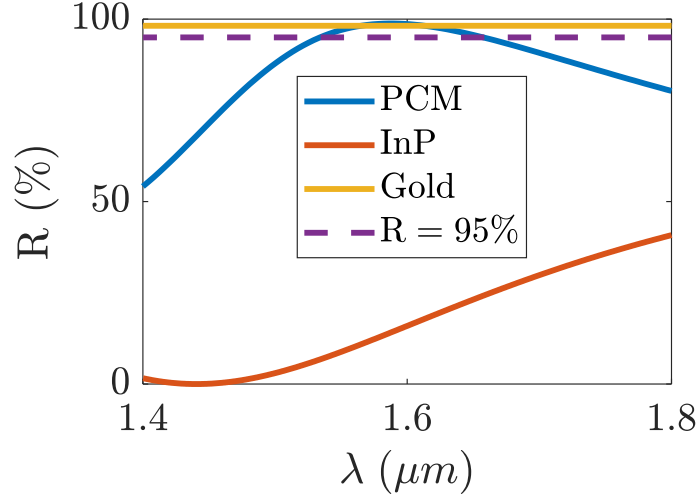


FIGURE 3.5: Reflectivity  $R(\lambda)$  spectra at normal incidence of the PCM membrane (RCWA simulations) with optimized lattice parameters and of non-structured suspended InP-made and gold-made membranes (calculated with Fresnel coefficients), all with a thickness of  $0.230 \mu m$ . The purple dashed line indicates the 95% limit of the reflectivity.

First, we have calculated theoretically using the Fresnel reflection coefficients (see Appendix C for details of the expressions), the reflectivity spectrum at normal incidence of a suspended non-structured  $0.23 \mu m$ -thick gold slab and obtained the yellow curve plotted in Figure 3.5. We have taken the dispersion relation of gold material from the experimental works [2]. The gold membrane exhibits a very high reflecting behaviour, with a reflectivity  $R$  stabilized at nearly 98 % over the entire spectral interval. However, Figure 3.5 also demonstrates a competitive PCM reflectivity, represented by a blue curve, which stays above the 95% high reflectivity limit over a  $130 nm$ -large interval. It even goes over the gold membrane curve, especially when reaching its maximum value of 99% at about  $1.56 \mu m$ . Despite excellent and broadband reflection properties, the gold material is also a source of optical losses that may heat up and damage the components in integrated devices. On the contrary, the InP material remains transparent in the near-infrared domain which allows for external optical excitation.

Second, we have confronted the PCM reflection properties to the theoretical reflectivity of a suspended non-structured  $0.23 \mu m$  InP membrane, again using Fresnel formulas, represented by a red curve in Figure 3.5. We notice that the InP membrane exhibits poor reflection properties as the reflectivity does not exceed 50 %. It even reaches a minimum at nearly  $1.45 \mu m$ , corresponding to a Fabry-Pérot transmission resonance:  $2hn_{\text{InP}} = p\lambda$ ,  $p \in \mathbb{Z}^*$ , with  $n_{\text{InP}} \sim 3.16$  the optical refractive index of InP at about  $1.55 \mu m$ . It proves the essential microstructure of the InP membrane to achieve a high and broadband reflecting behaviour in the spectral range of interest.

In conclusion, the PCM mirror combines both plain gold mirror and InP membrane advantages. It exhibits a high and broadband reflectivity while preserving the transparency properties of InP material. Most strikingly, the high reflectivity of the PCM originates from a micro-structured membrane mostly filled with air. Indeed, we estimate the fraction of air in the PCM, namely the air filling factor  $FF = 2\pi/\sqrt{3}(r/a)^2$ , to 58%.

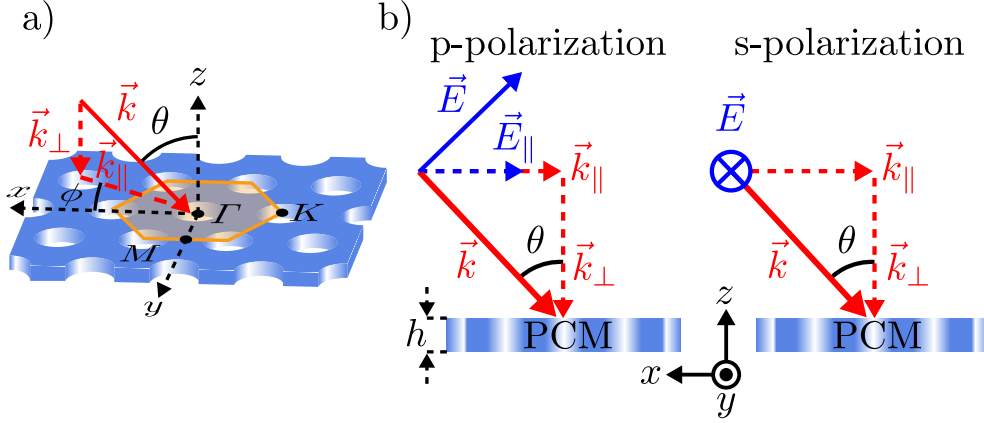


FIGURE 3.6: Deviation to normal incidence. a) Incident light on the PCM oriented by the wave-vector  $\vec{k}$  (red arrow) forming the angles  $\theta$  and  $\phi$  with the  $z$ -axis and  $x$ -axis directions respectively upon projection ( $\vec{k}_{\parallel}$ ) on the PCM plane. The points  $\Gamma$ ,  $K$  and  $M$  refers to the high-symmetry directions of the triangular lattice first Brillouin Zone (FBZ) with orange shading. b) The  $p$ - ( $s$ -) polarization for which the electric field  $\vec{E}$  represented as a blue arrow is contained (orthogonal) to the incidence plane.

### 3.2.3 Reflection properties at oblique incidence

We have demonstrated so far the advantages of using a PCM to create a non-absorbing broadband mirror operating in the near-infrared domain at normal incidence. We have also evaluated the robustness of the PCM reflection properties in the more general case of oblique incidence. To this end, we consider incoming light hitting the PCM surface with the direction of the wavevector  $\vec{k}$  forming an angle  $\theta$  with the  $z$ -axis and an angle  $\phi$  with the in-plane  $x$ -axis direction as depicted in Figure 3.6.a). We note  $\vec{k}_{\perp}$  and  $\vec{k}_{\parallel}$  the projections of  $\vec{k}$  onto the  $z$ -axis and the PCM plane, respectively. We identify the high symmetry directions of the photonic crystal,  $\Gamma$ ,  $K$  and  $M$  in the first Brillouin zone (FBZ) delimited by an orange area. Furthermore, we decompose the polarization of any incoming light in the basis of  $p$ -polarized and  $s$ -polarized radiations. For the two reference polarizations, the electric field  $\vec{E}$  is either contained or orthogonal to the incidence plane as schematized in the two drawings in Figure 3.6.b).

We have simulated the reflectivity of the PCM for  $\theta$  ranging from  $0^\circ$  to  $50^\circ$  with the RCWA method in four specific configurations with  $\phi = 0$  or  $90^\circ$  and  $p$ - or  $s$ -polarized light. We present the results of the simulations in Figure 3.7 and Figure 3.8. In both figures, the left drawings indicate the orientations of  $\vec{k}_{\parallel}$  and  $\vec{E}_{\parallel}$  with respect to the FBZ high symmetry directions. The right plots correspond to PCM reflectivity maps (in %) in the spectral range  $[1.4 - 1.8 \mu\text{m}]$  as a function of the angle  $\theta$ . We recall that, at normal incidence, a high reflectivity ( $R_p > 95\%$ ) zone covers the spectral interval  $[1.53 - 1.66] \text{ nm}$ .

For the four configurations, we report a global shrinking and red-shift of the original high reflectivity (HR) zone for increasing incidence angle  $\theta$ . To quantify the shrinking rate, noted  $\Delta_{\text{narrow}}$ , we extract the range and the bandwidth of the HR zone, noted HR range and  $\Delta\lambda_{\text{HR}}$  respectively, for each configuration at a fixed angle  $\theta = 14^\circ$ . This angle corresponds to the highest angle for which the simulation range  $[1.4 - 1.8] \mu\text{m}$  fully covers the HR zone spectral extent in each configuration. We also evaluate the relative deviation, noted  $\Delta_{\text{shift}}$  of each HR zone bandwidth in comparison to the  $130 \text{ nm}$ -large bandwidth obtained at normal incidence. We gather all the results in Table 3.1. We notice that increasing  $\theta$  up to  $14^\circ$  strongly reduces the HR zone spectral extent for  $s$ -polarized light and  $\phi = 90^\circ$ , with  $\Delta_{\text{narrow}}$  reaching 69%. On the contrary, the HR range



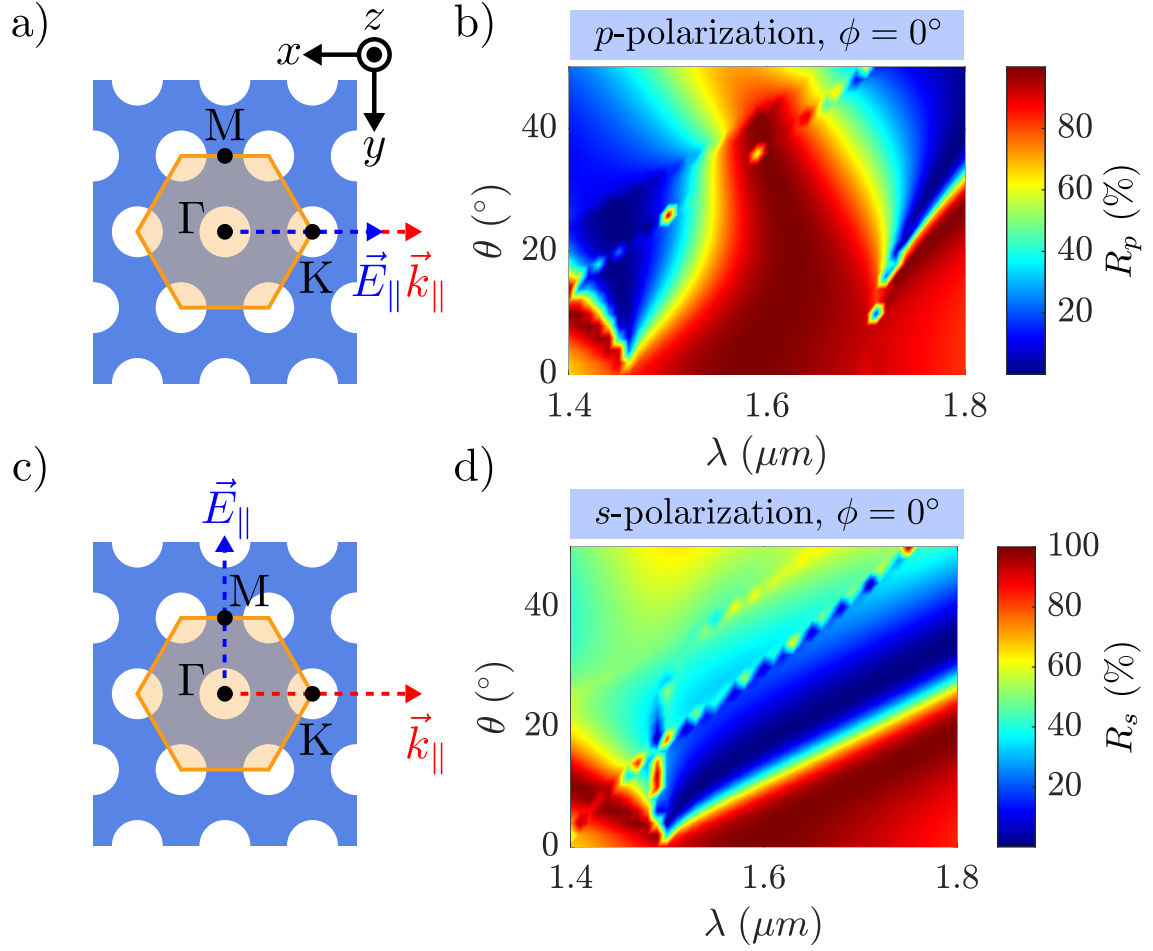


FIGURE 3.7: PCM's reflectivity  $R(\lambda)$  at oblique incidence (angle  $\theta$ ) and orientation  $\phi = 0^\circ$ . a) and c): Orientation of the projections of the electric field  $\vec{E}_{||}$  (dashed blue arrow) and the wavevector  $\vec{k}_{||}$  (dashed red arrow) onto the PCM plane for  $p$ - (upper drawing) and  $s$ - (lower drawing) polarizations. The points  $\Gamma$ ,  $K$  and  $M$  indicate the triangular lattice FBZ (orange zone) high symmetry points. b) and d): Maps of the PCM reflectivity  $R_{p,s}(\lambda)$  for  $p$ - (upper plot) and  $s$ - (lower plot) polarizations within the spectral range  $[1.4-1.8] \mu m$  as a function of the angle of incidence  $\theta$ .



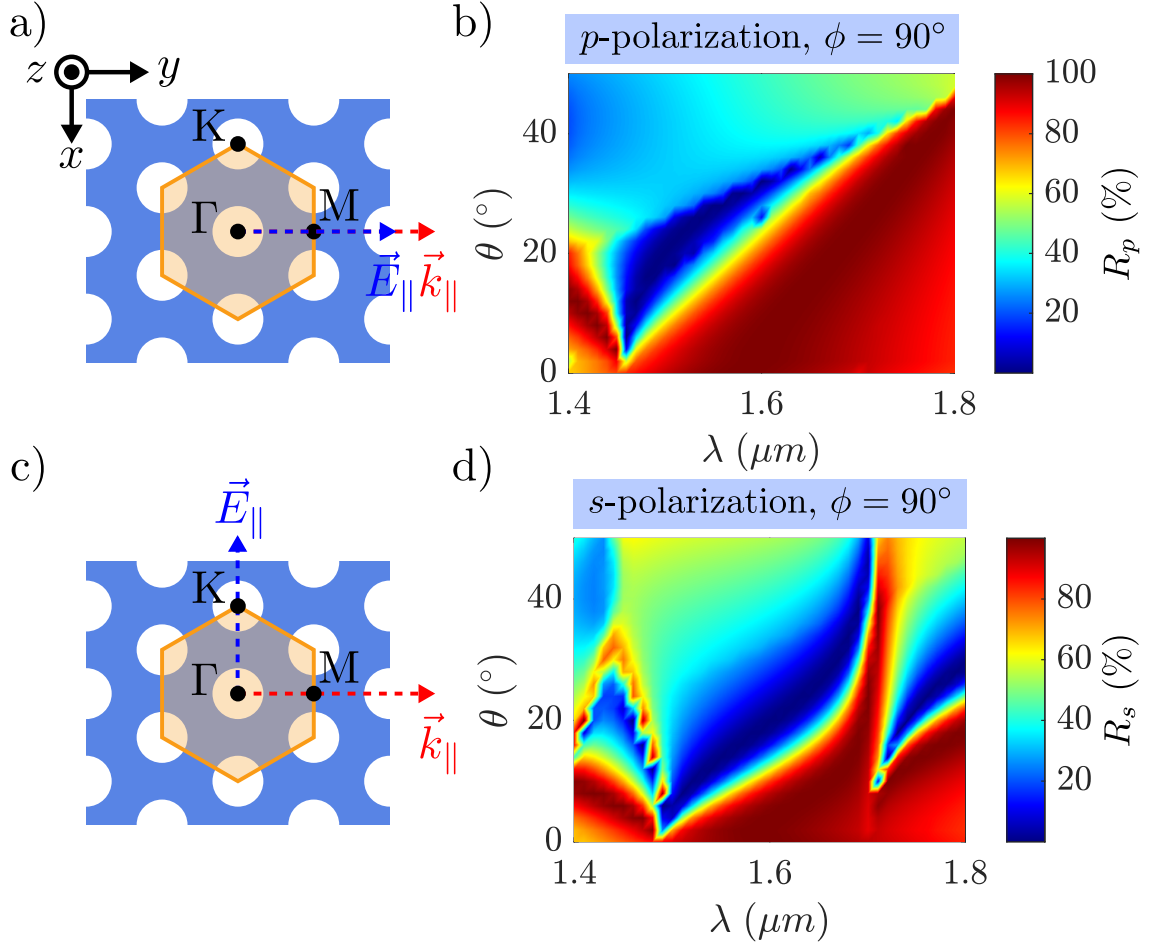


FIGURE 3.8: PCM's reflectivity  $R(\lambda)$  at oblique incidence (angle  $\theta$ ) and orientation  $\phi = 90^\circ$ . a) and c): Orientation of the projections of the electric field  $\vec{E}_{||}$  (dashed blue arrow) and the wavevector  $\vec{k}_{||}$  (dashed red arrow) onto the PCM plane for  $p$ - (upper drawing) and  $s$ - (lower drawing) polarizations. The points  $\Gamma$ ,  $K$  and  $M$  indicate the triangular lattice FBZ (orange zone) high symmetry points. b) and d): Maps of the PCM reflectivity  $R_{p,s}(\lambda)$  for  $p$ - (upper plot) and  $s$ - (lower plot) polarizations within the spectral range  $[1.4-1.8] \mu m$  as a function of the angle of incidence  $\theta$ .

for *p-polarized* light and  $\phi = 90^\circ$  exhibits quite robust behaviour to oblique incidence with the smallest  $\Delta_{\text{narrow}}$  of 15%.

$\phi$	Polar.	$\theta$ ( $^\circ$ )	HR Range ( $\mu m$ )	$\Delta\lambda_{\text{HR}}$ (nm)	$\Delta_{\text{narrow}}$ (%)	$\Delta_{\text{shift}}$ (%)
0	<i>p</i> -	14	1.58-1.68	100	23	3
0	<i>s</i> -	14	1.70-1.79	90	31	
0	<i>s</i> -	12	1.67-1.77	100		9
90	<i>p</i> -	14	1.60-1.71	110	15	
90	<i>p</i> -	18	1.63-1.73	100		6
90	<i>s</i> -	14	1.66-1.70	40	69	
90	<i>s</i> -	6	1.58-1.68	100		3

TABLE 3.1: Spectral characteristics of the PCM's high-reflectivity (HR) zones ( $R > 95\%$ ) recorded at oblique incidence  $(\theta, \phi)$  with *p*- or *s*- polarizations in Figure 3.7 and Figure 3.8. For each configuration, i.e.  $\phi = \{0, 90\}^\circ$  and *p*-/*s*-polarizations, we report the range, HR range in  $\mu m$ , and the bandwidth,  $\Delta\lambda_{\text{HR}}$  in nm, of the HR zone. The narrowing rate  $\Delta_{\text{narrow}}$  evaluates the relative deviation in % between the HR bandwidth at  $\theta = 0^\circ$  (130 nm) and  $\theta = 14^\circ$ . The shift rate  $\Delta_{\text{shift}}$  estimates the relative shift (in %) between the wavelength of the maximum reflectivity of a 100 nm-large HR zone at  $(\phi, -p/ -s, \theta)$  and at normal incidence.

To complete the previous results, we estimate for each configuration the maximum angle  $\theta$  preserving a 100 nm-large HR zone. According to Table 3.1, except for *s-polarized* light and  $\phi = 90^\circ$ , the HR zone shows robustness at oblique incidence as it maintains the 100 nm spectral width for  $\theta$  up to few tens of degrees. In particular, the configuration defined by *p-polarized* light with  $\phi = 90^\circ$  records the highest value of  $\theta$  estimated to  $18^\circ$ . We also report a red-shift of few units of % of the HR zone compared to normal incidence. On the contrary, we obtain the smallest  $\theta$  ( $6^\circ$ ) for robust behaviour of the 100 nm-large HR zone with *s-polarized* light and  $\phi = 90^\circ$ .

We have demonstrated that we could find a 100 nm-large spectral range within  $[1.4 - 1.8] \mu m$  where the PCM exhibits high reflecting behaviour for incidence angles up to a few tens of degrees. We also reported the most robust reflective behaviour in the case of *p-polarized* light oriented and  $\phi = 90^\circ$  for which the HR zone maintains its integrity up to  $18^\circ$  incidence angle. We have observed a redshift of the HR zone position to a few units of % of its original position at normal incidence. Finally, the PCM mirror's performances degrade for higher incidence angles as the HR zone shrinks progressively. We again note the smallest narrowing of the HR zone for *p-polarized* light and  $\phi = 90^\circ$ .

#### Key points of the section

We have managed to design a 2D PCM mirror with adjusted lattice parameters ( $a = 1.2, r = 0.48$ )  $\mu m$  and a thickness  $h = 0.23 \mu m$  and the following features:

- the PCM exhibits high reflection properties ( $R > 95\%$ ) at normal incidence over a large (130 nm) spectral window  $[1.53 - 1.66] \mu m$  in the near-infrared domain, comprising the 1.55  $\mu m$  wavelength of interest;
- unlike 1D PCM, the 2D PCM reflective response shows isotropic behaviour regarding the orientation of the electric field in the PCM plane, at normal incidence;
- the PCM is made out of non-absorbing InP material unlike equivalent gold membrane mirror and the structuring of the InP membrane is essential to achieve high reflection properties;
- the high reflectivity spectral zone of the PCM stays preserved but red-shifts at oblique incidence in the limit of inclinations angles of tens of degrees.

In keeping with the conception of photon cages based on rolled-up PCM mirrors, the next step focuses now on the simulation of the optical properties of tubular micro-cavity formed by the rolling of 2D PCM mirror, as introduced in the following section.

### 3.3 Analytical model of the cylindrical cavity resonator

We have completed the first stage of the tubular photon cages' conception by designing an efficient non-absorbing 2D PCM mirror operating within a broad near-infrared spectral range. The second step consists in simulating the optical response of the 3D hollow photonic micro-cavity formed by rolling the 2D PCM mirror up. We will first use the analytic model of the cylindrical cavity resonator to investigate the modes of our tubular cavity, approximating the photonic crystal membrane wall to a perfect mirror. This simple theoretical model will provide us with quick preliminary estimates of the type, spectral distribution, and field profiles of the modes supported by the cavity.

#### 3.3.1 Introduction to the model

A cylindrical resonant cavity is a common device in the microwave domain employed for high-sensitive detection of changes in materials' dielectric properties and as frequency meters. It consists of a hollow cylinder of inner radius  $\rho_c$  and length  $L$  with perfectly reflecting membrane wall as sketched in Figure 3.9.a), allowing strong confinement of the electromagnetic energy by exploiting resonances of the cavity. Its simple geometry and the knowledge of the boundary conditions enable the analytical resolution of Maxwell's equations inside the cavity. Consequently, we obtain the spectral and spatial distributions of the resonant modes supported by the cavity. In particular, we use this approach to obtain quick primary estimates of the optical response of rolled-up PCM tubular cavities, assimilating, in first approximation, the PCM to a perfect mirror. We summarize below the key results of the resolution of Maxwell's equations for one type

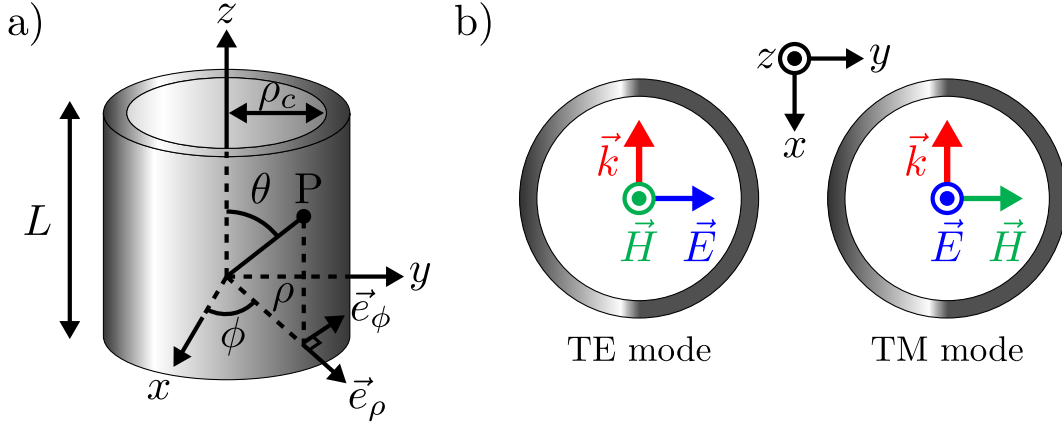


FIGURE 3.9: Cylindrical cavity resonator. a) Perspective view of a hollow cylindrical cavity resonator with inner radius  $\rho_c$ , a length  $L$  and perfectly reflecting membrane wall. The cylindrical coordinate system  $(\rho, \phi)$  is introduced here appropriately. b) Top view ( $xy$ -plane) of the cavity which supports two kinds of modes: transverse electric (TE) and transverse magnetic (TM) modes. For TE (TM)-polarized light propagating in the direction of the wave-vector  $\vec{k}$  (red arrow), the magnetic field  $\vec{H}$  (the electric field  $\vec{E}$ ) orients along the  $z$ -axis exclusively:  $\vec{H} = H_z \vec{e}_z$  ( $\vec{E} = E_z \vec{e}_z$ ).

of modes: transverse electric (TE) modes defined by  $E_z = 0$  as represented in Figure 3.9.b). We explain later in Section 2.3 regarding optical characterization measurements the choice to focus on TE modes. We note that similar calculations lead to the description of TM modes for which  $H_z = 0$ , hence not addressed in the present section. We will refer to Appendix D for a step-by-step construction of the TE solutions which follows a classical development used for instance in [5].

### 3.3.2 Infinite cylindrical cavities

We first investigate the modal properties of infinitely long cavities ( $L \rightarrow \infty$ ) filled with a dielectric homogeneous medium of optical refractive index  $n_{med}$  and negligible magnetic response ( $\mu = 1$ ) in the optical domain. For TE modes, the axial component of the magnetic field  $H_z$  verifies the *wave equation* or *Helmholtz equation*:

$$\nabla^2 H_z + k^2 H_z = 0, \quad (3.1)$$

with  $k = n_{med} \omega$  the wavenumber and  $\omega$  the pulsation. Assuming a plane wave solution propagating in the  $z$ -direction (axis of the cylinder)  $H_z(\rho, \phi, z) = h_z(\rho, \phi) e^{-j\beta z}$ , with  $\beta = \vec{k} \cdot \vec{e}_z$ , the Equation (3.1) becomes in the cylindrical coordinate system:

$$\left( \frac{\partial^2}{\partial \rho^2} + \frac{1}{\rho} \frac{\partial}{\partial \rho} + \frac{1}{\rho^2} \frac{\partial^2}{\partial \phi^2} + k_c^2 \right) h_z(\rho, \phi) = 0. \quad (3.2)$$

where  $k_c$  designates the transverse component of the wave-vector  $\vec{k} = \vec{k}_c + \beta \vec{e}_z$ . The notation  $k_c$  will be fully realised in the following developments. Using the method of separation of variables and considering the cylindrical symmetry, the general solution of the Equation (3.2) expresses as:

$$h_z^{(m)}(\rho, \phi) = (A \sin(m\phi) + B \cos(m\phi)) J_m(k_c \rho), \quad m \in \mathbb{N}, \quad (3.3)$$

where  $A$  and  $B$  are constants. The integer  $m$  corresponds to the *azimuthal* order of the TE mode and indicates the number of variations of the electromagnetic fields patterns

in the ortho-radial direction (along  $\vec{e}_\phi$ ). The function  $J_m$  relates to the first kind Bessel function at the order  $m$  described in Appendix D.

We determine the norm of the transverse wave-number  $k_c$  by applying a boundary condition. Interface electromagnetic conditions impose the continuity of the electric field tangential component  $\vec{E}_\parallel = \vec{E}_\phi + \vec{E}_z$ , which reduces to  $\vec{E}_\phi$  as  $\vec{E}_z = \vec{0}$  for TE modes. Furthermore, the perfectly reflecting wall of the cylindrical cavity starting at the inner radius  $\rho_c$  impedes the penetration of the electric field. Both conditions end in the following boundary condition:

$$E_\phi(\rho, \phi) = 0 \quad \text{at} \quad \rho = \rho_c. \quad (3.4)$$

Moreover, using Maxwell's equations in cylindrical coordinates, we derive the expression of the ortho-radial component of the electric field  $E_\phi(\rho, \phi)$  from the single axial component  $H_z$  so that, associated to Equation (3.3), we obtain:

$$E_\phi^{(m)}(\rho, \phi, z) = \frac{j\omega\mu}{k_c} (A \sin(m\phi) + B \cos(m\phi)) J'_m(k_c \rho) e^{-j\beta z}, \quad (3.5)$$

where  $J'_m$  stands for the first derivative with respect to the variable  $k_c \rho$  of the  $m$ -th order first kind Bessel function. The boundary condition established in Equation (3.4) becomes:

$$J'_m(k_c \rho_c) = 0, \quad (3.6)$$

which solutions correspond to the  $n$  ( $n \in \mathbb{N}^*$ ) roots of the function  $J'_m$  that we note  $p'_{m,n}$ . The first values of  $p'_{m,n}$  are listed in the Table D.1 of Appendix D. The integer  $n$  defines the *radial* order of TE modes and indicates the number of radial variations of the electromagnetic field pattern. The wave-number  $k_c$  takes therefore quantized values expressed as:

$$k_{c,m,n} = \frac{p'_{m,n}}{\rho_c}, \quad (3.7)$$

which corresponds to the cutoff wave-number  $k_{c,m,n}$  above which the mode  $\text{TE}_{m,n}$  exists and propagates inside the cavity. We associate the cutoff frequency  $f_{c,m,n}$  which writes then:

$$f_{c,m,n} = \frac{k_{c,m,n}}{2\pi n_{med}} = \frac{p'_{m,n}}{2\pi \rho_c n_{med}}. \quad (3.8)$$

We also deduce the dispersion relation for each modes  $\text{TE}_{m,n}$ :

$$k_{m,n}^2 = \frac{\omega_{m,n}^2}{c^2} n_{med}^2 = k_{c,m,n}^2 + \beta_{m,n}^2 = \left( \frac{p'_{m,n}}{\rho_c} \right)^2 + \beta_{m,n}^2, \quad (3.9)$$

where  $c$  stands for the speed of light and  $\omega_{m,n}$  corresponds to the pulsation of the mode  $\text{TE}_{m,n}$ . We have plotted in Figure 3.10.a) the dispersion diagrams  $\omega_{m,n} = f(\beta_{m,n})$  of the modes  $\text{TE}_{m,n}$  for the first values of the orders  $m = \{0, 1, 2\}$  and  $n = \{1, 2\}$ . We notice that all the present modes lie above the light line in air ( $\mu = \epsilon = 1$ ) defined by  $\omega_{m,n} = k_{m,n}c$ , with  $c$  the speed of light. This behaviour holds actually for every combinations of orders  $(m, n)$  of  $\text{TE}_{m,n}$  modes and it has a potential interest for optical characterization of the real micro-cavities. Indeed, such modes can couple more or less strongly with radiated modes so that we generally detect them with far-field measurements. We also note that the mode  $\text{TE}_{1,1}$  (yellow curve) is the first  $\text{TE}_{m,n}$  mode to emerge inside the cavity when increasing the excitation frequency. The propagation constant  $\beta_{m,n}$  corresponds to the norm of the projection of  $k_{m,n}$  onto the cavity axis coinciding with the  $z$ -axis:  $\beta_{m,n} = k_{m,n} \cos \theta$  with the angle  $\theta$  identified in Figure 3.9.a). By contrast with  $k_{c,m,n}$ , the component  $\beta_{m,n}$  can take *a priori* any values. In particular, for  $\beta_{m,n} = 0$ , the mode  $\text{TE}_{m,n}$  does not propagate along the axis of the cavity.

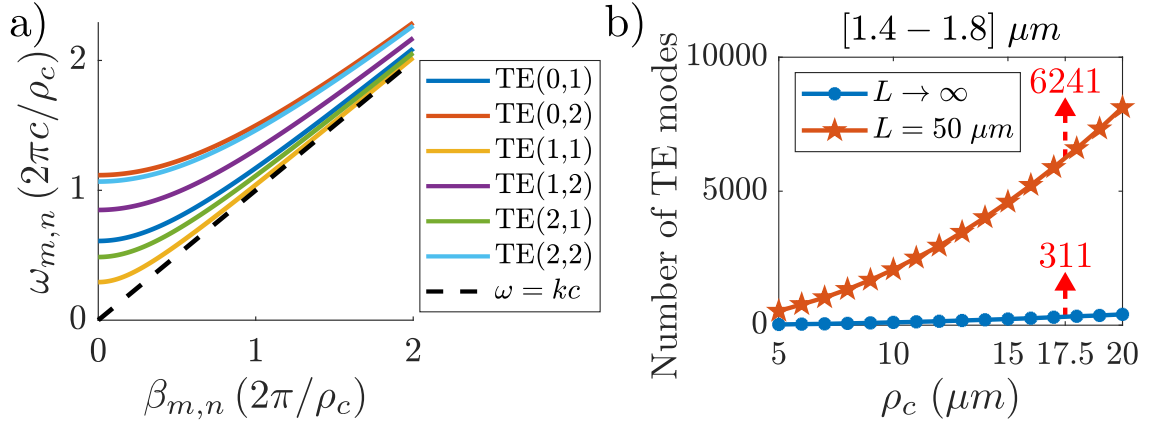


FIGURE 3.10: a) Dispersion diagrams of  $TE_{m,n}$  modes for the first orders  $(m, n)$  with a propagation constant  $\beta$  along the  $z$ -axis. The dashed black line refers to the light line in air ( $\mu = \epsilon = 1$ ) defined by the equation  $\omega = kc$ . b) Number of TE modes within the spectral range  $[1.4 - 1.8] \mu m$  as a function of the radius  $\rho_c$  of a cylindrical cavity resonator of infinite length  $L \rightarrow \infty$  (blue dot curve) and of length  $L = 50 \mu m$  (orange star curve).

In the perspective of the cavities' optical characterization, we estimate the number and spectral spacing of TE modes for a cavity of radius  $\rho_c$  within a prescribed spectral interval. We infer this information from the dispersion relation established in Equation (3.8). Intuitively, an increase of the curvature radius of the cavity will lead to a higher number of modes supported by the cavity. We represent the amount of TE modes in Figure 3.10.b) as a function of the radius  $\rho$  of an infinitely long ( $L \rightarrow \infty$ ) cavity, within the range  $[1.4 - 1.8] \mu m$ . We notice that the number of modes increases with the cavity radius, as expected. In particular, for a radius  $\rho_c = 17.5 \mu m$  obtained experimentally by rolling a PCM of thickness  $h = 0.23 \mu m$  and Gallium proportion  $x \sim 0.1$  in the InGaP layer, we observe that a maximum of 311  $TE_{m,n}$  modes coexist inside the cavity. Moreover, calculating the spectral spacing between consecutive  $TE_{m,n}$  modes, we report a minimum of 0.005 nm between the modes  $TE_{43,4}$  and  $TE_{59,1}$ . Though a high density of TE modes and reported extreme spectral proximity, the experimental discrimination of the modes also depends on the highest resolution achievable and the spectral overlap of the modes, namely their quality factors.

Furthermore, the resolution of Maxwell's equations allows us to find the analytic expressions of the magnetic and electric components  $H_z^{(m,n)}(\rho, \phi, z)$  and  $E_\phi^{(m,n)}(\rho, \phi, z)$  of  $TE_{m,n}$  modes. As mentioned previously, we derive the expressions of the remaining components from the axial magnetic component  $H_z^{(m,n)}(\rho, \phi, z)$  which gives:

$$E_\rho^{(m,n)} = \frac{-j\omega\mu m}{k_{c_{m,n}}^2 \rho} (A \cos(m\phi) - B \sin(m\phi)) J_m(k_{c_{m,n}} \rho) e^{j\beta_{m,n} z}, \quad (3.10)$$

$$E_\phi^{(m,n)} = \frac{j\omega\mu}{k_{c_{m,n}}} (A \sin(m\phi) + B \cos(m\phi)) J'_m(k_{c_{m,n}} \rho) e^{j\beta_{m,n} z}, \quad (3.11)$$

$$E_z^{(m,n)} = 0, \quad (3.12)$$

$$H_\rho^{(m,n)} = \frac{-j\beta_{m,n}}{k_{c_{m,n}}} (A \sin(m\phi) + B \cos(m\phi)) J'_m(k_{c_{m,n}} \rho) e^{j\beta_{m,n} z}, \quad (3.13)$$

$$H_\phi^{(m,n)} = \frac{-j\beta_{m,n} m}{k_{c_{m,n}}^2 \rho} (A \cos(m\phi) - B \sin(m\phi)) J_m(k_{c_{m,n}} \rho) e^{j\beta_{m,n} z}, \quad (3.14)$$

$$H_z^{(m,n)} = (A \sin(m\phi) + B \cos(m\phi)) J_m(k_{c_{m,n}} \rho) e^{j\beta_{m,n} z}. \quad (3.15)$$

The constants  $A$  and  $B$  relate to the initial conditions. They weight the contributions

of  $\sin(m\phi)$  and  $\cos(m\phi)$  terms which constitute acceptable solutions as they respect the cylindrical symmetry. Simplifying  $(A \sin(m\phi) + B \cos(m\phi))$  in  $C \cos(m\phi - \varphi)$  with  $C^2 = A^2 + B^2$  and  $\tan \varphi = A/B$ , we note that  $A$  and  $B$  result in a phase shift  $\varphi$  to the configuration ( $A = 0, B = 1$ ) for which  $\varphi = 0$ . Consequently, different  $A$  and  $B$  change the orientation of the fields' patterns. Without loss of generality, we fix the symmetry axes of the field patterns by setting  $A = 0$ . The theoretical patterns of normalized fields intensity  $|\vec{E}|^2 = E_\rho^2 + E_\phi^2 + E_z^2$  (right panel) and  $|\vec{H}|^2 = H_\rho^2 + H_\phi^2 + H_z^2$  (left panel) of  $\text{TE}_{m,n}$  ( $m = 0, 1, 2$  and  $n = 1, 2, 3$ ) modes are showed on Figure 3.11. The maps are plotted in the cylindrical cavity's cross-section. We focus on stationary modes defined by  $\beta_{m,n} = 0$  which lifetime in the cavity depends on the reflection power of the cavity wall. We notice that the intensity patterns of modes  $\text{TE}_{m,n}$  directly relate to the values of the orders  $m$  and  $n$ :

- the *azimuthal* order  $m$  indicates the number of nodal planes (white dashed lines) for the magnetic field intensity  $|\vec{H}|^2$ ;
- the *radial* order  $n$  refers to the number of radial nodes (lobes) of the magnetic (electric) field intensity  $|\vec{H}|^2$  ( $|\vec{E}|^2$ ).

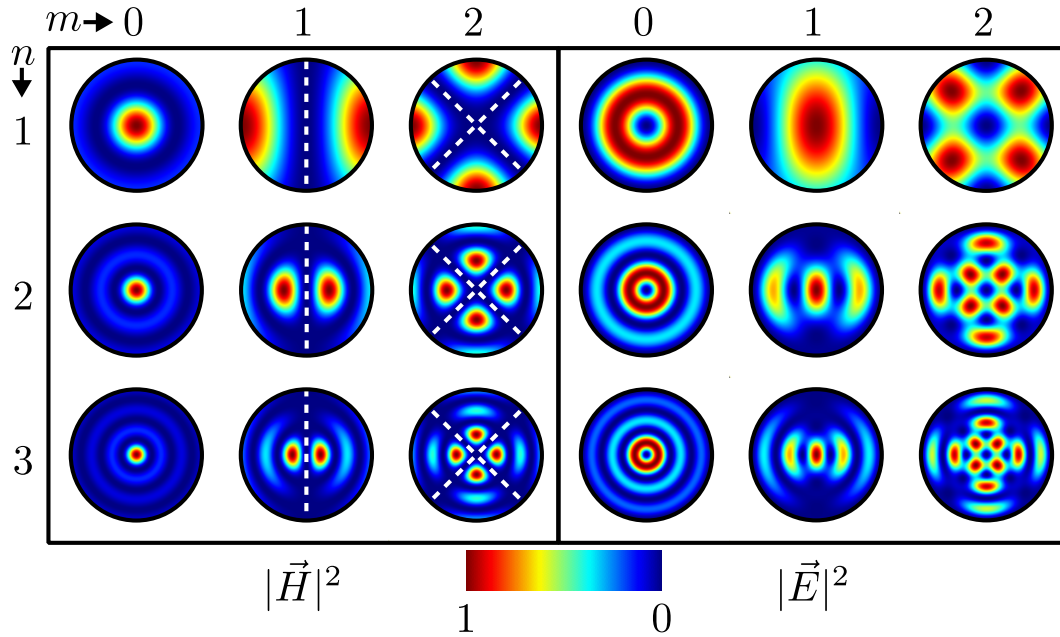


FIGURE 3.11: Theoretical patterns of normalized fields intensity  $|\vec{E}|^2 = E_\rho^2 + E_\phi^2 + E_z^2$  and  $|\vec{H}|^2 = H_\rho^2 + H_\phi^2 + H_z^2$  of  $\text{TE}_{m,n}$  modes with  $m = \{0, 1, 2\}$  and  $n = \{1, 2, 3\}$  in the cross-section of infinite cylindrical cavities delimited by a black circular line.

In particular, we observe that low azimuth order modes  $\text{TE}_{m,n}$ , especially  $m = \{0, 1\}$ , concentrate most of the electromagnetic energy in the centre of the cavity. This feature is all the more interesting as the key point in opto-fluidic detection applications consists in enhancing the overlap between the electromagnetic field and the sensing targets. We quantify the ability of any mode  $\text{TE}_{m,n}$  to concentrate the electric energy by calculating the mode surface  $S^{(m,n)}$  defined as:

$$S^{(m,n)} = \frac{\iint_c n_{med}^2 |E^{(m,n)}(\rho, \phi)|^2 \rho d\rho d\phi}{n_{med}^2 |E_{max}^{(m,n)}|^2}, \quad (3.16)$$



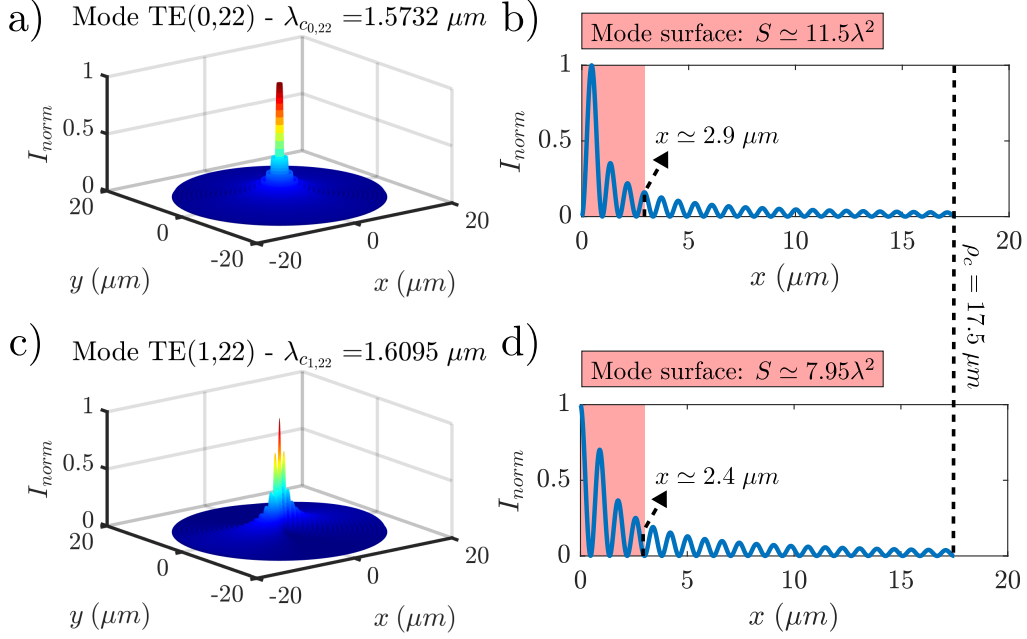


FIGURE 3.12: Surface maps of the normalized electric field intensity  $I_{norm}$  for a) the pure radial mode TE<sub>0,22</sub> and c) the mode TE<sub>1,22</sub> appearing respectively at the cutoff wavelengths  $\lambda_{c0,22} = 1.5732 \mu m$  and  $\lambda_{c1,22} = 1.6095 \mu m$  inside a cylindrical cavity of radius  $\rho_c = 17.5 \mu m$ . Profiles of b) the mode TE<sub>0,22</sub> and d) the mode TE<sub>1,22</sub> are extracted from the the associate surface maps along the  $x$ -axis. We indicate the mode surface of each of the modes expressed in units of  $\lambda^2$  with  $\lambda = 1.5 \mu m$ . The red zone delimits the radius of the disk (dashed black arrow),  $2.9 \mu m$  and  $2.2 \mu m$  for the modes TE<sub>0,22</sub> and TE<sub>1,22</sub> respectively, which concentrates most of the electric energy of the modes.

which corresponds to the inverse of the maximum of the normalized density of the electric energy. In other words, it estimates the area which contains most of the electric energy of the mode and hence where strong light-matter interaction occurs. In particular, we calculate  $S^{(0,22)}$  and  $S^{(1,22)}$  associated to radial modes TE<sub>0,22</sub> and TE<sub>1,22</sub> at  $\lambda_{c0,22} = 1.5732 \mu m$   $\lambda_{c1,22} = 1.6095 \mu m$  in a  $17.5 \mu m$ -radius cavity. We note that the wavelengths  $\lambda_{c0,22}$  and  $\lambda_{c1,22}$  stand close to the PCM reflectivity maximum located at about  $1.6 \mu m$ .

We notice the high concentration of light in the cavity centre for both modes on the surface maps of the electric field intensity  $|E|^2$  plotted in Figure 3.12.a) and c). We complete this appreciation by representing the profiles b) and d) of both modes extracted from the surface maps along the  $x$ -axis at  $y = 0$ . We estimate the mode surfaces of modes TE<sub>0,22</sub> and TE<sub>1,22</sub> to  $S^{(0,22)} \simeq 11.5\lambda^2$  and  $S^{(1,22)} \simeq 7.95\lambda^2$  in units of  $\lambda^2$  with  $\lambda = 1.5 \mu m$ . Knowing that the cavity cross-section covers an area  $A_c = \pi\rho_c^2 \simeq 428\lambda^2$ , the mode surfaces  $S^{(0,22)}$  and  $S^{(1,22)}$  thus represent about 2.7% and 1.9%, of the cavity cross-section. In other words, most of the electric energy is contained in disks of approximate radii  $2.9 \mu m$  and  $2.4 \mu m$  for the modes TE<sub>0,22</sub> and TE<sub>1,22</sub> respectively. The disks encompass the first three and four lobes of maximum electric intensity as shown of Figure 3.12.b) and d).

Finally, we observe that the surface of the first lobe of maximum of intensity, for any mode TE <sub>$m,n$</sub>  with low azimuthal order  $m = \{0, 1\}$ , shrinks as the radial order  $n$  increases. We should consider this second feature in the light of calculations of the modes' quality factors and Purcell factors to evaluate the ability of the cavity to improve for instance the spontaneous emission of external emitters.



### 3.3.3 Finite length cylindrical cavities

In their shortened versions, cylindrical cavities, referred to as cylindrical cavity resonators, have a finite length  $L$  and perfectly reflecting top and bottom edges. Consequently, the light also gets confined along the cavity axis coinciding with the  $z$ -axis direction. It bounces back and forth on the top and bottom boundaries to form stationary waves at quantized frequencies. We write the general form of the transverse electric fields  $(E_\rho^{(m,n)}, E_\phi^{(m,n)})$  of modes  $\text{TE}_{m,n}$  as the combination of two opposite waves propagating along  $+z$  and  $-z$ -axis direction:

$$E_t^{(m,n)}(\rho, \phi, z) = e_t^{(m,n)}(\rho, \phi)(A^+ e^{-j\beta_{m,n}z} + A^- e^{j\beta_{m,n}z}), \quad (3.17)$$

with  $A^+$  and  $A^-$  the waves' amplitudes. Placing the origin of the  $z$ -axis in Figure 3.9.a) at the cavity bottom edge, the top edge locates at  $z = L$ . By application of interface conditions at the perfectly reflecting top and bottom cavity frontiers, the tangent electric field cancels at  $z = 0$  and  $z = L$ . The boundary conditions derives then from Equation (3.17) as:

$$\begin{cases} A^+ + A^- = 0, \\ A^+ e^{-j\beta_{m,n}L} + A^- e^{j\beta_{m,n}L} = 0. \end{cases} \quad (3.18)$$

The first equation of the system imposes  $A^- = -A^+$  while the second reduces to  $\sin(\beta_{m,n}L) = 0$ , implying the quantization of the  $z$ -axis component of the wave vector according to:

$$\beta_{m,n,p} = \frac{p\pi}{L}, \quad p \in \mathbb{N}, \quad (3.19)$$

where the integer  $p$  designates the *axial* order and describes the variations of the electromagnetic fields patterns along the cavity axis. From the Equation (3.9), the dispersion relation of the modes  $\text{TE}_{m,n,p}$  changes into:

$$k_{m,n,p}^2 = \frac{\omega_{m,n,p}^2}{c^2} n_{med}^2 = k_{c,m,n}^2 + \beta_{m,n,p}^2 = \left( \frac{p'_{m,n}}{\rho_c} \right)^2 + \left( \frac{p\pi}{L} \right)^2, \quad p \in \mathbb{N}. \quad (3.20)$$

The expression of the cutoff wavelength of the mode  $\text{TE}_{m,n,p}$  derives from Equation (3.20) as  $\lambda_{m,n,p} = 2\pi/k_{m,n,p}$ . We plot in Figure 3.13.a) the evolution of the spectral spacing  $\Delta\lambda = \lambda_{0,24,p} - \lambda_{0,24,p+1}$  between consecutive  $p$  orders  $\text{TE}_{0,24,p}$  and  $\text{TE}_{0,24,p+1}$  supported by a cylindrical cavity of radius  $\rho_c = 17.5 \mu\text{m}$  and length  $L = 10, 20, 50, 100 \mu\text{m}$ . We first report an increase of  $\Delta\lambda$  for a cavity of length  $L = 10 \mu\text{m}$  until a maximum value of about  $40 \text{ nm}$  for  $p = 9$  (i.e. between modes  $\text{TE}_{0,24,9}$  and  $\text{TE}_{0,24,10}$ ) from which it then initiates a slow decrease. By contrast, the cavities with  $L > 10 \mu\text{m}$  record a single increase of  $\Delta\lambda$  over the range of  $p$  orders. In particular, the length  $L$  dictates the speed and the magnitude of the increase. Precisely, we estimate the spacing between first  $p$  orders  $\text{TE}_{0,24,1}$  and  $\text{TE}_{0,24,2}$  to  $0.11, 0.45, 2.81$  and  $11.06 \text{ nm}$  for cavities of lengths of  $10, 20, 50, 100 \mu\text{m}$  respectively. Similarly, the spacing reaches an ultimate value of  $0.78, 3.05, 16.13$  and  $39.95 \text{ nm}$  between the modes  $\text{TE}_{0,24,10}$  and  $\text{TE}_{0,24,11}$  in order of increasing lengths  $L$ . We have also plotted on Figure 3.13.b) the distribution of the cutoff wavelengths  $\lambda_{c,m,n,p}$  of the modes  $\text{TE}_{m,n,p}$  with successive orders  $p$  (colored dots) ranging from 1 to 20 for a cavity of radius  $\rho_c = 17.5 \mu\text{m}$  and length  $L = 50 \mu\text{m}$ . The label of the ordinate associate to each lines of dots indicate the couples of orders  $(m, n)$  with  $m = \{0, 1\}$  and  $n = \{21, 22, 23, 24\}$ . We highlight spectral overlaps for high  $p$  orders of modes  $\text{TE}_{m,n,p}$  with adjacent azimuthal orders  $m$  and a fixed radial

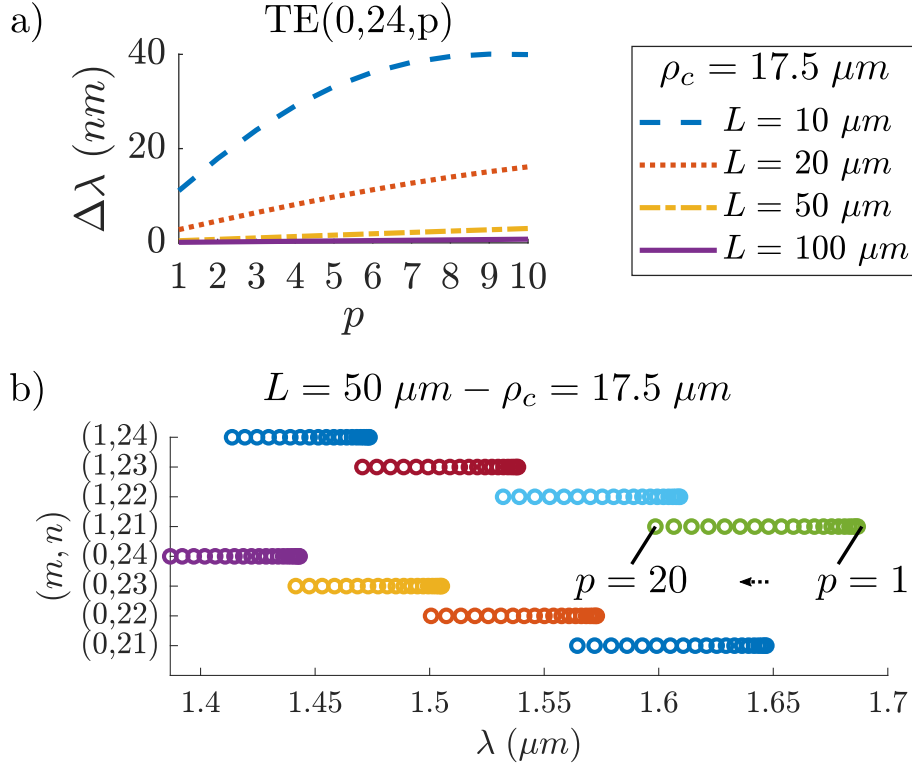


FIGURE 3.13: a) Evolution of the spectral spacing  $\Delta\lambda = \lambda_{0,24,p} - \lambda_{0,24,p+1}$  in nm between two consecutive modes  $TE_{0,24,p}$  and  $TE_{0,24,p+1}$  where  $p = \{1, 2, \dots, 10\}$  in a cylindrical cavity of radius  $\rho_c = 17.5 \mu m$  with increasing length  $L = \{10, 20, 50, 100\} \mu m$ . b) Spectral distribution of the modes  $TE_{m,n,p}$  with  $m = \{0, 1\}$ ,  $n = \{21, 22, 23, 24\}$  where  $p$  varies from 1 to 20, in a cylindrical cavity of radius  $\rho_c = 17.5 \mu m$  and length  $L = 50 \mu m$ .

order  $n$  and inversely. For instance, the modes  $TE_{1,22,7}$ ,  $TE_{0,21,15}$  and  $TE_{1,21,20}$  (green dot labelled on Figure 3.13.b)) appear successively at 1.59938, 1.59911 and 1.59855  $\mu m$ .

Similarly to infinite cylindrical cavities, we calculate the maximum number of  $TE_{m,n,p}$  modes supported by a cylindrical cavity resonator of radius  $\rho_c$  and length  $L$  within the spectral range  $[1.4 - 1.8] \mu m$ . In particular, we observe in Figure 3.10.b) that a 50  $\mu m$ -long cavity supports a fast-growing number of modes  $TE_{m,n,p}$  as the cavity radius increases, reaching a huge value of 6241 for the reference radius  $\rho_c = 17.5 \mu m$ .

Moreover, the expressions of the fields of modes  $TE_{m,n,p}$  in a cavity of length  $L$  become:

$$E_\rho^{(m,n,p)} = \frac{j\omega_{m,n,p}\mu m H_0}{k_{c_{m,n}}^2 \rho} \sin(m\phi) J_m(k_{c_{m,n}}\rho) \sin\left(\frac{p\pi z}{L}\right), \quad (3.21)$$

$$E_\phi^{(m,n,p)} = \frac{j\omega_{m,n,p}\mu H_0}{k_{c_{m,n}}} \cos(m\phi) J'_m(k_{c_{m,n}}\rho) \sin\left(\frac{p\pi z}{L}\right), \quad (3.22)$$

$$E_z^{(m,n,p)} = 0, \quad (3.23)$$

$$H_\rho^{(m,n,p)} = \frac{\beta_{m,n,p} H_0}{k_{c_{m,n}}} \cos(m\phi) J'_m(k_{c_{m,n}}\rho) \cos\left(\frac{p\pi z}{L}\right), \quad (3.24)$$

$$H_\phi^{(m,n,p)} = \frac{-\beta_{m,n,p} m H_0}{k_{c_{m,n}}^2 \rho} \sin(m\phi) J_m(k_{c_{m,n}}\rho) \cos\left(\frac{p\pi z}{L}\right), \quad (3.25)$$

$$H_z^{(m,n,p)} = H_0 \cos(m\phi) J_m(k_{c_{m,n}}\rho) \sin\left(\frac{p\pi z}{L}\right), \quad (3.26)$$

where  $H_0 = -2jA^+$ . We have mapped the distribution of the electric field magnitude

$|\vec{E}|$  in Figure 3.14 for the modes  $\text{TE}_{0,22,1}$  and  $\text{TE}_{0,22,2}$  in a cavity of radius  $\rho_c = 17.5 \mu\text{m}$  and length  $L = 100 \mu\text{m}$ . We notice that the order  $p$  corresponds to the number of lobes of maximum magnitude in the  $z$ -axis direction. We find for instance one and two lobes for the modes  $\text{TE}_{0,22,1}$  and  $\text{TE}_{0,22,2}$ , respectively. We also verify that the tangential electric field components vanish at the top ( $z = L \mu\text{m}$ ) and bottom ( $z = 0 \mu\text{m}$ ) edges of the cavity resonator. We finally remark that modes  $\text{TE}_{m,n,p}$  with an even (odd) *axial* order  $p$  will always exhibit a maximum (nodal plane) of the electric field in the middle plane of the cavity, at  $z = L/2$ .

We notify that the cylindrical cavity resonator model assumes perfect reflection on the membrane wall, top and bottom faces. Concerning the photonic crystal cavity, the impedance mismatch between the cavity hollow core and the free space ensures the reflection of light on top and bottom boundaries. It explains by the abrupt change in the group velocity of the modes inside and outside of the cavity. The reflection phenomenon occurs equivalently on top and bottom edges. Consequently, we compare the photonic cavity along the cylinder axis to a Fabry-Pérot resonator. The supported stationary modes appear at quantized propagation constants and describe  $p$  lobes along the cavity axis. Drawing the Fabry-Pérot analogy as developed in [4], the reflectivity of the equivalent mirror in the vertical direction of a 1D PCM-based photon cage of length  $L = 10 \mu\text{m}$  has for instance been estimated to  $R_v = 65\% \pm 10\%$  [6].

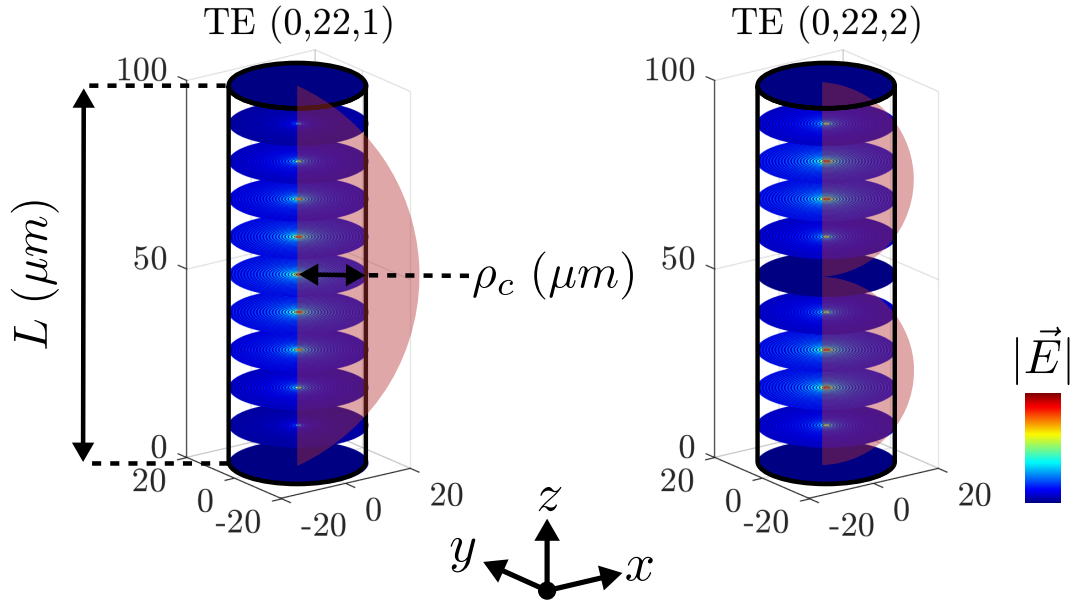


FIGURE 3.14: Slices in the  $z$ -direction of the electric field magnitude  $|\vec{E}|$  for the modes  $\text{TE}(0, 22, 1)$  and  $\text{TE}(0, 22, 2)$  existing in a cavity of radius  $\rho_c = 17.5 \mu\text{m}$  and of length  $L = 100 \mu\text{m}$ . The red patches indicate the distribution of the field in the  $z$ -axis direction.

### Key points of the section

In summary, we have first modelled tubular photon cages with ideal cylindrical cavity resonators considering the high and broadband reflection properties of the planar PCM. The simplicity of the model, a cylinder of radius  $\rho_c$ , length  $L$  and perfectly reflecting walls, allows for the analytical resolution of Maxwell's equations, providing an almost complete description of the supported modes. We recapitulate below the main properties of those modes:

- the cavity hosts two kinds of modes: transverse electric  $\text{TE}_{m,n,p}$  ( $E_z = 0$ ) and transverse magnetic  $\text{TM}_{m,n,p}$  ( $H_z = 0$ ) modes classified according to their orders  $m \in \mathbb{N}$ ,  $n \in \mathbb{N}^*$  and  $p \in \mathbb{N}^*$  which determine the variations of the electromagnetic fields in the *azimuthal*, *radial* and *axial* directions of the cylindrical coordinate system, respectively;
- we report a substantial number of TE modes coexisting in infinite and finite cylindrical cavities within the spectral range  $[1.4 - 1.8] \mu\text{m}$ ; this number increases for larger cavity radius;
- we observe an overlap of the spectral distributions of  $\text{TE}_{m,n,p}$  modes with spacing down to  $0.005 \text{ nm}$ ; we also note that the spectral spacing between consecutive modes  $\text{TE}_{m,n,p}$  and  $\text{TE}_{m,n,p+1}$  shrinks when the cavity length raises;
- we pointed out the interesting case of  $\text{TE}_{m,n,p}$  modes with a low azimuthal order  $m$  (typically  $m = \{0, 1\}$ ) which concentrate most of the electric field intensity over a small and centred fraction of the cavity cross-section;

In the following part, we aim to evaluate the consistency of the analogy with the cylindrical cavity model by simulating a more realistic model of the rolled-up 2D PCM cavity with the FDTD method.

## 3.4 Numerical study of tubular photon cages

The model of the cylindrical cavity resonator used hitherto to predict the optical response of rolled-up PCM cavities relies on two assumptions. First, it considers the cavity membrane wall as perfectly reflecting within the spectral range of interest. Second, it supposes that the membrane wall curvature does not impact its reflection performances. To evaluate the consistency of the two hypotheses in the study of rolled-up PCM cavities, we have also performed more realistic numerical simulations of the tubular photon cages using the FDTD method introduced in Section 2.1. We present the FDTD model of the tubular rolled-up PCM cavities in the first section. In the second section, we simulate the spectral and spatial distributions of the modes supported by infinite-length cavities. We confront the simulation results afterwards to the predictions of the analytical cylindrical cavity model. We complete the description of the modes by estimations of their quality factors. In the third section, we conduct simulations of the optical response of finite-length tubular cavities.

### 3.4.1 Numerical model of tubular photon cages

We present in Figure 3.15 different views (a), b) and c)) of the FDTD model of the rolled-up PCM cavity designed in the LUMERICAL 3D CAD environment. The perspective view a) shows the tubular photonic micro-cavity with an average radius  $\rho_{\text{avg}}$  and length  $L$ . The radius  $\rho_{\text{avg}}$  measures the distance between the centre of the tubular cavity and the median plane of the PCM wall as illustrated on the top view b). The PCM is represented by air holes (grey cylinders) etched in a  $h$ -thick membrane in InP material (pink contour). The air holes cylinders are slightly thicker than the InP slab for the needs of the simulation. We model the initial InGaP/InP bilayer membrane by a simple InP slab of total thickness  $h = h_{\text{InP}} + h_{\text{InGaP}}$  which exhibits similar optical response as InP/In<sub>1-x</sub>Ga<sub>x</sub>P bilayer for low Gallium compositions, typically  $x \simeq 0.1$ .

The lateral close-up view c) depicts the photonic crystal lattice: a triangular lattice, with a period  $a$ , of air holes of radius  $r$  embedded in InP material (pink background) medium. We set the rolling direction of the PCM along the high symmetry direction  $\Gamma\text{M}$  of the triangular lattice FBZ as indicated on the drawing c). Equivalently, the microtube axis coincides with the high symmetry direction  $\Gamma\text{K}$ . In this configuration, the reflection properties of the planar PCM at oblique incidence have been fully described in Figure 3.8.a) and b) for  $p$ - and  $s$ -polarizations. Moreover, we adjust the average perimeter  $2\pi\rho_{\text{avg}}$  to an integer number of periods along the  $\Gamma\text{M}$  direction to match the planar PCM edges upon rolling. The period of the photonic crystal along the  $\Gamma\text{M}$  direction equals  $\sqrt{3}a$ . Consequently, the value of the average radius is determined by the formula:

$$\rho_{\text{avg}} = \frac{N_p \sqrt{3}a}{2\pi}, \quad (3.27)$$

with  $N_p \in \mathbb{N}^*$  the number of periods along  $\Gamma\text{M}$ . We deduce the expressions of the inner and outer radii of the cavity,  $\rho_{\text{in}} = \rho_{\text{avg}} - h/2$  and  $\rho_{\text{out}} = \rho_{\text{avg}} + h/2$ , respectively. Furthermore, when the rolling of the PCM occurs along  $\Gamma\text{K}$ , the period along this direction becomes simply  $a$ . In the same way, the photonic crystal patterns span an integer number of half periods  $a/2$  along the tube's perimeter. We finally extend the InP membrane by  $a/2$  at each extremities of the microtube so that the length of the tubular microcavity  $L$  expresses as:

$$L = \frac{N_z a}{2} + a; \quad (3.28)$$

where  $N_z \in \mathbb{N}^*$  defines the number of half periods  $a/2$  along the tube axis.

In particular, we design a tubular cavity with the PCM lattice parameters,  $a = 1.206 \mu\text{m}$ ,  $r = 0.481 \mu\text{m}$  obtained in Section 3.2 and a membrane thickness  $h = 0.228 \mu\text{m}$  on the basis of fabricated samples. The previous set of parameters allows to achieve high and broadband PCM reflection properties according to Section 3.2. Furthermore, for typical compositions in Gallium element  $x \simeq 0.1$  in the InGaP layer and a ratio  $\xi = h_{\text{InGaP}}/h_{\text{InP}} \simeq 0.5$ , we report in Section 2.2 the fabrication of tubular microstructures of inner radius  $\rho_{\text{in}}$  in the order of  $17.5 \mu\text{m}$ . According to Equation (3.27), we draw a tubular cavity of average radius  $\rho_{\text{avg}} \simeq 17.62 \mu\text{m}$  by fixing  $N_p = 53$ , leading to  $\rho_{\text{in}} \simeq 17.5 \mu\text{m}$ , the perfectly matching with real structures' radius.

### 3.4.2 Simulations of infinite cavities

We emphasise the multi-scale nature of modelled tubular micro-cavities as  $a, r \ll \rho_{\text{avg}}, L$ , resulting in a very fine mesh of the micro-structure accordingly to the conformal mesh technology. We also note the delicate mesh of curved interfaces owing to the

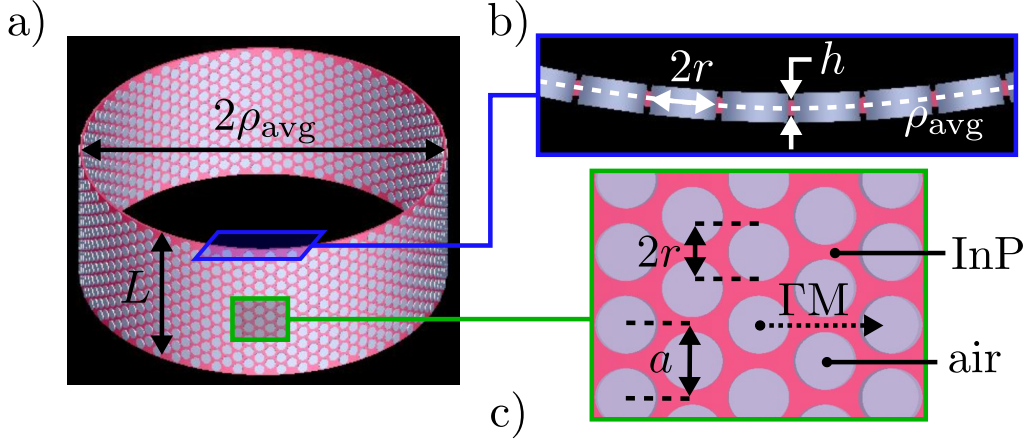


FIGURE 3.15: a) Perspective view of the tubular rolled-up PCM cavity with average radius  $\rho_{\text{avg}}$  and length  $L$  designed in LUMERICAL 3D CAD environment. b) Close-up view, on the top of the tubular cavity, of the PCM membrane wall which consists of air holes (grey cylinders) of radius  $r$  etched in an InP slab (pink membrane) of thickness  $h$ . The air holes are made intentionally thicker than the membrane for the needs of the simulation. c) Lateral close-up view on the photonic crystal pattern formed by a triangular lattice, of period  $a$ , of air holes arranged in the InP material. The black dashed arrow indicates the direction of the rolling of the planar PCM which coincides with the high symmetry direction  $\Gamma M$  in the first Brillouin zone of the triangular lattice.

Cartesian implementation of the FDTD algorithm which forces a very small mesh size and raises significantly the simulation time. Consequently, we have first conducted simulations of the optical response of infinitely long ( $L \rightarrow \infty$ ) rolled-up photonic cavities to reduce the memory requirements and the simulation time.

### Multiple dipole excitation

The Figure 3.16 presents cross-section (a) and lateral (b) views of the FDTD model of the rolled-up PCM cavity. We arrange a cloud of 15 electric dipole sources (blue arrows) randomly positioned in the hollow cross-section of the tubular cavity to excite all the possible modes while avoiding nodal planes. We use broadband sources with a bandwidth adjusted between  $1.275$  and  $1.825 \mu m$ . We ensure to collect selectively transverse electric (TE) modes by orienting the dipoles sources perpendicularly to the axis of the cavity. Moreover, all the dipoles point in the  $x$ -axis direction and they are included in the plane  $z = 0$  as shown on both views. We record the temporal evolutions of the electromagnetic fields with a cloud of 15 time monitors (yellow crosses) dispersed randomly in the plane of the dipole sources. With this specific planar configuration of the dipoles and the monitors, we seek to reproduce the experimental conditions of near-field optical measurements inside the cavity as described in Section 2.3. The brown rectangular contour on the cross-section view a) delimits the FDTD computation zone in the cavity cross-section. We apply perfectly matched layer (PML) boundary conditions of type *stretched coordinate PML* with a *standard* profile consisting of 8 layers of absorbing material.

The PML frontiers are placed at a distance of  $d_{\text{PML}} = 2 \times 1.55 \mu m$  from the outer radius of the cavity to prevent reflections of modes' evanescent tails on the PML. From preliminary tests, we set the simulation time to  $t_s = 30 ps$  as a compromise between a sufficient reduction of the final electromagnetic energy in the computation zone and a reasonable computation time. Indeed, we have shown in Section 2.1 that in the case of strong resonances, the remaining electromagnetic energy usually maintain above the

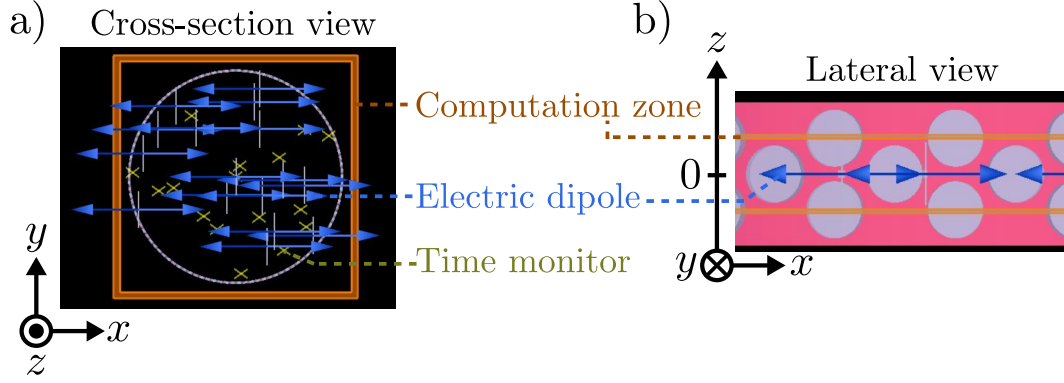


FIGURE 3.16: a) Cross-section and b) lateral views of the FDTD model of the tubular rolled-up PCM cavity with inner radius  $\rho_{\text{in}} \simeq 17.5 \mu\text{m}$ . Electric dipole sources (blue arrows) oriented along the  $x$ -axis and time monitors (yellow cross) are dispersed randomly in the cross-section  $z = 0$  plane of the cavity. The brown rectangular zone delimits the FDTD computation zone where perfectly matched layers (PML) boundary conditions are applied. The lateral view shows a part of the PCM wall with air holes (grey circles) in an InP membrane. The electric dipole sources are contained in the  $z = 0$  plane. The FDTD computation zone along the microtube axis consists of a unit cell repeated periodically along the  $z$ -axis to simulate an infinitely long cavity.

shutoff criteria level despite an increase of the simulation time. However, we achieve a precise estimation of the quality factors of the modes of the cavity as the time decay of the electromagnetic fields becomes sufficiently low. Along the axis of the cavity (i.e.  $z$  axis) as shown on the lateral view, the FDTD computation zone demarcates a unit cell repeated periodically on both sides by the application of periodic boundary conditions, in order to simulate an infinitely long cavity.

We plot in Figure 3.17.a) the spectral response of the infinitely long tubular cavity within the range  $[1.45 - 1.7] \mu\text{m}$ . The intensity  $I$  results from the Fourier transforms of the time data collected by all the monitors. We perform beforehand an apodization of the time signals with the parameters:  $t_c = 0.6t_s$  and  $\Delta t = 0.15t_s$ . This operation aims at removing all transient effects due for instance to the source pulse, before passing in the frequency domain as explained in Section 2.1. It is noteworthy that the intensity of the peaks in the spectrum depends mostly on the location of the sources and the monitors, and on the bandwidth of the dipole sources. Hence, we set the intensity axis in logarithmic scale to reveal potential modes weakly expressed. We notice a high density of modes in the region  $[1.58 - 1.7] \mu\text{m}$  with an important spectral overlap which leads mostly to broad and distorted peaks. Conversely, the interval spanning from 1.45 to about  $1.58 \mu\text{m}$  gathers fewer and more dispersed peaks. However, we distinguish four successive groups of peaks characterized by a similar pattern. Indeed, first overlapping and intense peaks are followed by secondary peaks with fading intensities and increasing spectral spacing. We also find that the number of secondary peaks in one group reduces strongly along with their intensities as the wavelength decreases.

We investigate the nature of the modes appearing in the spectrum by calculating maps of the electromagnetic fields at the wavelengths of some of the intensity peaks. To this end, we place a frequency monitor with apodization parameters  $t_c = 0.7t_s$  and  $\Delta t = 0.1t_s$  ( $t_s = 10 \text{ ps}$ ) which covers the entire FDTD computation zone in the cross-section of the cavity. We extract cartographies of the normalized magnetic field  $|\vec{H}|$  at three resonant wavelengths:  $\lambda_1 \simeq 1.5545 \mu\text{m}$ ,  $\lambda_2 \simeq 1.5625 \mu\text{m}$  and  $\lambda_3 \simeq 1.62 \mu\text{m}$ , displayed on Figure 3.17.b). Two black circular lines delimit the edges of the PCM membrane wall, namely the inner radius  $\rho_{\text{in}} \simeq 17.5 \mu\text{m}$  and outer radius  $\rho_{\text{out}} = \rho_{\text{in}} + h \simeq 17.73 \mu\text{m}$  of the tubular cavity, respectively. We recognise on the three maps typical patterns



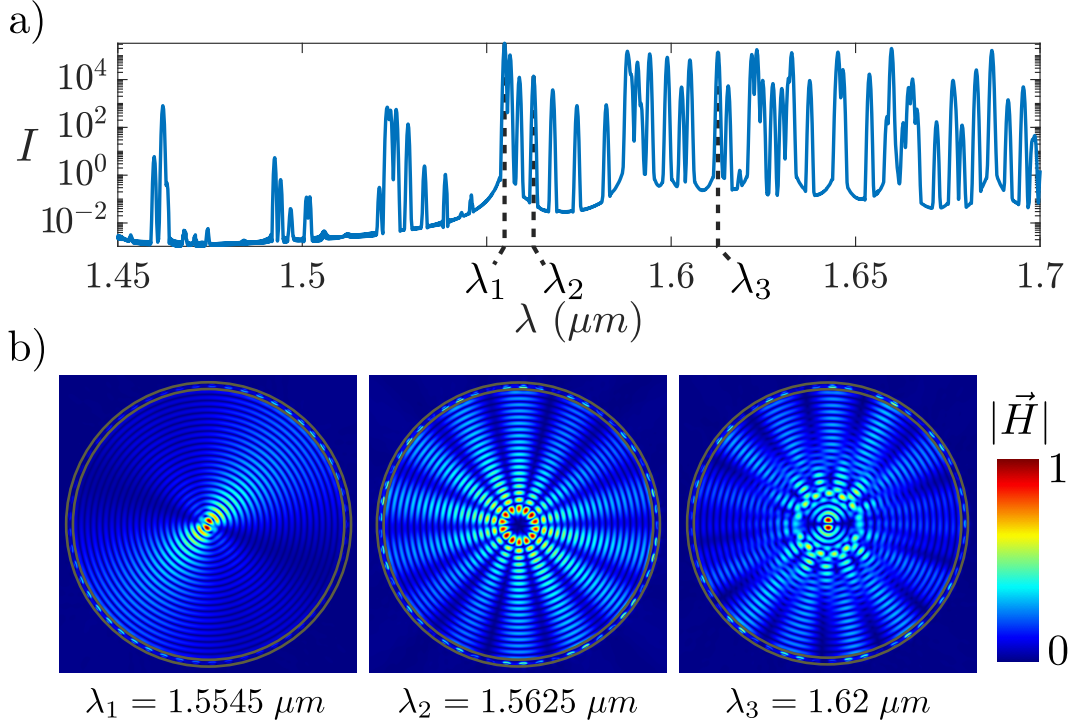


FIGURE 3.17: a) Spectral response of an infinitely long tubular rolled-up PCM cavity of average radius  $\rho_{\text{avg}} \simeq 17.5 \mu\text{m}$  within the spectral range  $[1.45 - 1.7] \mu\text{m}$ . b) Maps of the normalized magnetic field  $|\vec{H}|$  in the cross-section of the cavity and calculated at three different resonant wavelengths  $\lambda_1 = 1.5545 \mu\text{m}$ ,  $\lambda_2 = 1.5625 \mu\text{m}$  and  $\lambda_3 = 1.62 \mu\text{m}$  located on the previous spectrum. The grey lines delimit the edges of the PCM membrane wall of the cavity.

of cylindrical cavity modes  $\text{TE}_{m,n}$  described in Section 3.3. In particular, we observe at  $\lambda_1$  that one nodal line separates two groups of radial patterns extending from the centre of the cavity, which is the signature of a mode of type  $\text{TE}_{1,n}$ . We notice that the nodal line is not fully recovered as other modes patterns superimpose as indicated by the spectral overlap around  $\lambda_1$  on the previous spectrum. On the contrary, the peak detected at  $\lambda_2$  slightly detach from preceding modes so that we observe the whole pattern of a mode  $\text{TE}_{7,n}$ . Finally, the map obtained at  $\lambda_3$  illustrates the spatial overlap between one  $\text{TE}_{1,n}$  mode and cavity modes with higher azimuthal order  $m$  judging by the presence of several nodal lines, also in agreement with the overlap of peaks observed on the spectrum.

Unlike the azimuthal order, we can not access to the radial order  $n$  of the modes to the naked eyes. In particular, the superimposition of the modes' patterns observed on the map at  $\lambda_3$  encloses the mode  $\text{TE}_{1,n}$  emerging from the centre of the cavity and conceals a substantial part of the radial variations of the magnetic field. We also observe radial patterns overlaying along the nodal line of the mode  $\text{TE}_{1,n}$  detected at  $\lambda_1$ . Otherwise, we remark some distortions of the field patterns, especially for the first lobes of high amplitude in the maps of the modes calculated at  $\lambda_1$  and  $\lambda_2$ . Indeed, multiple dipole sources can excite the same mode at different locations in the cavity cross-section. It generates different orientations of the field patterns, more precisely of the nodal lines. These observations prove the delicate determination of the radial orders  $n$  of the mapped modes which will be the concern of the next series of simulations.

Combining the analyses of the spectrum and the maps, we correlate the spectral evolution of the modes' maps with the reflectivity spectrum  $R(\lambda)$  of the PCM membrane represented in Figure 3.8.a) for  $p$ -polarized light at normal and oblique incidences. We



suppose that the azimuthal order  $m$  of the cavity modes directly relates to the angle of incidence  $\theta$  of the incoming light as it occurs in the formation of whispering gallery modes (WGM):  $m$  increases along with  $\theta$ . We bring therefore the following statements:

- for  $1.45 \mu m < \lambda < 1.53 \mu m$ : the reflectivity  $R$  globally diminishes when  $\theta$  increases and  $R$  increases along with  $\lambda$  but maintains below the high reflectivity limit (95%). Consistently, the first intense peaks in the groups of modes observed in the spectrum correspond to cavity modes with low azimuthal orders, typically  $m = \{0, 1\}$  as illustrated on the map calculated at  $\lambda_1$ . Secondary peaks appear and reinforce gradually when  $\lambda$  increases and assimilate to  $TE_{m,n}$  modes with higher and increasing order  $m$  which is confirmed by the cartography at  $\lambda_2$ .
- $1.53 \mu m \leq \lambda \leq 1.66 \mu m$ : the reflectivity at normal incidence enters the high reflectivity (HR) zone of the PCM in which it stays above 95% and reaches a maximum value of about 99 % at about  $1.6 \mu m$ . For higher values of  $\theta$ , the HR zone is red shifted. Therefore, multiple  $TE_{m,n}$  modes can sustain in the cavity which results in the overlapping of patterns as observed for the map computed at  $\lambda_3$ . We note that the reflectivity at normal incidence at  $\lambda_3$  is quasi maximum which explains the clearness of the radial pattern in the centre of the cavity as compared to the dim azimuthal ring.
- $1.66 \mu m < \lambda \leq 1.7 \mu m$ : the reflectivity at normal incidence leaves the HR zone, while the HR zone is reached for higher values of  $\theta$  and shrinks progressively. Indeed, we have observed on additional maps that  $TE_{m,n}$  modes with high azimuthal orders  $m > 10$  appear and coexist while pure and quasi-pure radial modes ( $m = \{0, 1\}$ ) fade away.

We can already draw preliminary conclusions from the first series of FDTD simulations of spectral response and maps of the fields performed on infinitely long tubular rolled-up PCM cavities.

- We confirm the presence of cylindrical cavity modes  $TE_{m,n}$  in the tubular photonic crystal cavity when it is excited by electric dipole sources randomly disposed in a cross-section plane within the range  $[1.45 - 1.7] \mu m$ .
- The emergence of a mode  $TE_{m,n}$  depends on the reflection performances of the PCM membrane wall, function of the angle of the incident light  $\theta$ . Therefore, below  $1.53 \mu m$ , the modes with low azimuthal orders  $m < 10$  are predominant and overlap spectrally and spatially. Above  $1.53 \mu m$ , the reflectivity of the PCM improves at oblique incidence and even exceeds the reflectivity at normal incidence from  $1.66 \mu m$  which leads to the superimposition of modes with high azimuthal orders ( $m > 10$ ).

### Single dipole excitation

We also simulated the optical response of the rolled-up PCM cavity with a unique dipole source of electric and magnetic natures as depicted on the CAD views a) and c) in Figure 3.18, respectively. The dimensions of the photonic crystal microtube, the parameters of the calculation zone and the settings of the time monitors and of the dipole sources remain unchanged with respect to previous simulations to which we may refer. We orient the electric (magnetic) dipole along the  $x$ - ( $z$ -) axis to filter  $TE_{m,n}$  modes defined by  $E_z = 0$ . We also place both dipoles in the centre of the cavity to

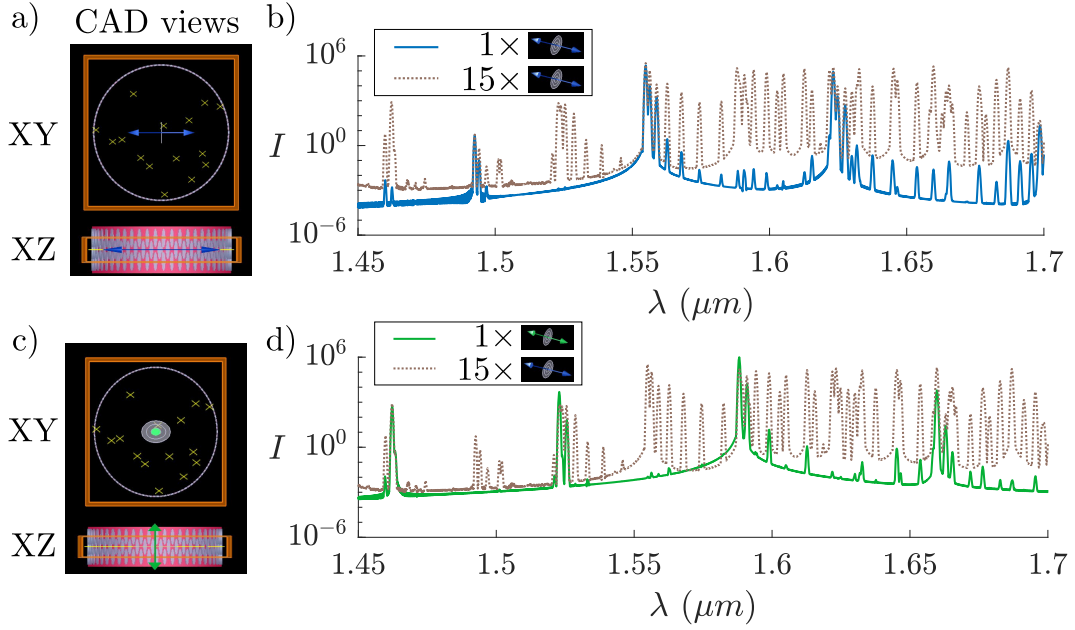


FIGURE 3.18: Left drawings: top (XY) and lateral (XZ) CAD views of the modelled rolled-up PCM microtube excited with a unique electric (a) or magnetic (b) dipole represented by blue and green arrows, respectively. A cloud of 15 monitors (yellow crosses), dispersed in the central ( $z = 0$ ) cross-section of the microtube, collect the time evolutions of the electromagnetic fields. Right plots: spectral responses of the cavity simulated with an electric (a) or magnetic (b) dipole. The grey dashed line spectrum indicates the optical response of the cavity when excited with a cloud of 15 electric dipoles described in the previous simulation.

extract preferentially  $TE_{m,n}$  modes with a low azimuthal order  $m$ . In particular, the position of the electric (magnetic) dipole coincides with the position of the first lobe of maximum electric (magnetic) field amplitude of the modes  $TE_{1,n}$  ( $TE_{0,n}$ ). As raised in Section 3.3, the potential interest in the modes  $TE_{m,n}$  with low azimuthal orders, especially  $m = \{0, 1\}$ , relies in their ability to concentrate most of the electromagnetic energy in the centre of the tubular cavity. The Fourier transform of the temporal data, recorded by the monitors and apodized beforehand, results in the two spectra showed in Figure 3.18.b) and d) corresponding to an electric (blue curve) and a magnetic (green curve) excitation, respectively. The dashed grey curve plotted on both spectra refer to the spectral response of the cavity obtained with a cloud of 15 electric dipoles randomly arranged and radiating in the hollow of the microtube. We notice an exact superimposition, in terms of spectral positions, of the peaks obtained with a unique dipole source excitation with the cavity modes resonances observed with the cloud of dipole sources. However, for a unique dipole excitation, only a couple of modes mostly express in the form of high intensity peaks. According to the maps of the previous simulation, we can infer that the two intense peaks detected at  $1.555 \mu m$  and  $1.63 \mu m$  correspond to  $TE_{1,n}$  cavity modes with distinct orders  $n$  whereas the weaker peak at about  $1.56 \mu m$  refers to a  $TE_{7,n}$  mode. This confirms the predominance of  $TE_{1,n}$  modes and the spectrally nearest  $TE_{m,n}$  modes with low azimuthal orders in the case of a unique and centred electric dipole excitation.

We confirm the nature of the modes detected in the spectra of single electric and magnetic dipole excitations by calculating maps of the normalized amplitude of magnetic component  $|H_z|$  in the cross-section plane  $z = 0$  of a tubular cavity of average radius  $\rho \simeq 17.62 \mu m$ . In particular, we present the cartographies in Figure 3.19 of two high-intensity peaks located at  $\lambda_e = 1.555 \mu m$  (a) and  $\lambda_m = 1.588 \mu m$  (b) in

the electric and magnetic excitation spectra, respectively. The two circular grey lines delimit the inside and outside frontiers of the PCM wall. We recognize at first glance typical patterns of modes  $TE_{1,n}$  at  $\lambda_e$ , characterised by one nodal line surrounded by pure radial patterns. Furthermore, the absence of nodal lines in the map at  $\lambda_m$  is the typical signature of a mode  $TE_{0,n}$ .

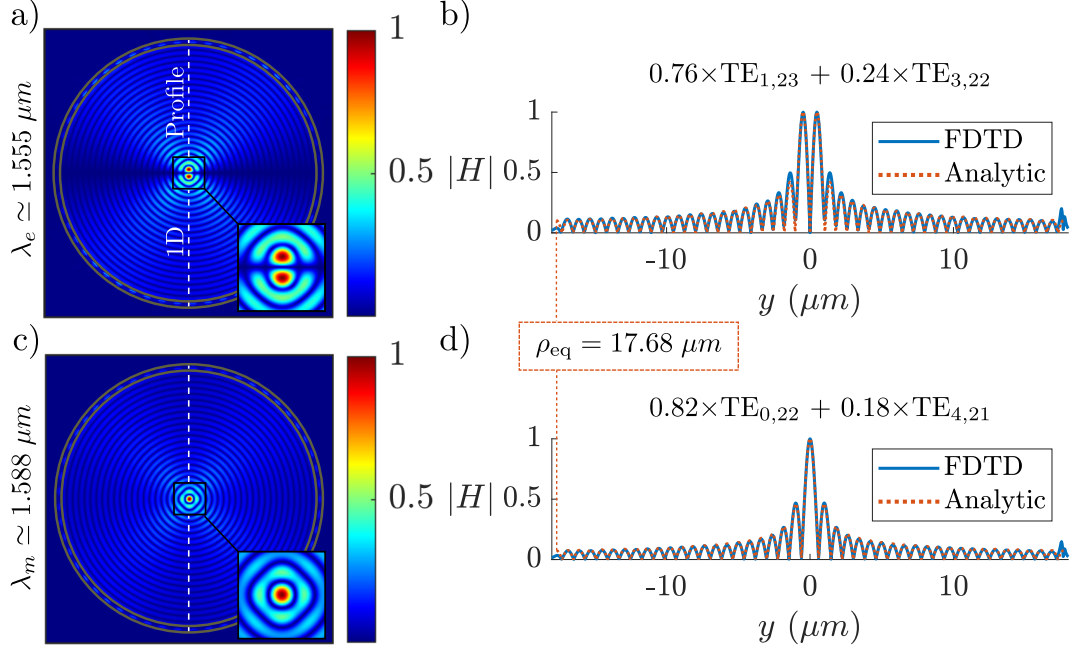


FIGURE 3.19: a) and c): Maps of the normalized magnetic field component  $H_z$  calculated in the cross-section of an infinite cavity of average radius  $\rho_{\text{avg}} \simeq 17.62 \mu\text{m}$  with the FDTD method at the wavelengths  $\lambda_e \simeq 1.555 \mu\text{m}$  and  $\lambda_m \simeq 1.588 \mu\text{m}$  with a single electric and magnetic dipole excitation, respectively. The two grey concentric circles delimit the inside and outside frontiers of the PCM cavity wall. The inset pictures show close up views of the central region of the maps. b) and d): 1D profiles (straight blue lines) extracted from maps a) and c) along the white dashed line diameter and fitted with theoretical profiles (dashed orange line) of the combination of modes  $0.76 \times TE_{1,23} + 0.24 \times TE_{3,22}$  and  $0.82 \times TE_{0,22} + 0.18 \times TE_{4,21}$  derived from the analytical cylindrical cavity model with an equivalent radius  $\rho_{\text{eq}} \simeq 17.68 \mu\text{m}$ .

We notice that the excitation of the cavity with a single dipole source provides well-defined maps of the magnetic field which allows *a priori* a clear determination of the radial order  $n$  of the modes. Toward this goal, we extract 1D profiles from the maps of modes  $TE_{1,n}$  (a) and  $TE_{0,n}$  (c) along the white dashed line diameter, which results in the blue straight curves of Figure 3.19.b) and d), respectively. Our strategy to identify the order  $n$  consists in fitting the FDTD 1D profiles with the theoretical profiles of generic modes  $TE_{1,n}$  and  $TE_{0,n}$  calculated with the cylindrical cavity model of equivalent radius  $\rho_{\text{eq}}$ , where  $n$  and  $\rho_{\text{eq}}$  are tunable parameters. We first fix the radius  $\rho_{\text{eq}}$  to  $16.6 \mu\text{m}$ , which corresponds approximately to the average radius of the FDTD model. We sweep then the integer  $n$  until minimizing the relative errors between the numerical and theoretical positions of the profiles' peaks. It occurs for  $n = 23$  and  $n = 22$  for the modes  $TE_{1,n}$  and  $TE_{0,n}$  represented in b) and d), respectively.

Nevertheless, we report significant relative errors of about 5% in the positions of the first peaks of both 1D profiles. Looking closely at both maps of the modes, two peculiar features suggest that we deal with the mixing of at least two modes. First, we notice that four glowing branches stand out of the global patterns in diagonal directions. Second, the close-up views on the central regions of both maps show a distortion of the

first lobes of maximum amplitude with respect to pure circular patterns expected for modes  $\text{TE}_{1,n}$  and  $\text{TE}_{0,n}$ . The spectral overlaps of the high intensity peaks observed in the spectra b) and d) of Figure 3.18 also reinforce the possibility of spatial coexistence of the modes  $\text{TE}_{1,23}$  and  $\text{TE}_{0,22}$  with their first and second nearest modes. According to Equation 3.8, the two nearest peaks, in order of increasing wavelength, after the mode  $\text{TE}_{1,23}$  ( $\text{TE}_{0,22}$ ) correspond to the modes  $\text{TE}_{3,22}$  and  $\text{TE}_{5,21}$  ( $\text{TE}_{2,22}$  and  $\text{TE}_{4,21}$ ). We obtain that the profile in b) (d) match the theoretical profile of a combination between  $\text{TE}_{1,23}$  and  $\text{TE}_{3,22}$  ( $\text{TE}_{0,22}$  and  $\text{TE}_{4,21}$ ) modes in proportions 0.76 and 0.24 (0.82 and 0.18), respectively. Finally, we adjust the radius of the equivalent theoretical cylindrical cavity to improve the fit so that we achieve a maximum relative error of 0.8% for  $\rho_{\text{eq}} = 17.68 \mu\text{m}$  delimited on both profiles.

Using the Equation 3.16, we estimate the surfaces  $S^{(1,23)}$  and  $S^{(0,22)}$  of the modes  $\text{TE}_{1,23}$  and  $\text{TE}_{0,22}$ , respectively. We integrate the normalized electric field intensity  $I = |E^{(m,n)}(\rho, \phi)|^2$  calculated numerically at  $\lambda_e$  and  $\lambda_m$  over the cross-section of an equivalent cavity of radius  $\rho_{\text{eq}} = 17.68 \mu\text{m}$ . The surface maps of the electrical intensity are plotted for each modes on Figure E.1.a) and c) in Appendix E. We find that most of the electrical energy concentrates in surfaces  $S^{(1,23)} \simeq 8.72\lambda^2$  and  $S^{(0,22)} \simeq 11.68\lambda^2$ , in units of  $\lambda^2 = (1.55)^2 \mu\text{m}^2$ , which represent about 2% and 2.68%, respectively, of the cavity cross-section surface  $A_c \simeq 436\lambda^2$ . Equivalently, the mode  $\text{TE}_{1,23}$  ( $\text{TE}_{0,22}$ ) contains most of the electromagnetic energy in a disk of radius  $2.5 \mu\text{m}$  ( $2.9 \mu\text{m}$ ) which encompasses the first four maxima of electrical intensity, as represented by red zones on Figure E.1. b) and d) in Appendix E. The analytical calculation of the modes' surfaces in a cylindrical cavity of radius  $\rho_c = 17.68 \mu\text{m}$  gives  $S^{(1,23)} \simeq 7.76\lambda^2$  and  $S^{(0,22)} \simeq 11.74\lambda^2$ . The errors obtained with the numerical computations, 12% and 1% for the modes  $\text{TE}_{1,23}$  and  $\text{TE}_{0,22}$ , respectively, stem mostly from the overlapping of modes  $\text{TE}_{5,21}$  and  $\text{TE}_{4,21}$  patterns in the maps of the fields.

$(m, n)$	$R$ (%)	$\lambda_{\text{FDTD}} (\mu m)$	$Q_{\text{FDTD}}$	$\lambda_{\text{th}} (\mu m)$	Relative error (%)
(0,24)	80	1.46238	$8.35 \times 10^3$	1.45824	0.283
(1,24)	88	1.49222	$1.56 \times 10^3$	1.48908	0.211
(0,23)	95	1.52256	$4.21 \times 10^3$	1.52097	0.105
(4,22)		1.52523	$3.48 \times 10^3$	1.52326	0.129
(1,23)	98	1.55460	$2.38 \times 10^4$	1.55455	0.003
(3,22)		1.55597	$2.44 \times 10^4$	1.55577	0.012
(5,21)		1.55853	$9.86 \times 10^3$	1.55734	0.076
(7,20)		1.56265	$6.91 \times 10^3$	1.56105	0.102
(0,22)	99	1.58784	$1.61 \times 10^5$	1.58934	0.094
(4,21)		1.59060	$2.07 \times 10^5$	1.59195	0.085
(6,20)		1.59392	$1.94 \times 10^5$	1.59524	0.083
(1,22)	97	1.62303	$8.19 \times 10^3$	1.62605	0.186
(3,21)		1.62449	$9.40 \times 10^3$	1.62745	0.183
(5,20)		1.62730	$1.12 \times 10^4$	1.63026	0.182
(0,21)	95	1.65952	$9.18 \times 10^4$	1.66414	0.278
(4,20)		1.66266	$2.95 \times 10^3$	1.66714	0.270
(1,21)	90	1.69841	$1.53 \times 10^3$	1.70445	0.356
(3,20)		1.69993	$1.12 \times 10^3$	1.70606	0.361

TABLE 3.2: Identification of some of the cylindrical cavity modes  $\text{TE}_{m,n}$  located on the FDTD spectra b) and d) of Figure 3.18 of an infinitely long tubular rolled-up PCM cavity. For each modes, we give the resonance wavelength  $\lambda_{\text{FDTD}}$  and the quality factor  $Q$  computed with harmonic inversion method from FDTD temporal data. We indicate the corresponding cutoff wavelength  $\lambda_{\text{th}}$  of each mode  $\text{TE}_{m,n}$  calculated theoretically in an infinitely long cylindrical cavity of radius  $\rho_c = 17.68 \mu m$ . We also assess the relative error (in %) between the analytical and numerical wavelengths of the modes. We highlight in blue the modes  $\text{TE}_{(m,n)}$  with low azimuthal order  $m = \{0, 1\}$  accompanied with the value of the reflectivity  $R$  (%) of the planar PCM at normal incidence assessed around the resonance wavelengths.

In the same way as performed with the modes  $\text{TE}_{1,23}$  and  $\text{TE}_{0,22}$ , we identify some of the remaining cavity modes detected in the spectra b) and d) of Figure 3.18 corresponding to single electric and magnetic dipole excitation of the cavity, respectively. We extract then for all the modes, the resonance wavelength  $\lambda_{\text{FDTD}}$  and we estimate the quality factor  $Q$  with the harmonic inverse method introduced in Section 2.1, gathered in Table 3.2. For the modes  $\text{TE}_{m,n}$  with  $m = \{0, 1\}$  highlit in blue, we notice that the value of the quality factor follows roughly the spectral evolution of the reflectivity  $R$  of the planar PCM wall at normal incidence. Indeed,  $Q$  increases from  $1.56 \times 10^3$  for the mode  $\text{TE}_{1,24}$  detected at  $1.4922 \mu m$  where  $R \simeq 88\%$  to  $1.61 \times 10^5$  for the mode  $\text{TE}_{0,22}$  at  $1.58784 \mu m$  for which  $R$  almost reaches its maximum value of about 99%. The quality factor then decreases as we leave progressively the high-reflectivity zone ( $R > 95\%$ ) of the planar PCM at normal incidence. This common evolution makes sense if we relate the angle of incidence of the incoming light to the azimuthal order  $m$  of any cavity mode. Following ray optics considerations, the number of azimuthal variations of the fields of one mode  $\text{TE}_{m,n}$ , namely  $m$ , increases along with the angle of incidence of the incoming light hitting the PCM wall. The temporal confinement of one mode  $\text{TE}_{m,n}$  generated from incident light inclined at angle  $\theta$ , hence its quality factor, is then conditioned by the reflection performances of the PCM at the angle  $\theta$ . We analyse the global evolution of  $Q$  for  $\text{TE}_{m,n}$  modes with  $m > 1$  in the light of the reflection power of the PCM for any incidence  $\theta$  and  $p$ -polarized light described in Figure 3.8.a):

- for  $\lambda \leq 1.58 \mu m$ : the reflectivity of the PCM always maintains at highest values at normal incidence. Therefore,  $Q$  decreases globally as the order  $m$  increases:  $Q_{0,23} > Q_{4,22}$  for instance.
- for  $\lambda > 1.58 \mu m$ : the reflectivity of the PCM slowly decreases at normal incidence while it tends towards maxima at higher wavelengths for oblique light rays, hence  $Q_{4,21} > Q_{0,22}$ , or  $Q_{5,20} > Q_{3,21} > Q_{1,22}$ .

We finally confront numerical and analytical models concerning the wavelengths of the cylindrical cavity modes. To this end, we assess the theoretical cutoff wavelengths of the modes in a cavity of radius  $\rho_{eq} = 17.68 \mu m$  equivalent to the FDTD model cavity. We report a very good compliance of the numerical results with the theoretical model as the relative errors maintain below a 0.5% limit in the spectral range of interest  $[1.45-1.7] \mu m$ .

#### Key points of the subsection

The simulations of the optical response of infinite rolled-up PCM cavities with the FDTD method bring out several key messages summarised here-under which validate the analogy with the cylindrical cavity model:

- The interpretation of the spectra combined with the analysis fields' maps have confirmed the existence of cylindrical cavity modes inside the tubular photonic cavity. Despite the induced curvature of the PCM wall, the high-aspect ratio of the photonic crystal microtube (radius  $\rho_c \simeq 17.5 \mu m \gg a \simeq 1.2 \mu m$ ) has preserved the integrity of the reflection properties of the PCM wall.
- We find an excellent agreement between the numerical and theoretical spectral distributions of the modes.
- We also report the coexistence of numerous and various TE cavity modes within the spectral interval  $[1.45-1.7] \mu m$  in compliance with theoretical predictions. The lifetime of the modes in the cavity, namely their quality factors, depends essentially on the reflection performances of the PCM wall. Therefore, below  $1.58 \mu m$ ,  $TE_{m,n}$  with low azimuthal orders ( $m \leq 1$ ), emerging at normal incidence, express predominantly and sustain longer in the cavity compared to high azimuthal orders. Above  $1.58 \mu m$ , the situation reverses progressively.

### 3.4.3 Simulations of finite cavities

To complete the numerical study of the photon cages, we perform optical simulations of finite-length rolled-up PCM cavities. We assimilate the photonic cavities to cylindrical cavity resonators introduced in Section 3.3, a shortened version of cylindrical cavities with perfectly reflecting top and bottom faces. In ideal cylindrical cavity resonators, the electromagnetic waves form stationary modes along the axis of the cylinder for quantized wavelengths. Tubular resonators support then  $TE_{m,n,p}$  and  $TM_{m,n,p}$  modes defined by quantized components of the wavevector along the tube axis:  $k_z = \beta_p = p\pi/L$  with  $p \in \mathbb{N}^*$  the axial order. Precisely, the order  $p$  denotes the number of

antinodes of the spatial distribution of the mode energy along the axial direction. Concerning tubular photon cages, we assume the reflection of light on top and bottom faces on account of group velocities mismatch between cavity and free space modes. The following simulations aim to validate the analogy between the model of cylindrical cavity resonators and tubular photonic micro-cavities. To this end, we will confront both cavity models according to spectral and spatial distributions of the supported modes.

We show in Figure 3.20 a cross-section view at  $z = 0$  (a) and a lateral view (b) of the 3D FDTD model of the finite rolled-up PCM cavity. The geometrical parameters of the PCM wall and the radius of the tubular cavity remain unchanged in comparison to the infinitely long cavity model, namely  $a = 1.206 \mu m$ ,  $r = 0.48 \mu m$ ,  $h = 0.228 \mu m$  and  $\rho_{\text{avg}} \simeq 17.62 \mu m$ . However, the cavity has now a finite length  $L$  as represented on 3.20.b) adjustable according to Equation (3.28). We simulate the spectral response of the cylindrical photonic microstructure with a single electric dipole oriented along the  $x$  axis and contained in the central cross-section plane located of equation  $z = 0$ . Such configuration illustrated on Figure 3.20.a) and b), we excite preferentially  $TE_{m,n}$  modes with low azimuthal  $m$  orders characterized by a maximum of the electric field energy in the middle of the cavity. This specific setting also allows to benefit from the symmetry properties of both the dipole source and the tubular microstructure by applying symmetric boundary conditions (transparent blue-shaded regions) in the half regions  $y < 0$  and  $z < 0$  of space. Consequently, the calculation zone delimited by a thick orange line restrains to complementary half planes  $y > 0$  and  $z > 0$  which reduces the computation time by a factor of four. As a precaution, we verify that the symmetry conditions do not affect the response of the tubular cavities. Moreover, the dipole bandwidth spans a  $550 \text{ nm}$ -large spectral window centred at  $1.55 \mu m$ . A cloud of 15 monitors (yellow crosses) are dispersed randomly over the simulation zone to record the temporal evolutions of the electromagnetic fields. We finally apply PML boundary conditions along  $x$ ,  $y$  and  $z$  Cartesian directions. In particular, the PML frontiers are at a distance  $d_{\text{PML}}^x = d_{\text{PML}}^y = 2\lambda$  with  $\lambda = 1.5 \mu m$  and  $d_{\text{PML}}^z = a(N_z - 2)/4$ , where the integer  $N_z$  is fixed with the cavity length, from the microstructure edges along  $x$ ,  $y$  and  $z$  axes respectively as illustrated on Figure 3.20.b).



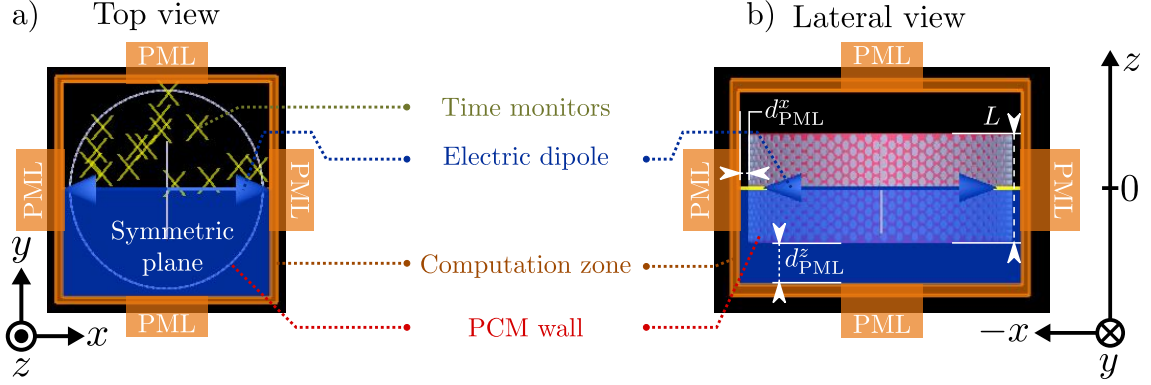


FIGURE 3.20: FDTD simulation model of a rolled-up PCM cavity of finite length  $L$  and radius  $\rho_{\text{avg}} \simeq 17.62 \mu\text{m}$  designed in LUMERICAL 3D CAD environnement. a) Cross-section view of the cavity at  $z = 0$ . An electric dipole (blue arrow) is placed in the centre of the cavity at  $z = 0$ , along the  $x$  axis, to excite  $\text{TE}_{m,n}$  modes with low  $m$  order. A cloud of 15 monitors (yellow crosses) distributed randomly in the upper-half region  $y \geq 0$  record the temporal evolutions of the electromagnetic fields. The thick orange line delimits the FDTD computation zone. The optical response in the shaded blue region is deduced by symmetry of the cavity and the source with respect to  $y = 0$  plane. PML boundary conditions are applied at the edges of the computation zone. b) Lateral view, at  $y = 0$ , of the PCM cavity with a length  $L$ . PML boundary conditions are used along the  $z$  axis at a distance  $d_{\text{PML}}^z = a(N_z - 2)/4$  from the top and bottom edges of the cavity.

### Cavity with a 10 micrometers length

We present in Figure 3.21 in blue thick line the intensity spectrum, in log scale, simulated for a 2D PCM tubular photon cage of length  $L \simeq 10 \mu\text{m}$  corresponding to  $N_z = 17$  in Equation (3.28). We have set the simulation time to  $t_s = 4500 \text{ fs}$  for a proper decay of the fields energy and apodization parameters to  $t_c = 0.7t_s$  and  $\Delta t = 0.15t_s$ . The spectrum shows four main broad peaks located around  $1.49$ ,  $1.55$ ,  $1.62$  and  $1.7 \mu\text{m}$ . The deformed and large shape of the spectral features suggest the overlap of multiple modes with large bandwidths, hence low quality factors  $Q$ . Accordingly, we have superimposed in dashed orange line, on indicative basis, the spectral response of an infinitely long ( $L \rightarrow \infty$ ) tubular photon cage presented earlier on Figure 3.18.b). We observe that the peaks of the finite cavity cover the peaks of cylindrical cavity modes  $\text{TE}_{m,n}$  with lowest azimuthal orders  $m = 1, 3, 5$  detected in the infinite cavity. Furthermore, we notice lobes on the left side of the broad peaks *a priori* unobserved in the infinite structure such as the features located around  $1.49 \mu\text{m}$  which hints the presence of additional modes.

We reveal the nature of the broad spectral features standing out in the spectrum of Figure 3.21 by mapping the electromagnetic fields in the cross-section and along the axis of the cylindrical cavity. In particular, we recognize typical patterns of cylindrical cavity modes on the spatial distribution of normalized magnetic field amplitude  $|H|$  shown on Figure 3.22.a) and calculated in the central cross-section plane of the cavity ( $z = 0$ ) at the wavelength  $\lambda = 1.553 \mu\text{m}$ . The grey circular contour outlines the PCM membrane wall. The presence of a central nodal line implies that we deal at least with a cavity mode of type  $\text{TE}_{1,n}$ . The four bright branches emerging from the centre of the map remind of the pattern obtained by the mixing of  $\text{TE}_{1,n}$  and  $\text{TE}_{3,n}$  modes as elucidated on Figure 3.19.a). We determine radial  $n$  and azimuthal orders involved in the hybrid mode pattern by best fitting of extracted profile along  $y$  axis at  $x = 0$ . We finally identify the mode displayed on Figure 3.22.a) to a combination of mainly cavity modes  $\text{TE}_{1,23}$  and  $\text{TE}_{3,22}$  in proportions estimated to  $0.62$  and  $0.38$ , respectively. In



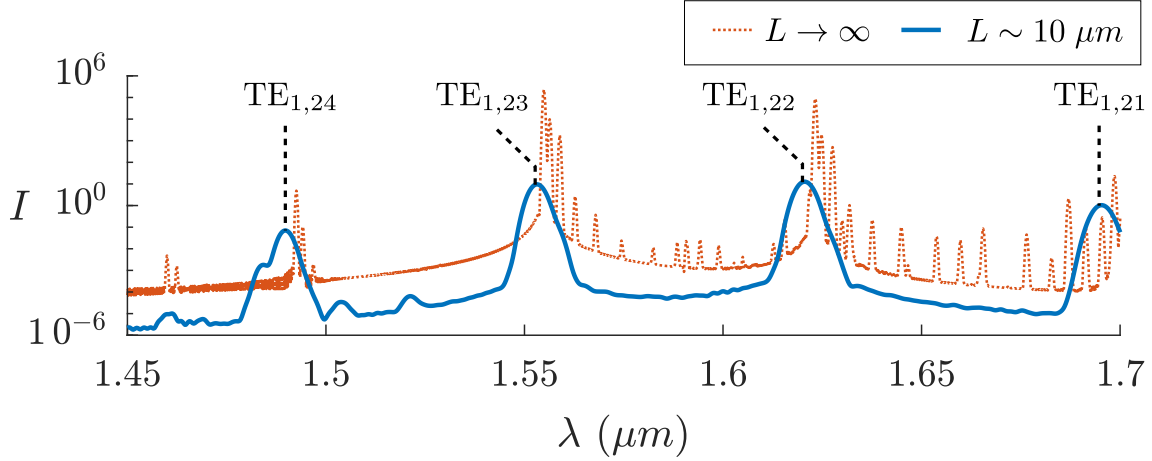


FIGURE 3.21: Intensity spectrum of a tubular photon cage with length  $L \sim 10 \mu m$  (thick blue line) simulated with an electric dipole source centred in the tube and oriented perpendicularly to the tube axis as depicted in the views of Figure 3.20. We indicate in orange dashed line the spectrum of an infinitely long ( $L \rightarrow \infty$ ) cavity simulated with the same excitation conditions and interpreted earlier.

the same way, we find that the remaining peaks observed around 1.49, 1.62 and 1.7  $\mu m$  correspond to combinations of modes  $TE_{1,24}$ - $TE_{3,23}$ ,  $TE_{1,22}$ - $TE_{3,21}$ ,  $TE_{1,21}$ - $TE_{3,20}$ , respectively.

We also notice weak crenellated patterns surrounding the central radial oscillations and typical of high azimuthal order cavity modes, zoomed on the inset picture in Figure 3.22.a). The presence of such extreme mode could be explained by *ad-hoc* high reflectivity of the planar PCM at grazing angles which are not investigated on Figure 3.8. By inspection, we find that the radius of the azimuthal ring matches that of cylindrical cavity mode  $TE_{55,3}$ . Under geometrical optics considerations, we assume that high azimuthal order modes form as light beams impinge on the PCM wall at grazing incidence. We establish then in first approximation a simple law of evolution of the angle of incidence  $\theta$  as a function of the order  $m$ ,  $\theta = (180 - 360/(2m))/2$ , plotted in Figure F.1.a) in Appendix F. We deduce that the azimuthal form defined by  $m = 55$  emerges at an angle  $\theta$  estimated to  $88.36^\circ$ . At such angle, the reflectivity of the PCM results from the bulk properties of the dielectric membrane rather than from the effect of the photonic crystal pattern. In particular, we represent in Figure F.1.b) in Appendix F the evolution of the reflectance  $R$  (%) as a function of the angle of incidence  $\theta$  of a 0.230  $\mu m$ -thick dielectric slab defined by an average value of the optical index which takes into account the index modulation of the PCM. For  $p$ -polarized incident light, the reflectivity  $R$  cancels out at the Brewster angle  $\theta_B \simeq 62.61^\circ$  and then soars up to 100% at  $90^\circ$  limit. In particular, at  $\theta \simeq 88.36^\circ$ , the reflectivity reaches a high value of about 98% which explains the emergence of the cavity mode  $TE_{55,3}$ . In the same way, cavity modes with higher value of  $m$  and cutoff wavelengths lying around 1.553  $\mu m$  also contribute to the final pattern in proportions defined by the distance to the wavelength of computation.

In addition, we present on Figure 3.22.b) the spatial distribution of normalized magnetic amplitude  $|H|$  computed at  $\lambda = 1.553 \mu m$  in the plane of equation  $x = 0$ . The grey straight and dashed lines delimit the PCM membrane wall and the virtual interfaces between top/bottom faces of the cavity and free space, respectively. We notice an important and seemingly uniform concentration of the mode energy in the vertical direction of the cylindrical cavity. For a better appreciation of the spatial extend of the field inside and outside the cavity, we plot on Figure 3.22.c) in blue straight line

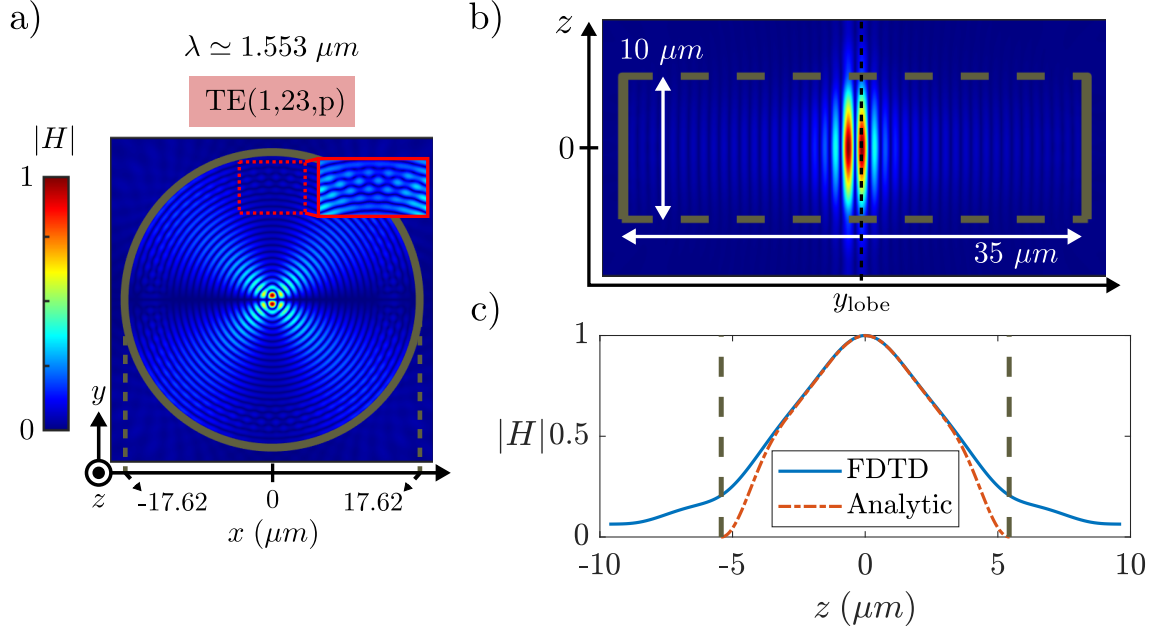


FIGURE 3.22: a) Map of the normalized magnetic field amplitude  $|H|$  calculated at  $\lambda \simeq 1.553 \mu\text{m}$  in the middle ( $z = 0$ ) cross-section plane of a  $10 \mu\text{m}$ -long tubular photon cage with average radius  $\rho_c \simeq 17.62 \mu\text{m}$ . The circular grey outline delimits the PCM membrane wall of the cavity. The field pattern corresponds to that of generic modes  $\text{TE}(1,23,p)$  with  $p \in \mathbb{N}^*$ . Inset picture: zoom on the peripheral azimuthal patterns with adjusted color gradient. b) Map of normalized  $|H|$  in the plane  $x = 0$ . c) Profile of normalized  $|H|$  (blue curve) along  $z$  axis of the cavity at  $y = y_{\text{lobe}}$ , the abscissa of the first maximum lobe. Vertical grey dashed lines indicate the top and bottom frontiers of the cavity within which the profile is fitted with harmonics (dashed orange line) of a Fabry-Pérot cavity.

a section of the map in b) following the black dashed line at  $y = y_{\text{lobe}}$ , the abscissa of the first lobe of maximum amplitude. We indicate with dashed grey lines the vertical top and bottom virtual frontiers of the cavity. We model the evolution of the field in between the top and bottom boundaries by a linear combination of harmonics of an equivalent Fabry-Pérot (FP) cavity:  $y_p(z) = \sum_p c_p \sin(p\pi z/L)$ ,  $p \in \mathbb{N}^*$  with weighting coefficients  $c_p$  of  $p$ -th harmonics and  $L$  the length of the FP cavity similar to that of the tubular cage. We find a good agreement between analytic (dashed orange line) and simulation data by considering the first five  $p$  orders in the following proportions:  $c_1 = 0.76$ ,  $c_2 = 0.11$ ,  $c_3 = 0.1$ ,  $c_4 = 0.02$ ,  $c_5 = 0.005$ . We can attribute the contributions of the first two  $p$  orders mainly to the emergence of cylindrical cavity modes  $\text{TE}_{1,23,p}$ ,  $\text{TE}_{3,22,p}$  and  $\text{TE}_{5,23,p}$  with  $p = 1, 2$  accordingly to their cutoff wavelengths specified in Table 3.3 contained to a larger extent in the broad peak observed at  $1.553 \mu\text{m}$ . The remaining contributions of  $p = 3, 4, 5$  orders stem from the expression of radial cavity modes  $\text{TE}_{0,22,3}$ ,  $\text{TE}_{1,22,4}$  and  $\text{TE}_{0,21,5}$  for the most part, which wavelengths allow their appearance in the final pattern of the mode, in weaker extent.

We finally examine the spatial damping of the hybrid mode in the vertical direction, outside of the cavity. Approaching the decay with a typical exponential form  $y(z) = e^{-z/L_p}$ , we estimate the penetration length of the field in free space  $L_p$  to  $3.271 \mu\text{m}$  which represents about 30% of the length of the cavity. It indicates therefore a low spatial confinement of the modes along the vertical direction.

### Cavity with a 50 micrometers length

We complete the analysis of the optical properties of finite tubular cages by simulating a cylindrical photonic cage with a length  $L = 50 \mu\text{m}$  corresponding to  $N_z = 83$

$p$	$\lambda_{\text{TE}_{1,23,p}}$	$\lambda_{\text{TE}_{3,22,p}}$	$\lambda_{\text{TE}_{5,21,p}}$	$\lambda_{\text{TE}_{0,22,p}}$	$\lambda_{\text{TE}_{1,22,p}}$	$\lambda_{\text{TE}_{0,21,p}}$
1	1.5499	1.5511	1.5535	1.5843	1.6207	1.6584
2	1.5361	1.5373	1.5396	1.5696	1.6050	1.6416
3	1.5139	1.5151	1.5173	1.5460	1.5797	1.6146
4	1.4845	1.4855	1.4877	1.5147	1.5463	1.5790
5	1.4490	1.4500	1.4519	1.4770	1.5060	1.5365

TABLE 3.3: Cutoff wavelengths  $\lambda_{m,n,p}$  in micrometers for first  $p$  orders,  $p = 1, 2, \dots, 5$ , of cylindrical cavity modes  $\text{TE}_{1,23,p}$ ,  $\text{TE}_{3,22,p}$ ,  $\text{TE}_{5,21,p}$ ,  $\text{TE}_{0,22,p}$  and  $\text{TE}_{1,22,p}$  supported by an ideal tubular cavity resonator of length  $L = 10 \mu\text{m}$  and average radius  $\rho_c = 17.62 \mu\text{m}$ .

in Equation (3.28). Keeping the same simulation settings, we obtain the intensity spectrum represented on Figure 3.23 as an orange-coloured curve. In substance, we retrieve the main four broad peaks detected in the spectrum of a  $10 \mu\text{m}$ -long cavity plotted in dashed blue line as a guide. However, we also discern multiple secondary peaks which stand out on the left side of the main spectral features located around  $1.49$ ,  $1.62$  and  $1.7 \mu\text{m}$ . Methodologically, we investigate the nature of the additional peaks by computing maps of the electromagnetic fields at different wavelengths around the main peaks.

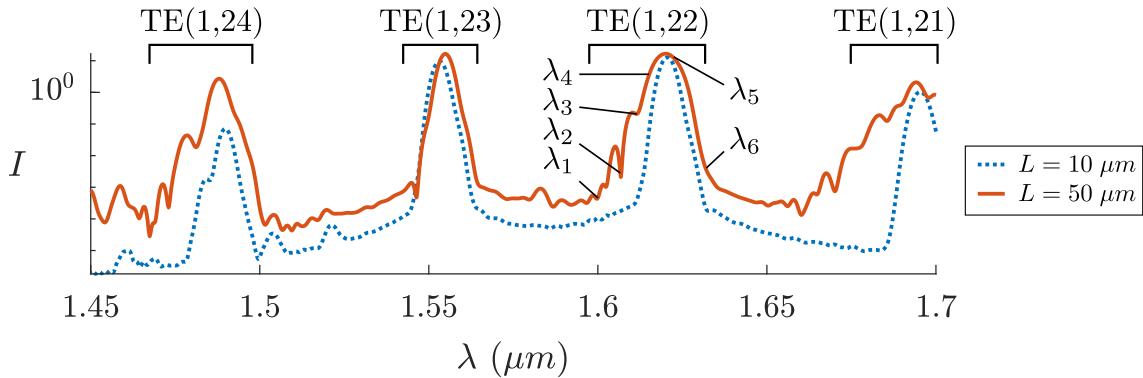


FIGURE 3.23: Intensity spectrum of a  $50 \mu\text{m}$ -long tubular cavity (orange line) with average radius  $\rho_c \simeq 17.62 \mu\text{m}$  simulated with a single electric dipole source placed in the central plane and oriented perpendicularly to the tube axis. We indicate the spectrum of a  $10 \mu\text{m}$ -long tubular cavity (dashed blue curve) obtained in the same excitation conditions.

In particular, we present on Figure 3.24 profiles of the magnetic field amplitude  $|H|$  in the central cross-section plane of the cavity for the first row and along the tube axis at  $x = 0$  for the second row. We calculated the maps at six distinct wavelengths:  $\lambda_1 = 1.6 \mu\text{m}$ ,  $\lambda_2 = 1.607 \mu\text{m}$ ,  $\lambda_3 = 1.612 \mu\text{m}$ ,  $\lambda_4 = 1.615 \mu\text{m}$ ,  $\lambda_5 = 1.621 \mu\text{m}$  and  $\lambda_6 = 1.633 \mu\text{m}$  pinned to the spectrum of Figure 3.23. Comparing the cross-section plots to theoretical patterns of cylindrical cavity modes, we identify the  $\text{TE}_{1,22}$  mode pattern which expresses predominantly until  $\lambda_6$  at which it shares comparable contribution with  $\text{TE}_{3,21}$  mode.

Furthermore, the vertical profiles represented on the lower plots in Figure 3.24 show a spatial distribution of the modes typical of Fabry-Pérot cavity modes with the order  $p$  defining the number of maximum amplitude lobes. In particular, we observe that the order  $p$  decreases from  $\lambda_1$  to  $\lambda_6$  in compliance with theoretical predictions, taking odd values from 11 down to 1. We explain the exclusive excitation of odd  $p$  orders by the particular position of the electric dipole located at field node shared by even  $p$  order modes. We focus here on the most representative  $p$  orders of the modes keeping in

mind that the mode profiles actually result from a combination of  $p$  orders as attested by the non-uniform intensity of the lobes.

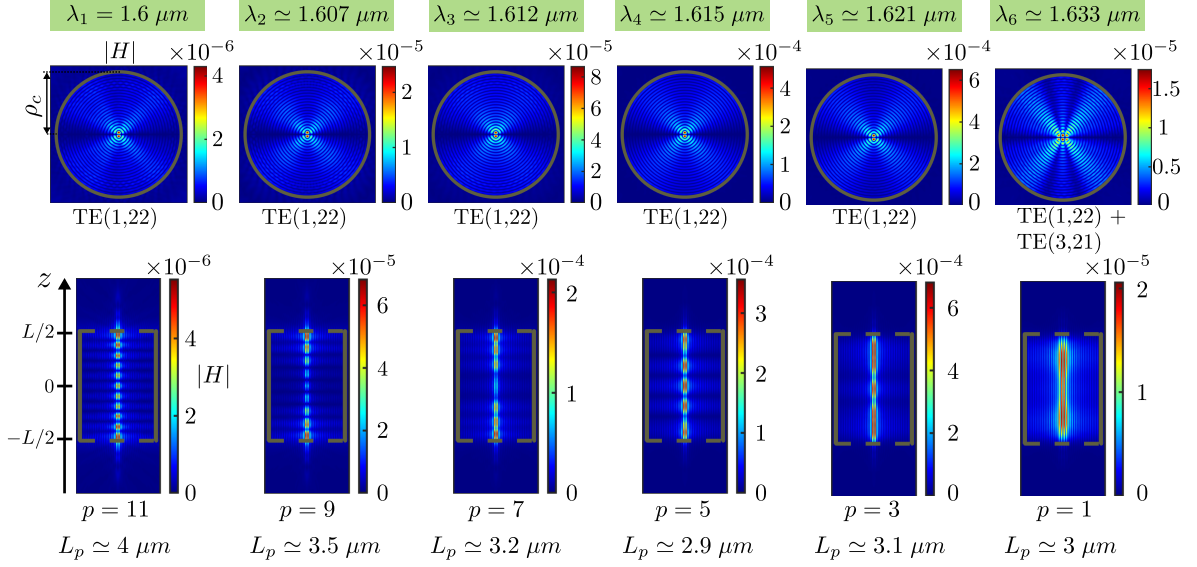


FIGURE 3.24: Maps of the magnetic field amplitude  $|H|$  calculated at different wavelengths from  $\lambda_1 = 1.6 \mu\text{m}$  to  $\lambda_6 = 1.633 \mu\text{m}$  in the cross-section (upper plots) and along the vertical axis (lower plots) of a tubular cage with length  $L = 50 \mu\text{m}$  and average radius  $\rho_c \simeq 17.62 \mu\text{m}$ . We identify the orders  $(m, n)$  and  $p$  in the cross-section and axial directions respectively of the predominant cavity modes patterns. A single electric dipole source is placed in the centre of the cavity and contained in the central cross-section plane to excite low  $m$  TE modes.

We also report Figure 3.24 a global decrease of the penetration length  $L_p$  of the modes in free space along with the diminishing of the axial order, showing a better axial confinement for low  $p$  orders. We note, however, a slight increase in the last two values of  $L_p$  that we explain by unsatisfying exponential modelling of the field decay into free space. Moreover, we note the independence of the penetration length with respect to the cavity length as we obtain a length  $L_p$  in the order of 3 to  $4 \mu\text{m}$  for the different  $p$  order modes existing the  $10 \mu\text{m}$  and  $50 \mu\text{m}$ -long cavities.

Finally, exploiting the spectrum shown on Figure 3.23 and the calculated maps, we give in Table 3.4 rough estimations  $\lambda_{\text{sim}}$  of the wavelengths of detection of the  $p = 1, 2, \dots, 11$  orders located around the peak at  $1.62 \mu\text{m}$ . The values of  $\lambda_{\text{sim}}$  show great consistency with theoretical cutoff wavelengths of modes  $\text{TE}_{1,22,p}$ ,  $\lambda_{\text{TE}_{1,22,p}}$ , as much as that of modes  $\text{TE}_{3,21,p}$ ,  $\lambda_{\text{TE}_{3,21,p}}$  with respective relative errors  $e_{1,22}$  and  $e_{3,21}$  remaining below 0.5 %. The compliance with both generic modes  $\text{TE}_{1,22,p}$  and  $\text{TE}_{3,21,p}$  explains by their high spectral proximity as the spectral spacing  $\Delta_{\text{ie}}$  at fixed  $p$  orders maintains below  $1.4 \text{ nm}$ . We also notice spectral spacing  $\Delta_{\text{ia}}$  of few nanometers between consecutive odd  $p$  orders.

$p$	$\lambda_{\text{TE}_{1,22,p}}$	$\lambda_{\text{TE}_{3,21,p}}$	$\Delta_{\text{ia}}$	$\Delta_{\text{ie}}$	$\lambda_{\text{sim}}$	$\Delta_{\text{sim}}$	$e_{1,22}$	$e_{3,21}$
1	1.6258	1.6272		1.398	1.6248		0.07	0.15
3	1.6241	1.6255	1.7	1.393	1.6215	3.3	0.16	0.25
5	1.6207	1.6221	3.4	1.385	1.6165	5.0	0.26	0.34
7	1.6156	1.6170	5.1	1.372	1.6103	6.2	0.33	0.41
9	1.6089	1.6103	6.7	1.355	1.6052	5.2	0.23	0.32
11	1.6006	1.6020	8.3	1.334	1.6016	3.6	0.06	0.03

TABLE 3.4: Cutoff wavelengths  $\lambda_{\text{TE}_{1,22,p}}$  and  $\lambda_{\text{TE}_{3,21,p}}$  in microns of modes  $\text{TE}_{1,22,p}$  and  $\text{TE}_{3,21,p}$  with  $p = 1, 3, 5, \dots, 11$  calculated for an ideal cylindrical cavity resonator of radius  $\rho_c = 17.68 \mu\text{m}$  and length  $L = 50 \mu\text{m}$ . Spectral spacing  $\Delta_{\text{ia}}$  in nanometers between two successive  $\lambda_{\text{TE}_{1,22,p}}$  or  $\lambda_{\text{TE}_{3,21,p}}$  with odd values of  $p$  order. Spectral spacing  $\Delta_{\text{ie}}$  in nanometers between  $\lambda_{\text{TE}_{1,22,p}}$  and  $\lambda_{\text{TE}_{3,21,p}}$  for identical  $p$  orders. Estimated wavelengths  $\lambda_{\text{sim}}$  and spectral spacing  $\Delta_{\text{sim}}$  in nanometers of  $p$  modes observed in the spectrum and maps in Figure 3.24. Relative errors  $e_{1,22}$  ( $e_{3,21}$ ) in % between simulated  $\lambda_{\text{sim}}$  and theoretical  $\lambda_{\text{TE}_{1,22,p}}$  ( $\lambda_{\text{TE}_{3,21,p}}$ ) wavelengths of  $p$  modes.

### Key points of the subsection

In summary, we shall retain the following key messages of the FDTD simulations performed on finite length 2D PCM photon cages with a single electric dipole source excitation:

- the cylindrical cavity modes  $\text{TE}_{m,n,p}$  are also confined along the axis of the tubular cavity in the form of stationary modes defined by  $p \in \mathbb{N}^*$  lobes of maximum intensity;
- we report a better vertical confinement for high aspect ratio cylindrical microstructures;
- for a given length of the cavity, the attenuation of the mode  $\text{TE}_{m,n,p}$  in free space is stronger for low values of  $p$  as it is related to a low group velocity;
- for a cavity of length  $L = 50 \mu\text{m}$ , the spectral proximity and bandwidths of successive orders  $p$  of modes  $\text{TE}_{1,n,p}$  at fixed  $n$  create a quasi-continuum of identical cross-sectional patterns in the vicinity of the fundamental mode  $\text{TE}_{m,n,1}$ . We extend the reasoning for the modes  $\text{TE}_{0,n,p}$  simulated preferentially by a single magnetic dipole source in the center of the cavity.

### 3.5 Conclusion of the chapter

In the present chapter, we have accomplished the theoretical study of tubular photon cages based on rolled-up 2D PCM. The study has divided into three main sections tackling the design of the planar PCM mirror, the analytical and numerical simulation of the cages' optical properties.

In the first section dedicated to the production of a highly reflective PCM membrane wall, we report the following key results:

- we have designed a non-absorbing polarization-independent highly efficient broadband 2D PCM mirror at normal incidence in the near-infrared domain;
- we have demonstrated the essential role of the photonic crystal pattern to achieve high reflective behaviour in comparison to poorly reflective plain membranes;
- we have attested the robustness of the PCM reflection properties up to a few tens of degrees of incidence angle.

In the second section, we have approached photon cages' optical response using in the first place the analytical model of the cylindrical cavity resonator. The model provides a almost complete description of the cavity's modal response with the following main features:

- the cavity supports transverse electric  $TE_{m,n,p}$  and transverse magnetic  $TM_{m,n,p}$  classified with  $m$ ,  $n$  and  $p$  the *radial*, *azimuthal* and *axial* orders defining the modes' distribution and patterns in the cylindrical geometry;
- we report a high density of modes in cavities of radius  $17.5 \mu m$  close to fabricated structures, and a high spectral proximity;

In the third section, we have conducted FDTD simulations to obtain a more realistic response of the photon cages. We highlight below the main results:

- the simulations of infinite and finite cavities have confirmed the emergence of TE cylindrical cavity modes in rolled-up PCM cages, validating the analytical predictions (spectral and spatial modes' distributions) and the efficiency of the curved PCM mirror wall;
- the simulations of infinite cavities have related, through the analysis of modes'  $Q$  factors and maps, the expression of  $TE_{m,n}$  modes with the PCM reflectivity spectrum;
- the simulations of finite cavities have revealed the axial confinement of the modes  $TE_{m,n,p}$  which quality depends on both the order  $p$  and the aspect ratio. For high aspect ratio cavities, the spectral proximity of  $p$  orders creates a quasi-continuum of modes at fixed  $(m, n)$  pairs.

We have finally brought a theoretical proof of photon cages based on rolled-up 2D PCM. The analytical cavity model constitutes a choice and powerful tool to predict the optical properties of the photon cages. The consistent theoretical study paves the way to the fabrication and optical characterization of real structures described in the following chapter.

### 3.6 References

- [1] S. Adachi. Optical dispersion relations for GaP, GaAs, GaSb, InP, InAs, InSb,  $\text{Al}_x\text{Ga}_{1-x}\text{As}$ , and  $\text{In}_{1-x}\text{Ga}_x\text{As}_y\text{P}_{1-y}$ . *Journal of Applied Physics*, 66(12):6030–6040, Dec. 1989. ISSN 0021-8979. doi: 10.1063/1.343580. URL <https://aip.scitation.org/doi/10.1063/1.343580>. Publisher: American Institute of Physics. 111
- [2] P. B. Johnson and R. W. Christy. Optical Constants of the Noble Metals. *Phys. Rev. B*, 6(12):4370–4379, Dec. 1972. doi: 10.1103/PhysRevB.6.4370. URL <https://link.aps.org/doi/10.1103/PhysRevB.6.4370>. Publisher: American Physical Society. 115
- [3] M. Kahn and D. Ritter. Strain relief by long line defects in tensile  $\text{Ga}_x\text{In}_{1-x}\text{P}$  layers grown on InP substrates. *Appl. Phys. Lett.*, 79(18):2928–2930, Oct. 2001. ISSN 0003-6951. doi: 10.1063/1.1412587. URL <https://aip.scitation.org/doi/abs/10.1063/1.1412587>. Publisher: American Institute of Physics. 114
- [4] P. Lalanne, C. Sauvan, and J. P. Hugonin. Photon confinement in photonic crystal nanocavities. *Laser & Photonics Reviews*, 2(6):514–526, 2008. ISSN 1863-8899. doi: 10.1002/lpor.200810018. URL <https://www.onlinelibrary.wiley.com/doi/abs/10.1002/lpor.200810018>. 128
- [5] D. M. Pozar. *Microwave Engineering*. Wiley, Hoboken, NJ, 4 edition edition, Nov. 2011. ISBN 978-0-470-63155-3. 121
- [6] C. Sieutat, R. Peretti, J.-L. Leclercq, P. Viktorovitch, and X. Letartre. Strong confinement of light in low index materials: the Photon Cage. *Opt. Express, OE*, 21(17):20015–20022, Aug. 2013. ISSN 1094-4087. doi: 10.1364/OE.21.020015. URL <https://www.osapublishing.org/oe/abstract.cfm?uri=oe-21-17-20015>. 128

# Chapter 4

## Fabrication and optical characterization of photon cages

*La Nature est un temple où de vivants piliers  
Laissent parfois sortir de confuses paroles ;  
L'homme y passe à travers des forêts de symboles  
Qui l'observent avec des regards familiers.*

---

CHARLES BAUDELAIRE  
(LES FLEURS DU MAL, CORRESPONDANCES)

### Contents

---

<b>4.1</b>	<b>Fabrication of tubular photon cages . . . . .</b>	<b>150</b>
4.1.1	Composition of the multi-layered precursors . . . . .	150
4.1.2	Production of the planar design . . . . .	151
4.1.3	Description of a typical sample . . . . .	153
4.1.4	Mechanical properties of the tubular microstructures . . . . .	154
<b>4.2</b>	<b>Optical characterization of the photon cages . . . . .</b>	<b>155</b>
4.2.1	Introduction . . . . .	155
4.2.2	Modal response of photon cages . . . . .	156
4.2.3	Reproducibility and vertical confinement . . . . .	163
4.2.4	Optical response for smaller radius cages . . . . .	168
<b>4.3</b>	<b>Conclusion of the chapter . . . . .</b>	<b>171</b>

---



We have achieved so far the theoretical study of photon cages based on rolled-up 2D PCM. We have first designed a 2D PCM mirror with broadband and high reflection properties in the near-infrared domain. We have then demonstrated theoretically and numerically that photonic tubular cavities, obtained by rolling the 2D PCM mirrors, support cylindrical cavity modes which strongly confine the light in air and in the three directions. The next stages aim to bring an experimental proof of the photon cages concept. The following section presents the main results of the fabrication of rolled-up 2D PCM cavities following the technical processes described in Section 2.2 based on the rolled-up nanotechnology. It finally reports on interesting elastic behaviour of the so-formed tubular photonic cavities when we try to detach them from the substrate.

## 4.1 Fabrication of tubular photon cages

### 4.1.1 Composition of the multi-layered precursors

The first step in the fabrication of 2D PCM photon cages consists in depositing successive layers of InGaAs (sacrificial layer), InP and  $\text{In}_{1-x}\text{Ga}_x\text{P}$  materials on top of a nominal InP substrate. As explained in Chapter 2.2, the epitaxial growth allows for a precise control of the composition and the thickness of each constitutive layer of the multilayered stack, related to the curvature radius of the final rolled-up microstructure according to Equation (1.21). We detail in Table 4.1 for three samples C2217, C2527 and C2579 used for later optical characterization:

- the thicknesses (in  $\mu\text{m}$ )  $h_{\text{InGaAs}}$ ,  $h_{\text{InP}}$ , and  $h_{\text{In}_{1-x}\text{Ga}_x\text{P}}$  of the InGaAs, InP and  $\text{In}_{1-x}\text{Ga}_x\text{P}$  material layers, respectively;
- the total thickness  $h = h_{\text{InP}} + h_{\text{In}_{1-x}\text{Ga}_x\text{P}}$  (in  $\mu\text{m}$ ) of the InGaP/InP bilayer and the ratio  $\xi = h_{\text{InGaP}}/h_{\text{InP}}$ ;
- the proportion  $x$  of Gallium element in the  $\text{In}_{1-x}\text{Ga}_x\text{P}$  layer;
- the lattice mismatch (in %)  $m$  or equivalently the tensile stress induced in the InGaP/InP bilayer;
- the theoretical radius  $\rho_{\text{th}}$  calculated according to Equation (1.21);
- the range of the experimental radius  $\rho_{\text{exp}}$  of the rolled-up microstructures estimated at the end of the fabrication process.

We estimate the mismatch lattice between InP and InGaP layers with the misfit parameter  $m$  defined earlier in Section 1.1. To this end, we approximate the lattice parameter  $a_{\text{In}_{1-x}\text{Ga}_x\text{P}}$  of the  $\text{In}_{1-x}\text{Ga}_x\text{P}$  layer according to the Vegard's law:

$$a_{\text{In}_{1-x}\text{Ga}_x\text{P}} = (1 - x)a_{\text{InP}} + xa_{\text{GaP}}, \quad (4.1)$$

with  $a_{\text{In}_{1-x}\text{Ga}_x\text{P}}$  and  $a_{\text{InP}}$  the lattice parameters of the InGaP and InP layers, respectively. We report, for  $x \in [0.1 - 0.15]$ , a uniform deposition of InGaP material up to a maximum thickness of about 80 nm. Above this limit, the layer-by-layer growth is not guaranteed anymore and 3D relaxations may occur. For the sample C2217, we have targeted a total thickness  $h$  of 230 nm of the InGaP/InP bilayer for which the corresponding InP-based PCM exhibits high and broadband reflection properties at normal incidence demonstrated in Section 3.2. For the sample C2527, we have slightly

reduced  $h$  down to 214 nm to achieve a smaller curvature radius in the order of 16.5  $\mu\text{m}$ , while preserving the PCM mirror performances. Indeed, according to Figure 3.8, the PCM high-reflectivity zone at normal incidence maintains around 1.6  $\mu\text{m}$  but the reflectivity initiates a faster decrease below 1.5  $\mu\text{m}$ . Finally, we have produced the sample C2579 with a thickness  $h \sim 86$  nm and a theoretical curvature radius of about 6  $\mu\text{m}$  to explore the optical response of high curvature cavities.

We notice a great consistency between the range of experimental curvature radius  $\rho_{\text{exp}}$  and the theoretical predictions  $\rho_{\text{th}}$ . We impute the observed differences mostly to the imprecision in the estimation of the real radius extracted from scanning electron microscopy (SEM) pictures of the final tubular cavities. In particular, the inclination and high-aspect ratio ( $h \ll \rho_{\text{exp}}$ ) of the tubular structures hinder the clear identification of the cavity centre and of the PCM wall frontiers. End-to-end contributions, we evaluate the radius measurement uncertainty to about 1  $\mu\text{m}$ . Finally, despite the high air fraction (FF  $\simeq$  58 %) in the PCM lattice, we presume a negligible influence of the bilayer microstructure on the strain homogeneous distribution, hence on the radius of the final tubular cavities, provided that the connection of the lattice pattern is preserved.

Sample	$h_{\text{InGaAs}}$	$h_{\text{InP}}$	$h_{\text{In}_{1-x}\text{Ga}_x\text{P}}$	$h$	$\xi$	$x$	$m$	$\rho_{\text{th}}$	$\rho_{\text{exp}}$
C2217	500	150	78	228	0.52	0.122	0.88	19,2	[17.5-19.4]
C2527	260	136	78	214	0.57	0.130	0.94	16,5	[14-15.5]
C2579	300	43	43	86	1	0.128	0.92	6	[5.1-6.2]

TABLE 4.1: Composition of the C2217, C2527, and C2579 multi-layered precursors consisting of successive InGaP, InP and InGaAs material layers deposited on top of a nominal InP substrate. The thicknesses  $h_{\text{In}_{1-x}\text{Ga}_x\text{P}}$ ,  $h_{\text{InP}}$ ,  $h_{\text{InGaAs}}$  and  $h$  of InGaP, InP, InGaAs layers and bilayer InGaP/InP, are expressed in nanometers, and  $\xi = h_{\text{In}_{1-x}\text{Ga}_x\text{P}}/h_{\text{InP}}$ . The proportion of Gallium element  $x$  in the  $\text{In}_{1-x}\text{Ga}_x\text{P}$  layer induces a tensile strength in the bilayer InGaP/InP, equivalent to the lattice mismatch  $m = (a_{\text{InP}} - a_{\text{In}_{1-x}\text{Ga}_x\text{P}})/a_{\text{InP}}$  (%) where  $a_{\text{InP}}$  and  $a_{\text{In}_{1-x}\text{Ga}_x\text{P}}$  stand for the lattice parameters of InP and InGaP material respectively. Using Equation 1.21, we calculate the theoretical curvature radius, in  $\mu\text{m}$  ( $\pm 1 \mu\text{m}$ ), of the bilayer upon rolling. We indicate the range of the radius  $\rho_{\text{exp}}$  in  $\mu\text{m}$  measured on the real structures.

### 4.1.2 Production of the planar design

The next step in the fabrication of the rolled-up 2D PCM cavity deals with the preparation of the planar design from the previous multi-layered stacks. It represents a milestone of the overall technical process. Indeed, it first brings the photonic functionalities of the final cavity by patterning the material layers to form the PCM mirror. Second, the orientation and the dimensions of the planar design determines the 3D shape of the final rolled-up microstructure. In particular, we show below that the planar layout illustrated on the scanning electron microscope (SEM) picture in Figure 4.1 leads to the production of vertically standing tubular cavities.

The 2D photonic crystal pattern consists of a triangular lattice with a period  $a$  of circular holes with a radius  $r$ . We create the PCM by imprinting the pattern down into the InGaP/InP bilayer of thickness  $h$  through a combination of e-beam lithography and reactive ion etching (RIE) processes as described in Section 2.2. We note that the parameters  $a$ ,  $r$  and  $h$  have been adjusted in Section 3.2 ( $a = 1.2 \mu\text{m}$ ,  $r = 0.48 \mu\text{m}$  and  $h = 0.23 \mu\text{m}$ ) to achieve high reflection properties of the PCM at normal incidence.

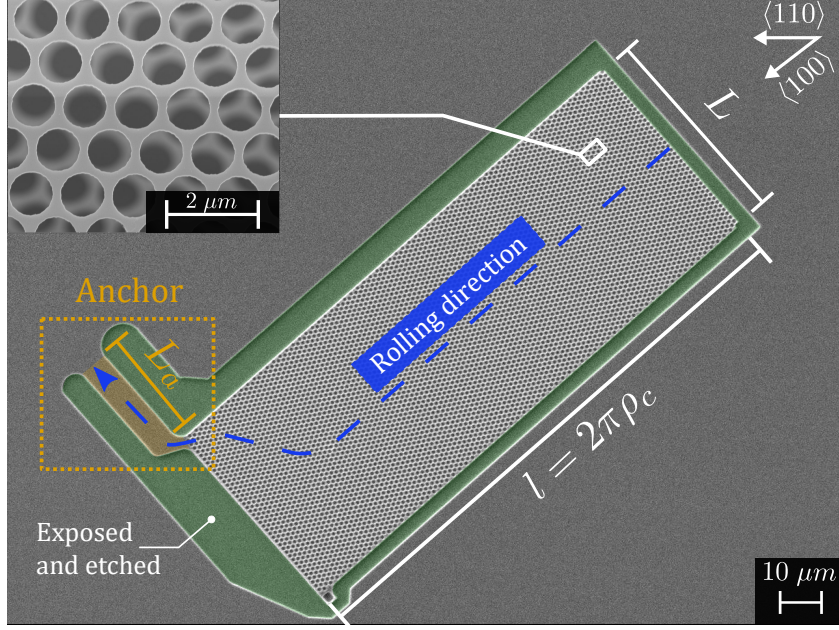


FIGURE 4.1: Scanning electron microscopy (SEM) picture of the planar design of the rolled-up 2D PCM cavity upon electron beam lithography and reactive ion etching (RIE) processes. The inset picture shows a close-up view of the 2D triangular lattice photonic crystal pattern. The under-etching step first occurs in the shaded green surrounding strip, exposed to e-beam and RIE beforehand, which triggers the rolling of the 2D PCM along the blue dashed arrow. It continues at the anchor level outlined in yellow dashed line and specifically designed to lift the so-formed microtube vertically. The dimension of the photonic crystal along the rolling direction  $L_p$  is set to  $2\pi\rho_c$ , with  $\rho_c$  the radius of the final tubular cavity, to achieve one rolling of the 2D PCM. In the perpendicular direction, the dimension  $L$  determines the length of the tubular cavity.

The inset SEM picture in Figure 4.1 shows a close-up view of the patterned InGaP/InP bilayer membrane obtained after the lithography and etching steps.

We intend then to roll the 2D PCM up into a tubular shape with a prescribed length  $L$  and radius  $\rho_c$ . Toward this goal, we design a rectangle of length  $l$  and width  $L$  which encompasses the photonic crystal pattern as depicted in Figure 4.1. We define the PCM rolling direction denoted by a blue arrow along the length  $l$  of this rectangle which coincides with the perimeter of the future tubular cavity. The other dimension  $L$  relates to the cavity length. We achieve  $n \in \mathbb{N}^*$  complete rolling of the PCM by adjusting  $l$  to  $n$  times the perimeter  $2\pi\rho_c$  of the final tubular microstructure.

The etching of the InGaAs sacrificial layer releases the stress contained in the InGaP/InP bilayer, which triggers the rolling of the PCM. On account of the anisotropic nature of the etching process, we need to make the PCM rolling direction (along  $l$ ), coincide with the direction of the highest etching rate to avoid the competitive rolling along the length  $L$ . In the (100)-oriented InP nominal substrate, the preferential etching direction, namely the crystal direction  $\langle 100 \rangle$ , orients at  $45^\circ$  with respect to the cleavage planes along  $\langle 100 \rangle$ . Moreover, due to the epitaxial growth mode, the InGaAs material layer shares the same crystallographic orientation as the underlying InP substrate, so that we identify the direction  $\langle 100 \rangle$  of the highest etching rate as represented in Figure 4.1. Finally, we add a strip (shaded green part) in the planar design and surrounding the PCM pattern, undergoing e-beam exposition and RIE etching processes. The strip facilitates the penetration of the etching solution towards the sacrificial layer, initiating the under-etching process. Looking closely at the border of the PCM, we remark the gradual extension of the plain membrane from the starting point of the rolling

direction until the end of the PCM pattern. This specific design feature allows delaying the sacrificial layer etching along  $L$  in aid of the etching and rolling along  $l$ .

The final part of the planar design deals with the vertical lifting of the tubular cavity in the prevision of the optical characterization measurements. To this end, we design a specific anchor of length  $L_a$  shaded in yellow in Figure 4.1 with a twofold function: lifting the rolled-up PCM and retaining it to the substrate. The under-etching of the PCM results in the formation of a horizontal microtubular cavity. It continues at anchor level to make the microtube axis rotate and orient along the normal to the sample surface. The elbow shape of the anchor favours the rolling along the longest dimension and prevents a deadlock situation due to the competitive rolling along the shortest dimension. We also turned original sharp corners delimiting the anchor into round corners to avoid high concentrations of stresses, leading potentially to cracking and fracture of the design during the under-etching. The rotation finally stops at the anchor's ending so that the microtube stands vertically but remains attached to the substrate. We adjust the length  $L_a$  to perform a  $90^\circ$ -rotation of the microtube from the sample surface, namely  $L_a = 1/4 \times 2\pi\rho_c$  with  $\rho_c$  the cavity radius.

### 4.1.3 Description of a typical sample

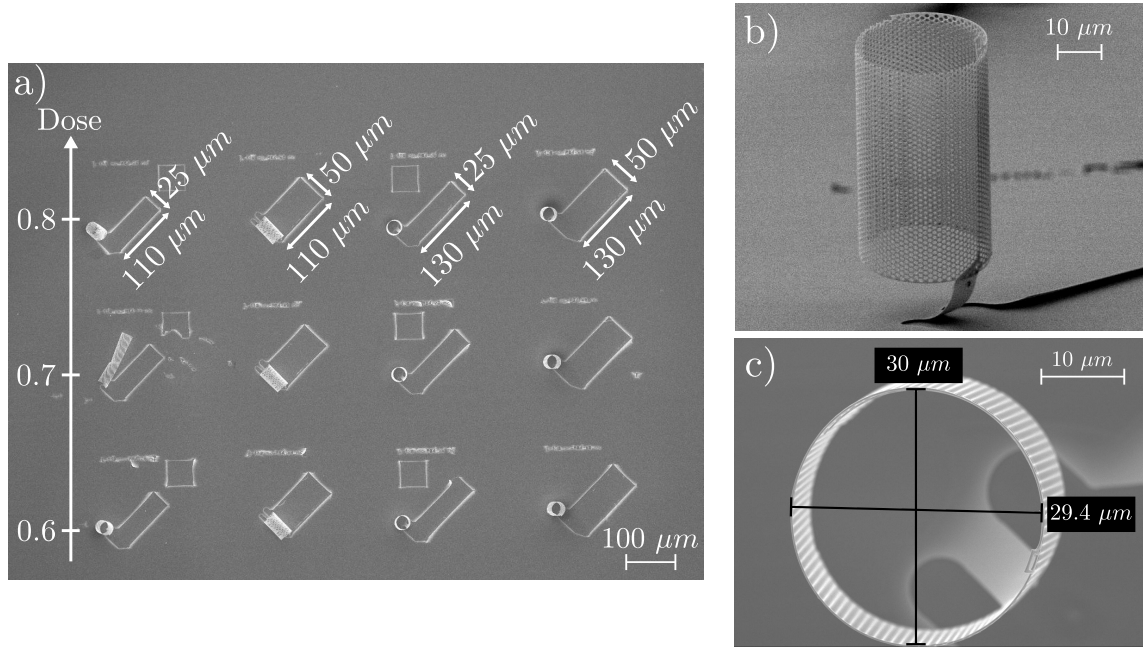


FIGURE 4.2: a) SEM picture from the top of a matrix of 12 microstructures produced after the under-etching and drying steps. Each row of structures corresponds to a different value of the exposure dose, from 0.6 to 0.8, starting at the bottom of the image. In the first (third) and second (fourth) columns, the length  $L$  of the planar designs is set to  $25\ \mu\text{m}$  and  $50\ \mu\text{m}$ , respectively, while the size  $L_p$  is fixed at  $100\ (130)\ \mu\text{m}$ , to achieve a bit more than one rolling (one rolling and a half) of the 2D PCM. b) SEM profile picture of a rolled-up 2D PCM microtube lifted vertically and retained by the anchor design to the substrate. c) SEM picture of the top of a rolled-up PCM cavity on which we estimate two orthogonal diameters.

In the final phase of the fabrication of tubular photon cages, we plunge the sample into a diluted  $\text{FeCl}_3$  solution to etch the InGaAs sacrificial layer. The operation triggers the rolling and vertical lifting of the PCM mirror, according to the planar design. We illustrate in Figure 4.2.a) a typical matrix of 12 microstructures from the sample C2527 obtained after completing one fabrication cycle. The three rows of the matrix

corresponds to three values of the exposures dose 0.6, 0.7 and 0.8, set during the lithography step. The sweep of the dose allows to find a good compromise between high resolved patterns and complete etching of the material layers. In the four columns, we change the dimensions of the planar design. We set the length  $l$  of the first (last) two designs to 110 (130)  $\mu m$  to achieve one rolling (one rolling and a half) of the PCM into a microtube of length 25  $\mu m$  and 50  $\mu m$ , alternatively.

We notice in Figure 4.2.a) the successful rolling and lifting of 8 structures out of the 12 planar designs of the matrix. Moreover, we count 3 horizontal rolled-up PCM while the remaining planar design has failed to roll and stand up. More generally, out of the 12 matrices of 12 microstructures in the sample C2527, we report about 49 % of successful rolling and lifting of the planar templates against 26 % and 24% of horizontal microtubes and unrolled/missing structures, respectively. The SEM picture in Figure 4.2.b) shows the successful vertical lifting of one rolled-up PCM specimen with almost 90° angle to the sample surface, which remains attached via the anchor. Furthermore, we estimate the diameter of the tubular cavity to 30  $\mu m$  and 29.4  $\mu m$  along orthogonal radial directions as depicted on SEM picture Figure 4.2.c) of the top of the vertical tubular cavity. We appreciate the uncertainty of the radius measurement due to the tilt of the cavity, as mentioned previously.

#### 4.1.4 Mechanical properties of the tubular microstructures

Some of the PCM structures manage to roll into a microtube but fail to stand up, as observed earlier. Thus, we have investigated on the possibility to detach manually the horizontal microtubes, to displace and make them stand vertically onto another substrate. Toward this goal and with the help provided by Solène Brottet, we have used the micromanipulator of a focused ion beam (FIB) device to handle a horizontal cavity specimen as illustrated on the FIB picture of Figure 4.3.a). The tip of the micromanipulator (green shaded object) is coated beforehand with a carbon deposit (red shaded cluster) to hook the microtube. We operate in a carbon atmosphere to avoid damaging the surface of the tubular cavity with the ion beam. We detach the microtube progressively away from the substrate as depicted on the SEM picture Figure 4.3.b). The operation requires careful manipulation not to tear the microstructure off. We have finally succeeded in completely removing the microtube of the substrate while preserving its integrity. We have then displaced the microtube and installed it onto a glass substrate, in a vertical position as represented on 4.3.d) and e). The experiment has proved, qualitatively, the elastic behaviour of the InP-made rolled-up PCM tubular cavities. Indeed, it deforms when solicited mechanically and softly but recovers its initial tubular shape when released from external strains. We also point out the opportunity to recycle horizontal microtubes in displacing them onto another substrate and in another position. Such an operation holds promises for the integration of tubular photonic cavities onto more complex platforms.

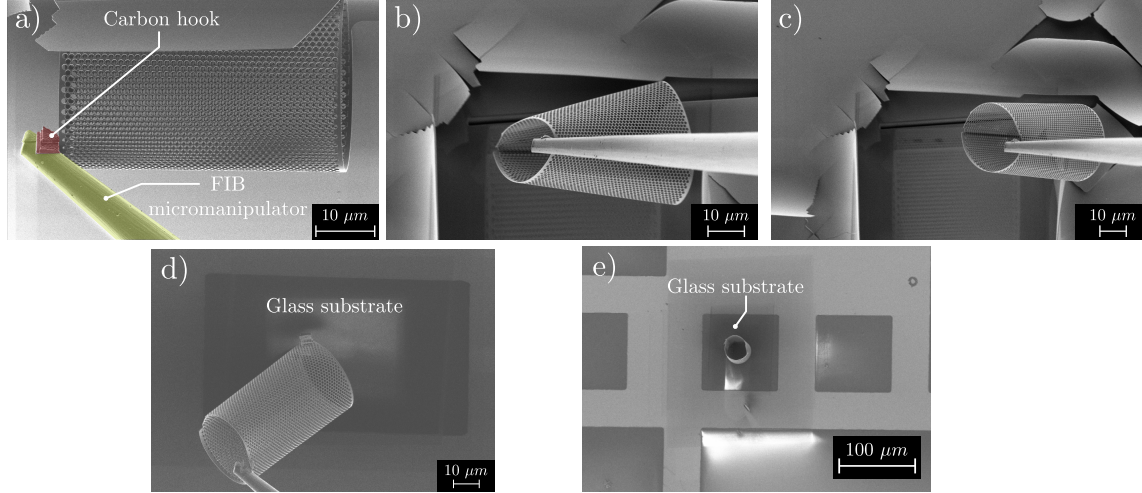


FIGURE 4.3: a) Focused ion beam (FIB) picture of an horizontal rolled-up 2D PCM being hooked by a carbon deposit (red shaded form) on the micro-manipulator (yellow shaded tip) of the FIB device. b) SEM picture of the photonic microtube which deforms as the micro-manipulator detaches it progressively from the substrate. c) SEM picture of the photonic tubular cavity back to its initial tubular shape and released completely from the substrate but bonded to the micro-manipulator. d) FIB picture of the tubular cavity being placed on a glass substrate. e) SEM picture of the tubular cavity standing vertically on the glass substrate.

#### Key points of the section

In conclusion to the section, we have presented typical fabrication results covering the entire production scheme of standing rolled-up PCM tubular cavities.

- We have detailed the composition of the multi-layered precursors C2217, C2527, and C2579 obtained upon molecular beam epitaxy (MBE) deposition. We have proved the consistency of the theoretical estimations of the final microtube radius with the measurements on real structures.
- We have emphasized the crucial role of the planar design to achieve the successful rolling and vertical lifting of the PCM into standing tubular photonic cavities.
- We report a reproducible fabrication of vertical tubular cavities, reckoned to almost 50 % at the scale of the whole sample C2527, for instance.
- We have finally demonstrated the possibility of transferring the so-formed rolled-up PCM cavities (vertical or horizontal) onto another substrate, holding promises for their integration onto more complex platforms.

## 4.2 Optical characterization of the photon cages

### 4.2.1 Introduction

The last step in the study of tubular photon cages deals with the optical characterization of the fabricated microstructures presented in the previous section. We aim to bring experimental proof of the 3D confinement of light in the hollow core of the



cylindrical cavities according to theoretical predictions of Chapter 3. In particular, we have shown in 3 that the scanning near-field optical microscopy (SNOM) represents a suitable method for probing the optical modes generated in the hollow part of the vertical tubular cavities. Moreover, using a bowtie nanoaperture (BNA) probe allows the selective detection of transverse electric (TE) modes.

In this section, we present SNOM measurements performed inside tubular microstructures from the samples C2217, C2527 and C2579 in the light of the analytical and numerical models. First, we investigate the modal response of the tubular photon cages in sample C2217 and its evolution while varying the excitation wavelength at fixed insertion depth of the probe in the hollow core. We propose a systematic post-process to analyze the scans and identify the emerging modes. Second, we assess the reproducibility of the SNOM measurements in cavities from the sample C2527. We also examine the vertical confinement of the modes by performing near-field scans at a fixed excitation wavelength but varying insertion depth of the probe. Finally, we explore the optical response of tubular cages with smaller curvature radius.

### 4.2.2 Modal response of photon cages

#### Tubular photon cages on sample C2217

We conduct a first set of SNOM measurements in tubular cavities fabricated from the C2217 multi-layered precursor described in Section 4.1. The sample C2217 contains 6 matrices of 15 planar PCM templates designed to roll up into vertical rolled-up PCM cavities with a length of 25 or 50  $\mu\text{m}$ . We report on average in one matrix the successful rolling and lifting of 7 templates into standing cavities. The remaining structures roll into horizontal microtubes or get damaged upon drying. We recall the key role of the lifting operation to facilitate the insertion of the SNOM probe inside the tubular microstructures. We show on the SEM picture in Figure 4.4.a) a part of one matrix of the sample C2217 upon fabrication. For instance, we have spotted three potential candidates for the measurements delimited in red dashed contour. In the close-up view in Figure 4.4.b), we appreciate the uplifting of one specimen attached to the substrate via the anchor design. According to 4.1, the radii of the tubular cages in sample C2217 span the interval  $[17.5 - 19] \mu\text{m} \pm 1\mu\text{m}$ .

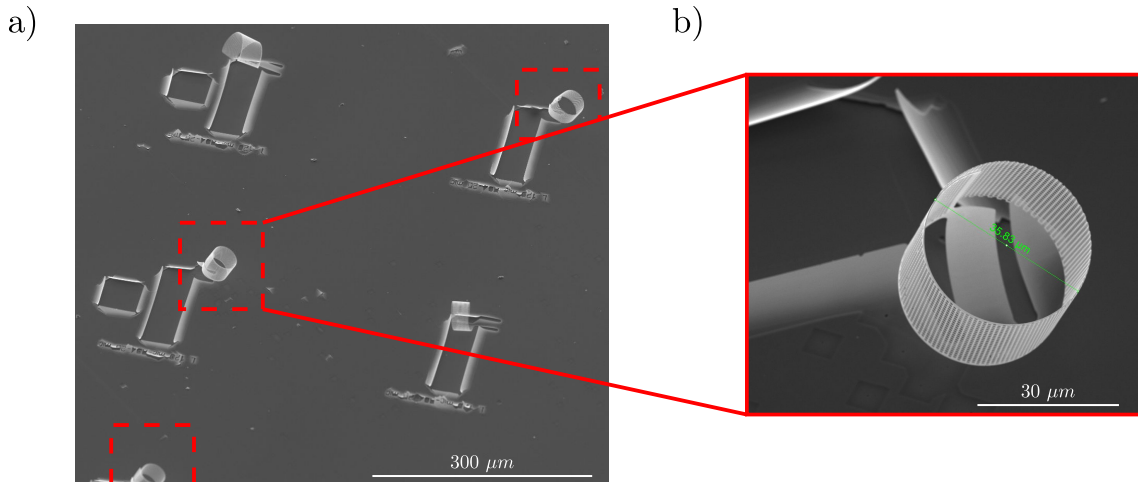


FIGURE 4.4: a) SEM picture of a part of a matrix of tubular photon cages on sample C2217. b) Close-up SEM view on a standing microtube.

### SNOM scans at various wavelengths

The first set of SNOM measurements investigates the modal response inside a  $50\ \mu\text{m}$ -long cavity specimen. In practice, we approach and centre the BNA probe with respect to the cavity, as described in Chapter 2. We insert the SNOM probe progressively down into the hollow core, close to the middle of the cavity, to detect the modes. We notify that the tapered shape of the probe not only limits the tip's insertion depth, noted  $d$  and measured from the top surface, but also the dimensions of the scan zone.

Fixing the depth of the probe's tip as sketched in Figure 4.5, we perform a series of scans of the electric field intensity  $|\vec{E}|^2$  covering a  $12 \times 12\ \mu\text{m}^2$  cross-section area. We sweep the excitation wavelength to span the entire range of the TUNICS laser source, from  $1.450\ \mu\text{m}$  to  $1.580\ \mu\text{m}$  with a  $10\ \text{nm}$  step. We present in Figure 4.5 the intensity maps recorded in order of increasing wavelengths. We observe a predominant pattern of concentric circles alternating between an antinodal (blue frame) and a nodal (green frame) central region. We note that, at  $1.5\ \mu\text{m}$ , the central region reveals a more complex pattern, preventing unambiguous classification. We recognize from Section 3.3 the pattern signatures of generic cylindrical cavity modes  $\text{TE}_{0,n}$  and  $\text{TE}_{1,n}$  with central nodes and antinodes, respectively. However, no clear spectral signature indicates the transition between the modes of the same family. We fail, for instance, to distinguish the three modes of type  $\text{TE}_{1,n}$  detected at  $1.47$ ,  $1.48$  and  $1.49\ \mu\text{m}$  due to their apparent pattern similarities. To overcome the difficulty, we identify the modes at each wavelength of the sweep by determining their radial order  $n$ . To this end, we follow a specific procedure described below to extract 1D profiles of the maps and compare them to theoretical profiles.

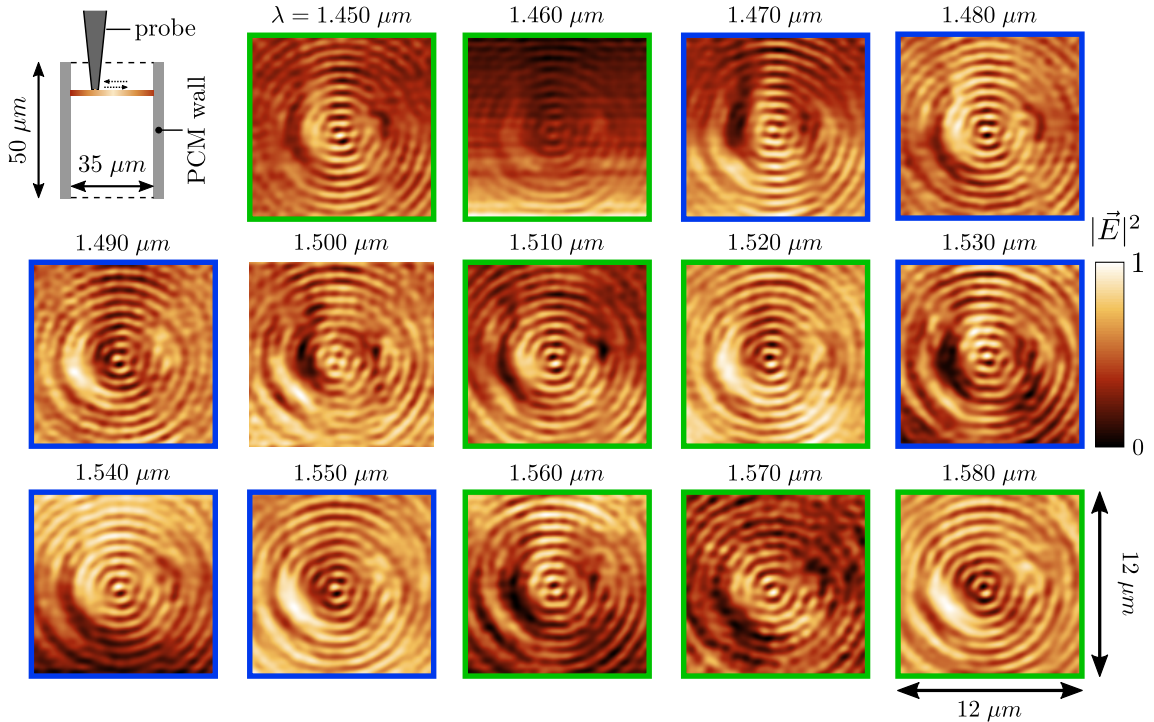


FIGURE 4.5: Schematics: scanning near-field optical microscope (SNOM) measurements inside a  $50\ \mu\text{m}$ -long tubular photon cage from sample C2217 of diameter in the order of  $35\ \mu\text{m}$ . Pictures:  $12 \times 12\ \mu\text{m}^2$  maps of the normalized electric field intensity  $|\vec{E}|^2$  recorded over a cross-section near the cavity centre for excitation wavelengths ranging from  $1.450$  to  $1.580\ \mu\text{m}$ .



### Analysis procedure of the maps

We realize the determination of the radial order  $n$  of the detected cavity modes  $TE_{0,n}$  and  $TE_{1,n}$  through a systematic three step procedure. We illustrate the procedure by identifying for instance the mode recorded at  $1.450 \mu m$  of type  $TE_{0,n}$  represented in Figure 4.6.a). We have included the maps of the mode in a scale drawing of a  $35 \mu m$ -diameter cavity and extended the intensity pattern schematically in the background to appreciate the fraction of the cavity cross-section covered by the scan zone. The close-up view of the map in 4.6.b) allows a better visualization of the intensity oscillations over the scan zone. We also notice the polarization effect of the BNA probe which optimizes the contrast of the intensity pattern along the BNA gap direction as outlined in blue dashed line.

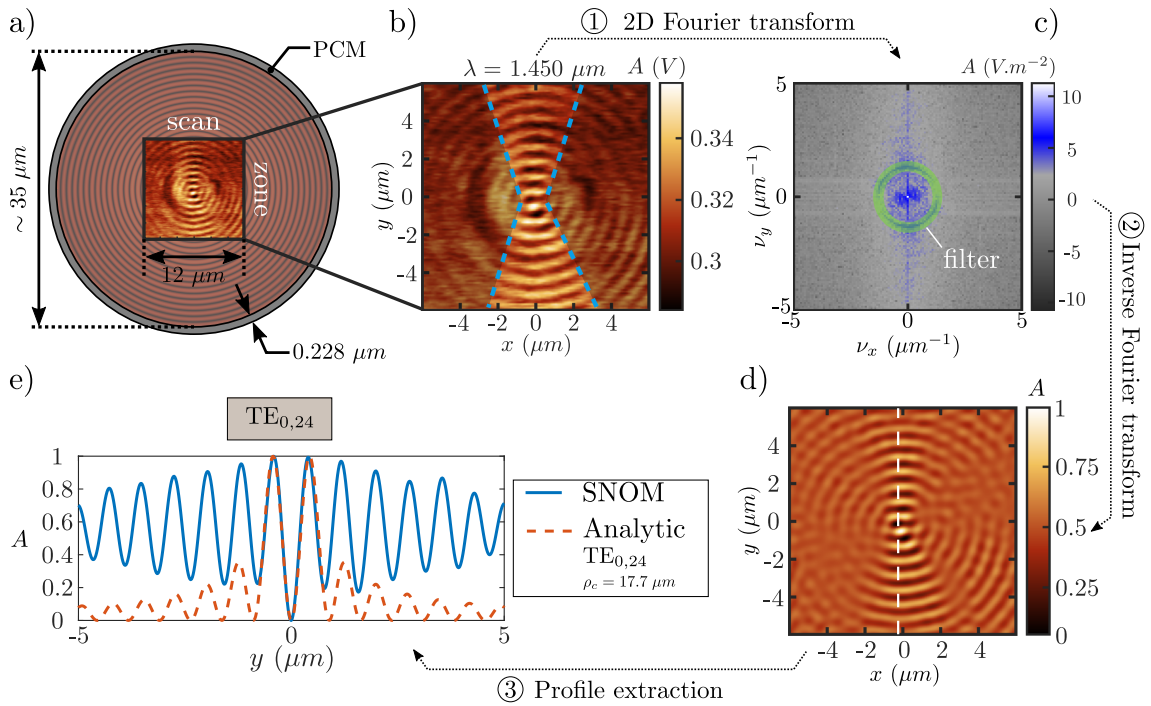


FIGURE 4.6: Analysis scheme of typical near-field optical scans obtained in tubular photon cages. a) Near-field optical scan of the electric field intensity spanning a  $12 \times 12 \mu m^2$  area in a cross-section plane of a tubular photon cage of diameter estimated to  $35 \mu m$  and wall thickness of  $0.228 \mu m$ . b) Close-up view of the electric intensity map recorded at  $\lambda_1 = 1.450 \mu m$ . The measured signal is a voltage with amplitude  $A$  in volts (V) directly related to the electric intensity. c) Fourier transform of the intensity map b) as a function of spatial frequencies  $\nu_x$  and  $\nu_y$  along the Cartesian directions  $x$  and  $y$ . We apply a band-pass filter represented by a pale green ring to isolate the radial pattern of the map. d) Inverse Fourier transform of the filtered map c). e) Profile of the electric intensity in blue line extracted from map d) along the white dashed line. The profile matches the theoretical profile of generic cylindrical cavity mode  $TE_{1,24,p}$  plotted in orange dashed line and calculated in a cavity of radius  $\rho_c = 17.7 \mu m$ .

We first isolate the main radial pattern observed. To this end, we calculate the 2D spatial Fourier transform of the intensity spatial distribution. In particular, we plot in Figure 4.6.c) the evolution of the complex coefficients modulus in logarithmic scale associated to each spatial harmonics within the interval  $[-5 \ 5] \mu m^{-1}$ . We observe a ring of high amplitude coefficients which relates to the radial intensity oscillations in the real space.

Second, we apply a band-pass filter (transparent green-shaded band) to select the spatial components responsible of the radial oscillations in real space exclusively. We

perform an inverse spatial Fourier transform of the filtered components to form the radial intensity pattern represented in real space on Figure 4.6.d).

Third, we extract a profile of the filtered map in d) along a diameter of the cavity (white dashed line) as plotted on 4.6.e) in blue straight line. We model the 1D experimental profile with the theoretical profile of a generic mode  $TE_{0,n}$  supported by an equivalent cylindrical cavity of tunable radius  $\rho_{eq}$  and order  $n$ . First fixing the radius at  $17.5 \mu m$ , we find a satisfying matching between theoretical and real data, minimizing the relative errors between the peaks' positions, for  $n = 24$ . We improve the fit by adjusting the value of  $\rho_{eq}$ : we report a better compliance for  $\rho_{eq} = 17.7 \mu m$  as depicted on Figure 4.6.e) with orange dashed theoretical profile. We report relative errors in the order of tens of % for almost all the peaks. For the first peaks taken from the origin at  $0 \mu m$ , the error reaches a few %, suggesting the presence of other modes not investigated here.

### Identification of the modes

We have applied the filtering procedure to compare the radial oscillations of the intensity maps and determine the radial orders  $n$  of the modes appearing at each of the sweep wavelengths. We have divided in Figure 4.7 the profiles in two categories including the modes of type  $TE_{0,n}$  or  $TE_{1,n}$ .

We observe that the profiles of the  $TE_{0,n}$  modes emerging at  $1.450 \mu m$  and  $1.460 \mu m$  coincide in Figure 4.7.a), implying identical radial orders  $n$ . We draw similar conclusions for the group of modes detected from  $1.5$  to  $1.52 \mu m$ , and from  $1.56$  to  $1.58 \mu m$ , considering matching profiles in Figure 4.7.b) and e), respectively. Similarly, in the  $TE_{1,n}$  family, the group of modes from  $1.470$  to  $1.490 \mu m$  show identical radial profiles, as well as the modes from  $1.530$  to  $1.550 \mu m$ , as shown on 4.7.f) and h).

Conversely, we infer from Figure 4.7.b) and d) that, though sharing the same azimuthal order  $n = 0$ , the modes recorded at  $1.450$  and  $1.510 \mu m$  on one hand, at  $1.510$  and  $1.560 \mu m$  on the other hand, exhibit distinct radial orders  $n$  according to the profile mismatch. Similarly, the modes at  $1.470 \mu m$  and  $1.530 \mu m$  belonging to the family of  $TE_{1,n}$  modes show shifted radial oscillations in their profiles as plotted in Figure 4.7.g).

We apply the remaining steps of the procedure to determine the radial orders  $n$  of each of the experimental modes. We find a good matching between the real profiles and the theoretical profiles calculated in an equivalent ideal cylindrical cavity of radius  $\rho_{eq} = 17.7 \mu m$  with the following classification:

- $\lambda = 1.450$  to  $1.460 \mu m$ : mode  $TE_{0,24}$ ;
- $\lambda = 1.470$  to  $1.490 \mu m$ : mode  $TE_{1,24}$ ;
- $\lambda = 1.500$  to  $1.520 \mu m$ : mode  $TE_{0,23}$ ;
- $\lambda = 1.530$  to  $1.550 \mu m$ : mode  $TE_{1,23}$ ;
- $\lambda = 1.560$  to  $1.580 \mu m$ : mode  $TE_{0,22}$ .

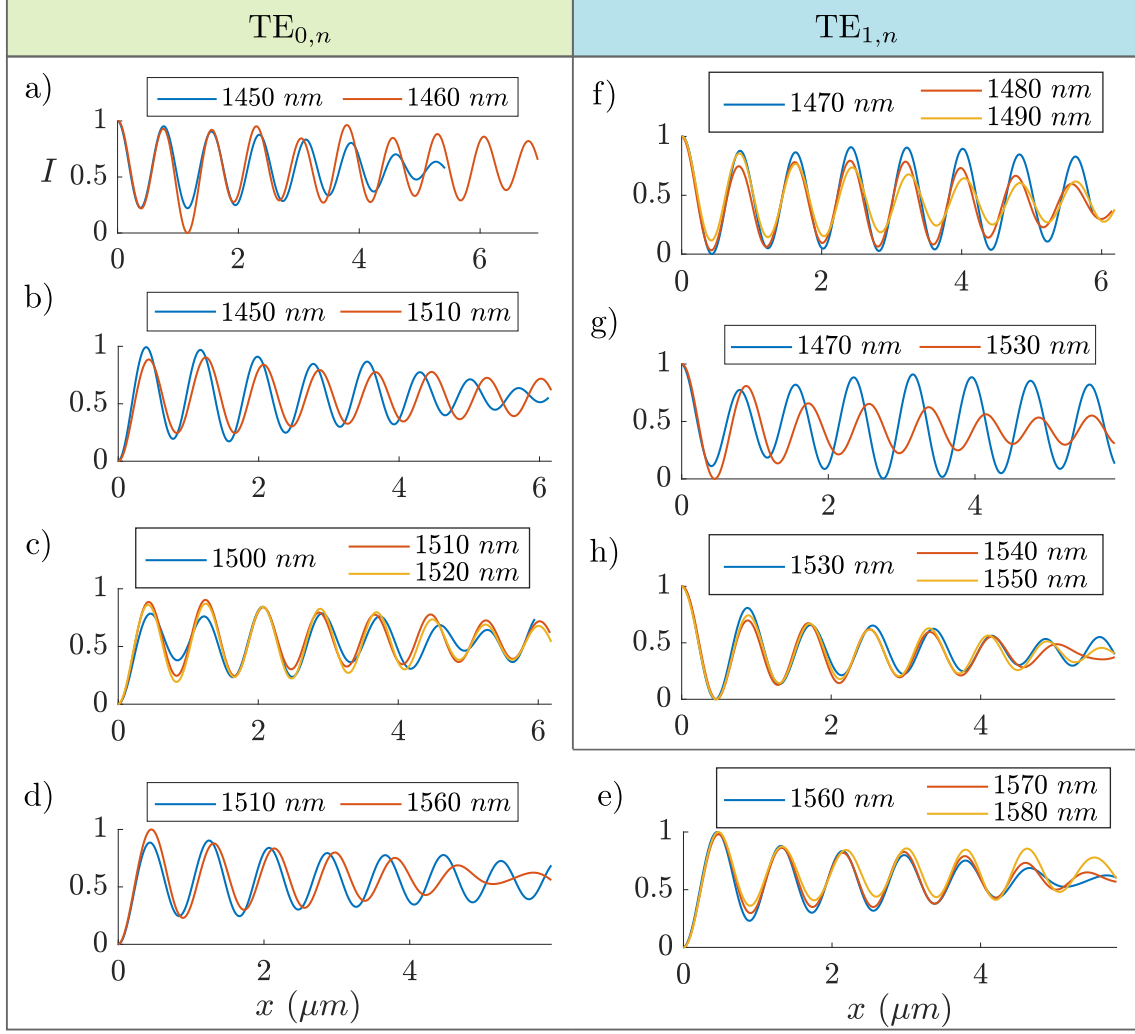


FIGURE 4.7: Comparison of profiles extracted from the electric field intensity maps of modes of type  $TE_{0,n}$  and  $TE_{1,n}$  recorded between 1.450 and 1.580  $\mu m$  and represented in Figure 4.5. Prior to the profiles' extraction, we apply a spatial filtering to the maps to filter radial oscillations.

### Discussion on the results

The identification of the experimental modes has revealed three essential features. First, we detect alternatively the presence of cavity modes of type  $TE_{0,n}$  and  $TE_{1,n}$  with decreasing radial orders  $n$  in order of increasing excitation wavelength  $\lambda$ . Indeed, the radial order of  $TE_{0,n}$  ( $TE_{1,n}$ ) evolves from 24 to 22 (from 24 to 23) over the entire source bandwidth. Those preliminary results concur with the theoretical predictions presented in Chapter 3 as we retrieve the same spectral distribution of cavity modes in tubular photon cages of radius 17.5  $\mu m$  simulated with the FDTD method.

The second feature concerns the absence of spectral signatures of the modes as we detect groups of cylindrical cavity modes  $TE_{0,n}$  and  $TE_{1,n}$  over the entire laser spectral range. Within each group of type  $TE_{0,n}$  ( $TE_{1,n}$ ), the modes share the same radial  $n$  and azimuthal  $m$  orders, hence exhibit the same intensity patterns. For instance, each of the electric field intensity maps generated between 1.470 and 1.490  $\mu m$  corresponds to the cylindrical cavity mode  $TE_{1,24}$  pattern. We have also performed  $12 \times 12 \mu m^2$  SNOM scans for excitation wavelengths varying from 1530 to 1532 nm down to 0.2 nm resolution. We have gathered the resulting maps of the normalized electric field intensity  $|\vec{E}|^2$  in Figure 4.8.a). We first remark the detection of cylindrical cavity modes

patterns with a central antinode, hence of type  $TE_{1,n}$ , at each wavelength. Using the spatial filtering procedure, we compare then the modes' profiles extracted along the BNA high contrast direction, coinciding with the  $y$ -axis direction in Figure 4.8.a). We find an exact matching of the profiles superimposed in Figure 4.8.b), implying a common radial order  $n = 23$  according to the previous results.

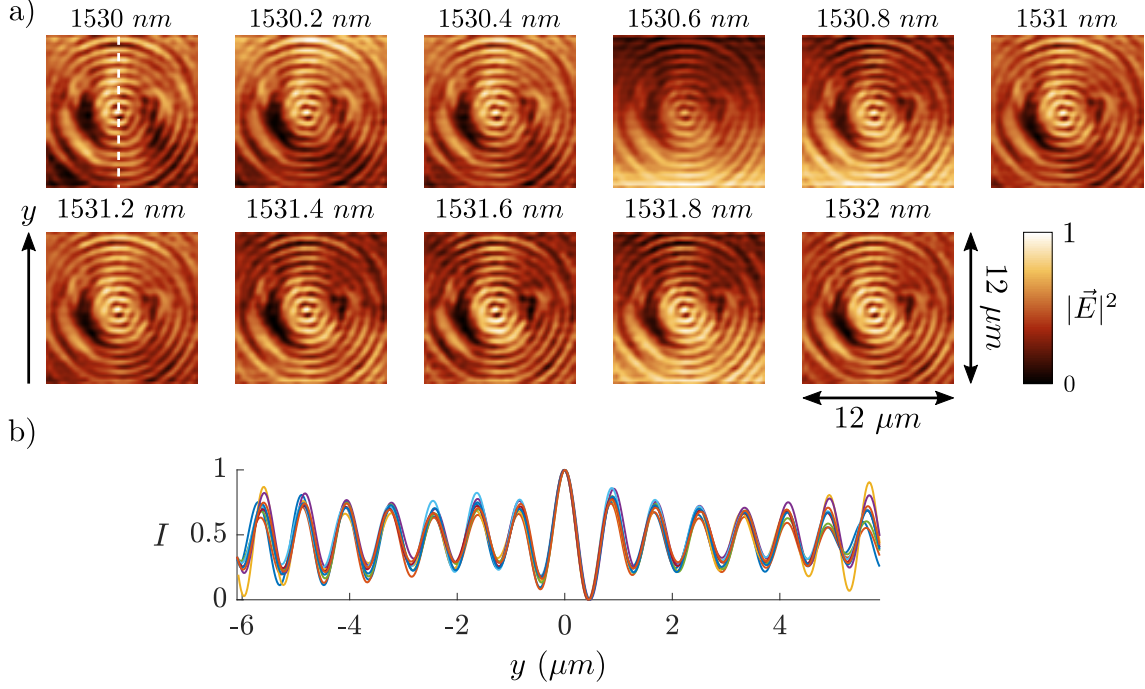


FIGURE 4.8: a) SNOM maps of the electric field intensity  $|\vec{E}|^2$  in normalized units over a  $12 \times 12 \mu m^2$  cross-section area inside a tubular photon cage from sample C2217. The excitation wavelength ranges from 1530 to 1532 nm with a 0.2 nm step. b) Superimposition of modes' profiles extracted from the maps in a) after spatial filtering along the  $y$  axis.

We explain the quasi-continuous detection of cavity modes' patterns defined with identical orders  $(m,n)$  by the presence of longitudinal ( $z$  axis) modes. Indeed, in addition to transverse confinement of light, finite-length cylindrical cavities host stationary modes forming along the cylinder axis upon reflection on top and bottom boundaries as explained in Chapter 3. The dispersion of  $TE_{m,n}$  modes along the cavity axis, hence the axial component  $k_z$  of the wavevector becomes quantized according to  $k_z = p\pi/L$  where  $L$  designates the cavity length and  $p \in \mathbb{N}^*$  the axial order. We describe the axial field distribution of modes  $TE_{m,n,p}$  for given  $(m,n)$  with the order  $p$  referring to the number of field lobes. Therefore, two consecutive modes  $TE_{m,n,p}$  and  $TE_{m,n,p+1}$  exhibit identical transverse profiles but differ of axial distributions.

We have plotted in Figure 4.9 the theoretical dispersions of the cavity modes  $TE_{0,22,p}$ ,  $TE_{1,23,p}$ ,  $TE_{0,23,p}$ ,  $TE_{1,24,p}$  and  $TE_{0,24,p}$  with  $p$  varying from 1 to 15 in a  $17.7 \mu m$ -radius tubular cavity of length  $L = 50 \mu m$ . The graph reveals the high density of modes in the spectral range of interest and the spectral proximity of the  $p$  orders. For instance, we count 13 modes  $TE_{1,24,p}$  with  $p = 2, 3, \dots, 14$  emerging successively in between the fundamental modes  $TE_{1,24,1}$  and  $TE_{0,24,1}$  at  $\lambda_{TE_{1,24,1}} \simeq 1.4906 \mu m$  and  $\lambda_{TE_{0,24,1}} \simeq 1.4597 \mu m$ , respectively. Moreover, we estimate the spectral spacing between the modes  $TE_{0,24,1}$  and  $TE_{0,24,2}$  to 0.5 nm. In theory, we could discriminate the two modes with a spectral resolution below 0.5 nm as provided by the TUNICS laser source. In reality, the cavity modes show a spectral extension related depend-

ing on their lifetime in the cavity, namely their quality factors noted  $Q$ . Therefore, a bandwidth of the modes  $\text{TE}_{0,24,1}$  and  $\text{TE}_{0,24,2}$  larger than  $0.25 \text{ nm}$  leads to a spectral overlap and allows the quasi-continuous probing of  $\text{TE}_{0,24,p}$  modes' transverse patterns. In particular, we apply the same reasoning to explain the quasi-continuous detection of the mode  $\text{TE}_{1,23,12}$  from  $1.53 \mu\text{m}$  to  $1.532 \mu\text{m}$  with a  $0.2 \text{ nm}$  step observed in Figure 4.8. We also project each wavelength of the  $10 \text{ nm}$ -sweep measurements presented in Figure 4.5 onto the theoretical dispersion curves to evaluate the  $p$  orders of the detected modes. We find that the  $p$  order varies from 1 to 12-13, accordingly to the values of the  $p$  orders (ranging from 1 to 11) calculated in a  $50 \mu\text{m}$ -long cavity of radius  $17.5 \mu\text{m}$  with the FDTD method in Chapter 3.

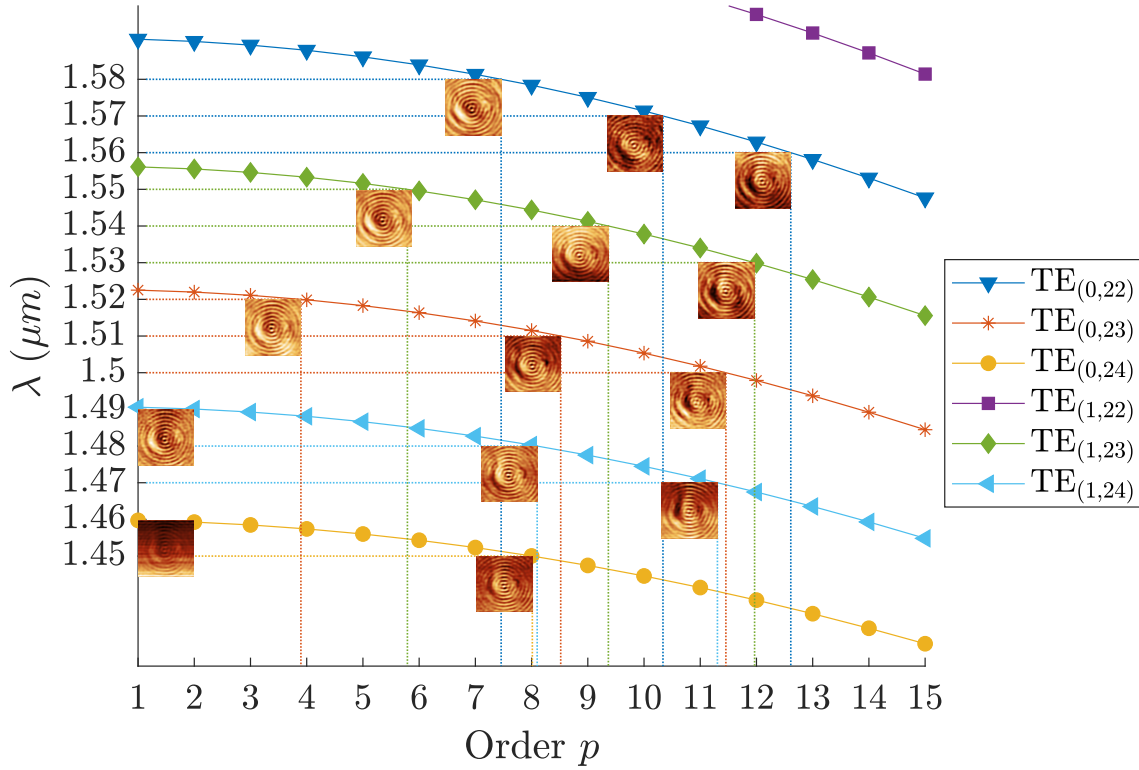


FIGURE 4.9: Theoretical dispersion curves of cylindrical cavity modes  $\text{TE}_{0,22,p}$ ,  $\text{TE}_{0,23,p}$ ,  $\text{TE}_{0,24,p}$ ,  $\text{TE}_{1,22,p}$ ,  $\text{TE}_{1,23,p}$  and  $\text{TE}_{1,24,p}$  as a function of the axial order  $p$  in a cylindrical cavity of radius  $\rho_{\text{eq}} = 17.7 \mu\text{m}$  and length  $L = 50 \mu\text{m}$ . We project the wavelengths and maps of the  $10 \text{ nm}$ -sweep scans presented in Figure 4.5 onto the dispersion curves to extract the corresponding  $p$  orders.

Finally, we report the selective detection of cylindrical cavity modes with low azimuthal orders, especially  $\text{TE}_{0,n,p}$  and  $\text{TE}_{1,n,p}$  modes, over the entire spectral range from  $1.450 \mu\text{m}$  to  $1.580 \mu\text{m}$ . We propose two reasons to account for this specific sensitivity, related to:

- the reflectivity of the PCM: according to Chapter 2, within the operational range of the TUNICS source, the PCM reflectivity at normal incidence remains higher as compared to oblique incidences. Moreover, for all incidence angles, the reflectivity decreases for smaller wavelengths until reaching a minimum at  $1.45 \mu\text{m}$  coinciding with a Fabry-Pérot resonance of the membrane. Assuming the dependence between high incidence angles and the formation of cavity modes with high azimuthal orders  $m$ , we understand the preferential detection of  $\text{TE}_{m,n,p}$  modes with low orders  $m$  in the spectral range of interest.
- the size of the scan zone: due to the tapered shape of the probe tip, the scan



zone area represents a limited fraction (about 15 %) of the cavity cross-section area. Moreover, the central node of the cross-section cavity mode  $TE_{m,n,p}$  pattern widens as the azimuthal order  $m$  increases. Therefore, we probe cylindrical cavity modes with low azimuthal orders for which the modes' intensity patterns form within the scan zone, exclusively.

We notice, however, a rather uniform distribution of the intensity in the patterns of the modes with azimuthal orders  $m = 0, 1$  contrary to high concentration of field energy predicted theoretically. This observation tends to reinforce the idea of an overlap of cavity modes patterns instead of the exclusive excitation of a single cavity mode.

#### Key points of the subsection

The first set of SNOM measurements performed inside tubular photon cages of sample C2217 have already shown great consistency with numerical and analytical predictions:

- First and foremost, we have evidenced the presence of cylindrical cavity modes in real tubular rolled-up 2D PCM experimentally, bringing practical demonstration of the photon cages concept.
- Second, the continuum of modes detected within the source spectral range, even down to the highest spectral resolution concur with the high spectral density of modes announced both by FDTD and analytic calculations on finite length cylindrical microresonators.
- Third, we have probed cylindrical cavity modes  $TE_{m,n,p}$  with low azimuthal orders  $m = 0, 1$  in agreement with the PCM reflection performances within the operational range at normal and oblique incidence calculated theoretically. Moreover, the spectral and spatial distribution of the detected modes  $TE_{0,24,p}$ ,  $TE_{1,24,p}$ ,  $TE_{0,23,p}$  and  $TE_{1,23,p}$  match the FDTD simulation results.

### 4.2.3 Reproducibility and vertical confinement

We have performed a second series of SNOM measurements inside tubular photon cages fabricated on sample C2527 with a two-fold objective: assess the reproducibility of the SNOM experiment and examine qualitatively the vertical confinement of the modes supported by the tubular cages.

#### Tubular photon cages on sample C2527

In sample C2527, we arrange 12 matrices of 12 planar templates designed to roll up into vertically standing tubular photon cages. One matrix divides into three rows of four planar designs. We adjust the exposure dose parameter of the e-beam lithography process for each row to 0.6, 0.7 and 0.8 starting from the bottom row. The first (last) two columns contain the templates of future tubular cages of length  $25 \mu m$  ( $50 \mu m$ ) produced by one rolling (one rolling and a half) of the PCM. We note the smaller thickness of the InGaP/InP bilayer estimated to  $0.214 \mu m$  as compared with sample C2217 (6% reduction). It implies shorter radii of the final tubular cages ranging from  $14$  to  $15.5 \mu m \pm 1 \mu m$ . We emphasize the negligible impact of the slight decrease of the

cages' radius on the PCM mirror performances at normal incidence according to the reflectivity spectra displayed in Chapter 3. We present in Figure 4.10.a) a titled SEM view including two matrices of 24 rolled-up microstructures created after completing the fabrication cycle. We report the successful rolling and lifting of 17 planar templates ( $\sim 71\%$ ) into standing tubular cages. The remaining templates generate horizontal microtubes (1 specimen) or membranes damaged upon drying (6 specimens). We spot the most vertical cages as the specimen of length  $25\ \mu\text{m}$  illustrated on the SEM close-up view in 4.10.a), constituting choice candidates for the SNOM measurements.

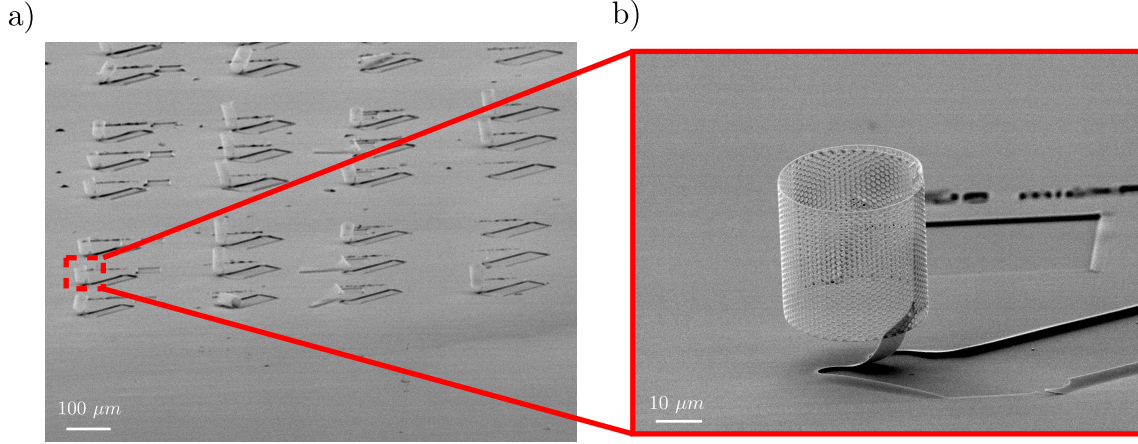


FIGURE 4.10: a) SEM picture of tubular photon cages on sample C2527. b) Close-up SEM view on a standing microtube.

### SNOM scans at various wavelengths

We introduce the SNOM probe inside one specimen of vertically standing tubular cages of radius  $\rho_c \simeq 29\ \mu\text{m}$  and length  $L \simeq 50\ \mu\text{m}$  at insertion distance  $d \simeq 10\ \mu\text{m}$  from the top boundary as schematized in Figure 4.11. In such a configuration, we ensure to position the probe tip deep enough inside the hollow core while enlarging the scan zone area as compared with the previous experiment. We perform in the first place near-field scans at fixed insertion depth of the probe  $d$  while sweeping the excitation wavelength from  $1.450$  to  $1.580\ \mu\text{m}$  with a  $10\ \text{nm}$  step.

We have gathered in Figure 4.11 the maps of the electric field intensity  $|\vec{E}|^2$  in normalized units spanning a  $15 \times 15\ \mu\text{m}^2$  area ( $\sim 27\%$  of the cavity cross-section area) generated at each wavelength of the sweep. We point out the three specific features standing out of the maps:

- similarly to the measurements on sample C2217, we notice radial oscillations spreading from the cavity centre and characteristic of cylindrical cavity modes  $\text{TE}_{m,n,p}$  with low azimuthal orders  $m$ ;
- apart from  $1.460\ \mu\text{m}$ , the central region of the maps reveals a more complex pattern, impeding the discrimination between central antinodes and nodes typical of  $\text{TE}_{0,n,p}$  and  $\text{TE}_{1,n,p}$  cavity modes realized with photon cages of sample C2217; at  $1.460\ \mu\text{m}$ , we recognize the pattern of a cylindrical cavity modes of type  $\text{TE}_{1,n,p}$  with a central antinode;
- we distinguish azimuthal patterns emerging at a certain radius delimited on the map at  $1.450\ \mu\text{m}$ , enclosing the central radial oscillations; it also seems that the

position of the first azimuthal ring appears at the same position for each of the maps.

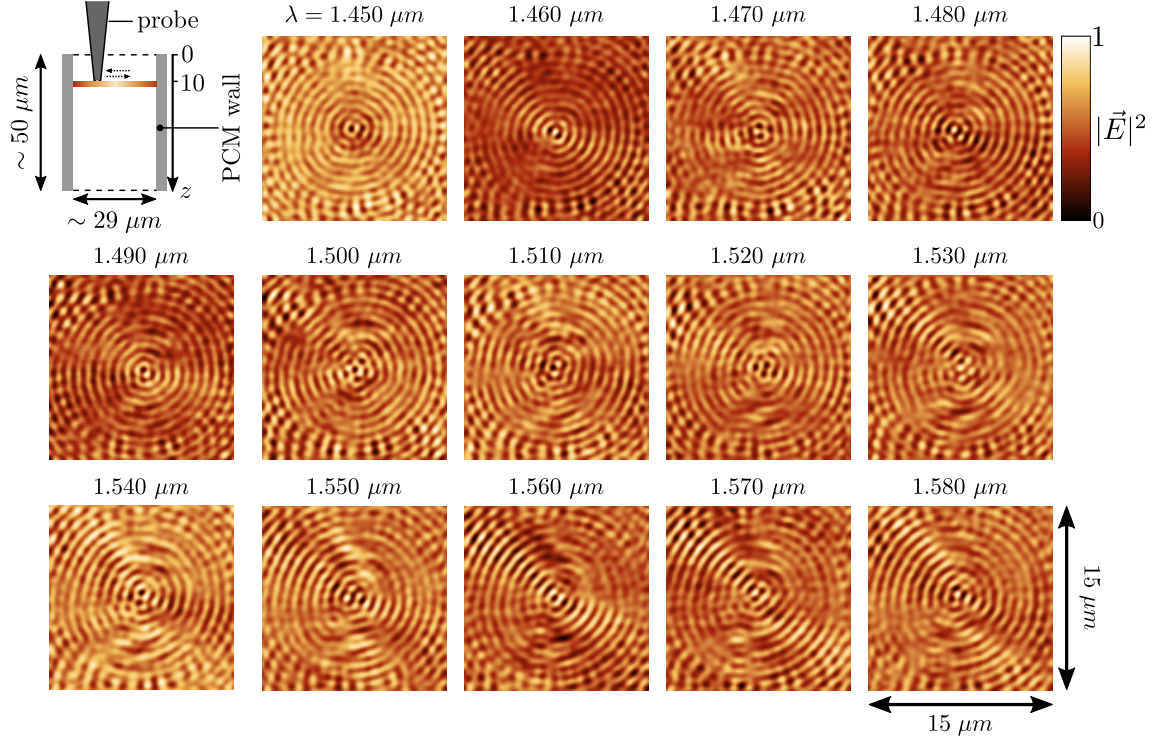


FIGURE 4.11: SNOM maps for various wavelengths in tubular photon cages of sample C2527.

### Identification of the mode at 1460 nm

We focus our analysis on the map generated at 1.460  $\mu m$  which exhibits a central antinode typical of  $TE_{1,n,p}$  cylindrical cavity modes. We present the distribution of the electric field intensity  $|\vec{E}|^2$  in Figure 4.12.a) within a scale drawing of the cage cross-section and schematic extension of the mode pattern in the background. The close-up view in Figure 4.12.b) allows a finer visualization of the modes' pattern across the scan zone area, composed of centred radial oscillations and surrounding azimuthal rings. In particular, we have delimited in blue dashed line the contour of the first azimuthal ring enclosing the central radial pattern.

Applying the spatial filtering method described in Section 4.2.2, we extract a profile over the cross-section map. We determine the radial order of the mode by comparison with theoretical profiles of generic mode  $TE_{1,n,p}$  in the cross-section of an ideal cavity of tunable radius  $\rho_{eq}$ . We find a good compliance between the experimental profile and the profile of the mode  $TE_{1,20,p}$  hosted by a cavity of radius  $\rho_{eq} = 14.4 \mu m$ . We report relative errors between experimental and theoretical positions of the profiles' peaks below 1 % except for the first peak for which the error reaches about 3%. Moreover, the polarizing effect of the BNA makes the identification of the azimuthal order of the azimuthal pattern delicate to the naked eye. To estimate the azimuthal order, we evaluate the inner radius  $\rho_a \simeq 6.2 \mu m$  of the first azimuthal ring enclosing the central radial region. We seek for the equivalent cylindrical cavity mode  $TE_{m,n,p}$  which central node extends until  $\rho_a$  in a cavity of radius  $\rho_{eq} = 14.4 \mu m$ . We first look at cavity modes showing spectral proximity to the mode  $TE_{1,20,p}$ . We finally associate the azimuthal intensity pattern to the cylindrical cavity mode  $TE_{28,9,p}$  which, combined to the  $TE_{1,20,p}$



mode pattern, results in the analytical intensity map presented in Figure 4.12.c). We note however that the fundamental mode  $TE_{28,9,1}$  emerges at a cutoff wavelength of about  $1.421 \mu m$ , far from the excitation wavelength  $1.460 \mu m$  at which we record the map in Figure 4.12.b).

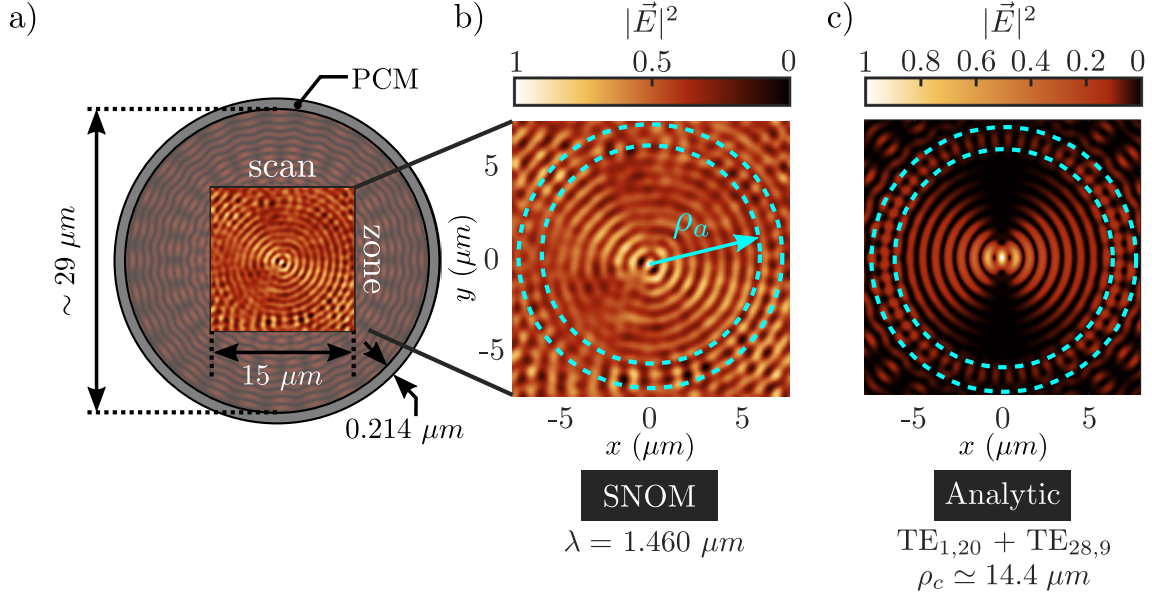


FIGURE 4.12: a) Near-field optical scan of the electric field intensity  $|\vec{E}|^2$  in normalized units generated at  $\lambda = 1.460 \mu m$  and covering a  $15 \times 15 \mu m^2$  area included in a cross-section of a cavity on sample C2527 drawn at scale. b) Close-up view of the scan realized at  $\lambda = 1.460 \mu m$ . We delimit in light dashed blue line the contour of the azimuthal ring surrounding the central radial pattern. c) Theoretical map of the electric field intensity  $|\vec{E}|^2$  for a combination of cylindrical cavity modes  $TE_{0,21}$  and  $TE_{28,9}$ . Similarly to b), we outline the azimuthal ring.

### Discussion on the results

The interpretation of the maps generated in a tubular microstructure of sample C2527 within the TUNICS source operational source along with the analysis of the mode detected at  $1.460 \mu m$  brings out the following remarks:

- we confirm the probing of cylindrical cavity modes in a tubular cage of sample C2527, reinforcing the experimental demonstration of the photon cages concept and proving the reproducibility of the SNOM experiment;
- despite the complexity central pattern, we appreciate a modal dynamics in the variation of the maps' central region in Figure 4.11, suggesting changes of the azimuthal orders of the modes;
- we detect the transverse mode pattern of generic cylindrical cavity mode  $TE_{1,20,p}$  at  $1.460 \mu m$  which shows consistency with the theoretical cutoff wavelength of the fundamental mode  $TE_{1,20,1}$  estimated to  $1.458 \mu m$ .
- at equivalent excitation wavelength of  $1.460 \mu m$ , we notice a decrease of the radial order of the detected cylindrical cavity mode, passing from 24 to 21, along with the reduction of the cavity radius, from  $17.5 \mu m$  to  $14.4 \mu m$  for the cavities on sample C2217 and C2527, respectively, in accordance with theoretical predictions;

- we have associated the azimuthal ring pattern enclosing the radial oscillations with  $\text{TE}_{28,9}$  mode profile; however, the inconsistency between the experimental excitation wavelength ( $1.46 \mu\text{m}$ ) and the theoretical cutoff wavelength of the fundamental mode  $\text{TE}_{28,9,1}$  ( $\sim 1.421 \mu\text{m}$ ) suggests that the formation of the azimuthal pattern is not related to the PCM microstructure; the presence of the azimuthal pattern on each maps of the sweep at similar positions reinforces the previous hypothesis; in Figure F.1 of Appendix F, we show the high reflectivity of a membrane with averaged optical properties at grazing incidence associate to the high azimuthal order  $m = 28$ , as a potential explanation for the formation of the azimuthal mode.

### SNOM scans at various altitudes

We perform a final series of measurements inside the tubular cage of sample C2527 to assess qualitatively the vertical confinement of the detected modes. In practice, we adjust the vertical position of the probe tip using a step motor with a  $0.7 \mu\text{m}$  increment. We measure the different insertion depths  $d$  of the tip from the top surface of the cavity as sketched in Figure 4.13. In particular, at  $d = 0 \mu\text{m}$ , the tip's apex locates at the top boundary of the cage.

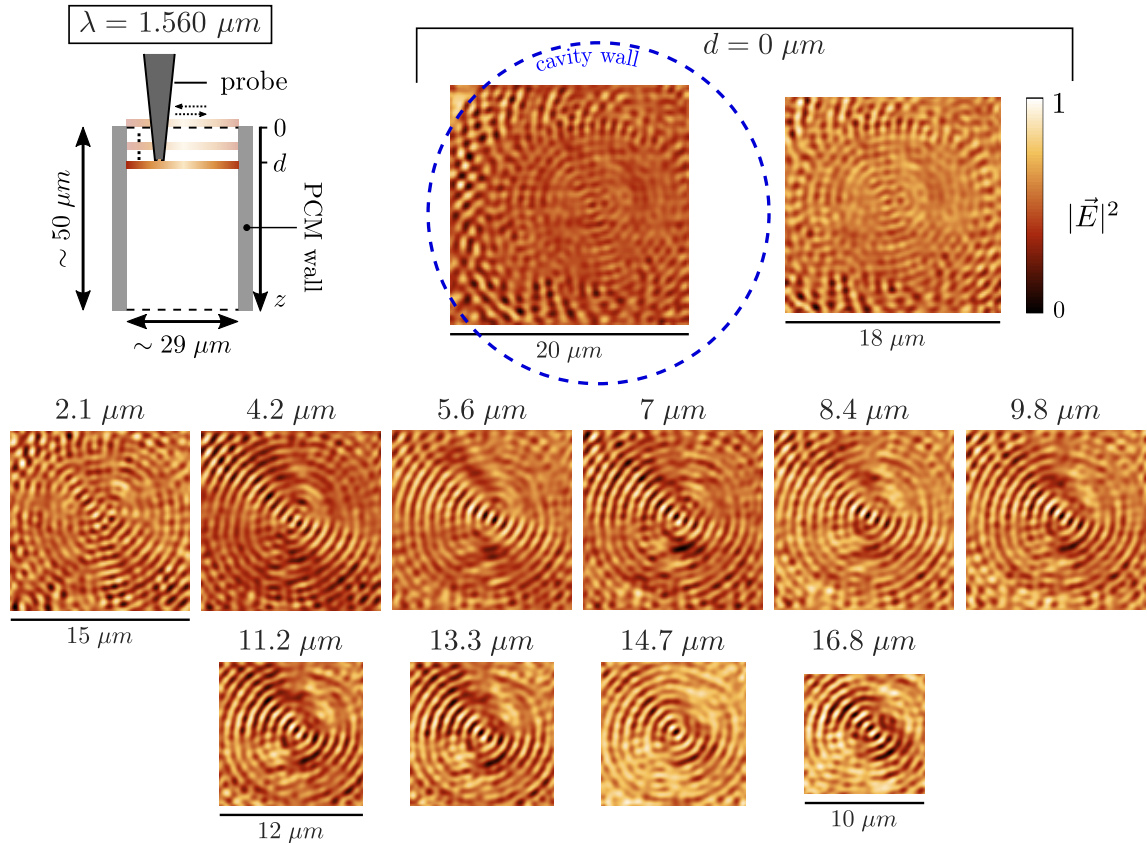


FIGURE 4.13: a) Schematics of near-field optical measurements realized inside in a  $50 \mu\text{m}$ -long tubular photon cage of diameter estimated to  $32 \mu\text{m}$  and  $0.214 \mu\text{m}$ -thick wall at various penetration depths of the probe  $d_1 \simeq 0 \mu\text{m}$ , level with the top face of the cage,  $d_2 \simeq 2 \mu\text{m}$  and  $d_3 \simeq 4 \mu\text{m}$ . b) Near-field optical maps of the electric field intensity performed at  $\lambda = 1.560 \mu\text{m}$  for the three penetration depths.

We present in Figure 4.13 electric field intensity  $|\vec{E}|^2$  maps generated at  $1.560 \mu\text{m}$  while progressively driving the probe tip down into the cage, at depths  $d$  varying from 0 to about  $16.8 \mu\text{m}$ . We notice the reduction of the scan area along with the insertion

of the tip down into the cage, due to the tapered shape of the probe. At  $d = 0 \mu m$ , we have realized two scans with the largest dimensions  $20 \times 20 \mu m^2$  and  $18 \times 18 \mu m^2$ . We delimit the frontiers of the cavity wall with a dashed blue line in the first scan. In the first two scans, we observe a large band of azimuthal patterns surrounding a central blurred region. We report a higher sensitivity and contrast in the detection of the azimuthal oscillations whereas we probe weakly contrasted traces of radial patterns. At  $d = 2.1 \mu m$ , the  $15 \times 15 \mu m^2$  map reveals an intricate assembly of patterns emerging in the central region still enclosed by azimuthal oscillations yet showing lower contrast. On the contrary, from  $d = 4.2 \mu m$  to  $d = 16.8 \mu m$ , we clearly distinguish predominant radial patterns with high contrast along the high sensitive BNA probe direction.

We interpret the near-field measurements realized for various insertion depths  $d$  of the probe tip inside the tubular cage in the following way:

- at  $d = 0 \mu m$  or at the very top of the cage, the large scan zone covering about 60 % of the cavity cross-section area reveals predominant azimuthal patterns bordering the cavity wall but weak traces of radial oscillations; we have proposed earlier an explanation to the presence of high azimuthal order modes based on the high reflection of the PCM slab at grazing incidence; moreover, the low sensitivity to radial patterns shows the minor penetration of low azimuthal order cavity modes outside of the microtube;
- at  $d = 2.1 \mu m$ , we observe a complex pattern probably resulting from the combination of the patterns of high  $p$  order modes detectable close to the cavity boundaries;
- from  $d = 4.2 \mu m$ , we probe more confined modes with predominant radial oscillations typical of cavity modes with low order azimuthal order;

#### 4.2.4 Optical response for smaller radius cages

The last series of near-field measurements explores the optical response of photon cages with smaller curvature radius. The interest of diminishing the cavity radius lies in the reduction of the number of modes supported by the cavity, facilitating their detection, yet at the expense of potential curvature effects.

##### Tubular photon cages on sample C2579

In this section, we perform near-field scans inside tubular photon cages fabricated on sample C2579. From the rolling of a 86 nm-thick InP/InGaP bilayer, we produce tubular cavities of radius varying between 5.1 and 6.2  $\mu m$ . The sample C2579 divides into 48 matrices of 4 planar templates for rolled-up PCM. In each matrix, we adjust the length of the cavity to 20 and 30  $\mu m$  in the columns, and the number of rolling of the PCM to 2 and 3 in the rows from the bottom row. By realizing multiple rolling of the PCM, we expect to compensate the higher optical losses and degradation of the PCM reflection properties owing to the thinner PCM. Indeed, for 86 nm-thick PCM, the PCM high reflectivity zone shrinks and shifts to 1.3  $\mu m$  as represented in Figure G.1 in Appendix G. We show on the SEM picture in Figure 4.14.a) an overview of a part of sample C2579 upon fabrication of the tubular cages. We report over 10 matrices (40 designs) for instance, the successful rolling and lifting of 23 cages ( $\sim 59$  %), 16 horizontal microtubes ( $\sim 40$  %) and one detached cavity. We illustrate on the SEM close-up view in Figure 4.14.b) a quasi-vertical photon cage of length 30  $\mu m$ .

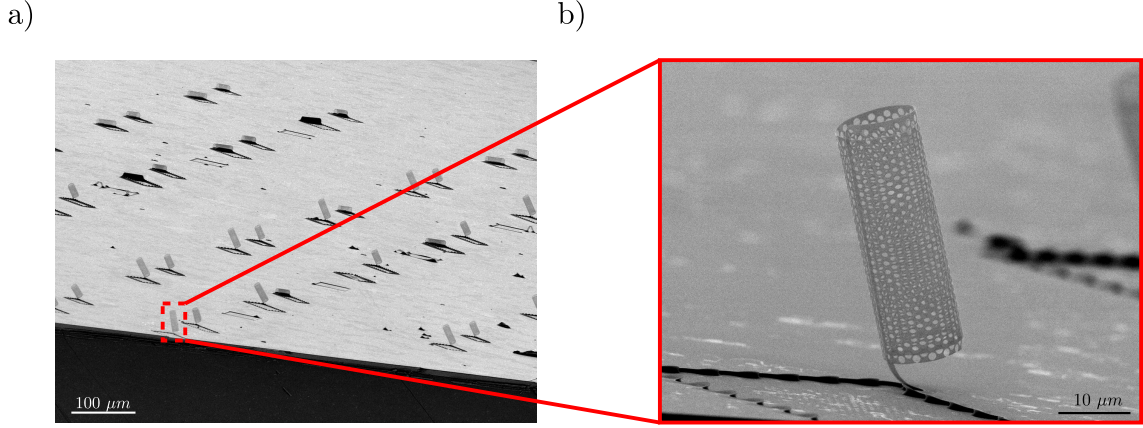


FIGURE 4.14: a) SEM picture of a part of sample C2579 upon fabrication of tubular photon cages. b) SEM close-up view of a tilted tubular cage specimen after rolling and lifting of the PCM.

### SNOM scans at the top of the cage

We perform a first set of near-field measurements at the top of one cage specimen of length  $20\ \mu\text{m}$  and radius close to  $11\ \mu\text{m}$  as sketched in Figure 4.15. The operation serves to the approach and centering of the probe tip with respect to the cage axis. It also allows preliminary estimates of the cavity optical response before the insertion of the probe tip inside the hollow core. We present in Figure 4.15  $30 \times 30\ \mu\text{m}^2$  maps of the electric field intensity  $|\vec{E}|^2$  in normalized units for an excitation wavelength  $\lambda$  ranging from  $1.5$  to  $1.530\ \mu\text{m}$  with a  $10\ \text{nm}$  step. The pattern of the four maps contain two specific features, attesting to the presence of the cavity: a thick pattern extending into free space and a central azimuthal pattern enclosing traces of radial variations. We note the invariance of the thick pattern to the spectral sweep that we attribute to the diffraction of the cavity's edges. Similarly, the azimuthal ring remains unchanged on the four maps and manifests probably the reflection of light onto the cavity wall at grazing incidence. Conversely, we observe variations of the pattern contained within the azimuthal ring as a function of the excitation wavelength, comforting a spectral sensitivity of the cavity delimited with a green dashed line.

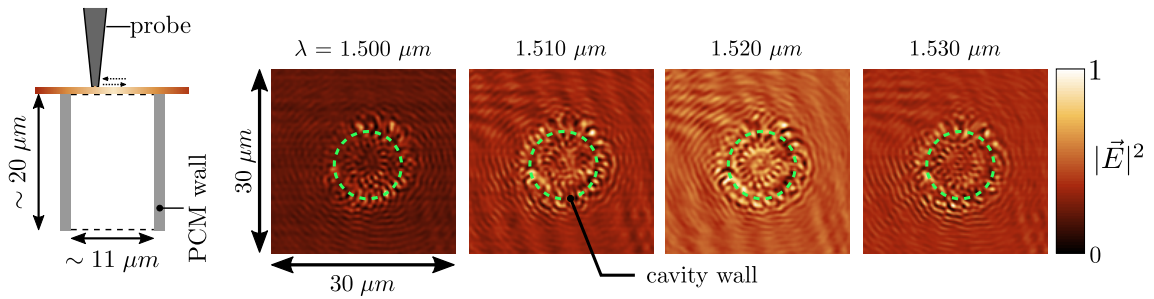


FIGURE 4.15: Schematics: near-field measurements at the top of a cage specimen on sample C2579 of radius and length estimated to  $11$  and  $20\ \mu\text{m}$ , respectively. Pictures:  $30 \times 30\ \mu\text{m}^2$  maps of the electric field intensity  $|\vec{E}|^2$  generated at various excitation wavelengths  $\lambda$  from  $1.5$  to  $1.53\ \mu\text{m}$  with a  $10\ \text{nm}$  step.

### SNOM scans at various wavelengths

We insert then the probe tip inside the cavity progressively to probe the modal response at a distance  $d = 6\ \mu\text{m}$  from the top surface of the cage as schematized in Figure 4.16.



Fixing the insertion distance  $d$ , we carry out near-field scans over the cavity cross-section while sweeping the excitation wavelength  $\lambda$  from 1.490 to 1.560  $\mu\text{m}$  with a 10 nm sweep. We present in Figure 4.16 the maps of  $|\vec{E}|^2$  in normalized units generated in order of increasing wavelengths and covering a  $4 \times 4$  scan area. We note the difficulty to enlarge the scan zone due to the attraction forces between the probe tip and the cavity wall.

From 1.490 to 1.5  $\mu\text{m}$ , we observe a complex intensity pattern emerging from the cavity center. It turns abruptly into radial oscillations at 1.52  $\mu\text{m}$  with a central node typical of cylindrical cavity modes  $\text{TE}_{0,n,p}$ . The radial pattern becomes clearer at 1.530 and 1.540  $\mu\text{m}$  before deforming progressively at 1.550 and 1.560  $\mu\text{m}$  into intricate geometries. Using the spatial filtering procedure, we analyze a filtered profile of the map generated at 1.530  $\mu\text{m}$ . By comparing to theoretical profiles of generic cavity modes  $\text{TE}_{0,n,p}$  in a cavity of radius  $\rho_{\text{eq}}$ , we find a good compliance of the experimental profile with transverse profiles of modes  $\text{TE}_{0,7,p}$  in a cavity of radius  $\rho_{\text{eq}} \simeq 5.6 \mu\text{m}$ . In particular, the excitation wavelength matches with the theoretical cutoff wavelength of the mode  $\text{TE}_{0,7,3}$  estimated to 1.536  $\mu\text{m}$ .

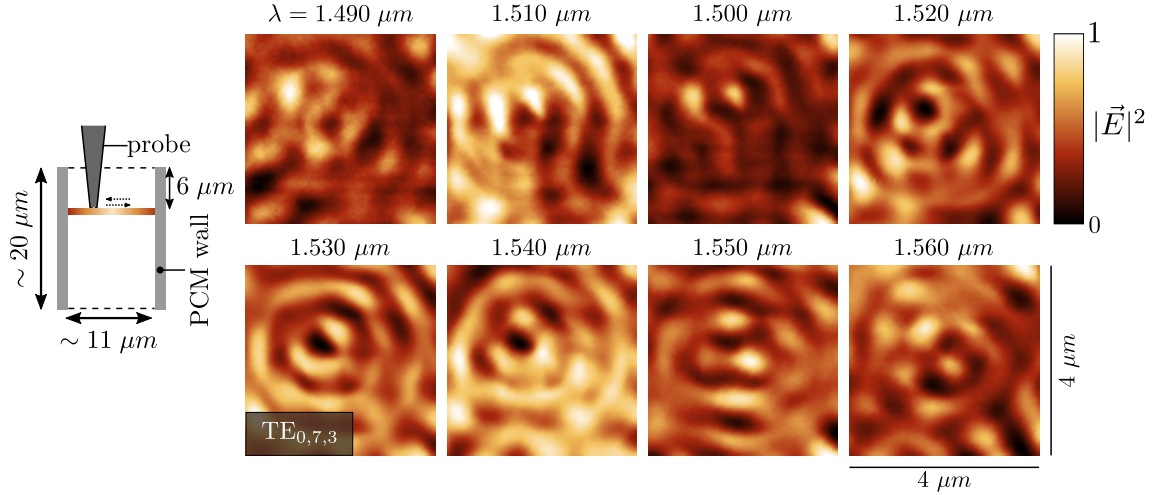


FIGURE 4.16: Schematics: near-field measurements at an insertion distance  $d = 6 \mu\text{m}$  of the probe tip from the top of a photon cage specimen on sample C2579 of radius and length estimated to 11 and 20  $\mu\text{m}$ , respectively. Pictures:  $4 \times 4 \mu\text{m}^2$  maps of the electric field intensity  $|\vec{E}|^2$  generated at various excitation wavelengths  $\lambda$  from 1.490 to 1.560  $\mu\text{m}$  with a 10 nm step.

### Discussion on the results

We have approached in the last series of measurements the modal response of a photon cage from sample C2579 with a radius and length estimated to 5.6  $\mu\text{m}$  and 20  $\mu\text{m}$ . We report the detection of cylindrical cavity modes confined in the cavity hollow core. The analysis of the map generated at 1.530  $\mu\text{m}$  has established the correspondence of the emerging pattern with the cylindrical cavity mode  $\text{TE}_{0,7,3}$ . Moreover, the decrease of the radial order as compared with equivalent measurements inside cavities of samples C2217 and C2527 proves the consistency of theoretical predictions. Considering the small cavity radius, the clear detection of cavity modes seems to occur near the resonance of fundamental modes  $\text{TE}_{m,n,p}$ , otherwise the intensity maps show more complexity. This observation would concur with the reduction of the modes supported by the cavity and the larger spectral spacing in between modes of distinct  $m$ ,  $n$  and  $p$  orders due to the small length of the cavity. The striking fact remains that the small

cavity radius, implying thinner PCM, alters significantly the reflectivity of the planar PCM judging by the reflectivity spectrum simulated with RCWA method, presented in Figure G.1 in Appendix G. Indeed, the PCM high reflectivity zone has shrunk into a thinner peak centred at around  $1.3 \mu m$  while the reflectivity decreases from about 60 % to 46 % in the spectral range  $[1.49-1.56] \mu m$ . At this level of reflection, we expect the presence of cavity modes to be hardly appreciable. Therefore, we may attribute the detection of the previous cavity mode to the high sensitivity of the BNA probe. The deeper understanding of the generated maps would however require a thorough quantitative analysis of the evolution of the recorded electric field intensity. We insist on the exploratory nature of these preliminary measurements conducted in the last period of this three year study.

### 4.3 Conclusion of the chapter

In conclusion to this chapter, we summarize below the main accomplishments bringing an experimental demonstration of the photon cages concept.

In the first section, we have successfully addressed the fabrication of tubular photon cages based on the rolling of 2D photonic crystal membranes (PCM), showing the following features:

- we have demonstrated our ability to produce tubular photon cages with great reproducibility and high control on the geometrical parameters;
- we have proved the efficiency of a specific anchor design to lift the rolled-up cavities vertically, facilitating the optical characterization of the microstructures;
- we have also opened the path to other applications of rolled-up PCM mirrors showing their elastic behaviour and the possible positioning of the microtubes onto other platforms.

In the second section, we have tackled the optical characterization of the fabricated tubular photon cages by probing the modal response in the hollow core through scanning near-field optical microscopy (SNOM) measurements. We highlight the main achievements resulting from measurements on three different samples C2217, C2527 and C2579 with different radius cavities:

- we have revealed the presence of cylindrical cavity modes  $TE_{m,n,p}$  in the air-filled core of the cavities confirming practically the potential of tubular photon cages to confine light in air;
- we have demonstrated the reproducibility of the SNOM measurements through the different scans conducted on various samples;
- we have showed the compliance of the orders and the wavelengths of the detected modes with the theoretical predictions provided by the FDTD and analytic models;
- we have assessed qualitatively the vertical confinement of the cavity modes by performing measurements at different insertion depths of the SNOM probe;

Finally, the results of the present and previous chapters provide a complete theoretical and experimental study on tubular photon cages which opens the path toward the integration of such microstructures in opto-fluidic application devices. We note that photon cages represent a typical combination between a photonic crystal pattern and a 3D tubular geometry accessible through the rolled-up nanotechnology. In particular, using the potential of the rolled-up nanotechnology platform, we investigate in the next chapter the optical properties of analogues of typical solid-states structures, graphene and carbon nanotubes, in the class of photonic crystals.

# Chapter 5

## Photonic crystal analogues of carbon nanotubes

*L'amour qui nous attache aux beautés éternelles  
N'étouffe pas en nous l'amour des temporelles ;  
Nos sens facilement peuvent être charmés  
Des ouvrages parfaits que le Ciel a formés.*

---

MOLIÈRE (TARTUFFE, ACTE III SCÈNE 3)

### Contents

---

<b>5.1</b>	<b>Graphene VS honeycomb lattice photonic crystal . . . . .</b>	<b>174</b>
5.1.1	Graphene . . . . .	174
5.1.2	Honeycomb lattice photonic crystal . . . . .	180
5.1.3	Conclusion of the section . . . . .	187
<b>5.2</b>	<b>Graphene ribbons and honeycomb lattice photonic crystal ribbons .</b>	<b>187</b>
5.2.1	Topology of graphene ribbons . . . . .	188
5.2.2	Topology of honeycomb lattice photonic crystal ribbons . . .	191
5.2.3	Conclusion of the section . . . . .	200
<b>5.3</b>	<b>Carbon nanotubes and rolled-up honeycomb lattice photonic crystal</b>	<b>200</b>
5.3.1	Carbon nanotubes . . . . .	201
5.3.2	Rolled-up honeycomb lattice photonic crystal . . . . .	210
5.3.3	Conclusion of the section . . . . .	222
<b>5.4</b>	<b>Conclusion of the chapter . . . . .</b>	<b>223</b>
<b>5.5</b>	<b>References . . . . .</b>	<b>224</b>

---



## 5.1 Graphene VS honeycomb lattice photonic crystal

In this section, we present successively the structures and properties of graphene and its equivalent in the class of photonic crystal membranes (PCM) corresponding to a honeycomb lattice PCM. First, we introduce briefly the origin of the planar honeycomb arrangement of carbon atoms in graphene. We present then the tight-binding approach used to calculate graphene electronic dispersion, emphasizing on the key features of the resulting dispersion. Second, we describe the structure of the honeycomb lattice PCM. We analyze then the dispersion of photonic graphene simulated with the FDTD method in the light of the solid-state model.

### 5.1.1 Graphene

#### Structural properties

In the class of 2D materials, graphene has become a flagship structure for its range of exceptional properties including high mobility of the charge carriers and mechanical flexibility. In particular, the excellent electronic transport properties originate from the specific planar arrangement of the carbon atoms according to a honeycomb lattice. We explain below the formation of the specific honeycomb crystallographic system considering the filling of carbon hybridized atomic orbitals.

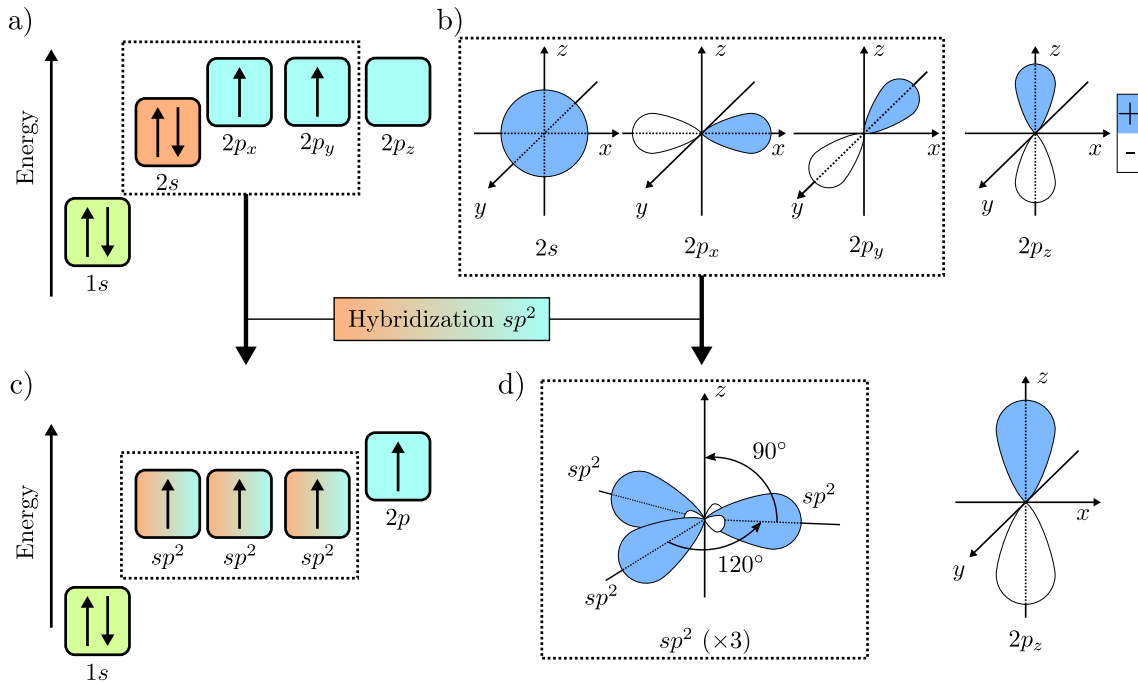


FIGURE 5.1: a) Energy diagram of the orbitals 1s, 2s, and 2p filled with the six electrons of a single carbon atom. The black arrows represent the orientation of the electrons' spin. The orbital 2p is degenerate into orbitals 2p<sub>x</sub>, 2p<sub>y</sub> and 2p<sub>z</sub>. b) Probability density of the orbitals 2s, 2p<sub>x</sub>, 2p<sub>y</sub> and 2p<sub>z</sub> in the Cartesian system. c) Energy diagram of the orbitals of a single carbon atom after sp<sup>2</sup> hybridization. d) Probability density of the sp<sup>2</sup> and 2p<sub>z</sub> orbitals in the Cartesian system.

One carbon atom possesses a total of six electrons distributed into three atomic orbitals 1s, 2s and 2p of increasing energies, leading to the following electronic configuration: 1s<sup>2</sup>2s<sup>2</sup>2p<sup>2</sup>. The orbital 2p is degenerate into three orbitals 2p<sub>x</sub>, 2p<sub>y</sub> and 2p<sub>z</sub> at the same energy level as illustrated in Figure 5.1.a). We also schematize in Figure 5.1.b) the density of probability of the different orbitals, showing spherical symmetry

for the orbital  $2s$  while orbitals  $2p_x$ ,  $2p_y$  and  $2p_z$  orient respectively along  $x$ ,  $y$  and  $z$  directions. The filling of electrons into the different orbitals follows Klechkowsky's rule, Hund's rule and Pauli's exclusion principle, placing two electrons in orbitals  $1s$  and  $2s$  and a single electron in each orbital  $2p_x$  and  $2p_y$  with parallel spins (black arrow). The electrons in lowest energy orbital  $1s$  constitute the core electrons tightly attached to the nucleus. Conversely, the four remaining electrons arranged in orbitals  $2s$  and  $2p$  form the valence electrons involved in the creation of chemical bounds. In particular, the two unpaired electrons in the  $2p$  orbitals associate to single electrons from other atoms to form chemical bound. However, the proximity in energy of orbitals  $2p$  and  $2s$  allows hybridization phenomena. According to the number of  $2p$  orbitals involved in hybridization with  $2s$  orbital, carbon atoms generate four, three or two hybridized orbitals noted  $sp^3$ ,  $sp^2$  or  $sp$ , respectively.

In graphene (and graphite *a fortiori*), the orbitals  $2s$ ,  $2p_x$  and  $2p_y$  hybridize into three orbitals  $sp^2$  sharing the same energy as shown in Figure 5.1.c). We also depict the geometry of the so-formed  $sp^2$  orbitals in Figure 5.1.d). Due to electrostatic interaction, the  $sp^2$  orbitals of one carbon atom repel with an angle of  $120^\circ$  angle. Head-on overlap between  $sp^2$  orbital from different carbon atoms leads to the creation of chemical covalent bonds, also called  $\sigma$  bonds due to the rotational symmetry with respect to the bond axis. Therefore, the planar arrangement of the carbon atoms form a honeycomb lattice. The last unhybridized orbital  $2p_z$ , orthogonal to the lattice plane, hosts the remaining unpaired electron. The overlap between  $2p_z$  orbitals produce weaker bonds than  $\sigma$  bonds called  $\pi$  bonds, which contribute to the free circulation of the electrons across graphene structure.

### Tight-binding model for graphene

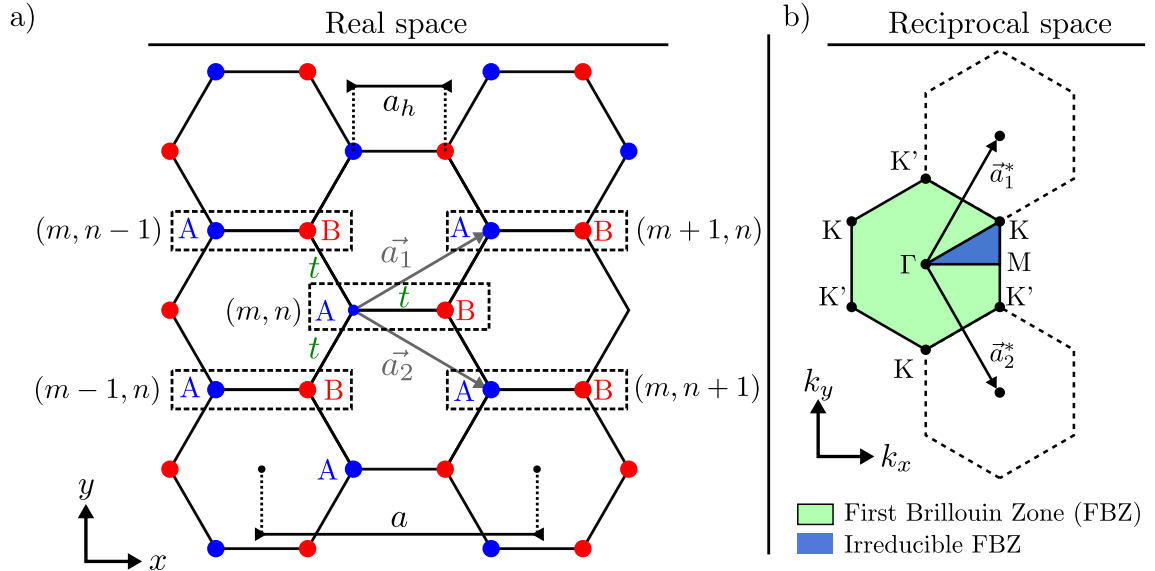


FIGURE 5.2: a) Schematized graphene honeycomb lattice with a period  $a_h$  and lattice vectors  $(\vec{a}_1, \vec{a}_2)$ . The honeycomb lattice unit cell comprises two sublattices A and B. We locate one unit cell with its coordinates  $(m, n)$  in the basis  $(\vec{a}_1, \vec{a}_2)$ . We note  $t$  the hopping energy for the electrons hop onto a nearest neighbour. The regular honeycomb lattice verifies  $a = 3a_h$ . b) Reciprocal lattice of the honeycomb pattern with lattice vectors  $(\vec{a}_1^*, \vec{a}_2^*)$ . The primitive cell (green zone) corresponds to the first Brillouin zone (FBZ) with high symmetry points  $\Gamma$ , K, K', and M. Due to  $\pi/3$ -rotational symmetry, the study of the FBZ reduces to the irreducible FBZ (blue zone).

For deeper insight on graphene electronic properties, we calculate the electronic

band structure of  $\pi$  electrons using the tight-binding approach. Considered as the analogue of the linear combination of atomic orbitals (LCAO) method used in chemistry, the tight-binding model, as the name suggests, describes the properties of tightly bound electrons in solids by approximating the overall wavefunction to the sum of isolated atomic orbitals. It suggests therefore a small overlap between atomic orbitals, implying minor, yet existing, interaction [1]. In particular, we use the tight-binding model to estimate the electronic dispersion for electrons contained in  $2p_z$  graphene out-of-plane orbitals. We may consult the reference book [1] for a detailed development of the tight-binding Hamiltonian in the general case and in the first quantization formalism. We build here graphene tight-binding Hamiltonian in the framework of second quantization particularly adapted to systems with a high number of undistinguishable particles. Though the following development belongs to classical academic exercises, we find it useful to reproduce the step-by-step procedure for non-familiar readers.

We consider graphene honeycomb lattice generated by the periodic repetition of a unit cell composed of two sublattices noted A and B symbolized in Figure 5.2.a) by blue and red dots respectively. The distance between A and B corresponds to the hexagon period  $a_h \simeq 2.46\text{\AA}$ . The lattice basis  $(\vec{a}_1, \vec{a}_2)$  expresses in the Cartesian system as:

$$\begin{aligned}\vec{a}_1 &= \frac{3}{2}a_h\vec{e}_x + \frac{\sqrt{3}}{2}a_h\vec{e}_y, \\ \vec{a}_2 &= \frac{3}{2}a_h\vec{e}_x - \frac{\sqrt{3}}{2}a_h\vec{e}_y.\end{aligned}\tag{5.1}$$

In a regular honeycomb lattice, the hexagon period also satisfies  $3a_h = a$ . We locate any unit cell A-B in the lattice with its coordinates  $(m, n)$  in the basis  $(\vec{a}_1, \vec{a}_2)$ . We assume, in first approximation, the interaction between nearest neighbours interpreted as the hopping of electrons from one site (A or B) to the adjacent one (B or A) and characterized by the hopping energy noted  $t$ . In this case, graphene tight-binding Hamiltonian writes in the following form:

$$H = t \sum_{m,n} [a_{m,n}^\dagger (b_{m,n} + b_{m,n-1} + b_{m-1,n}) + b_{m,n}^\dagger (a_{m,n} + a_{m,n+1} + a_{m+1,n})] \tag{5.2}$$

where  $a_{m,n}^\dagger$  ( $b_{m,n}^\dagger$ ) and  $a_{m,n}$  ( $b_{m,n}$ ) designate the fermionic operators of creation and annihilation, respectively, of one electron on site A (B) in the unit cell  $(m, n)$ . In the right part of the sum, the second term identifies with the Hermitian conjugate (*h.c.*) of the first term, leading to a more compact form of the Hamiltonian:

$$H = t \sum_{m,n} [a_{m,n}^\dagger (b_{m,n} + b_{m,n-1} + b_{m-1,n}) + h.c.] \tag{5.3}$$

Using the discrete translation symmetry of the lattice, we decompose the operators  $a_{m,n}^\dagger$  and  $b_{m,n}^\dagger$  in Fourier series according to:

$$\begin{aligned}a_{m,n}^\dagger &= \frac{1}{\sqrt{N}} \sum_{\vec{k}} e^{i\vec{k} \cdot (m\vec{a}_1 + n\vec{a}_2)} a_{\vec{k}}^\dagger, \\ b_{m,n}^\dagger &= \frac{1}{\sqrt{N}} \sum_{\vec{k}} e^{i\vec{k} \cdot (m\vec{a}_1 + n\vec{a}_2)} b_{\vec{k}}^\dagger,\end{aligned}\tag{5.4}$$

with  $N$ , the number of sites A (or B) and  $\vec{k}$  the momentum defined by  $|\vec{k}| = 2\pi/\lambda$ . Injecting expressions in Equation (5.4) in Equation (5.3), the Hamiltonian rewrites as:

$$H = t \sum_{m,n} \sum_{\vec{k}, \vec{k}'} \frac{1}{N} \left[ a_{\vec{k}}^\dagger b_{\vec{k}'} e^{j(\vec{k}' - \vec{k}) \cdot (m\vec{a}_1 + n\vec{a}_2)} \left( 1 + e^{-i\vec{k}' \cdot \vec{a}_1} + e^{-i\vec{k}' \cdot \vec{a}_2} \right) + h.c. \right]. \tag{5.5}$$

Using the orthonormality relation:

$$\frac{1}{N} \sum_{m,n} e^{j(\vec{k}' - \vec{k}) \cdot (m\vec{a}_1 + n\vec{a}_2)} = \delta_{\vec{k}, \vec{k}'}, \quad (5.6)$$

the Hamiltonian of the system reduces to:

$$H = t \sum_{\vec{k}} \left[ a_{\vec{k}}^\dagger b_{\vec{k}'} \left( 1 + e^{-i\vec{k} \cdot \vec{a}_1} + e^{-i\vec{k} \cdot \vec{a}_2} \right) + h.c. \right]. \quad (5.7)$$

In the basis  $(a_{\vec{k}}, b_{\vec{k}})$  of sub-lattices A and B,  $H$  writes in the matrix form:

$$H = \sum_{\vec{k}} \begin{pmatrix} a_{\vec{k}}^\dagger & b_{\vec{k}}^\dagger \end{pmatrix} H_{\vec{k}} \begin{pmatrix} a_{\vec{k}} \\ b_{\vec{k}} \end{pmatrix}, \quad (5.8)$$

where the Bloch hamiltonian  $H_{\vec{k}}$  expresses for any momentum  $\vec{k}$  as:

$$H_{\vec{k}} = t \begin{pmatrix} 0 & f(\vec{k}) \\ f^*(\vec{k}) & 0 \end{pmatrix}, \quad (5.9)$$

where  $f(\vec{k}) = 1 + e^{-i\vec{k} \cdot \vec{a}_1} + e^{-i\vec{k} \cdot \vec{a}_2}$ . The off-diagonal term  $f(\vec{k})$  in  $H_{\vec{k}}$  represent the phase shift acquired when hopping from site B to site A located in the same unit cell (zero phase shift) or in adjacent unit cells (phase shift of  $-\vec{k} \cdot \vec{a}_1$  or  $-\vec{k} \cdot \vec{a}_2$ ). Zero diagonal terms comes from two reasons:

- identical on-site energies for sub-lattices A and B fixed to zero as they only shift the  $H_k$  eigenvalues;
- we only consider nearest neighbours coupling.

### Graphene tight-binding band structure

We deduce the energy dispersion of graphene  $\pi$  electrons by calculating  $H_{\vec{k}}$  eigenvalues, leading to the following energy bands:

$$E_{\pm}(\vec{k}) = \pm t |1 + e^{-i\vec{k} \cdot \vec{a}_1} + e^{-i\vec{k} \cdot \vec{a}_2}| = \pm t |f(\vec{k})|. \quad (5.10)$$

Decomposing the momentum  $\vec{k}$  in the 2D Cartesian basis  $\vec{k} = k_x \vec{e}_x + k_y \vec{e}_y$ , the eigenvalues write as:

$$E_{\pm}(k_x, k_y) = \pm t \sqrt{1 + 4 \cos\left(\frac{3k_x a_h}{2}\right) \cos\left(\frac{\sqrt{3}k_y a_h}{2}\right) + 4 \cos^2\left(\frac{\sqrt{3}k_y a_h}{2}\right)}. \quad (5.11)$$

We find two types of degeneracy points in the band diagram, noted K and K' and defined by  $E_+(\vec{K}, \vec{K}') = E_-(\vec{K}, \vec{K}') = 0$ . We infer from Equation (5.10) that  $\vec{K}$  and  $\vec{K}'$  verify the following relations as roots of unity at the order 3:

$$\begin{aligned} \vec{K} \cdot \vec{a}_1 &= \frac{2\pi}{3} & \vec{K}' \cdot \vec{a}_1 &= -\frac{2\pi}{3} \\ \vec{K} \cdot \vec{a}_2 &= -\frac{2\pi}{3} & \vec{K}' \cdot \vec{a}_2 &= \frac{2\pi}{3}. \end{aligned} \quad (5.12)$$

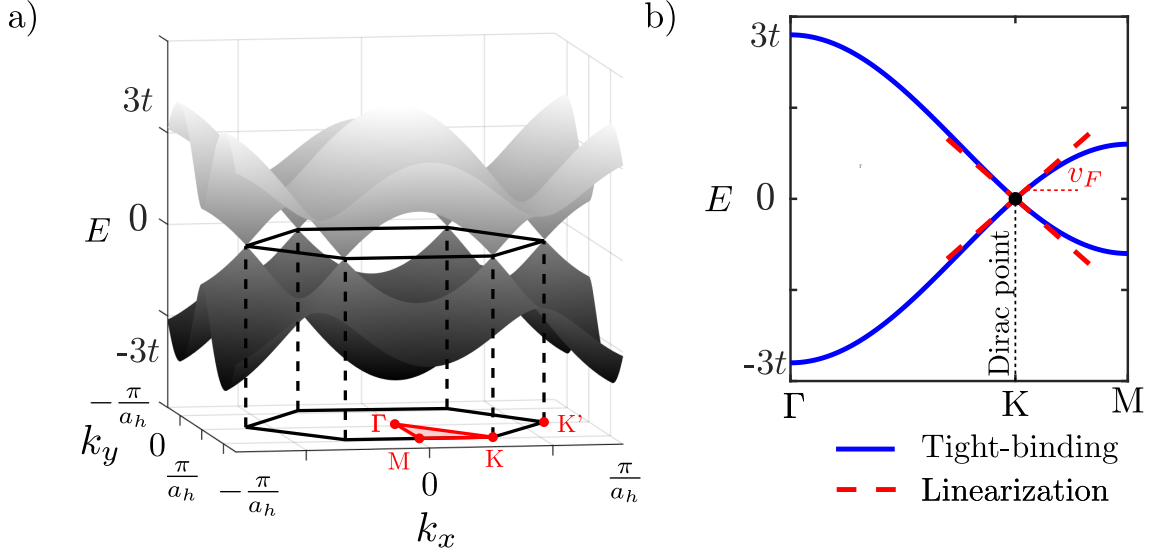


FIGURE 5.3: a) Surface plot of graphene energy band structure approximated with the tight-binding model. We delimit in black line the first Brillouin zone (FBZ) with high symmetry points  $\Gamma$ , K, K' and M. b) Previous band structure along the high-symmetry direction  $\Gamma$ -K-M in blue curve. The two bands cross at K point called Dirac point. Linearization in dashed red curve of the dispersion curve with a slope  $v_F$  corresponding to the Fermi velocity.

Moreover, in the honeycomb reciprocal lattice of basis  $(\vec{a}_1^*, \vec{a}_2^*)$ , the Dirac points K and K' have the following coordinates:

$$\begin{aligned}\vec{K} &= \frac{1}{3}(\vec{a}_1^* - \vec{a}_2^*), \\ \vec{K}' &= -\frac{1}{3}(\vec{a}_1^* - \vec{a}_2^*).\end{aligned}\tag{5.13}$$

The surface plot in the Figure 5.3.a) presents the dispersion of the two energy bands  $E_{\pm}(\vec{k})$  over graphene FBZ outlined in black line and projected in the plane  $(k_x, k_y)$  with high symmetry points  $\Gamma$ , K, K' and M. The upper  $E_+$  and lower  $E_-$  bands cross at the two triplets of degeneracy points K and K'. We plot in Figure 5.3.b) graphene electronic dispersion along the high-symmetry direction  $\Gamma$ -K-M. Developing the dispersion relation around K at  $\vec{k} = \vec{K} + \vec{q}$  with  $\vec{q} = q_x \vec{e}_x + q_y \vec{e}_y$ ,  $|\vec{q}| \ll |\vec{K}|$ , the anti-diagonal term of  $H_k$  rewrites as:

$$f(\vec{K} + \vec{q}) = 1 + e^{i\frac{3a_h q_x}{2}} \times 2 \left[ -\frac{1}{2} \cos\left(\frac{\sqrt{3}a_h q_y}{2}\right) - \frac{\sqrt{3}}{2} \sin\left(\frac{\sqrt{3}a_h q_y}{2}\right) \right]. \tag{5.14}$$

Expanding the previous equation in  $(q_x, q_y) = (0, 0)$  at the first order, the anti-diagonal term approximates to:

$$f(\vec{K} + \vec{q}) \simeq i\frac{3a_h}{2}(q_x + iq_y) + o(|q|^2). \tag{5.15}$$

The eigenvalues of  $H_k$  around the K point become:

$$E_{\pm}(q_x, q_y) = \pm \frac{3a_h t}{2} \sqrt{q_x^2 + q_y^2}, \tag{5.16}$$

The energy bands present therefore a conical evolution around the point K in the momentum space typical of Dirac's dispersion. In particular, for  $q_y = 0$  (equivalently

$q_x = 0$ ), the dispersion evolves linearly for both bands around the point K so called Dirac point, as illustrated in Figure 5.3.b). Moreover, the group velocity  $v_g$  expresses as:

$$v_g(q_y = 0) = \left. \frac{d\omega_{\pm}}{dk} \right|_{q_y=0} = \frac{1}{\hbar} \left. \frac{dE_{\pm}}{dk} \right|_{q_y=0} = \frac{1}{\hbar} \frac{3a_h t}{2} = v_F, \quad (5.17)$$

and identifies with the Fermi velocity  $v_F$ . We find a similar dispersion around the Dirac point K'. We also note that the tight-binding development for the honeycomb lattice holds true for any value of the hopping parameter  $t$ . In particular, the Fermi velocity  $v_F$  for graphene evaluates to about  $c/300$ , with  $c$  the speed of light in vacuum, corresponding to a hopping parameter  $t$  of about  $2 \text{ eV}$ .

### Graphene tight-binding wavefunctions

In the tight-binding approach, the Hamiltonian eigenfunctions write as linear combinations of the atomic wavefunctions noted  $\psi_{\vec{k}}(\vec{r})$ . Applied to graphene, the Hamiltonian eigenfunctions decompose in the basis of the two sublattices (A,B) as [2]:

$$\psi_{\vec{k}}(\vec{r}) = c_A(\vec{k})\psi_{\vec{k}}^A(\vec{r}) + c_B(\vec{k})\psi_{\vec{k}}^B(\vec{r}), \quad (5.18)$$

where  $\psi_{\vec{k}}^A(\vec{r})$  and  $\psi_{\vec{k}}^B(\vec{r})$  correspond to eigenstates of the Hamiltonian with associate coefficients  $c_A(\vec{k})$  and  $c_B(\vec{k})$ . Moreover, owing to the lattice periodicity, we search for eigenstates  $(\psi_{\vec{k}}^A(\vec{r}), \psi_{\vec{k}}^B(\vec{r}))$  in the form of Bloch functions  $\psi_{\vec{k}}(\vec{r}) = e^{i\vec{k}\cdot\vec{r}}u_{\vec{k}}(\vec{r})$  where the envelope  $u_{\vec{k}}(\vec{r})$  shares the same periodicity as the crystal. Introducing the atomic wavefunctions  $\phi(\vec{r})$  related to the  $2p_z$  orbitals of carbon atoms in graphene, the Hamiltonian wavefunction in Equation (5.18) rewrites as:

$$\psi_{\vec{k}}(\vec{r}) = \frac{1}{\sqrt{N}} \sum_j e^{i\vec{k}\cdot\vec{R}_j} \left[ c_A(\vec{k})\phi(\vec{r} - \vec{R}_j^A) + c_B(\vec{k})\phi(\vec{r} - \vec{R}_j^B) \right], \quad (5.19)$$

with  $N$  the number of graphene unit cells located at  $\vec{R}_j = m\vec{a}_1 + n\vec{a}_2$ , the multi-index  $j$  being a compact notation of the coordinates  $(m, n)$  in the lattice basis  $(\vec{a}_1, \vec{a}_2)$ . Similarly, the vectors  $\vec{R}_j^{A/B}$  indicate the atoms' positions on sites A and B, respectively.

We determine the expressions of the coefficients  $c_A(\vec{k})$  and  $c_B(\vec{k})$  by calculating the eigenvectors of the Hamiltonian  $H_k$  associate to the eigenvalues  $E_{\pm}$  and verifying:

$$H_k \begin{pmatrix} c_A(\vec{k}) \\ c_B(\vec{k}) \end{pmatrix} = E_{\pm} \begin{pmatrix} c_A(\vec{k}) \\ c_B(\vec{k}) \end{pmatrix}. \quad (5.20)$$

Introducing the phase  $\theta(\vec{k}) = -\arg[f(\vec{k})]$  of  $H_k$  anti-diagonal term  $f(\vec{k})$ , the general form of the Hamiltonian wavefunction in 5.19 rewrites as:

$$\psi_{\vec{k}}(\vec{r}) = \frac{1}{\sqrt{N}} \sum_j e^{i\vec{k}\cdot\vec{R}_j} \left[ \phi(\vec{r} - \vec{R}_j^A) \pm e^{i\theta(\vec{k})} \phi(\vec{r} - \vec{R}_j^B) \right]. \quad (5.21)$$

Knowing the form of the atomic orbitals  $\phi(\vec{r})$ , the above formula allows to map the Hamiltonian eigenfunction in real space for a given momentum  $\vec{k}$  across graphene lattice. For instance, we model  $\phi(\vec{r})$  with a Gaussian function centered on the atomic positions  $\vec{R}_j^{A/B}$ :

$$\phi(\vec{r} - \vec{R}_j^{A/B}) = e^{-\frac{(\vec{r} - \vec{R}_j^{A/B})^2}{2\sigma^2}}, \quad (5.22)$$

where  $\sigma$  refers to the width of the Gaussian function. The parameter  $\sigma$  also measures the overlap between atomic orbitals. In particular, we calculate the eigenfunctions  $\psi_+(\vec{r})$  and  $\psi_-(\vec{r})$  associate to the bands  $E_+$  and  $E_-$  plotted in Figure 5.4.a) along the direction  $\Gamma$ -K, at the specific momentum  $\vec{k} = 0.97\vec{K}'$  in preparation of further developments. We choose the Dirac point  $K'$  with coordinates  $(0, \frac{4\pi}{3\sqrt{3}a_h})$  in the FBZ depicted in Figure 5.2.b).

We present, therefore, the maps of square modulus  $|\psi_+(\vec{r})|^2$  and  $|\psi_-(\vec{r})|^2$  in Figure 5.4.b) for  $\sigma$  varying from  $0.2a_h$  to  $0.5a_h$  across a few unit cells of the honeycomb lattice. For  $\sigma = 0.2a_h$ , the eigenfunctions consists of the superimposition of the isolated atomic orbitals owing to the weak or quasi-nonexistent overlap between the Gaussian functions. At  $\sigma = 0.3a_h$ , the overlap between the orbitals initiate in the vertical and horizontal directions for  $\psi_+$  and  $\psi_-$ , respectively. At  $\sigma = 0.4a_h$  and  $\sigma = 0.5a_h$ , the significant overlap generates the spreading of the atomic wavefunctions between adjacent atomic sites in the vertical ( $\psi_+$ ) and horizontal ( $\psi_-$ ) directions.

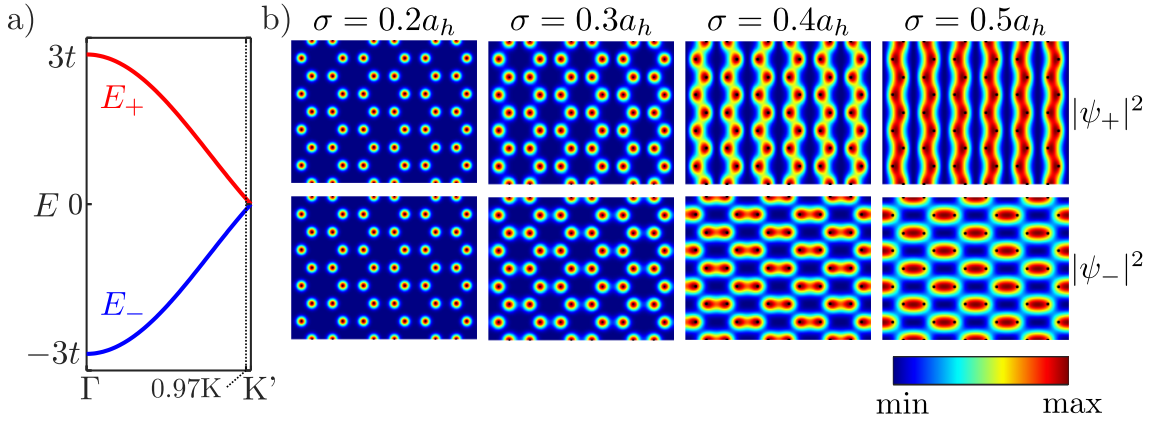


FIGURE 5.4: a) Graphene tight-binding energy dispersion  $E(\vec{k})$  along the high symmetry direction  $\Gamma$ -K in the FBZ. We note upper and lower bands  $E_+$  and  $E_-$ , respectively. b) Maps of graphene tight-binding wavefunctions square modulus  $|\psi_+|^2$  and  $|\psi_-|^2$  calculated in the upper and lower energy bands, respectively, at the momentum  $\vec{k} = 0.97\vec{K}'$  for various width of the Gaussian atomic function  $\sigma/a_h = 0.2, 0.3, 0.4, 0.5$ .

### 5.1.2 Honeycomb lattice photonic crystal

In the previous part, we have reviewed the main features of the tight-binding model used to calculate graphene energy band structure and wavefunctions' spatial distribution across the honeycomb lattice. The analogue of graphene in the class of photonic crystals consists of a honeycomb lattice photonic crystal membrane (HC-PCM). In the current part, we focus on the design of the HC-PCM constituting the building block of targeted photonic crystal analogues of carbon nanotubes (CNTs). We present the optical simulations of the photonic band structure and the modes' profiles of the PCM using the FDTD method. In particular, we analyze the photonic results in the light of the solid-state tight-binding model results.

#### 2D simulation of circular-hole HC-PCM

We perform a first series of FDTD simulations of a 2D honeycomb lattice photonic crystal (HC-PC) equivalent to an infinitely-thick HC-PCM. In addition to low simulation time and memory requirements, the 2D simulations offer a convenient testing

ground to approach, in first approximation, the dispersion curves of the HC-PCM while varying the model parameters. In particular, we calculate the HC-PC band structures for two different incident polarizations and we realize a first adjustment of the lattice parameters.

We present in Figure 5.5.a) a CAD view of the HC-PC FDTD model consisting of honeycomb lattice with a period  $a_h$  of circular air holes of radius  $r$  etched in an InP matrix ( $n_{\text{InP}} \simeq 3.16$  at  $1.55 \mu\text{m}$ ). We may refer to Chapter 2 Section 2.1 for a complete description of the simulation parameters. We apply Bloch boundary conditions (BC) to repeat the calculation cell (orange line) periodically. We set the simulation time  $t_s$  to 1000 fs and generate a non-uniform mesh with an accuracy level of 3. We place four pairs of two magnetic (electric) dipoles distributed symmetrically in the calculation zone and oriented along the  $z$  axis direction to excite TE (TM) modes. The spectral bandwidth of the dipoles spans the frequency range from 10 to 500 THz. A cloud of 15 monitors arranged randomly in the cell collect the fields' temporal evolutions. We finally calculate the band structure by Fourier transform of the temporal data apodized beforehand with the parameters  $t_c = 0.5t_s$  and  $\Delta t = 0.125t_s$ .

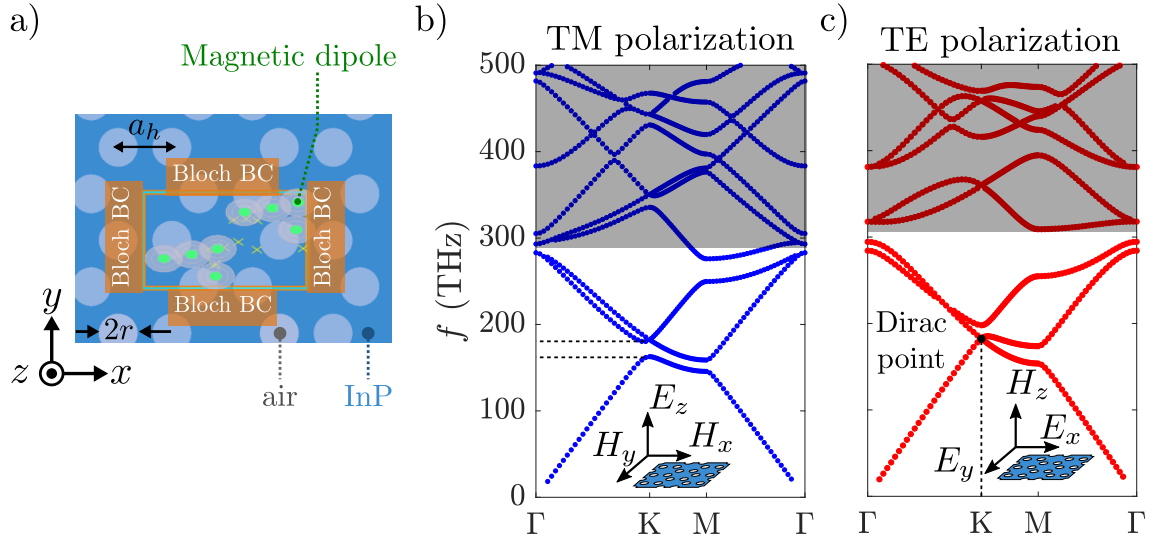


FIGURE 5.5: a) FDTD model of the honeycomb lattice photonic crystal (HC-PC) with a period  $a_h$  and air holes of radius  $r$  etched in InP material. We apply Bloch boundary conditions (BC) on the frontiers of the calculation zone (orange outline). We place magnetic dipoles (green arrows) oriented along the  $z$ -axis direction to excite TE polarized modes. b) and c): Band structures of the HC-PCM with  $a_h = 0.23 \mu\text{m}$  and  $r = 0.067 \mu\text{m}$ , calculated for TM and TE polarizations depicted on the inset drawings, respectively.

We plot in Figure 5.5.b) and c) the HC-PC band structures calculated for TM and TE polarizations, respectively, along  $\Gamma$ -K-M- $\Gamma$ . We have first fixed the period  $a_h$  and the air filling factor noted FF ( $\text{FF} = 4\pi r^2 / (3\sqrt{3}a^2)$ ) to arbitrary values of  $0.23 \mu\text{m}$  and  $0.2$ , giving a hole radius  $r = 0.067 \mu\text{m}$ . The inset drawings indicate the orientation of the electric and magnetic fields' Cartesian components for the two polarizations with respect to the photonic crystal plane. We concentrate on the low energy region below the gray-shaded where we distinguish three bands for both polarizations. We observe, for the TE polarization, the crossing of two bands with linear dispersion along  $\Gamma$ -K in K so called Dirac point. Conversely, we note that a band gap forms in K for the TM polarization. We focus in the following on the TE polarization configuration for which we retrieve a Dirac-like dispersion. We will clarify the bands' dynamics and nature of the modes in the later 3D simulations of HC-PC membrane.



In anticipation to the optical characterization of real active structures, we intend to position the dispersion key features close to the emission of the embedded quantum dashes (QDas) at about  $1.5 \mu m$ . In particular, we aim to move the Dirac point located at a wavelength  $\lambda_D$  toward the  $\lambda_{\text{ref}} = 1.5 \mu m$  reference. In Figure 5.5.c), for  $a_h = 0.23 \mu m$  and  $r = 0.067 \mu m$  (FF = 0.2), we find the Dirac point at about 183 THz ( $\lambda \sim 1.64 \mu m$ ), or 0.14 in normalized frequency units  $a_h/\lambda$ . Using scalable properties of Maxwell's equations, we shift the Dirac point to  $\lambda_{\text{ref}}$  by maintaining a constant ratio  $a_h/\lambda = 0.14$  but adapting  $a_h$  to obtain  $\lambda = \lambda_D = 1.5 \mu m$ . Keeping a filling factor FF = 0.2, the Dirac point locates, therefore, at  $1.5 \mu m$  for  $a_h = 0.212 \mu m$  and  $r = 0.061 nm$ .

We notice the delicate fabrication of highly resolved air holes with a radius  $r$  inferior, in a large extent, to  $100 nm$ . We increase the filling factor FF to obtain a larger value of  $r$  while maintaining the Dirac point position. Nevertheless, increasing FF diminishes the distance between two adjacent holes. It augments then the risk of pattern merging, considering the proximity effects generated during the lithography process. We opt for a filling factor FF of 0.32 leading to a radius  $r$  of  $77 nm$ . Repeating the Dirac spectral adjustment, we obtain the following set of parameters  $a_h = 0.232 \mu m$ ,  $r = 0.084 \mu m$  (FF  $\sim 0.32$ , serving as a starting point for the following 3D simulation.

### 3D simulation of circular-hole HC-PCM

We conduct then a series of 3D FDTD optical simulations of more realist HC-PCM structures of finite thickness  $h$ . We first calculate the band structure of a HC-PCM with a thickness  $h = 0.23 \mu m$  close to fabricated membrane thicknesses (see Section 4.1). We keep the same FDTD parameters as for the 2D case expect for PML boundary conditions with a *steep-angle* profile applied on each side of the photonic membrane at a distance  $d_{\text{PML}} = 5 \times h$ . We place out-of-plane magnetic dipoles to excite TE-polarized modes exclusively. Starting with the 2D set of lattice parameters,  $a_h = 0.232 \mu m$ ,  $r = 0.084 \mu m$  (FF  $\sim 0.32$ ), we adjust them to obtain a Dirac point at about  $1.5 \mu m$  as described previously.

We have plotted in Figure 5.6 the band structure (gray dotted line) calculated for a HC-PCM with  $a_h = 0.301 \mu m$ ,  $r = 0.109 \mu m$  exhibiting a Dirac point at about 194.5 THz ( $1.54 \mu m$ ). We also superimpose the two frequency bands derived from the tight-binding model with a hopping parameter  $t \simeq 25.6$  THz estimated by linearization of the numerical branches around the Dirac point. In the photonic band structure, we observe three bands that we note  $B_1$ ,  $B_2$  and  $B_3$ . In comparison to the tight-binding reference, we notice the following photonic specificities :

- the photonic band diagram comprises a band  $B_3$  in addition to the Dirac branches  $B_1$  and  $B_2$ ;
- along  $\Gamma$ -K direction:  $B_1$  ( $B_2$ ) deviates from the lower (upper) tight-binding branch as the frequency decreases (increases) and away from the Dirac crossing;
- along K-M direction:  $B_1$  follows accurately the lower tight-binding (TB) branch while  $B_2$  bends downwards the Dirac level;
- along M- $\Gamma$  direction:  $B_1$  deviates from the lower TB branch while  $B_2$  is shifted with respect to the upper TB branch.

As commonly observed in photonic crystal dispersion relations, at low frequencies, the optical wavelength increases until the PC pattern has no more diffractive effect

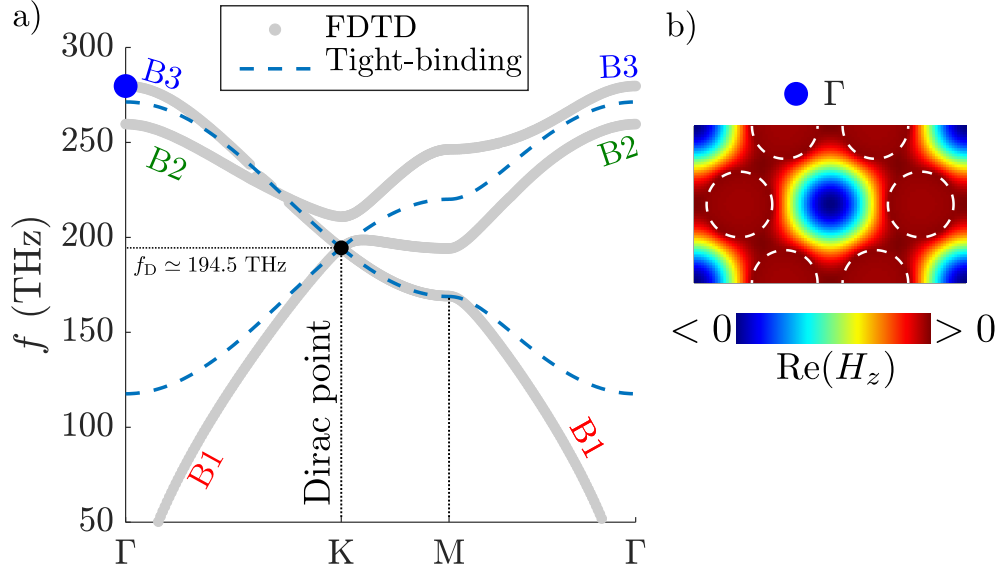


FIGURE 5.6: a) FDTD band structure along  $\Gamma$ -K-M- $\Gamma$  of a honeycomb lattice photonic crystal membrane (HC-PCM) with a period  $a_h = 0.301 \mu\text{m}$  of circular air holes of radius  $r = 0.109 \mu\text{m}$  in a  $0.228 \mu\text{m}$ -thick InP membrane. The dashed blue curve corresponds to the tight-binding model dispersion with a hopping parameter  $t \approx 25.6$  THz. b) Spatial distribution of the real part of the magnetic component  $H_z$  calculated on the band  $B_3$  in  $\Gamma$  (blue dot) over the HC-PCM unit cell.

on incident light so that the photonic dispersion becomes linear. This phenomenon accounts for the progressive divergence between  $B_1$  and the lower TB branch along  $\Gamma$ -K, away from the Dirac point.

We identify the nature of the modes existing along the band  $B_3$  by calculating the spatial distribution of the real part of the magnetic field component  $H_z$  over the PCM unit cell in  $\Gamma$  point. The resulting map is represented in Figure 5.6.b where the dashed white lines delimit the contour of the circular air holes. We remark that the photonic mode presents a monopolar distribution of the magnetic field, so that we refer to this mode as the monopolar mode in the following.

We note the concurrence between the photonic and TB bands in the close vicinity of the Dirac point, when both dispersion curves become linear. To complete the comparison between the two models, we confront the maps of the photonic modes with graphene wavefunction probability density for similar value of the momentum  $\vec{k}$  close to K. Therefore, we display in Figure 5.7.a) to d) the real part and square modulus of graphene TB wavefunctions  $\psi_+$  and  $\psi_-$  from the respective frequency bands  $f_+$  and  $f_-$  plotted in j) for the momentum  $\vec{k} = 0.97\vec{K}$ . The star markers indicate the centers of the Gaussian-type atomic orbitals with the overlap parameter  $\sigma = 0.5a_h$ . Similarly, we present in Figure 5.7.e) to h) the spatial distribution over the calculation zone depicted on the drawing i) of the real part and intensity of the magnetic components  $H_z^+$  and  $H_z^-$  on the upper and lower photonic bands coinciding with  $f_+$  and  $f_-$  branches in the plot j) at  $\vec{k} = 0.97\vec{K}$ . The star markers correspond to the holes' centers.

We observe a great consistency of the photonic fields' maps with the TB wavefunctions' real-space images calculated on the Dirac branches. In particular, the magnetic field's amplitude and intensity distributions share the same symmetries and amplitude extrema locations over the computation cell as the TB wavefunctions. In the TB model, the value of the Gaussian width  $\sigma = 0.5a_h$  assessed to reproduce the photonic maps suggests a significant overlap between the atomic orbitals in comparison to the TB model assumptions of weakly interacting atomic orbitals. Nevertheless, the TB model

provides a good approximation of the photonic dispersion and modes' profiles in the linear region, close to the Dirac point exclusively.

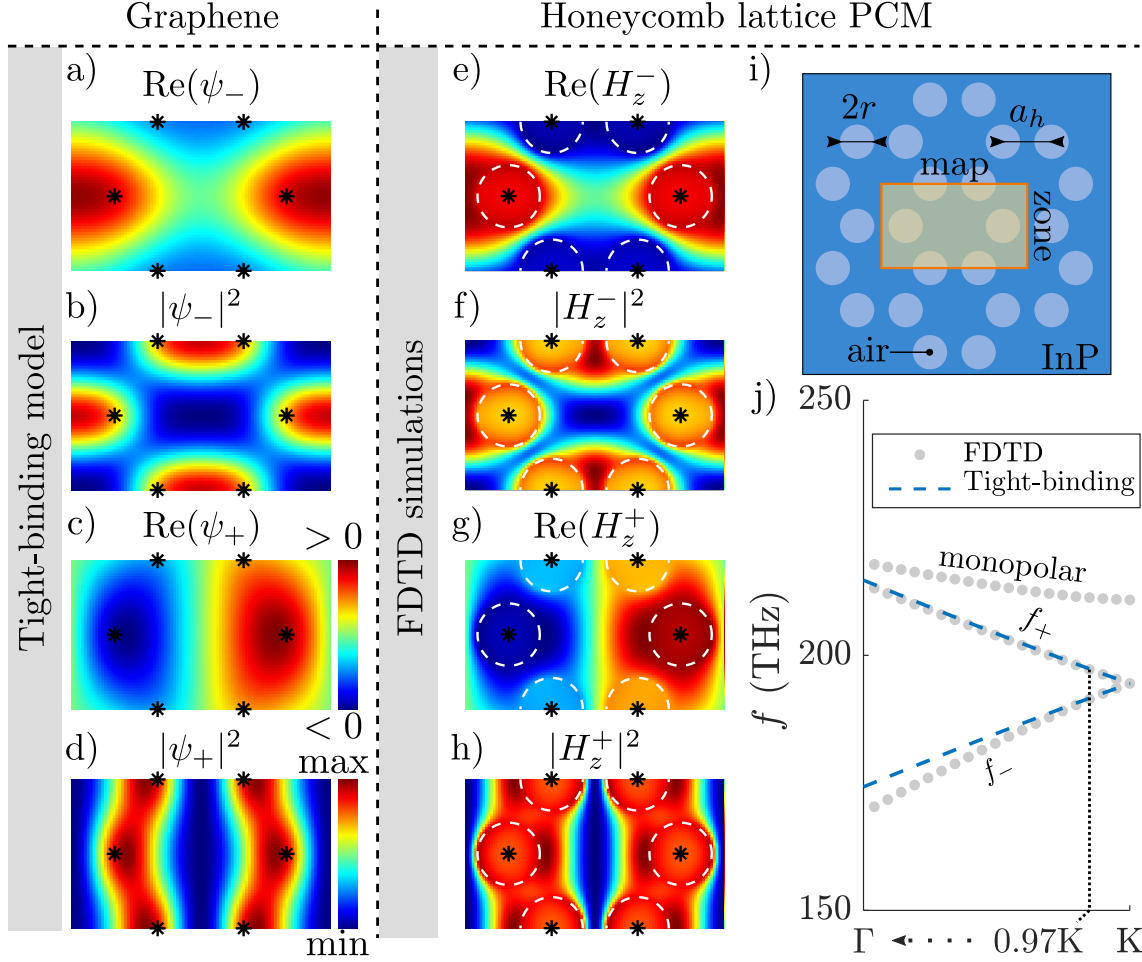


FIGURE 5.7: a) to d): Spatial distribution of the real part and square modulus of graphene TB wavefunctions  $\psi_+$  and  $\psi_-$  calculated for Gaussian-like atomic orbitals of width  $\sigma = 0.5a_h$ . e) to h) Maps over the calculation zone of the real part and intensity of the magnetic field components  $H_z^+$  and  $H_z^-$  for the wave vector  $\vec{k} = 0.97\vec{K}$ . i) Schematics of a circular-hole HC-PC with a period  $a_h$  and circular air holes of radius  $r$  etched in an InP matrix. j) Zoom of the band structure presented in Figure 5.6 around the Dirac K point.

We finally notice that the interaction between  $B_2$  and  $B_3$ , not investigated in this work, causes the bending of band  $B_3$  which passes below the Dirac point frequency  $f_D$  as depicted in Figure 5.6.a). Such a phenomenon may impede the opening of a gap at the level of the Dirac point as required to produce an insulating system showing potential non-trivial topological properties. A finer adjustment of the lattice parameters would allow the uplifting of band  $B_3$  to generate a small gap as reported by Anderson *et al.* in [3]. Another strategy proposed, for instance, by Barik *et al.* in [4], consists in replacing the circular holes by equilateral triangular air holes. In the following, we design an HC-PCM structure with triangular air holes in addition to the circular-hole version.

### 3D simulation of triangular-hole HC-PCM

Drawing inspiration from the design suggested in [4], the triangular-hole HC-PCM consists of equilateral triangular air holes with edges of size  $s$  etched in an  $h$ -thick InP membrane according to a regular honeycomb lattice of period  $a_h$  as schematized

in Figure 5.8.a). In particular, we note that the  $C_3$  ( $120^\circ$ ) rotational symmetry of the triangles preserves the honeycomb pattern system which, otherwise, turns into a triangular lattice. Indeed, the unit cell (dashed black contour) still contains two face-to-face triangular elements which generates the honeycomb lattice when repeated periodically along the lattice vectors ( $\vec{a}_1, \vec{a}_2$ ).

By contrast with circular-hole HC-PCM, the triangular-hole version has a monopolar mode which concentrates in a smaller region of the dielectric matrix (hexagons' centres), hence increasing the mode's frequency. Indeed, we observe in Figure H.1.a) a higher frequency monopolar mode for a triangular-hole HC-PCM with a period  $a_h = 0.301 \mu\text{m}$  and edge size  $s = 0.294 \mu\text{m}$  than the one obtained in the circular-hole HC-PCM (green dashed line) with the same period and holes' radius  $r = 0.109 \mu\text{m}$ . We determine the triangle edge size  $s$  so that triangular and circular holes cover the same areas. We also observe a smaller deformation of the Dirac upper branch for the triangular-hole HC-PCM due weak interaction with the monopolar mode.

To minimize the interaction with the monopolar mode and preserve at best the integrity of the Dirac bands, we increase the size edge  $s$  of the triangular-hole HC-PCM to move the monopolar mode as far as possible. We display in Figure H.1.a) to i) the band diagrams along K-M direction, fixing  $a_h$  to  $0.301 \mu\text{m}$  while varying  $s$  from  $0.294 \mu\text{m}$  to  $0.450 \mu\text{m}$ . We note that increasing  $s$  raises the monopolar mode frequency but also the Dirac branches which deform when approaching higher-order bands. We opt for  $s = 0.4 \mu\text{m}$  as a good compromise to remove the monopolar mode while maintaining Dirac bands far from upper bands. We adjust then the lattice parameters to position the Dirac point at about  $1.5 \mu\text{m}$  leading to the following geometry:  $a_h = 0.367 \mu\text{m}$  and  $s = 0.490 \mu\text{m}$  characterized by a Dirac frequency  $f_D \simeq 202.6 \text{ THz}$ .

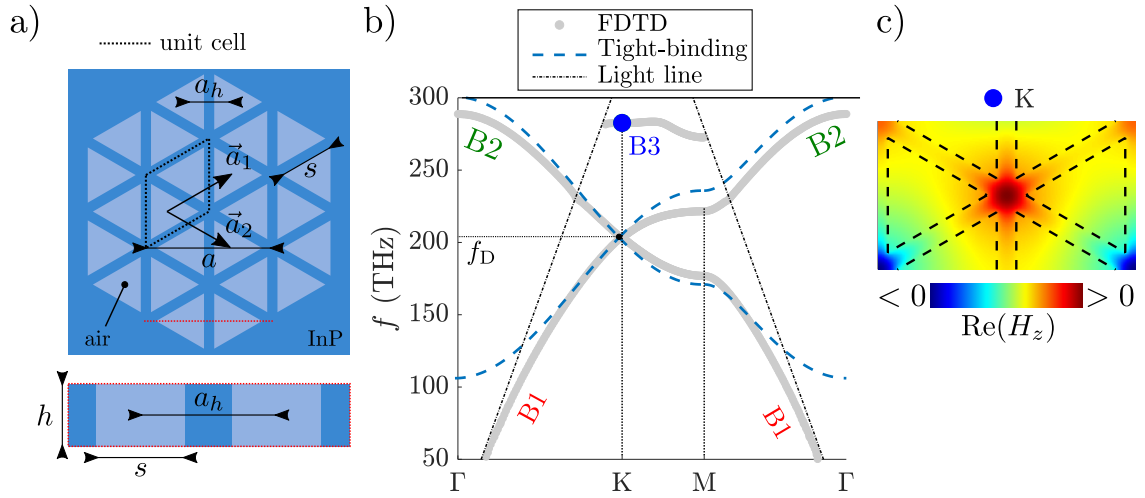


FIGURE 5.8: a) Schematics of a triangular-hole HC-PCM. Upper drawing: top view of the honeycomb lattice with a period  $a_h$  of equilateral triangular air holes of edge size  $s$  in InP material matrix. Lower drawing: lateral view of the InP membrane of thickness  $h$ . b) FDTD band structure of a triangular-hole HC-PCM of geometrical parameters  $a_h = 367 \mu\text{m}$ ,  $s = 0.490 \mu\text{m}$  and  $h = 0.228 \mu\text{m}$ . c) Spatial distribution of the real part of the magnetic component  $H_z$  calculated on the band  $B_3$  in K (blue dot) over the triangular hole HC-PCM unit cell.

We represent in Figure 5.8.b) the band structure simulated for a triangular-hole HC-PCM with  $a_h = 0.367 \mu\text{m}$ ,  $s = 0.490 \mu\text{m}$  and  $h = 0.228 \mu\text{m}$  along  $\Gamma$ -K-M- $\Gamma$  direction. We have superimposed the TB bands with a hopping parameter  $t \simeq 28.7 \text{ THz}$  obtained by linear fit around the Dirac point located at about  $203 \text{ THz}$  or  $1.48 \mu\text{m}$ . We count three photonic bands labelled  $B_1$ ,  $B_2$  and  $B_3$  partly recreated under the light lines

(oblique dark dashed lines). We identify bands  $B_1$  and  $B_2$  with the lower and upper TB bands, respectively. We investigate the nature of the spectrally remote branch  $B_3$  by calculating the spatial distribution of the real part of the magnetic field component  $H_z$  in K over the HC-PCM unit cell. The resulting map in Figure 5.8.c present a monopolar distribution of the magnetic field such that we associate the branch  $B_3$  to the monopolar mode.

Although a more accurate reproduction of the TB band shape along KM as compared to the circular hole structure dispersion, we still report a slight bending of  $B_2$  judging by the asymmetric splitting of  $B_1$  and  $B_2$  from the Dirac point level. Nevertheless, we observe that the band  $B_2$  is not crossing the Dirac level anymore on the K-M path, allowing for the opening of a gap and for the potential emergence of topological effects.

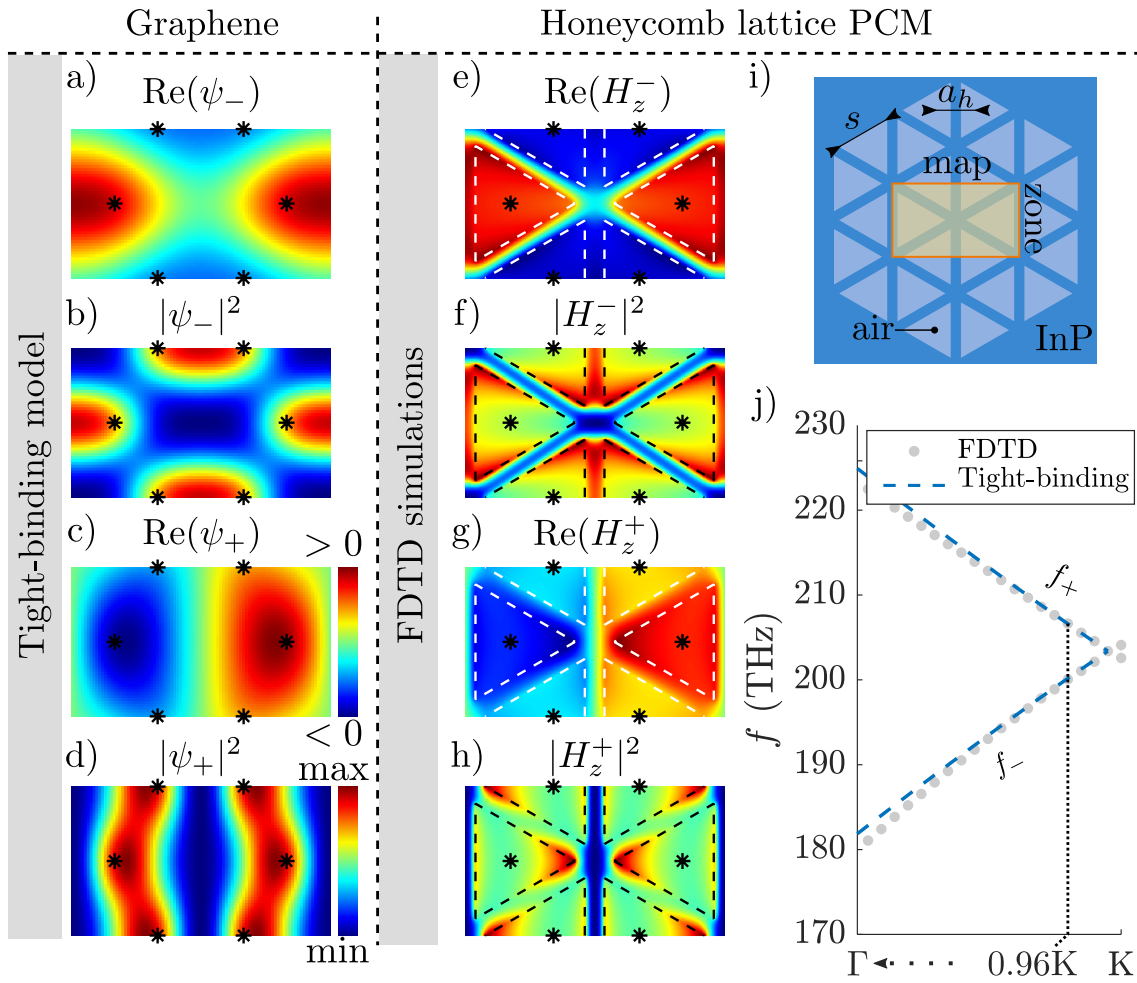


FIGURE 5.9: a) to d): Spatial distribution of the real part and square modulus of graphene TB wavefunctions  $\psi_+$  and  $\psi_-$  calculated for Gaussian-like atomic orbitals of width  $\sigma = 0.5a_h$ . e) to h) Maps over the calculation zone of the real part and intensity of the magnetic field components  $H_z^+$  and  $H_z^-$  for the wave vector  $\vec{k} = 0.97\vec{K}$ . i) Schematics of a triangular-hole HC-PC with a period  $a_h$  and triangular air holes of edge  $s$  etched in an InP matrix. j) Zoom of the band structure presented in Figure 5.8 around the Dirac K point.

We finally examine the analogies between the photonic modes' profiles over the HC-PCM unit cell depicted in Figure 5.9.i) and the spatial distributions of the TB wavefunctions around the Dirac point. Similarly to the air-hole structure, we calculate for both models the spatial location of the modes for  $\vec{k} = 0.96\vec{K}$  as indicated on the

band structures plotted in Figure 5.9.j). We note a shift of the position of the Dirac bands crossing due to an unsatisfying mesh of the triangular holes. In particular, for a Gaussian width parameter  $\sigma = 0.5a_h$ , the TB wavefunctions  $f_+$  and  $f_-$  distributions in amplitude (a) and c)) and intensity (b) and d)) match the photonic profiles  $H_z^-$  and  $H_z^+$  calculated on lower and upper photonic bands, respectively, in amplitude (e) and g)) and intensity (f) and h)). In other words, the spatial distributions of both models' solutions share the same symmetries and parities. Due to the proximity of the triangular holes, we observe an important spreading of the magnetic energy between adjacent triangles.

### 5.1.3 Conclusion of the section

#### Key points of the section

We have first reviewed the mains results of the tight-binding (TB) model used to approach graphene band structure and wavefunctions. We have then simulated with the band structures and modes' profiles of graphene photonic crystal analogues, honeycomb lattice photonic crystal membranes (HC-PCM), from which we can draw the following conclusions:

- in the natural HC-PCM analogue with circular air holes, we obtain the two Dirac bands with an additional band (monopolar band) specific to the photonic model; the interaction between the upper Dirac branch and the monopolar band causes the deformation and bending of the Dirac band below the Dirac frequency which may impede the opening of a gap at the Dirac point level towards the production of topological effects;
- in the HC-PCM version with triangular holes, the monopolar mode is removed at higher frequencies which globally preserves the Dirac dispersion integrity and free the Dirac level from any bands;
- the TB model provides a good approximation of the band structures and modes' profiles for both HC-PCM structures in close vicinity to the Dirac point;

Dirac materials show great potential to generate topological effects such as the emergence of unidirectional edge states. In particular, edge states emerge in graphene ribbons as planar intermediary of nanotubes, depending on the nature of the edge. In the following section, we investigate the topological properties of graphene ribbons' photonic crystal analogues based on HC-PCM structures.

## 5.2 Graphene ribbons and honeycomb lattice photonic crystal ribbons

In this section, we first review topological properties of graphene ribbons which depend on the edge shape specifically. In particular, we present the main results obtained by Deplace *et al.* in [5] which predict the existence of edge states in graphene ribbons for any type of edges by calculating a corresponding Zak phase. We then investigate the topological behaviour of photonic crystal analogues of graphene ribbons, namely



ribbons of HC-PCM. To this end, we propose two methods to assess numerically the existence of edge states in the photonic structures. The first method, based on Delplace's results, calculates a discrete version of the Zak phase for photonic ribbon specimens. The second method simulates the band structure of photonic ribbons defined by a given edge shape.

### 5.2.1 Topology of graphene ribbons

#### Construction of the Zak phase for graphene ribbons

The determination of graphene ribbons' topological properties as described in [5] involves the calculation of a Zak phase built from bulk graphene Hamiltonian and the definition of an edge-dependent Brillouin zone.

We recall from Section 5.1, graphene tight-binding Bloch Hamiltonian in the basis of sublattices (A,B) depicted in Figure 5.10, approaching graphene electronic properties:

$$H_k = t \begin{pmatrix} 0 & f(\vec{k}) \\ f(\vec{k}) & 0 \end{pmatrix} = t|f(\vec{k})| \begin{pmatrix} 0 & e^{-i\theta(\vec{k})} \\ e^{i\theta(\vec{k})} & 0 \end{pmatrix}, \quad (5.23)$$

where  $f(\vec{k}) = 1 + e^{-i\vec{k}\cdot\vec{a}_1} + e^{-i\vec{k}\cdot\vec{a}_2} = |f(\vec{k})|e^{-i\theta(\vec{k})}$ ,  $\theta(\vec{k}) = -\arg f(\vec{k})$ , expressed in the lattice vector basis  $(\vec{a}_1, \vec{a}_2)$  with  $\vec{a}_1 = (3a_h/2, -\sqrt{3}a_h/2)$  and  $\vec{a}_2 = (3a_h/2, \sqrt{3}a_h/2)$ . Graphene energy bands directly derive from  $H_k$  eigenvalues writing as  $E_{\pm} = \pm t|f(\vec{k})|$  as well as corresponding normalized eigenvectors  $|u_{k,\pm}\rangle$  expressing in the form:

$$|u_{k,\pm}\rangle = \frac{1}{\sqrt{2}} \begin{pmatrix} e^{-i\theta(\vec{k})} \\ \mp 1 \end{pmatrix}. \quad (5.24)$$

We emphasize that the previous eigenstates are defined by a gauge transformation, namely  $|\tilde{u}_{k,\pm}\rangle \rightarrow e^{i\phi_k}|u_{k,\pm}\rangle$ , with a  $\vec{k}$ -dependent phase factor  $\phi_k$ , also constitute a valid solution. We will show later that, by contrast with the Berry phase, the Zak phase is not invariant by any gauge transformation of the eigenstates.

In the Pauli matrices basis  $\vec{\sigma} = (\sigma_x, \sigma_y, \sigma_z)$ , the Hamiltonian  $H_k$  adopts the compact form:

$$H_k = t\vec{g}(\vec{k}) \cdot \vec{\sigma}, \quad (5.25)$$

where  $\vec{g}(\vec{k}) = |f(\vec{k})|(\cos \theta(\vec{k}), \sin \theta(\vec{k}), 0)$ . Therefore, the Hamiltonian  $H_k$  assimilates to the typical Bloch Hamiltonian of a 1D chain of dimers described in Chapter 1, except that  $\vec{k}$  momenta span a 2D parameter space. In particular, the winding of  $\vec{g}(\vec{k})$  around the  $\vec{k}$ -origin as  $\vec{k}$  varies across the Brillouin zone encodes the system's topological properties and information about the existence of edge states. Ryu and Hatsugai have originally used this approach in [6] to predict the presence of edge states in graphene ribbons with prescribed edges shape by calculating the Zak phase from an edge-*specific* Hamiltonian. Conversely, Delplace's strategy consists in describing any graphene ribbon with a *common* bulk Hamiltonian while constructing an edge-*specific* Brillouin zone to evaluate the Zak phase of the ribbon. In particular, this method has the merit to address a larger range of graphene ribbons.

We define one graphene ribbon's edges with connected dimers (A-B) of *fixed orientation* invariant by translation by  $\vec{T} = m\vec{a}_1 + n\vec{a}_2$ ,  $(m, n) \in \mathbb{Z}^2$ , so called *translation vector*, expressed in graphene lattice basis  $(\vec{a}_1, \vec{a}_2)$ . Assuming parallel edges, the edges deduce from one to the other by translation by an arbitrary vector  $\vec{C}$  written in graphene lattice basis. We illustrate different types of edges in Figure 5.10 constructed according

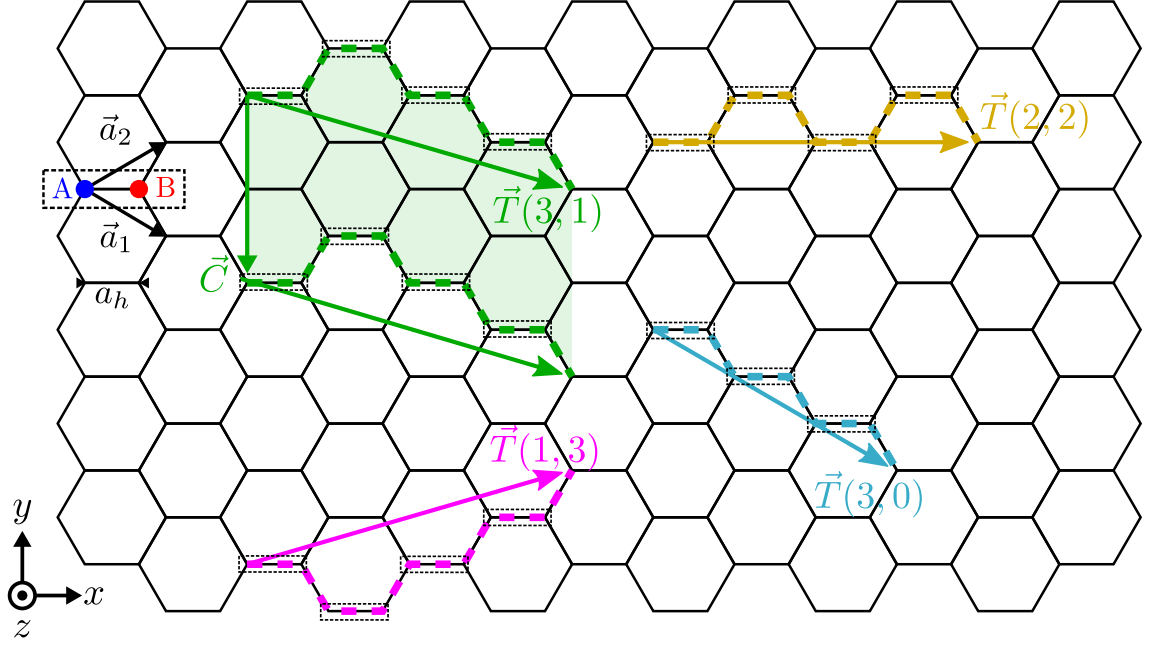


FIGURE 5.10: Illustration of different types of graphene ribbon edges as a function of the translation vector  $\vec{T}$ .

to predefined  $\vec{T}$  vectors with dimers (A-B) oriented along the  $x$ -axis direction<sup>1</sup>. We have, for instance, highlighted the pale green-shaded area delimited by edges defined by  $\vec{T}(3,1)$  and  $\vec{C}(2,-2)$ . We remark that translation vectors  $\vec{T}(3,1)$  (green arrow) and  $\vec{T}(1,3)$  (purple arrow) describe the same type of edges. Furthermore, graphene ribbons constructed with  $\vec{T}(2,2)$  and  $\vec{T}(3,0)$  belong to the generic classes of armchair ( $\vec{T}(m,m)$ ,  $m \in \mathbb{Z}$ ) and zig-zag ( $\vec{T}(m,0)$ ,  $m \in \mathbb{Z}$ ) ribbons owing to the so-formed edge shapes.

The calculation of the Zak phase for 1D systems such as the 1D chain of dimers described in Chapter 1, relies on the integral of the Berry connection over the 1D Brillouin zone. Extended to graphene ribbons, the integration path restrains to a section of the 2D graphene Brillouin zone along the direction perpendicular to the ribbon axis  $\vec{T}$  with associate momentum component  $k_{\perp}$ . Indeed, the projection of the momentum along  $\vec{T}$  noted  $k_{\parallel}$  represents a good quantum number due to the discrete translational symmetry. Therefore, we define the Zak phase  $\mathcal{Z}(k_{\parallel})$  of a graphene ribbon for a given  $k_{\parallel}$  by the integral of the Berry connection over the Brillouin zone along  $k_{\perp}$  direction.

In the simplest case of  $(m,n)$  coprime integers, we construct the ribbon's Brillouin zone  $(\vec{\Gamma}_{\parallel}, \vec{\Gamma}_{\perp})$  where  $\vec{\Gamma}_{\parallel}$  coincides with the 1D Brillouin zone along the  $\vec{T}$ -periodic direction. We define the second vector  $\vec{\Gamma}_{\perp}$  perpendicular to  $\vec{T}$  so that its norm verifies  $\vec{\Gamma}_{\parallel} \times \vec{\Gamma}_{\perp} = \vec{a}_1^* \times \vec{a}_2^*$ . In other words, the basis  $(\vec{\Gamma}_{\parallel}, \vec{\Gamma}_{\perp})$  covers the same area as generated by the reciprocal lattice vectors  $(\vec{a}_1^*, \vec{a}_2^*)$ . We obtain, therefore, the following coordinates of the vectors  $\vec{\Gamma}_{\parallel}$  and  $\vec{\Gamma}_{\perp}$  in the basis  $(\vec{a}_1^*, \vec{a}_2^*)$ :

$$\begin{cases} \vec{\Gamma}_{\parallel}(m,n) = \left[ \frac{n+2m}{2N} \right] \vec{a}_1^* + \left[ \frac{m+2n}{2N} \right] \vec{a}_2^*, \\ \vec{\Gamma}_{\perp}(m,n) = -n \vec{a}_1^* + m \vec{a}_2^* \end{cases} \quad (5.26)$$

<sup>1</sup>We note that in [5], the dimers orient along the  $y$ -axis in a lattice basis rotated with a  $90^\circ$  angle with respect to our present basis  $(\vec{a}_1, \vec{a}_2)$ .



with  $N = m^2 + n^2 + mn^2$ .

Introducing the unitary vectors  $\vec{e}_\parallel = \vec{\Gamma}_\parallel/|\vec{\Gamma}_\parallel|$  and  $\vec{e}_\perp = \vec{\Gamma}_\perp/|\vec{\Gamma}_\perp|$ , and decomposing  $\vec{k}$  in the basis  $(\vec{e}_\parallel, \vec{e}_\perp)$  as  $\vec{k} = k_\parallel \vec{e}_\parallel + k_\perp \vec{e}_\perp$ , the Zak phase  $\mathcal{Z}(k_\parallel)$  writes as:

$$\mathcal{Z}(k_\parallel) = i \oint \langle u_{k,\pm} | \partial_{k_\perp} u_{k,\pm} \rangle dk_\perp, \quad (5.27)$$

where  $\vec{k}_\perp$  evolves along  $\vec{\Gamma}_\perp$  of the Brillouin zone considered as a closed path. Identifying the eigenfunctions  $|u_{k,\pm}\rangle$  using Equation (5.27), the Zak phase becomes:

$$\mathcal{Z}(k_\parallel) = i \oint \partial_{k_\perp} \theta(\vec{k}) dk_\perp. \quad (5.28)$$

We note an identical expression of the Zak phase for the eigenvectors  $|u_{k,+}\rangle$  and  $|u_{k,-}\rangle$  located on the upper  $E_+$  and lower  $E_-$  graphene energy bands, respectively. By analogy with a 1D finite chain of dimers, the bulk-edge correspondence for a given  $k_\parallel$  reads:

$$\left| \frac{\mathcal{Z}(k_\parallel)}{\pi} \right| = \left| \frac{1}{2\pi} \oint \frac{d\theta(k_\parallel, k_\perp)}{dk_\perp} dk_\perp \right|, \quad (5.29)$$

evaluating the number of pairs of edge states from the bulk topological phase  $\mathcal{Z}(k_\parallel)$ .

### Graphical determination of the Zak phase

According to Equation (5.28), the evaluation of the Zak phase for any graphene ribbon  $\vec{T}(m, n)$  depends on the evolution of the phase  $\theta(\vec{k})$  in the  $k$ -space represented in Figure 5.11.a for  $\theta$  values restricted to  $[-\pi, \pi]$ . We indicate the contour of graphene Brillouin zones alternating non-equivalent Dirac points K and K' at the vertices. The plot  $\theta(\vec{k})$  reveals discontinuities connecting adjacent Dirac points in the  $k_y a$  axis direction. In particular, we obtain a non-zero Zak phase  $\mathcal{Z}(k_\parallel)$  when the integration path  $[k_\parallel, k_\parallel + \Gamma_\perp]$  crosses at least one of these discontinuities. Introducing  $d(k_\parallel)$  the number of intersections between the integration path and a line of discontinuity, the Zak phase determines, therefore, graphically as  $\mathcal{Z}(k_\parallel) = \pm\pi d(k_\parallel)$ . Moreover, the term  $d(k_\parallel)$  coincides with the number of pairs of edge states.

We illustrate the above graphical resolution method for a graphene ribbon of translation vector  $\vec{T}(0, 1)$ , in preparation to later developments. Using Equation (5.26), we first construct the corresponding Brillouin zone  $\vec{\Gamma}_\parallel(1, 0) = \vec{a}_1^* + \vec{a}_2^*/2$  and  $\vec{\Gamma}_\perp(1, 0) = \vec{a}_2^*/2$  that we report on the graph  $\theta(\vec{k})$  in Figure 5.11.a. The white shaded area covers the entire Brillouin zone generated by the basis  $(\vec{\Gamma}_\parallel(1, 0), \vec{\Gamma}_\perp(1, 0))$ . For  $\vec{k}_\parallel = \vec{k}_{\parallel,1}$ , the integration path of the Zak phase (dashed red arrow)  $[k_{\parallel,1}, k_{\parallel,1} + \Gamma_\perp]$  encounters no phase discontinuities, leading to  $\mathcal{Z}(k_\parallel) = 0$ . Conversely, for  $\vec{k}_\parallel = \vec{k}_{\parallel,2}$ , we report one crossing, spotted by a red cross, between the integration path and an oblique discontinuity line, resulting in  $\mathcal{Z}(k_\parallel) = \pm\pi$ .

More generally, we determine the size  $\Delta k_\parallel(m, n)$  of the range of  $\vec{k}_\parallel$  along  $\vec{\Gamma}_\parallel(m, n)$  for which we obtain a non-zero Zak phase, by projecting the discontinuity line onto the  $\vec{\Gamma}_\parallel(m, n)$ , leading to:

$$\Delta k_\parallel(m, n) = \frac{2\pi}{3\sqrt{3}a_h} \frac{|n - m|}{\sqrt{N}}, \quad (5.30)$$

---

<sup>2</sup>For  $(m, n)$  not coprime, we build a basis  $(\tilde{\Gamma}_\parallel, \tilde{\Gamma}_\perp)$  of the reciprocal lattice associate to  $(m = l\tilde{m}, n = l\tilde{n})$  and define the corresponding Zak phase  $\mathcal{Z}_{(\tilde{m}, \tilde{n})}(\vec{k}_\parallel)$ .

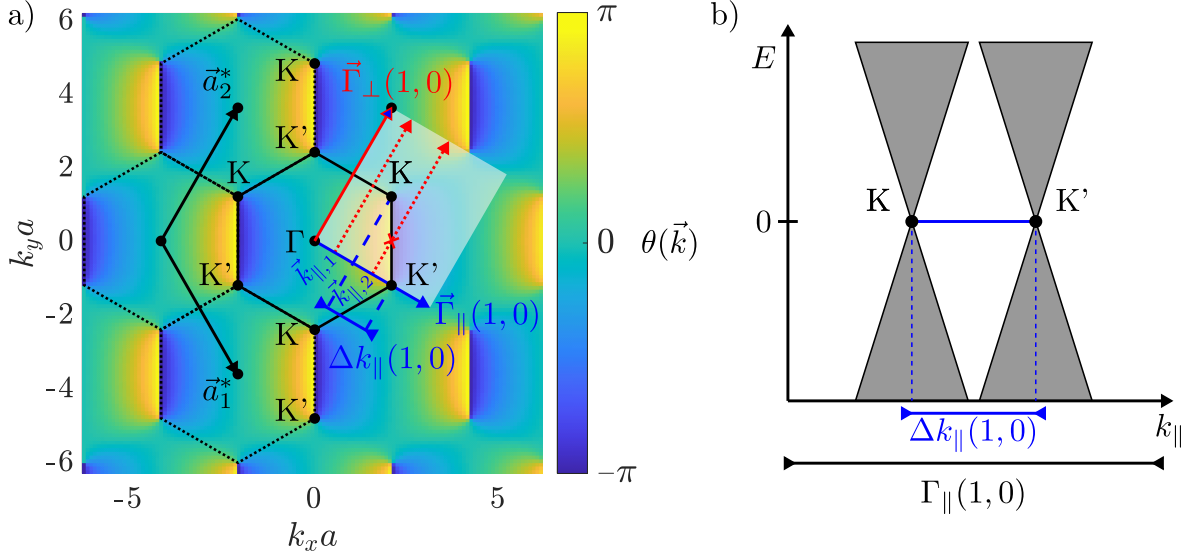


FIGURE 5.11: a) Evolution of the phase  $\theta(\vec{k})$  of graphene tight-binding eigenvectors in the reciprocal space. We indicate the Brillouin zone ( $\vec{\Gamma}_{\perp}(1,0), \vec{\Gamma}_{\parallel}(1,0)$ ) of the ribbon of translation vector  $\vec{T}(1,0)$ . b) Schematized band structure along  $\vec{\Gamma}_{\perp}(1,0)$  of the ribbon  $\vec{T}(1,0)$ .

which, divided by the length of the Brillouin zone  $|\vec{\Gamma}_{\parallel}(m,n)|$ , gives the ratio  $\mathcal{R}(m,n)$  expressed as:

$$\mathcal{R}(m,n) = \frac{|n-m|}{3}, \quad (5.31)$$

over which we expect at least one edge state existing in the graphene ribbon. For instance, we find a ratio  $\mathcal{R}(1,0) = 1/3$ , meaning that one edge state exists over one third of the Brillouin zone. More generally, according to Equation (5.31), almost every ribbons exhibit at least one edge state expect from armchair ribbons  $\vec{T}(m,m)$  characterized by  $\mathcal{R} = 0$ .

Finally, we note that the emergence of an edge state in the graphene ribbon  $\vec{T}(1,0)$  traduces by the presence of a zero-energy flat band (blue line) in graphene band structure schematized in Figure 5.11.b. It connects the two Dirac points K and K' and its symmetric distribution with respect to zero energy level directly reflect graphene chiral symmetry.

### 5.2.2 Topology of honeycomb lattice photonic crystal ribbons

On the basis of the solid-state results, we propose in this part to estimate the topological properties of graphene ribbons' photonic crystal analogues. Precisely, we intend to predict the existence of edge states for photonic ribbons according to two methods. The first method entails the numerical calculation of photonic ribbons' Zak phase using a discrete formulation of the 1D topological phase introduced previously. For the second method, we simulate the dispersion of the photonic ribbons interfacing two photonic materials of trivial topologies, to reveal potential edge states.

#### Discretized Zak phase

In the general case, an explicit expression of the eigenvectors  $|u_{k,n}\rangle$  on the  $n$ -th band as a function of  $k$  is not always accessible, preventing the integral evaluation of the Zak phase  $\mathcal{Z}$  according to Equation (5.27). We use, instead, a discrete formulation

involving numerical estimations of the normalized eigenvectors. In particular, we can consider the Zak phase as the continuum limit of the phase term [7]:

$$\phi_N = -\text{Im} \ln [\langle u_{k_1,n} | u_{k_2,n} \rangle \langle u_{k_2,n} | u_{k_3,n} \rangle \cdots \langle u_{k_{N-1},n} | u_{k_1,n} \rangle], \quad (5.32)$$

which corresponds to the geometrical phase accumulated by the vectors  $|u_{k,n}\rangle$  on the  $n$ -th band as  $k$  varies along the Brillouin zone with  $N$  discrete values  $k = k_i$  ( $i = 1, 2, \dots, N$ ). We note that the periodic Brillouin zone can be seen as a closed path in the  $k$ -space owing to the matching of the normalized edge states on the edges of the interval, formulated as  $u_{k_N,n} = u_{k_1,n}$ .

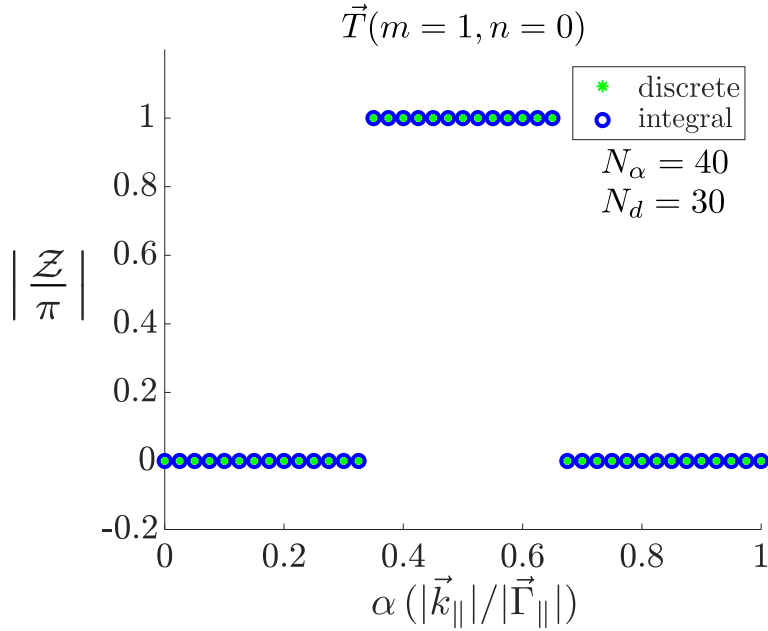


FIGURE 5.12: Evolution of the number of edge states  $|\mathcal{Z}/2\pi|$  for a graphene ribbon  $\vec{T}(1,0)$  as a function of the ratio  $\alpha = k_{||}/\Gamma_{||}$  calculated using the discrete (green stars) and integral (blue circles) formulation of the Zak phase. We choose a number  $N_\alpha = 40$  ( $0 \leq \alpha \leq 1$ ) of  $\vec{k}_{||}$  along  $\vec{\Gamma}_{||}$  and discretize the integration path in  $N_d = 30$  of samples  $k_\perp$ .

We apply, for instance, Equation (5.32) to the calculation of the Zak phase  $\mathcal{Z}(k_{||})$  of a graphene ribbon  $\vec{T}(1,0)$  for different  $k_{||}$  values, in comparison to the predictions obtained with the integral formulation. We first discretize the integration path  $[k_{||} \ k_{||} + \Gamma_\perp]$  into  $N = N_d$  samples of  $k_\perp$  component. We then evaluate, for instance, the normalized eigenvectors  $|u_{k_\perp,+}\rangle$  associate to the upper band  $E_+$  for each sample  $k_\perp$  according to Equation (5.24). We present in Figure 5.12 the evolution of the number of edge states  $|\mathcal{Z}(k_{||})/\pi|$  (green stars) as a function of the ratio  $\alpha = k_{||}/|\vec{\Gamma}_{||}|$  for  $N_d = 30$ . We report an exact matching with the number of edge states calculated with the integral Zak phase (blue circles). Indeed, we remark the existence of one edge state ( $|\mathcal{Z}(k_{||})/(2\pi)| = 1$ ) for  $\alpha$  ranging from 0.35 to 0.65 ( $\mathcal{R} = 1/3$ ) whereas we obtain a zero Zak phase for the remaining  $\alpha$  values. Moreover, we can show that the discrete Zak phase of the ribbon  $\vec{T}(1,0)$  rapidly converges toward its integral value with respect to the sampling rate  $N_d$ . Precisely, we obtain the superimposition of the discrete and integral curves from  $N_d = 5$ . We note that this superimposition depends upon the step and the initial value of the integration path  $[k_{||} \ k_{||} + \Gamma_\perp]$ .

### Numerical Zak phase of photonic ribbons

The propagation of light in photonic crystals is governed by the *master equation* derived from Maxwell's equations, written for the magnetic field  $\vec{H}(\vec{r})$  as:

$$\vec{\nabla} \times \left( \frac{1}{\varepsilon(\vec{r})} \vec{\nabla} \times \vec{H}(\vec{r}) \right) = \left( \frac{\omega}{c} \right)^2 \vec{H}(\vec{r}) \quad , \quad (5.33)$$

where  $\varepsilon(\vec{r})$  designates the dielectric constant. In particular, in periodic media, we search for solutions in the form of Bloch waves:

$$\vec{H}_{\vec{k}}(\vec{r}) = \vec{h}_{\vec{k}}(\vec{r}) e^{j\vec{k} \cdot \vec{r}} \quad , \quad (5.34)$$

where the envelope  $\vec{h}(\vec{r})$  shares the same periodicity as the crystal. The resolution of Equation (5.33) comes down to the resolution of an eigenvalue problem which eigenvalues correspond to the system energy bands  $E_{(n)}$  indexed by an integer  $n$ . Moreover, the eigenvectors associated to the energy band  $n$  are the Bloch waves  $\vec{H}_{\vec{k}}^{(n)}(\vec{r})$ , also referred to as the photonic crystal modes. In the following, we focus specifically on transverse electric (TE) polarized modes for which the magnetic field orients along the  $z$  axis normal to the photonic crystal plane. The Bloch waves solutions for TE polarization reduce then to scalar Bloch functions  $H_{z,\vec{k}}^{(n)}(\vec{r}) = h_{z,\vec{k}}^{(n)}(\vec{r}) e^{j\vec{k} \cdot \vec{r}}$ . In practice, we calculate the energy bands and the eigenvectors numerically with the FDTD method. The eigenvectors associated to the  $n$ -th energy band correspond to the distribution of the complex periodic envelope  $h_{z,k_i}^{(n)}$  computed over the photonic crystal unit cell at a given point on the band of coordinates  $(k_i, E_i)$ , with  $i = 1, 2, \dots, N_d$  and  $N_d$  the number of  $k$  points of the discretized band. Moreover, we introduce the Hermitian inner product associated to the eigenvalue problem formulated in Equation (5.33):

$$\langle h_{z,k_i}^{(n)} | h_{z,k_{i+1}}^{(n)} \rangle = \int_{\text{uc}} \mu(\vec{r}) \cdot h_{z,k_i}^{(n),*}(\vec{r}) \cdot h_{z,k_{i+1}}^{(n)}(\vec{r}) \quad , \quad (5.35)$$

where  $h_{z,k_i}^{(n)}$  and  $h_{z,k_{i+1}}^{(n)}$  designate two eigenfunctions calculated on the discretized  $n$ -th band over the spatially discretized photonic crystal unit cell (uc) for consecutive values of the momentum. In particular, at optical frequencies, the photonic crystal exhibit a low magnetic response so that we assume  $\mu(\vec{r}) = \mathbb{I}$ . According to the definition of the inner product in Equation (5.35), we express the normalized eigenfunction on the  $n$ -th band at the momentum  $k_i$ , noted  $u_{k_i,n}$ , as:

$$u_{k_i,n}(\vec{r}) = \frac{h_{z,k_i}^{(n)}(\vec{r})}{\langle h_{z,k_i}^{(n)} | h_{z,k_i}^{(n)} \rangle} \quad . \quad (5.36)$$

The numerical estimation of the Zak phase for the photonic crystal analogue of graphene ribbon decomposes therefore into the following steps:

1. We choose a chirality  $\vec{T}(m, n)$  for the ribbon and we determine the coordinates of the reciprocal vectors  $\vec{\Gamma}_{\parallel}$  and  $\vec{\Gamma}_{\perp}$  according to Equation (5.26) forming the ribbon's Brillouin zone.
2. We fix the momentum  $\vec{k}_{\parallel} = \alpha \vec{\Gamma}_{\parallel}$ , with  $0 \leq \alpha \leq 1$ , for which we will evaluate the Zak phase  $\mathcal{Z}(k_{\parallel})$ .

3. We simulate the band diagram of the honeycomb lattice photonic crystal membrane along the reciprocal path  $[\vec{k}_{\parallel} \ \vec{k}_{\parallel} + \vec{\Gamma}_{\perp}]$  with  $N_d$  values of the momentum component  $k_{\perp}$ .
4. For a given band indexed by  $n$ , we compute the normalized eigenfunctions  $u_{k_i,n}$  over the photonic crystal unit cell for each momentum components  $k_{\perp}$  along the band.
5. We finally estimate the numerical Zak phase  $\mathcal{Z}(k_{\parallel})$  in its discrete formulation according to Equation (5.32).

We apply this procedure to assess the Zak phase of a honeycomb lattice photonic crystal membrane ribbon of chirality  $\vec{T}(1,0)$  with circular and triangular air holes. The Brillouin zone  $(\vec{\Gamma}_{\parallel}(1,0), \vec{\Gamma}_{\perp}(1,0))$  of this ribbon is represented in Figure 5.11.a. Note that we translate the origin of this Brillouin zone from the  $\Gamma$  point to the K point located below. In such a configuration, we obtain non-zero Zak phase  $\mathcal{Z}(k_{\parallel})$  for  $k_{\parallel}$  values on the first third of the segment  $\vec{\Gamma}_{\parallel}$ . We then simulate the band structures of the photonic crystal membranes along the  $\vec{\Gamma}_{\perp}$  direction for  $\alpha$  varying between 0 and 1. We present in Figure 5.13.a, b and c, typical band diagrams simulated for the circular-hole photonic crystal membrane of period  $a_h = 0.301 \mu m$  and radius  $r = 0.109 \mu m$ , for  $\alpha$  fixed at 0.1,  $1/3$  and 0.4, respectively, with  $N_d = 30$  points of discretization. In the three diagrams, we observe three bands corresponding to the two Dirac branches (blue and red curves) and the monopolar mode (black curve). We have superimposed, as a guide, the tight-binding graphene upper (dashed red) and lower (dashed blue) energy bands. We remark, for  $\alpha = 0.1$  and  $\alpha = 0.1$ , a gap opening despite the alteration of the upper Dirac branch by interaction with the monopolar mode. At  $\alpha = 1/3$ , the upper and lower Dirac branches intersect and close the gap, hinting at a topological phase transition.

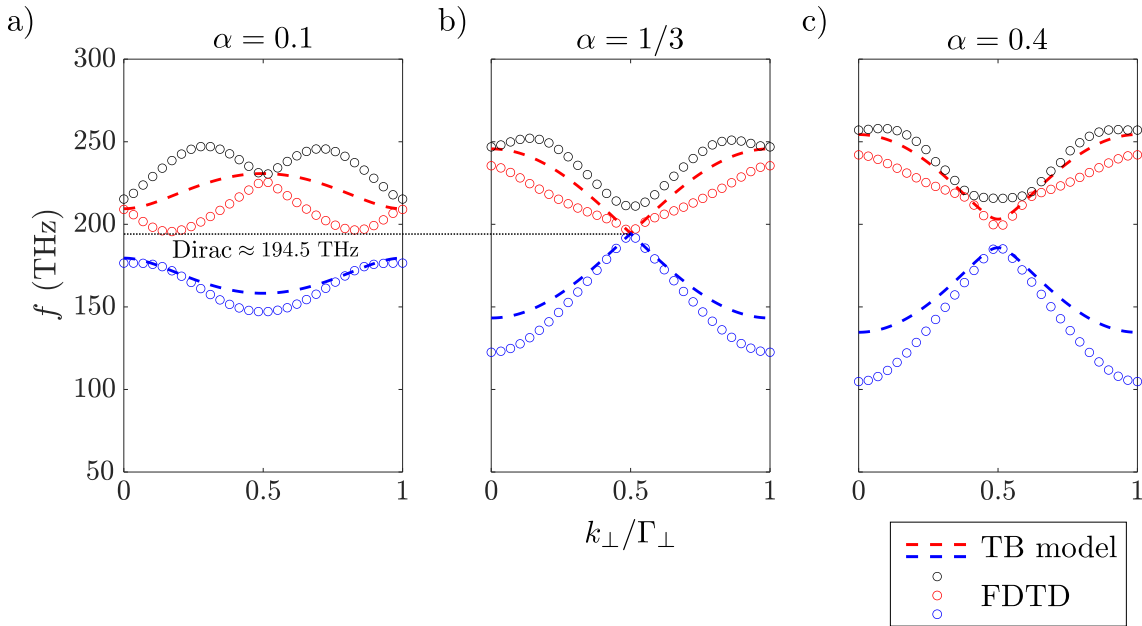


FIGURE 5.13: Band structures of a honeycomb lattice photonic crystal membrane of period  $a_h = 0.301 \mu m$  with circular air holes of radius  $s = 0.109 \mu m$  along the direction  $\vec{\Gamma}_{\perp}(1,0)$  of the Brillouin zone of a graphene ribbon of chirality  $\vec{T}(1,0)$  for  $\alpha = k_{\parallel}/\Gamma_{\parallel} = 0.1, 1/3$  and  $0.4$ .

We have performed similar calculations of band structures of a triangular-hole photonic crystal membrane of period  $a_h = 0.367 \mu m$  and triangle edge size  $s = 0.490 \mu m$ ,

gathered in Figure 5.14.a, b, and c for the three values of  $\alpha = 0.1, 1/3, 0.4$ . We notice that the monopolar mode has been removed to upper frequencies due to the triangular shape of the holes so that only the two Dirac branches remain. In particular, the tight-binding predictions match very satisfyingly with the photonic bands by contrast with the bands obtained with the circular-hole pattern. Moreover, we find that a gap opens at  $\alpha = 0.1$ , closes to form a Dirac point at  $\alpha = 1/3$  and opens again at  $\alpha = 0.4$ .

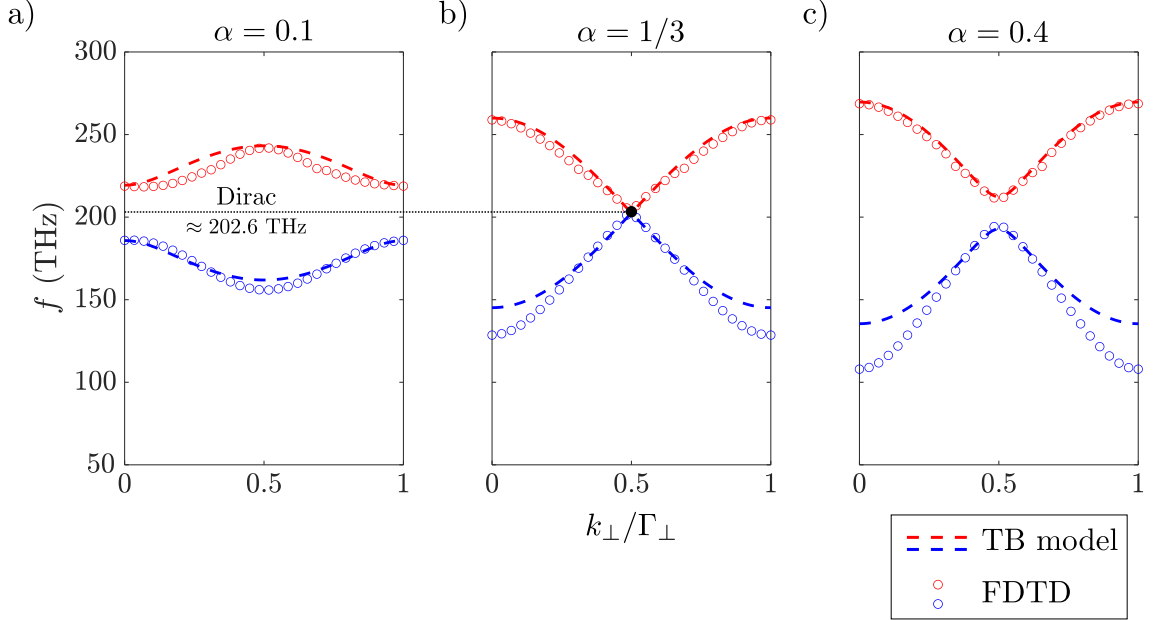


FIGURE 5.14: Band structures of a honeycomb lattice photonic crystal membrane of period  $a_h = 0.367 \mu\text{m}$  with triangular air holes of size  $s = 0.490 \mu\text{m}$  along the direction  $\vec{\Gamma}_\perp(1, 0)$  of the Brillouin zone of a graphene ribbon of chirality  $\vec{T}(1, 0)$  for  $\alpha = k_\parallel/\Gamma_\parallel = 0.1, 1/3$  and  $0.4$ .

We then compute the normalized eigenfunctions  $h_{z,k_i}^{(1)}$  along the first band of each band diagram of the circular and triangular hole structure simulated for  $\alpha$  varying between 0 and 1 with a step of 0.1, at the  $N_d = 30$  discretized values of the momentum  $k_i$  along  $\vec{\Gamma}_\perp$ . We have chosen to evaluate the Zak phase on the first band of the dispersion graphs as it is not altered by any coupling with the monopolar mode. Finally, injecting the normalized eigenfunctions into Equation (5.32), we assess the Zak phase for the photonic systems that we note  $\mathcal{Z}_{\text{ph}}$  and we deduce the number of edge states  $|\mathcal{Z}_{\text{ph}}/\pi|$ . The resulting Zak phase and edge state numbers are gathered in Table 5.1 as a function  $\alpha$  and are identical for both the circular and triangular hole pattern. We have also added the Zak phase derived from the tight-binding model, noted  $\mathcal{Z}_{\text{TB}}$ . For  $\alpha = 0, 1/3$  and  $1$ , the photonic bands touch so that the Zak phase is not well defined. Therefore, the Zak phase calculated numerically for the photonic ribbon of chirality  $\vec{T}(1, 0)$  cancels for  $\alpha = 0.1, 0.2, 0.3$  and equals  $-\pi$  for  $\alpha$  ranging from  $0.4$  to  $0.9$ . We deduce that one edge states exist for  $\alpha$  between  $0.4$  and  $0.9$ . However, for a graphene ribbon of similar chirality, the tight-binding model predicts the exact inverse situation for which the Zak phase  $\mathcal{Z}_{\text{TB}}$  cancels everywhere except for  $\alpha = 0.1, 0.2$  or  $0.3$  where it equals  $\pi$ . One way to explain this discrepancy relies on the fact that the Zak phase is not gauge invariant. Thus, for two distinct gauge choices, we will obtain different values of the phase. It is noteworthy that the gauge choice can not be controlled when the eigenfunctions are calculated numerically via the FDTD method. Hence, the Zak phase does not constitute a topological invariant in this case but the difference between the two Zak phases estimated with the two gauge choices does. Indeed, the quantity

$\mathcal{Z}_{\text{TB}} - \mathcal{Z}_{\text{ph}}$  remains invariant as a function of  $\alpha$  and always equals  $\pi$ .

$\alpha$	0	0.1	0.2	0.3	1/3	0.4	0.5	0.6	0.7	0.8	0.9	1
$\mathcal{Z}_{\text{TB}}$		$\pi$	$\pi$	$\pi$		0	0	0	0	0	0	
$\mathcal{Z}_{\text{ph}}$		0	0	0		$-\pi$	$-\pi$	$-\pi$	$-\pi$	$-\pi$	$-\pi$	
$ \mathcal{Z}_{\text{ph}}/\pi $		0	0	0		1	1	1	1	1	1	

TABLE 5.1: Evolution of the Zak phases  $\mathcal{Z}_{\text{TB}}$  and  $\mathcal{Z}_{\text{ph}}$  calculated with the tight-binding model for a graphene ribbon of chirality  $\vec{T}(1,0)$  and numerically for photonic ribbons of circular and triangular air hole of similar chirality, respectively, as a function of  $\alpha = k_{\parallel}/\Gamma_{\parallel}$  varying from 0 to 1. The number of edge states of the photonic systems equals  $|\mathcal{Z}_{\text{ph}}/\pi|$ .

### Dispersion of photonic ribbons

The two principal manifestations of non-trivial topological properties of a system are found in the description of its energy bands by a nonzero topological invariant, and in the emergence of edge states when the system interfaces with another structure of trivial topology. Following the 1D SSH modelling of graphene ribbons, we have calculated previously the numerical Zak phase of the honeycomb lattice photonic crystal ribbon of chirality  $\vec{T}(1,0)$  with circular and triangular holes. In particular, we have demonstrated the non-nullity of the Zak phase for a certain range of wavevector component along the ribbon axis, constituting the first indicator of the non-trivial topology of the ribbon.

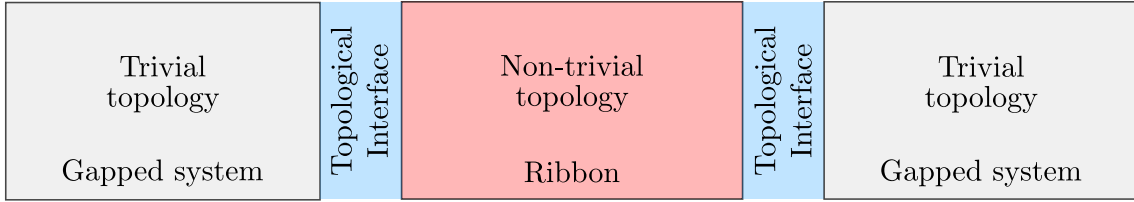


FIGURE 5.15: Schematics of the principle of a topological interface realized with a topologically non-trivial photonic crystal ribbon.

We intend, in this part, to confirm the topological properties of the photonic ribbon of chirality  $\vec{T}(1,0)$  established previously, by revealing the presence of edge states in its band structure when it is sandwiched by two structures exhibiting a trivial topology. Precisely, our strategy consists in realizing a topological interface as schematized in 5.15 and calculating the band diagram of the photonic ribbon at its edges. Indeed, the bulk-edge correspondence stipulates that edge states emerge at the interface between two gapped systems characterized by distinct topologies, namely trivial and non-trivial. It is noteworthy that the concept of topological interface can be used to explore the topology of photonic ribbons of different chiralities.

The first step toward the realization of the topological interface consists in calculating the band structure in the bulk of the ribbon  $\vec{T}(1,0)$ . We present in Figure 5.16.a the FDTD model of the photonic ribbon consisting of a HC-PCM of period  $a_h = 0.301 \mu\text{m}$  with circular air holes of radius  $r = 0.109 \mu\text{m}$ . We set the width of the ribbon to  $20|\vec{C}_h(1,0)| - a_h$  so as to get close to the large number of dimer limit required to produce edge states. We apply PML boundary conditions along the open boundary, separated to the photonic crystal pattern by a distance  $d_{\text{PML}} = 51a_h \simeq 15 \mu\text{m}$ . We set Bloch boundary conditions (BC) to repeat periodically the unit cell of length  $|\vec{T}(1,0)|$  along the ribbon axis ( $y$ -axis). We arrange 6 magnetic dipole sources (green dots) of



bandwidth [140-300] THz oriented along the normal of the ribbon and 15 time monitors (yellow cross) in the middle of the ribbon, to excite and detect the bulk modes. We obtain the band structure displayed in Figure 5.16.b simulated along the 1D Brillouin zone  $2\pi/|\vec{T}|$  of the ribbon. We explain the dense distribution of bands for frequencies above the Dirac frequency level of the HC-PCM ( $f_D \simeq 194.5$  THz) by the interaction between the Dirac branches and the monopolar mode. Most importantly, we notice a small band gap around the Dirac level extending from 193 (1.55  $\mu m$ ) to 196 THz (1.53  $\mu m$ ). Our next step consists in designing a photonic structure which present a band gap which overlaps with the ribbon band gap and has trivial topology, and will serve as the trivial material in the topological interface.

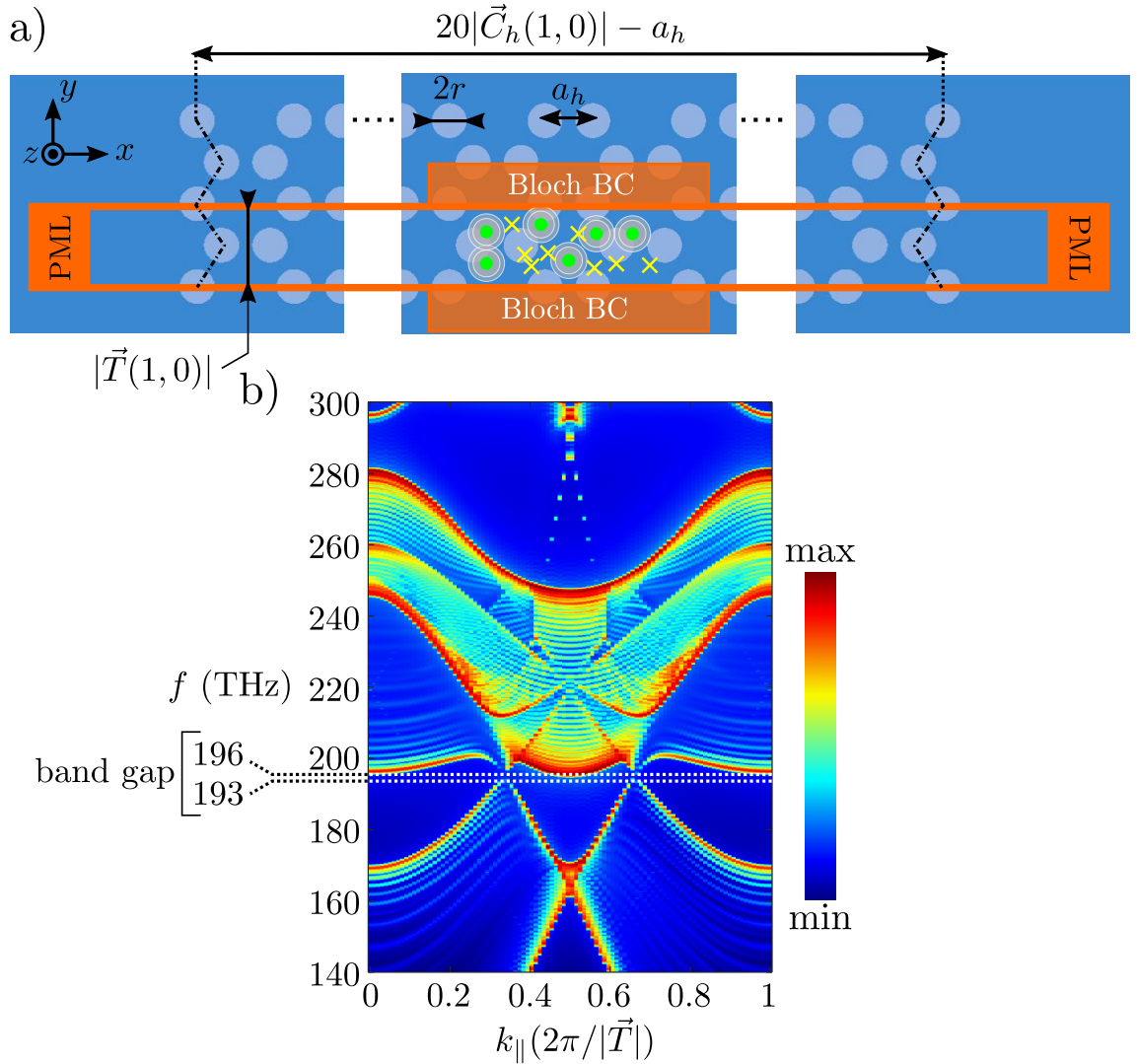


FIGURE 5.16: a) FDTD model of the honeycomb photonic crystal ribbon of chirality  $\vec{T}(1,0)$ . b) Band structure of the bulk of the photonic ribbon calculated over the ribbon's Brillouin zone.

In particular, we draw inspiration from the works of Bahari *et al.* in [8] to design a trivial material made out of a triangular lattice photonic crystal membrane characterized by a large low energy topologically trivial gap. Admissible designs of the triangular lattice photonic crystal of period  $a_{tri}$  and hole radius  $r_{tri}$  as depicted in Figure 5.17.a fulfil two requirements with respect to the ribbon: the compatibility of the computation unit cell and a sufficiently large trivial energy gap to include the ribbon's gap centred at 194.5 THz. In particular, no set of lattice parameters meet the second requirement



when we intend to adjust the period  $a_{\text{tri}}$  to a single ribbon's period. However, using a supercell of the ribbon containing two periods  $|\vec{T}(1,0)|$  as represented in Figure 5.17, we find one admissible couple ( $a_{\text{tri}} = 0.602$ ,  $r_{\text{tri}} = 0.216 \mu\text{m}$ ) which produces a large band gap containing the ribbon's gap (white dashed line) as showed on the simulated band structure in Figure 5.17.b. plotted along the triangular lattice Brillouin zone. We have also plotted in 5.17.d the band structure calculated within the ribbon's supercell. This band diagram results from the band folding of the dispersion relation of the ribbon with a single unit cell represented in 5.17.e. This remark is all the more important as the potential edge states will also be subjected to band folding when dealing with the interface.

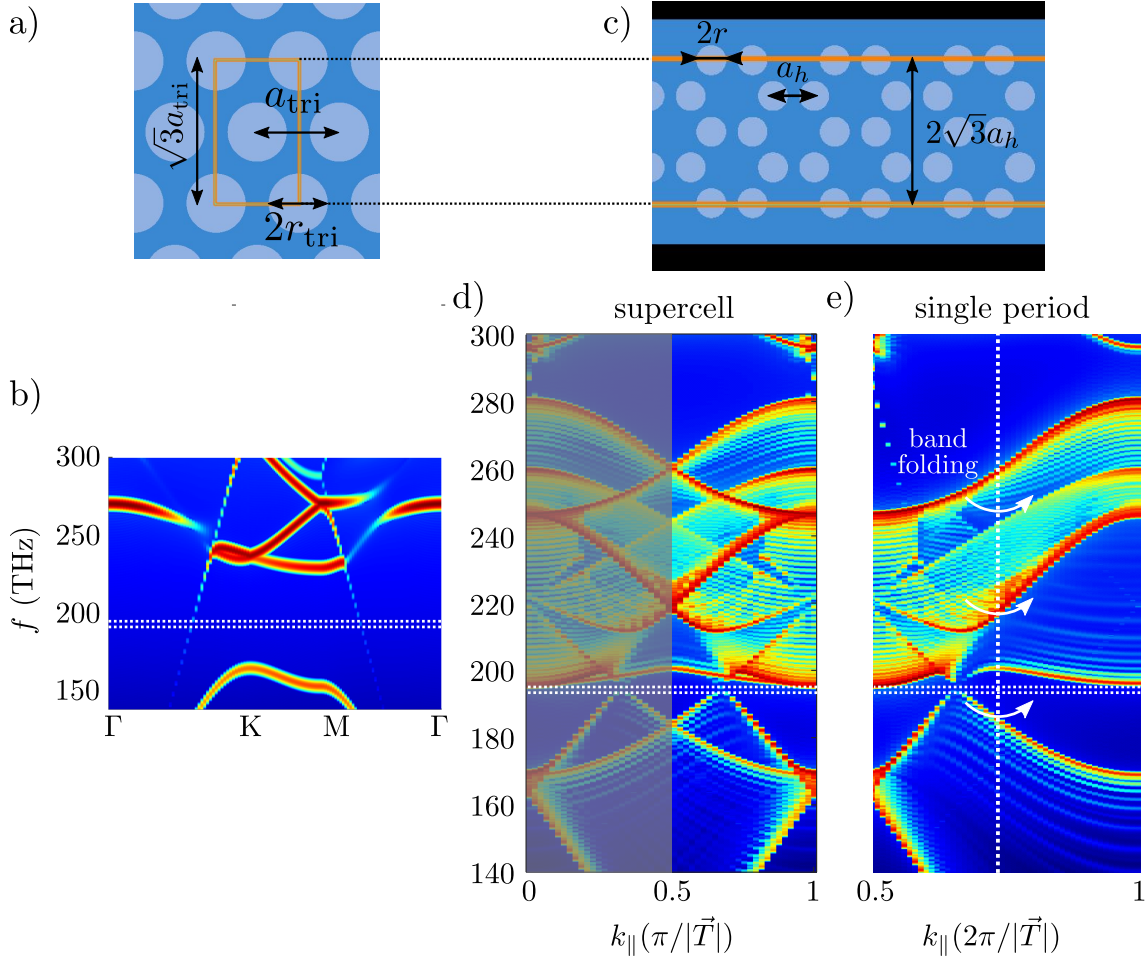


FIGURE 5.17: a) Triangular lattice of air holes of period  $a_{\text{tri}}$  and radius  $r_{\text{tri}}$  in InP membrane of thickness  $h = 0.228 \mu\text{m}$ . b) Band structure simulated for the triangular photonic crystal along the triangular lattice Brillouin zone for the set of lattice parameters  $a_{\text{tri}} = 0.602 \mu\text{m}$  and  $r_{\text{tri}} = 0.206 \mu\text{m}$ . c) FDTD model of the ribbon with a computation supercell corresponding to two times the translation vector  $\vec{T}(1,0)$ . Band structure of the ribbon's bulk calculated within d) the supercell, e) the single unit cell.

We finally consider the topological interface represented on the FDTD model in Figure 5.18.a which comprises the honeycomb photonic crystal ribbon  $\vec{T}(1,0)$  placed in the middle enclosed by two topologically trivial triangular photonic crystal systems with lattice parameters defined above. The computation unit cell (orange outline) encompasses the the three photonic systems repeated periodically along the ribbon's axis. We apply PML boundaries along the width of the ribbon. We position six magnetic dipole sources and 15 time monitors on the left edge of the ribbon to excite

and collect potential edge states as represented on the inset pictures. We show in Figure

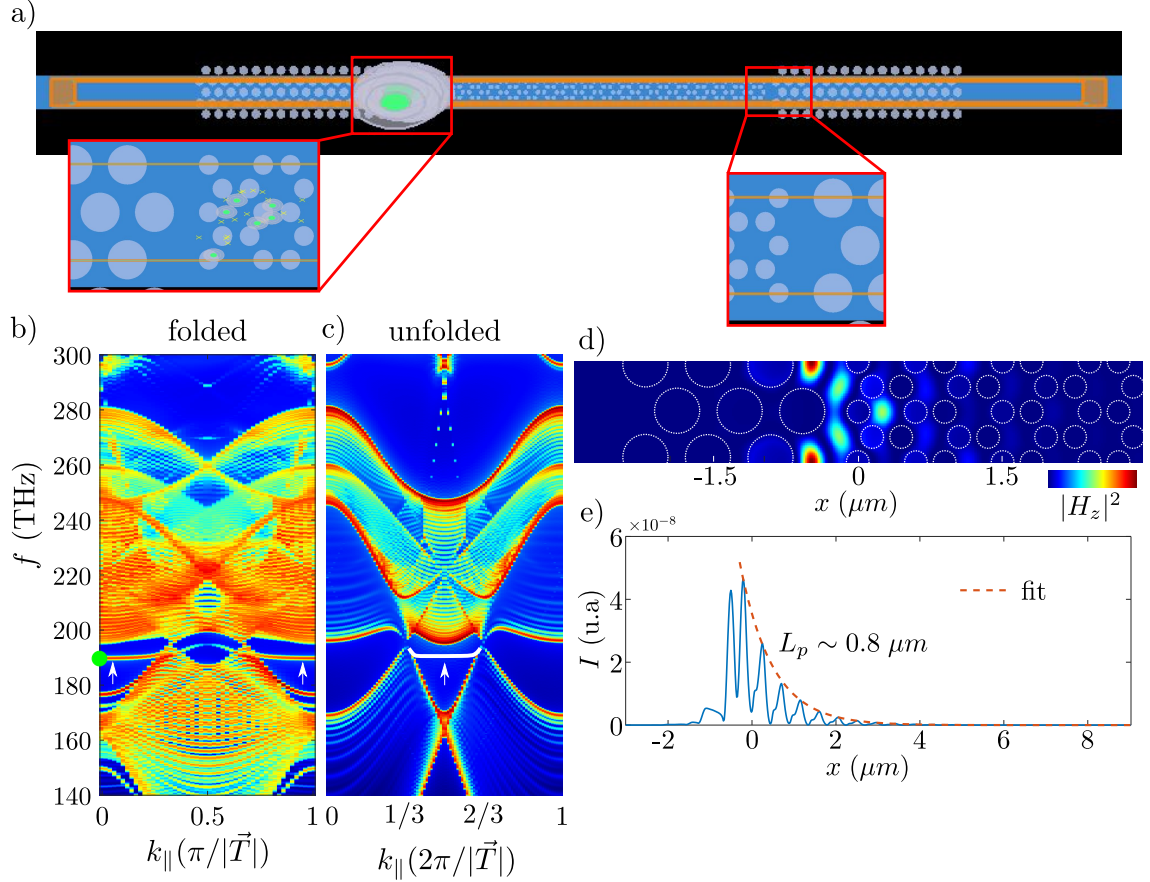


FIGURE 5.18: a) FDTD model of the topological platform consisting in the photonic ribbon places in the middle and enclosed by two topologically trivial triangular photonic crystals. The inset pictures show the shape of the ribbon's edges and the distribution the magnetic dipole sources and time monitors to excite and collect edge modes. b) Band structure simulated at the left edge of the photonic ribbon along the Brillouin zone of the ribbon's supercell. c) Band structure of the bulk ribbon on which we have added artificially the flat bands in the diagram of b) by virtual unfolding operation. d) Real-space map of the magnetic field intensity  $|H_z|^2$  calculated over a part of the computation cell centered on the interface between the ribbon and the trivial systems. e) Intensity integrated over the  $y$  coordinate in the previous map, plotted along  $x$  and fitted by an exponential decay function (red dashed line). The length  $L_p$  indicate the penetration length of the mode in the ribbon.

5.18.b the band diagrams simulated at the left edge of the ribbon along its Brillouin zone. We observe two nearly flat bands emerging at the Dirac energy level (194.5 THz) as indicated by the white arrows. As mentioned previously, the band structure of the supercell results from the band folding of the dispersion relation obtained when simulating the elementary unit cell of the ribbon. Therefore, in Figure 5.18.c, we have unfolded the flat bands and inserted them (white line) artificially onto the band diagram of the original bulk ribbon. In particular, the two branches unify to form a single branch sketched in a thick white line which extends in the middle of the ribbon's Brillouin zone. Precisely, the flat band appears at one third and vanishes at two third of the entire Brillouin zone, matching with the distribution of the non-zero Zak phase predicted for graphene ribbons in Figure 5.11.a and b.

We investigate the nature of modes existing on the previous flat bands by calculating the spatial distribution of the out-of-plane magnetic field component intensity  $|H_z|^2$  over the entire computation zone in  $\Gamma$  (green dot). A part of the resulting map focused on the interface region, displayed in Figure 5.18.d with white dashed outline of the

circular air holes, shows a localization of the magnetic intensity at the interface between the ribbon and the trivial crystal. To quantify this localization, we have plotted the evolution of the intensity integrated along the  $y$  coordinate and fitted the exponential decay of the envelope. In particular, we find that a penetration length in the ribbon of the mode of about  $0.8 \mu m$  which represents approximately 4 % of the total width of the ribbon. The strong localization of the mode on the ribbon's left edge finally proves that we deal with an edge state as predicted by the numerical calculation of the Zak phase.

### 5.2.3 Conclusion of the section

#### Key points of the section

In summary, we have explored the topological properties of photonic crystal analogues of graphene ribbons, namely ribbons of honeycomb lattice photonic crystal membranes.

- We have first reviewed the topological classification of graphene ribbons modelled as 1D SSH-like systems, with respect to their chirality. In particular, we have detailed the graphical determination of the Zak phase which analytical expression derives from graphene tight-binding calculation.
- We have then transposed the previous concepts toward the study of the analogue photonic ribbons, and approached their topology according to two approaches. In the first approach, we have estimated the Zak phase of the photonic ribbons via the numerical calculation of photonic graphene eigenvectors along the Brillouin zone of the ribbon. We have found a reverse distribution of the Zak phase values for the ribbon  $\vec{T}(1,0)$  along the Brillouin zone as compared to the solid-state results, due to the dependence of the Zak phase on the gauge choice.
- In the second approach, we have simulated the band structure of a topological interface consisting of the photonic ribbon  $\vec{T}(1,0)$  sandwiched between two topologically trivial photonic systems. We have demonstrated the existence of edge states in agreement with the solid-state predictions.

We emphasize that those results constitute a first step toward a more complete study of the topology of photonic graphene-like ribbons with different chiralities.

## 5.3 Carbon nanotubes and rolled-up honeycomb lattice photonic crystal

We first describe the structure of carbon nanotubes, introducing the main geometrical parameters.

### 5.3.1 Carbon nanotubes

#### Structural properties

Carbon nanotubes (CNTs) correspond to monolayer graphene sheets rolled up into hollow cylinders. The rolling of a single graphene sheet form single-walled nanotubes (SWNTs) whereas multi-walled nanotubes (MWNTs) comprise several concentric cylinders. There exists an infinite number of ways to roll graphene sheets into cylinders depending on the direction of rolling and the number of rolling, resulting in various tubes' diameters and microscopic structures. In practice, the fabricated structures have nanometric diameters and micrometric lengths, so that CNTs can be regarded as quasi-1D crystals with translational periodicity along their axis [9].

The direction of rolling or *chirality* of CNTs is defined on graphene planar pattern by the *chiral vector*  $\vec{C}_h$  expressed as:

$$\vec{C}_h = n\vec{a}_1 + m\vec{a}_2, \quad (5.37)$$

where the *chiral indices*  $(n, m) \in \mathbb{Z}^2$  refer to the coordinates of  $\vec{C}_h$  in graphene lattice basis  $(\vec{a}_1, \vec{a}_2)$  depicted in Figure 5.19. The black dots symbolize the carbon atom sites. The integer nature of  $(m, n)$  implies that the vector  $\vec{C}_h$  always join two carbon atom sites together. We derive from Equation (5.37) the norm of  $\vec{C}_h$  which coincides with the circumference of the nanotube of diameter  $d_t$ :

$$|\vec{C}_h| = \sqrt{3}a_h\sqrt{n^2 + m^2 + nm} = \sqrt{3}a_h\sqrt{N} = \pi d_t, \quad (5.38)$$

with  $N = n^2 + m^2 + nm$  and  $a_h \simeq 1.42 \text{ \AA}$  [10] the period of the honeycomb lattice or the distance between two nearest-neighbour carbon atoms.

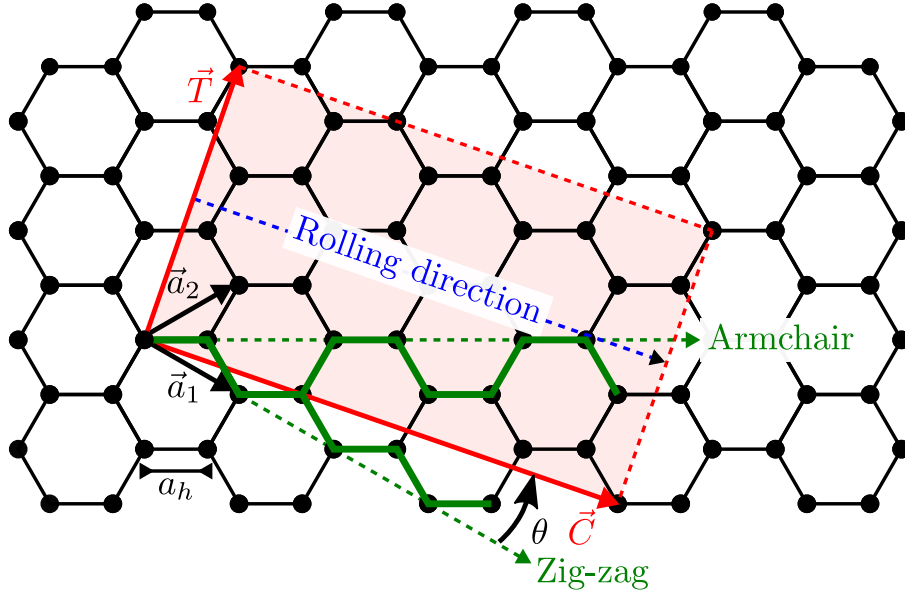


FIGURE 5.19: Planar unit cell  $(\vec{C}_h, \vec{T})$  of the carbon nanotube (CNT) of chirality  $\vec{C}_h(4, 1)$  where the chiral vector  $\vec{C}_h$  is expressed in graphene lattice basis  $(\vec{a}_1, \vec{a}_2)$ . The black dots represent carbon atom sites arranged according to a honeycomb lattice of period  $a_h$ . The orientation of  $\vec{C}_h$  indicates the direction of rolling of the graphene sheet and its norm fixes the circumference, hence the diameter, of the final nanotube. The translation vector  $\vec{T}(-2, 3)$ , also expressed in  $(\vec{a}_1, \vec{a}_2)$ , orients along the tube axis and its norm coincides with the tube's length. The chiral angle  $\theta$  measure the angular tilt between the chiral vector and zig-zag configurations of the form  $\vec{C}_h(n, 0)$ . We cover all possible chiralities with  $\theta$  varying between  $0^\circ$  (zig-zag) and  $30^\circ$  (armchair).

The dashed green arrows and green outlines in Figure 5.19 indicate the *zig-zag* and *armchair* chiralities defined by generic chiral vectors  $\vec{C}_h(n, 0)$  and  $\vec{C}_h(n, n)$ , respectively. In particular, the *chiral angle*, noted  $\theta$ , measures the angular distance between  $\vec{C}_h(n, m)$  and the zig-zag configuration expressed as:

$$\cos \theta(\vec{a}_1, \vec{C}_h) = \frac{\vec{a}_1 \cdot \vec{C}_h}{|\vec{a}_1 \cdot \vec{C}_h|} = \frac{2n + m}{2\sqrt{N}}. \quad (5.39)$$

Due to the  $60^\circ$ -rotational symmetry of the honeycomb lattice and the equivalence between chirality  $\theta$  and  $30^\circ - \theta$ , the study of all possible chiralities restricts to angles  $\theta$  within  $[0^\circ - 30^\circ]$ , namely  $n > m \geq 0$ .

We construct CNTs' unit cell from the orthogonal basis  $(\vec{C}_h, \vec{T})$  where  $\vec{T} = t_1\vec{a}_1 + t_2\vec{a}_2$  denotes the *translation vector* along the tube axis, satisfying the orthogonality relation:

$$\vec{C}_h \cdot \vec{T} = 0 \Rightarrow (2n + m)t_1 + (2m + n)t_2 = 0. \quad (5.40)$$

In particular, the translation vector associated to the smallest translational period along the tubes' axis writes:

$$\vec{T} = \frac{-(2m + n)}{d_R}\vec{a}_1 + \frac{(2n + m)}{d_R}\vec{a}_2, \quad (5.41)$$

with  $d_R = \gcd(2m + n, 2n + m)$ . Moreover, the norm of  $\vec{T}$ , coinciding with the length of the tube noted  $L$ , reads:

$$|\vec{T}| = \frac{3a_h\sqrt{N}}{d_R} = L. \quad (5.42)$$

We finally derive the number of graphene hexagons  $N_h$  within one CNT unit cell covered by the vectors  $\vec{C}_h$  and  $\vec{T}$  as the ratio of the unit cell area  $A_{uc}$  over one hexagon area  $A_h$ :

$$N_h = \frac{A_{uc}}{A_h} = \frac{|\vec{C}_h \times \vec{T}|}{\frac{3\sqrt{3}a_h^2}{2}} = \frac{2N}{d_R}, \quad (5.43)$$

from which we deduce the number of carbon atoms  $N_c$  within the CNT unit cell:

$$N_c = 2 \times N_h = \frac{4N}{d_R}. \quad (5.44)$$

### Electronic dispersion of CNTs: zone-folding scheme

From a bulk material to a lower dimension system, electronic states become quantized along the nanoscale directions. In particular, if the low-dimension system shares the same crystallographic structure as the parent bulk material, its electronic dispersion forms a subset of the bulk material electronic states. For instance, we construct the 1D band structure of a nanotube produced by rolling a 2D material sheet, by *cutting* the parent 2D electronic dispersion with a set of equidistant lines, so called *cutting lines* oriented along the nanotubes' 1D reciprocal space. The above procedure is better known as the *zone-folding scheme*. In particular, we apply this method to derive the band structure of quasi-1D CNTs from graphene 2D dispersion relation, following classical developments proposed in [11]. We first explain the principle of the method and then illustrate it by constructing the band structure of a  $\vec{C}_h(6, 6)$  nanotube. We finally highlight the main features of CNTs' electronic dispersion as a function of the chirality.

The first step of zone folding involves the construction of the unrolled reciprocal space of carbon nanotubes with arbitrary chirality  $\vec{C}_h(n, m)$ . We recall that graphene reciprocal lattice is generated by the reciprocal basis  $(\vec{a}_1^*, \vec{a}_2^*)$  verifying  $\vec{a}_i \cdot \vec{a}_j^* = 2\pi\delta_{i,j}$  with  $(i, j) = \{1, 2\}$  and graphene real-space lattice basis  $(\vec{a}_1, \vec{a}_2)$ . In a similar way, we define CNTs' reciprocal space vectors  $(\vec{K}_\perp, \vec{K}_\parallel)$  from the planar unit cell  $(\vec{C}_h, \vec{T})$  as:

$$\begin{aligned} \vec{C}_h \cdot \vec{K}_\perp &= 2\pi \quad ; \quad \vec{C}_h \cdot \vec{K}_\parallel = 0 \\ \vec{T} \cdot \vec{K}_\parallel &= 2\pi \quad ; \quad \vec{T} \cdot \vec{K}_\perp = 0. \end{aligned} \quad (5.45)$$

where  $\vec{K}_\perp$  and  $\vec{K}_\parallel$  point in the direction of  $\vec{C}_h$  and  $\vec{T}$ , respectively. The resolution of the previous system yields the following expressions of  $\vec{K}_\perp$  and  $\vec{K}_\parallel$  in graphene reciprocal basis  $(\vec{a}_1^*, \vec{a}_2^*)$ :

$$\begin{cases} \vec{K}_\perp = \frac{1}{N_h}(t_2\vec{a}_1^* - t_1\vec{a}_2^*), \\ \vec{K}_\parallel = \frac{1}{N_h}(-m\vec{a}_1^* + n\vec{a}_2^*), \end{cases} \quad (5.46)$$

from which we deduce the norms:

$$\begin{cases} |\vec{K}_\perp| = \frac{2}{d_t}, \\ |\vec{K}_\parallel| = \frac{2\pi}{|\vec{T}|}. \end{cases} \quad (5.47)$$

In particular, the norm  $|\vec{K}_\parallel|$  corresponds to the CNT's Brillouin zone in the direction of  $\vec{T}$ . We also infer from the first equation of the system (5.46) the relation  $N_h\vec{K}_\perp = (t_2\vec{a}_1^* - t_1\vec{a}_2^*)$  forming the smallest translation vector of graphene reciprocal space in the direction parallel to  $\vec{K}_\perp$ , as  $t_1$  and  $t_2$  have no common divisor by definition (see Equation (5.41)). Precisely, the  $N_h$  wavevectors along  $\vec{K}_\perp$  traduces the quantization of the electronic states along the nanotube's circumference. Introducing the unitary basis  $(\vec{e}_\perp, \vec{e}_\parallel)$ , we decompose any wavevector  $\vec{k}$  in the reciprocal space as  $\vec{k} = k_\parallel\vec{e}_\parallel + k_\perp\vec{e}_\perp$ . The discretization of  $\vec{k}$  along  $\vec{e}_\perp$  originate from the constructive interference between electronic waves after one circulation around the nanotube expressed by the phase-matching condition:

$$\vec{k}_\perp \cdot \vec{C}_h = 2p\pi, \quad (5.48)$$

with  $p$  an integer varying from  $(1-N_h/2)$  to  $N_h/2$ . Consequently, the allowed values for  $k_\perp$  in the CNT's reciprocal space write as:

$$\boxed{k_\perp = \frac{2p\pi}{|\vec{C}_h|} = \frac{2p}{d_t}; \quad p = \left\{1 - \frac{N_h}{2}, \dots, \frac{N_h}{2}\right\}}, \quad (5.49)$$

whereas the component  $k_\parallel$  along the tube's axis varies continuously along the Brillouin zone of size  $|\vec{K}_\parallel|$ . Therefore, the unrolled reciprocal space of the CNT forms  $N_h$  lines, the *cutting lines*, oriented along  $\vec{K}_\parallel$ , of size  $|\vec{K}_\parallel|$ , at the quantized values of  $k_\perp$ . We finally construct the CNT's electronic band structure by superimposing the 1D dispersion curves obtained by slicing graphene 2D band diagram along the cutting lines.



In practice, we inject the quantized values of  $k_{\perp}$  expressed in Equation (5.49) into graphene tight-binding energy bands established in Equation (5.11), using the change-of-basis formulas:

$$\begin{cases} k_x &= k_{\perp} \cos \theta - k_{\parallel} \sin \theta, \\ k_y &= k_{\perp} \sin \theta + k_{\parallel} \cos \theta \end{cases}, \quad (5.50)$$

with  $\vec{k}_{\parallel}$  running through the Brillouin zone.

In Figure 5.20, we illustrate the zone-folding procedure to build the band diagram of the armchair nanotube  $\vec{C}_h(6,6)$ . Using Equations (5.43) and (5.46), we identify in 5.20.a the unrolled reciprocal space of the CNT to the vectors  $\vec{K}_\perp = 1/12(\vec{a}_1^* + \vec{a}_2^*)$  and  $\vec{K}_\parallel = 1/12(-6\vec{a}_1^* + 6\vec{a}_2^*)$  which orientations coincide with  $k_x$  and  $k_y$  axes, respectively. We draw the  $N_h = 12$  cutting lines of length  $|\vec{K}_\parallel| = 2\pi/|\vec{T}|$  oriented along  $\vec{K}_\parallel$  and

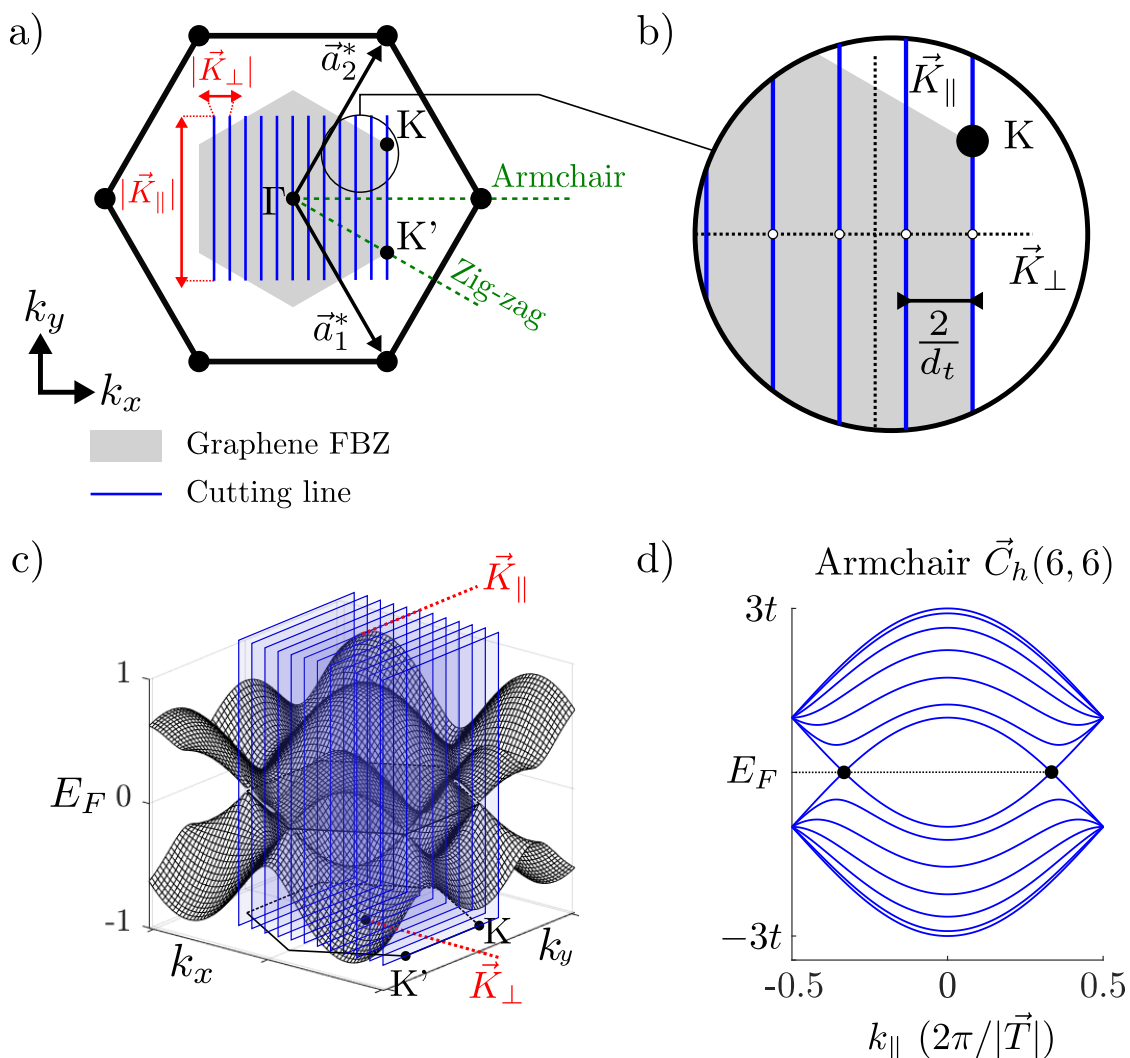


FIGURE 5.20: Illustration of the cutting lines method for the construction of the band diagram of a (6,6) armchair CNT. a) Section of the graphene FBZ by ( $m = n_1 = 6$ ) cutting lines oriented along the translation vector  $\vec{T}$  and regularly distributed along the chiral vector  $\vec{C}$ . b) 3D view of the cutting planes in the surface plot of graphene band diagram. c) Band structure,  $E = f(\vec{k}_{||})$ , of the (6,6) armchair CNT.

separated by the distance  $|\vec{K}_\perp| = 2/d_t$ . Precisely, starting from the  $\Gamma$  point, we add 6 and 5 lines on the right and left sides of graphene first Brillouin zone (FBZ) shaded

in gray, respectively. We also show in 5.20.b a close-up view of the lines distribution, approaching the edge of graphene FBZ. In the 3D perspective view of graphene tight-binding energy band structure in 5.20.c, the blue-shaded planes have replaced the cutting lines, which contain the dispersion curves at the quantized  $k_{\perp}$  values. We finally superimpose the dispersion curves extracted from the cutting planes to produce the energy band structure of the  $\vec{C}_h(6,6)$  armchair CNT plotted in 5.20.d. We count two pairs of six bands symmetrically arranged with respect to the Fermi energy level  $E_F$ , and forming the conduction ( $E > E_F$ ) and valence ( $E < E_F$ ). At the Fermi level, we also notice that the two closest conduction and valence energy bands cross linearly to create two Dirac points (black dots), conferring metallic properties to the nanotube.

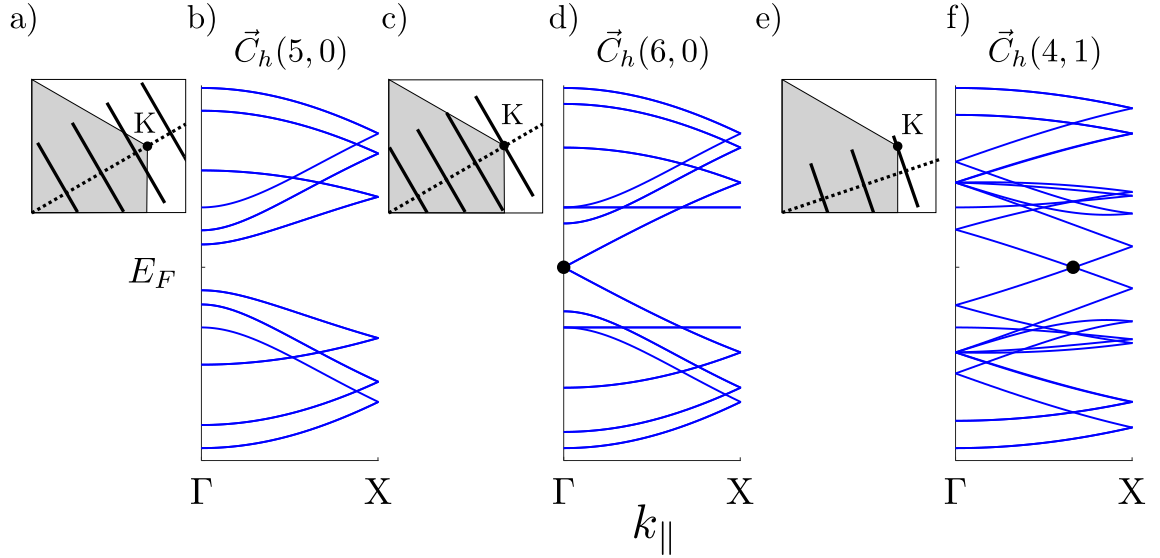


FIGURE 5.21: Schematized cutting lines a), c) and e) on graphene Brillouin zone and zone-folding dispersion diagrams b), d) and f) of (5,0)-zig-zag, (6,0)-zig-zag, and (4,1)-chiral CNTs, respectively.

We present in Figure 5.21.b, d and f, the electronic dispersion diagrams of three other chiralities  $\vec{C}_h(5,0)$ ,  $\vec{C}_h(6,0)$  and  $\vec{C}_h(4,1)$ , accompanied with sketches a, c and d, of the cutting lines in the vicinity of the K point on graphene Brillouin zone. Similarly to the armchair nanotube  $\vec{C}_h(6,6)$ , we observe a band crossing at the Fermi energy level  $E_F$  for  $\vec{C}_h(6,0)$  and  $\vec{C}_h(4,1)$  CNTs, implying a metallic behaviour confirmed by the intersection between the cutting lines and the high-symmetry K point. Conversely, the band structure of nanotube  $\vec{C}_h(5,0)$  exhibits a band gap centered on the Fermi level, revealing the semi-conducting nature of the tube.

More generally, we can predict the electronic behaviour (metallic or semiconducting) of any CNT with arbitrary chirality  $\vec{C}_h(n,m)$ . From a graphical viewpoint, a CNT will exhibit metallic behaviour if one of the cutting lines intersect one Dirac point of graphene FBZ. Equivalently, the CNT's band diagram will contain a Dirac crossing if the distance of the K point to the cutting line in  $\Gamma$  equals an integer number of the distance  $2/d_t$  between two consecutive cutting lines. The latter geometrical condition formulates with the chiral indices as:

$$\boxed{\text{Metallic } \vec{C}_h(n,m)\text{-CNT} \Leftrightarrow \text{mod}(2n+m, 3) = 0} \quad (5.51)$$

In particular, we infer from the previous equation that all the armchair nanotubes and zig-zag nanotubes provided  $\text{mod}(n, 3) = 0$  present a metallic behaviour.



Concerning metallic nanotubes, we notice that the chirality determines the position of the band crossing along the nanotube Brillouin zone. Indeed, for the CNT of chirality  $\vec{C}_h(6, 0)$  in Figure 5.21.d, the bands intersect in  $\Gamma$  ( $k_{\parallel} = 0$ ) while the crossing occurs in between  $\Gamma$  and X ( $k_{\parallel} = \pi/|\vec{T}|$ ) for the  $\vec{C}_h(4, 1)$  CNT. In particular, in anticipation of the optical characterization of analogue photonic structures, we emphasize the interest of having dispersion features located in  $\Gamma$  point (normal incidence) as we can probe them via far-field optical measurements.

Regarding semi-conductor CNTs, the existing band gap results from a misalignment of the cutting lines with respect to the K point, proportional to the inverse of the tube's diameter  $d_t$ . Therefore, we can estimate the band gap energy according to [9]:

$$E_g = 2 \left( \frac{\partial E}{\partial k} \right) \times \frac{2}{3d_t} = \frac{4\hbar v_F}{3d_t}, \quad (5.52)$$

where  $\partial E/\partial k = \hbar v_F$  corresponds to the slope of the energy linear dispersion around the K point with  $v_F$  the Fermi velocity. In particular,  $v_F \approx 10^6 \text{ m.s}^{-1}$  for graphene, leading to an energy gap of semi-conducting CNTs evolving as  $0,7/d_t$  in eV units with  $d_t$  expressed in nanometers.

In summary, the zone-folding scheme appears as a very competitive method to predict the CNTs' electronic dispersions. Indeed, it allows extremely fast calculations of the electronic properties of CNTs with arbitrary chirality, in agreement with *ab initio* predictions in the limit of large tubes' diameter ( $d_t > 1 \text{ nm}$ ) to prevent curvature effects. In particular, zone-folding shows high performances for nanotubes unit cells containing a high number of carbon atoms. We have shown that CNTs divide into two categories: metallic and semiconducting tubes, exhibiting a Dirac crossing and a band gap, respectively, in their energy dispersion. Moreover, the position of metallic tubes' crossing along the Brillouin zone depends upon the tubes' chirality. For semi-conducting CNTs, the energy gap is proportional to the inverse of the tubes' diameter. In particular, we can expect from the opening of a gap in Dirac materials to give rise to topological effects such as the emergence of edges states. We present in the following a 1D model of CNTs proposed recently by Okuyama *et al.* in [12] establishing a classification of CNTs according to their topological properties.

### Topological properties of CNTs

The description of gapped semiconducting CNTs in the framework of topology has drawn attention in the last decades, notably in relation to the emergence of topological superconducting states [13–15]. Several works [16, 17] have, for instance, examined the topological properties of CNTs using a 1D topological system derived from the well-known Su-Schrieffer-Heeger (SSH) model, which dispersion bands can be characterized by a winding number as the topological invariant. In particular, we review in the following the recent results obtained by Okuyama *et al.* in [12], establishing a topological classification of all possible CNTs' chiralities from an analytical formulation of the winding number.

To investigate the electronic properties of CNTs, we have introduced earlier a unit cell composed of  $N_h$  dimers A-B, generated by the chiral vector  $\vec{C}_h$  and the translation vector  $\vec{T}$  as depicted, for instance, in Figure 5.22.a for the chirality  $\vec{C}_h(6, 3)$ . We describe below another way to construct CNTs, exploiting their rotational and helical symmetry, which will prove convenient to derive the 1D lattice model.

First, a CNT of chirality  $\vec{C}_h(n, m)$  has a  $d$ -fold rotational symmetry around the tube axis where  $d$  corresponds to the great common divisor of  $n$  and  $m$ , namely  $d =$

$\gcd(n, m)$ . In particular, a rotation of angle  $2\pi/d$  around the tube axis corresponds to a translation by the vector  $\vec{C}_h/d$  onto graphene lattice. For instance, we notice in Figure 5.22.a that the chiral vector  $\vec{C}_h(6, 3)$  (green arrow) divides into three repetitions of the irreducible vector  $\vec{C}_h/d$  (blue arrow) where  $d = 3$ .

Second, the helical symmetry of the CNT is represented by the translation by a vector  $\vec{R} = p\vec{a}_1 + q\vec{a}_2$  expressed in graphene lattice basis  $(\vec{a}_1, \vec{a}_2)$ , where the integers  $p$  and  $q$  verify<sup>3</sup>:

$$mp - nq = d. \quad (5.53)$$

Precisely, the translation by  $\vec{R}$  traduces by a combination of a translation by  $a_z = |\vec{T}|d/N_h$  along the tube axis and a rotation by the angle  $\theta_z = 2\pi(t_1q - t_2p)/N_h$  around the tube axis. We represent, in particular, in Figure 5.22.a the vector  $\vec{R}$  given by  $p = 1$  and  $q = 0$ , describing the helical symmetry of the nanotube  $\vec{C}_h(6, 3)$ .

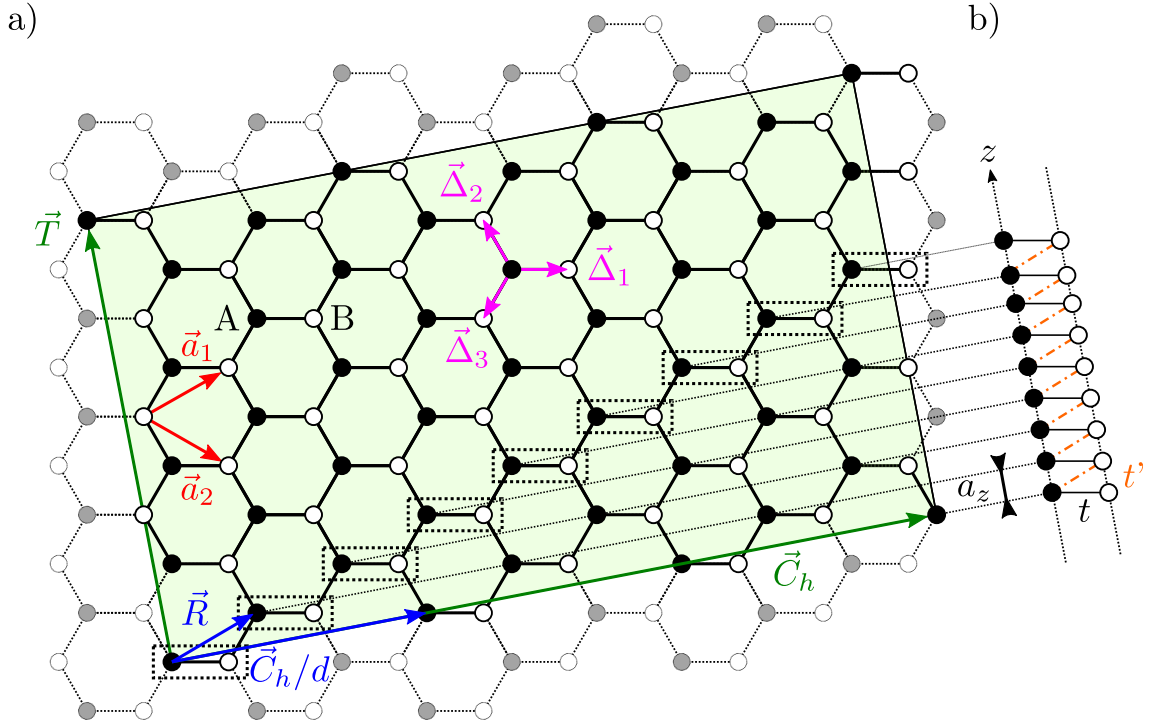


FIGURE 5.22: a) Unit cell of a carbon nanotubes of chirality  $\vec{C}_h(6, 3)$  on graphene lattice with the basis  $(\vec{R}, \vec{C}_h/d)$  related to the helical and rotation symmetries of the tubes. b) Associated 1D topological system.

Therefore, the vectors  $\vec{R}$  and  $\vec{C}_h/d$  constitute a new set of lattice vectors on graphene sheet where the positions of sublattices A and B, noted  $\vec{r}_A$  and  $\vec{r}_B$ , respectively, express as:

$$\begin{cases} \vec{r}_A = \ell\vec{R} + \nu(\vec{C}_h/d), \\ \vec{r}_B = \ell\vec{R} + \nu(\vec{C}_h/d) + \vec{\Delta}_1 \end{cases} \quad (5.54)$$

with integer indices  $\ell$  and  $\nu = 0, 1, 2, \dots, d-1$  and the translation vector  $\vec{\Delta}_1 = (\vec{a}_1 + \vec{a}_2)/3$  connecting A and B sites within a horizontal dimer A-B, as represented in Figure 5.22.a. The quantization of the indice  $\nu$  accounts for the periodic boundary conditions along the tube's circumference.

<sup>3</sup>Note that multiple couples  $(p, q)$  constitute admissible vectors  $\vec{R}$ .

To develop the 1D lattice model of the CNT, we consider graphene tight-binding Hamiltonian  $H$  involving nearest-neighbour interaction characterized by the hopping energy  $t$ :

$$H = \sum_{\vec{r}_A} \sum_{j=1}^3 t \left( c_{\vec{r}_A}^\dagger c_{\vec{r}_A + \vec{\Delta}_j} + \text{H.c.} \right) \quad (5.55)$$

with the creation (annihilation) operators  $c_{\vec{r}}^\dagger$  ( $c_{\vec{r}}$ ) of a  $\pi$  electron at the position  $\vec{r}$  and  $\vec{\Delta}_j$  ( $j = 1, 2, 3$ ) connecting sites A to B as drawn in Figure 5.22.a. Fourier expanding the  $\nu$  coordinate, the Hamiltonian  $H$  decomposes in the subspace of the orbital angular momentum  $\mu = 0, 1, 2, \dots, d-1$  as  $H = \sum_{\mu=0}^{d-1} H_\mu$  with

$$H_\mu = \sum_{\ell} \sum_{j=1}^3 t \left( e^{i2\pi\mu\Delta_j''/d} c_{A,\ell}^\mu c_{B,\ell+\Delta_j'}^\mu + \text{H.c.} \right). \quad (5.56)$$

The previous Hamiltonian describes a 1D lattice system consisting of a 1D chain of horizontal dimers A-B arranged along the CNT's axis with a period  $a_z$  as represented in Figure 5.22.b. It traduces the hopping of an electron with a given angular momentum  $\mu$  from the position indexed by  $\ell$  to one of the three adjacent sites located at  $\Delta_j'$  and  $\Delta_j''$  coordinates along  $\vec{R}$  and  $\vec{C}_h/d$ , respectively, defined by:

$$\vec{\Delta}_j - \vec{\Delta}_1 = \Delta_j' \vec{R} + \Delta_j'' \vec{C}_h/d. \quad (5.57)$$

After identification, we obtain the following expressions:  $\Delta_1' = \Delta_1'' = 0$ ,  $\Delta_2' = n/d$ ,  $\Delta_2'' = -p$ ,  $\Delta_3' = -m/d$  and  $\Delta_3'' = q$ . The Fourier transform of the Hamiltonian  $H_\mu$  along the  $\ell$  coordinate yields the following Bloch Hamiltonian  $H_\mu(\vec{k})$ , expressed in the basis of sublattices (A,B) in the form:

$$H_\mu(\vec{k}) = \begin{pmatrix} 0 & f_\mu(\vec{k}) \\ f_\mu^*(\vec{k}) & 0 \end{pmatrix}, \quad (5.58)$$

where  $\vec{k}$  varies across the 1D Brillouin zone along the tube axis  $[-\pi/a_z; \pi/a_z]$  and the anti-diagonal term  $f_\mu(\vec{k})$  writes as:

$$f_\mu(\vec{k}) = t \sum_{j=1}^3 e^{i2\pi\mu\Delta_j''/d} e^{i2\pi k a_z \Delta_j'}. \quad (5.59)$$

Moreover, in the basis of Pauli matrices  $\vec{\sigma} = (\sigma_x, \sigma_y, \sigma_z)$  the Hamiltonian  $H_\mu(\vec{k})$  rewrites as:

$$H_\mu(\vec{k}) = g(\vec{k}) \cdot \vec{\sigma}, \quad (5.60)$$

typical of a two-level system, where  $g(\vec{k}) = t(\text{Re}(f_\mu(\vec{k})), \text{Im}(f_\mu(\vec{k})), 0)$ . We deduce the eigenvalues of  $H_\mu(\vec{k})$  which correspond to the energy subbands  $E_\mu(\vec{k})$  for a given angular momentum  $\mu$ :

$$E_\mu^\pm(\vec{k}) = \pm |g(\vec{k})| = \pm |t f_\mu(\vec{k})|. \quad (5.61)$$

In particular, the CNT will exhibit a metallic behaviour when the two subbands  $E_\mu^\pm(\vec{k})$  are degenerate, namely for  $f_\mu(\vec{k}) = 0$  so that we retrieve the condition expressed in Equation (5.51). Conversely, we obtain a semiconducting CNT when  $f_\mu(\vec{k}) \neq 0$  for both bands over the entire Brillouin zone.

The topological properties of the semiconducting CNTs are encoded in the winding number  $w_\mu$  defined for each energy subbands  $E_\mu(\vec{k})$  as:

$$w_\mu = \frac{1}{2\pi} \oint_{\text{BZ}} \frac{\partial \arg f_\mu(\vec{k})}{\partial k} dk, \quad (5.62)$$

which counts the number of circulation of the Hamiltonian term  $f_\mu(\vec{k})$  around the origin of the complex plane when  $\vec{k}$  spans the entire Brillouin zone (BZ). For instance, we plot in Figure 5.23.a the component  $f_\mu(\vec{k})$  calculated for the CNT of chirality  $\vec{C}_h(6, 3)$  for  $\mu = 0$  (blue curve) and  $\mu = 1$  (orange curve) in the complex plane. For both  $\mu$ , we obtain a flower-shape curve composed of five lobes. However, we notice that for  $\mu = 1$ , one lobe enclose the origin  $(0, 0)$  resulting in a winding number  $w_\mu = w_1 = 1$  while we report no winding around the origin for  $\mu = 0$ , implying a zero-winding number  $w_0$ . We note that the winding number is not well defined for metallic nanotubes due to the zero-gap in the band-structure ( $f_\mu(\vec{k}) = 0$ ).

The winding number relates to the number of edge states  $N_{\text{edge}}$  existing at both ends of CNTs with arbitrary chirality, via the so-called *bulk-edge correspondence* expressed as:

$$N_{\text{edge}} = 4 \sum_{\mu=0}^{d-1} w_\mu. \quad (5.63)$$

where the factor 4 accounts for the edge states at the two ends of the nanotubes and the spin degeneracy.

We present in Figure 5.23.b the topological classification built from the previous equation and extracted from [12] which connects the chirality of the CNTs  $(n, m)$  in graphene basis  $(\vec{a}_1, \vec{a}_2)$  with the corresponding  $N_{\text{edge}}$ . Precisely, the color gradient of the cases, from white to dark blue, shows the evolution of  $N_{\text{edge}}$  in the ascending order. Cases with a cross indicate the CNTs with trivial topology (zero edge states). We

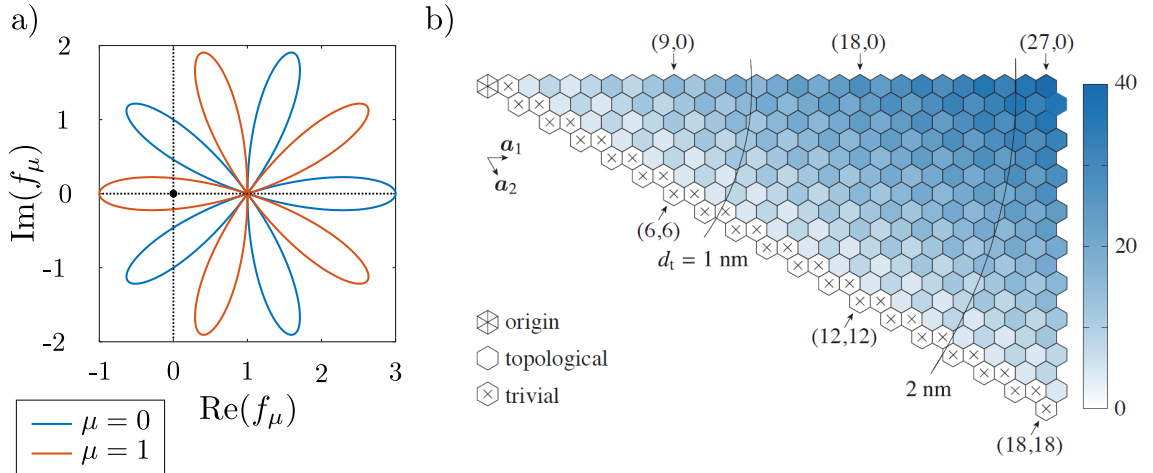


FIGURE 5.23: a) Representation of the Hamiltonian term  $f_\mu(\vec{k})$  in the complex plane for  $\mu = 0$  and  $\mu = 1$ . b) Topological classification of the CNTs: number of edge states (colour gradient) as a function of the tube's chirality.

infer from the reading of the diagram that the majority of CNTs present non-trivial topology and support  $N_{\text{edge}} \neq 0$  edge states expect for semiconducting  $\vec{C}_h(n + 1, n)$  and metallic armchair  $\vec{C}_h(n, n)$  nanotubes. We also mention that almost all CNTs experience a topological phase transition when subjected to a magnetic field increased

up to a critical threshold dependent on the chirality. However, the armchair variety constitutes the notable exception as it exhibits metallic behaviour irrespectively of the presence of a magnetic field and curvature effects.

### 5.3.2 Rolled-up honeycomb lattice photonic crystal

The previous section has revealed the versatility of carbon nanotubes (CNTs) regarding their electronic and topological properties mainly governed by their chirality. In particular, most of semiconducting CNTs exhibit non-trivial topological behaviour, conducive to the emergence of electronic edge states at both ends of the CNTs. Such edge states have attracted much attention toward, for instance, the conception of dissipationless devices. In the photonic domain, the realization of topological insulators have also appeared as a tantalizing route to achieve lossless optical communication.

In this section, we lay the foundations for the transposition of the physics of CNTs in the photonic domain. We intend notably to explore the optical properties of their photonic crystal analogues: rolled-up honeycomb lattice photonic crystal membranes (HC-PCM). We propose, therefore, two methods to calculate the dispersive features of the photonic microtubes. The first method inspires from the zone-folding procedure by calculating numerically (FDTD) the dispersion of a planar unit cell delimited on photonic graphene with periodic boundary conditions to reproduce the periodicity along the tube circumference. The principle of the second method relies on the numerical computation (FDTD) of the dispersion of more realist rolled-up photonic microtubes with circular hole pattern exclusively. We finally present preliminary results of the fabrication of real microtubes and their optical characterization through angular-resolved spectroscopy measurements.

#### Numerical zone folding

Our first approach to estimate the dispersive properties of rolled-up photonic graphene is based on zone folding method introduced previously to predict CNTs' band structures. We recall that the construction of CNTs entails the choice of a chiral vector  $\vec{C}_h(n, m)$  on graphene lattice defining the direction of rolling of the graphene sheet. We derive from the indices  $(n, m)$  the translation vector  $\vec{T}$  characterizing the periodicity along the tubes' axis. The basis  $(\vec{C}_h(n, m), \vec{T})$  constitutes therefore the unit cell of the CNT. The circulation of the electrons along the tubes' circumference implies the quantization of the wave vector component along  $\vec{C}_h$ . In the reciprocal space, the previous quantization traduces by a set of lines oriented along  $\vec{T}$  and positioned at the quantized values of the wave vector component along  $\vec{C}_h$ . The principle of zone folding involves the cutting of graphene 2D band diagram along these lines. We reconstruct then the 1D band structure of the CNTs by assembling the subbands resulting from the cutting operation along the CNTs' Brillouin zone.

It is noteworthy that the zone-folding approach supposes infinitely long nanotubes and neglect curvature effects. Being aware of these hypotheses, this method represents a powerful tool allowing extremely fast calculation of CNTs' energy dispersion, even for unit cells containing a large number of carbon atoms. For this reason, we use the zone-folding concept to obtain first estimations of the CNT-like photonic microtubes dispersion and test simple chiralities.

Following the zone-folding procedure, we define the photonic microtubes' unit cell on the planar pattern of an InP-made honeycomb lattice photonic crystal membrane

(PCM) presented in Figure 5.24.a and b) by top and lateral views of the 3D FDTD model with circular air holes. We set the lattice parameters to  $a_h = 0.301 \mu\text{m}$  for the honeycomb period and  $r = 0.109 \mu\text{m}$  for the holes' radius as adjusted in Section 5.1 to obtain a Dirac point at  $f_D \simeq 194.5 \text{ THz}$  (i.e.  $1.54 \mu\text{m}$ ). In the same way, we also fix the thickness of the dielectric membrane to  $h = 0.228 \mu\text{m}$ .

The FDTD computation zone (orange outline) coincides with the unit cell of the microtube generated by the chiral  $\vec{C}_h$  and translation  $\vec{T}$  vectors, indicated by purple arrows in Figure 5.24.a for the chirality  $\vec{C}_h(4, 1)$ . We note that the original honeycomb has been rotated appropriately to align  $\vec{C}_h$  and  $\vec{T}$  with  $y$  and  $x$  axes, respectively, to form a rectangular calculation region as required for Cartesian mesh. We apply periodic boundary conditions (BC) on the two frontiers perpendicular to  $\vec{C}_h$  to reproduce the periodicity along the tube's circumference. Moreover, Bloch BC simulate the periodicity along the tube's axis, namely in the direction of  $\vec{T}$ , while applying a phase correction on the fields when entering another cell. PML boundaries composed of 64 layers of *steep angle* profile absorb the electromagnetic energy in the out-of-plane direction ( $z$  axis direction) at a distance  $d_{\text{PML}} = 4h$  to the structure.

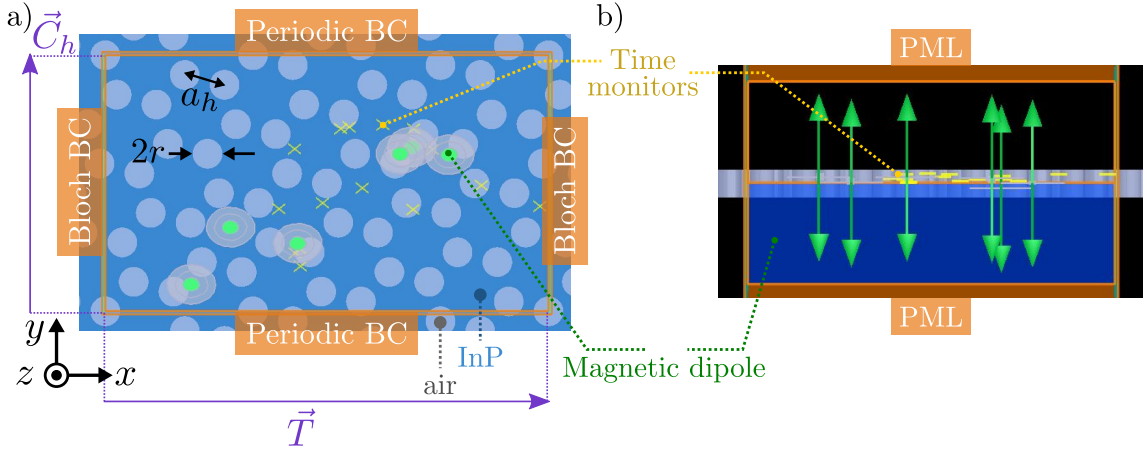


FIGURE 5.24: a) FDTD section view of the calculation unit cell of a rolled-up honeycomb lattice photonic crystal membrane microtube with periodic and Bloch boundaries conditions (BC) to reproduce the periodicity along the circumference and the axis of the tube as in the zone-folding method. b) FDTD lateral view of the model.

To calculate the spectral response of the HC-PCM unit cell, we place randomly 6 magnetic dipoles of emission bandwidth  $[50\text{-}300] \text{ THz}$  oriented along the  $z$ -axis to excite TE-polarized modes as depicted in 5.24.a. We enforce the detection of TE modes by applying symmetric boundary conditions over the blue-shaded half plane  $z < 0$  in 5.24.b. A cloud of 15 time monitors (yellow crosses) arranged randomly within the unit cell, record the temporal evolution of the electromagnetic fields. We set the simulation time to  $t_s = 3000 \text{ fs}$ . We finally extract the spectral response of the structure by Fourier transforming the time data apodized with the parameters  $t_c = 0.5t_s$  and  $\Delta t = 0.125t_s$  beforehand.

We present, therefore, in Figure 5.25.a, c and d the simulated band structures of unrolled photonic microtubes with chiralities  $\vec{C}_h(1, 0)$ ,  $\vec{C}_h(1, 1)$  and  $\vec{C}_h(2, 0)$ , respectively. We also superimpose the corresponding zone-folding bands in red dashed lines, calculated with a hopping parameter  $t = 25.6 \text{ THz}$  (see Section 5.1). We infer from the reading of the graphs that:

- we find two photonic bands in addition to the zone-folding bands;

- we retrieve the same dispersion features as in the electronic diagrams: the presence of a gap for the zig-zag chiralities  $\vec{C}_h(1,0)$  and  $\vec{C}_h(2,0)$  and a Dirac crossing for the armchair chirality  $\vec{C}_h(1,1)$ ;
- the zone-folding dispersion is well reproduced only in the vicinity of the Dirac crossing, notably for the armchair chirality  $\vec{C}_h(1,1)$ ;
- above the Dirac level, the frequency mismatch and the deformation of the photonic bands originate from the interaction between the zone-folding branches and the additional bands; precisely the supplemental band corresponds to the monopolar mode mentioned in Section 5.1 as confirmed by the map of the magnetic intensity  $|H_z|^2$  calculated at the green dot of the  $\vec{C}_h(1,0)$  band structure over the entire unit cell in Figure 5.25.b;
- below the Dirac level, the progressive divergence of the photonic band with respect to the zone-folding bands is attributed to the increase of the wavelength as compared to the lattice parameters, reducing the microstructure effect.

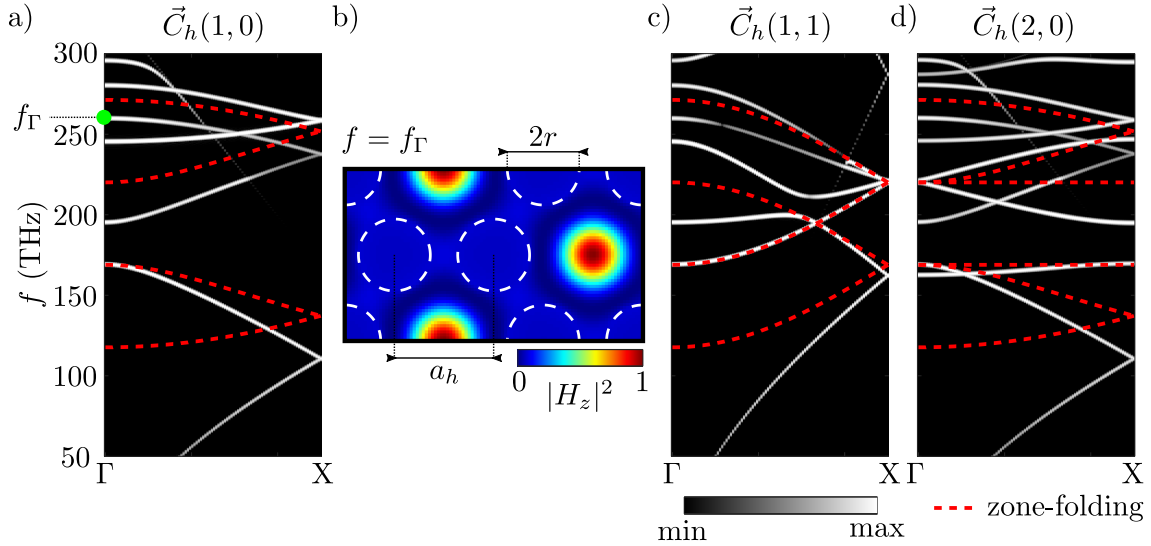


FIGURE 5.25: Simulated band structures of unrolled CNT-like photonic microtubes with circular air holes of chirality a)  $\vec{C}_h(1,0)$ , c)  $\vec{C}_h(1,1)$  and d)  $\vec{C}_h(2,0)$ . b) Real-space map of the magnetic field intensity  $|H_z|^2$  calculated over the unit cell of a CNT-like photonic microtube of chirality  $\vec{C}_h(1,0)$ .

We perform a similar series of simulations but replacing circular by triangular air holes to move the monopolar mode higher in frequency, away from graphene bands as carried out for photonic graphene in Section 5.1. A typical unit cell of the unrolled photonic microtube with triangular air holes is presented in Figure 5.26.a for the chirality  $\vec{C}_h(4,1)$ . In particular, we set the honeycomb period to  $a_h = 0.367 \mu\text{m}$  and the triangle edge size to  $s = 0.490 \mu\text{m}$  according to the adjustment of triangular-hole photonic graphene realized in Section 5.1. We use identical simulation setting for the calculation zone, the sources and the monitors as used for the case of circular-hole structure presented previously.

We present in 5.26.b, c and d the spectra obtained for the chiralities  $\vec{C}_h(1,0)$ ,  $\vec{C}_h(1,1)$  and  $\vec{C}_h(2,0)$  along one half of the microtube Brillouin zone extending from  $\Gamma$  to X point ( $k_z = \pi/|\vec{T}|$ ). We also overlay the zone-folding theoretical bands in red dashed line calculated with a hopping parameter  $t = 28.7$  THz. We confirm, therefore,



the removal of the monopolar mode which leaves folded graphene bands unaltered or quasi-unaltered. Indeed, we report a very good agreement, in shape and energy levels, with the zone-folding dispersion, except in the lower frequency domain (typically below 130 THz) where the photonic crystal diffraction effect vanishes so that the dispersion evolves linearly. We also remark the same dispersive behaviour as predicted for the electronic case at the Dirac level, namely the presence of a gap for chiralities  $\vec{C}_h(1,0)$  and  $\vec{C}_h(2,0)$  and a Dirac crossing for the armchair unit cell  $\vec{C}_h(1,1)$ .

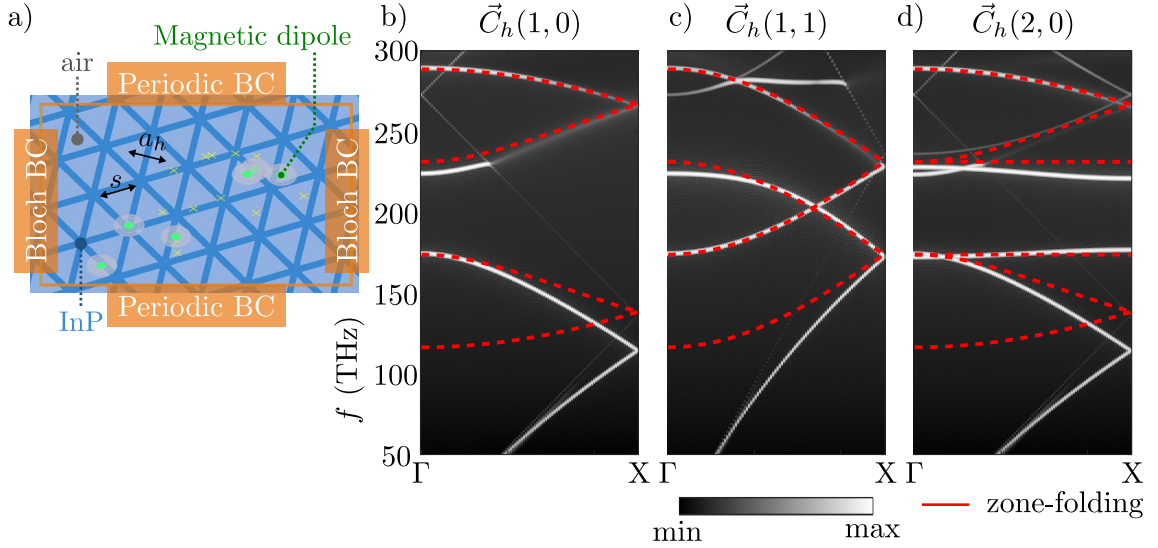


FIGURE 5.26: a) Computation unit cell of an unwrapped CNT-like photonic microtube with triangular air holes of chirality  $\vec{C}_h(4,1)$ . b) Simulated band structures of unrolled CNT-like photonic microtubes with triangular air holes of chirality a)  $\vec{C}_h(1,0)$ , c)  $\vec{C}_h(1,1)$  and d)  $\vec{C}_h(2,0)$ .

### Numerical band structure of rolled-up honeycomb lattice photonic crystal membrane

In the previous approach, we have simulated the band structures of CNT-like photonic microtubes, inspiring from the zone-folding method. It is noteworthy that the latter method gives reliable results assuming sufficiently long microtubes ( $L \gg a_h, r$ ) with large curvature radius noted  $\rho_t$ , namely  $\rho_t \gg a_h, r$ . In particular, we assess in the second approach the effect of curvature on the tube's dispersion by simulating the band structure of more realist CNT-like photonic microtubes with circular air holes.

We present in Figure 5.27.a, b and c, lateral, top and perspective views of the 3D FDTD design of the photonic microtube. It is built from the seamless rolling along a prescribed direction  $\vec{C}_h(m,n)$  defined on graphene lattice, of a honeycomb lattice photonic crystal membrane (HC-PCM). The HC-PCM consists of circular air holes of radius  $r = 0.109 \mu\text{m}$  etched in an InP membrane of thickness  $h = 0.228 \mu\text{m}$  arranged according to a honeycomb lattice of period  $a_h = 0.301 \mu\text{m}$ . Moreover, the chirality fixes the diameter of the tube  $d_t$  according to  $|\vec{C}_h| = \pi d_t$ , where  $|\vec{C}_h|$  coincides with the circumference of the tube.

The calculation zone (orange outline) encloses the rolled-up unit cell of the microtube, delimited by the norm of the translation vector  $\vec{T}$  along the tube axis, as depicted in Figure 5.27.a and b. To calculate the tube's band structure, we apply Bloch boundary conditions (BC) along its axis, coinciding with the  $z$  axis while we absorb incident light with PML boundaries with a *steep angle* profile comprising 64 absorbing layers distant to the tube surface by  $d_{\text{PML}} = 3\rho_t/2$ . We arrange magnetic dipoles sources



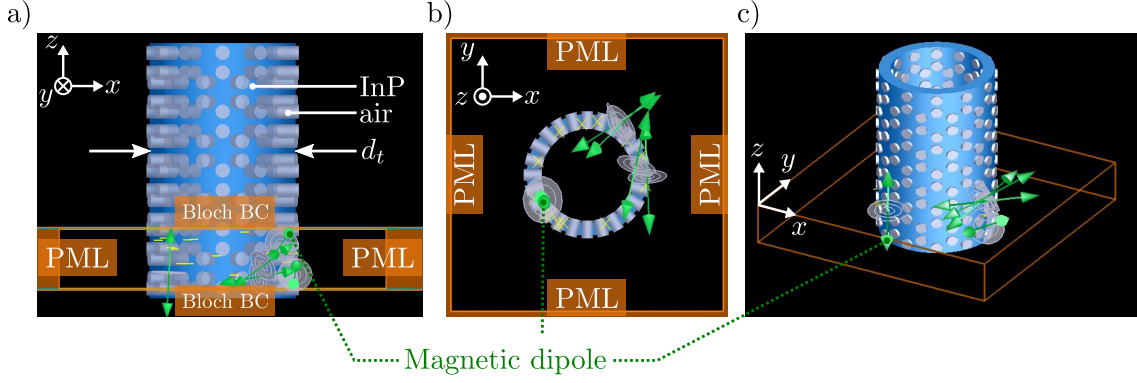


FIGURE 5.27: a) Lateral, b) cross-section, and c) perspective views of the FDTD model of a seamless rolled-up honeycomb lattice photonic crystal membrane microtube with circular air holes.

of bandwidth [50-300] THz and a cloud of time monitors inside the PCM around the tube's circumference to excite the modes and record the temporal evolution of the fields.

We simulate, therefore, the band structure of a HC-PCM rolled up along the direction  $\vec{C}_h(12,0)$  leading to a diameter  $d_t \simeq 1 \mu m$ . The diameter  $d_t$  increases along with the size of the unit cell which itself widens for larger values of the chiral indices  $(n, m)$ , which raises the computation time. We chose therefore to test the simple zig-zag chirality  $\vec{C}_h(12,0)$  represented in the 3D FDTD views in Figure 5.28.a, b and c, associated to a relatively small unit cell to minimize the memory requirements and the simulation time. This chirality also verifies the metallic condition expressed in Equation (5.51) so that we expect a Dirac crossing in the band diagram assuming weak curvature effects. We place 5 magnetic dipoles at random positions around the tube's circumference but oriented perpendicularly to the membrane plane to excite TE polarized modes exclusively as shown in Figure 5.28.b. We set the simulation time  $t_s$  to 10000 fs. A cloud of 15 monitors assembled randomly over the computation zone in the membrane and around the tube's circumference, collect the time data of the electromagnetic fields.

We present in Figure 5.28.d the frequency bands calculated along the tube's Brillouin zone  $\Gamma$ -X where X locates at  $k_z = \pi/|\vec{T}|$  and displayed in logarithmic scale. First of all, we observe a band crossing (red dot) at the level of the Dirac point (red dashed line) obtained in the photonic graphene structure, namely at  $f_D \simeq 194.5$  THz as expected for the chosen chirality. To facilitate the interpretation of the graph, we have added in Figure 5.28.g, as a guide, the band structure of the chirality  $\vec{C}_h(12,0)$  simulated with the zone-folding method on the photonic graphene unit cell represented in 5.28.e and f for TE polarization. We report, therefore, a good concurrence between the rolled-up and planar band structure, in terms of shape and energy levels of the bands. However, we notice extra bands in the diagram of the rolled-up tube which intersect the red dashed Dirac level. The presence of additional bands hints a potential mixing of TE and TM polarized modes. To validate this hypothesis, we have conducted another simulation of the planar photonic graphene cell with magnetic dipole sources of random orientation to excite both TE and TM modes, as represented on the FDTD top and lateral views in Figure 5.28.h and i. We have plotted the resulting band structure in Figure 5.28.j in which we retrieve all the bands of the rolled-up microtube.

In summary, we have achieved the simulation of the optical properties of CNT-like photonic crystal microtubes according to two methods from which we draw the following preliminary conclusions:

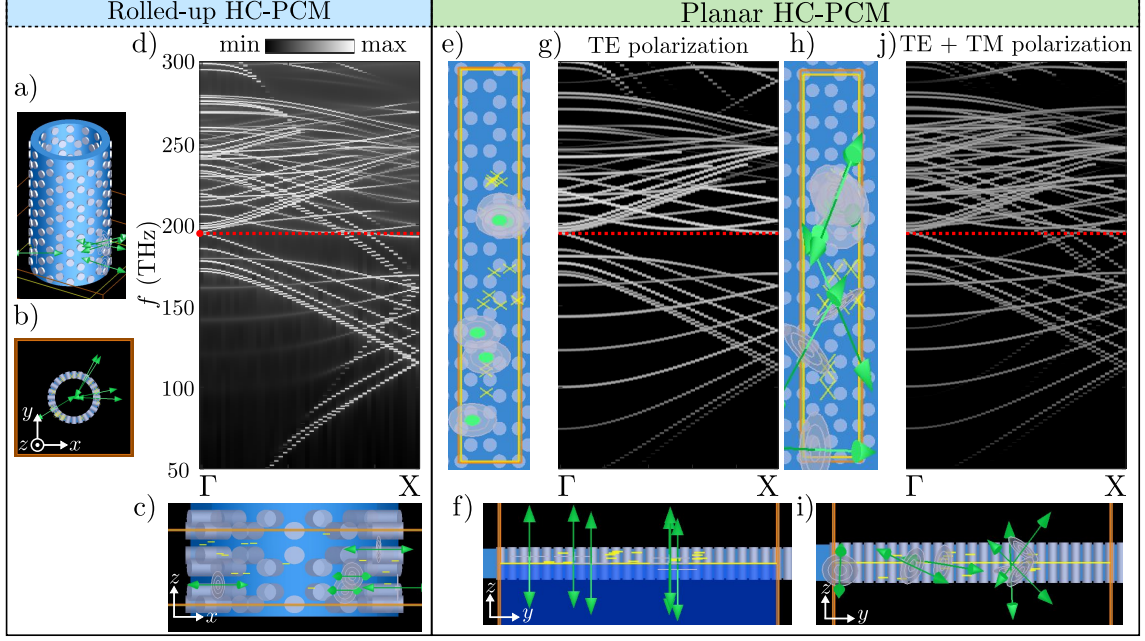


FIGURE 5.28: a) Perspective, b) top and c) lateral views of the FDTD model of a CNT-like photonic microtube with circular air holes. d) Simulated band structure of a CNT-like photonic microtube with circular air holes of chirality  $\vec{C}_h(12,0)$ . e) Top and f) lateral FDTD views of the planar computation unit cell of a CNT-like photonic microtube with circular air holes of chirality  $\vec{C}_h(12,0)$  with incident TE polarization. g) Simulated band structure of the unrolled microtube with TE polarization. h) Top and i) lateral FDTD views of the planar computation unit cell of a CNT-like photonic microtube with circular air holes of chirality  $\vec{C}_h(12,0)$  with incident TE and TM polarizations. j) Simulated band structure of the unrolled photonic microtube with TE-TM polarizations.

- numerical zone-folding: we have first estimated the CNTs optical response by calculating numerically the band diagrams of unrolled tubes in the way of zone-folding method. In particular, this method neglects the curvature effects. For chiralities with low chiral indices, we retrieve photonic equivalents of metallic and semiconducting behaviour predicted with the CNT zone folding, namely the presence of a Dirac crossing or a band gap. We also report a good matching between the zone-folding and photonic bands for triangular-hole PCM-based microtubes. By contrast, the presence of the monopolar mode in the circular-hole structure alters the bands located above the Dirac level.
- band structures of rolled-up photonic crystal membranes: in the second place, we have refined our estimation of the optical response of CNT-like photonic microtubes to take into account the finite curvature of the structures. To this end, we have simulated, for instance, the band structure of a realist photonic crystal microtube with circular air hole. We have showed that the bands match exactly with the dispersion of the unrolled tube, yet with mixed TE and TM polarizations. In this case, the tube's curvature generates negligible effects, making the planar simulations efficient and reliable toward the prediction of the CNT's optical features.

For the sake of completeness, the simulation of photonic crystal microtubes' band structures should be extended to other chiralities and diameters to get more representative results and draw conclusions on the relevance of the calculations on unrolled tubes. Moreover, we have not tested yet the triangular hole PCM-based microtube's

optical response for which the remote monopolar mode should barely affect the tube's final dispersion.

### Fabrication of rolled-up photonic graphene

In the previous part, we have investigated numerically the optical properties of photonic crystal analogues of carbon nanotubes. We have showed in particular that the presence of a Dirac crossing in the tubes' band structures was determined by their chirality. The first step toward the experimental validation of the numerical predictions involves the fabrication of the photonic microtube based on the rolled-up nanotechnology. In this section, we present main results of the fabrication process, from the description of the multi-layered precursor to the production of rolled-up honeycomb lattice photonic crystal membranes with various chiralities.

The first stage of the fabrication cycle deals with the successive epitaxial deposition of InGaAs (sacrificial layer), InP and InGaP material layers on top of an InP nominal substrate to form the multi-layered precursor. We focus, in particular, on the sample C2441 used for the later optical characterization measurements and composed of a 265 nm-thick InGaAs layer, 162 nm-thick InP layer and 74 nm-thick InP layer. We have also inserted a plane of InAs quantum dashes (QDas) at 58 nm to the bottom of the InP layer, characterized by an emission wavelength centered at around 1.5  $\mu m$  in preparation of later photoluminescence measurements. The Gallium proportion  $x_{Ga}$  in the InGaP layer reaches about 0.12 leading to a mismatch  $m$  between the InGaP and InP lattice parameters estimated to 0.8 %. According to Equation (1.21), we find a theoretical curvature radius of the rolled-up InP-InGaP bilayer of about 22  $\mu m$ . In practice, we measure real radii included in the interval [16.8 - 19]  $\mu m \pm 1 \mu m$ . The discrepancies between the theoretical and experimental data may be explained by the slight deformation of the tubes upon drying process.

The next step entails the production of the planar template to form the graphene-like photonic crystal membrane and achieve the rolling of the membrane into horizontal microtubes. For the sample C2441, the photonic crystal pattern consists of a honeycomb lattice with a period  $a_h = 0.294 \mu m$  of triangular air holes of edge size  $s = 0.287 \mu m$  as shown on the scanning electron microscopy (SEM) picture in Figure 5.29.b generated upon lithography and reactive ion etching (RIE) processes. The latter set of lattice parameters leads to a Dirac point about 1.5  $\mu m$ . The sample is organized in 4 matrices 12 planar rectangular templates. We fix the dimensions of all the rectangles to 50  $\mu m \times 140 \mu m$  where 50  $\mu m$  corresponds to the length and the perimeter to achieve a single rolling of the membrane. One matrix comprises three rows of four planar pattern designed to roll as shows on the SEM picture in 5.29.a. We sweep the value of the lithography exposure dose parameter from 0.7 to 0.9 for the three rows to find setting that allows highly resolved patterns and a complete etching. Each row decomposes into four orientations of the honeycomb pattern derived from the following elemental chiralities: armchair  $\vec{C}_h(1, 1)$ , metallic zig-zag  $\vec{C}_h(6, 0)$ , semiconducting (SC)  $\vec{C}_h(5, 3)$  and metallic  $\vec{C}_h(5, 2)$ . Dividing the 140  $\mu m$ -long perimeter of the tubes by an integer number of the norm of the previous elemental chiral vectors, we obtain microtubes' planar unit cells with armchair  $\vec{C}_h(56, 56)$ , metallic zig-zag  $\vec{C}_h(96, 0)$ , semiconducting  $\vec{C}_h(70, 42)$  ( $14 \times \vec{C}_h(5, 3)$ ) and metallic  $\vec{C}_h(75, 30)$  ( $15 \times \vec{C}_h(5, 2)$ ) chiralities.

In the matrix shown in 5.29.a, we report the successful rolling of all the 12 planar patterns to form photonic crystal microtubes. We note, however, that one specimen had its rolling direction deviated. On the scale of the entire sample, we observe a rate

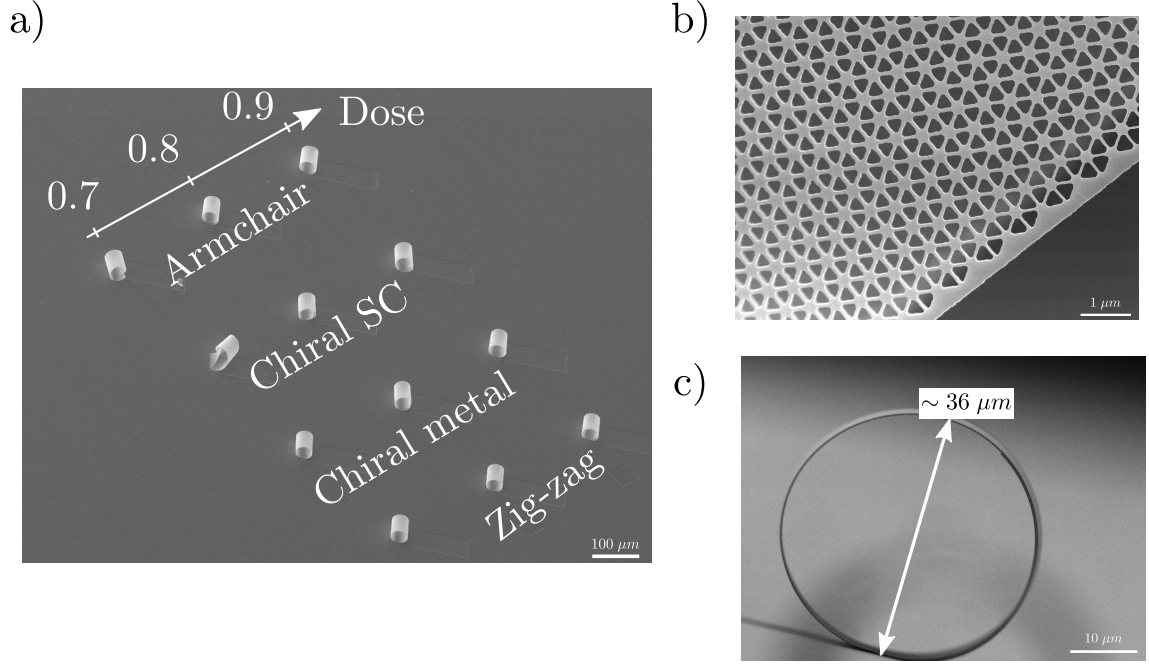


FIGURE 5.29: a) Scanning electron microscope (SEM) picture of a matrix of 12 rolled-up honeycomb lattice photonic crystal membrane microtube with triangular air holes upon rolling of planar templates with different e-beam lithography exposure doses and chiralities. b) Close-up SEM picture of the honeycomb lattice pattern with triangular air holes. c) SEM picture of a rolled-up photonic microtube.

of 94 % of successful rolling of the membranes. We appreciate the quality of the rolling on the SEM picture in Figure 5.29.c of a photonic microtube specimen with a diameter of about 36  $\mu\text{m}$ .

### Optical characterization of the honeycomb lattice photonic crystal microtubes

To finalize the study of CNT-like photonic microtubes, we have conducted a preliminary series of optical measurements to characterize the triangular air-hole photonic crystal microtubes fabricated on sample C2441 presented previously. Precisely, we have performed angular-resolved spectral measurements using a white light source to construct experimental band diagrams in reflectivity of the microtubes along their axis. In the following, we present and analyze the photonic bands extracted from zig-zag photonic microtubes exhibiting a metallic-like behaviour theoretically.

The sample C2441 contains photonic microstructures with four different chiralities, namely armchair  $\vec{C}_h(56, 56)$ , semi-conducting  $\vec{C}_h(70, 42)$ , metallic  $\vec{C}_h(75, 30)$  and zig-zag  $\vec{C}_h(96, 0)$ . As mentioned previously, those chiralities correspond to integer multiple of elemental chiralities  $\vec{C}_h(1, 1)$ ,  $\vec{C}_h(5, 3)$ ,  $\vec{C}_h(5, 2)$  and  $\vec{C}_h(6, 0)$  drawn, for instance, in Figure 5.30.a onto a honeycomb lattice of gray-shaded triangles. The zone-folding band structure of zig-zag  $\vec{C}_h(6, 0)$  tubes plotted in Figure 5.30.b along the Brillouin zone  $\Gamma$ -X in the direction of the tubes' axis, predicts a Dirac crossing located in  $\Gamma$ . We have showed earlier that the electronic zone-folding calculations matched with the numerical band diagrams of triangular air-hole honeycomb lattice PCM microtubes. In particular, photonic structures exhibiting dispersion features in  $\Gamma$ , or more generally above the light line (red dashed line), hold much interest for optical characterization as they are directly addressable via the surface. Among the above-mentioned chiralities, only the zig-zag  $\vec{C}_h(6, 0)$  microtubes are characterized by a band crossing occurring in  $\Gamma$ , in theory. We have, therefore, conducted a first series of angular-resolved spectral

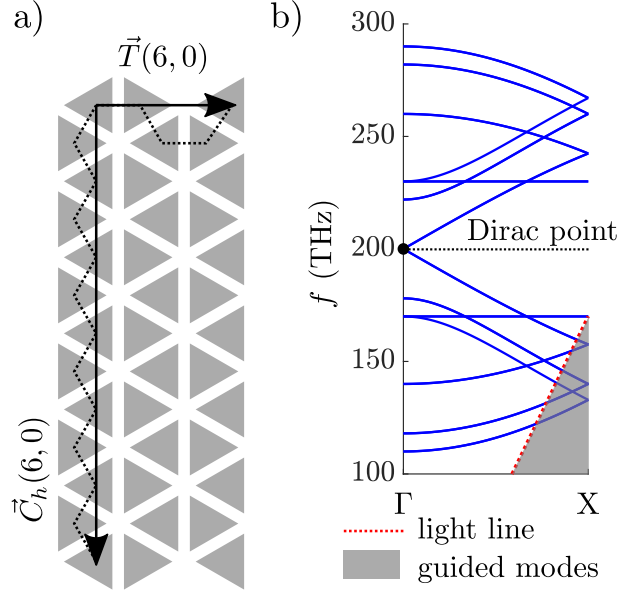


FIGURE 5.30: a) Unit cell of the zig-zag  $\vec{C}_h(6,0)$  microtube drawn onto a honeycomb lattice of gray-shaded triangles. b) Band structure of the zig-zag  $\vec{C}_h(6,0)$  microtube calculated with the zone-folding method along the Brillouin zone  $\Gamma$ - $X$ . For the photonic structures, the red dashed line corresponds to the light line which delimits the frontier between surface addressable modes and guided modes (gray region).

measurements which principle is described in Section 2.3, on the zig-zag microtubes to retrieve their dispersion relation along the tubes' axis experimentally.

When addressing the photonic modes via the microtubes' surface, the direction of the light waves given by the wave vector  $\vec{k}$  decomposes as  $\vec{k} = \vec{k}_{\parallel} + \vec{k}_{\perp} + \vec{k}_{\text{out}}$ , where  $\vec{k}_{\parallel}$  orients along the tube's axis while  $\vec{k}_{\perp}$  and  $\vec{k}_{\text{out}}$  coincide with the radial and orthoradial components as depicted on the schematic perspective and top views of the tube in Figure 5.31.a and b. To extract the band diagram of the tube along its axis, we filter out the  $\vec{k}_{\perp}$  component by orienting the slit delimited by dashed black lines in 5.31.a, along  $\vec{k}_{\parallel}$ . In doing so, we ensure to collect the angular dispersion represented by the angle  $\theta$  in 5.31.c from which we deduce the norm of  $\vec{k}_{\parallel}$  according to  $k_{\parallel} = \vec{k}_{\parallel} \cdot \vec{e}_z = |\vec{k}| \sin \theta$  which constitutes the abscissa of the dispersion relation  $\omega = f(k_{\parallel})$ .

In practice, we illuminate the horizontal microtubes with the white light source which, after focusing into the objective, generates an  $10 \mu m$ -large ovoid excitation spot symbolized by the yellow ellipse on the upper schematics in Figure 5.32.a, b and c spreading along the tubes' axis. We then collect the reflected beam through the same objective, that we orient along the slit axis by rotation of the Dove's prism. The spectral information of the modes is finally dispersed spectrally when entering the spectrometer. In particular, we use the grating A of period 150 lines/mm to diffract the spectral components over a 114 nm-large window. Moreover, we perform multiple measurements at different central wavelengths that we combine to reconstruct the band diagram over a broader spectral interval.

Therefore, we present in Figure 5.32.a, b and c the experimental dispersion diagrams in reflectivity of a zig-zag microtube specimen generated for frequencies ranging from 180 to 320 THz ( $0.94 \mu m$  to  $1.67 \mu m$ ) for three positions of the excitation spot, in the middle, on the left and right sides of the microtube, respectively. The wave vector components  $k_{\parallel}$  are normalized by the size of the honeycomb lattice Brillouin zone  $2\pi/a_h$  with the period  $a_h = 0.294 \mu m$ . The borders of the graphs are limited by the

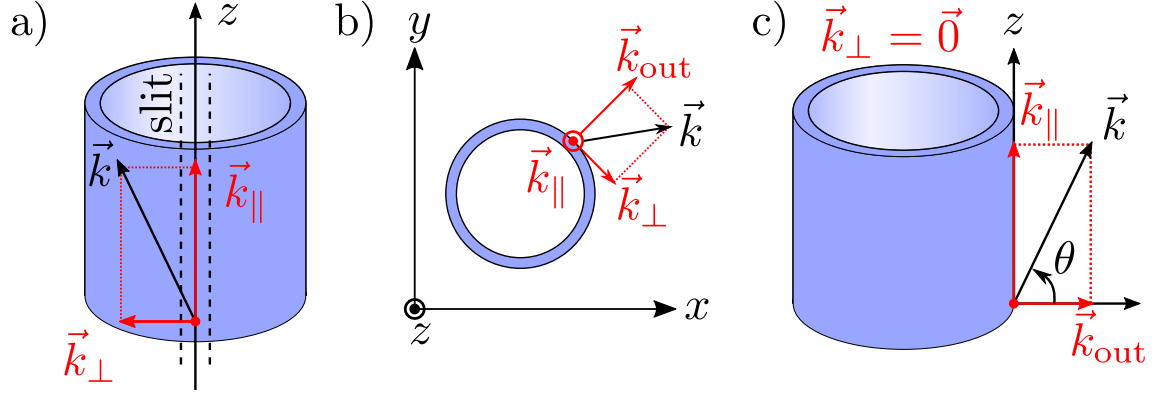


FIGURE 5.31: a) Schematic front view of incident light hitting the microtube and oriented along the wave vector  $\vec{k}$  which decomposes into a component along the microtube axis ( $z$  axis) noted  $\vec{k}_{\parallel}$  and a component along the orthonormal direction noted  $\vec{k}_{\perp}$ . The slit of the angular-resolved spectral setup is oriented along the tube's axis to select the component  $\vec{k}_{\parallel}$  exclusively. b) Cross-section view of the microtube where the wave vector divides into the radial and orthonormal components noted  $\vec{k}_{\text{out}}$  and  $\vec{k}_{\perp}$ , respectively. c) Decomposition of the incident  $\vec{k}$  with an angle  $\theta$  into  $\vec{k}_{\parallel}$  and  $\vec{k}_{\text{out}}$  for zero  $\vec{k}_{\perp}$  component.

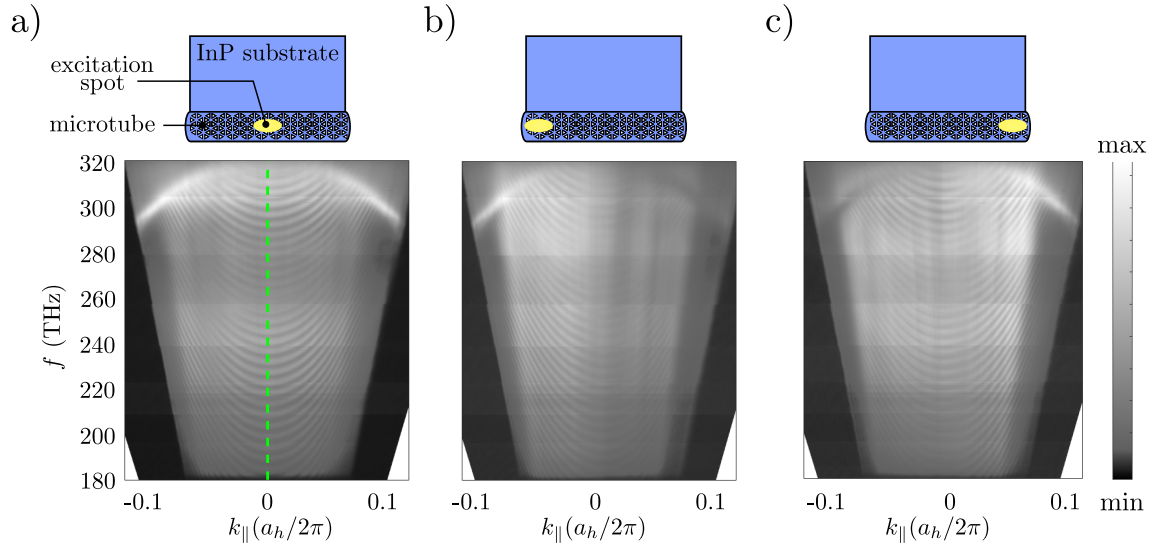


FIGURE 5.32: Upper drawings: schematics of the experimental configuration where we send a white light beam (yellow ovoid zone) in a) the middle, b) the left end and c) the right end of a triangular air-hole honeycomb lattice photonic crystal membrane microtube rolled up on a InP substrate. Graphs: experimental band diagrams in reflectivity of the fabricated zig-zag photonic microtubes when the excitation spot locates a) in the middle, b) on the left end, and c) right end of the tube.



numerical aperture of the objective ( $NA = 0.42$ ) yielding a maximum value of the normalized modulus  $|k_{\parallel}|$  estimated to 0.13 at a frequency (wavelength) of 320 THz ( $0.94 \mu m$ ). Note that we have also removed background reflection signal produced by the optical components, especially the objective, by realizing measurements where the sample is hidden by an absorbing material sheet.

We remark on the first graph displayed in Figure 5.32.a two distinct dispersive features: a bright curved branch emerging at about 320 THz in  $\Gamma$  ( $k_{\parallel} = 0$ ) and reaching 295 THz at the diagram frontiers in  $k_{\parallel}$ , and fringes regularly arranged along the entire spectral range. We retrieve only one half on the branch on the two other dispersion curves in 5.32.b and c, which position on the reciprocal space depends on the location of the excitation spot on the microtube. Conversely, the fringes are totally preserved irrespective of the spot location.

The dependence of the bright branch upon the spot location demonstrates that it corresponds to a mode propagating along the tube's wall membrane. Indeed, when the spot is positioned, for instance, on the left end of the tube, the mode can only travel on the right direction leading to a single branch on the diagram for which the sign of  $k_{\parallel}$  indicate the direction of propagation. However, we do not retrieve the dispersive signature of the zig-zag chiralities characterized by a Dirac point at 200 THz as presented in Figure 5.30. By deduction, the detected mode should correspond to a mode of the PCM membrane. To validate this hypothesis, we have joined in Figure 5.33.a the experimental band structure to the photonic bands of the triangular-hole honeycomb lattice PCM calculated with the FDTD method. The dispersion of the PCM with a period  $a_h = 0.294 \mu m$  and triangle edge  $s = 0.287 \mu m$  along the  $\Gamma$ -K reciprocal segment is showed in 5.33.b where the red dashed line indicate the frontier between surface-addressable modes and guided modes. The inset picture illustrates the photonic crystal membrane with triangular hole. In particular, we have extracted part of the monopolar and Dirac branch (green dashed zone) in the spectral and momentum space of interest. Though the shift in energy levels imputed to experimental deviations with respect to the targeted lattice parameters, we note the same curvature for the experimental and theoretical branches so that we may attribute the Dirac or monopolar modes to the bright mode observed experimentally. Finally, we explain the absence of the tube's distinctive dispersive features (Dirac bands) by the absorption of photons before completing at least one circulation along the large tube's circumference. The impossible circulation of photons prevents, therefore, the formation of the quantized modes around the tube, hence of the zone-folded dispersion.

Furthermore, the fringes pattern are typical of interference phenomenon between the optical signals reflected from the microtube surface. To get more insight on the interaction of the light beam with the sample, we have schematized in Figure 5.34.a the path of the incident light (yellow arrow) at normal incidence ( $\theta = 0^\circ$ ) inside the tube produced by the self-rolling of the InP/InGaP bilayer upon removal of the sacrificial InGaAs layer lying on the InP substrate. In our case, we consider low concentration of Gallium element in the InGaP layer so that the InGaP/InP assimilates to a simple InP layer of total thickness  $h = 0.24 \mu m$ . The whole structure is equivalent to an air-filled cavity which thickness  $L$  coincides with the tube's inner diameter  $d_t$  enclosed by an upper  $0.240 \mu m$ -thick InP layer and an InP substrate layer. We have, therefore, simulated the reflection spectrum of this cavity at normal incidence while varying the thickness  $L$ . In particular, we show in Figure 5.34.b that the cavity reflectivity range pattern matches within [214-230] THz the fringes extracted in  $\Gamma$  of the experimental band diagram along the green dashed line drawn in Figure 5.32.a with a thickness ad-

justed to  $L = 32.5 \mu\text{m}$ . We note that the spikes of the experimental curve correspond to mismatched jointing regions of the multiple measurements realized at different central wavelengths.

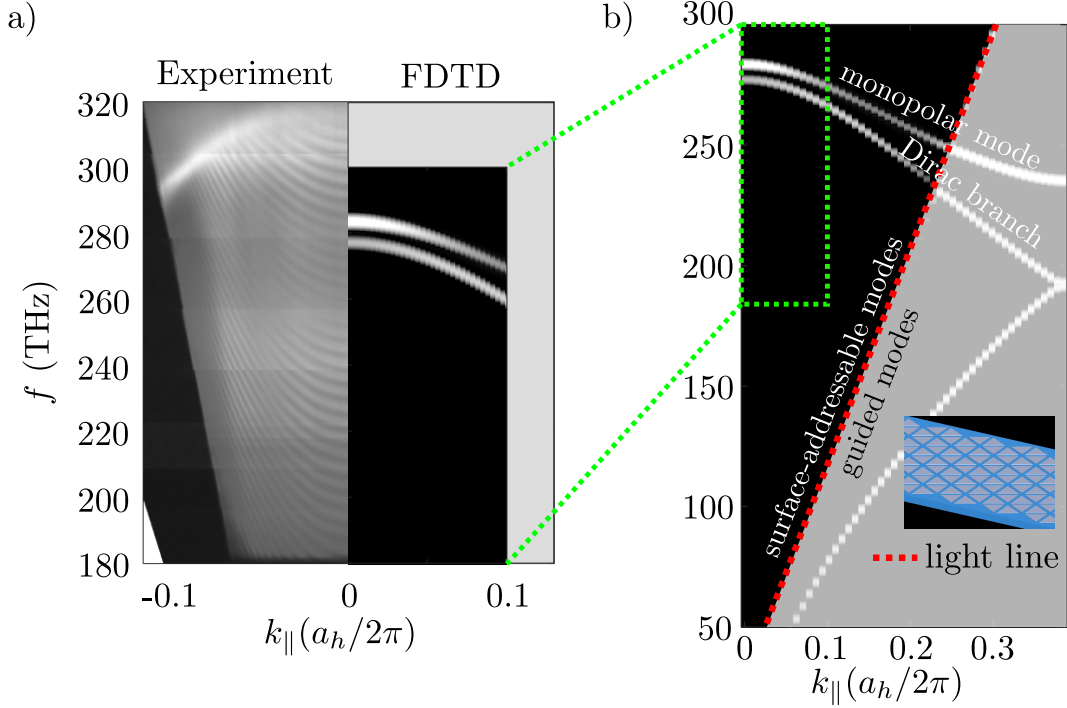


FIGURE 5.33: a) Experimental band diagram in reflectivity of the photonic microtube facing part of the band structure of a triangular air-hole honeycomb lattice photonic crystal membrane with a period  $a_h = 0.294 \mu\text{m}$  and edge size  $s = 0.287 \mu\text{m}$ . b) Band diagram of the photonic crystal membrane plotted on the reciprocal segment  $\Gamma$ -K. The inset picture shows the geometry of the photonic system.

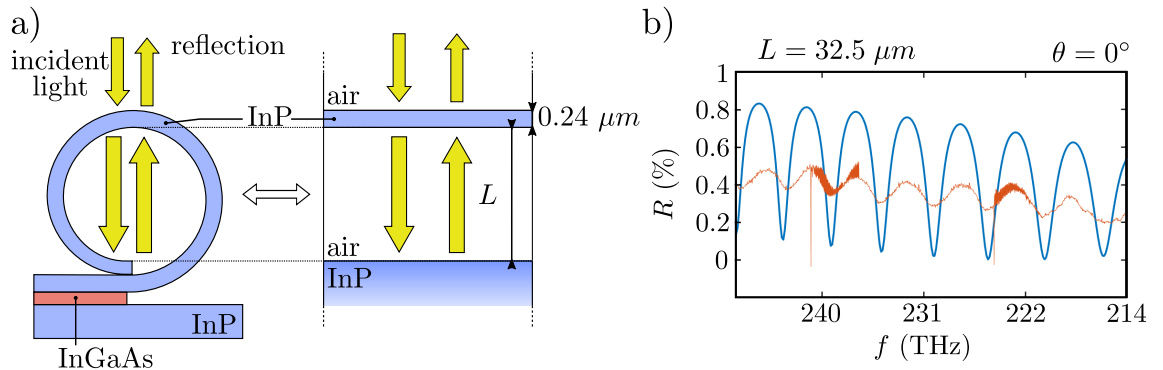


FIGURE 5.34: a) Modelling of the photonic microtube of diameter  $d_t$  rolled up upon the removal of the sacrificial InGaAs layer lying on an InP substrate by an air-filled cavity of thickness  $L = d_t$  enclosed by an upper  $0.24 \mu\text{m}$ -thick InP layer and an InP substrate. b) Reflectivity spectra of the microtube (orange curve) extracted along the green dashed line on the experimental band diagram in Figure 5.32.a and the cavity model (blue curve) calculated with the RCWA method.



### 5.3.3 Conclusion of the section

#### Key points of the section

In summary, we have addressed the main steps of the theoretical study, the practical conception and optical characterization of photonic crystal microtubes analogues of carbon nanotubes.

We have first reviewed the principal electronic and topological properties of carbon nanotubes (CNTs) which depend primarily on their chirality  $\vec{C}_h(n, m)$  or the direction of rolling of the graphene sheet:

- CNTs exhibit either metallic or semiconducting behaviour which is well predicted by the zone-folding method in the limit of tubes with large curvature and length;
- modelling CNTs as 1D topological systems derived from the SSH model, we obtain a topological classification of every possible chiralities revealing that almost all semiconducting CNTs exhibit non-trivial topology.

In the second part, we have investigated theoretically and experimentally the optical properties of rolled-up honeycomb lattice photonic crystal membranes (HC-PCM) as photonic analogues of CNTs.

The numerical calculation of the band structures of the photonic microtubes have brought the following the results:

- we have first assessed the band diagrams using a zone-folding method applied to the unrolled unit cell of the microtubes; in particular, the calculations have revealed the matching between electronic and photonic bands for triangular-hole HC-PCM unrolled microtubes by contrast with the circular-hole structure which dispersion is altered by the additional monopolar mode;
- we have then calculated the band diagrams of realist rolled-up circular-hole HC-PCM which have proven consistent with the zone-folding photonic predictions. Simulations with the triangular-hole HC-PCM are under study.

We have then tackled the fabrication of the photonic crystal microtubes based on the rolled-up nanotechnology. We have demonstrated the successful production of high-quality self-rolling photonic crystal membranes with different orientations of the honeycomb pattern to reproduce the chiralities of CNTs.

Finally, we have carried out a first series of angular-resolved spectral measurements to build the experimental dispersion diagrams of zig-zag microtubes. We have yet not been able to recover the distinctive dispersion features of the photonic crystal microtubes predicted by zone-folding calculations, due to the absorption of photons around the tubes' circumference. Instead, we have observed modes of the photonic crystal membrane wall. To circumvent this issue, we are conducting measurements on tubes with smaller radius. We also plan to evaluate the circulation of photons around non-structured tubes as a testing ground before moving on to photonic crystal tubes.

## 5.4 Conclusion of the chapter

This chapter was dedicated to the exploration of the optical properties of carbon nanotube-like photonic crystal analogues, namely rolled-up honeycomb lattice photonic crystal membranes microtubes. Before addressing the study of the carbon nanotubes-like photonic microtubes, we have simulated the optical and topological properties of intermediary structures that are honeycomb lattice photonic crystal membrane (HC-PCM) and ribbons of HC-PCM corresponding to photonic analogues of graphene and graphene ribbons. For each photonic system, we have first reviewed the models used to apprehend the electronic and topological properties of the associated solid-state structure.

In the first section, we have presented graphene electronic properties derived from the tight-binding approach and the simulated optical properties of the HC-PCM. In particular, we have calculated the optical dispersion of two designs of the HC-PCM, one with circular air holes, the other with triangular air holes. For both designs, we retrieve a Dirac dispersion typical of graphene-like structures. We have also observed a third band on which the modes' intensity exhibits a monopolar distribution interacting with the upper Dirac branch. The triangular hole design was used, in particular, to move the monopolar mode up to higher frequencies, in prevision to a gap opening for the realization of topological effects. We have finally noticed that the tight-binding bands match the photonic only in the vicinity of the Dirac points.

In the second section, we have presented the 1D SSH-like topological model used to predict the topological properties of graphene ribbons via the calculation of the Zak phase. We have showed that graphene ribbons topology depends mainly on the ribbon's chirality. Similarly, we have estimated the topology of the analogue photonic ribbons of elementary zig-zag chirality  $\vec{T}(1, 0)$  according to two methods consisting in calculating numerically the Zak phase and simulating the band structure of the ribbon. Both methods agree on the non-trivial topology of the ribbon, hence on the existence of edge states when the ribbon interface a topologically trivial structure, in accordance with the results obtained for the graphene ribbons.

In the third section, we have reviewed the electronic properties and the topological classification of carbon nanotubes (CNTs), using a zone-folding approach and a 1D topological system, respectively. Both electronic and topological behaviour of the CNTs depend of the nanotubes' chirality. We have then assessed numerically the optical dispersion of the equivalent photonic microtubes with simple chiralities according a zone-folding like method and by simulating the dispersion of more realist structures. We have showed, in particular, the concurrence between the electronic and photonic zone-folding predictions. We have then presented typical results of the fabrication of CNT-like microtubes based on the rolled-up nanotechnology, emphasizing the high reproducibility. We have finally addressed the experimental optical characterization of a photonic microtube specimen with metallic zig-zag chirality through angle-resolved spectral measurements. We have reported typical dispersion features of the photonic membrane wall and interference patterns but yet no spectral signature of the microtube dispersion probably due to the absorption of photons upon circulating around the tube.

## 5.5 References

- [1] N. D. Ashcroft, Neil W.; Mermin, *Solid State Physics*. Philadelphia: Saunders College Publishing, 1976. 176
- [2] C. Bena and G. Montambaux, “Remarks on the tight-binding model of graphene,” *New J. Phys.*, vol. 11, p. 095003, Sept. 2009. Publisher: IOP Publishing. 179
- [3] P. D. Anderson and G. Subramania, “Unidirectional edge states in topological honeycomb-lattice membrane photonic crystals,” *Opt. Express, OE*, vol. 25, pp. 23293–23301, Sept. 2017. 184
- [4] S. Barik, H. Miyake, W. DeGottardi, E. Waks, and M. Hafezi, “Two-dimensionally confined topological edge states in photonic crystals,” *New J. Phys.*, vol. 18, no. 11, p. 113013, 2016. 184
- [5] P. Delplace, D. Ullmo, and G. Montambaux, “Zak phase and the existence of edge states in graphene,” *Phys. Rev. B*, vol. 84, p. 195452, Nov. 2011. Publisher: American Physical Society. 187, 188, 189
- [6] S. Ryu and Y. Hatsugai, “Topological Origin of Zero-Energy Edge States in Particle-Hole Symmetric Systems,” *Phys. Rev. Lett.*, vol. 89, p. 077002, July 2002. Publisher: American Physical Society. 188
- [7] D. Vanderbilt, *Berry Phases in Electronic Structure Theory: Electric Polarization, Orbital Magnetization and Topological Insulators*. Cambridge: Cambridge University Press, 2018. 192
- [8] B. Bahari, A. Ndao, F. Vallini, A. E. Amili, Y. Fainman, and B. Kanté, “Nonreciprocal lasing in topological cavities of arbitrary geometries,” *Science*, vol. 358, pp. 636–640, Nov. 2017. Publisher: American Association for the Advancement of Science Section: Report. 197
- [9] S. Reich, C. T. physicien, C. Thomsen, and J. Maultzsch, *Carbon Nanotubes: Basic Concepts and Physical Properties*. John Wiley & Sons, Mar. 2004. Google-Books-ID: w\_xpdFx0C4MC. 201, 206
- [10] P. R. Wallace, “The Band Theory of Graphite,” *Phys. Rev.*, vol. 71, pp. 622–634, May 1947. Publisher: American Physical Society. 201
- [11] G. G. Samsonidze, A. R. Saito, D. A. Jorio, E. M. A. Pimenta, E. A. G. Souza Filho, F. A. Grüneis, D. G. Dresselhaus, and M. S. Dresselhaus, “The Concept of Cutting Lines in Carbon Nanotube Science,” *Journal of Nanoscience and Nanotechnology*, vol. 3, pp. 431–458, Dec. 2003. 202
- [12] R. Okuyama, W. Izumida, and M. Eto, “Topological classification of the single-wall carbon nanotube,” *Phys. Rev. B*, vol. 99, p. 115409, Mar. 2019. 206, 209
- [13] J. D. Sau and S. Tewari, “Topological superconducting state and Majorana fermions in carbon nanotubes,” *Phys. Rev. B*, vol. 88, p. 054503, Aug. 2013. Publisher: American Physical Society. 206

- [14] C.-H. Hsu, P. Stano, J. Klinovaja, and D. Loss, “Antiferromagnetic nuclear spin helix and topological superconductivity in  $^{13}\text{C}$  nanotubes,” *Phys. Rev. B*, vol. 92, p. 235435, Dec. 2015. Publisher: American Physical Society.
- [15] W. Izumida, L. Milz, M. Marganska, and M. Grifoni, “Topology and zero energy edge states in carbon nanotubes with superconducting pairing,” *Physical Review B*, vol. 96, Sept. 2017. arXiv: 1707.02934. 206
- [16] W. Izumida, R. Okuyama, A. Yamakage, and R. Saito, “Angular momentum and topology in semiconducting single-wall carbon nanotubes,” *Physical Review B*, vol. 93, May 2016. 206
- [17] X. Zang, N. Singh, and U. Schwingenschlögl, “Topological characterization of carbon nanotubes,” *J. Phys.: Condens. Matter*, vol. 30, p. 335301, July 2018. Publisher: IOP Publishing. 206



# General conclusion

## Tubular photon cages

### The proof of concept

The first objective of this thesis consisted in the conception of tubular photon cages based on the rolling of 2D photonic crystal membrane (PCM) mirrors. To address this issue, we have covered the entire process of design, simulation, fabrication and optical characterization of these photonic microresonators. We have first achieved the design of the cages' membrane wall consisting of a highly-efficient non-absorbing broadband 2D PCM mirror operating in the near-infrared range. We have then simulated the optical properties of the final tubular cavity using both the analytical model of the cylindrical cavity resonator and more realistic finite difference time domain (FDTD) simulations. Both models have predicted the confinement of light in the hollow part of the cylindrical photonic cavities in the form of cylindrical cavity modes. We have then reported the fabrication of the tubular photon cages following the rolled-up nanotechnology processes with a high degree of control on the structural parameters of the final 3D shape. We have finally demonstrated experimentally through scanning near-field optical microscopy (SNOM) measurements the presence of confined modes inside real hollow cylindrical microresonators showing spectral and spatial distribution in compliance with the theoretical previsions. The results of this work bring therefore the proof of concept of tubular photon cages as photonic microresonators capable of 3D confinement of light in air.

### In quest of a spectral signature

Tubular photon cages hold much interest for a wide variety of applications in demand of strong light-matter interaction including biosensing or optical tweezer. Indeed, they realize the confinement of light in air which enhances the overlap between the mode field and the micro- and nano-sized targets to which they offer great accessibility to the hollow part. The optical performances of these tubular microresonators depend notably on the quality of the confinement in the air-filled core directly related to the modes' lifetime in the cavities. In particular, we have demonstrated theoretically high quality factors of the cylindrical cavity modes emerging in infinitely long tubular cavities, proving the efficiency of the PCM mirror. However, for finite-size cavities with large curvature radius, the numerical determination of the quality factors of the modes remains challenging owing notably to the high density and spectral overlap of the modes. For the same reasons, the experimental extraction of the spectral signature of cylindrical cavity modes in fabricated tubular microstructures through near-field measurements has not been reported yet.

A alternative way to access the tubular cavities' spectral signature would consist

in probing the modes of the microstructures with an optically active material inserted inside the microtube. To this end, quantum dots (QDs) can be attached at the apex of the SNOM probe emitting within a broad spectral range. Pumping the active nanostructures with an external source, we can collect the photoluminescent signal in the SNOM probe after potential coupling with the cavity modes. This method allows then for a direct probing of the modes provided a sufficient interaction with the QDs emission.

Another strategy considers the reduction of the diameter of the tubular cages. Indeed, we have estimated a total of 6241 modes likely to emerge in a cavity of radius  $17.5 \mu m$  and length  $L = 50 \mu m$  within the spectral range  $[1.4-1.8] \mu m$ . Similar computations show that the number of modes reduces down to 528 for  $5 \mu m$ -radius cavity with identical length and in the same spectral range. In addition, the decrease of the radius removes part of the high azimuthal order modes which increases the chance to achieve a strong concentration of light in the center of the cavity, an appealing feature for trapping applications for example. We also note that such a concentration of the electric field intensity in the center of the cavities has not been observed on the near-field maps. However, we should be aware that the diminishing of the radius can be at the cost of the degradation of the confinement in the cavity. Indeed, smaller radius implies thinner membrane wall which causes optical leakage of the modes. Moreover, for high curvatures, the reflectivity of the membrane wall degrades as it deviates from the planar reflection properties of the PCM.

## **Toward versatile photon cages**

Among potential applications of tubular photon cages, we have mentioned the realization of opto-fluidic micro-sensors as the cages combine transport facilities and optical functionalities. We first remark, though, that for small tubes' diameter, potential capillarity effects should be considered as they may hinder the transport of the targets. We also note that preliminary tests should be conducted to evaluate the optical response of the cavity in different atmospheres and especially to appraise the mechanical stability of the microtubes in contact with liquid targets. We have also illustrated the elastic behaviour of the tubular cages via focused ion beam (FIB) micromanipulation. We can therefore envision to trigger the unfolding of the PCM mirrors via electrical actuation and create reconfigurable photonic microdevices. We finally notify the design flexibility of the photonic microtubes which enables to transpose the functionalities of the micro-objects toward different spectral domains.

## **Photonic crystal analogues of carbon nanotubes**

The second objective of this thesis concerned the exploration of the optical and topological properties of carbon nanotubes photonic crystal analogues produced by the rolling of honeycomb lattice photonic crystal membranes. Preliminary studies were conducted to assess the optical and topological properties of graphene and graphene ribbons' photonic crystal analogues. All the results concerning the photonic crystals have been analyzed in the light of the solid-state reference models.

## Summary of the main results

We have first addressed the simulation of the optical properties of graphene analogues in the class of photonic crystals, namely honeycomb lattice photonic crystal membranes (HC-PCM). In particular, two designs of HC-PCM, with circular and triangular air holes, were investigated. For both designs, we have retrieved a Dirac dispersion typical of graphene-like structures. We have also reported the presence of an additional photonic mode with a monopolar concentration of the electromagnetic field, consistent with the literature. In the circular hole structure, the interaction between one Dirac branch and this monopolar mode makes the Dirac branch bend at the energy level of the Dirac, not boding well for a potential gap opening and the emergence of topological properties. By contrast, the triangular design allows to move the monopolar mode up at higher frequencies and preserve the Dirac bands' original curvature. Finally, we have noted a good correspondence between the photonic bands energy levels and curvatures, and graphene tight-binding band structure and spatial distribution of the wavefunctions, near the Dirac point exclusively.

We have then examined the topological properties of ribbons of HC-PCM. We have first assessed numerically the Zak phase of a photonic ribbon of chirality  $\vec{T}(1, 0)$  with circular air holes following the solid-state methodology applied to graphene ribbons. We found a non-zero Zak phase for a certain range of momentum along the ribbon's axis, implying the non-trivial topology of the ribbon and the existence of an edge state according to the bulk-edge correspondence. In particular, we have noticed inverse distribution of the range of momentum characterized by a non-zero Zak phase estimated with the photonic and the solid-state models attributed to a different gauge choice. In this case, the difference of Zak phases evaluated with two gauges constitutes the topological invariant. We have confirmed the non-trivial topology of the ribbon by calculating the band structure at the edge of the ribbon interfacing a trivial material which has revealed the existence of a zero-energy edge state. Those results have showed, more specifically, that a gap opening and the emergence of an edge state were possible with the circular hole design despite the downward bending of the upper Dirac band at the Dirac energy level.

In the final part, we have addressed the conception and optical characterization of rolled-up HC-PCM. We have first simulated numerically the optical dispersion diagrams of unwrapped photonic microtubes of simple chiralities, with circular and triangular air hole PCM, in the way of the solid-state zone-folding method. We have noticed the concurrence between photonic and solid-state bands for the triangular hole design. By contrast, we have observed the alteration of the bands of the circular hole pattern due to the interaction with the monopolar mode. We have then computed the band structure of more realist microtube of chirality  $\vec{C}_h(12, 0)$  with circular hole and noticed an excellent compliance with the zone-folding predictions. Our next step concerned the fabrication of the photonic microtubes following the rolled-up nanotechnology processes. We have showed the quality and the high reproducibility of the rolling of HC-PCM with triangular air holes into horizontal microtubes of different chiralities. We have finally tackled the optical characterization of the fabricated microtubes of metallic zig-zag chirality through angle-resolved spectral measurements. We have reconstructed the experimental band structure of the microtube on which we have noticed bands from the tubes' membrane wall and interference cavity mode patterns. However, we have not recorded the dispersive signature of the microtube probably on account of the absorption of photons before completing one circulation around the tube.



## Perspectives

We emphasize that the simulation and characterization results presented above remain of an exploratory nature. Our strategy was to study simple cases and establish a methodology toward deeper analysis of the optical properties of photonic ribbons and microtubes. In particular, we summarize hereinafter ongoing and future works as complement to the present study. Concerning photonic HC-PCM ribbons, our next tasks will first consist in investigating the topological properties of circular hole ribbons with various chiralities other than  $\vec{T}(1,0)$  by the calculation of the Zak phase and band structures within a topological interface. We also plan to perform similar work with triangular hole photonic ribbon. Concerning HC-PCM microtube, our future works will focus on simulating the band structure of microtubes with circular and triangular air hole of different chiralities. These results will then be exploited to assess the topological properties of the microtubes in accordance with our initial objective. The angular-resolved measurements have not revealed the dispersive signature of the CNT-like photonic microtubes but rather the dispersion of the membrane wall due to the absorption of photons upon circulation around the tubes. We are currently fabricating new samples with microtubes of smaller radius to allow at least one circulation of the photons. We also propose to measure beforehand the dispersion of non-structured microtubes of small curvature radius to detect the presence of whispering gallery modes, giving the green light for the measurements on structured microtubes. We will also perform angular-resolved measurements on photonic microtubes with various chiralities to attest the change of dispersion. We finally mention that we are working to establish an analytical model to predict the photonic dispersion of graphene-like photonic crystals which will be useful to assess analytically the topological properties of the HC-PCM-based structures.

# Appendix A

## Mechanical model

We evaluate the efforts  $\mathbf{F}$  in the bilayer membrane as the integral of the reduced constitutive laws established in Equation 1.11 for each layer, over the entire thickness of the bilayer  $h = h_1 + h_2$ :

$$\mathbf{F} = \int_{-h/2}^{h/2} \boldsymbol{\sigma} dx_3 = \int_{-h/2}^{h/2} \hat{\mathbf{C}}(x_3) [\boldsymbol{\varepsilon} + \mathbf{m}(x_3)] dx_3. \quad (\text{A.1})$$

Integrals in Equation 1.17 decompose in two parts according the concerned layer:

- Layer A<sub>1</sub> for  $x_3 \in [-h/2, -h/2 + h_1]$ :  $\hat{\mathbf{C}} = \hat{\mathbf{C}}^{(1)}$  and  $\mathbf{m} = \mathbf{0}$ .
- Layer A<sub>2</sub> for  $x_3 \in [-h/2 + h_1, h/2]$ :  $\hat{\mathbf{C}} = \hat{\mathbf{C}}^{(2)}$  and  $\mathbf{m} = \begin{pmatrix} m \\ m \\ 0 \end{pmatrix}$ .

Identifying  $\boldsymbol{\varepsilon}$  in Equation 1.14, the effort  $\mathbf{F}$  becomes:

$$\boxed{\mathbf{F} = \mathbf{A}\boldsymbol{\varepsilon}^0 + \mathbf{B}\boldsymbol{\kappa} + h_2\hat{\mathbf{C}}^{(2)}\mathbf{m},} \quad (\text{A.2})$$

where the coefficients  $\mathbf{A}$  and  $\mathbf{B}$  are defined by:

$$\mathbf{A} = h_1\hat{\mathbf{C}}^{(1)} + h_2\hat{\mathbf{C}}^{(2)}, \quad \mathbf{B} = \frac{h_1h_2}{2} \left( \hat{\mathbf{C}}^{(2)} - \hat{\mathbf{C}}^{(1)} \right). \quad (\text{A.3})$$

Similarly, we obtain the expression of the moment  $\mathbf{M}$  of the bilayer membrane by integrating the reduced constitutive law multiplied by  $x_3$  beforehand, over the total thickness  $h$ :

$$\mathbf{M} = \int_{-h/2}^{h/2} x_3 \boldsymbol{\sigma} dx_3 = \int_{-h/2}^{h/2} x_3 \hat{\mathbf{C}}(x_3) [\boldsymbol{\varepsilon} + \mathbf{m}(x_3)] dx_3. \quad (\text{A.4})$$

Using the same decomposition of the integral as performed previously and according to the layer, the moment  $\mathbf{M}$  writes as:

$$\boxed{\mathbf{M} = \mathbf{B}\boldsymbol{\varepsilon}^0 + \mathbf{D}\boldsymbol{\kappa} + \frac{h_1h_2}{2}\hat{\mathbf{C}}^{(2)}\mathbf{m},} \quad (\text{A.5})$$

where the coefficient  $\mathbf{D}$  identifies as:

$$\mathbf{D} = \frac{1}{12} \left[ \hat{\mathbf{C}}^{(1)} (h_1^3 + 3h_1h_2^2) + \hat{\mathbf{C}}^{(2)} (h_2^3 + 3h_2h_1^2) \right]. \quad (\text{A.6})$$

In the case of a free bilayer and without consideration of the boundary conditions, the internal strains and curvatures adjust to cancel out the forces  $\mathbf{F}$  and the moments  $\mathbf{M}$ :

$$\mathbf{F} = \mathbf{0}, \quad \mathbf{M} = \mathbf{0}. \quad (\text{A.7})$$

The third equations of the two systems expressed in Equation A.7 implies that:

$$\varepsilon_{12}^0 = 0, \quad \kappa_{12}^0 = 0. \quad (\text{A.8})$$

Furthermore, the resolution of the two remaining sets of equations in A.7 imposes that  $\varepsilon_{11}^0 = \varepsilon_{22}^0$  and  $\kappa_{11}^0 = \kappa_{22}^0$ . For the simplification of later calculation developments, we introduce conveniently the Young modulus  $E$  and the Poisson coefficient  $\nu$ , adapted for the material of each layer, and related to the Hooke tensor according to:

$$C_{11} = \frac{E(1-\nu)}{(1+\nu)(1-2\nu)}, \quad C_{12} = \frac{E\nu}{(1+\nu)(1-2\nu)}. \quad (\text{A.9})$$

Consequently, the *reduced elastic constants* transform into:

$$\hat{C}_{11} = \frac{E}{1-\nu^2}, \quad \hat{C}_{12} = \frac{\nu E}{1-\nu^2}, \quad \hat{C}_{11} + \hat{C}_{12} = \frac{E}{1-\nu}. \quad (\text{A.10})$$

We also introduce the *contrast* between the two materials of the two layers, which defines as:

$$C = \frac{E_1}{1-\nu_1} \times \left( \frac{E_2}{1-\nu_2} \right)^{-1} \quad (\text{A.11})$$

The first equations of both systems in Equation A.7 read:

$$\begin{aligned} (A_{11} + A_{12})\varepsilon + (B_{11} + B_{12})\kappa &= -mh_2 \quad (\hat{C}_{11}^{(2)} + \hat{C}_{12}^{(2)}), \\ (B_{11} + B_{12})\varepsilon + (D_{11} + D_{12})\kappa &= -m\frac{h_1h_2}{2} \quad (\hat{C}_{11}^{(2)} + \hat{C}_{12}^{(2)}), \end{aligned} \quad (\text{A.12})$$

Using the third identity of Equation A.10 and the contrast defined in Equation A.11, we show that the previous two equations rewrite as:

$$\begin{aligned} (Ch_1 + h_2)\varepsilon + \frac{h_1h_2}{2}(1-C)\kappa &= -mh_2, \\ \frac{h_1h_2}{2}(1-C)\varepsilon + \frac{1}{12}(C(h_1^3 + 3h_1h_2^2) + h_2^3 + 3h_2h_1^2)\kappa &= -m\frac{h_1h_2}{2}. \end{aligned} \quad (\text{A.13})$$

Introducing the dimensionless quantities  $\xi = h_2/h_1$  and  $\hat{\kappa} = h_2\kappa$ , the system A.13 reduces to the more compact form:

$$\begin{aligned} (C + \xi)\varepsilon + \frac{1}{2}(1-C)\hat{\kappa} &= -m\xi, \\ (1-C)\varepsilon + \frac{1}{6}\left(C\left(\frac{1}{\xi^2} + 3\right) + \xi + \frac{3}{\xi}\right)\hat{\kappa} &= -m \end{aligned} \quad (\text{A.14})$$

# Appendix B

## 1D SSH model

The Hamiltonian  $H$  of the SSH system writes in the second quantization formalism as:

$$H = t' \sum_n \hat{b}_n^\dagger \hat{a}_n + t \sum_n \hat{b}_{n-1}^\dagger \hat{a}_n + \text{H.c.}, \quad (\text{B.1})$$

where  $\hat{b}_n^\dagger$  ( $\hat{a}_n^\dagger$ ) and  $\hat{b}_n$  ( $\hat{a}_n$ ) designate the creation and annihilation operators, respectively, of a particle on the  $n$ -th site B (A), and H.c. refers to the Hermitian conjugate. Due to the periodicity of the chain, the Fourier expansion of the operator  $\hat{b}_n^\dagger$ , for instance, expresses as:

$$\hat{b}_n^\dagger = \frac{1}{N} \sum_k \hat{b}_k e^{ikna}, \quad (\text{B.2})$$

where  $N$  corresponds to the number of dimers, so that the Hamiltonian rewrites as:

$$H = t' \sum_k \hat{b}_k^\dagger \hat{a}_k + t \sum_k \hat{b}_k^\dagger \hat{a}_k e^{-ika} + \text{H.c.}. \quad (\text{B.3})$$

In the basis of the sublattices  $(\hat{a}_k^\dagger, \hat{b}_k^\dagger)$ , the Hamiltonian decomposes as the sum of each Bloch Hamiltonian  $H_k$  for each momentum  $k$ :

$$H = \sum_k \begin{pmatrix} \hat{a}_k^\dagger & \hat{b}_k^\dagger \end{pmatrix} H_k \begin{pmatrix} \hat{a}_k \\ \hat{b}_k \end{pmatrix}, \quad (\text{B.4})$$

with the following expression of  $H_k$ :

$$H_k = \begin{pmatrix} 0 & t' + te^{-ika} \\ t' + te^{ika} & 0 \end{pmatrix} \quad (\text{B.5})$$

# Appendix C

## Fresnel coefficients

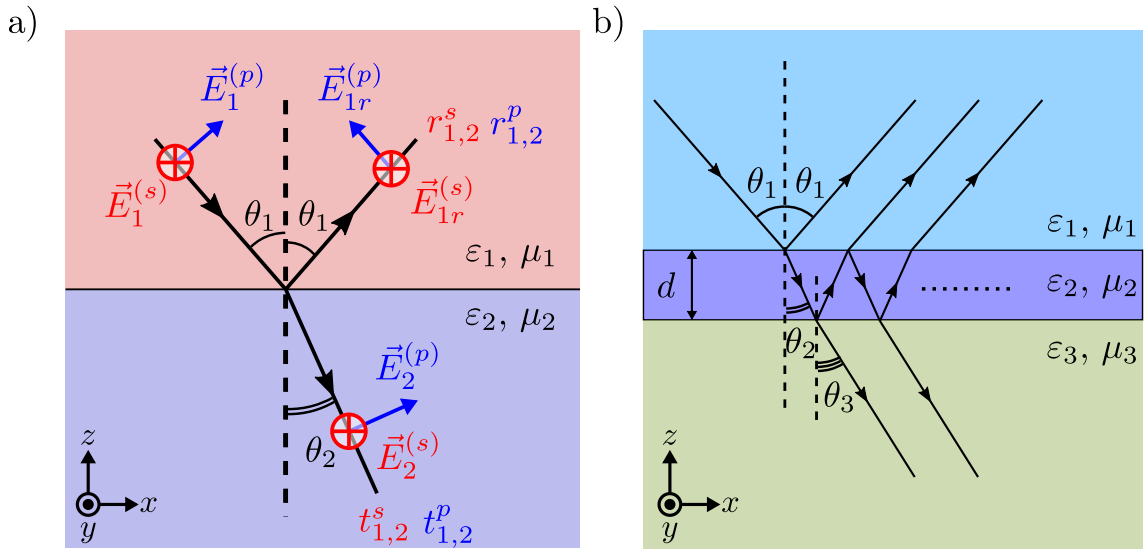


FIGURE C.1: a) Schematized reflection with angle  $\theta_1$  and refraction with angle  $\theta_2$  of light at the interface between dielectric medium 1 ( $\epsilon_1, \mu_1 = 1$ ) and medium 2 ( $\epsilon_2, \mu_2 = 1$ ) for  $p$ - and  $s$ -polarized incident light in proportion  $r_{1,2}^p$  ( $r_{1,2}^s$ ) and  $t_{1,2}^p$  ( $t_{1,2}^s$ ), respectively. For  $p$ -polarized ( $s$ -polarized) light, the electric field  $\vec{E}$  is contained into (normal to) the plane of incidence coinciding with the  $(x, z)$  plane. b) Schematized reflection and refraction of light onto a  $d$ -thick dielectric slab ( $\epsilon_2, \mu_2 = 1$ ) comprised between the dielectric medium 1 ( $\epsilon_1, \mu_1 = 1$ ) and 3 ( $\epsilon_3, \mu_3 = 1$ ).

At the interface between two dielectric media 1 and 2, incident light gets reflected with an angle  $\theta_1$  into medium 1 and refracted with an angle  $\theta_2$  into medium 2 taken from the normal of the interface, as illustrated in Figure C.a). Fresnel coefficients express the reflection  $r_{1,2}^s$  ( $r_{1,2}^p$ ) and transmission  $t_{1,2}^s$  ( $t_{1,2}^p$ ) rates for  $s$ -polarized ( $p$ -polarized) incident radiation as:

$$\begin{aligned} r_{1,2}^s &= \frac{\sqrt{\epsilon_1} \cos \theta_1 - \sqrt{\epsilon_2} \cos \theta_2}{\sqrt{\epsilon_1} \cos \theta_1 + \sqrt{\epsilon_2} \cos \theta_2}, & r_{1,2}^p &= \frac{\sqrt{\epsilon_2} \cos \theta_1 - \sqrt{\epsilon_1} \cos \theta_2}{\sqrt{\epsilon_2} \cos \theta_1 + \sqrt{\epsilon_1} \cos \theta_2}, \\ t_{1,2}^s &= \frac{2\sqrt{\epsilon_1} \cos \theta_1}{\sqrt{\epsilon_1} \cos \theta_1 + \sqrt{\epsilon_2} \cos \theta_2}, & t_{1,2}^p &= \frac{2\sqrt{\epsilon_1} \cos \theta_1}{\sqrt{\epsilon_2} \cos \theta_1 + \sqrt{\epsilon_1} \cos \theta_2}, \end{aligned} \quad (\text{C.1})$$

where  $\epsilon_1$  and  $\epsilon_2$  designate the permittivity of medium 1 and 2 respectively. We also suppose that both medium show weak magnetic responses or permeability, i.e.  $\mu_1 = \mu_2$ . For  $s$ -polarized ( $p$ -polarized) light, the electric field is orthogonal to (contained into) the plane of incidence. In particular, at normal incidence, i.e. for  $\theta_1 = \theta_2 = 0^\circ$ , the

coefficients in Equation C.1 reduce to:

$$\begin{aligned} r_{1,2}^s &= \frac{\sqrt{\epsilon_1} - \sqrt{\epsilon_2}}{\sqrt{\epsilon_1} + \sqrt{\epsilon_2}}, & r_{1,2}^p &= \frac{\sqrt{\epsilon_2} - \sqrt{\epsilon_1}}{\sqrt{\epsilon_1} + \sqrt{\epsilon_2}} = -r_{1,2}^s, \\ t_{1,2}^s &= t_{1,2}^p = \frac{2\sqrt{\epsilon_1}}{\sqrt{\epsilon_1} + \sqrt{\epsilon_2}}. \end{aligned} \tag{C.2}$$

Using Fresnel coefficients in Equation C.1, we also derive the reflection and transmission coefficients of a  $d$ -thick slab made of material 2 ( $\epsilon_2$ ) comprised between media 1 ( $\epsilon_1$ ) and 3 ( $\epsilon_3$ ), represented in Figure C.1.b), as:

$$\begin{aligned} r^{(p,s)} &= \frac{r_{1,2}^{(p,s)} + r_{2,3}^{(p,s)} e^{i\frac{2\pi}{\lambda} 2d\sqrt{\epsilon_2} \cos \theta_2}}{1 + r_{1,2}^{(p,s)} r_{2,3}^{(p,s)} e^{i\frac{2\pi}{\lambda} 2d\sqrt{\epsilon_2} \cos \theta_2}}, \\ t^{(p,s)} &= \frac{t_{1,2}^{(p,s)} t_{2,3}^{(p,s)} e^{i\frac{2\pi}{\lambda} d\sqrt{\epsilon_2} \cos \theta_2}}{1 + r_{1,2}^{(p,s)} r_{2,3}^{(p,s)} e^{i\frac{2\pi}{\lambda} 2d\sqrt{\epsilon_2} \cos \theta_2}}, \end{aligned}$$

with  $\lambda$  the wavelength of the incident wavelength.

# Appendix D

## Cylindrical cavity model

We develop the dispersion relation of transverse electric (TE) modes defined by  $E_z = 0$  in the cylindrical system supported by a cylindrical cavity with perfectly reflecting wall. We first manipulate the expressions of Maxwell's equations to derive the transverse fields components  $(E_\rho, E_\phi, H_\rho, H_\phi)$  from the longitudinal components  $(E_z, H_z)$  in the cylindrical coordinate system, according to:

$$E_\rho = \frac{-j}{k_c^2} \left( \beta \partial_\rho E_z + \frac{\omega \mu}{\rho} \partial_\phi H_z \right), \quad (\text{D.1})$$

$$E_\phi = \frac{-j}{k_c^2} \left( \frac{\beta}{\rho} \partial_\phi E_z - \omega \mu \partial_\rho H_z \right), \quad (\text{D.2})$$

$$H_\rho = \frac{j}{k_c^2} \left( \frac{\omega \epsilon}{\rho} \partial_\phi E_z - \beta \partial_\rho H_z \right), \quad (\text{D.3})$$

$$H_\phi = \frac{-j}{k_c^2} \left( \omega \epsilon \partial_\rho E_z + \frac{\beta}{\rho} \partial_\phi H_z \right). \quad (\text{D.4})$$

In particular, for TE modes defined by  $E_z = 0$ , the transverse fields components solely depend on the longitudinal component  $H_z$  of the magnetic field as:

$$E_\rho = \frac{-j}{k_c^2} \frac{\omega \mu}{\rho} \partial_\phi H_z, \quad (\text{D.5})$$

$$E_\phi = \frac{j}{k_c^2} \omega \mu \partial_\rho H_z, \quad (\text{D.6})$$

$$H_\rho = \frac{-j}{k_c^2} \beta \partial_\rho H_z, \quad (\text{D.7})$$

$$H_\phi = \frac{-j}{k_c^2} \frac{\beta}{\rho} \partial_\phi H_z. \quad (\text{D.8})$$

Therefore, the determination of the fields' expressions comes down to the resolution of the *wave equation* or *Helmholtz equation* for time-harmonic solutions. Applied to  $H_z$  component, the equation writes as:

$$\nabla^2 H_z + k^2 H_z = 0, \quad (\text{D.9})$$

where  $k = \omega \sqrt{\epsilon \mu}$  refers to the wave number. In the cylindrical coordinate system and for a plane wave solution in the  $z$ -direction  $H_z(\rho, \phi, z) = h_z(\rho, \phi) e^{-j\beta z}$ , the Equation D.9 becomes:

$$\left( \frac{\partial^2}{\partial \rho^2} + \frac{1}{\rho} \frac{\partial}{\partial \rho} + \frac{1}{\rho^2} \frac{\partial^2}{\partial \phi^2} + k_c^2 \right) h_z(\rho, \phi) = 0. \quad (\text{D.10})$$

Using the method of separation of variables,  $h_z(\rho, \phi) = R(\rho)P(\phi)$ , the Equation D.10 rewrites as:

$$\frac{\rho^2}{R} \frac{dR^2}{d\rho^2} + \frac{\rho}{R} \frac{dR}{d\rho} + \rho^2 k_c^2 = -\frac{1}{P} \frac{d^2 P}{d\phi^2}. \quad (\text{D.11})$$

The previous equality holds true for any pair  $(\rho, \phi)$  provided both left and right terms in Equation D.11 equal to a constant that we note  $k_\phi^2$ , leading to the following relations:

$$\rho^2 \frac{dR^2}{d\rho^2} + \rho \frac{dR}{d\rho} + (\rho^2 k_c^2 - k_\phi^2) R = 0; \quad (\text{D.12})$$

$$\frac{d^2 P}{d\phi^2} + k_\phi^2 P = 0. \quad (\text{D.13})$$

The solutions of Equation D.13 express in the general form:

$$P(\phi) = A \sin(k_\phi \phi) + B \cos(k_\phi \phi). \quad (\text{D.14})$$

Due to the cylindrical symmetry of the problem, the function  $P$  and  $h_z(\rho, \phi)$  are necessarily  $2\pi$ -periodic with respect to  $\phi$ , implying  $k_\phi = m \in \mathbb{N}$ . Substituting  $k_\phi$  by  $m$  in Equation D.12, we find the following relation:

$$\rho^2 \frac{dR^2}{d\rho^2} + \rho \frac{dR}{d\rho} + (\rho^2 k_c^2 - m^2) R = 0, \quad (\text{D.15})$$

which corresponds to a typical Bessel's differential equation of general solution:

$$R(\rho) = C J_m(k_c \rho) + D Y_m(k_c \rho), \quad (\text{D.16})$$

where  $C$  and  $D$  are constants, and  $J_m$  and  $Y_m$  refer to Bessel functions of the first and second kinds, respectively, at the order  $m$ . In particular, we have plotted the functions  $J_m$  with orders  $m = 0, 1, \dots, 4$  in Figure D.1.a). As the function  $Y_m(k_c \rho)$  diverges when  $\rho$  tends to zero, only the constant  $C$  keeps a physical meaning, so that  $D = 0$ . The general form of the solution  $h_z(\rho, \phi)$  writes then as:

$$h_z(\rho, \phi) = (A \sin(m\phi) + B \cos(m\phi)) J_m(k_c \rho), \quad (\text{D.17})$$

where the constants  $A$  and  $B$  encompass the constant  $C$ .

Finally, we determine  $k_c$  by applying a proper boundary condition. Here, the perfectly reflecting membrane wall and the continuity of the tangential component of the electric field  $E_{tan} = E_\phi$  (as  $E_z = 0$ ) at  $\rho = a$  imposes the condition:

$$E_\phi(\rho, \phi) = 0 \quad \text{at} \quad \rho = a. \quad (\text{D.18})$$

Combination Equations D.6 and D.17, we find the expression of  $E_\phi$  component:

$$E_\phi(\rho, \phi, z) = \frac{j\omega\mu}{k_c} (A \sin(m\phi) + B \cos(m\phi)) J'_m(k_c \rho) e^{-j\beta z}, \quad (\text{D.19})$$

where  $J'_m$  refers to the first derivative of the  $m$ -th order first kind Bessel function, plotted in Figure D.1.b) for  $m = 0, 1, \dots, 4$ , with respect to its argument  $k_c \rho$ . The boundary condition established in Equation D.18 becomes then:

$$J'_m(k_c a) = 0. \quad (\text{D.20})$$



which solutions correspond to the roots of the  $m$ -th order function  $J'_m$  that we note  $p'_{m,n}$  with  $n \in \mathbb{N}^*$  indexing the  $n$ -th root indicated in Table D.1 for  $m = 0, 1, \dots, 4$  and  $n = 1, 2, \dots, 5$ . The wave-number  $k_c$  can then only takes quantized values given by:

$$k_{c_{m,n}} = \frac{p'_{m,n}}{a}. \quad (\text{D.21})$$

The modes  $\text{TE}_{m,n}$  are thus defined by their orders  $m$  and  $n$  which describe the number of azimuthal and radial variations of the electromagnetic fields. They only exist above the cutoff limit  $k_{c_{m,n}}$  of  $k_c$  evaluated in Equation D.21. The dispersion relation of each  $\text{TE}_{m,n}$  mode is given by:

$$k_{m,n}^2 = k_{c_{m,n}}^2 + \beta^2 = \left( \frac{p'_{m,n}}{a} \right)^2 + \beta^2. \quad (\text{D.22})$$

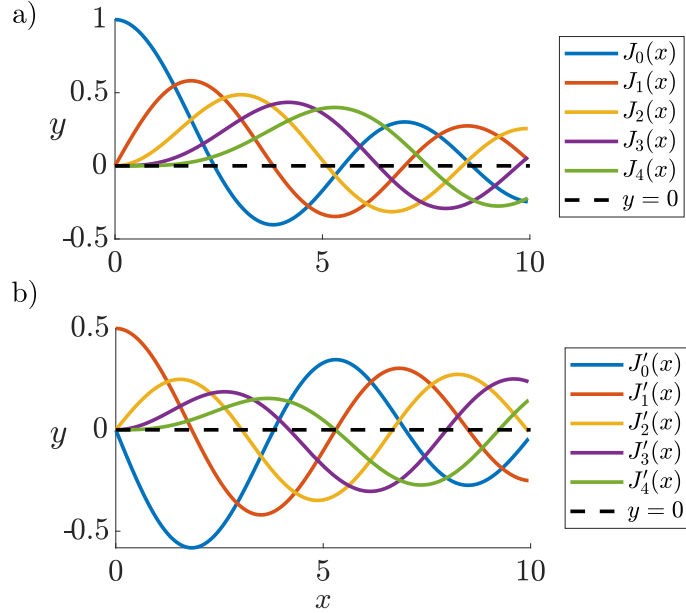


FIGURE D.1: Plots of a) Bessel functions of first kind  $J_m(x)$  at the order  $m = 0, 1, \dots, 4$ , b) their first derivatives  $J'_m(x)$  with respect to the variable  $x$ . Both plot blocks are accompanied with a black dashed line of equation  $y = 0$ .

Roots $p'_{m,n}$	$J'_0$	$J'_1$	$J'_2$	$J'_3$	$J'_4$
1	3.8317	1.8411	3.0542	4.2011	5.3175
2	7.0155	5.3314	6.7061	8.0152	9.2823
3	10.1734	8.5363	9.9694	11.3459	12.6819
4	13.3236	11.706	13.1703	14.5858	15.9641
5	16.4706	14.8635	16.3475	17.7887	19.1960

TABLE D.1: First five roots of the first derivative of first kind Bessel functions  $J'_m$  with  $m = 0, 1, 2, 3, 4$ .

# Appendix E

## Mode surface of FDTD modes

We present in Figure E.1.a) and c) surface maps of the normalized electric field intensity  $I$  of cavity modes  $TE_{0,22}$  and  $TE_{1,23}$  calculated in an infinitely-long rolled-up PCM cavity of average radius  $\rho_{\text{avg}} \simeq 17.62 \mu\text{m}$  with the FDTD method at wavelengths of  $1.58808 \mu\text{m}$  and  $1.55484 \mu\text{m}$ , respectively. We extract then the profile of each mode along the  $x$  axis direction at  $y = 0$  represented in Figure E.1.b) and d). We indicate the modes' surfaces  $S^{(0,22)}$  and  $S^{(1,23)}$  quantifying the concentration of light in the cavity centre and the equivalent radius of the disks sharing the same area.

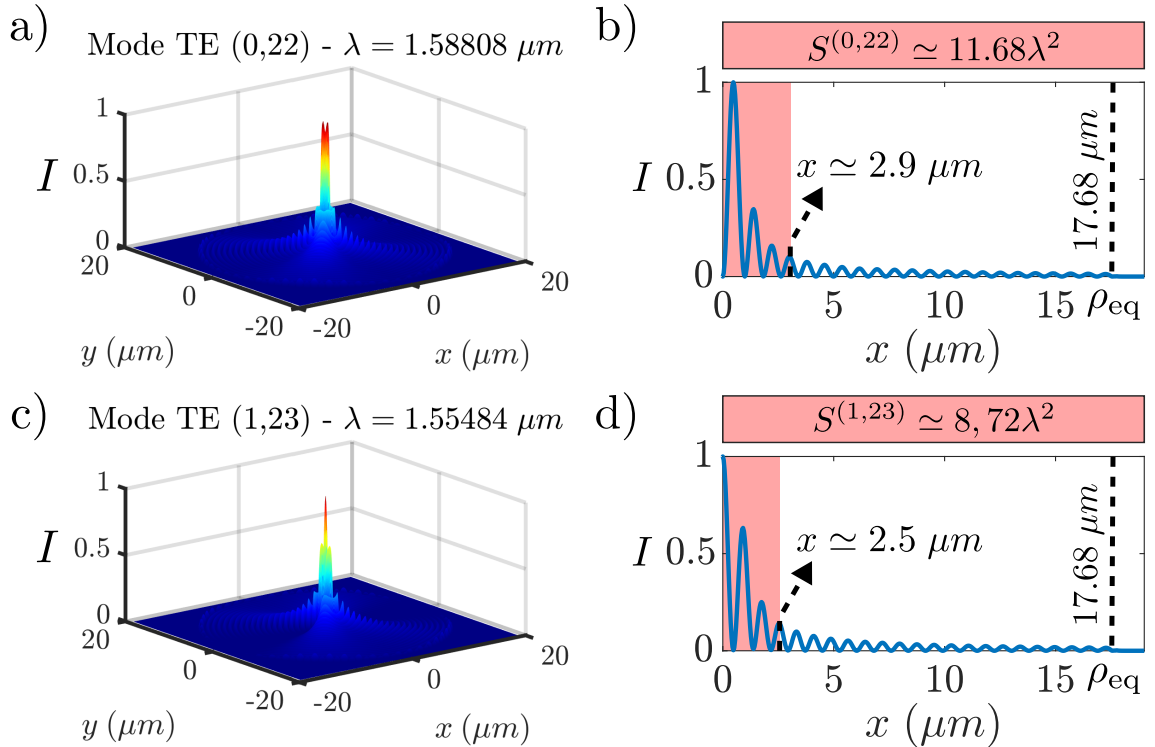


FIGURE E.1: a) and c): Surface maps of the normalized electric field intensity  $I$  calculated with the FDTD method at  $\lambda = 1.58808 \mu\text{m}$  (a) and  $\lambda = 1.55484 \mu\text{m}$  (c) in a rolled-up PCM cavity of average radius  $\rho_{\text{avg}} \simeq 1.62 \mu\text{m}$ . We identified in Section 3.4.2 the patterns in (a) and (c) as being mostly that of modes  $TE_{0,22}$  and  $TE_{1,23}$ , respectively. b) and d): 1D profile extracted from the maps a) and c) along the  $x$  axis direction from the centre of the map until the radius  $\rho_{\text{eq}} = 17.68$  of an theoretical cylindrical cavity. The red zone delimits the radii of the disks which cover the same areas as the surfaces  $S^{(0,22)}$  and  $S^{(1,23)}$  of the modes  $TE_{0,22}$  and  $TE_{1,23}$  indicated above each plot. The modes' surfaces are expressed in units of  $\lambda^2$  with  $\lambda = 1.5 \mu\text{m}$ .

# Appendix F

## Grazing reflection onto the PCM

Using geometrical optics, we can see the modes with given azimuthal order  $m$  existing in a cylindrical cavity with perfectly reflecting wall, as the result of incident light beams bouncing  $2m$  times on the wall before coming back to initial position, as schematized on the inset drawing of Figure F.a). Moreover, we can associate a given  $m$  with the angle of incidence  $\theta$  of the light beams on the wall according to the simple law:

$$\theta = \frac{1}{2} \left( 180 - \frac{360}{2m} \right), \quad (\text{F.1})$$

plotted in F.a). We note that the reasoning stays valid for  $m \geq 2$ . We observe a rapid increase of  $\theta$  at first values  $m$  followed by an asymptotic evolution toward  $90^\circ$ . For instance, for  $m = 55$ , the angle  $\theta$  reaches  $88.36^\circ$ . We deduce that the azimuthal form defined by  $m = 55$  emerges at an angle  $\theta$  estimated to  $88.36^\circ$ . At grazing incidence, the reflectivity of the PCM results mainly from the bulk properties of the dielectric membrane. We show in Figure F.1.b) the evolution of the reflectance  $R$  (%) as a function of the angle of incidence  $\theta$  of a  $0.230 \mu\text{m}$ -thick dielectric slab. The refractive index of the InP-based PCM is approximated to  $n \simeq \text{FF}_{\text{air}} n_{\text{air}} + (1 - \text{FF}_{\text{air}}) n_{\text{InP}} = 0.57 \times 1 + (1 - 0.57) \times 3.16 \simeq 1.93$  where  $\text{FF}_{\text{air}}$  designates the air filling factor of the PCM with the lattice parameters  $a = 1.206 \mu\text{m}$  and  $r = 0.480 \mu\text{m}$ .

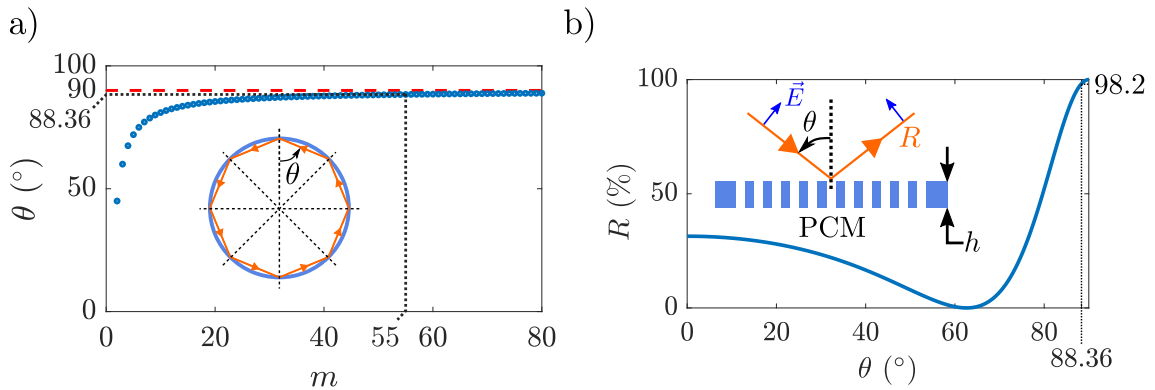


FIGURE F.1: a) Evolution of the angle of incidence  $\theta$  in degrees as a function of the azimuthal order  $m$ . We indicate in red dashed line the  $90^\circ$  asymptotic limit. Inset drawing: optical beams (orange arrows) bouncing with a angle  $\theta$  on a perfectly reflecting wall of a cylindrical cavity. b) Variation of the reflectance  $R$  (%) of a photonic crystal membrane of thickness  $h = 0.230 \mu\text{m}$  calculated with Fresnel reflection coefficients as a function of the angle  $\theta$  of incident  $p$ -polarized light (electric field (blue arrow) contained in the plane of incidence).

# Appendix G

## Reflection of small radius photon cages

We estimate the reflection performances at normal incidence of tubular photon cages' PCM wall fabricated on sample C2579. The PCM consists of a triangular lattice, with a period  $a = 1.2 \mu m$ , of air holes of diameter  $2r \simeq 0.960 \mu m$  etched in an  $86 \text{ nm}$ -thick InP membrane as depicted in Figure G.1.a). We present in Figure G.1.b) the PCM reflectivity spectrum  $R(\lambda)$  at normal incidence in the range  $[1-1.8] \mu m$  calculated with the RCWA method. We observe a broad peak culminating at about 98 % at  $1.34 \mu m$ .

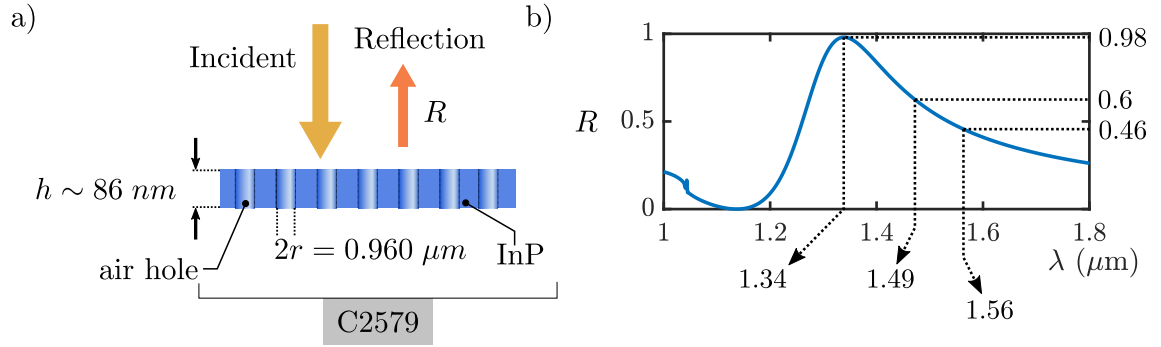


FIGURE G.1: a) Schematized profile of a PCM structure fabricated on sample C2579 based on a triangular lattice of air holes of diameter  $2r \simeq 0.960 \mu m$  etched in an InP-based membrane of thickness  $h \simeq 86 \text{ nm}$ . b) Reflectivity  $R$  spectrum of the PCM in the spectral range  $[1-1.8] \mu m$  at normal incidence.

# Appendix H

## Parameters of triangular-hole HC-PCM

We present in Figure H.1.a) to i) the band structures of triangular-hole photonic crystal membranes with a period  $a_h = 0.301 \mu m$  and a triangle edge  $s$  varying from 294 to 450 nm, calculated with the FDTD method. Increasing the edge size  $s$  reduces the size of the region where the monopolar mode (pointed by the red arrow) energy concentrates. Consequently, the frequency of the monopolar mode increases along with  $s$  which reduces the probability of coupling with the Dirac dispersion bands below.

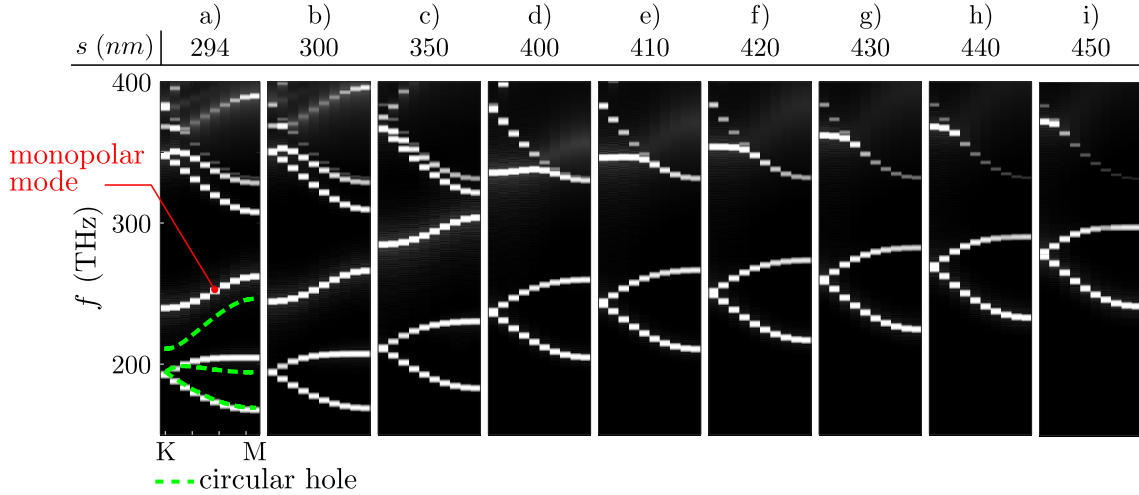


FIGURE H.1: a) to i): FDTD band structures of triangular-hole photonic crystal membranes with a period  $a_h = 0.301 \mu m$  and a triangle edge  $s$  varying from 294 to 450 nm. The green dashed curve indicate the band structure calculated for a triangular-hole photonic crystal membrane with a period  $a_h = 0.301 \mu m$  and holes' radius  $r = 0.109 \mu m$ .

# Appendix I

## Résumé long en français

### Introduction

L'histoire de la nanophotonique a connu un tournant majeur avec l'avènement à la fin des années 80 des cristaux photoniques, analogues photoniques artificiels des cristaux à l'état solide. En particulier, l'analogie entre la propagation des électrons dans les semi-conducteurs et la propagation de la lumière dans les cristaux photoniques a ouvert de nouvelles perspectives pour le contrôle spatial et temporel de la lumière, à l'échelle de la longueur d'onde et selon une, deux ou trois directions. De surcroît, la diversité et la flexibilité des mailles des cristaux photoniques a permis d'obtenir une large palette de fonctionnalités optiques telles que le guidage, le piégeage ou le ralentissement de la lumière. Les cristaux photoniques 1D constitués d'empilements de multicouches diélectriques sont, par exemple, utilisés comme revêtements réfléchissants ou comme miroirs à haute réflectivité dans les cavités laser. Des effets optiques similaires ont été observés avec des cristaux photoniques 2D obtenus en structurant des membranes diélectriques. La production de cristaux photoniques 3D présentant une bande interdite photonique complète a également suscité beaucoup d'intérêt pour le contrôle omnidirectionnel de la lumière. Cependant, la réalisation de telles architectures 3D de cristaux photoniques fait généralement appel à des technologies de fabrication complexes basées par exemple sur l'empilement de couches bidimensionnelles, la gravure laser ou le perçage sous différents angles.

Dans la perspective du développement de structures photoniques 3D, le projet ANR PHOLDING (pour FoLDING PHOTonic Crystals : Semiconductors ORIGAMI), dans lequel s'inscrit cette thèse, propose d'appliquer la technologie de relaxation des contraintes aux membranes à cristaux photoniques. En effet, la relaxation élastique de multicouches structurées précontraintes permet de fabriquer des micro-objets 3D dont les formes 3D finales sont dictées par la répartition initiale des contraintes dans les couches. Les structures ainsi créées sont parfois appelées "Origamis photoniques" en référence à l'art japonais du pliage papier dont s'inspire la méthode de microfabrication. L'objectif général de ce travail est d'explorer les voies ouvertes par cette méthode de fabrication pour produire des structures photoniques originales.

Des nouvelles familles de micro-résonateurs optiques creux 3D permettant un piégeage efficace et une exaltation de la lumière dans un milieu à faible indice optique, sont particulièrement ciblées. Dans ces microrésonateurs, le confinement de la lumière repose sur le concept de « cages à photons » qui consiste à encercler une petite région de l'espace en repliant une membrane à cristaux photoniques présentant une réflectivité élevée et large bande dans la gamme de longueurs d'onde d'intérêt. L'idée est de réaliser

des résonateurs très ouverts où une forte interaction lumière-matière peut être exploitée dans des dispositifs optiques comprenant un matériau optiquement actif intégré dans une matrice à faible indice comme un polymère, un liquide ou même un gaz. En effet, les résonateurs 3D creux présentent un grand intérêt pour les opérations de détection car ils maximisent non seulement le confinement 3D de la lumière mais optimisent également le recouvrement entre champ électromagnétique et les potentielles cibles de détection micrométriques. En utilisant la technique d'ingénierie des contraintes, ces microrésonateurs 3D peuvent être fabriqués en enroulant des membranes à cristaux photoniques 2D pour former des « cages à photons » tubulaires. Si le concept de cages à photons a été étudié théoriquement à l'INL dans le cas d'un cristal photonique unidimensionnel, aucune validation expérimentale n'a encore été apportée. Dans cette thèse, nous nous intéressons tout d'abord à la conception et la caractérisation optique de cages à photons tubulaires produites par auto-enroulement de miroirs à base de membranes à cristaux photoniques 2D. En particulier, notre objectif est d'obtenir une preuve expérimentale du confinement de la lumière à l'intérieur des cages à photons tubulaires.

Une autre application des origamis photoniques vise à prolonger la correspondance entre les propriétés des systèmes de la matière condensée et des systèmes photoniques. En effet, la production d'analogues des cristaux atomiques dans la classe des cristaux photoniques a ouvert de nouvelles perspectives pour la manipulation de la lumière. En particulier, les cristaux photoniques empruntant le réseau cristallin en nid d'abeille du graphène ont suscité beaucoup d'intérêt car, comme leurs homologues électroniques, ils présentent des propriétés remarquables telles que la présence d'un point de Dirac dans leur diagramme de bandes. Cependant, contrairement aux cristaux atomiques, leurs équivalents à cristaux photoniques présentent un design flexible permettant notamment d'adapter les paramètres de maille, et ainsi d'explorer de nouveaux effets optiques. En particulier, au-delà de la dispersion linéaire autour du point de Dirac, il a été prouvé qu'en générant une bande interdite autour de ce point, des états de bords topologiques pouvaient être observés.

La méthode de fabrication basée sur l'ingénierie des contraintes nous permet également de poursuivre cette analogie et d'explorer les propriétés des analogues à cristaux photoniques des nanotubes de carbone, à savoir les microtubes formés par l'enroulement de membranes à cristaux photoniques avec un réseau en nid d'abeille. En effet, selon la direction d'enroulement du feuillet de graphène, appelée chiralité, les nanotubes de carbone peuvent (ou non) présenter une bande interdite électronique. Par conséquent, une question naturelle que nous abordons dans ce travail concerne l'existence d'une bande interdite induite par l'enroulement des membranes à cristaux photoniques en microtubes photoniques. Si tel est le cas, une autre question légitime que nous soulevons porte sur la nature topologique de cette bande interdite générée.

## Chapitre 1

Nous montrons dans ce chapitre que la nanotechnologie par enroulement de nanomembranes représente une alternative compétitive à la fabrication de micro-objets 3D polyvalents. Le principe de cette technique repose sur l'auto-enroulement de membranes précontraintes caractérisées par une épaisseur de l'ordre du micron. La réalisation d'une géométrie 3D souhaitée passe par deux étapes essentielles : l'ingénierie des contraintes et la conception du design plan des membranes. Les architectures 3D populaires produites avec la nanotechnologie enroulée incluent les microtubes, les micro-bobines ou encore les hélices. De plus, la large gamme de matériaux couverts par la micro-fabrication, comprenant des métaux, des semi-conducteurs ou des polymères, permet l'utilisation des micro-objets 3D ainsi formés pour diverses applications. En particulier, les microstructures de forme tubulaire, agissant à la fois comme des microcanaux et des microrésonateurs optiques, ont été très prometteuses dans la réalisation de dispositifs de détection opto-fluidiques compacts et efficaces.

Dans cette thèse, notre approche consiste à utiliser la nanotechnologie par enroulement pour enrouler des membranes à cristaux photoniques afin de former deux types de structures : des cages à photons et des analogues de cristaux photoniques de nanotubes de carbone.

En premier lieu, nous abordons la conception de cages à photons tubulaires basées sur l'auto-enroulement d'une membrane à cristaux photoniques 2D cristalline très réfléchissante en utilisant la nanotechnologie par enroulement. Une telle structure est capable de confiner la lumière dans l'air. Notre objectif consiste à apporter une preuve de concept expérimentale de ces cages à photons.

En second lieu, nous avons l'intention d'explorer théoriquement et expérimentalement les propriétés optiques et topologiques d'analogues cristallins photoniques de nanotubes de carbone constitués de membranes cristallines photoniques en nid d'abeille enroulées. À la lumière des propriétés électroniques et topologiques des nanotubes de carbone, nous visons à répondre aux deux questions suivantes. Comment évolue la dispersion photonique du microtube photonique de type CNT en fonction de la chiralité du microtube ? Les microtubes photoniques présentent-ils des propriétés topologiques non triviales ?

Dans le chapitre suivant, nous présentons les méthodes numériques et de fabrication pour réaliser les différentes étapes de la conception des structures précédentes : la conception, la simulation des propriétés optiques, la fabrication et la caractérisation optique des structures.



## Chapitre 2

Dans ce chapitre, nous présentons les différentes méthodes de simulation, de fabrication et de caractérisation optique pour la conception et l'étude des propriétés optiques des membranes à cristaux photoniques 2D enroulées.

Dans la première section, nous décrivons la méthode d'analyse rigoureuse des ondes couplées (RCWA) et la méthode de calcul de différences finies dans le domaine temporel (FDTD) employées pour simuler :

- le spectre de réflectivité d'une membrane à cristaux photoniques 2D en incidence normale et oblique (RCWA) ;
- la réponse spectrale de cavités tubulaires (méthode FDTD) ;
- le diagramme de dispersion de structures photoniques périodiques avec une géométrie quelconque (méthode FDTD).

Dans la deuxième section, nous détaillons le processus de fabrication de microtubes à base de membrane à cristaux photoniques 2D enroulées à partir des principales étapes suivantes :

- la production de précurseurs multicouches de matériaux semi-conducteurs par épitaxie par jets moléculaires (MBE) ;
- la conception, la fabrication et le transfert du masque planaire de la membrane à cristaux photoniques par des procédures successives de lithographie par faisceau électronique et de gravure ionique réactive (RIE) ;
- le laminage du MCP sous une forme tubulaire par procédé de sous-gravure et le séchage de l'échantillon ;

L'ensemble de ces étapes ont été réalisées au sein de la plateforme NanoLyon par Philippe Regreny (dépôt des couches) et Pierre Cremillieu (lithographie électronique, gravure, sous-gravure et séchage).

Dans la troisième section, nous décrivons les deux principaux montages dédiés à la caractérisation optique des micro-objets tubulaires fabriqués :

- un montage personnalisé de microscopie optique à champ proche à balayage (SNOM) pour cartographier les modes qui se forment à l'intérieur des cages à photons tubulaires ;
- un montage de spectroscopie résolue en angle pour construire le diagramme de bandes des structures fabriquées en collectant le signal de photoluminescence ou de réflexion.

En particulier, nous appliquons les méthodes précédentes dans le chapitre suivant pour la conception et la caractérisation de cages à photons tubulaires.

## Chapitre 3

Dans ce chapitre, nous réalisons l'étude théorique des cages à photons tubulaires à base de cristaux photoniques membranaires (PCM) enroulé. L'étude se divise en trois sections principales abordant la conception du miroir planaire PCM, la simulation analytique et numérique des propriétés optiques des cages.

Dans la première section consacrée à la production d'une paroi en membrane PCM hautement réfléchissante, nous rapportons les résultats clés suivants :

- nous avons conçu un miroir PCM 2D large bande non absorbant, indépendant de la polarisation et très efficace en incidence normale dans le domaine du proche infrarouge ;
- nous avons démontré le rôle essentiel du réseau cristallin pour obtenir un comportement hautement réfléchissant par rapport à des membranes simples peu réfléchissantes ;
- nous avons attesté la robustesse des propriétés de réflexion du PCM jusqu'à quelques dizaines de degrés d'angle d'incidence.

Dans la deuxième partie, nous avons abordé la réponse optique des cages à photons en utilisant en premier lieu le modèle analytique de la cavité cylindrique résonante. Ce modèle fournit une description presque complète de la réponse modale de la cavité avec les principales caractéristiques suivantes :

- la cavité supporte des modes transverse électrique  $TE_{m,n,p}$  et transverse magnétique  $TM_{m,n,p}$  classés avec les indices  $m$  (*azimutal*),  $n$  (*radial*) et  $p$  (*axial*) décrivant la distribution spatiale des modes dans la cavité cylindrique ;
- nous rapportons une forte densité de modes dans des cavités de rayon  $17,5 \mu m$  proches des structures fabriquées, et une grande proximité spectrale.

Dans la troisième section, nous avons mené des simulations FDTD pour obtenir une réponse optique plus réaliste des cages photoniques. Nous soulignons ci-dessous les principaux résultats :

- les simulations de cavités de longueur infinies et finies ont confirmé l'émergence de modes de cavité cylindrique TE dans des cages à PCM enroulées, validant les prédictions analytiques (distributions spectraux et spatiaux des modes) et l'efficacité de la paroi miroir à PCM incurvée ;
- les simulations de cavités infinies ont permis de relier, à travers l'analyse des facteurs  $Q$  et des cartographies des modes, l'expression des modes  $TE_{m,n}$  avec le spectre de réflectivité du PCM ;
- les simulations de cavités finies ont révélé le confinement axial des modes  $TE_{m,n,p}$  dont la qualité dépend à la fois de l'ordre  $p$ . Pour les cavités à rapport d'aspect élevé, la proximité spectrale des ordres  $p$  crée un quasi-continuum de modes à des paires  $(m, n)$  fixes.

Nous avons enfin apporté une preuve théorique des cages à photons à base de PCM 2D enroulé. Le modèle de cavité analytique constitue un outil puissant pour prédire les propriétés optiques des cages photoniques. L'étude théorique ouvre donc la voie à la fabrication et à la caractérisation optique des structures réelles décrites dans le chapitre suivant.

## Chapitre 4

Dans ce chapitre, nous apportons une démonstration expérimentale du concept de cages à photons.

Dans la première section, nous avons abordé avec succès la fabrication de cages à photons tubulaires basées sur l'auto-enroulement de cristaux photoniques membranaires (PCM) 2D, présentant les caractéristiques suivantes :

- nous avons démontré notre capacité à produire des cages à photons tubulaires avec une grande reproductibilité et un contrôle précis des paramètres géométriques ;
- nous avons prouvé l'efficacité d'un design d'ancrage spécifique pour soulever verticalement les cavités enroulées, afin de faciliter la caractérisation optique future des microstructures ;
- nous avons également ouvert la voie à d'autres applications impliquant des miroirs CPM enroulés en montrant leur comportement élastique et leur intégration dans d'autres plateformes plus complexes.

Dans la deuxième section, nous avons abordé la caractérisation optique des cages à photons tubulaires fabriquées en sondant la réponse modale dans le noyau creux par des mesures de microscopie optique en champ proche (SNOM). Nous récapitulons ci-après les principaux résultats de mesures réalisées sur trois échantillons différents C2217, C2527 et C2579 avec des cavités de rayons différents :

- nous avons mis en évidence la présence de modes de cavités cylindriques  $TE_{m,n,p}$  dans le cœur rempli d'air des cavités confirmant, en pratique, le potentiel des cages à photons tubulaires à confiner la lumière dans l'air ;
- nous avons démontré la reproductibilité des mesures du SNOM à travers les différents scans réalisés sur différents échantillons ;
- nous avons montré la conformité des ordres et des longueurs d'onde des modes détectés avec les prédictions théoriques fournies par les modèles FDTD et analytiques ;
- nous avons évalué qualitativement le confinement vertical des modes de cavité en effectuant des mesures à différentes profondeurs d'insertion de la sonde SNOM ;

Enfin, les résultats du présent chapitre et des chapitres précédents fournissent une étude théorique et expérimentale complète sur les cages à photons tubulaires qui ouvre la voie à l'intégration de telles microstructures dans des dispositifs d'application opto-fluidiques. Nous notons que les cages à photons représentent une combinaison typique entre un motif de cristal photonique et une géométrie tubulaire 3D accessible grâce à la nanotechnologie par enroulement. En particulier, en utilisant le potentiel de la plate-forme de nanotechnologie enroulée, nous étudions dans le chapitre suivant les propriétés optiques d'analogues de structures de la physique du solide, le graphène et les nanotubes de carbone, dans la classe des cristaux photoniques.

## Chapitre 5

Ce chapitre est consacré à l'exploration des propriétés optiques de microtubes de cristaux photoniques membranaires en réseau en nid d'abeille (HC-PCM) enroulés, analogues photoniques des nanotubes de carbone. Avant d'aborder l'étude de ces microtubes photoniques, nous avons simulé les propriétés optiques et topologiques de structures intermédiaires que sont le cristal photonique membranaire en nid d'abeille (HC-PCM) et les rubans de HC-PCM correspondant aux analogues photoniques du graphène et des rubans de graphène. Pour chaque système photonique, nous avons d'abord passé en revue les modèles utilisés pour appréhender les propriétés électroniques et topologiques de la structure solide associée.

Dans la première section, nous présentons les propriétés électroniques du graphène dérivées de l'approximation des liaisons fortes (TB) et les propriétés optiques simulées du HC-PCM. En particulier, nous avons calculé la dispersion optique de deux architectures de HC-PCM, l'une avec des trous d'air circulaires, l'autre avec des trous d'air triangulaires. Pour les deux designs, nous retrouvons une dispersion de Dirac typique du graphène. Nous observons également une troisième bande photonique pour laquelle les modes présente une distribution monopolaire, interagissant avec la branche supérieure de la dispersion de Dirac. La design avec trous triangulaires a notamment été utilisée pour déplacer le mode monopolaire à des fréquences plus élevées, en prévision d'une ouverture de bande photonique interdite (BIP) pour la réalisation d'effets topologiques. Nous avons enfin remarqué que les bandes du modèle TB coïncident avec les bandes photoniques uniquement autour des points de Dirac.

Dans la deuxième section, nous avons présenté le modèle topologique 1D de type SSH pour prédire les propriétés topologiques des rubans de graphène via le calcul de la phase de Zak. Nous avons montré que la topologie des rubans de graphène dépend principalement de la chiralité du ruban. De même, nous avons estimé la topologie des rubans photoniques de chiralité élémentaire zig-zag  $\vec{T}(1,0)$  selon deux méthodes consistant à calculer numériquement la phase Zak et à simuler la structure de bandes du ruban. Les deux méthodes s'accordent sur la topologie non triviale du ruban, donc sur l'existence d'états de bord lorsque le ruban interface une structure topologiquement triviale, conformément aux résultats obtenus pour les rubans de graphène.

Dans la troisième section, nous avons passé en revue les propriétés électroniques et la classification topologique des nanotubes de carbone (CNT), en utilisant respectivement une approche de repliement de zone et un modèle topologique 1D. Le comportement électronique et topologique des CNT dépend de la chiralité des nanotubes. Nous avons ensuite calculé la dispersion optique des microtubes photoniques équivalents avec des chiralités simples selon une méthode de type repliement de bandes et en simulant la dispersion de structures plus réalistes. Nous avons montré, en particulier, la concordance entre les prédictions de repliement de zone électronique et photonique. Nous avons ensuite présenté des résultats typiques de la fabrication reproductible de microtubes de type CNT basés sur la nanotechnologie par enroulement. Nous avons enfin abordé la caractérisation optique expérimentale d'un échantillon de microtube photonique avec une chiralité métallique en zigzag par des mesures spectrales résolues en angle. Nous avons rapporté des caractéristiques de dispersion typiques de la paroi de la membrane photonique et des motifs d'interférence, mais encore aucune signature spectrale de la dispersion du microtube probablement due à l'absorption de photons lors de leur circulation autour du tube.

## Conclusion

Le premier objectif de cette thèse consistait en l'étude théorique et expérimentale de cages à photons tubulaires basées sur l'auto-enroulement de miroirs à membranes à cristaux photoniques 2D (PCM). Pour résoudre ce problème, nous avons couvert l'ensemble du processus de conception, de simulation, de fabrication et de caractérisation optique de ces microrésonateurs photoniques. Nous avons d'abord réalisé la conception de la paroi membranaire des cages constituée d'un miroir PCM 2D large bande non absorbant très efficace fonctionnant dans le proche infrarouge. Nous avons ensuite simulé les propriétés optiques de la cavité tubulaire finale en utilisant à la fois le modèle analytique de la cavité cylindrique résonante et des simulations plus réalistes à l'aide la méthode FDTD. Les deux modèles ont prédit le confinement de la lumière dans la partie creuse des cavités photoniques cylindriques sous forme de modes de cavités cylindriques. Nous avons ensuite rapporté la fabrication des cages à photons tubulaires suivant les processus de nanotechnologie par enroulement avec un contrôle précis des paramètres structurels et de la forme 3D finale. Nous avons enfin démontré expérimentalement par des mesures de microscopie optique à balayage en champ proche (SNOM) la présence de modes à l'intérieur des microrésonateurs cylindriques creux présentant des distributions spectrales et spatiales conformes aux prévisions théoriques. Les résultats de ce travail apportent donc la preuve de concept des cages à photons tubulaires en tant que microrésonateurs photoniques capables de confiner la lumière dans les trois directions de l'espace et dans l'air.

Le deuxième objectif de cette thèse concernait l'exploration des propriétés optiques et topologiques des analogues de cristaux photoniques de nanotubes de carbone produits par l'auto-enroulement de membranes à cristaux photoniques en nid d'abeille. Des études préliminaires ont été menées pour évaluer les propriétés optiques et topologiques du graphène et des analogues des rubans de graphène dans la classe des cristaux photoniques. Tous les résultats concernant les cristaux photoniques ont été analysés à la lumière des modèles de référence de la physique du solide.

Nous avons d'abord abordé la simulation des propriétés optiques des analogues du graphène dans la classe des cristaux photoniques, à savoir les membranes à cristaux photoniques en nid d'abeille (HC-PCM). En particulier, deux designs de HC-PCM, avec des trous d'air circulaires et triangulaires, ont été étudiées. Pour les deux designs, nous avons retrouvons une dispersion de Dirac typique des structures dérivées du graphène. Nous avons également rapporté la présence d'un mode photonique supplémentaire avec une concentration monopolaire du champ électromagnétique, en accord avec la littérature. Dans la structure à trous circulaires, l'interaction entre une branche de la dispersion de Dirac et ce mode monopolaire fait que la branche de Dirac se plie au niveau du Dirac, empêchant potentiellement l'ouverture d'une bande interdite photonique (BIP) et l'émergence de propriétés topologiques. En revanche, le design triangulaire permet de remonter le mode monopolaire à des fréquences plus élevées et de préserver la courbure d'origine des bandes de Dirac. Enfin, nous avons noté une bonne correspondance entre les niveaux d'énergie et les courbures des bandes photoniques, et la structure des bandes tirée du modèle des liaisons fortes du graphène et la distribution spatiale des fonctions d'onde, à proximité du point de Dirac exclusivement.

Nous avons ensuite examiné les propriétés topologiques des rubans de HC-PCM. Nous avons d'abord évalué numériquement la phase Zak d'un ruban photonique de chiralité  $\vec{T}(1, 0)$  avec des trous d'air circulaires en suivant la méthodologie appliquée aux rubans de graphène. Nous avons trouvé une phase Zak non nulle pour une certaine plage

de la norme du vecteur d'onde le long de l'axe du ruban, impliquant une topologie non triviale du ruban et l'existence d'un état de bord selon la correspondance volume-bord. En particulier, nous avons remarqué une distribution complémentaire de la plage de la norme du vecteur d'onde caractérisée par une phase de Zak non nulle estimée avec les modèles photonique et de la physique du solide attribuée à un choix de jauge différent. Dans ce cas, la différence de phases Zak évaluée avec deux jauges constitue l'invariant topologique. Nous avons confirmé la topologie non triviale du ruban en calculant la structure de bande au bord du ruban interfaçant un matériau de topologie triviale, révélant l'existence d'un état de bord. Ces résultats ont montré, plus spécifiquement, qu'une ouverture de gap et l'émergence d'un état de bord étaient possibles avec la conception de trou circulaire malgré la l'altération de l'une des branches de la dispersion de Dirac.

Dans la dernière partie, nous avons abordé la conception et la caractérisation optique des HC-PCM enroulés. Nous avons d'abord simulé numériquement les diagrammes de dispersion optique de microtubes photoniques non enroulés avec des chiralités simples, à trous d'air circulaires et triangulaires PCM, en suivant la méthode de repliement de zone. Nous avons remarqué la correspondance entre les bandes photoniques et de la physique du solide pour design de trous triangulaires. En revanche, nous avons observé l'altération des bandes du motif de trous circulaires due à l'interaction avec le mode monopolaire. Nous avons ensuite calculé la structure de bande d'un microtube plus réaliste de chiralité  $\vec{C}_h(12, 0)$  à trous circulaires et remarqué une excellente conformité avec les prédictions de repliement de zone. Notre prochaine étape concernait la fabrication des microtubes photoniques suivant les procédés de nanotechnologie par enroulement. Nous avons montré la qualité et la haute reproductibilité de l'auto-enroulement de HC-PCM avec des trous d'air triangulaires pour former des microtubes horizontaux de différentes chiralités. Nous avons enfin abordé la caractérisation optique des microtubes fabriqués de chiralité zigzag par des mesures spectrales résolues en angle. Nous avons reconstitué la structure de bande expérimentale du microtube sur laquelle nous avons remarqué des bandes issues de la paroi membranaire des tubes et des modes de cavité Fabry-Pérot. Cependant, nous n'avons pas enregistré la signature dispersive du microtube probablement à cause de l'absorption de photons avant d'avoir terminé une circulation autour du tube.



## **AUTORISATION DE SOUTENANCE**

Vu les dispositions de l'arrêté du 25 mai 2016,

Vu la demande du directeur de thèse

Madame, Monsieur S. CALLARD et A. DANESCU

et les rapports de

M. A-P. RUEDIGER

Professeur - Centre Energie Matériaux Télécommunications - 1650 bd Lionel-Boulet -  
Varennes (Québec) J3X 1S2 - Canada

et de

Mme S. BOUCHOULE

Directrice de Recherche CNRS - C2N (UMR 9001) CNRS - Université Paris Saclay –  
10 bd Thomas Gobert - 91120 Palaiseau


**Monsieur BRICHE Rémi**

est autorisé à soutenir une thèse pour l'obtention du grade de **DOCTEUR**

**Ecole doctorale MATERIAUX**

Fait à Ecully, le 13 juillet 2021

P/Le directeur de l'E.C.L.  
Le directeur des Formations



Grégory VIAL